



Forschungsberichte

itke  
39

Thiemo Fildhuth

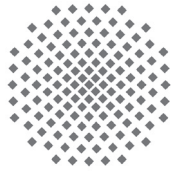
# Design and Monitoring of Cold Bent Lamination- Stabilised Glass

Investigated by Applying  
Fibre Optic Sensors









Forschungsberichte

itke

aus dem Institut für Tragkonstruktionen  
und Konstruktives Entwerfen,  
Universität Stuttgart

Herausgeber:  
Professor Dr.-Ing. Jan Knippers

Institut für Tragkonstruktionen und Konstruktives Entwerfen:  
Forschungsbericht 39

**Thiemo Fildhuth:**

Design and Monitoring of Cold Bent Lamination-Stabilised Glass  
Investigated by Applying Fibre Optic Sensors

Stuttgart, August 2015

ISBN 978-3-922302-39-1

D 93

© Institut für Tragkonstruktionen  
und Konstruktives Entwerfen  
Universität Stuttgart  
Keplerstraße 11  
D-70174 Stuttgart



Alle Rechte, insbesondere der Übersetzung,  
bleiben vorbehalten. Vervielfältigung jeglicher Art,  
auch auszugsweise, ist nicht gestattet.

# **Design and Monitoring of Cold Bent Lamination-Stabilised Glass**

## **Investigated by Applying Fibre Optic Sensors**

Von der Fakultät Architektur und Stadtplanung der Universität Stuttgart  
zur Erlangung der Würde eines Doktor-Ingenieurs (Dr.-Ing.)  
genehmigte Abhandlung

Vorgelegt von  
Thiemo Fildhuth  
aus Bad Pyrmont

Hauptberichter:	Prof. Dr.-Ing. Jan Knippers
Mitberichter:	Prof. Dr.-Ing. Bernhard Weller
2. Mitberichter:	Prof. Dr. Johannes Roths

Tag der mündlichen Prüfung:	20. Juli 2015
-----------------------------	---------------



*Für Christine*





## Abstract

Continuously curved, highly transparent façades or roofs are increasingly demanded in architecture. Regularly curved or free-form building envelope shapes represent a rapidly growing market field in construction and project design. For such transparent roof or façade claddings, the necessary durability, strength and safety require laminated safety glass as the principle material. Whereas the faceting of curved surfaces to apply planar glass elements is a frequently used cladding solution, the employment of curved glass modules permits a more precise, smooth achievement of curved envelopes. Recent improvements in the industrialised fabrication of curved glass render the use of such elements increasingly attractive. The two main, but different, production methods to shape these modules are the heat bending and cold bending of glass. Plastic heat bending results in a stable glass shape permitting high curvature. However, any potential optical surface bumps, any remaining irregular local interior stress from production and the limited applicability of toughened glass impose restrictions on the use of heat bent glass.

In contrast, elastic cold bending only allows for low curvature but provides high optical surface quality and permits the unrestricted use of toughened glass. Stabilisation of the curved shape of cold bent glass without a retaining substructure can be achieved through the establishment of a shear compound of several elastically bent glass panes via lamination with polymeric interlayers. The bending stress remains in the glass. Despite the potential of this type of cold bent glass for construction purposes, comprehensive research approaches and the necessary stress- and shape-monitoring methods for glass laminates are lacking. Therefore, the characteristic properties and parameters influencing manufacture, the short- and long-term behaviour of cold bent glass, applicable numerical form-finding models and shape- and interior stress-monitoring methods have been investigated in the present work. The testing of real scale cold bent glass specimens with respect to displacement and stress permits the verification of the analyses. Close range photogrammetry has been applied to measure the three-dimensional shape and recovery behaviour of bent laminates. A new method for permanent real-time monitoring of the interior stress in the laminate by applying thin, barely visible, fibre optic Bragg-grating sensors with transparent adhesive bonding has been developed. Fibre optical sensing has been examined and evaluated and is discussed as a possible monitoring system applicable to multi-layered glass units. Based on the accumulated modelling and testing results, information regarding the behaviour and the design of cold bent lamination-stabilised glass and the potential of fibre optic monitoring for glass laminates is provided as a working basis in the conclusion to this work.



## Zusammenfassung

Angesichts der zunehmenden Bedeutung der Freiformarchitektur wächst bei Bauherren, Planern und Herstellern die Nachfrage nach Lösungen für kontinuierlich gekrümmte, transparente Gebäudehüllen. Dabei ist Verbund Sicherheitsglas aufgrund der Ansprüche an die Widerstandsfähigkeit, Sicherheit und Dauerhaftigkeit das primäre Konstruktionsmaterial. Die häufig verwendete Methode, gekrümmte Fassaden oder Dächer zu facetieren, um plane Glasbauteile zur Eindeckung verwenden zu können, steht jedoch im Widerspruch zu den gewünschten fließenden, sanft gekrümmten Formen. Ein Erreichen dieses Ziels ist hingegen durch den Einsatz gekrümmter Gläser möglich, die durch neue oder weiterentwickelte Fertigungstechniken in der Glasveredelung immer präziser hergestellt werden können. Plastische *Heißverformung* von Glas ermöglicht große und verschiedenartige Krümmungen, durch das Herstellungsverfahren können jedoch optische Unregelmäßigkeiten der Glasoberflächen und lokale, eingeprägte Spannungen im Glas entstehen. Abhängig von der Krümmung und Fertigungsart kann teilweise kein thermisch vorgespanntes Glas verwendet werden.

Beim *Kaltbiegen* hingegen sind teilvorgespanntes und Einscheibensicherheitsglas beliebig anwendbar. Die erzielbaren Krümmungen sind begrenzt, es wird aber eine hohe optische Oberflächenqualität des Glases erzielt. Besonders interessant ist das Verfahren des Kaltbiegens mit Krümmungserhalt durch Herstellung eines Schubverbunds zwischen den einzelnen, gebogenen Gläsern per Lamination mittels Polymer-Zwischenschichten. Die Biegespannungen bleiben im Glas erhalten. Für diese Gläser kann möglicherweise auf eine architektonisch störende, formerhaltende Unterkonstruktion verzichtet werden. Übergreifende Forschungsansätze für solche kaltgebogenen, laminationsstabilisierten Glaslamine fehlen noch weitgehend. Eine weitere Einschränkung stellt die mangelnde Verfügbarkeit von anwendbaren Messmethoden zur Kontrolle der Formgebung und der eingeschlossenen Spannungen dar. In der vorliegenden Arbeit werden daher zunächst die charakteristischen Eigenschaften und die bei der Herstellung, Formgebung und im Langzeitverhalten einflussnehmenden Parameter von kalt gebogenen, laminationsstabilisierten Verbundgläsern untersucht. Numerische Modelle zur Analyse und Formfindung sowie Ansätze zum Monitoring der Spannungen sowie der dreidimensionalen Form der Gläser werden entwickelt und durch Versuche an realmaßstäblichen, kalt gebogenen Gläsern überprüft. Zur Beobachtung der Krümmungsform und des Rückstellverhaltens der Glaslamine kommt ein photogrammetrisches Verfahren zum Einsatz. Erstmals werden für die dauerhafte Erfassung von Oberflächenspannungen des Glases in den Schichten des Laminats faseroptische Sensoren mit Bragg-Gittern eingesetzt und Applikationsverfahren mit transparenten Klebstoffen entwickelt. Die Ergebnisse der Arbeit stellen auf Grundlage vorgenommenen Untersuchungen eine Arbeitsbasis betreffend das Verhalten, die prinzipiellen Parameter und die Modellierung kalt gebogener, laminationsstabilisierter Gläser sowie für das Monitoring mit faseroptischen Sensoren bereit.





## Preface

The present thesis is the result of research on cold bent laminated glass and involves the related development of a method for stress measurement in such laminates based on fibre optical sensors conducted during my work at the Institute of Building Structures and Structural Design (ITKE) at the University of Stuttgart / Germany. At first, the research was dedicated to the application possibilities for cold bent lamination-stabilised glass, whereby its use in modular shell structures serving as facades or roofs was examined in particular. However, it quickly became evident that the low curvature of glass modules largely limits such load-bearing applications in architecture and causes extremely high joint forces in the shell. Furthermore, the existing fundamental research and publications on cold bent glass stabilised through lamination have proved to be fragmentary. To overcome these obstacles, my ongoing research has therefore been oriented towards form-finding, testing and applicable monitoring techniques of such laminates with regard to their geometrical shape and interior stress. This process has culminated in the idea of examining the incorporation of small, nearly invisible, fibre optic sensors in glass laminates as a possible solution for short- and long-term stress-monitoring during manufacture and in later practical use. The principal research and development findings related to sensor applicability are valid not only for cold bent glass, but also for planar glass laminates and other glass constructions necessitating a highly transparent stress-sensing solution.

I would like to express my gratitude to my principal examiner and supervisor, Prof. Dr.-Ing. Jan Knippers, for the opportunity to conduct this work at his institute and for his confidence in my research topic and methodology. I am also very grateful to Prof. Dr.-Ing. Bernhard Weller (TU Dresden) and Prof. Dr. Johannes Roths (University of Applied Sciences Munich) for their co-examination of the thesis.

Much of the research, testing and development necessary for this work were made possible through the funding granted by the Central Innovation Program SME (ZIM) of the Federal Ministry of Economic Affairs and Energy (BMWi) for two projects carried out with the companies sedak GmbH & Co. KG on cold bent glass applications and with GuS GmbH & Co. KG for fibre optic sensor integration into laminates. I would like to thank both companies for the collaboration. My sincere thanks go to Dipl.-Ing. Olaf Krätzig from GuS for the multiple research and development tasks conducted together in the field of glass laminates and fibre optic sensing. I would also like to express my gratitude to Dr.-Ing. Christiane Kothe and Dr.-Ing. Silke Tasche from TU Dresden for their laboratory support in the development of a transparent application technique of fibre optic sensors. The photogrammetric monitoring of the cold bent glass became possible thanks to Prof. Dr.-Ing. Norbert Haala and Dipl.-Ing. Alessandro Cefalu from the Institute for Photogrammetry (IFP) at the University of Stuttgart. I am very thankful to Prof. Dr.-Ing. habil. Manfred Bischoff for allowing many opportunities to follow lectures at his institute IBB and for helpful discussions on modular shells.

Major technical, financial and material support was granted for the fabrication and testing of cold bent lamination-stabilised glass with integrated fibre optic sensor networks by RFR Paris (through the European Research project FP7-PEOPLE-IAPP project 230520) with Niccolo Baldassini, Dr. Eric Lindner and Dr. Jan van Roosbroeck from FBGS Technologies GmbH / FBGS International NV, Martin Sulzer from Bischoff Glastechnik AG (BGT) and Petra and Manfred Arnold with their team from INGLAS Produktions GmbH. I am very thankful for the involvement of all these persons in the work.

My special thanks go to my colleagues at the ITKE for supporting my research, namely Jian-Min Li and Axel

## 0 | PREFACE

Körner, Michael Tondera from the faculty testing laboratory for his practical advice and particularly the student collaborators Antje Ehret, Oliver Hainbuch, Franziska Häuptle, Hu Yang, Elisabeth Holzheimer, Norbert Jundt, Jonas Landsberger and Sebastian Lippert for their dedicated participation and contribution.

Finally, I would like to express my deepest gratitude towards my wife, Christine Fildhuth, for her support, patience and advice during the time of my work on this doctorate thesis.

Stuttgart, August 2015

Thiemo Fildhuth

# Contents

<b>Abstract</b>	<b>I</b>
<b>Zusammenfassung</b>	<b>III</b>
<b>Preface</b>	<b>V</b>
<b>Contents</b>	<b>VII</b>
<b>Notation</b>	<b>XI</b>
<b>1. Introduction</b>	<b>1</b>
1.1. Motivation . . . . .	2
1.2. Research Objective . . . . .	5
1.3. Methodology . . . . .	5
<b>2. Background</b>	<b>9</b>
2.1. The cladding of Transparent Curved Building Envelopes . . . . .	10
2.2. Cold Bending of Glass . . . . .	12
2.3. Thermally Curved Glass . . . . .	16
<b>3. Problem Statement</b>	<b>21</b>
3.1. Behaviour of Cold Bent, Lamination-Stabilised Glass, Monitoring Solution . . . . .	22
3.2. Excluded Topics . . . . .	23
<b>4. Solution Concept</b>	<b>25</b>
4.1. Testing and Monitoring . . . . .	26
4.1.1. Monitoring of Stress, Strain and Structural Integrity . . . . .	28
4.1.2. Displacement Monitoring . . . . .	30
4.2. Numerical Simulation . . . . .	32
<b>5. Analysis, Diagnostic</b>	<b>35</b>
5.1. Fibre Optic Sensing . . . . .	36
5.1.1. Fibre Optics and Applicable Sensing Principles . . . . .	36
5.1.1.1. Optical Fibres . . . . .	36
5.1.1.2. Light Propagation and Guidance in Optical Fibres . . . . .	37
5.1.1.3. Fibre Optic Sensors and Photosensitivity . . . . .	40
5.1.1.4. Bragg Gratings . . . . .	42
5.1.1.5. Coupled Mode Theory for Fibre Bragg Gratings . . . . .	45
5.1.1.6. Derivation of the Strain and Temperature Sensitivity of FBGs . . . . .	47
5.1.1.7. Free FBG Sensor Strain and Temperature Sensitivity . . . . .	49
5.1.1.8. Surface Bonded FBG Sensor Strain and Temperature Sensitivity . . . . .	51
5.1.2. Strain Transfer Models . . . . .	55
5.1.2.1. Axial Strain Transfer Models . . . . .	55
5.1.2.2. Bending Strain Transfer Model Development . . . . .	56

5.1.3.	Adhesive Choice for FBG Sensor Bonding . . . . .	64
5.1.3.1.	Adhesive Preselection and Cure Conditions . . . . .	65
5.1.3.2.	Dynamic Mechanical Analysis . . . . .	67
5.1.3.3.	Axial Tensile Tests . . . . .	71
5.1.3.4.	Differential Scanning Calorimetry . . . . .	73
5.1.3.5.	Adhesive Application and Joint Geometry . . . . .	73
5.1.4.	FBG Sensor Property Determination . . . . .	76
5.1.4.1.	Gauge Factor Determination . . . . .	76
5.1.4.2.	Determination of the Thermo-Optic Coefficient . . . . .	79
5.1.4.3.	Transverse Strain Effects . . . . .	82
5.1.4.4.	FBG Sensor Property Summary . . . . .	84
5.1.5.	Testing of Glass-Bonded Bragg Sensors . . . . .	85
5.1.5.1.	Test Setup . . . . .	85
5.1.5.2.	Four-Point Bending Preliminary Tests . . . . .	86
5.1.5.3.	Four-Point Bending Constant Load Tests . . . . .	89
5.1.5.4.	Summary . . . . .	94
5.1.6.	FE Micro-Modeling . . . . .	95
5.1.6.1.	Micro Model Setup . . . . .	95
5.1.6.2.	Bending Load Application . . . . .	98
5.1.6.3.	Axial Load Application . . . . .	101
5.1.6.4.	Thermal Load Application . . . . .	102
5.1.6.5.	Summary . . . . .	103
5.2.	Close Range Photogrammetry Principle . . . . .	105
5.3.	Material Models for Numerical Simulation . . . . .	109
5.3.1.	Glass Laminates . . . . .	109
5.3.2.	Ionomer Interlayer . . . . .	109
5.3.3.	Viscoelastic PVB Interlayers . . . . .	111
<b>6.</b>	<b>Application, Comparison</b> . . . . .	<b>115</b>
6.1.	Real Scale Testing . . . . .	116
6.1.1.	Real Scale Test Setup . . . . .	116
6.1.2.	Equipment of the Samples with FBG . . . . .	119
6.1.3.	Photogrammetry Application to the Specimens . . . . .	122
6.2.	Finite Element Model Setup . . . . .	125
6.2.1.	FE Models Adapted to the Tests . . . . .	125
6.2.2.	Form-Finding FE Models . . . . .	126
6.3.	Comparison of FEA and Testing Results . . . . .	127
6.3.1.	Displacement Results . . . . .	127
6.3.2.	Surface Curvature Quality . . . . .	128
6.3.3.	Strain and Stress Results . . . . .	131
6.3.3.1.	Results from the Two- and Three-Ply Specimens . . . . .	131
6.3.3.2.	Results from the Four-Ply Specimens . . . . .	135
6.3.4.	Summary of the Testing Results . . . . .	138
<b>7.</b>	<b>Discussion, Transfer</b> . . . . .	<b>139</b>
7.1.	Monitoring Feasibility of Glass Laminates by Applying Fibre Optic Sensors . . . . .	140
7.1.1.	FBG Transverse Effect Results and Sensor Robustness . . . . .	140
7.1.2.	FBG Result Evaluation . . . . .	143
7.1.2.1.	Analysis with the Micro-Mechanical FE Model . . . . .	144
7.1.2.2.	Potential Influence of the Adhesive Bond . . . . .	145
7.1.2.3.	Autoclave Process Monitoring . . . . .	146
7.1.2.4.	Transient Numerical Model . . . . .	148
7.1.2.5.	Handling, Application Feasibility and Operation of Fibre-Optic Sensors . . . . .	150

7.2. Numerical Cold Bent Glass Analysis Method Evaluation . . . . .	152
7.2.1. Analysis of Cold Bent Glass Behaviour and Appropriate Modelling Methods . . . . .	152
7.2.1.1. Test Result Interpretation . . . . .	152
7.2.1.2. Cylindrical Model . . . . .	154
7.2.1.3. Fixed Point Iteration Model . . . . .	156
7.2.2. Examination of Principal Cold Bending Shapes . . . . .	158
<b>8. Conclusion</b>	<b>165</b>
8.1. Cold Bent Glass Analysis and Monitoring . . . . .	166
8.2. Further Research, Future Work . . . . .	168
<b>References</b>	<b>169</b>
<b>List of Figures</b>	<b>181</b>
<b>List of Tables</b>	<b>187</b>
<b>Appendix</b>	<b>189</b>
<b>A. Bragg Grating Sensors</b>	<b>191</b>
A.1. Fibre Optic Sensor Categories . . . . .	192
A.2. Photoelasticity . . . . .	192
A.3. Strain and Temperature Sensitivity of FBGs . . . . .	193
<b>B. Adhesive Bonding of Fibres</b>	<b>195</b>
B.1. Adhesive Classification . . . . .	196
B.2. Adhesive Testing Results . . . . .	197
B.3. Adhesive Bond Section Data . . . . .	204
<b>C. Sensor Property Testing Results</b>	<b>207</b>
C.1. FBG Coefficient Determination . . . . .	208
C.2. Four-Point Bending Tests of FBGs Bonded to Glass . . . . .	210
<b>D. Micro-Mechanical FEM Results</b>	<b>213</b>
<b>E. Real Scale Tests</b>	<b>219</b>
E.1. Photogrammetry . . . . .	220
E.2. Numerical Cold Bending Model . . . . .	222
E.3. Real Scale Testing Results . . . . .	225
E.4. Result Comparison . . . . .	237
<b>F. Curriculum Vitae</b>	<b>241</b>





# Notation

## Minuscule Latin Symbols

<i>Symbol</i>	<i>Units</i>	<i>Description</i>
$a$	$\mu\text{m}$	radius of a fibre core
$b$	-	normalised propagation constant
$b_{f,e}$	mm	effective elongation value of a fibre relative to a substrate
$b_i$	mm	$i = (1, 2, 3, 4)$ arc lengths of the different interfaces bent substrate - adhesive - fibre
$b(V)$	-	normalised propagation constant (depending on the V-parameter)
$c$	m/s	speed of light in vacuum
$c_{1,2}$	-	WLF coefficients
$\vec{e}_{jt}$	-	normalised, transverse mode field vector
$\vec{e}_{jt}^*$	-	complex conjugate (of normalised, transverse mode field)
$f$	Hz or 1/s	frequency
$h_a$	mm	effective adhesive thickness between the fibre and the substrate
$i$	-	imaginary unit (complex numbers)
$j$	-	incident mode number in a fibre in coupled mode theory
$k$	-	diffracted or reflected mode number in a fibre in coupled mode theory
$k_0$	-	wavenumber
$k_T$	-	thermal gauge factor of a bonded FBG
$k_E$	-	gauge factor (of a bonded FBG)
$l$	-	integer; azimuthal mode order
$m$	-	integer; radial distribution index (mode definition)
$m_d$	-	diffraction order (integer)
$n$	-	refractive index of a material (fibre core, fibre cladding, coating etc.)
$n_{eff}$	-	effective refractive index of the fibre core at the Bragg grating
$\bar{n}_{eff}$	-	mean effective refractive index of the fibre core at the Bragg grating
$n_{p,q}$	-	refractive indices in the p and q axes in the $x_2$ - $x_3$ -plane
$n_0$	-	initial refractive index at the Bragg grating initial at constant temperature and zero mechanical strain
$n_1$	-	refractive index of the fibre core
$n_2$	-	refractive index of the cladding
$n_{p,q}$	-	refractive indices of the transverse optical axes $p, q$
$\Delta n$	-	difference of the refractive index in a fibre
$\overline{\Delta n_{eff}}(z)$	-	change of the refractive index averaged over the grating period; "DC-term" of the refractive index change
$\Delta n_{eff}(z)$	-	perturbation of the effective index of refraction (of the guided mode) in the waveguide core
$\Delta n_{AC}(z)$	-	modulated, AC-part of the index change in a fibre core
$\Delta n_{DC}(z)$	-	constant, DC-part of the index change in a fibre core
$o_a$	-	adhesive overhang

## 0 | NOTATION

$p$	-	fringe visibility due to the index change [Oth99, p. 191]; contrast from the visibility of the UV fringe pattern [Leb01, p. 3-3]; ratio of the amplitude of the refractive index change and the refractive index averaged over a grating period
$p$	-	transverse optical axis, see also $q$
$p_e$	-	photoelastic or strain-optic coefficient
$p\overline{\Delta n_{eff}}(z)$	-	modulation amplitude; “AC-term” of the refractive index change
$p_{ij}$	-	general Pockels coefficient
$p_{11,12}$	-	Pockels coefficients for isotropy
$q$	-	transverse optical axis, see also $p$
$r$	$\mu\text{m}$	general radius direction of a fibre
$r_f$	$\text{mm}$	radius of the optic fibre and the FBG
$r_i$	$\text{mm}$	$i = (1,2,3,4)$ bending radii of the different interfaces bent substrate - adhesive - fibre
$r_{\epsilon,s}$	-	ratio of the mechanically induced bending strain at the surface of the substrate below the FBG and the bending strain et the opposite surface of the substrate
$t_a$	$\text{mm}$	adhesive thickness between the tip point of the fibre and the substrate
$t_s$	$\text{mm}$	thickness of the substrate (glass)
$u_f$	$\text{mm}$	expansion of the fibre gravity axis attributable to bending
$u_s$	$\text{mm}$	expansion of the surface of the substrate attributable to to bending
$u_3$	$\text{mm}$	expansion of the fibre bottom surface attributable to bending
$x^*$		fixed point variable in a fixed point iteration
$z$	$\text{nm}$	distance along the longitudinal axis of the fibre
$z_{cb}$	$\text{nm}$	vertical z-coordinates of the cold bent geometry
$z_{des}$	$\text{nm}$	vertical z-coordinates of the desired final glass geometry
$\Delta z$	$\text{nm}$	difference of the z-coordinates of the desired and achieved shape after springback / relaxation

## Majuscule Latin Symbols

<i>Symbol</i>	<i>Units</i>	<i>Description</i>
$A_a$	$\text{mm}^2$	section area of the adhesive bond
$A_c$	$\text{mm}^2$	section area of the coating
$A_f$	$\text{mm}^2$	section area of the fibre and cladding
$A_s^f$	$\text{mm}^2$	shear area at the interface of the coating and adhesive of a bonded sensor fibre
$A_{tot}$	$\text{mm}^2$	total fibre section area, including coating, cladding and core
$B_i$	-	normalised (symmetrical) dielectric tensor (or relative dielectric impermeability)
$B_{ij}$	-	dielectric indicatrix tensor
$B_{1,2}$	-	constants in the differential equations for strain transfer
$\vec{D}_i$		electrical displacement field
$E$	-	electric field phasor
$E_a$	$\text{N}/\text{mm}^2$	Young’s modulus of the adhesive for gluing the fibre
$E_c$	$\text{N}/\text{mm}^2$	Young’s modulus of fibre’s coating
$E_f$	$\text{N}/\text{mm}^2$	Young’s modulus of the optical fibre and FBG (silica)
$E_{f,eff}$	$\text{N}/\text{mm}^2$	general, effective Young’s modulus of the fibre including the coating
$E_{f,eff,L}$	$\text{N}/\text{mm}^2$	effective Young’s modulus of the fibre including the coating as per Liu
$E_{f,eff,V}$	$\text{N}/\text{mm}^2$	effective Young’s modulus of the fibre including the coating as per Voigt
$E_s$	$\text{N}/\text{mm}^2$	Young’s modulus of the substrate (glass)

$\vec{E}_j$		electrical field vector
$\vec{E}(x, y, z, t)$	-	electric field vector (Cartesian space, time); also $\vec{E}_{ij}$
$E^*$	$N/mm^2$	complex Young's modulus (DMA)
$E'$	$N/mm^2$	storage Young's modulus (DMA)
$E''$	$N/mm^2$	Young's loss modulus (DMA)
$F_f$	N	resultant force in the bent fibre
$F_{x,z}$	N	force components of $F_f$
$G_a$	$N/mm^2$	shear modulus of the adhesive for gluing the fibre
$G_c$	$N/mm^2$	shear modulus of the coating of the fibre
$G(t)$	$N/mm^2$	relaxation shear modulus
$G(0)$	$N/mm^2$	initial, elastic shear modulus
$G^*$	$N/mm^2$	complex shear modulus (DMA)
$H$	-	magnetic field phasor
$H_{transf}$	-	4x4 homogeneous transformation matrix
$K, K^2$	-	simplification factor in the analytical strain transfer equations, shear lag factor
$K_e$	-	elastic stiffness
$K_g$	-	initial stress stiffness
$K_{kn}^t(z)$	-	transverse coupling coefficient
$K_{kn}^l(z)$	-	longitudinal coupling coefficient
$K_{s,1}$	-	axial sensor strain sensitivity [Ste 97]
$K_{s,T}$	-	temperature sensitivity [Ste 97]
$K_{s,d}$	-	differential strain sensitivity [Ste 97]
$K_{s,h}$	-	average strain sensitivity [Ste 97]
$K_{s,s}$	-	sensitivity to maximum shear strain $\gamma_{max}$ [Ste 97]
$K_T$	-	tangential stiffness (geometrically non-linear analysis)
$K_T$	-	or: temperature coefficient on an FBG
$K_u$	-	initial displacement stiffness
$K_\varepsilon$	-	strain sensitivity coefficient, K-factor
$L$	nm	grating length
$L_a$	mm	adhesive joint length of a bonded sensors
$L_b$	mm	length of the FBG
$LP_{lm}$	-	linearly-polarised mode of indices l and m, e.g. $LP_{01}$
$M$	-	approximate total number of possible guided modes in a multimode-fibre
$NA$	-	numeric aperture
$O$	-	perspective centre (photogrammetry); $O'$ is the projection of $O$ on the photograph
$P$	-	object point (photogrammetry); $P'$ is the projection of $P$
$R$	mm	Curvature radius of a single-curved (bending) shape
$R_e$	-	power reflection coefficient, Bragg grating reflectivity (coupled mode theory)
$R_{ij}$		9 rotational entries ( $i, j = \{1 \dots 3\}$ ) of the homogeneous transformation matrix $H_{transf}$
$R_r$		radial distribution of the axial fibre direction component of the electric field phasor E
$R_s$	mm	bending radius of the substrate, related to the centre line
$R(z)$	-	incident wave (coupled mode theory)
$R_{1,2}$	mm	Curvature radii of double-curved geometrical (bending) shapes
$S(z)$	-	reflected wave (coupled mode theory)
$T_g$	$^\circ\text{C}, \text{K}$	glass transition temperature
$T_k$		3 translation entries ( $k = \{X, Y, Z\}$ ) of the homogeneous transformation matrix $H_{transf}$

## 0 | NOTATION

$\Delta T$	°C, K	temperature difference or change related to a reference $T_0$
$V$	-	normalised frequency, V-parameter
$X$	-	normalised transverse propagation constant
$Y$	-	attenuation / decay constant

### Minuscule Greek Symbols

<i>Symbol</i>	<i>Units</i>	<i>Description</i>
$\alpha_g$	-	thermal expansion coefficient of the sensor (silica material)
$\alpha_n$	-	thermoelastic or thermo-optic coefficient
$\alpha_s$	-	thermal expansion coefficient of a substrate material supporting a bonded Bragg sensor
$\alpha_T(T)$	-	temperature shift factor (WLF)
$\beta$	-	propagation constant
$\beta_{li}$	-	propagation constant for the incident mode
$\beta_{2d}$	-	propagation constant for the diffracted mode
$\gamma_a$	rad	shear deformation angle of the adhesive between substrate and fibre
$\delta$	rad	phase angle (DMA); $\tan \delta$ is the damping
$\epsilon_i$	mm/mm	strain (general), $i = 1 \dots 6$
$\epsilon_0$	-	electric field constant
$\epsilon_{ij}^{di}$	-	dielectric constant
$\epsilon_f$	mm/mm	longitudinal strain at the optical fibre or FBG surface
$\epsilon_s$	mm/mm	longitudinal strain at the surface of the substrate
$\epsilon_{i,f}$	mm/mm	strain in the core of the FBG, $i = \{1 \dots 3\}$
$\epsilon_{i,s}$	mm/mm	strain at the surface of the substrate, $i = \{1 \dots 6\}$
$\epsilon_{1,s,e}$	mm/mm	ideal bending strain in 1-direction in the fibre core extrapolated from the substrate strain below the FBG
$\epsilon_{i,s,m}$	mm/mm	mechanically induced strain of the substrate $i = \{1 \dots 6\}$
$\Delta\epsilon(x, y, z)$	-	permittivity perturbation (perturbation of the dielectrical field constant)
$\eta_i$	-	damping (visco-elasticity)
$d\vartheta$	rad	angle of the bent section of the substrate
$\theta_{2d}$	rad	angle of the diffracted, reflected light to the grating plane
$\theta_a$	rad	acceptance angle
$\theta_c$	rad	critical angle
$\bar{\theta}_c$	rad	complementary critical angle
$\theta_{1i}$	rad	angle of the incident light to the grating plane
$\kappa$	-	Gaussian curvature
$\kappa_{AC}$	-	AC-coupling coefficient for two counterpropagating $LP_{01}$ -modes
$\lambda_c$	nm	cutoff wavelength
$\lambda_B$	nm	Bragg wavelength
$\lambda_D$	nm	design wavelength
$\lambda_i$	nm	relaxation time
$\nu$	-	Poisson's coefficient, general
$\nu_c$	-	Poisson's coefficient of the coating of a sensor fibre
$\nu_f$	-	Poisson's coefficient of the coating of the core / cladding of a sensor fibre
$\rho$	-	amplitude reflection coefficient (coupled mode theory)
$\rho^2 = R_e$	-	power reflection coefficient
$\sigma_i$	$N/mm^2$	stress, general ( $i = 1 \dots 6$ , or $i = x, y, z$ )
$\sigma_f(x)$	$N/mm^2$	stress in longitudinal direction at the surface of the fibre
$\sigma_s(x)$	$N/mm^2$	stress in longitudinal direction at the surface of the substrate
$\zeta_i$	-	strain transfer coefficient



$\hat{\sigma}$	-	general DC coupling coefficient
$\tau$	$N/mm^2$	shear lag (strain) at the interface of the fibre and the bonding adhesive, or general shear strain
$\varphi(z)$	rad	grating chirp
$\omega$	1/s	radian frequency; $\omega = 2\pi f$

### Majuscule Greek Symbols

<i>Symbol</i>	<i>Units</i>	<i>Description</i>
$\Gamma$	-	confinement factor
$\bar{\Gamma}^2$	-	shear coefficient
$\Delta$	-	fractional refractive index
$\Delta$	mm	or: shear lag length between substrate and bonded fibre
$\Lambda$	nm	period
$\Psi_c$	-	volume fraction of the coating
$\Psi_f$	-	volume fraction of the fibre core and cladding
$\Omega$		angle formed by the $x_2$ -axis and the grating vector projected onto the $x_2 - x_3$ -plane

### Acronyms

ANG	annealed glass (float glass)
APDL	ANSYS Parametric Design Language
CAD	computer-aided design
CAM	computer-aided manufacturing
CMT	coupled mode theory
CSG, CTG	chemically tempered glass (chemically toughened glass)
DMA	dynamic mechanical analysis
DSC	differential scanning calorimetry
FBG	fibre-Bragg grating
FBGS	fibre-Bragg grating sensor
FOS	fibre-optic sensor
FPS	Fabry-Pérot sensor
FTG	fully tempered glass (fully toughened glass)
GODC	Germanium-oxygen deficient centres
HSG	heat strengthened glass
IGU	insulating glass unit
IRS	infrared spectroscopy
LSG	laminated safety glass
MCVD	modified chemical vapour deposition
MFD	mode field diameter
MMD	mode field diameter of an optical fibre
MMF	multi-mode fibre
NURBS	non-rational uniform B-spline
OBR	optical backscatter reflectometer
OFDR	optical frequency-domain reflectometry
OSA	optical spectrum analyser
OTDR	optical time-domain reflectometry
PC	polycarbonate

## 0 | NOTATION

PDL	polarisation-dependent loss (of FBG)
PMMA	polymethyl methacrylate
PU	polyurethane
PVB	polyvinyl butyral film
RTD	resistance temperature detectors, e.g. PT100
SBS	stimulated Brillouin scatter
SG	SentryGlass® ionomer film
SMF	single mode fibre
TMM	transfer matrix method
UV	ultra-violet light / radiation
WLF	Williams-Landel-Ferry shift equation (linear visco-elasticity)

# 1 Introduction

### 1.1. Motivation

During the past three decades, curved geometry and free-form architecture have rapidly developed from theoretical or experimental attempts, such as the embryonic house by Greg Lynn / FORM or the water pavilion from 1997 by NOX / Lars Spuybroek [Zel99], into a rapidly growing market field in construction and project design business. The continuous evolution of the design process, computational methods, material research and production together with the knowledge transfer between various industries have permitted an increase in complexity in free-form building design. The resulting necessary interaction and close coupling of geometrical shaping and production technology have been pointed out by Schiffner et al. [Sch 13] and Vaudeville et al. [Vau 13]. However, in order to achieve the desired smoothly curved shapes of free-form architecture, geometrically suited construction materials are necessary. In complex geometrical design, the building envelope mainly conveys the haptic and visual expression of the desired architectural shape. As can be seen from recent examples, such as the Nordkettenbahn funicular stations in Innsbruck in fig. 1.1 or the Fondation Louis Vuitton pour la Création in Paris in fig. 1.2, glass plays a major role as the principal, transparent and slick cladding material in such envelopes.



**Figure 1.1.:** Funicular station “Congress” of the Nordkettenbahn at Innsbruck (Arch.: Zaha Hadid).

The polymer materials PMMA or PC, although having previously been used for some transparent building purposes as shown in [Eck 10, p. 431] and [Cac 04, p. 72], are applied to a lesser extent, as they have a Young’s modulus inferior to that of glass and show less resistance to fire, ageing and scratching.



**Figure 1.2.:** Fondation Louis Vuitton pour la Création, Paris (Arch. F.O. Gehry). Photo: Courtesy of Niccolo Baldassini, Paris.

Typically, the desired three-dimensional curved envelope shape is rationalised in order to permit cladding with planar triangular, figure 1.4, or quadrangular panels, figure 1.3. These planarity rationalisational approaches usually necessitate changes in the original design of the envelope and limit the choice of feasible geometries. Furthermore, the approximation of the surface and the faceting as a necessary condition for applying planar elements conflicts with the desired smooth continuous envelope appearance.

Use of single- or double-curved glass modules instead of planar elements permits the more precise aesthetic achievement of smoothly curved claddings as proposed in fig. 1.5. Important research activities have been carried out in this field, leading to an increasing number of tessellation methods and panelisation software for complex geometry surface rationalisation, see section 2.1. In addition, the use of curved glass is rendered increasingly attractive by recent improvements in industrialised fabrication processes, particularly concerning glass bending and tempering furnaces [Kar 08].



**Figure 1.3.:** Translational grid shell with quadrangular mesh, Bosch-Areal, Stuttgart (Arch.: Prof. Ostertag + Vornholdt; Eng.: Schlaich, Bergermann und Partner).

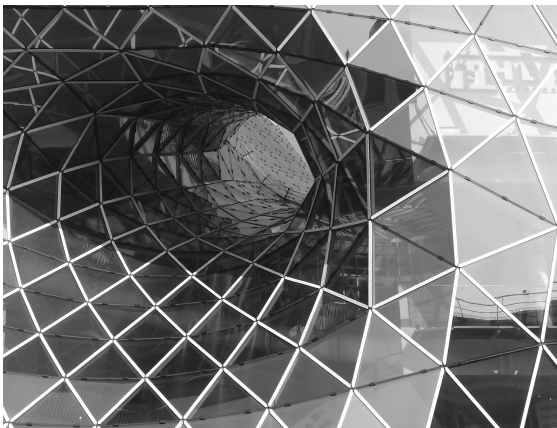


**Figure 1.4.:** MyZeil shopping mall with a triangulated glass grid shell façade, Frankfurt a. M. (Arch.: Massimiliano Fuksas architetto).

The main curvature generation methods for glass are heat bending and cold bending [Fil 12a, p. 135], both of which are discussed in chapters 2.2, 2.3. Heat bending results in a stable glass shape permitting high curvature, e.g. for application in strongly curved claddings such as that in fig. 1.1. However, potential optical surface bumps, any remaining irregular local interior stress from production or limitations for toughening impose restrictions on heat bent glass use. The feasible size of heat bent glass depends on the bending furnace dimensions. In contrast, all types of toughened glass are applicable for cold bending and most coatings can be used [Tei 14, p. 82]. However, only low curvature is obtained through cold bending, which generally results in a smooth, high optical surface quality. An example of cold bent glass use is the façade of the main station of Strasbourg, fig. 1.6.

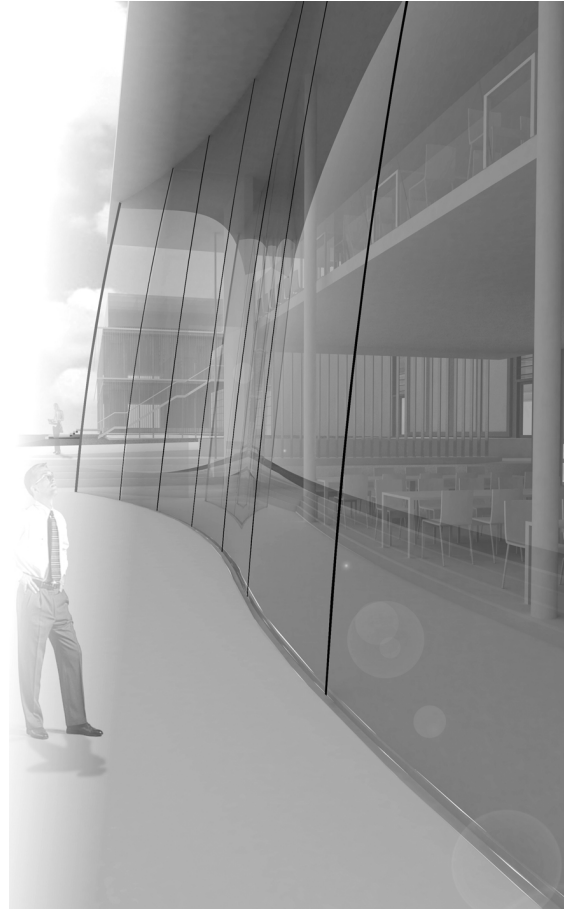


**Figure 1.5.:** Smooth, double curved façade from cold bent glass. Rendering: N. Jundt, ITKE

As elastically cold bent glass tends to return to its initial planar state, the curved shape has to be stabilised by interior or exterior constraints. This is achieved either through permanent fixing on a frame-like substructure or by creating a shear compound of several elastically bent glass panes via lamination. The bending stress thus remains within the glass. This type of cold bending with shape-conserving shear coupling through lamination (designated “cold bent lamination-stabilised glass” in this work) is particularly interesting, as curved glass modules without a retaining frame can be obtained. However, depending on temperature and the interlayer shear stiffness, the laminate can be subject to indetermined curvature changes attributable to relaxation throughout its life span [Lou 14, pp. 105-112].

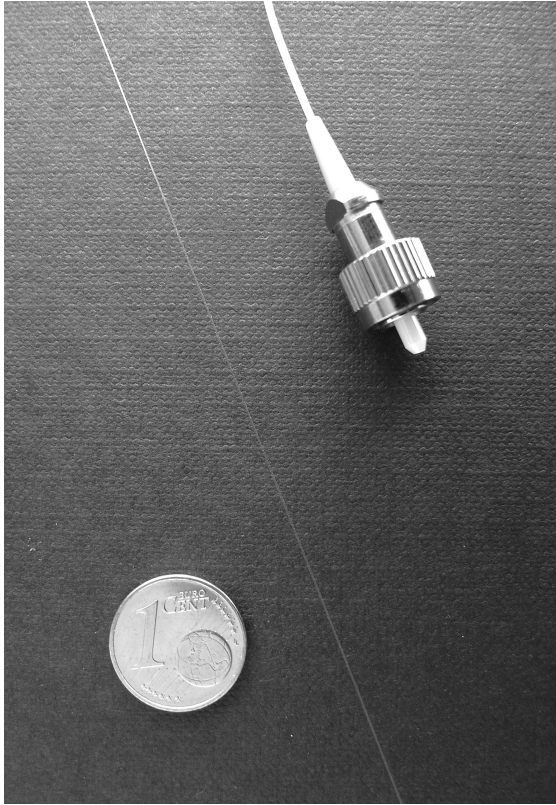


Figure 1.6.: Cold bent glass façade of Strasbourg Central Station.

Despite the potential of cold bent, lamination-stabilised glass for construction purposes, this recent technology lacks comprehensive research approaches, definitions and methods to identify and monitor its principal behaviour parameters. Standards, technical approvals or guidelines covering curved glass are mostly limited to heat bent glass, see section 2.3, even though the topic of cold bending of glass is planned to be treated in future codes. Apart from publications on project examples regarding the application of cold bent glass [Kas 11], scientific publications exist for the cold bending of monolithic and of laminated glass or for IGU. Analytical approaches regarding cold bending of developable glass shapes have also been published as explained in section 2.2. Systematic practical research approaches on the topic of cold bent lamination-stabilised glass, however, are missing so far.

The situation described above shows the necessity for examining the behaviour of cold bent glass and for providing methods for numerical modelling and form-finding. The application potential in curved building envelopes has to be studied to identify the parameters governing the use of cold bent glass and to provide shaping recommendations. However, these tasks necessitate the testing of cold bent glass specimens and the proposal for a monitoring solution for the stress permanently preserved in the laminate.

The current proposal for the long-term monitoring of glass laminates, beyond pure experimental use, in practical applications (e.g. façades, vehicles) favoured searches for a nearly invisible solution to avoid obstruction of the transparency. Because of their optical appearance and possible creep effects [Hof 87], electrical strain gauges were discarded. The recent technology of fibre optic strain- and stress-sensing with Bragg sensors inscribed into fused silica optical fibres [Udd 06, pp. 1-8], [Oth 06, pp. 189-261], which has previously been examined at the ITKE with regard to embedment into GFRP-bridge structures [Gab 12], emerged as a possible solution. Fibre optic sensors (FOS) are robust, resist high thermal load and are insensitive to electromagnetic influences [Sch 10, pp. 1-3]. Their small diameter of less than 0.2 mm, as shown in fig. 1.7, allows their integration into the interlayer zones of glass laminates. Measurements with fibre Bragg grating sensors are expressed as wavelength values and are therefore an “[...] absolute quantity [...]” [Leb 04, p. 1], which is an advantage compared with electrical strain gauges. Furthermore, this technique permits the integration of several sensors into a single fibre. Thus, the topic of cold bent glass can be complemented via fibre optic sensor networks for permanent long-term strain-monitoring within of glass laminates and their possible contribution to the enhancement of glass safety.



**Figure 1.7.:** Size comparison of an optical fibre and its FC/APC-plug.

## 1.2. Research Objective

As demonstrated above, cold bent lamination-stabilised glass has a high potential for use in curved building envelopes. Systemic research on the behaviour of this laminate type and the development of applicable monitoring methods are a necessary prerequisite for its application in building practice. Thus, the present work aims at examining the short- and long-term behaviour of cold bent lamination-stabilised glass and at identifying the principal applicability parameters. Numerical modelling and form-finding procedures for the bent glass elements have to be established and verified through the testing of representative samples. A major focus of this work is to solve the issue of continuous interior stress-monitoring of the sample laminates by a novel method of applying thin, barely visible, fibre optic sensors with Bragg gratings. To maintain the optical properties of the glass laminate, transparent bonding techniques of the sensors to the glass need to be developed. The reliability of the sensors in the bending and lamination process and in subsequent

use has to be investigated. Based on the findings, principles of the behaviour and design of cold bent glass and the feasibility of the monitoring of glass laminates by using fibre optic Bragg sensors will be obtained as a principal base for further research and developmental work.

## 1.3. Methodology

Principally, the work is organised on the basis of applying a linear deductive approach involving testing, material research and both numerical and analytical models. An overview of the research methodology is provided in fig. 1.8. This scheme reveals that the work comprises eight main sections. The first (present) section is dedicated to an introduction and approach to the topic.

Section 2 uses a top-down approach in order to establish the background of the research. It starts with a basic investigation on the possible use of curved glass in building envelopes. Based on this, the shaping methods for fabricating curved glass modules through heat and cold bending are described. The method of cold bending of glass with shape conservation through lamination is pointed out as a principal topic necessitating investigation.

In section 3, the short- and long-term behaviour and interior stress-monitoring of this laminate type are identified as key research problems. The chosen topic range for this work is delimited to short- and long-term laminate behaviour and monitoring techniques applicable to laminated glass, while excluding aspects related to building physics, joining and envelope construction.

Section 4 is dedicated to the solution concept for the above research problems. The complex behaviour of glass laminates is characterised by the succession of cold bending, lamination and later changes in the shape and interior stress attributable to springback and relaxation during the lifetime of the laminate. Therefore, numerical modelling procedures applicable for cold bent glass simulation have been identified. One modelling approach determines the behaviour of cold bent, lamination-stabilised glass starting from a given initial bending shape. Another procedure is aimed at form-finding of the initial bending shape to achieve a certain long-term shape. For the verification of the models, parallel testing options are discussed. With regard to the latter, close range photogrammetry for the displacement and the new technique of fibre optic sensors with Bragg gratings for the interior stress-

monitoring of the bent laminates are proposed after reviewing possible alternatives. An outline of the principle tests performed with real scale specimens and their manufacturing is given.

In section 5, the foundation for performing the testing, monitoring and modelling is laid. As a main prerequisite, the new method of fibre optic sensor application into the laminate had to be developed. Therefore, the theoretical base of fibre Bragg sensors is outlined first and the role of the fixing of the sensor to the glass in order to obtain sufficient strain transmission is demonstrated. Applicable transparent adhesive bonding procedures have been developed and tested therefore. Both a numerical micro-FE-model and an analytical approach are established for simulating and examining the strain transfer between the glass and the sensor. The topic of transverse strain influence on the sensors is discussed. The resulting sensor bonding system is used in the manufacture of the specimens for the testing program. Furthermore, the principles of the applied close range photogrammetry and of the

numerical models, particularly with respect to the polymer interlayer material model, are given.

The detailed real-scale test setup with nine specimens of three compositions and the related numerical model approaches are explained in section 6. A cold bent glass arch permitting stress-sensing through an integrated Bragg sensor network exhibited at the glasstec trade fair 2014 is presented as a demonstrator for possible sensor applications. Test results from the Bragg sensors and the photogrammetry analyses are provided and compared with the numerical results.

On this basis, an evaluation of results and the related deduction of the cold bent glass laminate behaviour, possible modelling and design methods and the feasibility of fibre optic sensor monitoring are discussed in section 7. Finally, in section 8, conclusions are drawn from the above research regarding the behaviour cold bent glass and for applying fibre optic stress-sensing in the context of laminated glass. References and appendices are presented after section 8.



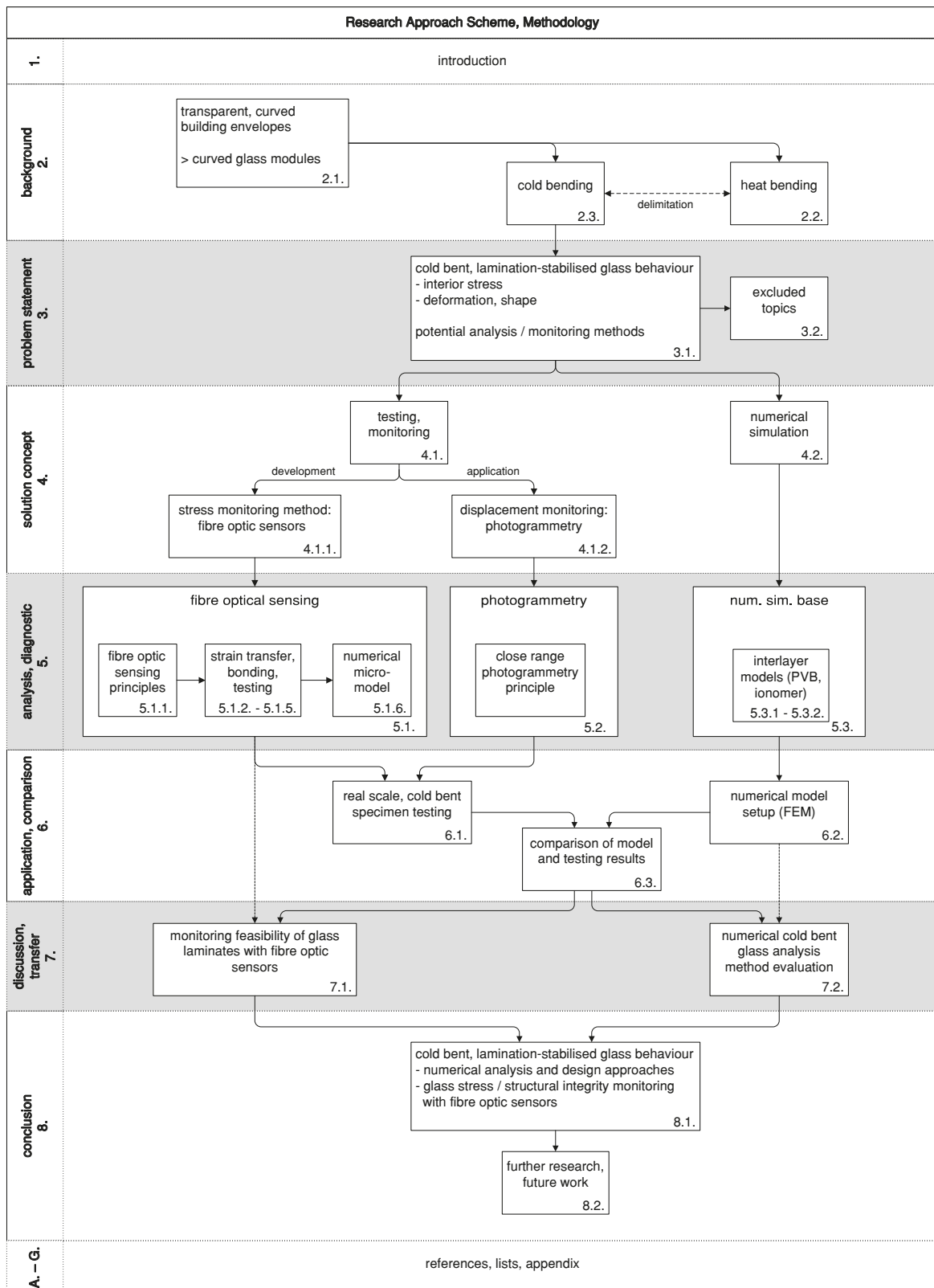


Figure 1.8.: Research approach and methodology overview in flow chart depiction.



## 2 Background

## 2.1. The cladding of Transparent Curved Building Envelopes

The primary geometrical problem regarding the building envelope is the panelisation, which has to satisfy not only aesthetic, but also building physical, constructional and structural requirements. As the geometrical shape of the envelope conveys the design and appearance intention, it has gained the utmost importance in freeform architecture, which tends to favour curved, fluent shapes. Initially, the design approaches aimed at a rationalisation of the geometrical shape into a triangulated mesh with planar triangular panels or, if possible, into double-curved surfaces allowing for a cladding with planar quadrangular elements, as described by Schlaich [Sch 98], Schober [Sch 02] or in [Fuc 09]. Both approaches are still widely used today with an increasing technical refinement [Fre 09]. Recent research aims at achieving a maximum degree of repetition of the planar panels by proposing equilateral mesh optimisation and voxel meshes [Hua 14]. Hexagonal planar panelling has strongly gained in importance because of its structural advantages [Bag 10] for shells and its affinity to developable surfaces and polyhedral meshes [Jia 14]; a method for application of a periodic hexagonal mesh to a double-curved surface aligned with the boundaries has been presented by [Rör 14]. However, all types of planar panelisation lead to a faceting of the surface, which is often not desired and becomes ever more visible because of the reflection behaviour of glass.

Other approaches thus focus on “[...] the approximation of the design surface by a union of patches [...] panels, that can be manufactured with a selected technology at reasonable cost, while meeting the design intent and achieving the desired aesthetic quality of panel layout and surface smoothness” [Eig 10]. Research on geometrical methods for tessellation and panelling optimisation applicable to free form shapes has, for example, been carried out as shown in [Wal 11], [Vou 12], [Sch 13] and has led to the development of software solutions such as evolute tools [Gmb 14a]. In order to achieve the maximum smoothness and maximum correspondence with any given freeform design based on NURBS surfaces, the use of curved panels becomes necessary to avoid faceting. The manufacturing of double-curved glass panels of various shapes necessitates the use of expensive customised moulds; moreover, the risk of visible optical surface flaws from the thermal bending with moulds arises. A proposal for a surface approximation method by Eigensatz et al. [Eig 10] focuses on the smooth continuous panelling of double curved surfaces while reducing the number of diverse panel shape types to simplify production. With regard to glass, the application of developable cladding element shapes for the panelling of a surface constitutes the most efficient method, as both cold bending (see section 2.2) and modern inline fabrication technology for thermal bending as in section 2.3 can be applied; both fabrication technologies permit the use of heat-strengthened or toughened glass.

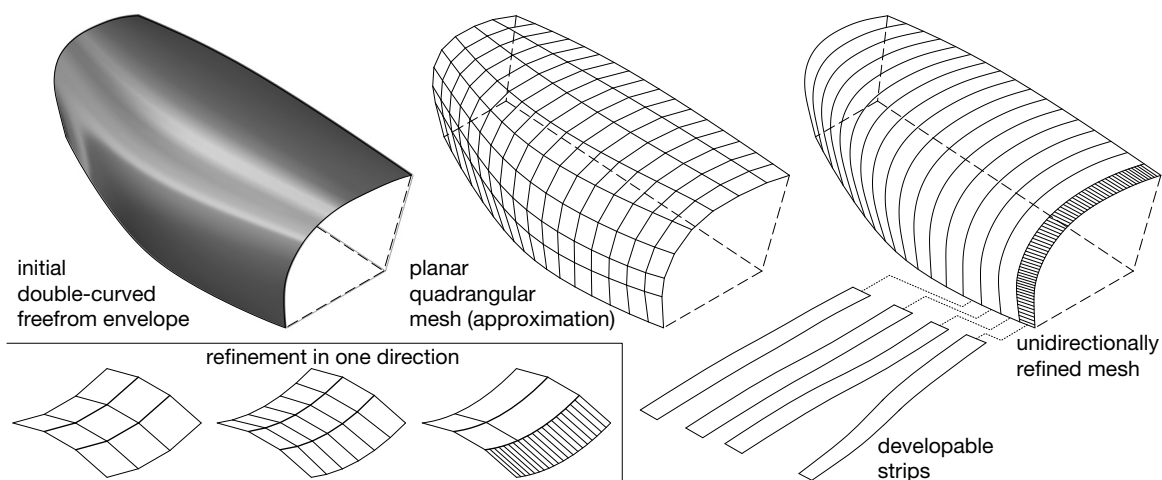
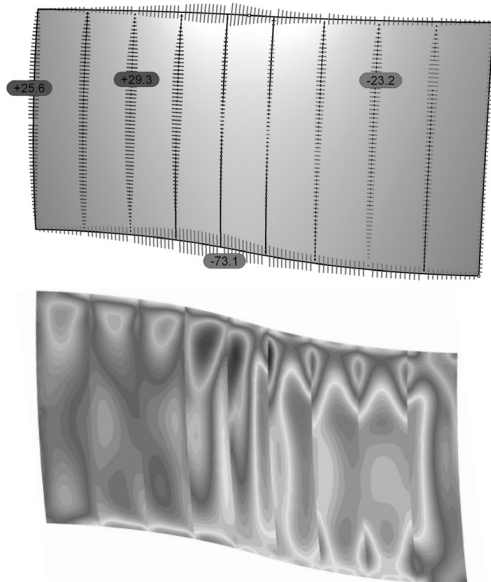


Figure 2.1.: Principle of the developable strip approximation (bottom) and its application to a freeform façade (top).

Progress in the geometrical rationalisation and optimisation of freeform NURBS surfaces has led to algorithmic procedures aimed at the discretisation of a surface into developable strips, thus enabling the efficient use of single-curved glass elements. The D-strip method [Pot08], [Flö 13] is based on the rationalisation of a given surface into a planar quad mesh and then the subdivision of one direction of the quads until it is curved, fig. 2.1. Thus, the strips are developable surfaces with the rulings being orthogonal to the centreline of the strip surface. Geometrical approximation and optimisation procedures for the panelisation of double-curved freeform glazing applied in the context of real projects are presented in [Sch 13] for the Eiffel tower pavilions or in [Vau 13] for the Fondation Louis Vuitton pour la Création. The aim in all cases has been to achieve a surface approximation that is as smooth as possible combined with the application of as few as possible different types of curved or planar glass panels. Most of these panelisation methods have either been developed without a connection to structural aspects or by assuming the existence of a load-bearing supporting substructure. A design approach regarding self-supporting vault surfaces with a quad meshing for planar glass elements inspired by P. Block is presented in [Vou 12].



**Figure 2.2.:** Cold bent glass façade study with wind load and self weight. Top: normal joint forces; bottom: principal stress  $\sigma_1$ .

The use of single- or double-curved glass elements having a low curvature for glass shells is approached in [Fil 12a]. The focus there is laid on

the occurring joint forces depending on the structural joint pattern of the glass shell. Horizontal shells, where both the bent glass laminates and the joints are permanently exposed to the self-weight loads, are estimated to be problematic from the structural point of view. On the contrary, shell-like façades from cold bent glass elements without supporting substructures are an attractive option [Fil 12b], as mainly short-term wind loads act on the glass and on the joints. Even with low glass element curvature, a partial membrane load-bearing behaviour can be established. As a consequence, both the cladding of façade substructures with curved glass elements and the potential use for full glass constructions are fields of application for cold bent glass stabilised by lamination. Studies of full glass façades such as shown in figs. 1.5, 2.2 and shells as per fig. 2.3 assembled from cold bent glass elements have subsequently been performed, see [Fil 11], [Fil 12b]. Structural application of this glass type, however, necessitates permanent shape stability and a knowledge of the behaviour and interior glass stress attributable to the bending process. This is the point at which the present work starts.

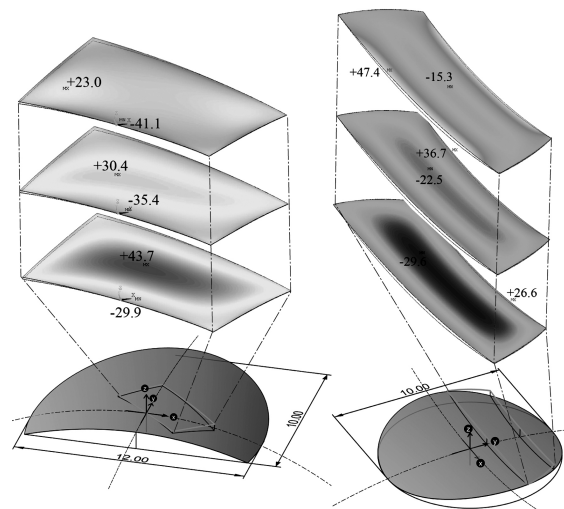


**Figure 2.3.:** Form-finding studies of double curved, cold bent glass laminate panels for a paraboloid / saddle shell.

The dimensions and the shape of curved glass elements are defined by the project requirements and by the manufacturing, statics, construction and assembly constraints. The choice of a particular glass processing company also defines the producible glass curvature and other properties mainly depending on the available machinery and equipment. Some standard and maximum size information is provided in table 2.1.

## 2.2. Cold Bending of Glass

The term “cold bending” principally describes the application of a large elastic deformation to a glass pane. The main issue for the usage in a building envelope is the permanent preservation of the bent shape of the glass, which can be attained in two ways:

- Cold bending of single glass panes and shape preservation by fixing to a substructure: The glass plate is forced onto a rigid substructure in the workshop or on site and then firmly attached to it by point fixings or linear clamping. Laminated glass can also be cold bent [Bel 07a, pp. 123-146], but to a lesser degree, as its short-term stiffness and stress level are higher than for a single glass plate. Insulating glass units have also been elastically bent but the possible deformation is limited to avoid leakage of the edge seal.
- Cold bending with shape stabilisation by lamination: Stacked glass panes and interlayer sheets in a vacuum bag are elastically bent on a mould / rig. Fixed on the mould, the stack is laminated in an autoclave at 140°C and slowly cooled afterwards. After release from the mould, the laminate shows a springback and recovery behaviour depending on time and temperature.

In the literature, no clear nomenclature for cold bent lamination-stabilised glass has as yet been established. “Cold lamination bending”, “cold bending by lamination” or “cold bending during lamination” are among the expressions used to define the glass product. In this work, the descriptive term *cold bent lamination-stabilised glass* is applied, as it is unambiguous regarding the manufacturing process and the function principle of the bent glass.

Cold bending of glass generally enhances the behaviour of the glass with respect to exterior loads, such as wind or snow, because of the curved shape, which partially allows the load-carrying behaviour by membrane forces. Thus, the span of the glass can be increased or its thickness can be reduced. However, the bending and membrane stress attributable to the cold bending process included in the glass limit the extent of the acceptable exterior load level. Increasing the cold bending deformation causes the interior stress to rise but it also leads to an increase in the membrane load-bearing behaviour. Thus, the exterior load application has to be studied

in close connection with the distribution and position of the stress from the bending procedure in order to identify and use synergies of both and to avoid conflict.

Cold bending into a developable shape mainly induces bending in glass and, subsequently, the convex glass surface is subjected to tensile stress and the concave surface to compressive stress. The achievable curvature radii depend on the thickness of the glass and the acceptable tensile stress of the glass; the minimum radii are usually assumed to be larger than 3m. As a rule of thumb, the relationship of the bending moment and the curvature or radius can be used in context with the thickness to determine the induced stress for single-curved glass bending [Fil 11, pp. 384-385], [Tei 14, p. 76].

Deformation into a double-curved shape causes high membrane and bending stress in the laminate and results in high bending radii above 25m. In this case, the dimensions of the glass plate and the intended deformation are the main limitation aspects for the achievable curvature. Local or global buckling during the bending is an additional issue. As shown by Eekhout and Staaks [Eek 09] and again by Datsiou and Overend [Dat 14], the hyper-like deformation of a glass pane supported along two edges or three corners by displacing the free corner normal to the glass surface is possible until a very low curvature is reached at which the glass buckles and restabilises as a single-curved shape. The feasible double curvature depends upon the boundary conditions, for example, linear or point support or the constraint of additional points of the glass surface. Unpublished studies undertaken by the author have shown that the hyper deformation of a glass pane with vertical supports along all four edges and along the cross-wise centre rulings leads to four local buckling areas in the free areas of the glass after passing a limit deformation.

As mentioned above, the glass can be fixed to a substructure in order to preserve the bending shape. The substructure has to be designed to support the clamping forces, the self-weight and the exterior loads acting on the bent glass.

Stabilisation of the bent shape by lamination with a polymer interlayer is more complex, as it involves non-linear material behaviour depending upon time and temperature. The glass panes are stacked alternating with interlayer sheets in a vacuum bag and are mechanically bent on a shape-providing bending mould, fig. 2.4.

This forcing of the glass-interlayer stacks to the bending mould can be carried out in various ways:

- By local, linear or point-like clamp devices such as the lateral bars shown in fig. 2.4
- By a grid of clamping bars or points pushing the glass towards the mould
- By a continuous surface acting as a punch, which is shaped as the positive of the negative form given by the mould below; this way of shaping is, however, a rather theoretical approach, as it is difficult to achieve in practice
- Use of vacuum drawing or pressure for fitting the glass to an underlying mould

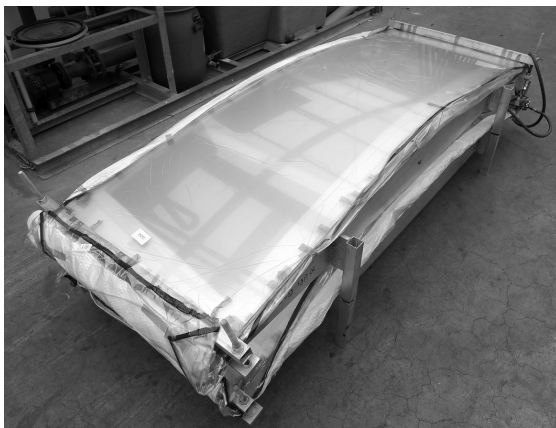


**Figure 2.4.:** Cold bent glass on a mould in an evacuated vacuum bag.

Lamination is performed in an autoclave at a temperature of 140°C and a pressure of about 12bar to 14bar during a process lasting several hours. The interlayer melts and is uniformly distributed in the interstice between the glass panes. After cooling down, the shear compound of the glass by the solidified interlayer is operational. Once the laminate is released from the mould, it starts to recover; the cold bending curvature decreases and the interior bending stress state changes. The behaviour of cold bent glass stabilised by lamination at the moment of the release from the bending mould

and in the long-term can be characterised by two principal stages as in [Pen 13], [Gal 14b].

At the moment of release, a quasi-elastic springback of the laminate occurs and the shear compound is activated by the related partial recovery of the bending deformation. The springback mainly depends on the elastic properties of the interlayer and on the composition of the laminate, namely the number and thickness of glass panes and interlayers. The viscoelastic behaviour of the interlayer causes a short- and long-term relaxation / creep behaviour in parallel. The viscoelastic properties of the interlayer, mainly expressed by the time- and temperature-dependent shear modulus, govern the recovery behaviour and the shape preservation of the laminate. The equilibrium state in the sandwich structure at each infinitely short moment in time can be described in a simplified one-dimensional manner by the shear force couple at the interface of the interlayer and the glass opposed to the bending moments of the glass panes [Pen 13, p. 288]. The principal behaviour is comparable to the sandwich plate model established by [Sta 74].

A softer interlayer such as PVB with a long-term shear modulus decreasing towards 0.1MPa or less leads to a continuous, though decreasing, recovery of the laminate at room temperature. The curvature successively decreases, as does the stress. Subsequently, clamping is necessary to preserve the bending shape, as in the façade of Strasbourg station [Roy 11].

An interlayer such as SentryGlas® having a high shear modulus with a sufficient range of temperatures has thus to be used to preserve the bending shape without clamping. This is the solution usually applied. For the mean temperature levels in countries with a moderate climate, a stable shape over a long period of time can be achieved in this way. Teich [Tei 14, pp. 79-80] proposes causing an anticipated springback<sup>1</sup> and relaxation effect for cold bent lamination-stabilised glass by temperature treatment to obtain a stable curved shape exhibiting practically no further relaxation in the built-in state in, for example, a façade.

<sup>1</sup>The springback of a single-curved, bent laminated glass 450x900mm, 2x6mm FTG and 1.52mm SG interlayer was anticipated by applying a constant temperature of 68°C for 6h. The initial cold bending rise was 29.1mm, which reduced by 8mm at room temperature after one month and by 20mm by anticipated heating.

The permanently included, cold bending stress and the relaxation behaviour of cold bent glass and the related curvature changes are a downside of cold bent lamination-stabilised glass. However, a high optical quality with a smooth, continuously curved surface can be produced by this technology. Possible uneven areas from the bending process are mostly compensated and smoothed by the springback and relaxation effect, as can be seen from curvature analysis at various stages, see section 6.3.1. Cold bending with shape stabilisation by lamination is thus particularly efficient for applications necessitating continuous low curvature, whereby thermally curved glass usually cannot offer the same optical quality level. With respect to the included permanent stress from bending, heat-strengthened or fully toughened glass has to be used for cold bending to provide sufficient resistance reserve for additional exterior loading.

Standards, technical approval or guidelines covering curved glass are limited for some aspects regarding thermally curved glass, see section 2.3 below. In the JRC guidance for the development of Eurocodes on the structural design of glass components [Fel13, pp. 116-117] dated 2013, recommendations are given to address cold bent glass in the future Eurocode. The German DIN standards on glass do not consider cold bending; it is planned to integrate cold bent glazing elements into the future DIN 18008-7 [Sie12a, p. 30]. An indirect crosslink can be established between the German general technical approval Z-70.3-175 [DiB12], which refers to safety glass laminated with an SG ionomer interlayer and indicates temperature- and load-duration-dependent shear moduli for the interlayer, which can be taken into account for the design within the scope of the German TRLV [DiB06b], TRAV [DiB03] and TRPV [DiB06a]. The stress limits for cold bent curved glass elements mentioned in various publications, e.g. [Tei14, pp. 75-83], generally refer to 50MPa for fully toughened glass, which complies with the German TRLV [DiB06b] for linearly supported glass. No references to codes with partial safety factors have been made so far.

Double-curved cold bent glass with shape stabilisation by fixing to a substructure has, for example, been used with point-fixings in the façade of the Floriade building in Hoofddorp [Eek08, pp. 551-553] and in the roof of the tramway station Zuidpoort in Delft [Eek07, p. 219] or in the roof of

the Victoria and Albert Museum in London [Eek07, p. 221]. Example projects for the application of cold bent glass with shape stabilisation by lamination include the Strasbourg Central Rail Station [Roy11, p. 378], the Park House in London [Tei14, p. 78], the roof of the Apple Cube 2 in New York [Tei14, p. 81] and the Städel Museum in Frankfurt on the Main [Tei14, p. 81]. In a number of projects, the use of cold bent glass has been intended, but combinations of thermally curved glass and planar elements have been used instead following structural and cladding optimisation studies. The double-curved glazing of the Eiffel tower pavilion [Sch13], the transparent sail-like envelope of the Fondation Louis Vuitton pour la Création [Vau13] or the structural glass façades of the Bombay Sapphire Distillery greenhouses [Web13] are among these projects.

Research into the circular cold bending of PVB laminated toughened glass has been performed by Belis et al. [Bel07a], [Bel07b]. The specimens mostly did not meet the normative design criteria with respect to the necessary failure load but exhibited a good post breakage stability. The importance of correctly managing the surface geometry of cold bent glass and avoiding stress concentrations or bumps is underlined by Eekhout et al. [Eek09, pp. 408-412], [Eek07, pp. 213-220], who also give a number of project examples regarding this task.

A limited number of analytical approaches concerning the description of the general cold bending of glass and regarding the behaviour of cold bent lamination-stabilised glass have been published so far:

The inextensional theory for bent plates by [Ash63] and Mansfield [Man89] is applied in [Roy11] and [Est13] for the analytical calculation of the exact deformation and stress occurring in the large pure bending deformation of plates into a single-curved developable shape. In the boundary layers along the curved edge of the elastically bent glass, this theory predicts a tensile normal force in the curvature direction adding to the bending moments in the glass and a slight anticlastic deformation along the edges. The bending in the transverse direction is also taken into account. Comparison with finite element analyses has shown a correspondence and the analytical approach is estimated as being conservative.



The diploma work by Keller [Kel 12] conducted together with the ITKE and the IBB at the University of Stuttgart has examined the applicability of linear Kirchhoff plate theory, non-linear v. Kármán plate theory and non-linear shell theory for the cold bending of a single glass sheet into double-curved shapes. In order to solve the constituting equations, the exact three-dimensional nodal displacement field of the glass pane into the desired curved shape has to be known. As a result, the strong sensitivity of the analytic approach to the displacement field data has to be mentioned. Even a slight deviation of a node in the horizontal coordinate directions leads to a large increase in membrane stress in the glass in the case of double curvature. In general, the non-linear shell approach is a precise approach for cold bending calculation, if the displacement field in all three coordinate directions is exactly known. Unfortunately, this exact coordinate or displacement data is an unknown parameter with double curvature. The only work referring to the relaxation behaviour of cold bent lamination-stabilised glass has been published by Galuppi and Royer-Carfagni [Gal 14b]. The authors divide the process into three stages: the cold bending, the springback / relaxation after lamination and the final forcing of the laminate by clamping it to a substructure. The cold deformation is considered as being purely flexural. An initial shear distortion of the interlayer from the shift of the bent glass plies is assumed and integrated into the equilibrium equation based on a method by Newmark for the sandwich. A viscoelastic solution of the equilibrium equations by using a method by Galerkin and a linear viscoelastic approach with a quasi-elastic equilibrium approximation are compared. The quasi-elastic solution underestimates the stress in the panel during the relaxation phase and overestimates the clamping force in the third phase. The full viscoelastic solution, taking into account the viscoelastic memory of the interlayer, is recommended for the performance of studies of the precise stress and deformations of the springback and relaxation phase.

No research on glass bending exists regarding to the potential effects of the initial stress stiffness part<sup>2</sup>  $K_g$  from the change of the interior forces during large deformation.

Some recent research and development proposals tend towards the use of very thin, chemically strengthened glass for cold bending [Gmb 14b]. At the glasstec 2012 trade fair, a cold bent lamination-stabilised element from thin chemically strengthened glass was shown. However, this glass type, which is mainly used for mobile phones and laptops, is still extremely expensive and thin glass elements are more prone to buckling.

A summary of the main cold bending parameters in comparison with thermally curved glass can be found in table 2.1. With the exception of the above-mentioned work, a lack of systematic research publications can be noted with regard to the topic of cold bent lamination-stabilised glass. To date, glass processing companies dominate this segment of research development.

<sup>2</sup>The entire tangential stiffness  $K_T$  in a geometrically non-linear analysis consists of the elastic stiffness  $K_e$ , the initial displacement stiffness  $K_u$  and the initial stress stiffness part  $K_g$  (geometrische Steifigkeit)

### 2.3. Thermally Curved Glass

In the present work, the term “thermally curved glass” is used generally to designate curved glass fabricated by heat bending, a glass-shaping process by heating flat glass to a temperature in the range of its softening point at 550°C to 620°C [Sie 12b, pp. 20-22] in order to curve it plastically. Through cooling, the curved shape becomes permanent. This is the main difference compared with elastic cold bending by which the curved shape has to be preserved by clamping or lamination. Generally, mouldless techniques and procedures involving moulds can be applied. Considerable improvements of heat-bending technology, machinery and product quality have been achieved in the last decade. The following heat-bending methods can be distinguished as in [Fel 13, pp. 50-51], [Sie 12b, pp. 20-22] and [Tim 14, pp. 141-149], fig. 2.5:

- Gravity (sag) bending, slumping: Heated glass is deformed by gravity over or into a custom-made mould. The mould either defines the entire bending surface or it provides only the boundaries for the glass shape. Depending on the mould shape, the furnace size and the glass thickness, nearly all single- and double-curved forms can be produced. It is possible to bend two stacked glass panes simultaneously; this permits to obtain two curved glass elements being highly suited for lamination. Usually only slow cooling is possible and annealed glass is the resulting quality. If fast cooling is technically possible with the furnace and the mould, heat-strengthened or fully toughened glass can be obtained. However, chemical strengthening is more typical for gravity-bent custom-curvature glass products used, for example, in the marine glazing of yachts.
- In line bending with an adjustable quench tool: This fully automated technique is mainly used for producing developable, mostly cylindrical, curved glass in two steps in an inline process. The glass is heated first and then deformed by means of two parallel adjustable curvature-shape-giving quench devices consisting of movable chords containing the cooling nozzles. Fast cooling by the nozzles permits the prestressing of the glass to the heat-strengthened or fully toughened level. Good optical surface quality can be achieved. A process modification allowing the manufacturing of bi-arc-curved glass, for example, cone-like shapes, has recently been published [Chi 13, p. 343].

- Press bending: The glass pane is thermally curved by means of a press and blow process, typically combined with a mould defining the target surface shape and a hollow ring mould providing the edge support for the glass. Various single-curved and double-curved shapes are possible. Fast cooling is possible in order to obtain a heat-strengthened or fully toughened glass quality. Press bending is mainly used for the production of curved automotive glazing.

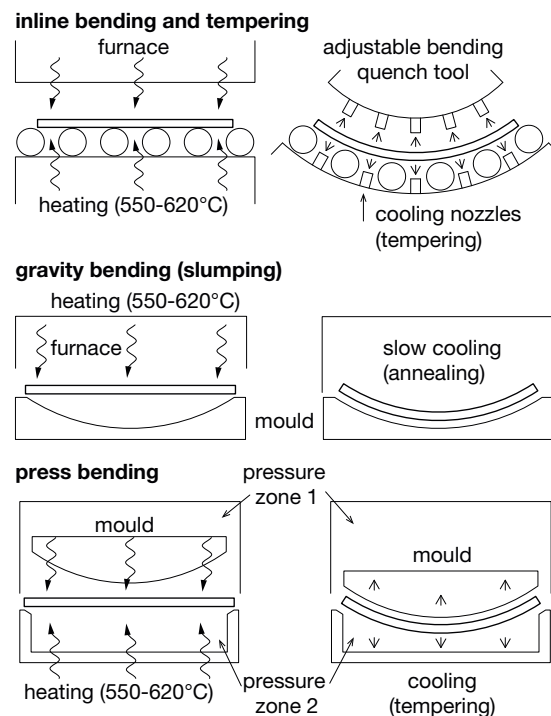


**Figure 2.5.:** Schematic depiction of the principal heat bending processes.

Classification of bent glass shapes is provided by the standard ASTM C1464-06 (2011) [C14 11], defining cylindrical, elliptical, multiple, compound, serpentine and single bends. The available dimensions, radii and curvature heights of thermally curved glass products depend on the manufacturing offers in the market and on the necessary properties and quality of the glass product. For single curvature glass with fully toughened quality, a maximum of 2850mm x 12800mm is offered in a single case [nor 15], 4200mm x 2440mm are mentioned as standard size limits by [Fed 13, p. 99] and 5000mm x 3210mm with minimum radii of 2m to 3m are available from a known glass processing company [sed 15].

Annealed moulded sag-bent glass is available with maximum dimensions of 2.9m x 7.00m [Cri 15]. The curvature direction in all cases corresponds to the shorter dimension. The chemical strengthening of curved glass as feasible for sizes up to 5m x 2.8m [Chi 13, p. 343] up to 2014. Typical minimum bending radii are in a range of 1m to 2m, even though minimum radii of 0.1m are possible. For gravity bending with moulds, the maximum bending height or rise is about 0.80m [Wel 10] to 1.00m [Cri 15]. For more details and an overview in comparison to cold bent glass, see also table 2.1.

US standard ASTM C1464-06 (2011) [C14 11], the guideline of the German Bundesverband Flachglas [BF 11] or the British Glass and Glazing Federation Manual [Fed 13] provide quality requirements regarding the quality and geometrical tolerances of thermally curved glass. Depending on the glass thickness and the curvature, the maximum acceptable tolerances given by [BF 11, p. 9] are  $\pm 3\text{mm/m}$  shape accuracy,  $\pm 2\text{mm/m}$  to  $3\text{mm/m}$  edge straightness and  $\pm 3\text{mm/m}$  twist. ASTM C1464-06 (2011) [C14 11, pp. 4-5] stipulates shape accuracy, height, crossbend and twist deviations depending on glass thickness and curvature height being usually below  $\pm 3.2\text{mm}$  (glass thickness up to 12mm) or  $\pm 4.8\text{mm}$  ( $>12\text{mm}$ ). Other quality issues with thermally curved glass are quench marks (stress anisotropies) becoming visible from certain viewing angles or lighting conditions, ring / pock marks, bumps and blurs. With low curvature, potential surface defects can become more visible, fig. 2.6.



**Figure 2.6.:** Optical distortion of a single curved, thermally bent insulating glass unit.

The application of soft magnetron sputter coatings such as low-e layers is performed on flat glass. Subjecting the coated glass to a thermal bending process can damage or cause deterioration of the optical quality of the coating. Fast process types such as adjustable quench inline bending are better suited, as the heat acts on the coating over a period lasting only a few minutes. Usually, the soft coating can only be applied to the surface of glass opposite to the rollers or the mould [Tim 14, pp. 146-147]. Hard coatings can be applied because of their resistance to thermal influence. In any case, the applicability of coatings in the context of thermally curved glass has to be tested and mock ups are recommended prior to any decision being made. Testing performed with a low-e triple silver soft coating subjected to a thermal bending process for producing annealed glass and toughened glass is described in [Chi 13, p. 341]; only minor deterioration of the coating at the edges of the glass occurred in the bending process and was judged acceptable by the author of the paper. No further details on the coating or its long-term stability were discussed.

However, no specific codes or standards regarding strength specifications for thermally curved glass exist so far. The ISO-standards 11485-1 to -3 [Sta 14], [Sta 11b], [Sta 11a] cover the terminology, quality requirements and the fracture behaviour of tempered and laminated thermally curved glass but do not provide strength values [Fel 13, p. 51]. In general, research results correspondingly show a reduced characteristic bending strength with cylindrical thermally shaped glass [Kas 03],[Buc 09]. Strength testing in research is based on four-point bending as in DIN EN 1288-3 [DIN 00]. The German guideline [BF 11, p. 14] provides characteristic strength values based on the research of [Buc 09, pp. 23-28] of 40MPa for float glass<sup>3</sup> and of 31MPa for the edges; a 55MPa characteristic strength is given for heat-strengthened glass and 105MPa for fully toughened glass. Particularly with heat-strengthened glass, the fragmentation pattern of thermally curved glass deviates from planar glass [Sch 12, p. 193]; this depends mainly on the manufacturing process. If manufactured correctly, good quality annealed glass exhibits little to no local residual stress; values of 2MPa to 3MPa have been published for such stress [Chi 13, p. 337].

<sup>3</sup>In [Buc 09, p. 27], a strength of 45MPa for float glass and a reduction by 20% for the glass edges are given.

The German technical guidelines for vertical linearly supported glass TRLV [DiB 06b] and for vertical safety barrier glazing TRAV [DiB 03] are also applicable for thermally curved glass [Sch 12, p. 195]. In Germany, thermally curved glass is a non-regulated building product [Sch 12], [BF 11] necessitating general national or European approval (German AbZ, European ETA) or German exceptional approval (ZiE) for use in construction. Examples of German general approvals for single annealed curved glass and curved safety glass laminates are [DIB 13] and [DIB 10]. A detailed European Technical Approval for annealed and fully toughened, heat soaked curved glass with minimum bending radii of 1500mm has been available since 2013 [EOT 13]. For the ETA, verifications of the curved glass have been made in accordance with four-point bending tests as in EN 1288-3 and fragmentation as in EN 12150-1 [DIN 12]; quality control includes the use of polarisation filters for detecting stress anisotropies. If a general approval as mentioned above is available, the related thermally bent glass product can be used with the strength specifications given in the approval. A critical review of the application of four-point bending tests as in EN 1288-3 is given by Krampe and Weller [Wel 11b], who describe the effect of additional membrane stress developing in a large bending deformation of glass.

Insulating glass units assembled from cylindrical or conical curved glass have been examined, for example, by Neugebauer [Neu 08], [Neu 09],[Neu 13]. Whereas the curvature of the glass causes the internal pressure to increase compared with flat glass, the load-bearing behaviour and distribution of the curved glass layers with respect to exterior loads is more complex. Generally, curved glass subjected to exterior loads such as wind show a stiffer behaviour than planar glass, as their load-bearing behaviour is characterised by both membrane forces and bending [Nij 11, p. 394]. This is also the case with curved insulating glass [Pen 14]. Smaller deflections and stress are positive results from the curved shape. However, an increasing stiffness can also attract higher load and thus design calculation has to be undertaken with care. Local displacement of the supports of curved glass can cause high stress. One of the few structural applications of thermally curved glass has been made with the pleated curved greenhouse structures described in [Web 13, pp. 328-334].

A concise summary of curved glass types in comparison is provided in table 2.1 below.

	heat bending		cold bending	
	with mould or frame	mouldless	clamping to substructure	lamination-stabilised
<b>principle</b>	plastic deformation, permanent shape preservation	plastic deformation, permanent shape preservation	elastic deformation, shape preservation by clamping to a substructure	elastic deformation, shape preservation by interlayer shear compound
<b>technology</b>	sag / gravity bending, adjustable moulds, press forming	bending quench / bending conveyor (inline heating, bending and quench cooling / toughening)	bending / clamping: - on-site - on a frame in prefabrication	bending of glass- interlayer stacks on a mould / rig, autoclave lamination, release, springback / relaxation
<b>process temp.</b>	550-620°C	550-620°C	-	140°C
<b>residual production stress</b>	none or local stress peaks (cooling, quench pattern)	none or local stress peaks (cooling, quench pattern)	depends on glass thickness, dimensions and bent shape	depends on glass thickness, dimensions and bent shape
<b>applicable glass type</b>	ANG, CSG* (HSG* for single-curvature)	ANG, HSG*, FTG*	HSG, FTG, CSG	HSG, FTG, CSG
<b>feasible shapes</b>	- single curvature - synclastic - anticlastic (limited)	usually cylindrical, some developable surfaces (torsal ruled surfaces)	- developable surfaces (torsal ruled surfaces), - anticlastic	- developable surfaces (torsal ruled surfaces), - synclastic (limited) - anticlastic (theory)
<b>interlayer (laminated glass)</b>	lamination after bending, all interlayer types possible	lamination after bending, all interlayer types possible	PVB, PU, EVA, cast resins; lamination prior to bending (cold bending of laminated glass causes high stress)	high shear stiffness and high glass transition $T_g$ necessary (e.g. SentryGlas®)
<b>min. radii (cold bending: 50MPa max. tens. stress)</b>	max. rise or depth: 1m <sup>(1)</sup>	0.1m - 0.3m [Tei 14] 1m - 2m <sup>(4)</sup>	single curvature: 2.5-7m** or ~1500-R <sup>(3)</sup>	single curvature: 4-9m** or ~1500-R <sup>(3)</sup> synclastic: >25-30m anticlastic: >35m***
<b>max. dimensions</b>	ANG: 2.95m x 7m <sup>(1)</sup> CTG: 2.8m x 5m <sup>(2)</sup> ANG, HSG: 3m x 7.6m <sup>(2)</sup>	typical: 5m x 3m <sup>(3)</sup> 2.85m x 12.8m <sup>(4)</sup>	limited by glass size, substructure / frame and exterior loads	depending on autoclave size, max. 15m x 3m <sup>(3)</sup>
<b>optical surface quality</b>	stress anisotropies, bumps, blur possible	good	high	high
<b>shape stability</b>	permanent	permanent	provided by substructure / clamping	provided by the interlayer (shear modulus G), depending on temperature and time; possible relaxation
<b>temperature influence</b>	none (temperature differences can cause breakage in case of strong local stress anisotropies)	none	none (clamps must allow for in-plane movement)	permanent high temperature increases springback / relaxation (curvature decreases)
<b>loads on substructure</b>	none	none	forces from bending process (permanent)	loads from springback / relaxation (depending on time, temperature)
<b>coatings, finishes</b>	limited: soft coatings partially applicable to concave surface; hard coatings more suited	limited: soft coatings partially applicable to concave surface; hard coatings more suited	hard and soft coatings, ceramic frit	hard and soft coatings, ceramic frit
<b>IGU fabrication</b>	possible	possible	limited (bending of the entire IGU necessary)	possible (all IGU glass layers are bent laminates, possible edge compound problems from relaxation)

<sup>(1)</sup> [cri 15]<sup>(2)</sup> [sun 14]<sup>(3)</sup> [sed 15]<sup>(4)</sup> [nor 15]

\* toughening performed after bending \*\* depends on glass thickness / limit stress \*\*\* values determined theoretically

**Table 2.1.:** Comparative summary of curved glass manufacturing methods and properties (partially based on [sun 14], [sed 15], [cri 15], [nor 15]).



### **3 Problem Statement**

### 3.1. Behaviour of Cold Bent, Lamination-Stabilised Glass, Monitoring Solution

As shown in 2.2, cold bending with shape stabilisation through lamination is of particular interest, as it allows for the production of stable curved glass elements of high optical quality without the need for clamping to a support structure. For the application of this complex relatively recent glass product, however, knowledge of the interior stress caused by cold bending, the production process and its development with time is necessary in order to determine the exploitable level of additional stress resulting from exterior loads. The interior stress from manufacturing is maintained throughout the lifetime of the glass product. Preliminary FE analyses have shown, that the interior stress on the glass interfaces with the interlayer can possibly become higher than the stress on the outside faces with time during the relaxation of the laminates. This is an aspect of importance for structural design with such glass elements and it could become a future topic of interest, if the presence of the maximum tensile glass stress at the interior laminated faces of the glass turn out to be an advantage with respect to crack formation and breakage safety. As a first step, the systematic monitoring of the interior stress contributes to these aspects and could also help to make lamination-stabilised cold bent glass accessible for potential later use as a structural element. Lifetime stress monitoring of special glass products can potentially be applied to raise the safety level. Furthermore, the 3D bending geometry and its development with time need to be known to ascertain the production and preservation of the correct desired shape for application in, for example, a building. This work is intended to contribute to these issues based on the following problem-oriented topics:

Numerical simulation methods:

- Proposal, comparison and application of various numerical modelling procedures characterising the short- and long-term behaviour of cold bent glass
- Definition of the time- and temperature-dependent stress inside the glass and the 3D geometry of the glass elements as principal aspects for evaluating cold bent, lamination-stabilised glass

- Development of a procedure for determining the initial cold bending rig or mould shape to obtain a final product exhibiting a specific desired shape after springback and relaxation

Verification / comparison aspects by testing:

- Development of experimental procedures for the monitoring of the interior stress and deformation of cold bent lamination-stabilised glass throughout a testing period of more than half a year
- Concept and fabrication of respective characteristic specimens allowing comparison with numerical models

Choice of monitoring and evaluation methods for the experimental set-up:

- Proposal and applicability testing of a monitoring method for permanent real-time stress measurement in glass laminates
- Performance of monitoring and capture of the 3D-shape and time-dependent deformation of cold bent lamination-stabilised glass

Application potential and principal requirements regarding the monitoring solution:

- Possible application proposals with regard to complex glass laminates in architectural, vehicle, aerospace and naval settings as a stress-sensitive measurement device; permanent monitoring of very large glass elements or special shapes and of glass under extreme situations or for experimental purposes; possible safety factor enhancement
- Demand for maximum transparency and clearness for the monitoring solution in order that the field of view through the glass is not obstructed
- Resistance of the chosen technique to manufacturing and autoclave conditions for usage in interior stress monitoring
- Requirement to have sufficiently small dimensions to fit between the glass layers for a minimum glass pane distance of 0.76mm (PVB interlayer) or 0.89mm (SG interlayer)



### 3.2. Excluded Topics

As the focus of this work is directed to the elaboration of principal aspects of cold bending with the lamination-stabilisation of glass, the identification of transparent monitoring solutions for the interior glass stress and the respective time-dependent deformation and geometrical shape, the following aspects are not covered herein:

Architectural and construction aspects:

- Construction and architectural aspects involving cold bent glass would not decisively contribute to the topics and conclusions of this work and are therefore not examined. The field of construction and architecture remains closely linked to specific building designs and must thus be treated on the basis of research approaches different from this work.
- Joining of curved panels used, for example, for façade design is a topic that does not influence cold bending procedures and its monitoring. It is thus not treated here.

Building-physical and safety aspects:

- Solar protection, thermal insulation, fire protection and weatherproofing are entire research fields of their own and go beyond the scope of this work.
- Breakage and post-breakage behaviour of cold bent lamination-stabilised glass is not covered in detail and no experiments have been undertaken related to this topic. However, some mention of the potential use of continuous interior stress monitoring for enhancing the structural safety of glass usage is given in section 8. This aspect also constitutes an entire research field of its own.
- Durability aspects of cold bent glass and monitoring techniques concerning environmental influences such as solar / UV radiation, humidity or cleaning agents are not treated because of the limited available testing time of less than one year and of the large amount of testing and research necessary to cover this topic.

Other aspects concerning curved glass:

- Heat bending of glass is outlined in section 2.3 for the purpose of comparison and conceptual delimitation to cold bending. As heat bending is a large topic of its own with manufacturing conditions, material resistance and application possibilities differing strongly from those of cold bent glass, no further thematic discourse is provided regarding this glass type. As heat bent glass might develop local residual stress from the manufacturing process, particularly the cooling after plastic deformation, an applicable monitoring solution would differ extensively from the tracking of the stress systematically included in the entire cold bent glass.
- Cold bending and shape stabilisation through the clamping of the boundaries of single glass panes or of previously laminated glass, with the latter, for example, having been examined by [Bel 07a, pp. 123-146] and [Gal 15], is not covered here, as the present work focuses on shape stabilisation by lamination and the attractive feature of the possibility of omitting architecturally disturbing clamping and support constructions.
- Testing of the relaxation behaviour of cold bent laminates at temperature levels above room temperature was not possible, as no sufficiently large climatic chamber was available. The subject is of importance for further, future research.
- Analytical formulations of the cold bending and relaxation behaviour of lamination-stabilised glass are not dealt with in detail in this work because of their great extent and complexity. An overview of emerging approaches and the state of research is, however, presented and a cold bending analysis study in the context of this research work is briefly mentioned. The material models used for the description of polymer interlayers used in the laminates are covered by an analytical approach, see section 5.3.

In the description of the background of this work in sections 2.1, 2.2, 2.3, some of the excluded aspects mentioned above are basically touched upon by reference to current states of technology and research. Wherever possible, however, important aspects concerning the excluded topics related to the methodology and results of this work will be indicated as future work and research proposals.



## 4 Solution Concept

#### 4.1. Testing and Monitoring

For examining the behaviour of cold bent glass with shape stabilisation through lamination, tests have been performed with real-scale samples adapted to usage in building and construction. These tests have been accompanied by corresponding finite-element modelling with various degrees of model complexity. The principal information necessary for the description of the behaviour of cold bent glass is the interior stress and the deformation or global shape of the curved glass panes. Thus, a stress measurement method applicable in the interior of the laminate and permitting continuous short- or long-term real-time monitoring has been sought, see section 4.1.1 below. Another requirement for this measurement method is the avoidance of obstructing the transparency of the glass laminate. This demand is in compliance with the possible future use in built-in glass elements in buildings or vehicles for which transparency is the principal feature offered by glass. The research of such an interior glass stress / strain measurement technology thus aims at the market field of the continuous long-term or real-time monitoring of glass elements in everyday operation.

For curved architectural and automotive glass, the smoothness and continuity of the curvature are of major importance: surface irregularities, bumps and other disturbances are readily perceived because of the reflectivity and transparency of glass. Therefore, various surface control methods and instruments are available as outlined in section 4.1.2. However, for the performance of such controls expensive technical equipment is often necessary but has not been available in the context of this work. The size of architectural glass laminates often surpasses the maximum monitoring dimensions offered by industrialised methods. As a consequence, a method allowing for application in situ and applicable to large glass dimensions has been sought and identified in section 4.1.2 below. Furthermore deformation monitoring serves as an additional control and calibration method for the finite element model in comparison with stress monitoring.

For the tests, single-curved specimens have been used with respect to technical feasibility and for facilitating the strain and deformation monitoring. A metallic bending mould of a given cylindrical shape has been applied to perform the bending, fig. 4.1. Samples produced by the application of such a mould thus have a known initial bending shape, which is also the basis for subsequent monitoring and FE modelling. During the tests, the initial geometrical shape changes after release from the mould as a result of the relaxation of the polymer interlayer applied for lamination. Double-curved cold bent glass has not been tested, as its production is complex, the feasible shapes and the degree of curvature are severely limited and the description of the interior stress states is more complex than that with single-curved glass bending, as membrane and plate effects prevail. Only synclastic spherical laminates have actually been successfully produced by double-curvature cold bending and lamination so far<sup>4</sup>. The achieved curvature radii in a range of 20 to 35m (section 7.2) are relatively large and therefore the monitoring of the geometrical shape and its change with time can be imprecise because of measurement errors relative to the small real displacement of the tested object.

In the tests, various laminate compositions have been applied for an understanding of the influence of the thickness of the laminate, interlayer materials and number of glass layers and for the inclusion of typical examples used in building and construction. For the interlayers, the most widespread polymer materials of poly-vinyl-butylal (PVB) and high shear stiffness ionomer (SG) have been used and modelled. Two to four glass layers have been applied. The bending process of the glass used for tests is shown in fig. 4.2. Alternating layers of glass and polymer interlayer sheets are stacked (1), placed in a vacuum bag and bent upon the mould (2, 3) by applying transverse bars at the ends of the glass. The whole package is laminated in an autoclave (4) in a process that involves the simultaneous application of pressure, temperature and vacuum (in the bag). After lamination and cooling, the shear compound of the glass layers is established by the interlayers.

<sup>4</sup>Circular spherical glass units produced for the Städel Museum in Frankfurt / Main and some test laminations carried out by sedak / Gersthofen. Anticlastic bending has only be achieved by forcing glass onto substructures by means of clamping for low curvature and limited deformation control.

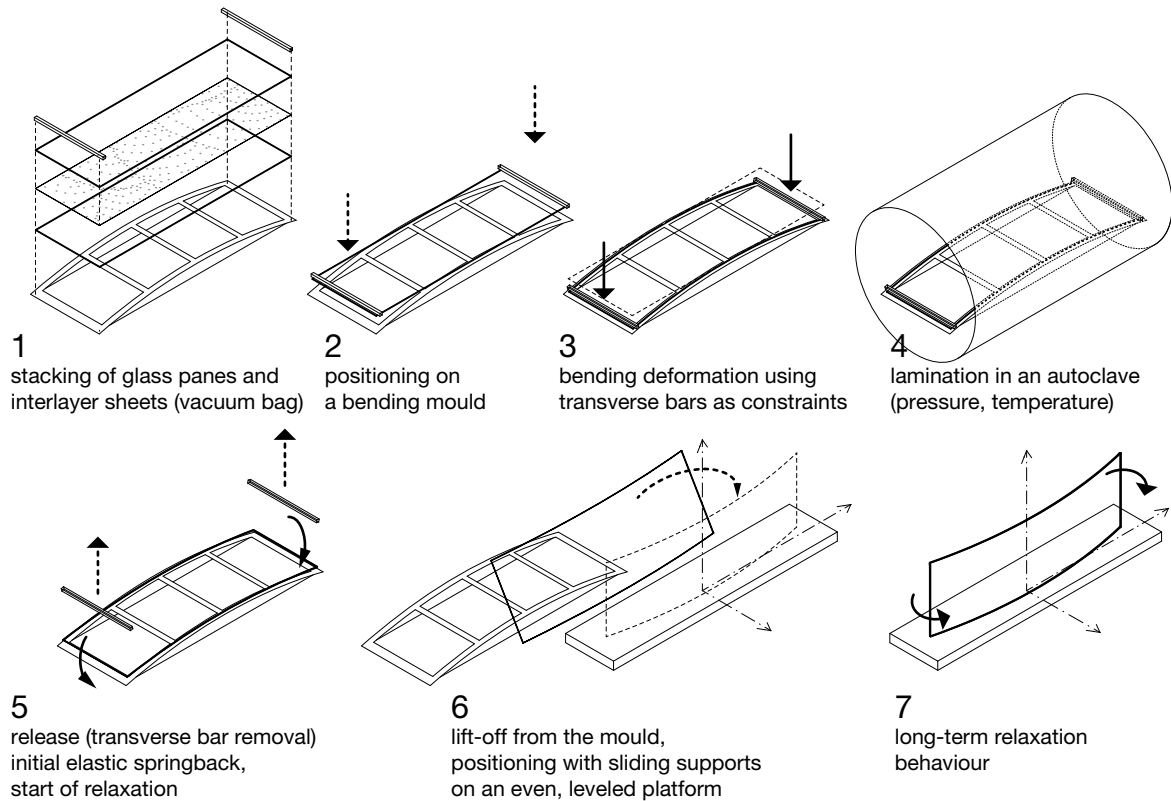


**Figure 4.1.:** Schematic workflow depiction of the glass cold bending, lamination and relaxation procedure applied in this research.

Release of the laminate from the bending mould by removal of the transverse bars (5) results in an initial elastic springback [Fil 14d, p. 113] and in a following relaxation (recovery) depending on time and temperature. For minimising the influence of the weight of the glass itself on the relaxation, the laminates are placed on their curved edges with sliding supports (6). The long-term recovery behaviour can then be monitored (7). The test set-up is explained in detail in section 6.1.1.

The bending technique on a metallic rig / mould providing linear support along the edges of the glass described above can be regarded as typical for single-curved glass for building. Depending on the desired bending shape, such a mould can also be an entire, continuous surface or comprise several parallel curved supports acting as a grid and with a negative form from that of the glass shape. The forcing of the glass onto such a mould, which is carried out from the side opposite to the mould surface, can be performed in various ways, as mentioned in section 2.2.



**Figure 4.2.:** Cold bending aluminium mould with glass-interlayer stacks wrapped in an evacuated vacuum bag applied in this research.

#### 4.1.1. Monitoring of Stress, Strain and Structural Integrity

The measurement of the stress introduced into the glass panes in the cold bending process and the conservation and functionality of the chosen measurement method during and after the autoclave lamination process are the major problems addressed in this thesis. As stated above, the interior stress of the glass at the interface with the interlayers is particularly important, because a considerable stress level is possibly conserved there during the lifetime of the bent glass. In addition to the required resistance of the measurement device to the temperature conditions of the autoclave, maximum transparency and ease of continuous monitoring of the stress are two demands imposed upon the solution sought.

Among the passive (contact-less) techniques applied for strain measurement, photogrammetry and strain-optical methods have to be mentioned. *Close-range photogrammetry* can be used for identifying the 3D deformation of glass subjected to a known load scenario. Comparison of both the unloaded and the loaded situation then permits the calculation of the related strain. The possible examination area dimensions depend on the resolution of the camera and the desired measurement resolution of the sample. Industrial systems such as provided by GOM (ARAMIS) typically allow for the examination of areas up to a square meter, but areas of 100x100 to 300x300mm are more realistic for obtaining sufficient accuracy. The manufacturer reports a best strain accuracy of 0.005%, but an accuracy of 0.01% has also been mentioned [Wel 14b, p. 541]. Successful application of photogrammetry to monitor the local strain of glass elements is reported by Weller and Tautenhahn [Wel 14a, p. 197] for thin glass plates and Mähr [Mäh 13, pp. 415-418] for a glass fin. A stochastic black-and-white speckled pattern needs to be applied to the glass surface for the identification of relative movement by photogrammetry.

Photogrammetry only allows for the identification of surface strain through deformation measurement; thus, no residual strain, e.g. from tempering, can be tracked. The principal advantage of photogrammetric strain measurement is the possibility of measuring the strain of an entire area without contact and not at a discrete point only. The limited dimensions of the monitoring area are

a momentary disadvantage. The curved glass units in this thesis are too large for achieving this type of photogrammetry strain tracking.

*Strain optic methods* are principally based on the photo-elasticity of glass. If glass is subjected to a state of stress, it becomes birefringent. This effect modifies the polarisation of electromagnetic light waves passing through the transparent material and thus allows the identification of the polarised light. Typical methods permit either local strain / stress measurement on the glass surface or through the thickness. Aben [Abe 08, p. 40], for example, gives an introduction to various strain-optical methods.

*Polarisation filters* are applied for visualising the strain / stress distribution of an entire glass panel. Therefore, light is sent through a linear or circular polarisation filter prior to being passed through the photo-elastic glass material. In the glass, the light wave is resolved into components along the principal stress directions. The stress birefringence of the isotropic glass generates two different refractive indices for the principal directions, a process that causes a phase lag of the two light wave parts. When passing through the second polarisation filter, only the phase-shifted components of the light corresponding to the filter direction are made visible for analysis. A comprehensive description of stress analysis of glass with polarisation filters is given by Feldmann, Kasper and Langosch in [Fel 12, pp. 67-85]. The main application is the quality control of the residual glass stress from tempering. The measurement of edge stress and local surface stress of glass is achieved with polariscopes by using the refraction of light at the surface of the glass [Red 04].

Through-the-thickness determination of stress states in glass is made possible with *scattered light polarimeters*, see [Abe 10, p. 150], [Abe 14, p. 241]. A laser wave passes through the glass at 45° and is subjected to a modification of its polarisation by the birefringence effect described above. The scattered light of the laser beam is polarised perpendicular to the beam direction. The scattered light intensity, tracked by a camera in the device, then allows the determination of the phase shift of the light components and thus the calculation of the stress through the thickness of the glass.

However, none of the strain optic methods are quantitatively applicable to laminated glass<sup>5</sup>, as the interlayer influences the light transfer through the laminate. Most photo-elastic measurement methods, with the exception of the above-mentioned polarisation filters, only allow for local / discrete point stress determination. An advantage of these methods is that no devices have to be inserted into the laminate (contactless).

Strain gauges of various kinds, which are fixed to a discrete point of an object at which a strain measurement is to be made, form the a large group of strain measurement devices involving contact. The most widespread technique is the bonding of temperature-resistant *electrical strain gauges* to the object of interest. Schuler [Sch 03, pp. 89-90] and Ensslen [Ens 05, pp. 146-147] report the successful application of electrical strain gauges inside of glass laminates in bending tests. However, both authors used the gauges for strain measurement only after the lamination process and no reference to the state prior to lamination was thus needed. The testing of surface-bonded electrical strain gauges as performed in the context of this thesis on small glass samples subjected to a temperature of 140°C and permanent bending strain as in section 5.1.5.2 led to erroneous results. Temperature-curing adhesives have not been used as their application to gauge bonding has been considered as not being feasible for large architectural glass samples. Another problem of electrical strain gauges for the long-term monitoring of cold bent glass comes from the fact that no relationship to an absolute measurement quantity is given. Furthermore, the gauges and their cables disturb the transparency of the glass and are therefore only of use for experimental assessment.

*Piezoelectric sensors* function based on the measurement of the electrical signal emitted by a crystal subjected to a load. The electrical charge is proportional to the applied load. They are offered, for example, as load cells or film or cable sensors. As these sensors are not well suited for long-term static loads and elevated temperature, they have been considered not being applicable for the given cold bending problem. Piezoelectric sensors integrated into yacht glazing have been proposed by [Sch 15].

*Fibre optic sensors with Bragg-gratings* are identified as a possible solution for continuous stress / strain monitoring in glass laminates. Laser light propagating in thin optical fibres of 0.12 to 0.2mm diameter is partially reflected at the gratings of the sensor. The reflected parts of the light are in phase and add up to a measurable signal of a particular wavelength. This allows the identification of the sensor location in the fibre, as a characteristic Bragg wavelength is allocated with each grating sensor. Multiplexing is possible, as several sensors can be integrated into one fibre. The fibres are thin enough to permit integration into the interlayers of glass laminates and they are barely visible. They withstand autoclaving temperatures when a suitable fibre coating is used or even when no coating is applied at all. If the fibre, which has to be glued to the glass surface at discrete points at which measurement is intended, is subjected to strain from the glass, the reflected characteristic wavelength signal exhibits a measurable shift. Measurement based on wavelength as an absolute quantity is helpful for monitoring possible changes introduced by glass bending, during the autoclave process and after release from the bending mould. Long-term monitoring is possible, as the fibre can always be used for measurement by an interrogator device. Depending on the measurement frequency of the interrogator, typically in a range of 500Hz to 1Hz, few or many wavelength-shift results can be recorded with time. The disadvantages of FBG are the adhesive bond, the installation technique and the strain tracking only at discrete locations.

More detailed explanations of FBG are given in sections 5.1.1.3 and 5.1.1.4. In the context of this work, research conducted on FBGs bonded to glass being laminated in an autoclave process has been published in [Fil 13], [Fil 14b, p. 61], [Fil 14a, pp. 289-300], [Fil 14c, p. 105]. So far, no other research on the integration of FBG in glass laminates for glass surface stress measurement has been published. Haase [Haa 14, p. 249] has proposed the use of two, equally oriented fibre Bragg grating sensors laminated into the interlayer of glass laminates to calculate the shear angle and shear stress in the interlayer as a theoretical approach.

<sup>5</sup>With the scattered light method, analyses of two-ply laminates have been conducted by measurement on both outer surfaces of the laminate, although this method does not apply to more than two glass layers.

#### 4.1.2. Displacement Monitoring

Various methods can be applied for monitoring 3D shape, deformation or displacement. Among the mechanical methods involving contact with the object of interest, *extensometers / path transducers* are frequently used in engineering. The mechanically induced movement of a transducer touching a point on the deforming object of measurement is either mechanically translated into a proportional displacement value and shown on a dial gauge or is measured electronically and processed by software. Depending on the extensometer, 1/10 and 1/100mm are typical precision values reached; 1/1000mm also exists but is highly sensitive to environmental influence. As each extensometer only tracks the displacement of one specific point, they are not suitable for the systematic 3D monitoring of the glass specimens. Extensometer dial gauges (1/100mm) applied for the measurement of the relaxation behaviour of cold bent glass in the context of this work have proved unreliable because of their sensitivity to secondary effects from the test set-up. *Surface roughness contour measurement* along a given line on the glass surface is another mechanical technology used for surface quality control. It is not applicable here, as building glass dimensions are too large for the available immobile measurement devices.

Among the contact-less techniques, laser-scanning, interferometry, deflectometry and photogrammetry can be named. *Laser scanning* typically applies the measurement of the reflection of a laser point projected onto the surface of interest. Via triangulation, the distance of the laser emitter and the 3D coordinates of the laser point on the surface are calculated and assembled into a 3D model. Laser scanning of the glass specimens has been tested with a hand-held scanning equipment but does not permit valid results to be obtained because of the transparency and reflection of the glass. A typical volumetric accuracy of such scanners is  $0.02\text{mm} \pm 0.1\text{mm/m}$ ; the scanning area is often in a range of less than  $300 \times 300\text{mm}$ . Application of a contrast spray to the glass surface for the laser has been discarded, as the total glass surfaces are too large.

*Interferometry* is a general standard application in quality control of curved surfaces. Superposition of (electromagnetic) light waves leads to interference patterns providing information concerning the

waves and, for example, their reflection from surfaces. Newton interferometry, holographic interferometry, phase shifting interferometry and vertical scanning interferometry are amongst the most typical techniques. Compensation optics with prefabricated holograms specifically adapted to a certain surface shape are often used for automated in-line quality control but they only apply to large series of identical products. Most interferometric techniques are not readily applicable to glass because of its transparency and reflection behaviour. For the assessment of the quality of car windshield production, some distortion control techniques, for example, with Moiré-patterns are used.

*Phase measuring deflectometry* (PMD) has been described to allow the measurement of the local slope of curved transparent surfaces [Kna04]. Deflectometry in general means procedures for measuring and interpreting the deflection of reflected or transmitted light. This is mainly carried out by combining a camera and a light-emitting source. Reflections of sinusoidal fringe patterns projected, for example, to a free-form surface show distortions, if the reflecting surface has discontinuous curvature, slope or other irregularities. The fringe pattern reflected from the testing object is mapped to the image plane of a camera. The change of these fringe patterns allows the mathematical calculation back onto the 3D-surface and its curvature. Precision can reach the nanometre level. This technology, applied to car windscreens as a maximum object size and small areas of  $d=0.1\text{mm}$  as a minimum size [Kna09, p. 175], was not available for this work, as it is mostly based on immobile devices in vehicle glass testing stands or as in-line testing for glass products. Large area scans for architectural glass are not yet possible, and high precision in the placement of the monitored glass with respect to the camera is needed. For the regular 8-month long-term tracking necessary for cold bent glass monitoring and for the size of the testing specimen, no access to deflectometry devices and software was possible.

To obtain complete 3D data and height information of the inspected glass objects, *stereo-deflectometry* is applied in industry for the quality control of glossy, highly reflective surfaces and of curved glass. Therefore, a second camera is added to the PMD set-up. As with photogrammetry, the identification of the same point on the glass by the two cameras from different viewing angles is used to calculate the 3D position of this point.



Mercier [Mer 14, p. 215] reports a measurement tolerance of  $\pm 0.05\text{mm}$  for this technique and a maximum glass size of  $3.40 \times 6.00\text{m}$ . This recent technology was also not available for the long-term measurement of the cold bent glass in the context of this thesis. It is, however, an attractive method for glass quality surface control for companies with a sufficiently large glass treatment output and / or high quality requirements. The typical application spectrum for interferometric / deflectometric methods in the glass business is the detection of optical defects, curvature discontinuities and other shape deviations of glass products.

With the passive contactless technique of *close range photogrammetry*, central projection is used for calculating the 3D shape of an object from at least two photographs showing the object from different angles. Therefore, photographs of sufficient quality and resolution from two positions and the interior data of the involved camera, notably the focal length, the lens distortion and the digital sensor size / resolution, have to be available. From each corresponding image point on the photographs, the spatial position of the related object point can be calculated by the intersecting bundles of rays related to the camera positions / directions (exterior orientation), the image points and the object points. Photogrammetry is becoming increasingly popular and is now even possible with mobile-phone cameras and related software solutions. As photogrammetry is applicable with high-resolution consumer digital cameras and allows a possible best measurement accuracy of  $10\mu\text{m}$  [Luh 14, p. 562], it is an attractive low-cost measurement solution of high interest for solving the issues of glass shape and displacement monitoring. Furthermore, photogrammetry analysis software is readily available at most universities and is also included in specific solutions or systems offered by the market.

However, the transparency of glass makes an application of close-range photogrammetry for shape and displacement calculations difficult, as no image points can be identified. Therefore, the proposal of measuring a grid of circular standard points attached to the glass surfaces was proposed in collaboration with the Institute of Photogrammetry (IFP) at the University of Stuttgart. This grid permits a 3D point cloud to be obtained, which serves as a base for reconstructing curved surfaces passing through the points. As shown in fig. 4.1, both fast springback deformations of the curved

glass and long-term relaxation movements have to be tracked. With close-range photogrammetry, either one camera used to take photographs of an object from different angles can be applied for monitoring of the 3D shape of glass in cases in which extremely slow or no movements are involved or 2-3 synchronised fixed cameras can be used for tracking deformations at short time intervals in order to trace relatively fast changes. Thus as it meets most criteria necessary for the shape and deformation monitoring of curved glass, close-range photogrammetry was chosen for the testing in the context of this work [Fil 14d, p. 113]. The method is explained in detail in section 5.2. No references related to 3D glass deformation monitoring were identified in the literature at the time of writing. However, strain monitoring based on industrial photogrammetry techniques has been applied to glass surfaces in recent research projects at the TU Dresden [Wel 14b, p. 541], [Wel 14a, p. 197].

## 4.2. Numerical Simulation

For comparison with the experimental stress and deformation measurements and for the general future calculation of cold bending and relaxation processes, both analytical and numerical calculation methods are possible. In this work, analytical methods as outlined in section 2.2 have not been used for characterising cold bending and relaxation. In the past four years, a number of proposals for the cold bending behaviour of single plates, e.g. by [Roy 11], [Est 13] and [Dat 14], have been made. Relaxation behaviour in cold bending is treated in [Gal 14b], [Gal 14a] and [Gal 15]. However, the approaches do not cover all cases necessary for modelling the experimental set-ups. The diploma work of Keller [Kel 12] conducted together by the ITKE and the IBB in the context of cold bending research at the University of Stuttgart has examined the applicability of linear Kirchhoff plate theory, non-linear v. Kármán plate theory and non-linear shell theory for the cold bending of a single glass sheet into double-curved shapes. For solving the constituting equations, the exact, 3D nodal displacement field of the glass pane into the desired curved shape has to be known in order to obtain valid stress results. Usually, this displacement data is not known exactly. Instead, numerical analysis with finite elements is applied, as it offers the potential to model the complex behaviour of glass bent to any kind of shape on a mould, including non-contact situations and local lift-off.

Only a few publications mentioning numerical modelling results of cold bending, lamination and relaxation are available, notably [Bel 07b], [Kas 11], [Fil 12a, p. 135], [Fil 14d, p. 113] and [Tei 14, p. 75]. Various modelling approaches can be applied, depending on the objective of the respective studies. Basically, the following starting situations can be considered for the objective of a cold bending process, compare fig. 4.5 (top):

- An initial bending geometry is given for the glass by the respective mould. After cold bending and lamination, the time- and temperature-dependent, initially unknown, springback and relaxation shape is determined. This calculation (FSD) only involves the two stages of the cold bending and the springback / relaxation. As large deformations are applied, non-linear geometrical analysis has to be used. The polymer interlayer is simulated by a material non-linear model.

- A desired final shape of the glass to be accomplished after a fixed relaxation period and temperature is given. The necessary bending mould geometry to achieve the desired shape is sought. This form-finding calculation in a finite element analysis necessitates an iterative approach (FPI). In the context of this work, this is carried out by fixed-point iteration. In each iteration step, the entire bending and relaxation process is calculated and the obtained shape is compared with the desired geometry. The difference  $\Delta x, \Delta y, \Delta z$  between the two shapes is then added to the cold bending deformation set and the analysis is run again. These steps are repeated until a defined tolerance between the shapes is met.

Fixed-point iteration in a numerical analysis [Mey 03, p. 132] is applied to calculate a fixed point  $x^*$  by iterating a function  $f(x_n)$

$$x_{n+1} = f(x_n) \quad n = \{0, 1, 2, \dots\} \quad (4.1)$$

which, starting with an initial arbitrary values of  $x_0$  and following  $x_1, x_2$  etc., should converge to the point  $x^*$ . Figure 4.5 schematically depicts the two principal model approaches outlined above. Furthermore, the two basic methods FPI and FSD each give rise to different boundary conditions for approximating the cold bending process:

- A given forced nodal displacement (FPI.1, FSD.1) is applied to each node of the mesh of the glass to achieve an exact cold bending shape. This can either be any point cloud or an explicit shape function describing the bending geometry. This deformation method is easily applied in a model but it does not correspond to the bending shape achievable on a real bending mould on which the homogeneous application of a deformation to the entire glass surface will not be possible. The forced displacement of only the nodes along the edges of the glass is also possible; this corresponds more closely to the real deformation applicable on a bending mould as shown in figs. 4.2, 4.3.
- For a more realistic approach, contact and target elements are used (FSD.2). Contact elements are applied to the bottom surfaces of the glass panes and target elements to the surface of the mould. These contact elements have to permit friction and the possible lifting of the glass from the mould during the bending process. The symmetry of the specimens allows the establishment of a quarter model as shown in fig. 4.3.

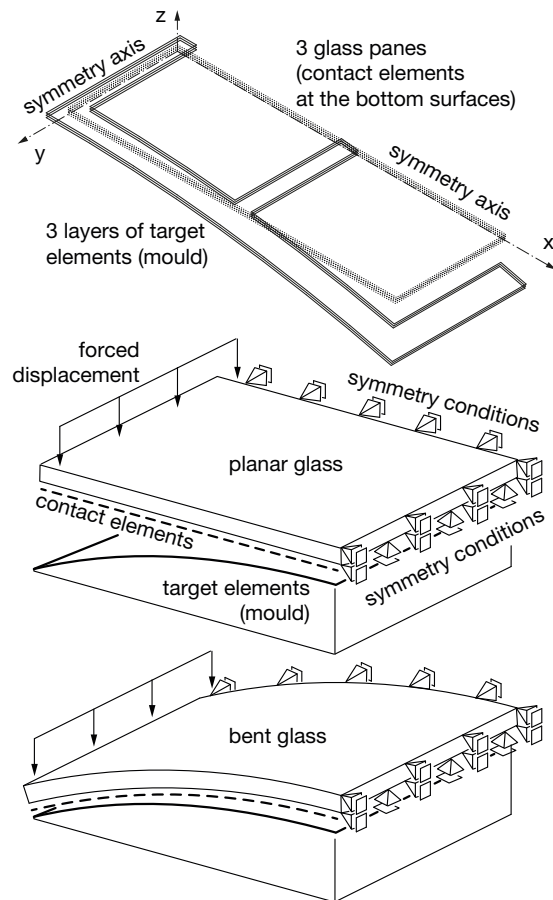


**Figure 4.3.:** Target and contact element configuration of a symmetric quarter model of the bending mould and glass panes.

The contact element model can also be applied in the fixed point iteration, although this results in an extremely large model with long solution periods and is therefore not considered further here. In figure 4.5 (bottom), the modelling strategies explained at the top of the same figure are applied to the example of a single-curved bent glass.

For numerically simulating the cold bending tests performed in this work, in which the glass is bent upon a given mould geometry, the first principal method (FSD, fig. 4.5) can be applied. The model set-up is given in section 6.2. Based on this, the iterative bending mould form-finding approach is explained in section 7.2.1 in fig. 7.13.

As mentioned in section 2.2, the time- and temperature-dependent shear properties of the interlayer are decisive for the recovery behaviour of the entire laminate. In the present work, both PVB and SentryGlas® interlayers have been used

for the lamination of the cold bent specimens for testing. PVB can be described as a viscoelastic material with a time-dependent decrease of the shear modulus mathematically expressed by a Prony series [And 14], [Gal 14b] (section 5.3). This method also applies to SG, even though the material mainly has an elastically behaviour at room temperature. Depending on their composition, the bent and laminated glass specimens exhibit a pronounced initial springback at the moment of release from the bending mould, fig. 4.4. The initial springback is necessary to activate the shear compound of the glass panes and the interlayer and is principally comparable with the sandwich effect and an applied exterior load [Sta 74]. The springback with the related recovery deformation causes a sudden shear strain in the interlayer constrained between the two glass layers; this leads to a quasi-elastic short-term reaction of the interlayer. Thus, this initial part of the springback is mainly governed by the elastic properties of the interlayer and can have a strong influence in the model. In parallel, the molecular chains of the interlayer shift against each other and a time-dependent viscous behaviour (entropy-elasticity) takes place that gradually reduces the shear stress in the interlayer. However, this leads to a loss of curvature of the laminate and the shear angle of the interlayer increases. The recovery process thus depends on the time, temperature and the acting shear. Principally, the time-dependent recovery behaviour of the glass laminate can be described with both the terms of creep or of relaxation. Neither the stress nor the shear in the interlayer are exactly constant with time, as the recovery of the bent laminate causes a continuous change of both quantities. In the literature, the rheological behaviour of the interlayer is usually described as relaxation by using the Maxwell-Wiechert model with a Prony series. This accepted method has therefore been chosen for this work in section 5.3.

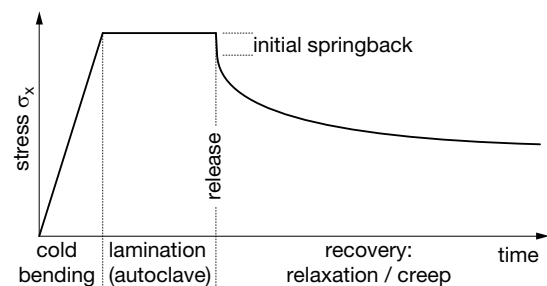


**Figure 4.4.:** Schematic diagram depicting the principal phases of cold bent and lamination.

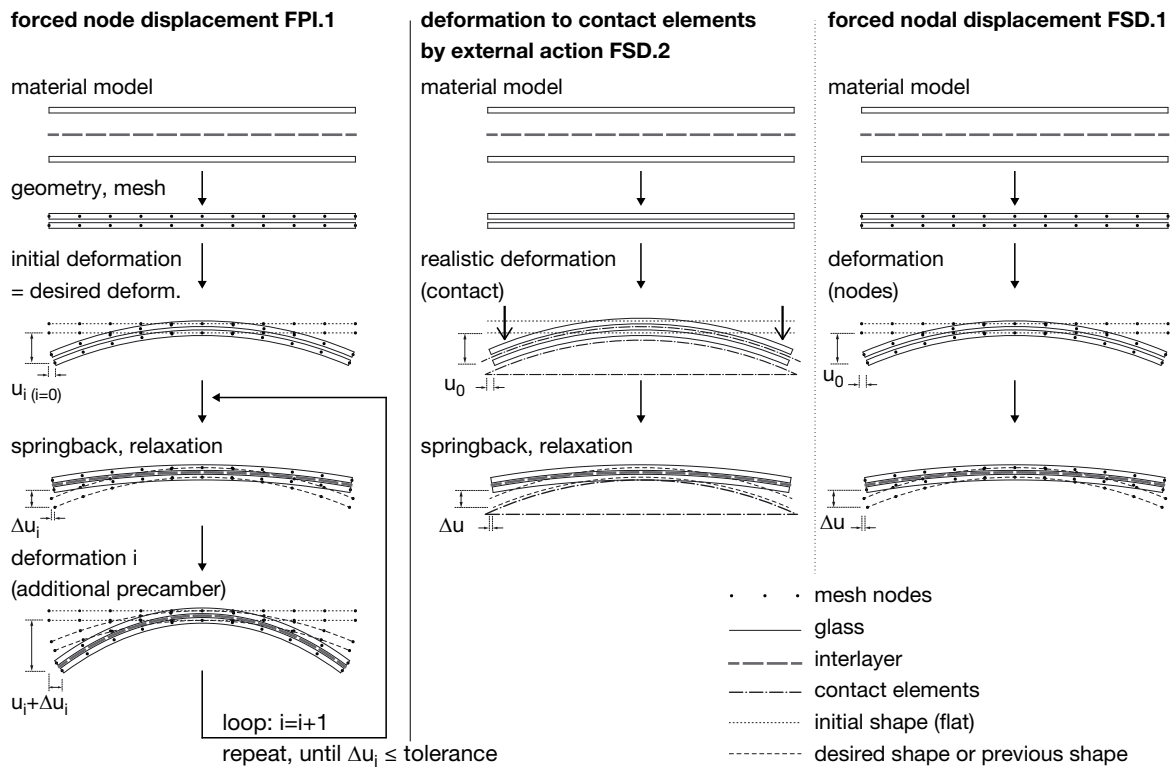
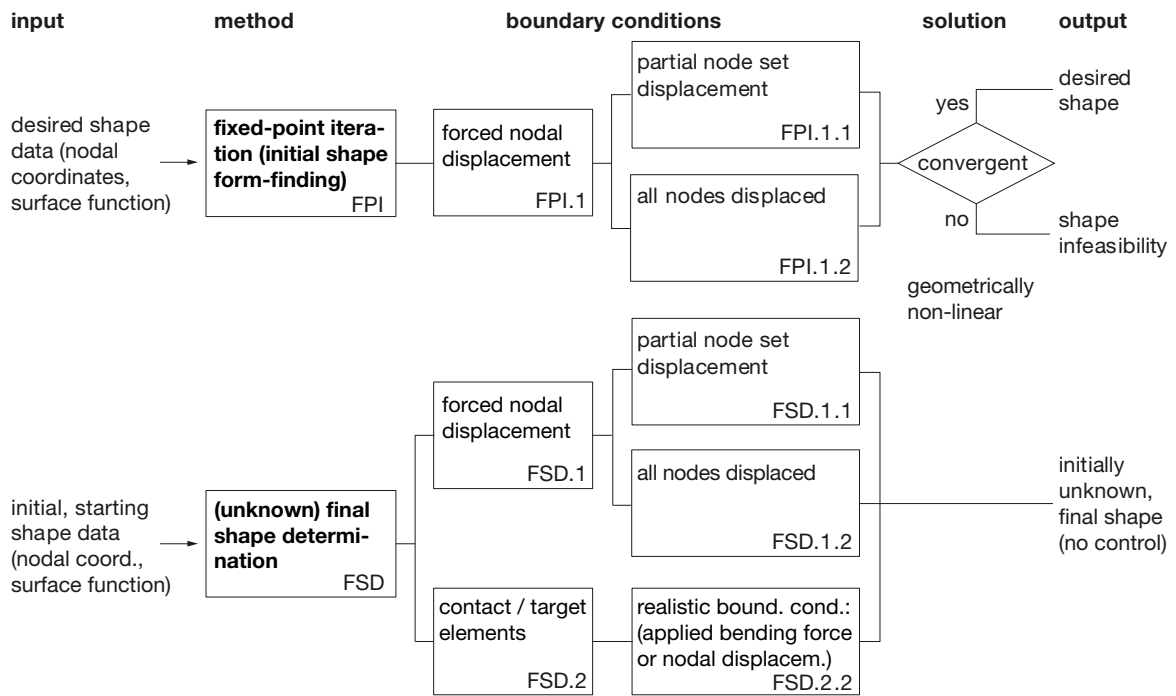


Figure 4.5.: Top: diagram of the applicable finite element design strategies for cold bending and relaxation modelling of glass; bottom: application of the FE-modelling procedures from above for single curvature bending.

## **5 Analysis, Diagnostic**

## 5.1. Fibre Optic Sensing

### 5.1.1. Fibre Optics and Applicable Sensing Principles

The basic choice of fibre Bragg gratings for strain sensing in this work is described in section 4.1.1. Multiple parameters affect strain / stress measurements by optical fibres in laminated glass: the cold bending and lamination processes in an autoclave have an influence on the strain transmission in-between the glass substrate and the fibres glued to its surfaces. Furthermore, temperature effects have a strong influence on the fibres and the sensor results. The sensor response consists of temperature- and strain-related components that have to be separated in order to interpret the actions to which the fibre and glass are exposed to. Silica waveguides with Bragg gratings have not yet been used in laminated glass and its manufacturing procedures; they represent a new topic for engineers and designers working with building glass. Therefore, the following sections give a synopsis of the theory behind fibre optic sensing, provide an overview of the state of technology and of research and describe the principal parameters necessary for the understanding, processing and interpretation of the samples tested with optic sensing equipment presented in this work.

#### 5.1.1.1. Optical Fibres

Optical fibres nowadays are commonly used for light signal transmission, filtering and amplification in telecommunications and for physical, chemical and temperature monitoring in sensing networks. This is based on the development of optical waveguides having a low loss of the transmitted light during the 1960s [Oth99, p. 1]. Optical fibres, typically made from fused silica glass ( $SiO_2$ ), can be characterised as dielectric optical waveguides having a cylindrical axis of symmetry [Bro95]. Most optical fibres consist of a small core, surrounded by a cladding and a protective coating. Glass fibres of the type used for sensing purposes usually have a typical cladding diameter of  $125\ \mu\text{m}$  or, less frequently, of  $60\ \mu\text{m}$  or  $80\ \mu\text{m}$ . The waveguiding core measures  $9\ \mu\text{m}$  or  $4.3\ \mu\text{m}$  in diameter. Typically, the fibre is produced in a drawing-out process from a silica glass preform. The cross section and composition of the preform, having a diameter of several centimetres,

has affinity to the much smaller final fibre diameter. The preform is often produced through the modified chemical vapour deposition (MCVD) process: the inner surface of a heated rotating silica glass tube is coated with silica glass particles doped with additional gaseous chemical substances. Finally, the resulting tube is collapsed into the massive preform shape by heating, fig. 5.1. For guiding a lightwave in the core by total internal reflection, the refractive index of the silica core needs to exceed the index of the cladding. Therefore, doping substances such as Germanium-oxide  $GeO_2$  are added to the core during the production of the preform. In order to obtain the final optical fibre, the preform is heated in an oven to about  $1850\text{-}2000^\circ\text{C}$  and then drawn out to the final dimensions in a vertical process. For choosing a fibre type, the following properties given by the manufacturer have to be known.

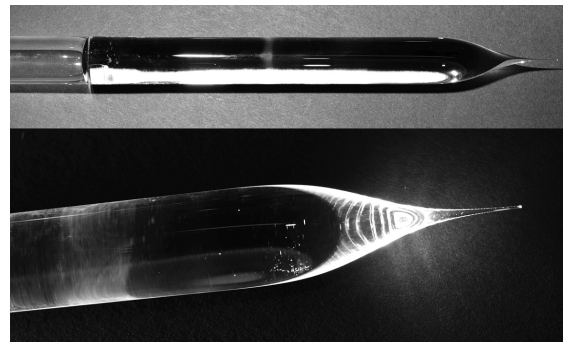


**Figure 5.1.:** Fused silica preform for optical fibre drawing (top) and tip detail (bottom). Source: Courtesy of FBGS Technologies GmbH, Jena

The basic type of an optical fibre is the *step index fibre*, fig. 5.2. The constant indices of refraction of the fibre core  $n_1$  and the cladding  $n_2$  are different to allow the total reflection of passing light rays at the boundary of the core and cladding. For enhancement of the speed of communication in a fibre by minimising the modal dispersion [Sal91, p. 273], *graded index fibres* are used. The refractive index is graded from its maximum in the core towards the cladding. For the continuous guidance of light rays in the fibre core, the lightwaves must comply to a self-interference condition. A limited number of paths, which are analogous to the propagation of electro-magnetic modes in the core, adheres to this constraint. Typical fibres for structural monitoring have a small core allowing only a few modes to propagate. This type of fibre is principally described with the help of Maxwell's equations.

### 5.1.1.2. Light Propagation and Guidance in Optical Fibres

Light rays, e.g. from a laser, are guided through a fibre core by total internal reflection, if their incidence angle on the interface of the core and the cladding is larger than the critical angle  $\theta_c$ .

$$\theta_c = \arcsin\left(\frac{n_2}{n_1}\right), \quad (5.1)$$

where  $n_1$  is the refractive index of the fibre core and  $n_2$  the refractive index of the cladding, fig. 5.2. Total reflection necessitates  $n_1$  in the fibre core to be increased compared with the index of the cladding,  $n_2$ . As the difference of both indices is usually small, the change of the fractional refractive index  $\Delta$  can be expressed by

$$\Delta = \frac{n_1^2 - n_2^2}{2n_1^2} \approx \frac{n_1 - n_2}{n_1} \quad (5.2)$$

Four different types of ray propagation paths can occur in an optical fibre, fig. 5.2: *Meridional rays* pass through the symmetry axis; they adapt to the self-interference condition. Meridional rays propagate in a plane passing through the fibre axis  $z$ . Their angle with the fibre axis has to be smaller than the complementary critical angle  $\bar{\theta}_c$  [Sal 91, p. 275]

$$\bar{\theta}_c = \frac{\pi}{2} - \theta_c = \arccos\left(\frac{n_2}{n_1}\right), \quad (5.3)$$

comparable to the guiding condition formulated above. *Leaky rays* are nearly totally reflected internally but their propagation is limited. *Cladding modes* are formed by rays leaving the core to be reflected at the boundary of the cladding and coating. *Skew rays* propagate in the fibre core, but do not pass through the  $z$ -axis. Skew rays lie in planes<sup>6</sup> parallel to the fibre axis and follow a helical path within the core.

A ray entering the fibre from outside is guided, if it is refracted into the core with an angle smaller than  $\bar{\theta}_c$  (see fig. 5.2). Snell's law of refraction<sup>7</sup> dictates the acceptance angle  $\theta_a$  in the air for incident light

and the angle  $\bar{\theta}_c$  in the core, which are related by:

$$\frac{\sin \theta_a}{\sin \bar{\theta}_c} = \frac{n_1}{1} \quad (5.4)$$

$$\Rightarrow \sin \theta_a = n_1 \sqrt{1 - \cos^2 \bar{\theta}_c} = \sqrt{n_1^2 - n_2^2}$$

The expression  $\sqrt{n_1^2 - n_2^2}$  is called the numerical aperture  $NA$ , which thus is related to the acceptance angle by:

$$\theta_a = \arcsin NA \quad (5.5)$$

$NA$  can also be written as:

$$NA = n_1 \sqrt{2\Delta} \quad (5.6)$$

by using  $\Delta 2n_1^2 = n_1^2 - n_2^2$ . The NA-parameter basically provides information about the refractive index difference of the core and the cladding of an optical fibre and about the capacity of an optical fibre to gather light. The acceptance angle describes an incidence cone that rays coupled from outside into the fibre have to meet to be guided inside the fibre [Sal91, p.277].

Generally, optical fibres are distinguished as single mode fibres (SMF) and multi-mode fibres (MMF). Whereas the latter allow the propagation of several modes<sup>8</sup> in the fibre and therefore have a large waveguiding core diameter ( $> 50\mu\text{m}$ ), an SMF has a small core diameter below  $9\mu\text{m}$ . In the present work, SMF are used exclusively, as they are readily available from various commercial manufacturers and are typically applied for the inscription of fibre-Bragg sensors for strain measurement purposes. Advanced fibres such as polarisation-maintaining fibres with a different section build-up have not been used, as they are still the object of research, e.g. [Sin 12], see section 5.1.4.2. SMF are mostly produced as step-index fibres. An SMF allows only for the propagation of the so-called  $LP_{01}$  transverse mode. The field analysis and solution for a step index fibre cited here is principally based on the work of Buck [Buc 95, pp. 51-63], where more details can be found.

<sup>6</sup>These planes have an angle  $\phi$  with the normal to the core boundary and a constant distance from the axis; thus, they do not pass through the axis.

<sup>7</sup>Snell's law:  $\frac{\sin \theta_1}{\sin \theta_2} = \frac{n_2}{n_1}$

<sup>8</sup>Modes designate the spatial distribution possibilities of waves in the fibre. Each mode corresponds to a particular electromagnetic field pattern. Typical modes in an optical fibres are transverse modes, which are orthogonal to the fibre's longitudinal axis.

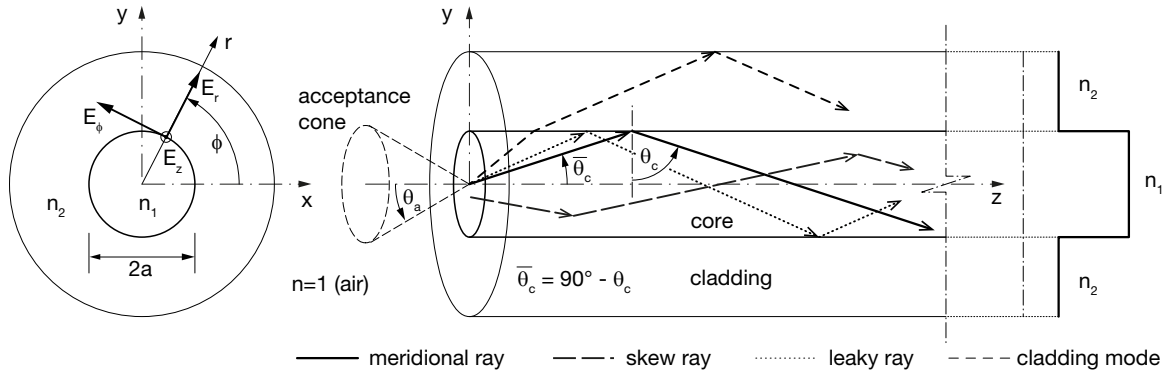


Figure 5.2.: Ray propagation types and relevant angles in step-index fibre.

Monochromatic light propagating in a step index fibre can be described by electromagnetic theory. The electric and magnetic fields then have to comply with Maxwell's equations and the boundary conditions given by the cylindrical dielectric silica fibre core. A light ray propagating in a fibre is associated with two plane waves. Only certain angles  $\theta$  permit rays to propagate, each possible angle corresponds to a single mode in the waveguide. The electric and magnetic components of the plane waves are expressed by the electric ( $E$ ) and magnetic ( $H$ ) field phasors<sup>9</sup>. For guidance of the wave in the fibre, the respective propagation constant  $\beta$  has to exceed the combined wavenumber  $k_0$  and refractive index  $n_2$  in the cladding, but must be smaller than both values  $n_1 k_0$  in the core:

$$n_2 k_0 < \beta < n_1 k_0 \quad (5.7)$$

The important radial distribution  $R(r)$  of the axial fibre direction component of  $E$  can be expressed by a Helmholtz equation, which is solved by two differential equations and by Bessel functions  $J_l(x)$ ,  $K_l(x)$  of the order  $l$ . For the  $LP_{01}$  mode mentioned above, a Gaussian-shaped concentration of  $R(r)$  and the related mode field energy in the fibre core and a fast decay in the cladding are shown in fig. 5.3. The decay in the cladding is described by the mode field diameter (MFD)<sup>10</sup> The  $LP_{11}$  mode has less energy concentrated in the core and reaches into the cladding. Each mode is defined by the azimuthal index  $l$  and the respective radial distribution indices

$m$  in the linearly polarised form of  $LP_{lm}$  [Lin 12, p. 6].

The V-parameter, called the normalised frequency, describes the relationship of the fibre geometry, its refractive index conditions and the guided modes and is also related to the numerical aperture  $NA$  by

$$\begin{aligned} V &= \sqrt{X^2 + Y^2} = a k_0 \sqrt{n_1^2 - n_2^2} = a k_0 NA \\ &= 2\pi \frac{a}{\lambda_0} NA \end{aligned} \quad (5.8)$$

The effective refractive index  $n_{eff}$  of a fibre for guided modes is defined for each propagation constant and wavenumber by eq. 5.9 [Buc 95, p. 72] [Lin 12, p. 7]

$$n_{eff} = \frac{\beta}{k_0}, \quad n_1 < n_{eff} < n_2 \quad (5.9)$$

For V-parameters roughly between 1.5 to 2.5,  $n_{eff}$  lies between  $n_1$  and  $n_2$ . Large V-parameters occur for  $n_{eff}$ -values close to the core index  $n_1$ ; the waves propagate with reflection angles larger than the critical angle and stay in the core (fast decay in the cladding). If  $n_{eff}$  becomes equal to the value of  $n_2$  of the cladding, the respective mode is no longer guided in the core. This limit is called the *cut-off* value for the mode. In the case of the fundamental mode  $LP_{01}$ , which is not cut-off with  $V < 2.405$ , this value of V also delivers the limit for a SMF, which guides only this single mode  $LP_{01}$ . The cutoff

<sup>9</sup>A phasor is a phase vector describing a sinusoidal function, such as a wave. The amplitude, frequency and phase are time-invariant and are separated into three independent factors in the phasor.

<sup>10</sup>The MFD of the FBGs applied in this work with a  $\lambda_{B,0}$  between 1510nm to 1590nm is given by the manufacturer as  $6\mu\text{m}$ . This is slightly larger than the core diameter of  $4.3\mu\text{m}$  of the fibre; thus a small part of the Gaussian-shaped intensity profile of the transverse  $LP_{01}$ -mode is reaching into the cladding.



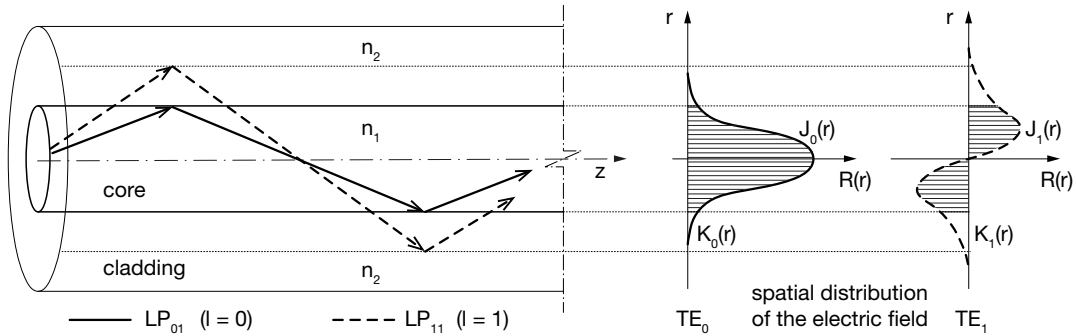


Figure 5.3.: Radial distribution  $R(r)$  for  $l = 0$  and  $l = 1$  based on [Sal 91, p. 278]; hatches indicate the part in the fibre core.

wavelength  $\lambda_c$  for an SMF can be calculated by

$$\lambda_c = \frac{2\pi na}{2.405} \sqrt{2\Delta} = \frac{2\pi a}{2.405} NA \quad (5.10)$$

The refractive indices of the SMF used in this work are  $n_1 = 1.454$  and  $n_2 = 1.43$  giving  $NA = 0.263$ . The core diameter is  $2a = 4.3\mu\text{m}$  and subsequently  $V = 2.35 < 2.405$ . The cut-off wavelength for  $LP_{01}$  as in eq. 5.10 for  $V = 2.405$

gives  $\lambda_c = 1478\text{nm}$ . The conditions for a SMF are fulfilled. An NA of 0.26 indicates a fast decay of the intensity profile of the mode  $LP_{01}$  in the cladding and thus the fibre should show little energy loss in bending.

In conclusion, the principal control and characterisation parameters of optical waveguides are summarised in table 5.1.

symbol	unit	definition	title, description
$V$	[-]	$V = \sqrt{X^2 + Y^2} = ak_0\sqrt{n_2^2 - n_1^2} = ak_0NA = 2\pi \frac{a}{\lambda_0} NA$	normalised frequency; V-parameter (determines the possible modes and cut-off in a step-index fibre); if $V < 2.405$ , only one fundamental mode exists, no cutoff
$NA$	[-]	$NA = \sqrt{n_1^2 - n_2^2} = n_1\sqrt{2\Delta}$	numerical aperture (describes the range of angles allowing light to enter and / or to propagate in it)
$\Delta$	[%]	$\Delta = \frac{n_1^2 - n_2^2}{2n_1^2} \approx \frac{n_1 - n_2}{n_1}$	normalised refractive index difference; assuming $n_1$ being only slightly bigger than $n_2$
$n_{eff}$	[-]	$n_{eff} = \frac{\beta}{k_0} = \sqrt{bNA^2 + n_2^2}$	effective refractive index of a mode (effective guide index); condition for mode guidance: $n_1 > n_{eff} > n_2$
$M$	[-]	$M = \frac{V^2 4}{\pi^2}$ for $V \gg 1$ or $M = \frac{V^2}{2}$ for large $V$	total number of guided modes in a multimode fibre
$b$	[-]	$b = 1 - \frac{X^2}{V^2} \approx \frac{n_{eff} - n_2}{n_1 - n_2}$	normalised propagation constant; change of the amplitude of a propagating wave in a fibre ( $0 < b < 1$ for modes to propagate)
$\beta$	[-]	$\beta = \frac{2\pi}{\lambda} n_{eff}$	propagation constant of a mode; if $\beta < n_2 k_0$ , power is lost from the core into the cladding.

Table 5.1.: Summary of the principal control parameters of optical waveguides

### 5.1.1.3. Fibre Optic Sensors and Photosensitivity

The fibre and light guidance properties described above enable the use of a waveguide as a fibre optic sensor. Numerous sensing purposes can be fulfilled by fibre optic sensors, for example, of mechanical (strain, pressure, cracks, vibration, rotation, flow), chemical (aggregate states, substances) or environmental (temperature, humidity) influence. Basically, the measurement of either transmitted or reflected light in the fibre is possible. Furthermore, the various properties and modulation of the light give rise to the following sensor categories [Yin 08, pp. 2-34]:

- interference-based types (phase modulation)
- intensity-based types (intensity modulation)
- spectrally-based types (wavelength / spectrum modulation)
- polarisation-based types (polarisation modulation)

The sensor type can additionally be distinguished by the sensor region. With *extrinsic* (hybrid) sensors (also called extrinsic fibre etalon), the light modulation by an exterior action happens outside the fibre core. The fibre itself is used as a light carrier. A frequently used, common, extrinsic type is the Fabry-Pérot sensor (FPS). This sensor type is made up of a gap in the fibre. With *intrinsic* (all-fibre) sensors, the sensing region is situated directly inside the fibre as an integrated part of it. In this case, the light passing through the fibre is modulated by exterior actions affecting the fibre or the sensing region. Intrinsic sensors thus do not necessitate the interruption of the fibre. Discrete fibre Bragg gratings (FBG) in which the refractive index of the core material is permanently changed to reflect a particular wavelength band of the light are a common example of an intrinsic sensor type. An overview and categorisation of fibre optical sensors is shown in table A.1 in appendix A.1.

*Intensity-based* sensors as the most basic sensor type, rely on the measurement of a changing intensity of light passing through a waveguide. The fibre itself acts as a propagation medium for the light

input and output. The sensor is usually situated outside the fibre. The FPS mentioned above is a typical member of the intensity-based category. Typically, only one sensor can be applied per fibre.

*Interference-based* sensors rely on the measurement of differential light propagation in a fibre. The light propagation velocity differs depending upon the refractive indices of the fibre. The refractive index itself is changed by temperature and mechanical strain. Typically, the light velocity differences are extremely small. Michelson, Mach-Zehnder and Sagnac interferometers or ring resonators are typical methods of interference-based sensing.

*Spectrally-based* fibre optic sensors are widely used for a broad application range including strain, temperature, viscosity, humidity and chemical sensing. They measure the modulation of the wavelength (spectrum) of light propagating in a fibre caused by exterior action on the fibre. The most common sensor of this type is the Bragg<sup>11</sup> grating. Its function is comparable to that of an electrical strain gauge. Bragg gratings rely on the periodic modulation of the refractive index of the core of an optic fibre serving as a reflection filter for particular wavelength bands. The reflected wavelength shows a measurable shift if the fibre is subjected to mechanical strain or temperature. The advantages of fibre optic sensors are [Yin 08, p. 2]:

- Small fibre diameter, barely visible, lightweight
- Immunity against electromagnetic radiation / fields
- Low power consumption
- Passive system
- Accepts high strain rates
- Robustness: can withstand high temperature and harsh environmental conditions
- Large bandwidth
- High sensitivity
- Multiple sensors in one fibre (quasi-distributed), multiplexing

<sup>11</sup>Sir William Henry Bragg and William Lawrence Bragg were awarded the 1915 Nobel Prize in physics for their description of the constructive interference and related angles of X-irradiation scattered in crystal lattices through Bragg's law (or Bragg condition).

<sup>12</sup>As in 2014, Bragg grating interrogators necessitate investment in a range of 13,000€ - 30,000€. Expenses for optic fibres and sensors depend on the applied sensing technology, fibre types and coatings; 10€ to 50€ per meter fibre length including one or more Bragg sensors are the typical cost range.

The disadvantages include the high cost of measurement equipment<sup>12</sup>, the sensitivity to accidental mechanical rupture, the difficulty of separating temperature-induced effects from mechanical strain. In addition, gratings show birefringence for reflected light if subjected to transverse loads, making interpretation of strain results difficult.

Multiplexing [Yin 08, p. 24] is possible for some of the intrinsic or extrinsic sensor types and is applied in large sensor networks or long fibres with many sensors. A single optical channel can be used to measure a large number of sensors. Fibres with multiple inscribed sensors (e.g. many Bragg gratings in a single fibre), multiplexing or arrays of sensor fibres can be used to establish *quasi-distributed sensor networks*. However, this approach still uses discrete sensors with particular locations in the fibres and is limited by the number of fibres connected to an interrogator or multiplexer and the number of sensors supported by a fibre<sup>13</sup>.

In contrast to quasi-distributed sensors, *distributed sensors* allow the spatial measurement of strain or temperature along the entire optical fibre length as a function of position and time or frequency. The fibre itself functions as a sensor. The method principally relies on the scattering patterns of light caused by the imperfections in the fibre material and their changes attributable to strain and temperature influences. For the sensing and monitoring, optical backscatter reflectometers (OBR) are used. Two principal methods are applicable:

*Brillouin scattering* occurs when light propagating in a fibre interacts with acoustic waves developing through the influence of density and refractive index variations<sup>14</sup>. Shifts in the SBS frequency are caused by strain and temperature influencing the refractive index variations of the fibre. The time lag between the signal input and output is used to identify the location of the reflected signal.

The measurement technique is thus called optical time-domain reflectometry (OTDR). Actually, 0.5m resolution and distances of more than 20km are feasible [Nöt 14].

In contrast to non-linear Brillouin scatter, linear *Rayleigh scattering*<sup>15</sup> is caused by random density and index variations of the fibre material. Optical frequency-domain reflectometry (OFDR) is used to track the Rayleigh scattering intensity profile, which is shifted by strain in the fibre, along an optic low-loss fibre passed by light signals. Spatial resolutions of about 1cm can be attained depending on the bandwidth of the interrogator; fibre lengths are below 70m [Sam 12].

Densely spaced Bragg gratings of the same wavelength each can also be measured using an OFDR device. This technique permits a spatial resolution below 1mm; the minimum spacing of FBGs for this device is 10mm. OTDR and OFDR technology are attractive monitoring technologies, as they provide high measurement resolution along the entire fibre length. However, the cost of interrogation instruments for this relatively recent technology is still very high<sup>16</sup>.

The propagation of light in an optical fibre can be influenced by modifications of the refractive index of the silica material, as mentioned in section 5.1.1.2. Refractive index changes are typically generated by taking advantage of the *photosensitivity* of waveguides, that designates the permanent modification of the refractive index of the fibre core, when exposed to light of a certain intensity and wavelength characteristics. This is typically reached by applying UV laser light. The photosensitivity of waveguides was detected in 1978 by Hill et al. [Hil 78]. The grating was established because of the sensitivity of the fibre to a standing wave pattern formed by light reflected from the fibre end interfering with the light passing through the waveguide [Hil 97, p. 1264]. This periodic modulation of the refractive index

<sup>13</sup>Most interrogator devices, e.g. for fibre Bragg gratings, procure 4, 8 or 16 channels. A maximum 25 up to 40 sensors per fibre and channel is possible depending on the necessary spacing between the Bragg wavelengths of the single gratings.

<sup>14</sup>Léon Brillouin theoretically described the interaction of acoustic waves and light causing a scatter photons of the latter in 1922. High power (laser) light can cause such acoustic excitation in an optic fibre resulting a backscatter of light particles, called stimulated Brillouin scatter (SBS).

<sup>15</sup>Rayleigh scattering is named after John William Strutt, 3rd Baron Rayleigh. Light waves are scattered through particles or density variations being substantially smaller than the wavelength of the light.

<sup>16</sup>State-of-the-art OFDR optical backscatter reflectometers cost about 120,000€.

is called a “Hill grating”. Meltz et al. in 1989 exposed the side of a Germanium-doped fibre to two intersecting beams of UV-light, thus inscribing a periodically modified index grating into the fibre core, called the “transverse holographic technique” [Hil 97, p. 1264], [Oth 99, p. 3].

Previously existing defects in the silica core and a modification of its interior stress state through exposure to light are considered as two main aspects affecting photosensitivity [Lin 12, p. 8]: core defects occur during preform manufacturing as so-called germanium-oxygen deficient centres (GODC). These defects are photo-sensitive to certain wavelengths of UV laser radiation, e.g. 240 nm. The UV-induced transmutation of the initial defects reacting to 240nm light causes a change of the refractive index of an order of magnitude of  $10^{-5}$  to  $10^{-3}$  in the section of the core exposed to the UV-laser. This effect is described by the “F-centre model (colour centre model)” [Lin 12, p. 9]. The second approach is to assume a modification of interior stress states in the glass through UV-light influence by means of the “stress relief model” and the “compaction model”. Other approaches are discussed in [Oth 99, pp. 60-76].

Doping the preform of the core with Germanium linearly affects the number of defects in the silica and thus the sensitivity to a UV-induced modification of the refractive index [Lin 12, p. 10]. Furthermore, the chemical environment during the collapsing of the preform tube influences the sensitivity. Other methods to achieve an increased photosensitivity are a pre-exposure to UV laser light of a radiation below 240nm or an exposure of the glass to a hydrogen saturated atmosphere prior to the inscription of the gratings. In this way, a  $\Delta n$  of up to  $10^{-2}$  has been achieved [Hil 97, p. 1264].

In the present research, measurement of mechanically induced strain in laminated glass has to be performed. In the case of cold bent glass, the FBG bonded to the glass has to measure correct strain rates prior to and following the autoclave process. The main conditions with which such a sensor has to comply with are:

- Fit into the interlayer thickness (minimum 0.76mm) between the glass layers
- High strain rate acceptance (thermal expansion at 140°C)

- No obstruction of the laminate transparency
- Application of multiple sensors in one fibre, arrays
- Robustness and resistance with respect to lamination procedure in an autoclave: T=140°C, pressure up to 13bar, vacuum bagging
- Short- and long-term monitoring
- Applicable bonding technique, e.g. adhesives resisting autoclave conditions
- Availability, partial industrialisation, price-competitiveness

Electrical strain gauges are not applicable, as the gauges and the electrical cables obstruct the transparency of the glass. Furthermore, the electrical resistance can be altered in the autoclave. The strain transmission under high temperature can be incomplete attributable to the small available adhesion area around the gauge grid. Thus, fibre optic sensors have been chosen because of their robustness with regard to temperature and their small diameter below 0.2mm. From the technologies explained above, FBGs comply with the project requirements. The fibres (d=0.195mm) used in the context of this project are manufactured in a draw tower process applying a 248nm (UV) Krypton-Fluoride excimer laser. The core is doped with 18mol% Germanium; no hydrogenation has been undertaken. The maximum operation temperature is 200°C. A stiff and resistant inorganic-organic hybrid polymer coating is available for this fibre type.

#### 5.1.1.4. Bragg Gratings

A Bragg grating inscribed in an SMF as described in section 5.1.1.2 is formed by a periodic index modulation along a short section of a length  $L$  of the fibre core. Because of the reflection of incident light at the periodic grating fringes, a resonant coupling of reflected or diffracted modes of a selected wavelength band  $\lambda_B$  can be achieved, fig. 5.4. Each grating along  $L$  consists of a zone with a modified refractive index, which causes a small portion of the light wave to be reflected<sup>17</sup>. For a refractive index period  $\Lambda$  measuring half of the wavelength  $\lambda_B$ , the reflected portions interfere and form a strong, measurable counterpropagating wave. The Bragg grating thus functions as a selective, dielectric-like wavelength mirror or a reflection filter.

<sup>17</sup>Fresnel reflection principle, see [Lin 12, p. 13].

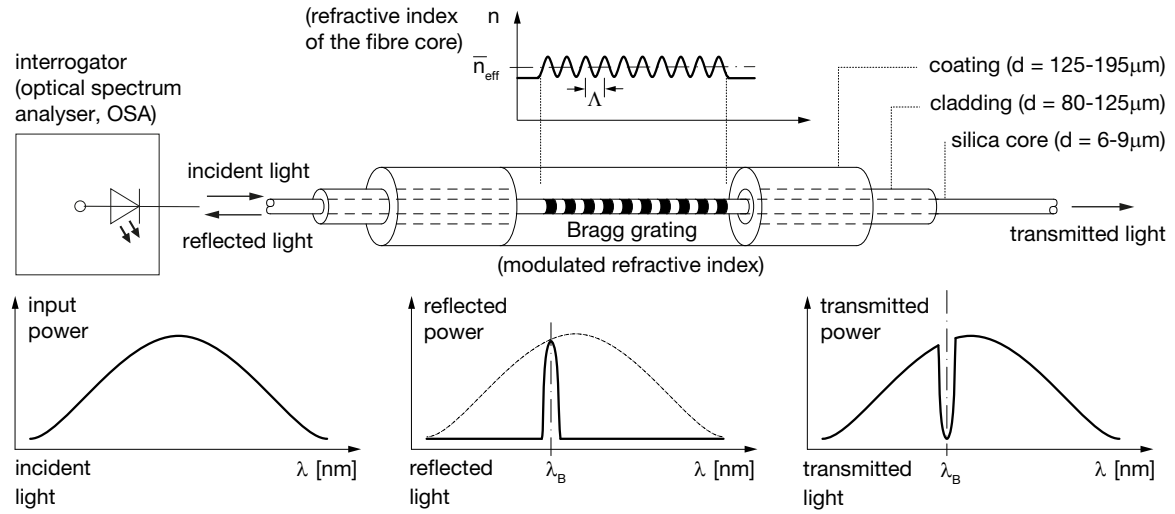


Figure 5.4.: Schematic diagram of the function principle and reflection of a Bragg grating inscribed in a fibre core.

Perturbations to the effective refractive index  $\Delta n_{eff}$ , see 5.1.1.3 and 5.1.1.2, of the guided mode can be expressed by the sinusoidal expression [Oth 99, p. 191], [Erd 97, p. 191], [Hil 97, p. 191]

$$\Delta n_{eff}(z) = \overline{\Delta n_{eff}}(z) \left[ 1 + p \cos \left( \frac{2\pi}{\Lambda} z + \varphi(z) \right) \right] \quad (5.11)$$

as a periodic waveform with a modulated phase and amplitude.  $\overline{\Delta n_{eff}}(z)$  is called the *DC-part* of the averaged index change over the grating period,  $p$  defines the contrast (ratio of the amplitude of the index change and the averaged index change) of the index change indicated by the fringe pattern visibility of the grating.  $\overline{\Delta n_{eff}}(z)p$  in the equation thus defines the *AC-part* of the amplitude of the index change.  $z$  is the distance along the longitudinal fibre axis,  $\Lambda$  is the nominal Bragg period and  $\varphi(z)$  takes a possible grating chirp into account. The averaging of the refractive index is always related to just one respective Bragg period. The AC-term, which describes the refractive index amplitude change (modulation amplitude), can be replaced by  $\Delta n_{AC}(z)$ ; the DC-term correspondingly by  $\Delta n_{DC}(z)$  [Lin 12, p. 14]. The DC-term expresses the difference of the core index  $n_1$  and the averaged effective refractive index  $\overline{n_{eff}}$  of the grating (index modulation). This simplifies (5.11) to the index modulation equation

$$\Delta n_{eff}(z) = \Delta n_{DC}(z) + \Delta n_{AC}(z) \cos \left( \frac{2\pi}{\Lambda} z + \varphi(z) \right) \quad (5.12)$$

Figure 5.5 schematically depicts the reflection of a wave at the periodic gratings and the related index change parameters.

The index change  $\Delta n_{eff}(z)$  and the grating period along the fibre core axis  $z$  are the key parameters for controlling the optical behaviour and properties of a grating. For *uniform gratings*,  $\Delta n_{DC}$  and  $\Delta n_{AC}$  do not depend on  $z$ ;  $\varphi$  becomes zero. The period is constant. Figure 5.5 shows the principle of a uniform Bragg grating. Non-uniform gratings can be either tilted, chirped or apodised. Periodic superstructures and discrete phase shifts are other non-uniform grating types.

The principles of photosensitivity allowing gratings to be inscribed in a silica fibre by locally and periodically changing the refractive index of the core is outlined in section 5.1.1.3. Bragg gratings are usually inscribed into fibres by UV-laser such as an argon (244nm) or krypton fluoride (excimer) laser (248nm). The *interferometric transverse holographic method* first developed by Meltz allows gratings to be created with reflection wavelengths different from the inscription wavelength [Lin 12, p. 23]. It applies a laser beam split into two branches interfering at the intended location of the grating in the fibre. The light can pass the fibre cladding and the grating inscription is limited to the fibre core. The *phase mask technique* is a standard method for inscribing gratings by interference of UV laser light following transmission through a diffraction phase mask [Hil 97, p. 1266].

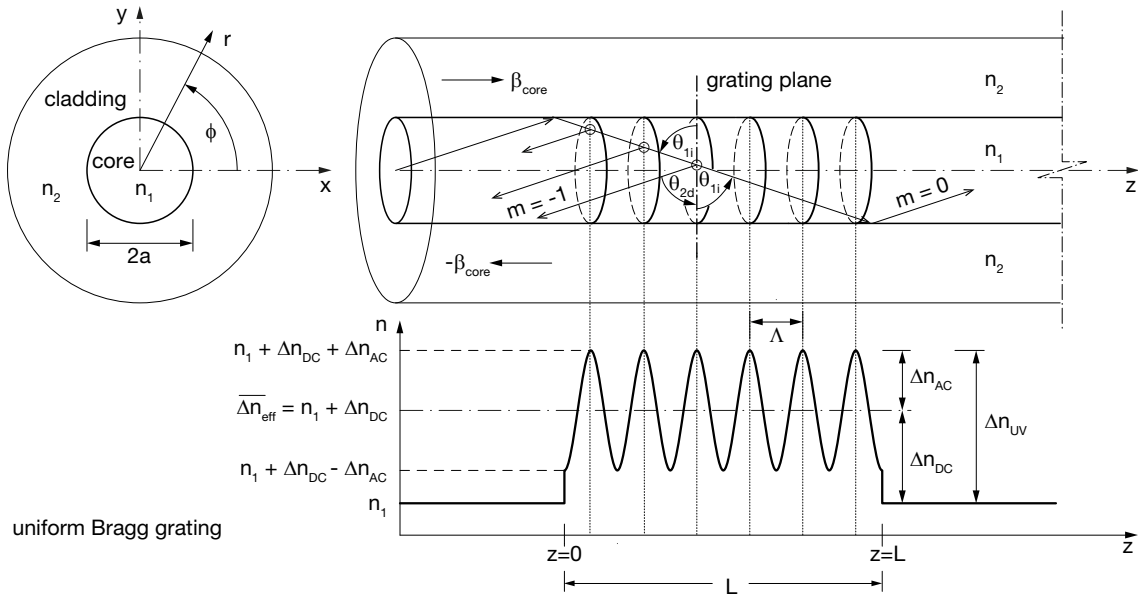


Figure 5.5.: Schematic representation of the modulated index amplitude (AC) and the DC-index change (offset) of a Bragg grating.

The Bragg wavelength (eq. 5.17) depends on the period of the applied phase mask. Combination of both the phase mask and the interferometric transverse holographic technique are possible by applying a Talbot interferometer [Lin 12, p. 53]: The splitting of the laser beam is made by a phase mask, with the resulting two beams then being reflected in an adaptable angle through rotating or moveable mirrors towards an interference location in the fibre core. The Bragg gratings used in the this research work are fabricated in this way.

The doping and fibre drawing method from preforms is described in section 5.1.1.1. Typically, the fibres are produced in a vertical draw tower process, fig. 5.6: The preforms pass through a graphite furnace, where they are molten at nearly 2000°C and then drawn into the required fibre diameter. The Bragg gratings are inscribed into the moving fibre, which is coated directly afterwards. In this way, the fibre is not structurally damaged<sup>18</sup> and high mechanical strength is achieved (>50N and 5% strain).

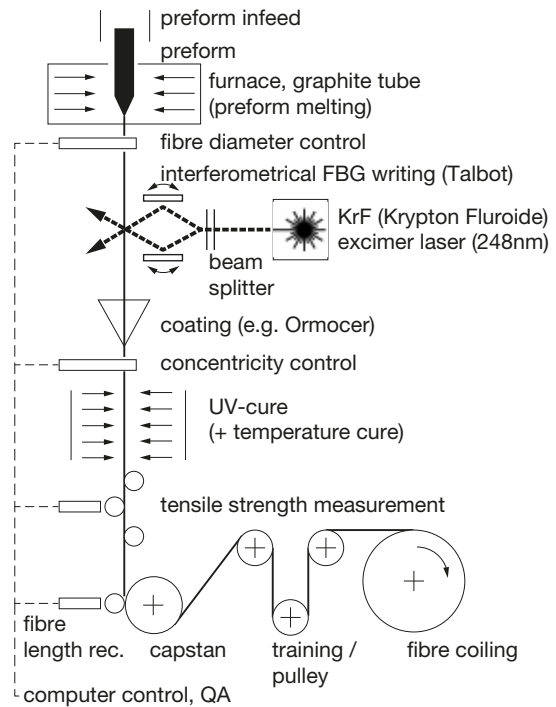


Figure 5.6.: Schematic diagram of a draw tower process with holographic inscription of Bragg gratings.

<sup>18</sup>Other procedures use a previously coated fibre, whereby the coating must be stripped off the fibre prior to the grating inscription. After that, the grating zone is coated again. This process leads to low tensile strength of the fibre.

Coatings are applied to shield the fibres from exterior disturbance or damage and for additional stiffening against breakage, e.g. through bending. The coating thickness has a range of  $10\mu\text{m}$  to  $25\mu\text{m}$ . The fibres are coated with acrylic polymer with a maximum Young's modulus of about  $1000\text{MPa}$  or  $2000\text{MPa}$  [Gab 12] or with Polyimide. Soft acrylic coatings can be applied if the fibre is subjected to transverse strain to reduce the related birefringence effects on the sensor response. Metallic coatings, such as gold, exist for elevated temperature applications of about  $800^\circ\text{C}$ . Recent material developments such as Ormocer<sup>®</sup> combine good surface adhesion to the fibre, temperature resistance, transparency and the passage of UV-laser light to inscribe gratings and the establishment of very thin coatings. The fibres used in this work have an inorganic-organic hybrid Ormocer<sup>®</sup> coating of  $35\mu\text{m}$  thickness. The hybrid polymer coating is UV-cured directly in the production in-line process. Additional thermal post-cure is added because of heating through the UV-lamp, see figure 5.6. Ormocer<sup>®</sup> hybrid polymers have been analysed in this work regarding a possible application as mounting adhesive for sensor fibres coated with the same material, see section 5.1.3.

An incident light wave with an angle  $\theta_1$  to a grating plane can either pass the grating without diffraction (transmission grating) or is diffracted and has an angle  $\theta_2$  to the grating thereafter, fig. 5.5. The order of diffraction is given by an integer  $m_d$ . For transmission,  $m_d = 0$ , for diffraction or reflection,  $m_d = -1, -2, \dots$ . Equation [Erd 97, p. 1278]

$$n \sin \theta_{2d} = n \sin \theta_{1i} + m_d \frac{\lambda}{\Lambda} \quad (5.13)$$

permits the description of a constructive interference; furthermore, the wavelength, whereby the grating achieves the maximum coupling (resonance) of two modes, can be found. Bragg gratings, as used here, are short-period reflectors in which mode coupling is achieved for waves propagating in opposite directions (contradirectional coupling, as shown in fig. 5.5). The mode propagation constant

$$\beta = \frac{2\pi}{\lambda} n_{eff} \quad (5.14)$$

(where  $n_{eff} = n_1 \sin \theta$ ) is substituted into eq. (5.13). Designating the propagation constant for the incident mode  $\beta_{1i}$  and for the diffracted mode  $\beta_{2d}$ , these

expressions yield for guided modes [Erd 97, p. 1278] [Yin 08, p. 301]

$$\beta_{2d} - \beta_{1i} = m_d \frac{2\pi}{\Lambda} \quad (5.15)$$

To allow for a resonant coupling of modes (power amplification of the sensor), the path of light reflected from uniform neighbouring grating planes should be an integer multiple of the wavelength of the light travelling through the fibre. First order diffraction with  $m_d = -1$  is the typical case for Bragg gratings with a contradirectional mode coupling. A negative value is used for the propagation constant applying to reflected modes in an opposite (-z) direction to the incident light:  $\beta_{2d} < 0$ . The wavelength necessary to obtain resonance in contradirectional coupling of a mode having an index  $n_{eff,1i}$  with a reflected mode  $n_{eff,2d}$  then is

$$\lambda = (n_{eff,1i} + n_{eff,2d}) \Lambda \quad (5.16)$$

For an ideal resonant Bragg reflection in a SMF, both modes are the same:  $n_{eff,1i} = n_{eff,2d}$ . By insertion of eq. 5.14 into 5.15, this condition yields the Bragg condition as the principal equation for uniform Bragg grating sensors in which  $\lambda_D$  means the design wavelength of the fibre and  $\lambda_B$  designates the Bragg wavelength.

$$\lambda_B = 2n_{eff}\Lambda = \lambda_D \quad (5.17)$$

#### 5.1.1.5. Coupled Mode Theory for Fibre Bragg Gratings

Several methods are available for describing the coupling behaviour of modes in optical fibres, namely coupled mode theory (CMT) and transfer matrix method (TMM) [Lin 12, p. 19]. Most often, either CMT or TMM are used to describe the diffraction and coupling of propagating and/or reflected modes in a fibre. CMT offers analytical solutions for homogeneous Bragg gratings but does not permit the solving of equations of non-uniform gratings, such as chirped or apodised gratings, for which TMM is applied. However, as uniform Bragg gratings are used in the present work, a short description of the CMT method is given hereafter. The reflectivity  $R_e$  calculated by means of CMT is applied with optical spectrum analyser devices (OSA) to calculate and visualise the reflected spectrum of a FBG.

Principally, CMT describes the diffraction of guided modes at fibre gratings, the coupling, spectral properties and disturbing effects such as dielectric perturbation, fibre imperfections and inhomogeneities. In an entirely unperturbed waveguide, no exchange of energy between different modes occurs. However, perturbation of the dielectric properties of a fibre, e.g. a change of the index of refraction, leads to the coupling of the different amplitudes of the modes  $j, k$ , which is described through coupling coefficients. Whereas the coefficient for longitudinal coupling is small and is thus omitted, the transverse coupling coefficient is kept to define the coupling of counterpropagating mode amplitudes along the fibre axis  $z$ .

The change of the amplitude of a mode  $j$  depends on the dielectric perturbation, the mode fields and the other mode amplitudes in the fibre [Tru01, p. 19]. The change of the refractive index in a step index fibre along its axis  $z$  is assumed to be sinusoidal and contains a constant DC-portion  $\Delta n_{DC}(z)$  and a modulated AC-portion  $\Delta n_{AC}(z)$ , compare eq. 5.12 and fig. 5.5. Two coupled differential equations with the mode amplitudes of the incident wave  $R(z)$  and the reflected wave  $S(z)$  are obtained for the  $LP_{01}$ -mode

$$\frac{dR(z)}{dz} = i\hat{\sigma}_{DC}(z)R(z) + i\kappa_{AC}(z)S(z) \quad (5.18)$$

$$\frac{dS(z)}{dz} = -i\hat{\sigma}_{DC}(z)R(z) - i\kappa_{AC}(z)R(z) \quad (5.19)$$

with  $\kappa_{AC}$  being the transverse AC coupling coefficient,  $\overline{\Delta n_{eff}}$  being the refractive index averaged over the grating period and  $\hat{\sigma}_{DC}$  being the general DC coupling coefficient. Perfect phase matching of two counterpropagating  $LP_{01}$ -modes is given for a grating without chirp, if the general DC-term becomes zero and results in the Bragg condition  $\lambda_B = 2\overline{\Delta n_{eff}}\Lambda$ .

These principal coupled mode differential equations (5.18, 5.19) can be solved for the case of gratings being uniform in the  $z$ -direction and for perfect phase matching, see [Erd97, p. 1280]: In this particular case, which applies to the Bragg grating sensors used in the present work,  $\overline{\Delta n_{eff}}$ ,  $\hat{\sigma}_{DC}$  and  $\kappa_{AC}$  are constants. The ratio of the incident and the reflected mode and the *amplitude reflection coefficient*  $\rho$  can now be determined analytically by applying the relation

$$\rho = \frac{S(-0.5L)}{R(-0.5L)}. \quad (5.20)$$

From this, the power reflection coefficient  $R_e = \rho^2$  can be calculated:

$$R_e = \frac{\sinh^2\left(\sqrt{\kappa_{AC}^2 - \hat{\sigma}_{DC}^2}L\right)}{\cosh^2\left(\sqrt{\kappa_{AC}^2 - \hat{\sigma}_{DC}^2}L\right) - \frac{\hat{\sigma}_{DC}^2}{\kappa_{AC}^2}} \quad (5.21)$$

By applying the normalised wavelength equation from [Erd97, p. 1280], where  $N = \frac{L}{\Lambda}$  defines the number of gratings, eq.

$$\frac{\lambda}{\lambda_B} = \frac{1}{1 + \frac{\hat{\sigma}_{DC}L}{\pi N}} \Leftrightarrow \hat{\sigma}_{DC} = \frac{\pi N}{L} \left( \frac{1}{\frac{\lambda}{\lambda_B}} - 1 \right) \quad (5.22)$$

permits the calculation of typical Bragg grating reflectivity spectra. Figure 5.7 shows an example plot of the reflectivity  $R_e$  against the normalised wavelength  $\frac{\lambda}{\lambda_B}$  for two different values of  $\kappa_{AC}L = 2$  and  $\kappa_{AC}L = 8$ , both with  $L = 6\text{mm}$ .  $N$  has the same value in both cases. A smaller AC-coupling constant thus results in a narrower wavelength spectrum and shows a more pointed maximum peak. For  $L = 3\text{mm}$  and  $\kappa_{AC} = 1$ ,  $N$  is smaller and, subsequently, the reflectivity  $R_e$  is reduced.

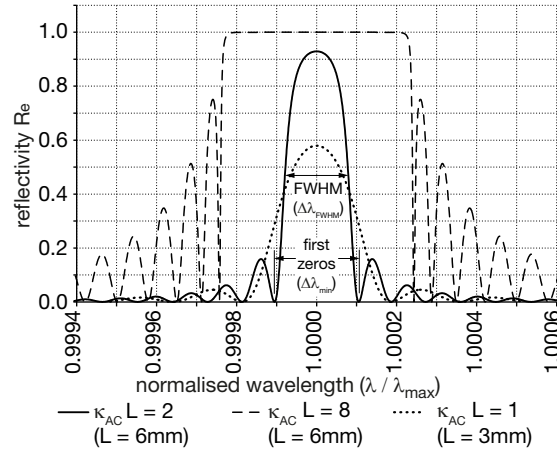


**Figure 5.7.:** Normalised reflectivity  $R_e$  plotted against the normalised wavelength  $\lambda / \lambda_{max}$ .

Either the normalised reflectivity  $R_e$  (as shown in fig. 5.7) or the intensity in a logarithmic scale (fig. 5.8) for the spectra are issued by the OSA and its respective software.



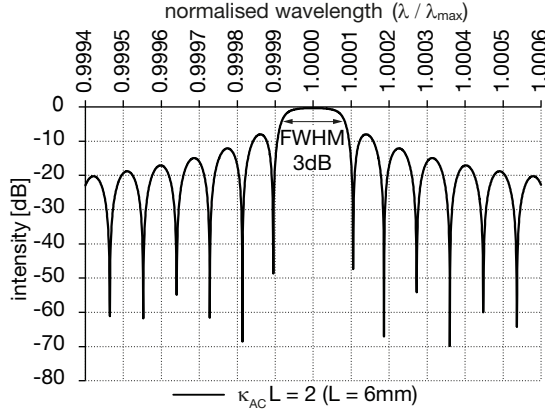


**Figure 5.8.:** Intensity plot ( $\log_{10}$ ) of a FBG spectrum for normalised wavelength  $\lambda/\lambda_{max}$ .

Identification of the Bragg wavelength  $\lambda_B$  from measured spectra in the present work is made by applying the full-width-half-maximum (FWHM) of the maximum peak: The spectral width  $\Delta\lambda_{FWHM}$  is identified at  $0.5R_{e,max}$  (compare fig. 5.7) or at a distance of  $-3\text{dB}$  from the peak in the case of an intensity plot, fig. 5.8. A second method is the measurement of the spectral bandwidth  $\Delta\lambda_{min}$  between the first zeros (minima) situated on both sides of the maximum point [Yin 08, p. 312] between the centre peak and first two sidelobes.

#### 5.1.1.6. Derivation of the Strain and Temperature Sensitivity of FBGs

As mentioned above (section 5.1.1.4), multiple FBG can be inscribed into a single fibre. They can be distinguished by their respective Bragg wavelength  $\lambda_B$  depending on the period  $\Lambda$  and the mean effective refractive index  $\bar{n}_{eff}$ . If either mechanically- or temperature-induced strain is caused in the fibre, the period  $\Lambda$  of the sensor is subjected to a linear geometrical length change corresponding to the exterior strain action. The related proportional shift can be seen from the Bragg condition depending on mechanical strain  $\epsilon_i$  (with the principal components  $i$ ) and temperature  $T$ ,

$$\lambda(\epsilon_i, T) = 2\bar{n}_{eff}(\epsilon_i, T)\Lambda(\epsilon_i, T) \quad (5.23)$$

compare eq. 5.17. A temperature change has two effects on the gratings in the fibre core: it causes a real strain length modification of the period attributable to the thermal expansion of the silica material and an apparent strain attributable to the temperature-induced change of the refractive index.

For the following deductions, temperature and strain are assumed to be homogeneous across the section of the fibre core. The fibre diameter is extremely small compared with the thickness of surrounding structural members such as glass and interlayers. Thus, the fibre is subjected to practically the same temperature as the material to which it is glued or in which it is embedded and the above hypothesis holds. The bending radii of a fibre glued to a bent curved glass surface are in an order of 3m to 5m in the specimen used for tests in this work and are far from a range causing inhomogeneous stress in the fibre because of bending effects. However, the FE-model developed in section 5.1.6 is used to quantify such an influence. As given by the producer of the FBGs used in this work [Int 14], the light signal attenuation for bending radii above 3.75mm is negligible.

Fibres bonded to the surface of a material subjected to bending are situated in either the tensile or compressed zone of the cross section of the bent substrate. The fibre core diameter  $<9\mu\text{m}$ , is small compared with the glass thickness of 4mm to 6mm applied in this work. The bending strain of the fibre attributable to its bending stiffness is extremely small and the strain state caused in the fibre by the bending of the glass substrate to which the sensor is bonded is close to axial; a homogeneous strain state in the fibre core can be assumed. Verification of the strain hypothesis is made by finite element micro-models in section 5.1.6. The influence of strain and a temperature change on the wavelength shift in a fibre sensor can then be generally expressed as

$$d\lambda(\epsilon_i, T) = \lambda_{\epsilon_i} d\epsilon_i + \lambda_T dT, \quad (5.24)$$

with the partial differentials

$$d\lambda(\epsilon_i, T) = \frac{\partial\lambda}{\partial\epsilon_i} d\epsilon_i + \frac{\partial\lambda}{\partial T} dT. \quad (5.25)$$

A linear approximation of  $d\lambda$  can thus be derived by the total differential of the Bragg condition eq. 5.23 including the respective partial differentials:

$$\begin{aligned} d\lambda(\epsilon_i, T) = & 2 \left( \Lambda \frac{\partial\bar{n}_{eff}}{\partial\epsilon_i} + \bar{n}_{eff} \frac{\partial\Lambda}{\partial\epsilon_i} \right) d\epsilon_i + \\ & + 2 \left( \Lambda \frac{\partial\bar{n}_{eff}}{\partial T} + \bar{n}_{eff} \frac{\partial\Lambda}{\partial T} \right) dT \end{aligned} \quad (5.26)$$

The first term describes the influence of strain on the wavelength change; the second term the changing wavelength attributable to the temperature difference. The initial Bragg wavelength  $\lambda_{B,0}$  not subjected to any temperature change or strain contains the initial, unchanged refractive index  $\bar{n}_{eff,0}$  and period  $\Lambda_0$  of the grating:

$$\lambda_{B,0} = 2\bar{n}_{eff,0}\Lambda_0 \quad (5.27)$$

Dividing eq. 5.26 by eq. 5.27 yields the expression

$$\begin{aligned} \frac{d\lambda}{\lambda_{B,0}}(\varepsilon_i, T) = & \left( \frac{1}{\bar{n}_{eff,0}} \frac{\partial \bar{n}_{eff}}{\partial \varepsilon_i} + \frac{1}{\Lambda_0} \frac{\partial \Lambda}{\partial \varepsilon_i} \right) d\varepsilon_i + \\ & + \left( \frac{1}{\bar{n}_{eff,0}} \frac{\partial \bar{n}_{eff}}{\partial T} + \frac{1}{\Lambda_0} \frac{\partial \Lambda}{\partial T} \right) dT. \end{aligned} \quad (5.28)$$

In this equation, the wavelength shift attributable to temperature and strain is related to the initial Bragg wavelength of the respective sensor. In addition, dependency on the refractive index and its change can be seen. As described by Pockels<sup>19</sup> [Poc 89], in a transparent material such as a silica glass fibre, the change of the refractive index can be expressed as a function of the strain caused by mechanical influence or temperature. This is carried out by relating the photoelastic optical effects in the fibre to the strain acting in the fibre.

The fibre axis ( $z$ ) is oriented in  $x_1$ -direction, figs. 5.5, 5.11. Principal components for strain and stress are assumed for the fibre core. This hypothesis has to be examined and verified for various load cases, see section 5.1.6. The related expressions are thus denoted with the index “1” if acting in the direction of the longitudinal fibre axis. For strain and stress tensors, contracted notation as in Voigt is applied ( $\varepsilon_{11} = \varepsilon_1, \varepsilon_{22} = \varepsilon_2, \varepsilon_{33} = \varepsilon_3, \varepsilon_{23} = \varepsilon_{31} = \varepsilon_4$ , etc., eq. ??).

The fibre is assumed to be optically isotropic with the optical axes being aligned with the fibre axes. This is described by two transverse optical axes  $p, q$  in the  $x_2$ - $x_3$ -plane being orthogonal to the fibre axis. Both axes are associated with the respective refractive indices  $n_p, n_q$ . As shown in eq. A.2 in appendix A.3, strain and temperature cause a relative proportional change of the refractive indices in the transverse polarisation directions  $p, q$  with the

proportionality Pockels coefficients  $p_{ij}$  given by the photoelastic Pockels matrix, eq. A.1 in appendix A.2 [Ste 97, p. 277]. Small deformations and difference in the fibre are assumed. Thus, the infinitesimal small values of  $d\lambda, d\varepsilon_i$  and  $dT$  in eq. 5.28 above are replaced by  $\Delta\lambda, \Delta\varepsilon_i$  and  $\Delta T$  and the differential  $d$  becomes a linear function of  $\Delta$ :  $d \approx \Delta$ . Wavelength shift differences  $\Delta\lambda$  measured with an FBG sensor then have to be related to initial reference values  $\lambda_{B,0}, \varepsilon_{0,i}$  and  $T_0$ . The relative change of the refractive index attributable to mechanical strain and temperature is described in eq. A.2 for the  $p, q$ -directions. For uniaxial fibre strain and isotropy, the mean refractive index  $\Delta\bar{n}_{eff}$  equals  $\Delta n_{p,q}$ . Based on these assumptions, the full expression for a free fibre Bragg grating in an isotropic fibre subjected to mechanically induced strain and temperature is derived as shown briefly in appendix A.3

$$\begin{aligned} \frac{\Delta\lambda}{\lambda_{B,0}} = & \varepsilon_1 \left( 1 - \frac{n_0^2}{2} p_{12} \right) - \frac{n_0^2}{2} \left[ \left( \frac{p_{11} + p_{12}}{2} \right) (\varepsilon_2 + \varepsilon_3) \right. \\ & \left. \pm \left( \frac{p_{11} - p_{12}}{2} \right) (\varepsilon_2 - \varepsilon_3) \right] + \Delta T \left( \alpha_g + \frac{1}{n_0} \frac{dn_0}{dT} \right) \end{aligned} \quad (5.29)$$

This corresponds to the expression provided by Gabler [Gab 12, p. 48]. For simplicity, the strain differences  $\Delta\varepsilon_i$  are expressed by  $\varepsilon_i$ , as the change in strain is always related to an initial strain-state.

In the following sections, the cases of a free sensor and of a sensor bonded to the surface of an object are set up. Approaches to describe embedded or substrate-bonded sensors exist, e.g. in v. Steenkiste [Ste 97], but none so far covers the case of a sensor bonded to an isotropic substrate with a large Young’s modulus being laminated by applying polymer interlayers, as is the case in this work. In the case of laminated glass, the purpose is the measurement of glass surface strain inside of the laminate based on the general expression eq. 5.29. The sensor is bonded to the glass with an adhesive providing high bond stiffness with respect to the softer interlayer. The sensor is assumed to depend on the strain state of the glass surface; the shear influence of the interlayer is assumed negligible. This hypothesis, which is examined throughout this work, allows the application of the equations for sensors bonded to the surface of a substrate.

<sup>19</sup>Friedrich C. A. Pockels (1865-1913) discovered the influence of electrical fields or mechanical strain on the refractive index change in birefringent glass material

## 5.1.1.7. Free FBG Sensor Strain and Temperature Sensitivity

For the case of purely axial loading of a free fibre ( $\Delta T = 0$ ), the sensor is only subjected to axial strain  $\varepsilon_1$ . because of isotropy, the remaining two principal strain components become

$$\varepsilon_2 = \varepsilon_3 = -\nu \varepsilon_1. \quad (5.30)$$

Substitution of the above expression into eq. 5.29 and  $\Delta T = 0$  yields

$$\frac{\Delta\lambda}{\lambda_0} = \varepsilon_1 \left[ 1 - \frac{n_0^2}{2} (p_{12} - \nu (p_{11} + p_{12})) \right] \quad (5.31)$$

The term

$$\frac{n_0^2}{2} [p_{12} - \nu (p_{11} + p_{12})] \quad (5.32)$$

is called the *photoelastic* or *strain-optic coefficient*  $p_e$ , see 5.1.4.1. From this, the *strain sensitivity coefficient* or *K-factor*  $K_\varepsilon = 1 - p_e$  can be defined, and eq. 5.31 simplifies to:

$$\frac{\Delta\lambda}{\lambda_{B,0}} = \varepsilon_1 K_\varepsilon \quad (5.33)$$

A free fibre without a mechanically induced axial load, which is subjected to pure temperature change ( $\Delta T \neq 0$ ), remains mechanically unstrained but nevertheless shows a wavelength shift. As eq. 5.29 contains temperature-induced strain effects, the relative wavelength shift for a pure temperature influence can be found by setting the mechanically induced strains  $\varepsilon_i = 0$ :

$$\frac{\Delta\lambda}{\lambda_{B,0}} = \Delta T \left( \alpha_g + \frac{1}{n_0} \frac{dn_0}{dT} \right) \quad (5.34)$$

The last term is the *thermoelastic* or *thermo-optic coefficient*, which describes the change of the refractive index of the fibre attributable to temperature, compare 5.1.4.2

$$\alpha_n = \frac{1}{n_0} \frac{dn_0}{dT} \quad (5.35)$$

Combining this coefficient and the thermal expansion coefficient of the fibre permits the definition of a temperature coefficient  $K_T$  to describe the behaviour of the fibre under temperature load:

$$K_T = \alpha_g + \alpha_n$$

With the temperature coefficient, eq. 5.34 becomes:

$$\frac{\Delta\lambda}{\lambda_0} = \Delta T K_T \quad (5.36)$$

The relation of the wavelength shift and the strain of a free fibre subjected to both axial mechanical load  $\Delta\varepsilon_1$  and temperature  $\Delta T$  is calculated based on eq. 5.29 and 5.30:

$$\begin{aligned} \frac{\Delta\lambda}{\lambda_0} &= \varepsilon_1 \left[ 1 - \frac{n_0^2}{2} (p_{12} - \nu (p_{11} + p_{12})) \right] + \\ &+ \Delta T \left( \alpha_g + \frac{1}{n_0} \frac{dn_0}{dT} \right) \\ &= (1 - p_e) \varepsilon_1 + \left( \alpha_g + \frac{1}{n_0} \frac{dn_0}{dT} \right) \Delta T \\ &= K_\varepsilon \varepsilon_1 + K_T \Delta T \end{aligned} \quad (5.37)$$

Van Roosbroeck and Chojetzki [Van09, p. 60] point to an error occurring by approximating the differential of the wavelength  $d\lambda$  through  $\Delta\lambda$ , which is based on the engineering (Cauchy-) strain, for small changes related to an initial value  $\lambda_{B,0}$

$$\frac{d\lambda}{\lambda_{B,0}} \approx \frac{\Delta\lambda}{\lambda_{B,0}}$$

Taking into account the photoelastic coefficient  $K_\varepsilon = 1 - p_e$ , integration of expression 5.37 leads to

$$\ln \left( \frac{\lambda}{\lambda_{B,0}} \right) = K_\varepsilon (\varepsilon_i - \varepsilon_{i,0}) + \sum (T - T_0), \quad (5.38)$$

where  $\lambda_{B,0}$  is the initial reference wavelength at the reference conditions  $\varepsilon_0$  and  $T_0$ .  $\lambda$  is the measured wavelength. This expression corresponds to the true, logarithmic (Hencky-) strain formulation. The authors indicate an error of 0.2% relative strain for an applied total of strain 0.5% caused by the approximation. As this error is relatively small, it is neglected in this work.

If a free fibre is subjected to transverse loading, birefringence effects occur. For an ideal circular fibre core section (not being polarisation-maintaining) with straight parallel Bragg gratings orthogonal to the fibre axis, both polarisation directions p and q of a propagating wave typically remain orthogonal to each other; they do not exchange energy and thus have identical propagation constants and a constant polarisation state. Bragg gratings are intrinsic sensors and thus can be subject to birefringence. Mechanical deformation of a fibre attributable to transverse forces orthogonal to the fibre axis cause the fibre section to ovalise or to

become an ellipsoid, fig. 5.9. The propagation velocity of the waves changes for the two principal polarisation directions  $p, q$ . Thus, the refractive index of the fibre  $n_{p,q}$  is also modified. The principal axes of the polarisation directions  $p, q$  can be assumed to be parallel (3) and orthogonal (2) to the loading direction and, thus  $n_{p,q} = n_{2,3}$  ([Leb 04, pp. 2-9]).

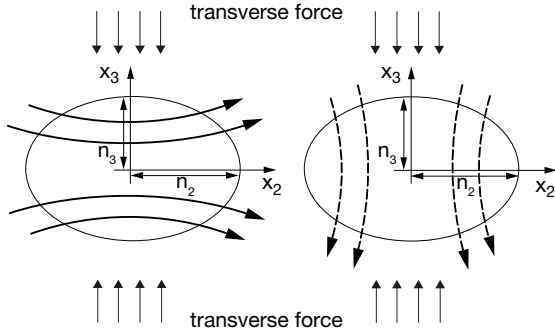


**Figure 5.9.:** Sketch of the modification of the two polarisation directions of the electric field caused by fibre deformation attributable to transverse forces (based on [Sch 10, p. 16]).

Assuming homogeneous strain  $\epsilon_3$  in transverse direction<sup>20</sup>  $x_3$ , the components  $\epsilon_1, \epsilon_2$  are again related to  $\epsilon_3$  through Poisson's ratio  $\nu$  [Gab 12, p. 50]:

$$\epsilon_1 = \epsilon_2 = -\nu \epsilon_3; \quad \epsilon_3 \neq 0; \quad \epsilon_2 \neq \epsilon_3 \quad (5.39)$$

With eq. 5.29, the resulting wavelength differences for the  $p, q$ -polarisation directions read for  $\Delta T = 0$ :

$$\frac{\Delta \lambda_{p,q}}{\lambda_{B,0}} = \epsilon_3 \left[ -\nu \left( 1 - \frac{n_0^2}{2} p_{12} \right) - \frac{n_0^2}{4} \left( (p_{11} + p_{12}) \cdot (-\nu + 1) \pm (p_{11} - p_{12})(-\nu - 1) \right) \right] \quad (5.40)$$

The above equation permits the calculation of two reflection peaks for the  $p, q$ -polarisation directions shifted by  $\Delta \lambda_{p,q}$  with respect to the initial Bragg wavelength  $\lambda_{B,0}$ . Typically, this effect occurs as a broadening of the reflection spectrum by  $\pm 0.5 (\Delta \lambda_p - \Delta \lambda_q)$  from  $\lambda_{B,0}$ . Subsequently, the quasi-homogeneous average wavelength shift can be approximately expressed by the average  $0.5 (\Delta \lambda_p + \Delta \lambda_q)$  ([Gab 12, p. 50]). However, the test and OSA-measurement of a fibre mechanically

loaded in the transverse direction often does not show a clear double peak spectrum, but just a broadened spectrum, making it difficult to distinguish the  $p, q$ -results described above.

Trutzel [Tru 01, pp. 275-276] proposes an analytical approach for a fibre exposed to a transverse linear force  $q_F = F/l_F$ , where  $F$  is the applied transverse single load acting in the 3-direction and  $l_F$  the application length of the single load on the fibre surface, fig. 5.10.

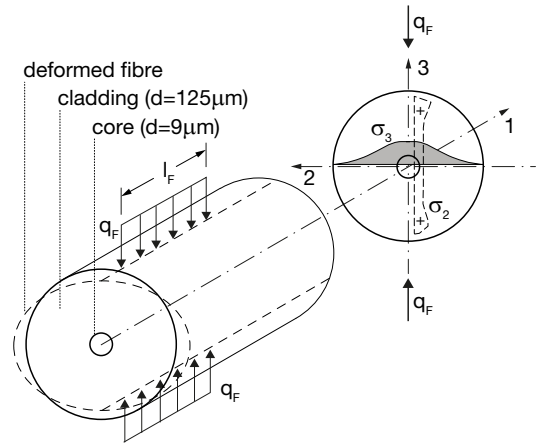


**Figure 5.10.:** Principal stress in the cylindrical fibre caused by transverse linear force acting in 3-direction (based on [Gab 12, p. 51]).

Assuming principal stresses (principal axe system) and infinitesimally small geometrical changes of the fibre geometry (the fibre approximately remains circular in the deformed state), the stress components of free fibre are [Gab 12, p. 51]

$$\sigma_1 \approx 0 \quad \sigma_2 \approx \frac{1}{\pi r} q_F \quad \sigma_3 \approx -\frac{3}{\pi r} q_F \quad (5.41)$$

The above approximation is only valid for the fibre core, where a constant transverse stress state can be assumed for a linear transverse load orthogonal to the fibre axis, as the core diameter ( $< 9 \mu m$ ) is very small compared with the cladding ( $< 125 \mu m$ ) or coating ( $< 195 \mu m$ ) diameter and the load acts either on the cladding or on the coating, fig. 5.10. The principal strain components in the isotropic fibre core are thus [Gab 12, p. 51]

<sup>20</sup>Constant transverse strain in the fibre core can be assumed for a linear, transverse load orthogonal to the fibre axis, as the core diameter ( $< 9 \mu m$ ) is very small compared with the cladding ( $< 125 \mu m$ ) or coating ( $< 195 \mu m$ ) diameter and the load acts either on the cladding or on the coating.

$$\begin{aligned}
 [\varepsilon_i] &= \frac{1}{E_{fibre}} \begin{bmatrix} 1 & -\nu & -\nu \\ -\nu & 1 & -\nu \\ -\nu & -\nu & 1 \end{bmatrix} \cdot \begin{bmatrix} \sigma_1 \\ \sigma_2 \\ \sigma_3 \end{bmatrix} = \\
 &= \begin{bmatrix} -\frac{\nu}{E} (\sigma_2 + \sigma_3) \\ \frac{1}{E} (\sigma_2 - \nu \sigma_3) \\ \frac{1}{E} (-\nu \sigma_2 + \sigma_3) \end{bmatrix}
 \end{aligned} \quad (5.42)$$

Substituting the stress and strain expressions from eq. 5.41, 5.42 into eq. A.2 and 5.29 with  $\Delta T = 0$  yields:

$$\begin{aligned}
 \frac{\Delta \lambda_p}{\lambda_{B,0}} &= -\frac{n_0^2}{2} \frac{q_F}{E \pi r} \left[ p_{11} (1 + 3\nu) + p_{12} (-3 + \nu) - \frac{4\nu}{n_0^2} \right] \\
 \frac{\Delta \lambda_q}{\lambda_{B,0}} &= -\frac{n_0^2}{2} \frac{q_F}{E \pi r} \left[ -p_{11} (3 + \nu) + p_{12} (1 + 5\nu) - \frac{4\nu}{n_0^2} \right]
 \end{aligned} \quad (5.43)$$

In contrast, Trutzel [Tru 01, pp. 275-276] assumes plane strain conditions with  $\varepsilon_1 = 0$ ; this results in the following equations for the wavelength shift of the birefringent fibre:

$$\begin{aligned}
 \frac{\Delta \lambda_p}{\lambda_{B,0}} &= -\frac{n_0^2}{2} \frac{q_F}{E \pi r} \left[ p_{11} (1 + 3\nu) - p_{12} (3 + \nu) \right] \\
 \frac{\Delta \lambda_q}{\lambda_{B,0}} &= -\frac{n_0^2}{2} \frac{q_F}{E \pi r} \left[ -p_{11} (3 + \nu) + p_{12} (1 + 3\nu) \right]
 \end{aligned} \quad (5.44)$$

#### 5.1.1.8. Surface Bonded FBG Sensor Strain and Temperature Sensitivity

If an FBG is bonded to the surface of an object subjected to an exterior load, it can be used to determine the local surface strain of this object at the discrete location to which the FBG is fixed. Some of the coefficients in the equations determined above have then to be adapted to take into account the influence of the substrate and the bond on the sensor. The approach used for the free fibre subjected to an axial load is based on isotropy, on a homogeneous strain state with respect to the fibre axis and on constant strain along the sensor length. For a sensor fixed to another, substantially larger element or embedded into another material, all six possible strain components  $\varepsilon_1 \dots \varepsilon_6$  of the FBG can be influenced by potential multiaxial strain states of the element. The bond properties coupling the sensor to the element and the coating of the fibre influence the transmission of the strain from the element into the sensor. The shear angles and the

strain components are related by

$$[\varepsilon_{kl}] = \begin{bmatrix} \varepsilon_{xx} & \varepsilon_{xy} & \varepsilon_{xz} \\ \varepsilon_{yx} & \varepsilon_{yy} & \varepsilon_{yz} \\ \varepsilon_{zx} & \varepsilon_{zy} & \varepsilon_{zz} \end{bmatrix} = \begin{bmatrix} \varepsilon_{xx} \\ \varepsilon_{yy} \\ \varepsilon_{zz} \\ 2\varepsilon_{yz} \\ 2\varepsilon_{xz} \\ 2\varepsilon_{xy} \end{bmatrix} = \begin{bmatrix} \varepsilon_1 \\ \varepsilon_2 \\ \varepsilon_3 \\ \varepsilon_4 \\ \varepsilon_5 \\ \varepsilon_6 \end{bmatrix} \quad (5.45)$$

in Voigt notation with the shear strain angles  $\gamma_{yz} = 2\varepsilon_{yz}$ ,  $\gamma_{xz} = 2\varepsilon_{xz}$  and  $\gamma_{xy} = 2\varepsilon_{xy}$ .

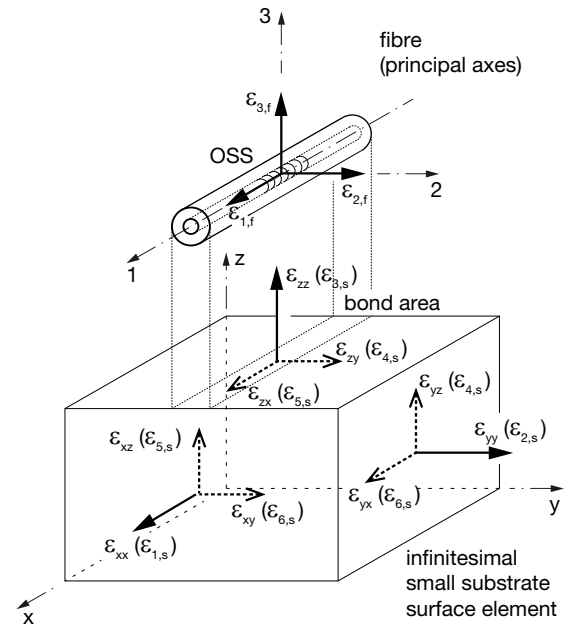


**Figure 5.11.:** Sensor fibre and substrate strain directions with the respective coordinate systems.

In the following, strain or stress related to the fibre or the substrate are accorded the indices  $f$  and  $s$ , respectively. The coordinate system axes  $x, y, z$  of the structure and of the surface-bonded sensor 1, 2, 3 are assumed to be aligned, fig. 5.11. All sensors used in this work are bonded to locations on the glass substrate where the principal strain / stress directions correspond to the axes of the fibre and the substrate as given in fig. 5.11. Thus, the same indices 1...3 apply for the fibre and the substrate and their aligned principal axes. However, this correspondence assumption for the principal axes and the validity of the principal strain assumption has to be verified for each structure studied. Following the argumentation of Trutzel [Tru 01, p. 127], the strain components  $\varepsilon_{1,f}, \varepsilon_{2,f}, \varepsilon_{3,f}, \varepsilon_{4,f}$  corresponding to the strain components  $\varepsilon_{1,s}, \varepsilon_{2,s}, \varepsilon_{3,s}, \varepsilon_{4,s} = \varepsilon_{zy}$  of the

substrate affect the sensor signal, whereas the other two shear components have nearly no influence on the sensor wavelength shift. This is attributable to the longitudinal electro-magnetic field component of the wave being negligible compared with the transverse field:  $\epsilon_{xz} = \epsilon_{xy} = 0$ . In the coupled mode theory section, this is correspondingly assumed by omitting the longitudinal coupling coefficient.

The ratio of the strain transfer from the structure to the fibre can be described by a general strain transfer coefficient  $\zeta_i$ , compare [Jül 13, p. 2]:

$$\zeta_i = \epsilon_{i,f} / \epsilon_{i,s} \quad (5.46)$$

This ratio varies from 0 to 1 depending on the quality of the strain transfer between the structure and the sensor bonded to its surface for the case of axial strain in the substrate<sup>21</sup>. The strain transfer ratio mainly depends on the material properties of the adhesive and of the fibre coating and on the bond geometry (thickness, overhang, length, width) and the coating thickness. In the case of the bending of the substrate, the fibre strain result has to be corrected for the additional strain from the distance between the fibre axis and the substrate surface, see section 5.1.2.2. Based on the works of v. Steenkiste [Ste 97, p. 80] and Trutzel [Tru 01, pp. 127-128] the strain components of the structure and of the sensor bonded to it are related by

$$\begin{aligned} \epsilon_{1,f} &= \zeta_1 \epsilon_{1,s} \\ \epsilon_{2,f} &= \zeta_2 \epsilon_{2,s} \\ \epsilon_{3,f} &= \zeta_3 \epsilon_{3,s} \\ \epsilon_{4,f} &= \zeta_4 \epsilon_{4,s} \end{aligned} \quad (5.47)$$

The fibre axis 1 is set to be aligned with the 1-axis of the substrate. The sensor is required to measure the axial component 1 of the farfield strain from the substrate and subsequently only this component from the substrate will be transferred into the sensor fibre. In this case, for an isotropic fibre and principal strain conditions, the axial strain and the two other strain components are linked as in equation 5.30:  $-\nu \epsilon_1 = \epsilon_2 = \epsilon_3$ . If the FBG is aligned to the principal force directions / axes of the substrate, the 4-shear strain is assumed to be 0 and the general strain transfer coefficients of the remaining three principal directions as per eq. 5.47 are

$$\begin{aligned} \zeta_1 &= \frac{\epsilon_{1,f}}{\epsilon_{1,s}} \\ \Rightarrow \zeta_2 &= -\nu \zeta_1 \frac{\epsilon_{1,s}}{\epsilon_{2,s}} \\ \Rightarrow \zeta_3 &= -\nu \zeta_1 \frac{\epsilon_{1,s}}{\epsilon_{3,s}} \end{aligned} \quad (5.48)$$

Following the approach of Trutzel, the formulations derived in section 5.1.1.7, eq. 5.37, can also be used as a base for describing a surface-bonded fibre. The above conditions in eq. 5.48 comply with this demand. The strain in the structure and the sensor can be induced mechanically ( $\epsilon_{1,s,m}, \epsilon_{2,s,m}, \epsilon_{3,s,m}$ ) or by temperature changes  $\Delta T$ . In contrast to a free FBG, the thermal expansion of a surface-bonded sensor is mainly governed by the thermal expansion behaviour of the substrate described by its coefficient of thermal expansion  $\alpha_s$ . The thermal dilatation of the fibre  $\alpha_g$  is most often neglected compared with the thermal dilatation of the structure, as the former is usually very small because of to the low coefficient of thermal expansion of the silica fibre:  $\alpha_g = 0.51 - 0.55 \cdot 10^{-6} 1/K$  for the fibre, but  $\alpha_s = 23.10 \cdot 10^{-6} 1/K$  for a substrate from aluminium. Replacing the general strain expressions  $\epsilon_{1,s}, \epsilon_{2,s}, \epsilon_{3,s}$  by the sum of both temperature and mechanically induced strain ( $\epsilon_{1,s,m} + \Delta T \alpha_s$ ), the fibre strain formulations in eq. 5.47 together with eq. 5.48 become:

$$\begin{aligned} \epsilon_1 &= \zeta_1 (\epsilon_{1,s,m} + \Delta T \alpha_s) \\ \epsilon_2 &= -\nu \zeta_1 (\epsilon_{1,s,m} + \Delta T \alpha_s) \\ \epsilon_3 &= -\nu \zeta_1 (\epsilon_{1,s,m} + \Delta T \alpha_s) \end{aligned} \quad (5.49)$$

With the expression for the thermoelastic coefficient  $\alpha_n$  from 5.35 and substitution of eq. 5.49 into A.2 and then together with A.4 into A.3, the discrete, mechanically induced strain of the structure at the sensor location and in axial sensor direction is given by

$$\begin{aligned} \frac{\Delta \lambda(\epsilon, T)}{\lambda_{B,0}} &= \zeta_1 \epsilon_{1,s,m} \left[ 1 - \frac{n_0^2}{2} (p_{12} - \nu p_{11} - \nu p_{12}) \right] + \\ &+ \Delta T \left[ \zeta_1 \alpha_s \left( 1 - \frac{n_0^2}{2} (p_{12} - \nu p_{11} - \nu p_{12}) \right) + \alpha_n \right] \end{aligned} \quad (5.50)$$

<sup>21</sup>For bending, it can be >1 depending on the distance of the fibre from the substrate. If the fibre strain is corrected (eq. 5.61) with respect to the distance from the substance for bending, the ratio varies from 0 to 1.

Applying the photoelastic coefficient expression

$$p_e = \frac{n_0^2}{2} [p_{12} - \nu (p_{11} + p_{12})],$$

eq. 5.50 for the relationship of the measured, relative wavelength shift of the sensor and the strain of the structure in fibre axis direction becomes:

$$\frac{\Delta\lambda(\varepsilon, T)}{\lambda_{B,0}} = \zeta_1 \varepsilon_{1,s,m} (1 - p_e) + \Delta T [\zeta_1 \alpha_s (1 - p_e) + \alpha_n] \quad (5.51)$$

Eq. 5.37 for a free fibre contains the photo-elastic coefficient  $K_\varepsilon = 1 - p_e$ . The general strain transfer coefficient  $\zeta_1$  introduced above quasi acts in addition to  $K_\varepsilon$ . Whereas  $\zeta_1$  characterises the bond quality with respect to strain transfer into the fibre,  $K_\varepsilon$  describes the effect of strain in the fibre itself on the respective wavelength shift of the FBG. Both coefficients can be combined into the gauge factor  $k_\varepsilon$ :

$$k_\varepsilon = \zeta_1 K_\varepsilon = \zeta_1 (1 - p_e) \quad (5.52)$$

With eq. 5.52, eq. 5.51 becomes

$$\frac{\Delta\lambda(\varepsilon, T)}{\lambda_{B,0}} = k_\varepsilon (\varepsilon_{1,s,m} + \alpha_s \Delta T) + \alpha_n \Delta T \quad (5.53)$$

If the structure is only subjected to a change in temperature, eq. 5.51 simplifies to:

$$\begin{aligned} \frac{\Delta\lambda(T)}{\lambda_{B,0}} &= \Delta T [\zeta_1 \alpha_s (1 - p_e) + \alpha_n] \\ &= \Delta T (k_\varepsilon \alpha_s + \alpha_n) \end{aligned} \quad (5.54)$$

Subtraction of eq. 5.54 from eq. 5.53 allows us to obtain the purely mechanically induced strain from a specimen with one sensor bonded in an area subjected to both temperature and mechanical strain and a second one in an area without mechanically induced strain, the latter acting as a temperature compensation FBG:

$$\frac{\Delta\lambda(\varepsilon, T)}{\lambda_{B,0}} - \frac{\Delta\lambda(T)}{\lambda_{B,0}} = k_\varepsilon \varepsilon_{1,s,m} \quad (5.55)$$

If no area on the substrate without mechanical strain is available for fixing a temperature compensation sensor, a free sensor can be used instead. To calculate the compensation, eq. 5.34 is solved for  $\Delta T$  and substituted into eq. 5.53:

$$\varepsilon_{1,s,m} = \frac{1}{k_\varepsilon} \left( \frac{\Delta\lambda(\varepsilon, T)}{\lambda_{B,0}} - \frac{\Delta\lambda(T)}{\lambda_{B,0}} \frac{k_\varepsilon \alpha_s + \alpha_n}{\alpha_s + \alpha_n} \right) \quad (5.56)$$

However, this method has some major disadvantages: A free sensor is usually subjected to a different temperature regime from that of the bonded sensor, because it is not thermally linked to the substrate but is influenced by the temperature of the surrounding atmosphere. Furthermore, compensation with a free sensor directly depends on the coefficients of thermal expansion of the silica fibre and substrate. If these values are not exactly known, the compensation will be erroneous. Both topics can lead to substantial compensation errors. The coefficients  $k_\varepsilon$  and  $\alpha_n$  are determined in sections 5.1.4.1 and 5.1.4.2 below.

Eq. 5.51 is usually sufficient for calculating a fibre bonded to a substrate, as the thermal expansion coefficient of the fibre is small compared with other materials, e.g. soda-lime silica glass  $\alpha_s = 9.00 \cdot 10^{-6} 1/K$ . However, the different thermal expansion of the bonded sensor fibre and the substrate can cause real strain in the fibre. By taking the additional differential strain caused by the thermal expansion coefficient difference of the substrate and the fibre  $\alpha_s - \alpha_g$  into account through the terms

$$\begin{aligned} \varepsilon_{1,f}(T) &= \Delta T (\alpha_s - \alpha_g) \\ \varepsilon_{2,f}(T) &= -\nu \Delta T (\alpha_s - \alpha_g) \\ \varepsilon_{3,f}(T) &= -\nu \Delta T (\alpha_s - \alpha_g) \end{aligned} \quad (5.57)$$

and proceeding as above by substitution into eq. A.2 and then into eq. A.3 together with eq. A.4, the full term for a surface-bonded fibre subjected to both mechanical strain from the substrate and thermal loads reads in analogy to eq. 5.29:

$$\begin{aligned} \frac{\Delta\lambda(\varepsilon, T)}{\lambda_{B,0}} &= \\ &= \varepsilon_{1,f} \left( 1 - \frac{n_0^2}{2} p_{12} \right) - \frac{n_0^2}{2} \left[ \left( \frac{p_{11} + p_{12}}{2} \right) (\varepsilon_{2,f} + \varepsilon_{3,f}) \pm \right. \\ &\pm \left. \left( \frac{p_{11} - p_{12}}{2} \right) (\varepsilon_{2,f} - \varepsilon_{3,f}) \right] + \Delta T \left[ \frac{1}{n_0} \frac{dn_0}{dT} + \right. \\ &\left. + (\alpha_s - \alpha_g) \left( 1 - \frac{n_0^2}{2} (p_{12} - \nu (p_{11} + p_{12})) \right) \right] \end{aligned} \quad (5.58)$$

Again, for the case of pure axial loading of the fibre,  $-\nu \varepsilon_1 = \varepsilon_2 = \varepsilon_3$  applies and, by additionally substituting  $K_\varepsilon$  in the above equation, we obtain

$$\frac{\Delta\lambda(\varepsilon, T)}{\lambda_{B,0}} = K_\varepsilon \varepsilon_{1,f} + \Delta T [K_\varepsilon (\alpha_s - \alpha_g) + \alpha_n] \quad (5.59)$$

As above,  $K_\epsilon$  can be replaced by the gauge factor  $k_\epsilon$  if the strain transmission effects are being taken into account:

$$\frac{\Delta\lambda(\epsilon, T)}{\lambda_{B,0}} = k_\epsilon [\epsilon_{1,s,m} + \Delta T (\alpha_s - \alpha_g)] + \Delta T \alpha_n \quad (5.60)$$

Expression 5.59 corresponds to the equation provided by van Roosbroeck et al [Van09]. The authors also mention the change of the thermo-optic coefficient of a fibre with temperature, which in this work is taken into account by using the expressions for  $\alpha_n$  derived in section 5.1.4.2.

If the fibre is bonded to a substrate subjected to bending, the result obtained from eq. 5.59 and 5.51 leads to fibre strain results  $\epsilon_{1,f}$  differing from those on the substrate's surface  $\epsilon_{1,s,m}$  because of the distance between the fibre axis and the surface of the substrate. The strain calculated from the fibre therefore has to be corrected by [VDE 10, p. 34]:

$$\epsilon_{1,s,m} = \epsilon_{1,f} \frac{\frac{t_s}{2}}{\frac{t_s}{2} + t_a + r_f} \quad (5.61)$$

In this equation,  $t_a$  is the adhesive thickness directly below the fibre,  $r_f$  the fibre radius and  $t_s$  the substrate thickness. More details are provided in the following section 5.1.2. Please note, that this equation contains a small error attributable to the different bending radii on the top and bottom surface of the glass. In case of considerable differences, for example, thick substrates with high bending curvature, equation 5.61 can be replaced by:

$$\epsilon_{1,s,m} = \frac{\epsilon_{1,f}}{\frac{(t_s + r_f + t_a) \left(1 - \frac{1}{r_{\epsilon,s}}\right)}{t_s} + \frac{1}{r_{\epsilon,s}}} \quad (5.62)$$

$$r_{\epsilon,s} = \frac{\epsilon_{1,s,m}}{\epsilon_{1,s,o}}$$

where  $\epsilon_{1,s,m}$  is the strain on the surface of the substrate beneath the fibre bond and  $\epsilon_{1,s,o}$  is the strain on the surface of the substrate opposite to the bond. This equation thus necessitates to know the reference strain on the top and bottom surface of the substrate. Alternatively, these can be obtained from the bending radii of both glass surfaces. An assumption can be gained by a finite element model or measurement of the geometrical shape in a test. However, this method only applies if the reference strain or substrate bending values are known. In most practical applications, the difference of the pure bending strain on both glass surfaces will be negligible because of the small curvature feasible by

cold bending. In the case of considerable normal (membrane) forces adding to the bending, the use of the bending strain correction in eq. 5.61 can cause an error in the calculation of the strain on the glass surface.

In section 5.1.6, a mechanical FE-model of microscopic scale, representing a small, densely meshed 3D-section of a surface-bonded fibre is analysed for obtaining the gauge factor  $k_\epsilon$  for the case of a fibre subjected to 3D-principal strain states as in eq. 5.58. The basic principle of these studies is to evaluate the possible application of a gauge factor in eq.5.51, 5.53 for the strain calculation in cold bent glass laminates.



5.1.2. Strain Transfer Models

In the case of the cold bending of glass, the bonded fibres are glued to the glass surface prior to the bending process. In this way, the fibres include the bending prestress when being subjected to the autoclave process for lamination. The related heating to temperatures of 140°C cause the Young’s modulus / shear modulus of the adhesive to decrease, as shown in section 5.1.3. During the entire process, a suitable shear bond of the fibre and the glass substrate has to ensure full strain transfer from the glass into the fibre core to preserve the bending prestress. At the beginning of the bond, the strain transfer ratio between the fibre and the substrate  $\epsilon_f/\epsilon_s$  is at 0% and increases along the length of the bond. Gluing methods and joint geometries have to be established to guarantee a 100%-ratio in the fibre before the location of the FBG itself in order to avoid strain gradients in the sensor. The bonding length of the fibre thus plays an important role in the strain transfer. Basically, a soft adhesive with a small shear modulus will necessitate a longer bond length of the fibre to assure full strain transfer at the FBG, whereas an adhesive having a high shear modulus allows a shorter bond. The bond length should be as short as possible to allow bonding in the substrate’s constant strain zone but also as long as necessary to arrive at full strain transfer at the FBG itself, see fig. 5.13. The parameters influencing the strain transfer ratio are:

- The deformation of the substrate and related surface strain type  $\epsilon_s$ , e.g. bending with a radius  $R_s$ .
- The adhesive properties: Youngs’ modulus  $E_a$ , shear modulus  $G_a$ .
- The mechanical properties of the substrate  $E_s$ ,  $\nu_s$  and the fibre  $E_f$ ,  $\nu_f$ .
- The total bond length  $2L_a$  and the included FBG length  $2L_b$ .
- The minimum bond thickness  $t_a$  below the fibre and possible effective thickness  $h_a$ .
- The substrate thickness  $t_s$ .

These values are depicted in figures 5.13, 5.14 and 5.15 below. The focus of the analytical approach developed here is on the determination of sufficient bond length depending on the above-mentioned parameters and on establishing a basic bond-length-dimensioning tool for practical application purposes. The potential strain states of a fibre bonded to a glass surface subjected to axial or bending strain and for a bent laminate are shown in fig. 5.12.

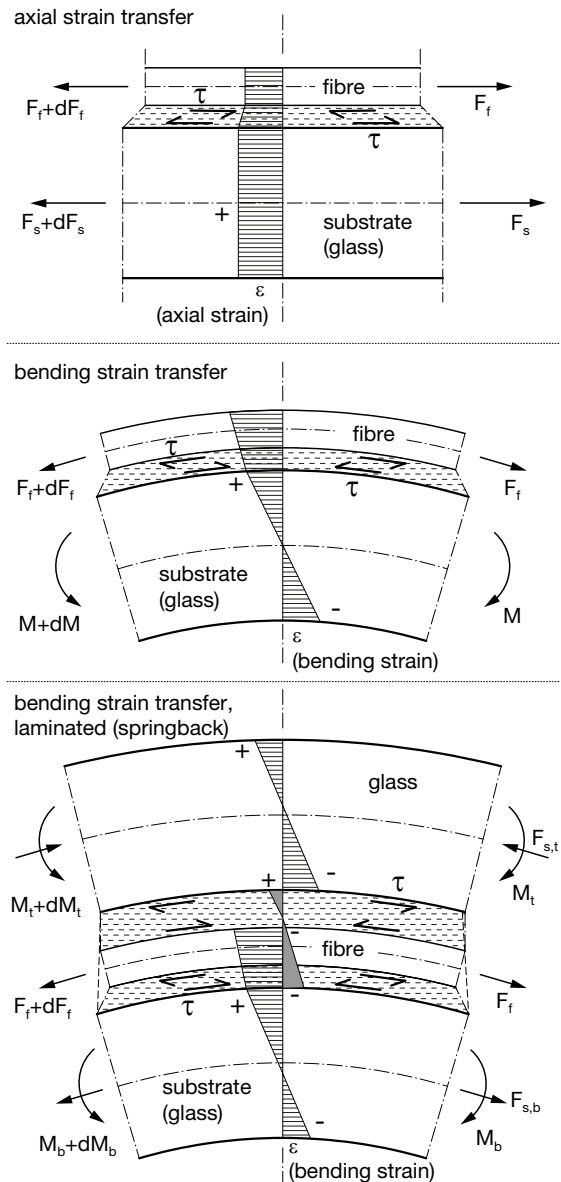


Figure 5.12.: Schematic axial and bending models of a FBG bonded to a substrate and inside of a laminate.

5.1.2.1. Axial Strain Transfer Models

Cheng et al. have developed a linear-elastic 1D strain transfer model [Che05, p. 3908] based on the assumption of continuous axial strain across the interfaces of the axially loaded substrate, the adhesive and the bonded fibre. A shear coefficient  $\bar{\Gamma}^2$  describes the shear lag occurring because of the low stiffness of the bond compared with the fibre and the substrate:

$$\bar{\Gamma}^2 = \frac{G_a L_a^2}{E_f t_f t_a} \left( 1 + \frac{1}{\frac{t_s E_s}{t_f E_f}} \right) \quad (5.63)$$

Based on this, Schlüter [Sch 10, p. 25] has replaced the bond thickness below the fibre  $t_a$  by an effective thickness  $h_a$ , which is defined to take into account the geometry of the bond section. The effective thickness of an adhesive bond having the same width as the fibre diameter (fig. 5.13) is determined by

$$h_a = t_a + r_f \left( 1 - \frac{\pi}{4} \right) \quad (5.64)$$

with  $r_f$  being the fibre radius,  $t_a$  the minimum adhesive thickness between the fibre bottom and the substrate and  $h_a$  the effective thickness of the adhesive bond, see fig. 5.13. For an adhesive joint with a lateral overhang  $o_a$ , Schlüter proposes a different equation:

$$h_a = \frac{2r_f t_a + 2 \left( r_f^2 - 0.25 \pi r_f^2 \right) + o_a (t_a + r_f)}{2r_f + o_a} \quad (5.65)$$

The shear lag K-factor introduced by Schlüter is defined by

$$K = \sqrt{\frac{G}{E_f h_a r_f}} \quad (5.66)$$

The solution for the differential equation describing the strain ratio of the fibre and the substrate is

$$\frac{\varepsilon_f(x)}{\varepsilon_s} = \left[ 1 - \frac{\sinh(Kx)}{\sinh(KL_a)} \right] \quad (5.67)$$

The analytical strain transfer model by Her and Huang [Her 11, pp. 6927-6941] additionally incorporates the effect of the coating. The model is based on the longitudinal stress equilibrium of the fibre and the substrate and on the shear continuity at the interfaces of the substrate, adhesive, coating and fibre. The fibre bond geometry is shown in fig. 5.14. The shear lag K-factor is

$$K = \sqrt{\frac{2r_f}{\pi r_c^2} \left( \frac{\pi r_c^2}{2t_s r_f E_s} + \frac{1}{E_f} \right)} \cdot \sqrt{\int_0^{\cos^{-1}\left(\frac{b_a}{r_f}\right)} \left[ \frac{1}{\frac{r_c(1-\sin\theta)}{G_a} + \frac{r_f}{G_c} \ln\left(\frac{r_f}{r_c}\right)} \right] d\theta} \quad (5.68)$$

where  $G_a$  is the shear modulus of the adhesive and  $G_c$  the shear modulus of the coating.

The ratio of the fibre / substrate strain is

$$\frac{\varepsilon_f}{\varepsilon_s} = \frac{1}{E_f \left( \frac{\pi r_c^2}{2t_s r_f E_s} + \frac{1}{E_f} \right)} \left[ 1 - \frac{\cosh(Kx)}{\cosh(KL_a)} \right] \quad (5.69)$$

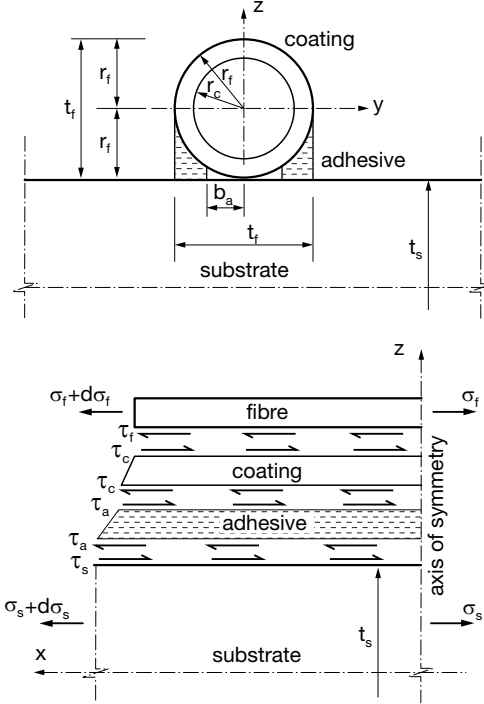


Figure 5.14.: Transverse and longitudinal section model of a surface-bonded FBG [Her 11, p. 6928].

### 5.1.2.2. Bending Strain Transfer Model Development

All models presented in the previous section have been developed for axial loading; bending is not covered. However, glass laminates used in building or vehicles or cold bent glass are mainly subjected to bending. For low bending curvature and small fibre dimensions or thin bonds one might argue that the strain state from the substrate surface influencing the fibre core is actually close to being axial but this hypothesis neglects the bending influence and leads to an error increasing with the distance of the fibre axis from the surface of the substrate. As the fibre radius and the adhesive's added thickness are typically more than 0.19mm, the error is not negligible. The simplified bending model developed hereafter aims at means of determining the necessary bond length to achieve full bending strain transfer from a bent substrate to an FBG glued to its surface. The following assumptions are defined:

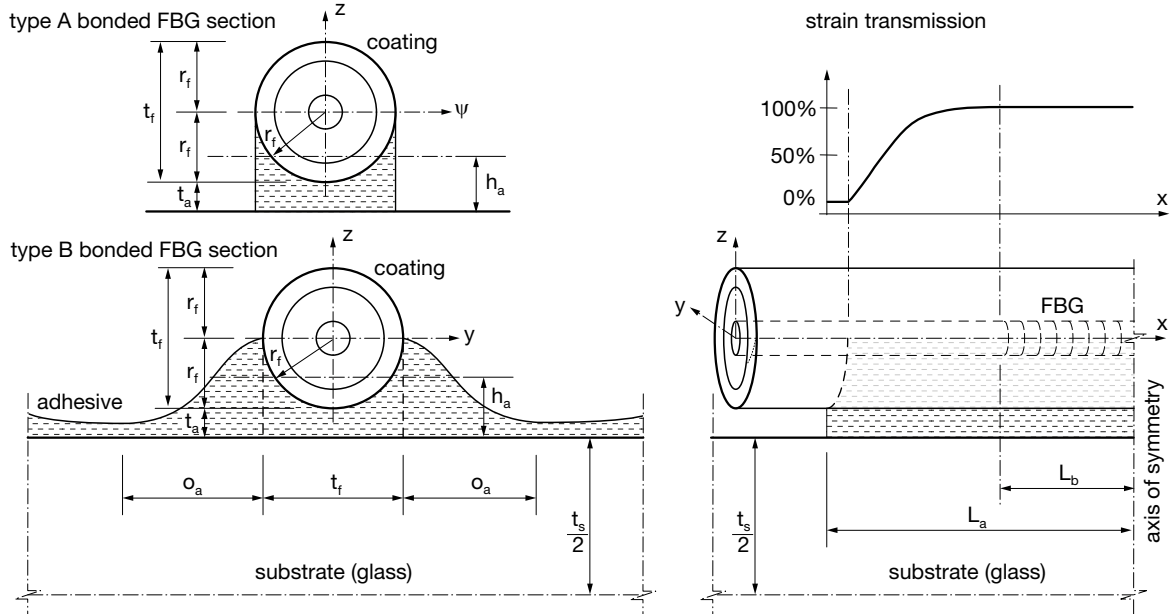


Figure 5.13.: Schematic transverse and longitudinal sections of a surface-bonded fibre.

- Perfect bonding of the fibre to the glass, strain continuity at all interfaces.
- Strain in longitudinal fibre direction (1D model).
- Linear-elastic, isotropic materials.
- Linear theory applies for bending with small deformations.
- Bernoulli's hypothesis is valid for the glass and the fibre.
- Shear deformation (Timoshenko) of the section of the substrate or the fibre is not taken into account.
- The bending radius  $R_s$  of the substrate surface and the bending moment are assumed to be constant along the the bond length  $L_a$ .
- The effect of the coating is not considered.
- The adhesive works in shear only.
- Bending of the substrate causes a force along the fibre axis. The bending stiffness of the fibre itself is negligible.

The procedure for setting up the equilibrium formulations is inspired by the methods applied by Schlüter [Sch 10, pp. 25-31] and Her et al. [Her 11, pp. 6927-6941]. All geometrical variables are depicted in fig. 5.15 and fig. 5.13. The thickness of the glue below the fibre changes along the circular interface between the fibre and the adhesive. For this analysis, the simplified bonding section of type A shown in the left upper part of fig. 5.13 applies. The whole model cannot, however, take three-dimensional or plain strain states into

account, that are more closely examined by FEA in section 5.1.6. For the effective adhesive bond thickness  $h_a$  of the simplified section type A in the  $z$ -direction, a factor having an important influence on the strain transfer from the substrate into the fibre, two possible hypotheses are assumed, see eqs. 5.70, 5.71:

$$h_{a,t} = t_a \quad (5.70)$$

$$h_a = \frac{1}{3} \frac{r_f^2 (3\pi - 10) + r_f t_a (3\pi - 12) - 6t_a^2}{r_f (\pi - 4) - 4t_a} \quad (5.71)$$

Whereas the first equation only takes the minimum thickness of the adhesive directly below the fibre into account, the latter equation assumes the centre of the area of the adhesive bond section as being the thickness affecting the strain transfer. As the first hypothesis from eq. 5.70 largely overestimates the stiffness of the bond, the centre of area-assumption  $h_a$  is examined here. The effect of the coating is not included in the following derivation. Therefore, the fibre and the coating are modelled by using an effective Young's modulus  $E_{f,eff}$  as given by Voigt [Kel 14, pp. 3-15] for a composite section of axial, parallel isotropic material bars and loading in axial direction. It is composed of the area-weighted Young's modulus of the coating  $E_c$  and the fibre  $E_f$ :

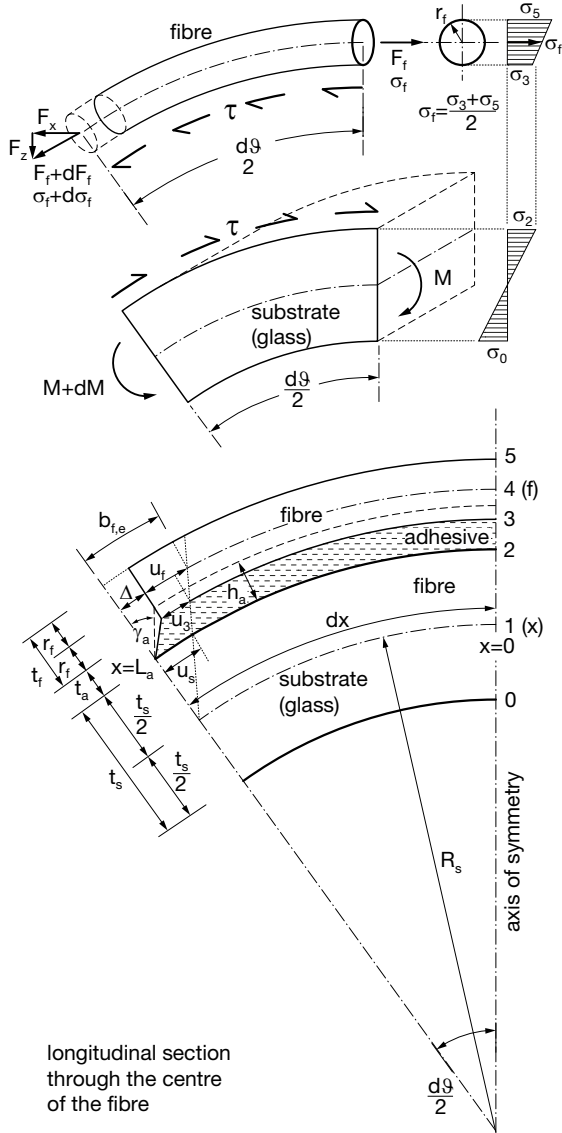


**Figure 5.15.:** Schematic depiction of a surface-bonded fibre subjected to bending.

$$E_{f,eff,V} = \psi_c E_c + \psi_f E_f \quad (5.72)$$

where the volume fractions  $\psi_c$ ,  $\psi_f$  of the coating section area  $A_c$  and the fibre cladding / core section area  $A_f$  related to the total area of the coated fibre  $A_{tot}$  are:

$$\psi_c = \frac{A_c}{A_{tot}} \quad \psi_f = \frac{A_f}{A_{tot}} \quad (5.73)$$

Potential Poisson-effects as proposed by Liu et al. [Liu 09, p. 2200] are neglected, as the fibre's layers are assumed to have only insignificant lateral expansion obstruction.

The bending radii at the various layers of the substrate-fibre-bond are defined by

$$\begin{aligned} r_2 &= R_s + \frac{t_s}{2} \\ r_3 &= R_s + \frac{t_s}{2} + r_f + t_a - \sqrt{r_f^2 - y^2} \\ r_4 &= R_s + \frac{t_s}{2} + t_a + r_f \end{aligned} \quad (5.74)$$

The related full arc lengths, without taking into account the shear lag, at the layers in the entire system<sup>22</sup> are

$$\begin{aligned} b_2 &= r_2 d\vartheta = \left( R_s + \frac{t_s}{2} \right) d\vartheta \\ b_3 &= r_3 d\vartheta = \left( R_s + \frac{t_s}{2} + r_f + t_a - \sqrt{r_f^2 - y^2} \right) d\vartheta \\ b_4 &= r_4 d\vartheta = \left( R_s + \frac{t_s}{2} + t_a + r_f \right) d\vartheta \end{aligned} \quad (5.75)$$

where  $d\vartheta = \frac{dx}{R}$  is the bending angle. The effective elongation values  $u_s, b_{f,e}$  and the shear lag  $\Delta$  of the layers attributable to bending for the symmetric half of the system are:

$$u_s(x) = \frac{1}{2} (b_2 - dx) = \frac{t_s}{4} d\vartheta \quad (5.76)$$

$$b_{f,e}(x) = \frac{1}{2} (b_4 - dx) = \left( \frac{t_s}{4} + \frac{t_a}{2} + \frac{r_f}{2} \right) d\vartheta \quad (5.77)$$

$$\Delta = b_{f,e}(x) - u_f(x) = \left( \frac{t_s}{4} + \frac{t_a}{2} + \frac{r_f}{2} \right) d\vartheta - u_f(x) \quad (5.78)$$

The variable  $dx$  is the arc length value along the substrate's axis depending on the bending angle, which is given by transforming eq. 5.76:

$$d\vartheta = \frac{4}{t_s} u_s(x) \quad (5.79)$$

Substitution of eq. 5.79 into eq. 5.78 yields

$$\Delta = u_s(x) \left( 1 + \frac{2t_a}{t_s} + \frac{2r_f}{t_s} \right) - u_f(x) \quad (5.80)$$

<sup>22</sup>The further derivation uses only half of the entire bent system because of axial symmetry

The above equations permit the definition of the shear deformation angle by

$$\gamma_a = \frac{\Delta}{h_a} = u_s(x) \left( \frac{1}{h_a} + \frac{2t_a}{t_s h_a} + \frac{2r_f}{t_s h_a} \right) - \frac{u_f}{h_a} \quad (5.81)$$

The force equilibrium of the fibre and the boundary layer with the adhesive (fig. 5.15) are established in the next step. As shown in the upper part of fig. 5.15, the resultant force  $F_f + dF_f$  at the left side of the bent fibre consists of two force components  $F_x, F_z$ :

$$F_x = \cos\left(\frac{d\vartheta}{2}\right) (F_f(x) + dF_f(x)) \quad (5.82)$$

$$F_z = \sin\left(\frac{d\vartheta}{2}\right) (F_f(x) + dF_f(x))$$

The typical bending radii of bent glass are usually  $> 2000mm$  and the bond lengths FBGs have lengths  $2L_a < 60mm$ . For these conditions,  $|d\vartheta/2| \ll 1$  applies and the force components can be approximated by

$$\sin\left(\frac{d\vartheta}{2}\right) \approx \frac{d\vartheta}{2} \Rightarrow F_z \approx 0 \quad (5.83)$$

$$\cos\left(\frac{d\vartheta}{2}\right) \approx 1 \Rightarrow F_x \approx F_f(x) + dF_f(x),$$

The shear area  $A_s^f$  at the interface of the adhesive with the fibre and the cross section area  $A_f$  of the fibre is assumed to be a part of a torus and is

$$A_s^f = \frac{d\vartheta}{2} \int_{-r_f}^{r_f} \left[ \left( R_s + \frac{t_s}{2} + t_a + r_f - \sqrt{r_f^2 - y^2} \right) \cdot \sqrt{1 + \frac{y^2}{r_f^2 - y^2}} \right] dy \quad (5.84)$$

assuming a semi-circle for the adhesive-fibre-interface.

$$A_f = \pi r_f^2 \quad (5.85)$$

The horizontal equilibrium of the fibre is obtained by equating the axial forces and the shear stress  $\tau$  along the shear area  $A_s^f$ :

$$\begin{aligned} \sum \vec{N}_f = 0: F_f - (F_f + dF_f) - \tau A_s^f &= 0 \\ \Leftrightarrow -dF_f = \tau A_s^f & \end{aligned} \quad (5.86)$$

After the performance of different design insertion and transformation operations, the equilibrium equation of the fibre becomes

$$\frac{d\sigma_f(x)}{dx} = -\tau \frac{1}{2\pi r_f^2 R_s} \int_{-r_f}^{r_f} \left[ \left( R_s + \frac{t_s}{2} + t_a + r_f - \sqrt{r_f^2 - y^2} \right) \sqrt{1 + \frac{y^2}{r_f^2 - y^2}} \right] dy \quad (5.87)$$

Assuming the involved material modules  $E_s, E_{f,eff}, G_a = const.$  and linear elasticity, the stress acting on the substrate's surface and in the fibre is

$$\sigma_s(x) = \varepsilon_s(x) E_s \quad (5.88)$$

$$\sigma_f(x) = \varepsilon_f(x) E_s \quad (5.89)$$

and the strain is

$$\varepsilon_s(x) = \frac{du_s}{dx}; u_s = u_s(x) \quad (5.90)$$

$$\varepsilon_f(x) = \frac{du_f}{dx}; u_f = u_f(x) \quad (5.91)$$

The shear strain at the interfaces with the adhesive depends on the shear angle and shear modulus:

$$\tau = G_a \gamma_a \quad (5.92)$$

Next, eq. 5.89 is differentiated with respect to  $x$  and the result is equated with eq. 5.87.  $\tau$  is substituted by eq. 5.92 and  $\gamma_a$  with 5.81. Differentiation ( $x$ ) of the expression obtained and substitution of the strain eqs. 5.90 and 5.91 leads to the second order differential equation

$$\begin{aligned} \varepsilon_f''(x) &= -\frac{G_a}{2\pi r_f^2 E_{f,eff} R_s h_a} \cdot \\ &\cdot \left[ \varepsilon_s(x) \left( 1 + \frac{2t_a}{t_s} + \frac{2r_f}{t_s} \right) - \varepsilon_f(x) \right] \int_{-r_f}^{r_f} \left[ \left( R_s + \frac{t_s}{2} + t_a + r_f - \sqrt{r_f^2 - y^2} \right) \sqrt{1 + \frac{y^2}{r_f^2 - y^2}} \right] dy \end{aligned} \quad (5.93)$$

For simplification reasons, a shear lag parameter  $K^2$  is isolated from the above eq. 5.93:

$$\begin{aligned} K^2 &= \frac{G_a}{2\pi r_f^2 E_{f,eff} R_s h_a} \int_{-r_f}^{r_f} \left[ \left( R_s + \frac{t_s}{2} + t_a + r_f - \sqrt{r_f^2 - y^2} \right) \sqrt{1 + \frac{y^2}{r_f^2 - y^2}} \right] dy \end{aligned} \quad (5.94)$$

$K$  depends on the bond geometry and the materials involved. It can thus be seen as a parameter expressing the bond strain transfer efficiency and stiffness. Substituting the expression for  $K^2$  in eq. 5.93 and solving this equation leads to

$$\varepsilon_f(x) = e^{Kx} C_2 + e^{-Kx} C_1 - \frac{K \left( \frac{t_s}{2} + t_a + r_f \right) e^{-Kx}}{t_s} \cdot \left[ \left( \int e^{-Kx} \varepsilon_s(x) dx \right) e^{2Kx} - \left( \int e^{Kx} \varepsilon_s(x) dx \right) \right] \quad (5.95)$$

The boundary conditions to determine the constants  $C_1, C_2$  in eq. 5.95 are as follows: directly at the end of the adhesive bond of the fibre,  $x = L_a$ , no strain is transferred into the fibre as yet.

$$\varepsilon_f(x = L_a) = 0 \quad (5.96)$$

At  $x = 0$ , the centre of the bonded fibre and the symmetry axis in this model, full strain transfer is assumed to be accomplished. The difference of the strain in the fibre from the surface strain of the substrate attributable to bending is taken into account using the following:

$$\varepsilon_f(x = 0) = \varepsilon_s(x) \frac{2t_a + t_s + 2r_f}{t_s} \quad (5.97)$$

The expressions  $e^x$  and  $e^{-x}$  in eq. 5.95 are replaced by trigonometric functions and the boundary condition constants are determined and then substituted into 5.95, which leads to the fundamental equation describing the strain transfer ratio between the fibre and the substrate:

$$\frac{\varepsilon_f}{\varepsilon_s}(x) = \left( 1 + \frac{2r_f}{t_s} + \frac{2t_a}{t_s} \right) \left[ 1 - \frac{\sinh(Kx)}{\sinh(KL_a)} \right] \quad (5.98)$$

Once  $\varepsilon_s(x)$  is known and it has been assured that no strain gradient occurs along the FBG bond length, either the sensor strain  $\varepsilon_f(x)$  or the ratio of the strains can be calculated. Full transfer is reached if the calculated strain ratio depending on the length position  $x$  from the FBG centre remains constant. For bending, this ratio is  $|\varepsilon_f(x)/\varepsilon_s(x)| > 1.0$ , as the sensor lies at a distance from the substrate's surface.  $L_a$  should be set so as to reach full strain transfer even at a minimum distance of  $x = L_b$ , which is half of the FBG length<sup>23</sup>, from the centre.

Analytical and numerical results have been compared; the FE-micro-model used is described in detail in section 5.1.6. Additional parameter studies have been undertaken to examine the sensitivity of the strain transfer to varying shear modulus and bond thickness. Both the realistic bond type-B section with  $o_a = 0.18\text{mm}$  overhang and the simplified type-A joint without overhang  $o_a = 0$ , as shown in fig. 5.13, are applied in the FE model. The other parameters are set as follows:

- $t_a=0.001206\text{mm}$  as a fixed value or as a parameter varying from 0.0001mm to 0.2mm
- Adhesive shear modulus as a variable parameter  $G_a=10\text{MPa}$  to 600MPa or fixed to 10MPa, 570MPa or 600MPa
- Bending radius  $R=3552\text{mm}$
- Glass substrate thickness  $t_s=3.848\text{mm}$
- Fibre radius  $r_f=0.091769\text{mm}$
- Young's modulus of the fibre  $E_f=73,000\text{MPa}$
- Coating modulus  $E_c=1,500\text{MPa}$
- Effective fibre modulus  $E_{f,eff}=34,664.55\text{MPa}$  as per eq. 5.72

In fig. 5.16, the analytical approach (without overhang) is compared with numerical results with and without adhesive overhang  $o_a$  in the bond section. 20mm of the bonded length are examined. The strain transfer curves indicate the necessary length to achieve full strain transfer (99.99% to 100%). From the curves we can see that, on the assumption of full strain transfer, the predicted maximum bending strain level of about  $\varepsilon_f = 1.054\varepsilon_s$  in the analytical and the numerical model correspond.

For a high adhesive shear modulus  $G_a=570\text{MPa}$ , the analytical model slightly underestimates the necessary length to reach full strain transfer for a bond geometry. A bond length of approximately 6mm is necessary to obtain full strain transfer. For the low adhesive shear modulus  $G_a=10\text{MPa}$ , neither the numerical nor the analytical model achieve full strain bending transfer from the substrate into the fibre at  $x=20\text{mm}$ . The analytical model gives a strain transfer curve very close to the FE-analysis results; the necessary bond length is slightly overestimated in comparison with the FE model. For practical application, this tendency is generally safe, as slightly longer bonds than necessary will be calculated in the case of softer adhesives;

<sup>23</sup>Low reflectivity FBG in SMF have a typical length range of 1mm to 10mm. In this work, 8mm long FBGs are used, thus  $x = L_b = 4\text{mm}$ .

this reduces the risk of an incomplete strain transfer to the FBG. In the numerical model, the behaviour of the bonds with and without overhang show only minor differences in strain transfer behaviour and curve gradient for low adhesive shear modulus.

The numerical model with an overhang bond generally shows an increased strain transfer ratio and resulting shorter bond length  $x$  for achieving full strain transfer in comparison with the bond without overhang; the adhesive joint with overhang thus exhibits a more efficient strain transfer. However, the analytical results are close to the values found through FE-analysis and basically validate the principal applicability of the theoretical approach for the pre-dimensioning of the bond lengths. The analytical approach approximately covers a bond geometry both with and without overhang, fig 5.16. However, the limitations discussed above have to be kept in mind during the use of the equations.

The strain transfer ratio is normalised in the following parameter studies to facilitate comparison. Results for a variable adhesive shear modulus values in a range of 10MPa to 600 MPa for a constant  $t_a = 0.012\text{mm}$  are shown in fig. 5.17. The dependency of the shear lag factor  $K$  and of the strain transfer length along  $x$  to obtain 99.99% strain transfer from the substrate into the fibre is strongly non-linear (bottom of fig. 5.17). Below a value of the shear modulus of  $G_a = 50\text{MPa}$  to  $100\text{MPa}$ , bond lengths needed to achieve full strain transfer show a rapid non-linear rise with decreasing  $G_a$ .

The top of fig. 5.18 depicts a parameter study for the adhesive thickness  $t_a$  in range of 0 to 0.2mm with a constant, low shear modulus of the adhesive  $G_a = 10\text{MPa}$ . The symmetric bond lengths needed to achieve full strain transfer are more than 40mm. The influence of the adhesive thickness on the bond length shows the importance of using a  $t_a$  as small as possible in order to reduce the shear lag in case of a very soft adhesive. Both the  $K$ -factor and the 99.99% strain transfer ratio show a non-linear dependency on  $t_a$ , although the non-linearity is less pronounced than that with a variable shear modulus. The same parameter variation of  $t_a$  is made for  $G_a = 600\text{MPa}$ . Results are given at the bottom of fig. 5.18. In this case, the  $K$ -factor shows a more accentuated non-linearity depending on  $t_a$ , than in the case of a small adhesive shear modulus. Moreover, the influence of the bond thickness on the bond length necessary to reach 99.99% strain transfer is smaller than for adhesives with low  $G_a$ .

As a conclusion, the shear modulus of the adhesive is the most influential parameter regarding the bond length and the strain transfer ratio. Values above 50MPa to 100MPa provide an efficient ratio of bond length and shear transfer capacity. The adhesive thickness has less influence, but has to as small as possible, in particular for adhesives having a low  $G_a$ . A bond overhang can slightly improve the strain transfer from the substrate into the fibre. The adhesives applied for the FBG bonding in this work (5.1.3.5) show shear modulus values larger than 1000MPa at room temperature but decrease to  $G_a \approx 55\text{MPa}$  (adhesive KB OB642) or about 10MPa (adhesive KB4552) for autoclave temperatures of 140°C. Subsequently, bonding lengths of  $L_a = 25\text{mm}$  (fig. 5.17) are applied on either side of the 8mm long FBGs, leading to a maximum bond length of 60mm. Constant strain at the surface of the substrate along the bond length has to be provided. In the tests, this is achieved by producing constant bending radii and therefore constant bending moments through four-point bending, section 5.1.5, or bending on cylindrical moulds, section 6.1, in the glass at the sensor positions.

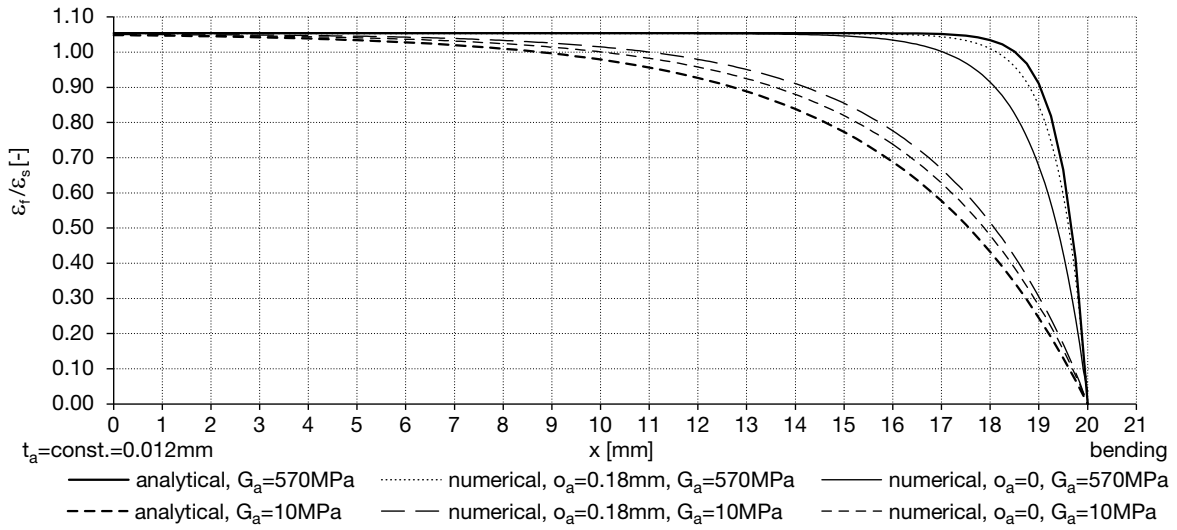


Figure 5.16.: Comparison of numerically and analytically determined bending strain for different  $G_a$  and bond types A, B.

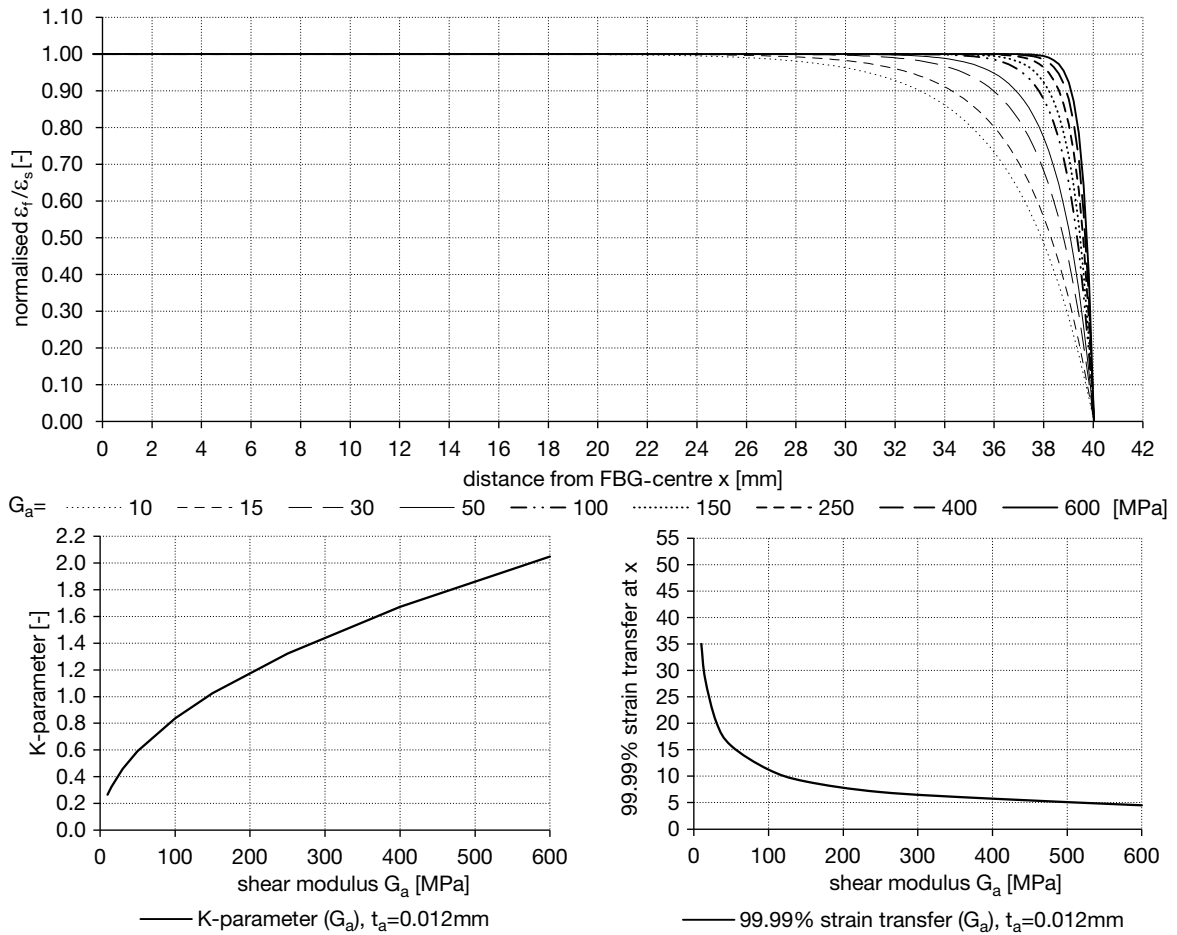


Figure 5.17.: Bending strain transfer ratio with varying  $G_a$  for  $t_a=0.012$ mm.



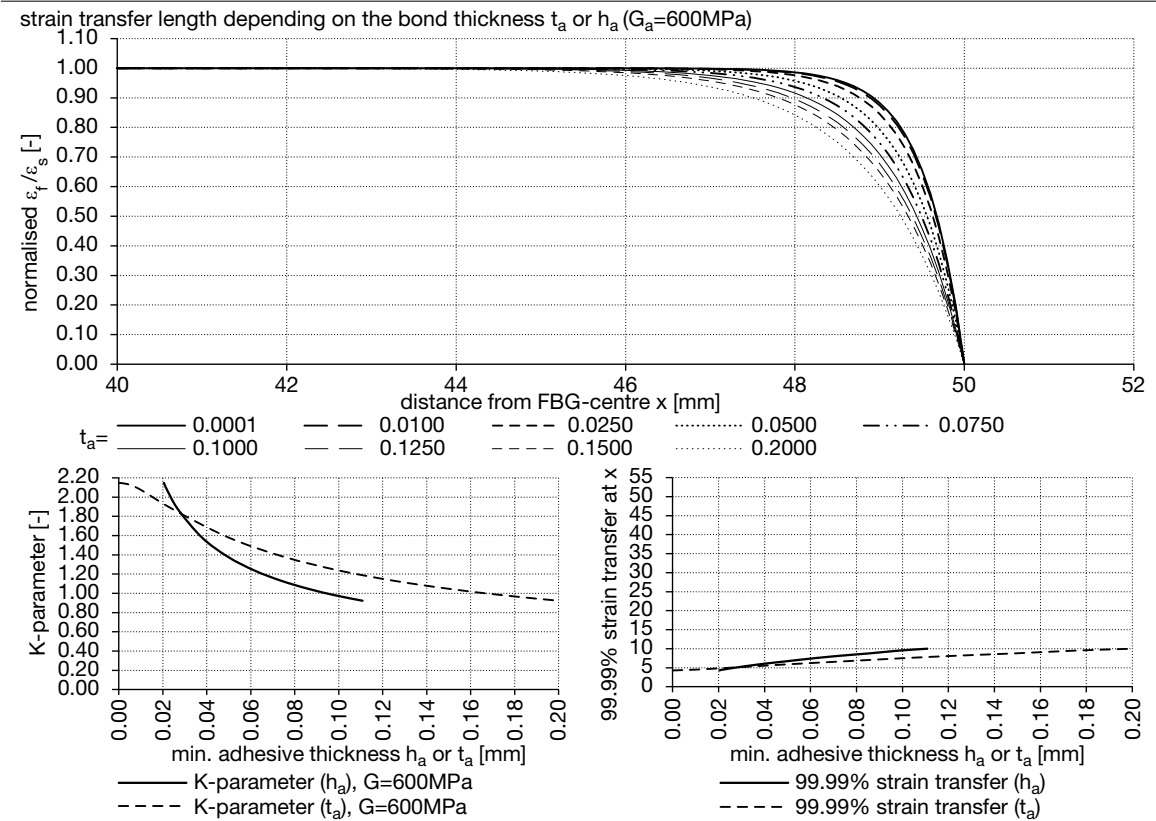
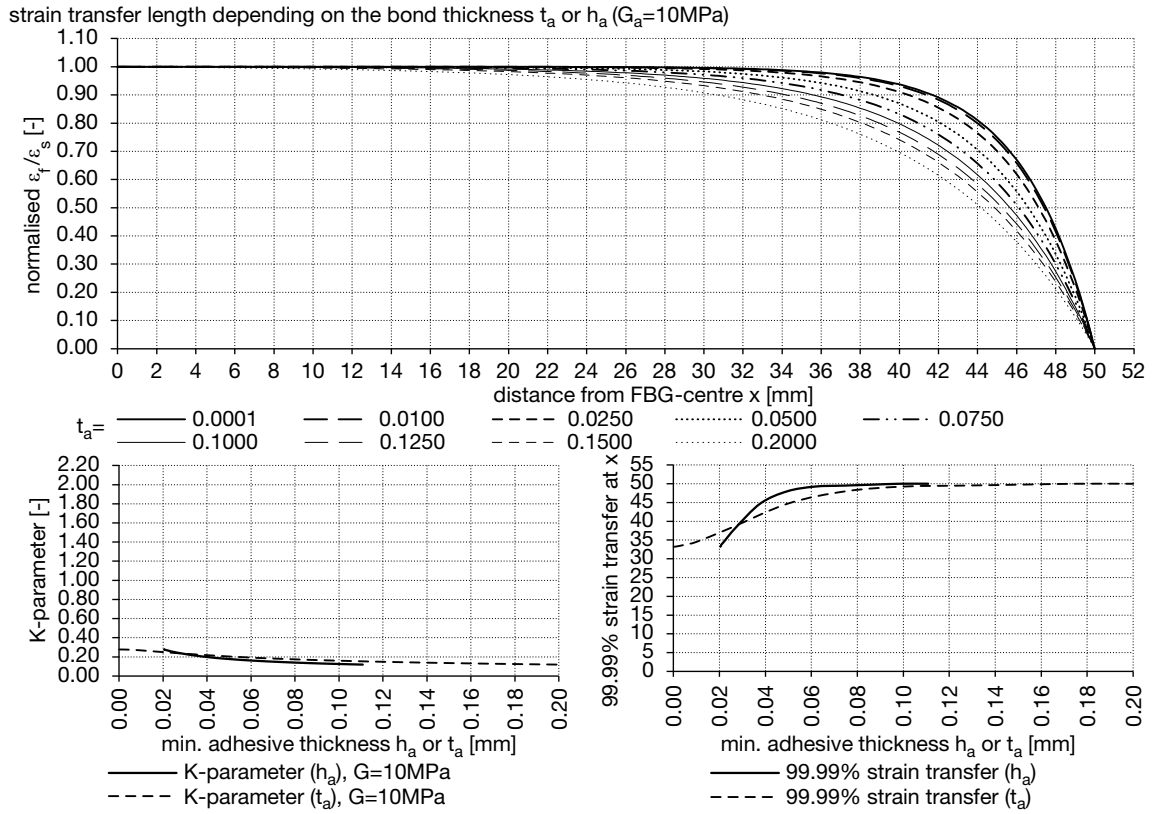


Figure 5.18.: Bending strain transfer ratio with varying  $t_a$  for  $G_a=10\text{MPa}$  (top) and  $G_a=600\text{MPa}$  (bottom).

### 5.1.3. Adhesive Choice for FBG Sensor Bonding

The quality of strain measurement provided by an FBG notably depends on the properties of the adhesive bond, which attaches the fibre to a substrate's surface. Although various adhesive solutions have been proposed, e.g. [Sch 10, p. 43], no system is available for FBG bonding on glass subjected to the temperature conditions occurring during lamination. Furthermore, only a few techniques are available for establishing a reproducible bond with constant dimensions. The company FBGS has commercialised a UV-curing bonding system with a silicone pad for mounting the fibre with the adhesives Z70, X60 or Norland NOA61<sup>24</sup>. Other solutions rely on fibres in a GFRP-patch<sup>25</sup>. Trutzel [Tru 01, p. 181] used a stamp-like application device. However, no solution exists that focuses on transparent bonding to glass. Thus, the following section is dedicated to the identification of an adhesive for use in FBG-bonding in the context of glass laminates. The conditions that the adhesive is subjected to and the related material parameters are:

- Adhesion to soda-lime silica glass and to the Ormocer<sup>®</sup> coating of the fibre.
- Transparency, colourlessness after cure; refractive index similar to soda-lime silica glass ( $n \sim 1.52$ ).
- High stiffness bond for obtaining sufficient strain transfer from the glass into the fibre and for reducing the bond length. The recommended shear modulus is  $>50$  MPa to 100MPa at peak autoclave temperature to preserve FBG prestress from cold bending of glass during the lamination process, see previous section 5.1.2.2.
- Resistance to autoclave conditions (13bar pressure, 140°C temperature for a period of up to 5h), no major chemical alterations, phase changes or degradation of the adhesive. After autoclaving, the adhesive has to regain the stiffness properties and transparency that it had prior to the process. The glass transition temperature  $T_g$  as a reference value should thus be high and ideally exceed 140°C.
- Low viscosity of approximately 1,000-

10,000mPas for minimising the bond thickness  $t_a$ , permitting a good flow behaviour of the adhesive for adapting to the fibre section geometry and for gap-filling.

- Sufficient viscosity to prevent uncontrolled dispersal on substrate's surface and for obtaining an even bond surface of constant thickness.
- Adhesive application technique and glue viscosity need to be designed allowing for reproducible constant bond geometry and quality.
- Tack-free glue surface after curing.
- Controllable cure of the adhesive with respect to maintaining the fibre position in the bond. This condition favours UV-curing adhesives, as these can be cured in a short-time period after correctly positioning the fibre in the liquid adhesive. The orientation and position of the fibre on the substrate determines the strain component that it will measure in use.
- No thermal post-cure effects of the adhesive during the autoclave process, as such effects might cause shrinkage of the bond, which can induce unwanted residual fibre strain.

With regard to the sheer number of available adhesives, the examination performed in the context of this work is forcedly limited to a comparison of basic adhesive parameters chosen with respect to the above conditions. For choosing an appropriate adhesive for FBG bonding onto glass, several basic analyses have been made in this work to determine the temperature-dependent Young's modulus  $E_a$  of the adhesive, the glass transition temperature  $T_g$ , the thermal behaviour and possible post-cure effects by uniaxial tensile tests, dynamic mechanical analysis (DMA), differential scanning calorimetry (DSC) and infrared spectroscopy (IRS). Furthermore, the processibility, bond quality and geometrical bond quality have been analysed, the last mentioned by surface roughness measurement. In addition to identifying a suitable adhesive, an adequate application technique has been developed; this is, however, not a topic included in this work.

<sup>24</sup><http://www.fbgs.com/productsadv/be-en/5/detail/item/36/page/1/>

<sup>25</sup><http://www.hbm.com/en/menu/products/strain-gages-accessories/optical-strain-gauges/k-ol/>

### 5.1.3.1. Adhesive Preselection and Cure Conditions

According to the above criteria, several commercially available adhesives were preselected from an initial list of about 50 products. Therefore, the adhesion to glass, the glass transition temperature, the operational temperature range, the cure mechanism, the viscosity and the transparency were used as entry and sorting criteria. An overview of these data as provided by the manufacturers can be found in table B.1 in appendix B.1. Most adhesives used in the context of this work are UV-curing, as this allows for the positioning of an FBG in the liquid adhesive and then its rapid fixation in the chosen position by UV activation of the adhesive.

Apart from adhesives readily available on the market, the performance of the coating material of the fibre, Ormocel<sup>®</sup> NM850, applied for bonding has also been examined. Contrary to the other adhesives, no cure intensity and time information is provided for the particular Ormocel<sup>®</sup> NM850 material applied here. The manufacturer generally recommends UV-cure at a power of 100W/cm, a UV dose 0.5-5J/cm<sup>2</sup> and a curing time of 0.5 to 20 seconds depending on thickness. Therefore, the necessary data were determined by infrared spectroscopy (ISC) with using a PerkinElmer Spectrum 400 device, see below. Detailed information on curing mechanisms of adhesives and related ISC-testing can, for example, be found in a paper by Weller and Kothe [Wel 11a, p. 566].

Ormocer<sup>®</sup> is an inorganic-organic hybrid polymer for applications in optics, opto-electronics and coating technology [Büs 01]. Its properties can be described as a mixture of ceramics, organic polymers, silicones and glass. As in [Büs 01, p. 182], the material is synthesised in two steps by “[...] inorganic polycondensation of [...] silane molecules via sol-gel reaction [...] followed by crosslinking of the organic side chains resulting in three-dimensional duroplastic materials.” Chemically, the material is based on organoalkoxysilanes (diphenylsilanediol and 3 methacryloxypropyltrimethoxysilane) and an inorganic Si-O-Si network. Its viscosity (below 15,000mPas), thermal expansion coefficient ranging from 60 to 250 · 10<sup>-6</sup>1/K and Young’s modulus are adjustable. The Ormocel<sup>®</sup> coating used here is a UV-curable material providing heat resistance up to 250°C and a refractive index ranging from 1.42-1.59 suitable for coatings of 20-50µm of

materials such as PC, PMMA and glass [Ros 13]. On request, the company providing the optical fibres with Ormocel<sup>®</sup>-coating used in this work specified a value of E=1,500MPa for the coating at room temperature and about 500MPa at 120°C.

Testing performed in the context of the present research work revealed a curing time of 90s with a UV-lamp at an intensity level of 60mW/cm<sup>2</sup>. The related test was performed by infrared spectroscopy, in which oscillations of molecules in the polymer specimen are triggered by introducing IR radiation. The different molecular groups in the specimen have absorption bands of different strength and therefore absorb characteristic parts of the introduced energy. These regions are subsequently missing in the related spectra and can thus be identified. In the case of Ormocel<sup>®</sup> NM850, such changes at different UC-curing times (after 0s, 53s and 168s) can, for example, be observed for the band at 807 and the double band 1619, 1635cm<sup>-1</sup>. These bands are related to carbon double-bonds, which are opened during curing and therefore vanish from the spectrum, see fig. 5.19, left. A zoom into the spectrum showing the bands is depicted at the bottom of the same figure. The graphs on the right-hand side in the same figure show the reaction turnover of the bands with time. The reaction turnover (or conversion) is calculated from the area of the bands in the spectrum. After 90s, more than 80% absorption has been reached and the cure reaction is basically achieved.

The tests in the following sections were performed in the context of this work and a joint industry research project at the ITKE / University of Stuttgart for selecting adhesives suitable for FBG-bonding adapted to glass lamination, table 5.2. The testing was conducted at the Friedrich-Siemens-Laboratory of the TU Dresden. Because of the brittleness of some of the adhesives, especially for the DMA, the number of specimens that could be successfully tested, varied. All testing was performed with bulk adhesive specimen cured following the manufacturer recommendations. For some promising adhesives, additional specimens were produced by UV-cure and subsequent tempering at 140°C, comprising 1h heating, 3.5h constant temperature and subsequent cooling. These tests served to examine the adhesive behaviour after an autoclave process. Temperature-curing Epo-Tek 353ND was not tested in this project but is also listed in the tables, as it was used in some of the four-point bending pretests.

5 | ANALYSIS, DIAGNOSTIC

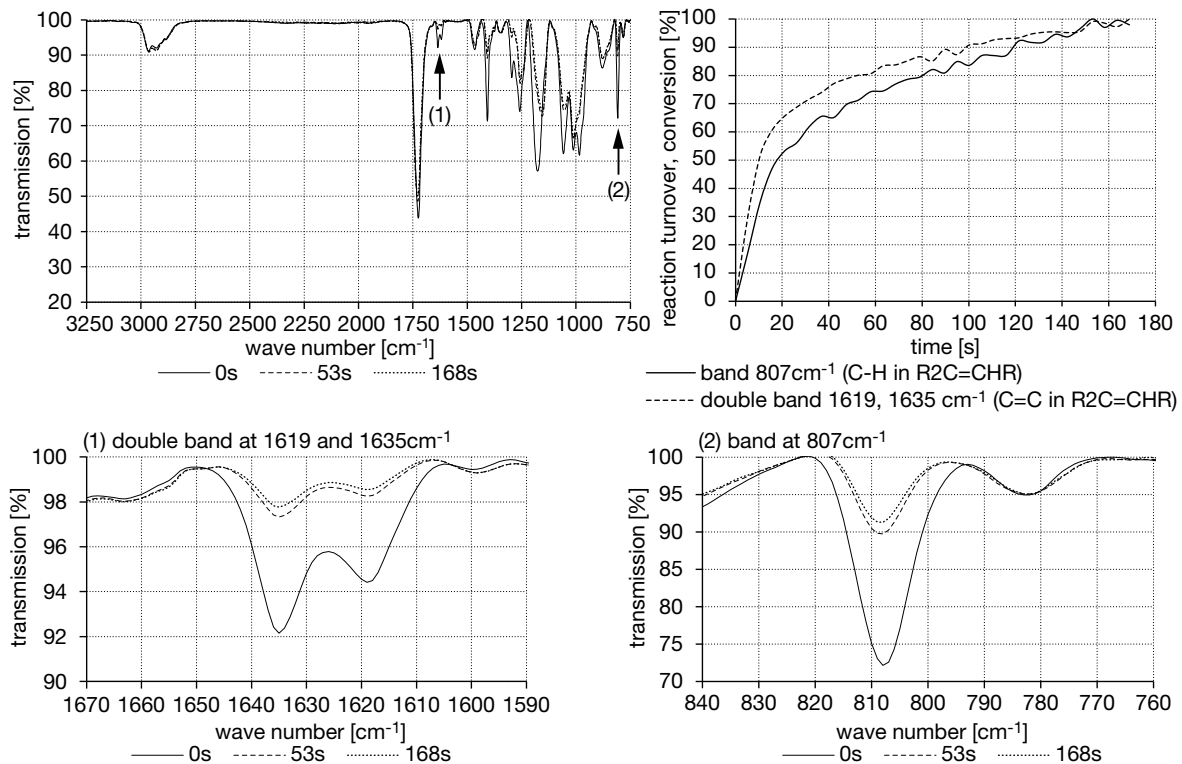
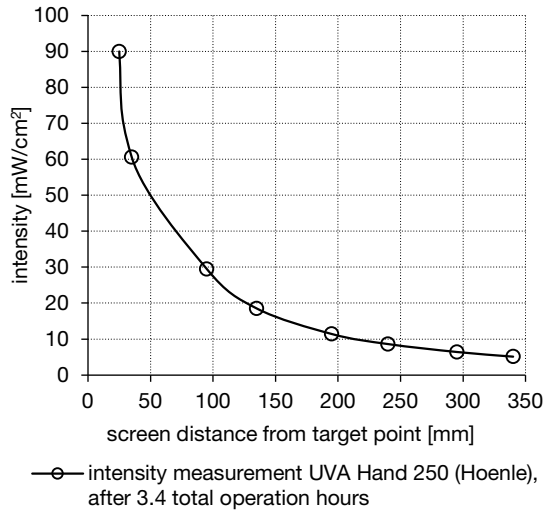


Figure 5.19.: Infrared spectroscopy of Ormocer® NM850: Transmission spectrum (top left), reaction turnover (top-right) and detailed bands of the transmission spectrum (bottom).

no.	manufacturer	brand name	UV-cure			UV-cure and tempering		
			DSC	DMA	tensile test	DSC	DMA	tensile test
1		KB4552	1	2	3	1	1	3
2	DELO	KB AD640	1	6	3	-	2	2
3		KB OB642	1	2	3	1	1	3
4	Dymax	Ultra Light-Weld 431	-	1	3	-	-	-
5	Epoxy Technologies	EPO-TEK 353ND	-	-	-	-	-	-
6	Fraunhofer ISC	Ormocer NM850	1	1	3	-	-	-
7		Ormocer AL1029	1	1	3	-	-	-
8		Loctite 3301	-	1	3	-	-	-
9	Henkel	Loctite 3494	-	1	3	-	-	-
10		Loctite 4090	-	-	2	-	-	-
11		Vitralit UV1605	1	-	3	1	-	3
12	Panacol	Vitralit UV2020	1	1	3	1	-	3
13		Vitralit UC1608	1	3	3	1	-	1
14	Permabond	UV632	1	2	3	-	-	-
15		UV681	1	2	3	-	-	-
16	Polytec	UV2144	1	1	3	-	-	-
17		Catiowell 3052	-	3	3	-	-	-
18	Wellmantech	Catiowell 3052 (thixotr.)	1	1	4	1	1	3
19		Photowell 1044	-	-	-	-	-	-
20	3M	Scotch-Weld UV50	-	1	3	-	-	-
21		Scotch-Weld DP804	-	1	-	-	-	-

Table 5.2.: Overview of the tests carried out with different adhesives.

The lamp used for curing is a Hönle UVA Hand 250 with a metal halide lamp. The intensity of the lamp has been checked by using a DELOLUXControl UV-measurement device prior to application. The resulting intensity profile depending on the lamp's protective screen distance from the curing object is given in fig. 5.20.



**Figure 5.20.:** UV-intensity measurement of UVA Hand 250 lamp depending on light source distance from cure object.

### 5.1.3.2. Dynamic Mechanical Analysis

Adhesives are polymers and thus can be characterised by their viscoelastic behaviour, comprising an elastic part and a viscous Newtonian fluid part. A typical analysis technique used for this is dynamic mechanical analysis (DMA). In DMA, a test sample is excited into oscillation by the application of a cyclic external force or a cyclic deformation. In the first case, the sample is subjected to sinusoidal stress depending on the applied force, and the related sinusoidal strain is calculated from the measured deformation. For the latter testing method, a predefined cyclic deformation applied to the sample causes sinusoidal strain, which allows for the calculation of the respective sinusoidal stress. The phase lag of the exciting or response stress and strain sinus waves, their amplitudes and the applied forces or deformations are used to calculate the viscoelastic material properties. Apart from the oscillation frequency, the temperature can be varied in DMA in order to obtain temperature-dependent material properties. The Netzsch DMA 242 C device shown in fig. 5.21 was used in this work to determine

both the glass transition temperature  $T_g$  and the dependency of Young's modulus on temperature.

The ideal elastic behaviour of a polymer subjected to a sinusoidal force application is characterised by an in-phase strain response ( $\delta = 0$ ). For ideal viscosity, the strain sinus curve shows a phase lag of  $\delta = \pi$  to the excitation stress curve. For a viscoelastic material, the phase lag of the sinusoidal curves is  $0 \leq \delta \leq \pi$ . As polymers are subjected to both elastic and viscous effects, a complex Young's  $E^*$  or shear modulus  $G^*$  is used to describe this behaviour. These complex modules comprise two components: The storage modulus  $E'$ , or  $G'$  for shear, describes the recoverable energy stored in the excited polymer and thus the elastic properties of the material. The loss modulus  $E''$  or  $G''$  is used to define the viscous part corresponding to the energy loss in the oscillated polymer material. As, for example, shown with Menard [Men99, p. 66] or Habenicht [Hab02, p. 696], the complex Young's modulus can be calculated from the storage and loss modulus by

$$E^* = E' + iE'' = \sqrt{E'^2 + E''^2} \quad (5.99)$$

with  $i$  being the imaginary unit  $i^2 = -1$ . This absolute value is analogous to the Young's modulus derived, for example, from tensile tests. Below the glass transition temperature,  $E^*$  and  $E'$  have similar values, as the material behaviour is close to elasticity and the loss modulus is small. The damping  $\tan \delta$  with the phase angle  $\delta$  and the modules  $E'$ ,  $E''$  are linked through the equation

$$\tan \delta = \frac{E''}{E'}; \quad \delta = \arctan \frac{E''}{E'} \quad (5.100)$$

The same formulations apply for the shear storage, loss and complex modules  $G'$ ,  $G''$ ,  $G^*$ . Conversion of the complex Young's modulus  $E^*$  and the complex shear modulus  $G^*$  is usually carried out assuming linear elasticity and isotropy through equation

$$G^* = \frac{E^*}{2(1+\nu)} \quad (5.101)$$

This conversion, however, is only valid for a fixed temperature and depends on the Poisson coefficient. The latter is rarely determined for adhesives and is usually not provided in the technical data-sheets of adhesive manufacturers. Habenicht [Hab02, p. 254] generally lists a range of 0.25 to 0.49 and shows a list of adhesive types with various curing mechanisms ranging from 0.385 to 0.44.

Principally, adhesives tend towards near-incompressibility  $\nu=0.499$  with rising temperature and declining Young's modulus. In general, application of linear elasticity and isotropy is assumed to be sufficiently exact in the literature, e.g. [Hab 02, p. 253].

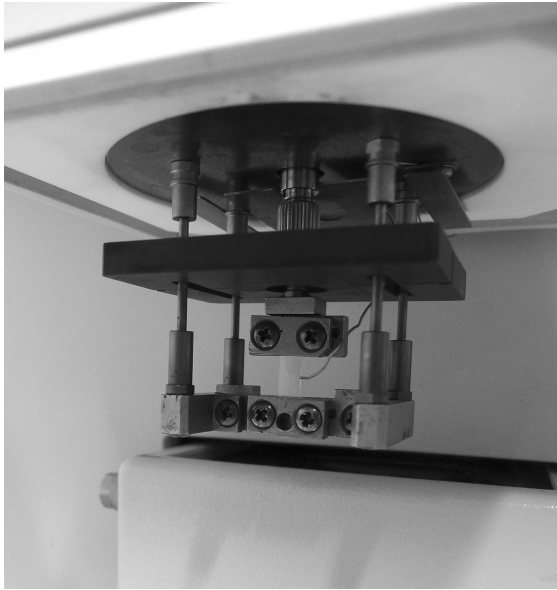


Figure 5.21.: DMA testing device (Netzsch DMA 242 C).

Various methods are applicable for determining  $T_g$ . Menard [Men 99, p. 101] mentions the options of using the onset or the peak of the  $\tan \delta$ -curve, the onset of the decline of the storage modulus  $E'$  and the onset or peak of the loss modulus  $E''$ -curve. A further often-used method is the calculation of the inflexion point of the  $E'$ -curve. Depending on which analysis type and analysis frequency is used,  $T_g$ -results vary.  $T_g$ -values determined by DMA typically differ from the  $T_g$  results obtained from DSC. As per DIN EN 6032 [Nor 13, pp. 4-5], the glass transition temperature can be determined by three methods in DMA tests:

- The onset  $T_g$  is determined by the temperature at the intersection of the extrapolated tangent lines of the storage modulus  $E'$ -curve prior to and after the glass transition.
- The loss  $T_g$  is related to the temperature at the maximum value of the loss modulus  $E''$ -curve
- The peak  $T_g$  refers to the temperature at the maximum value of the  $\tan \delta$ -curve.

As many of the adhesives applied in the context of this work have high stiffness and therefore tend

to be brittle, only basic axial tensile oscillation tests have been made for determining the principal applicability of the tested adhesives. More elaborated tests and the exact determination of the shear modulus are recommended.

DMA-testing was carried out for most of the UV-cured adhesives in table 5.2. For the Delo-adhesives and Catiowell 3052, DMA of tempered samples was undertaken in addition to examine the possible behaviour after autoclaving. The results for all tested adhesives are displayed in appendix B.2, figs. B.1 and B.2. Both the storage and loss modulus are plotted against each other in the graphs. Delo KB AD640 exhibits an initial  $E'$  of  $\sim 1750$ MPa at room temperature and maintains 130MPa at  $140^\circ\text{C}$ , table 5.3. Tempering negatively affects the storage modulus. Depending on the interpretation of the curves, glass transition occurs at around  $70^\circ\text{C}$ . This adhesive was tested many times, as it displayed a good behaviour. However, KB AD640 was recently withdrawn from the market and replaced by KB OB642. Results for the latter and Delo KB4552 are shown below in fig. 5.22. Whereas the storage modulus of KB4552 drops to low values of 25MPa at  $140^\circ\text{C}$ , OB 642 has an  $E'=175$ MPa at this temperature level. The tempered specimen even reaches  $E'=541$ MPa at a temperature of  $140^\circ\text{C}$ . Catiowell 3052 exhibits the maximum storage modulus of all tested, UV-cured adhesives, namely 360MPa at  $140^\circ\text{C}$ , as shown in table 5.3 and fig. B.2. Vitralit UC1608 also performs well under the given conditions, with  $E'=108$ MPa at  $140^\circ\text{C}$ .

Depending on the method, the results of  $T_g$  vary. The glass transition temperatures for peak  $\tan \delta$ , peak  $E''$  and onset  $E'$  of these adhesives determined by DMA are listed in tables B.2, B.3 in appendix B.2. Identification of clear  $T_g$ -values, however, remains problematic for the tested adhesives. KB OB642 and Catiowell 3052 exhibit two typical drops of the storage modulus. This behaviour can possibly be explained by the different behaviour of the chemical components of the adhesive, which react at separate temperature levels. The chemical composition of both adhesives from at least two different monomers supports this hypothesis. The adhesives, KB OB642, Vitralit UC1608 and Catiowell 3052, have  $T_g$ -values of  $70^\circ\text{C}$ ,  $55\text{-}77^\circ\text{C}$  and  $88\text{-}105^\circ\text{C}$ , respectively, related to peak  $E''$ -points. The respective  $E'$  onset results are  $52^\circ\text{C}$  (OB642),  $40^\circ\text{C}$  to  $45^\circ\text{C}$  (UC1608) and  $45^\circ\text{C}$  to  $50^\circ\text{C}$  (Catiowell 3052).

The results can vary with the same adhesive for several specimens, as can be seen for Vitralit UC1608. Tempering of KB OB624 causes a rise of the glass transition temperature (peak  $E''$ ) to 130°C. For other adhesives, for example, Catiowell 3052 and KB4552, such an influence of tempering does not occur.

The complex Young's modulus values obtained through DMA for the adhesives mainly applied in the context of the present work can be seen in the graphs at the bottom of fig. 5.22. For analytical and numerical calculation, values of

approximately  $E'=1800\text{MPa}$  at room temperature for KB OB642 and  $E'=1520\text{MPa}$  for KB4552 are applied in this thesis. On the assumption of a Poisson coefficient comprised between 0.35 and 0.49, the respective shear modules are roughly  $G=600\text{MPa}$  to  $670\text{MPa}$  for KB OB642 and  $420\text{MPa}$  to  $463\text{MPa}$  for KB4552. Based on these findings for KB OB642, the analytical strain transfer parameter study in section 5.1.2.2 applies values of  $570\text{MPa}$  and  $600\text{MPa}$  for the adhesive, the first value being a safe-side approximation for  $G_a$ , which is also used in the numerical micro-model analyses throughout this work.

**arithmetic mean Young's modulus values**

product	30°C		115°C		140°C	
	E'	E''	E'	E''	E'	E''
	[MPa]	[MPa]	[MPa]	[MPa]	[MPa]	[MPa]
KB4552	1524.62	70.70	71.64	26.28	25.08	3.21
KB4552 autoclave	1582.55	89.89	148.10	36.80	80.10	10.12
KB AD640	1773.69	38.79	189.19	18.61	129.19	4.60
KB AD640 autoclave	1290.30	37.04	168.51	16.17	131.57	2.94
KB OB642	1802.68	42.83	436.74	104.82	176.45	33.06
KB OB642 autoclave	2412.95	37.26	1365.29	101.47	541.07	100.26
Ultra Light-Weld 431	855.17	95.72	4.84	3.83	-	-
EPO-TEK 353ND	-	-	-	-	-	-
Ormocer NM850	710.27	83.95	**	**	**	**
Ormocer AL1029	4.86	2.05	4.50	0.04	-	-
Loctite 3301	767.65	74.18	1.99	1.07	-	-
Loctite 3494	682.70	135.97	1.61	0.42	-	-
Loctite 4090	-	-	-	-	-	-
Vitralit UV1605	**	**	**	**	**	**
Vitralit UV2020	2338.08	38.95	**	**	**	**
Vitralit UC1608	2701.69	105.29	245.31	132.63	108.49	55.68
UV632	268.76	110.84	1.49	-0.01	-	-
UV681	182.87	93.16	3.52	0.00	0.06	-0.01
UV2144	1471.92	86.33	31.41	14.32	-	-
Catiowell 3052	1757.67	44.67	600.37	132.20	362.23	95.14
Catiowell 3052 (thixotr.)	1995.76	55.81	296.93	138.20	27.22	10.15
Catiowell 3052 (thixotr.) autoclave	2595.29	27.84	80.03	56.63	21.15	4.31
Photowell 1044	-	-	-	-	-	-
Scotch-Weld UV50	240.69	93.56	0.83	0.33	-	-
Scotch-Weld DP804	1570.09	134.56	6.04	6.56	-	-

\*\* too brittle for testing or early rupture due to brittleness

**Table 5.3.:** Mean storage and loss moduli from DMA at temperatures of 30°C, 115°C and 140°C.

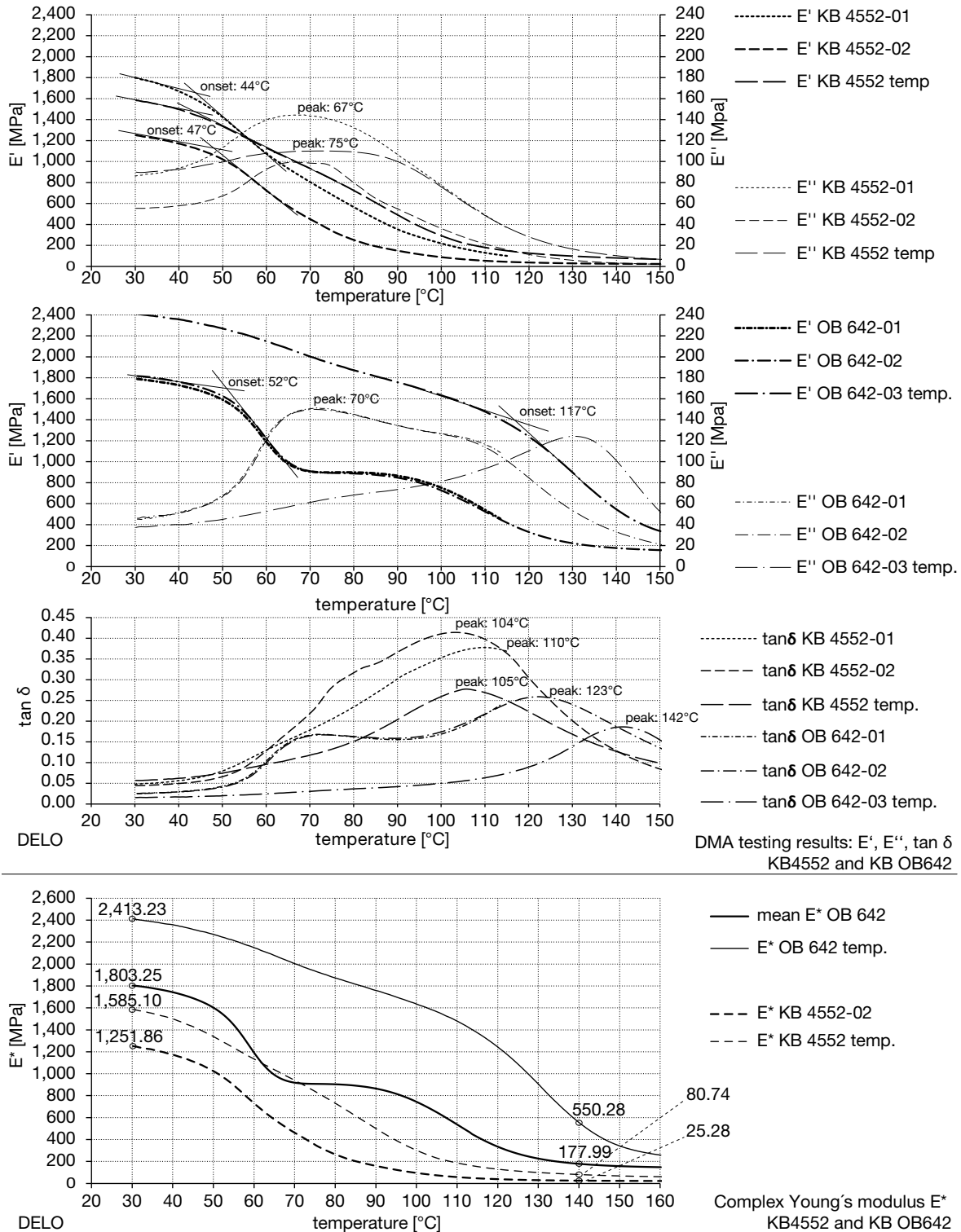
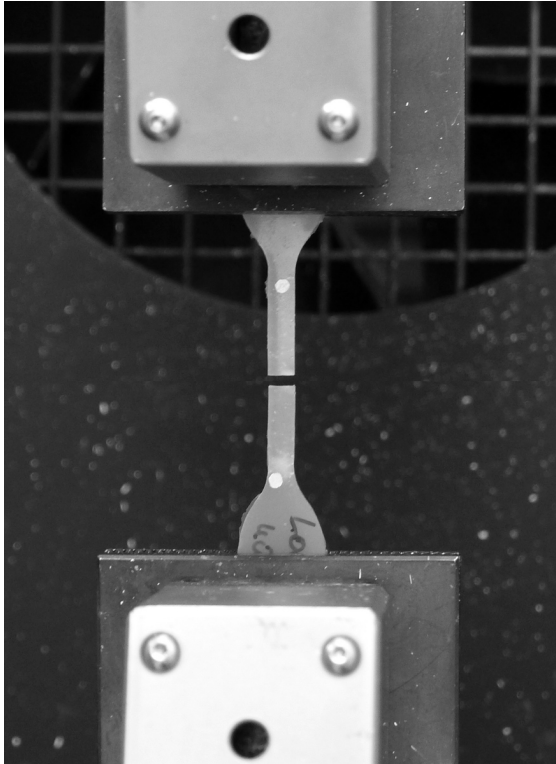


Figure 5.22.: DMA testing results  $E'$ ,  $E''$  of Delo KB4552 and KB OB642 (top) and complex Young's modulus  $E^*$  (bottom).



### 5.1.3.3. Axial Tensile Tests

Tensile testing of bulk dumbbell specimens of type S1 as in DIN 53504 and DIN EN ISO 527-1 to 2 was performed at room temperature (21-24°C) at a rate of 0.25mm/min with an universal testing machine Instron UPM 5881 having a climatic chamber and video-extensometer, see fig. 5.23.



**Figure 5.23.:** Bulk adhesive sample axial tensile testing with an Instron UPM 5881.

Three specimens of each adhesive from table 5.2 were tested and the mean Young's moduli were determined from the results, which are given in appendix B.2 in figures B.3, B.4 and in tables B.2, B.3. In addition, seven short-listed adhesives have been tested with UV-cured and autoclave-like tempered specimens. For the two adhesives used in the projects and tests related to this work, namely Delo KB4522 and KB OB642, the strain-stress curves are plotted in fig. 5.24. KB4552 exhibits a mean tensile strength of 40MPa at a mean strain of 0.036mm/mm. A big part of the stress-strain curve is non-linear. Tempering seems to reduce the tensile strength. The mean tensile Young's modulus  $E$  of KB4552 is 1,881MPa and drops to 1,456MPa for the tempered dumbbells. KB OB642 shows a more brittle behaviour with an ultimate mean tensile strength of approximately 21MPa and 0.0095mm/mm strain. The stress-strain curve is almost linear. The mean  $E$  is 2,516MPa for the UV-cured specimen, whereas the UV-cured, tempered (autoclaved) dumbbells have a slightly increased mean  $E=2,610$ MPa. All tensile Young's modulus results are significantly higher than the values obtained through axial tensile DMA, see section 5.1.3.2. Therefore, the DMA-results of  $E'=1,803$ MPa for OB642 and  $E'=1,525$ MPa for KB4552 are subsequently used in this work.

In future research, further testing is necessary to determine the shear modulus from shear testing directly. Furthermore, as the material properties of an adhesive can differ for bulk specimen and for the application as a joint between two substrate materials, testing with the latter configuration is recommended. Some examples are given in the work of Habenicht [Hab 02, pp. 670-703].

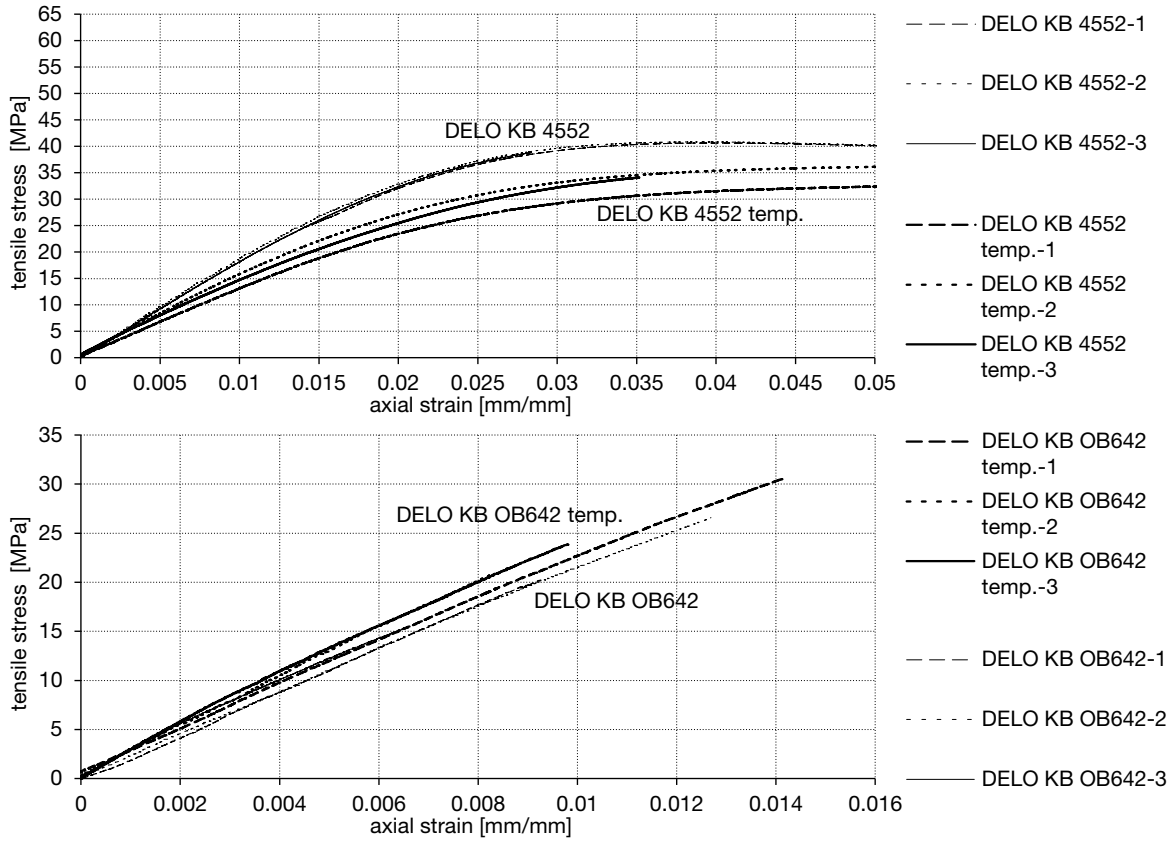


**Figure 5.24.:** Tensile stress-strain diagrams for Delo KB4552 (top) and KB OB642 (bottom) after UV cure only and UV cure with autoclave-like tempering.

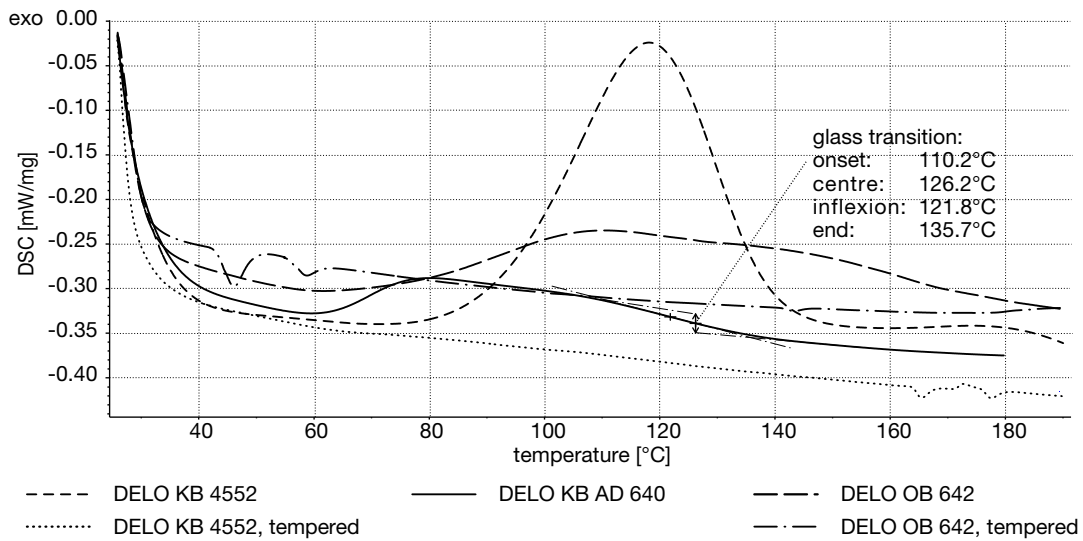


**Figure 5.25.:** Comparison of DSC analyses for Delo KB4552, KB AD640 and KB OB642.

#### 5.1.3.4. Differential Scanning Calorimetry

In DSC analysis, a polymer sample in a crucible and an empty reference crucible are simultaneously subjected to identical variable temperature levels. Temperature differences between the sample and the reference occur because of exothermic or endothermic reactions of the polymer depending on the temperature. Thermal energy is either acquired or emitted by the sample. DSC is performed to determine the glass transition temperature and to examine the chemical reaction behaviour of the adhesive at various temperature levels. A Netzsch DSC 204 F1 Phoenix differential scanning calorimeter was used for the analyses. From most of the adhesives, one sample was analysed, with some additional tempered specimens also being examined, see table 5.2. All resulting curve plots are given in the appendix, section B.2, fig. B.5. Only in a few cases, namely Polytec UV2144, Permabond UV632 / 681 and modified Ormocer AL1029, can a glass transition temperature be determined from the analyses. Many of the adhesives show a sudden change in the heat flux in a temperature range of 60 to 160°C; this indicates that a chemical reaction occurs with rising temperature. This effect is most likely to be related to thermal post-cure effects of the adhesives and is notably seen with the Vitralit adhesives, Delo KB4552 and Catiowell 3052. DSC analyses with tempered (autoclaved) samples no longer show post-cure behaviour with these adhesives underlining the hypothesis of a thermal post-cure mechanism.

Such post-cure not only changes the material properties, but also might cause shrinkage of the adhesive. The differential expansion of the adhesive with respect to the substrate and the bonded fibre can possibly cause residual fibre strain, which modifies the measured FBG signal if related to a  $\lambda_{B,0}$  value recorded prior to cold bending and lamination. Glue-induced birefringence could be another consequence. Such effects are repeatedly examined in the literature, for example, [Hel 14], [Sto 97] and [Par 10].

Two strategies can be deduced from this. First, FBG measurement should be related to different initial Bragg wavelengths  $\lambda_{B,0}$ . In the case of cold bent glass, this means that, after lamination but prior to release from the bending device, a reference wavelength value has to be recorded and all subsequent monitoring results  $\Delta\lambda$  are related to

this value. This method, however, only works if the cold bending stress level in the glass is assumed to remain constant prior to and after lamination in the autoclave. Thus, the glass stress measured prior to the thermal treatment can be used as a reference. Second, the chosen adhesive should exhibit as little thermal post-cure as possible. This is the case with Delo KB OB642 plotted versus the KB4552 for comparison in fig. 5.25. Furthermore, the KB OB642 adhesive shows a high glass transition of  $T_g=122^\circ\text{C}$  (peak  $\tan\delta$ ) /  $71^\circ\text{C}$  (peak  $E''$ ). Ormocer<sup>®</sup> NM850, Permabond UV632 and 681 and Polytec 2144, see fig. B.5, do not show post-cure effects and are therefore well adapted to the fibre bonding task from a DSC-related point of view. However, UV632 and 681 do not provide sufficient strength, Ormocer<sup>®</sup> NM850 proves to be too brittle and UV2144 shows zero stiffness beyond 120°C. Thus, KB OB642 proves to be the most adapted adhesive for the FBG bonding task with respect to the Young's modulus at room temperature and at 140°C, the post-cure behaviour, transparency and processibility, see section 5.1.3.5 below.

#### 5.1.3.5. Adhesive Application and Joint Geometry

Related to the above testing methods, the main parameters and criteria necessary for choosing an adhesive for application to FBG bonding in the context of laminated glass are: 1.) Young's modulus at various temperatures, 2.) colourless transparency, 3.) no or little post-cure behaviour with rising temperature, 4.) strength and 5.) high glass transition  $T_g$ . A comparison of these aspects in the previous sections leads to the choice of Delo KB OB642 as the best-suited adhesive; this is mainly attributable to the high Young's modulus at 140°C and at room temperature, the optical quality and the negligible, little post-cure effects. The processibility for bonding is very good. Catiowell 3052 is also well suited but tends to have a yellowish appearance and proves to be either too liquid or too viscous in the thixotropic version for producing a constant, regular bond film. However, if the viscosity can be customised for the task, Catiowell 3052 might even be the best-suited solution, providing that an undertone in colour is acceptable for the bonding task. Nano-particle filled Vitralit UC1608 is another alternative but is subject to strong post-cure effects. In general, all UV-curing adhesives tested here have some disadvantages for the temperature level of 140°C.

High-temperature-suited 2K epoxy adhesives with filler particles are more adapted to such temperatures, but nearly all of these necessitate either temperature curing, which is not feasible in the case of large glass panes equipped with FBG, and are mostly opaque or strongly coloured, e.g. Epo-Tek 353ND. Furthermore, many of these epoxies have too high a viscosity or thixotropy to be adaptable for a thin FBG bond.

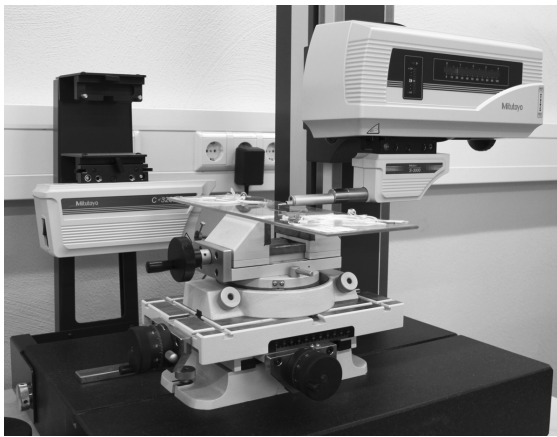
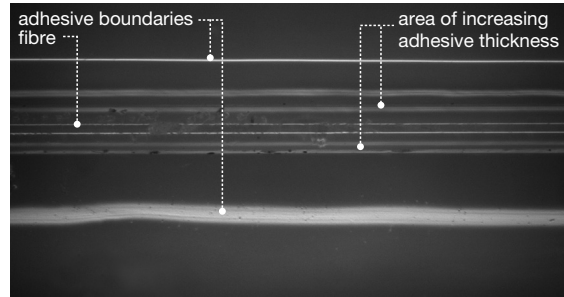


**Figure 5.26.:** Mitutoyo SV-C3200-H4 surface roughness contour measurement device.

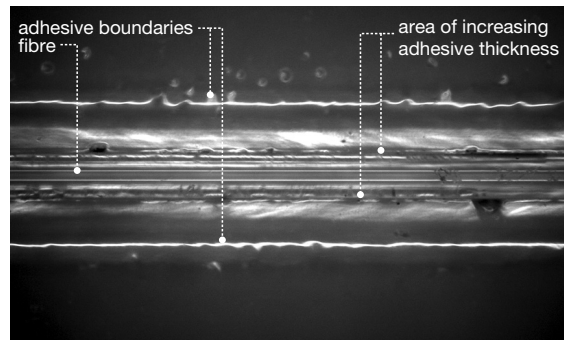


**Figure 5.27.:** Surface roughness contour measurement gauge head.

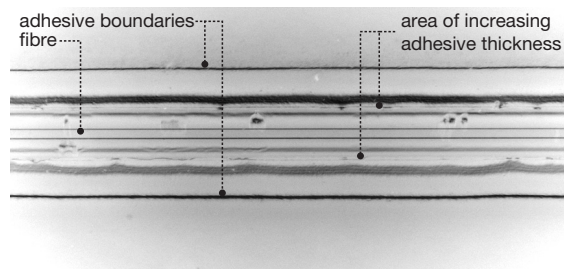
In order to bond a fibre, the glass substrate is first cleaned by pyrolytic surface silicating and then an even regular adhesive film of 60mm length and approximately 5mm width is applied. After the placing of the fibre on the film, the adhesive is cured through UV-light. For each of the two chosen adhesives mentioned above, six fibre bonds in total on a glass substrate were geometrically examined by means of a Mitutoyo SV-C3200-H4 surface roughness contour measurement device, fig. 5.26. By applying a diamond or sapphire needle, this instrument measures the surface contour along a given line, fig. 5.27.



Microscopic plan view on a bonded FBG (specimen FTG\_KB4552-02, sensor 2-2)



Microscopic plan view on a bonded FBG (specimen FTG\_KB OB642-01, sensor 1-1)



Inverted microscopic plan view on a bonded FBG (specimen FTG\_KB OB642-06, sensor 6-3)

**Figure 5.28.:** Microscopic plan view images of surface-bonded FBGs.

Three transverse contour profiles were measured; one across the centre of the adhesive joint, and one at a 20mm distance to the left and one at the same distance to the right of the centre. Chosen characteristic results are graphically shown in appendix B.3, figs. B.6, B.7. In order to obtain the adhesive thickness  $t_a$  below the fibre, the circular cross section of the embedded fibre was fitted to the upper part of the measured contour curve.

The fitting revealed that the typical fibre exposed a smaller radius of about 0.093 to 0.094mm compared with the nominal radius of 0.0975mm. The statistical results from these measurements are listed in table 5.4. Typical cross sections of a bond established with KB4552 and KB OB642 are plotted in fig. 5.29: The low-viscosity KB4552 leads to a broad bond with a small gradient in the decreasing adhesive thickness on both sides of the fibre. In contrast, KB OB642 forms a relatively constant film thickness, which reduces near the fibre and then strongly climbs towards the fibre's section flanks. The various viscosity and flow behaviour of the adhesives also causes the KB4552 bond to expose a lower average thickness  $t_a=5.33\mu\text{m}$  below the fibre than KB OB642 with its average of  $t_a=8.03\mu\text{m}$ .

Generally, the bond cross section geometries

produced here comply with the findings of, for example, Schlüter [Sch 10, p. 54], as shown by REM images of polished thin sections of surface-bonded fibres.

The mean values from table 5.4 are directly applicable for modelling or analytical calculation, for example, of the strain transfer into the fibre, see section 5.1.2.2. However, for the parameter studies in the analytical approach presented in the aforementioned section, slightly different values  $t_a=0.01206\text{mm}$  and  $r_f=0.091769\text{mm}$  are used; which correspond to the example of specimen ftg\_kb-ob642-04.

Additional microscopic examination of the adhesive joints shows the straightness and regularity of the bonds produced with the procedure applied in the context of this work, fig. 5.28.

		$r_f+t_a$	$r_f$	$t_a$	bond sect. width incl. lat. disturb.	reg. bond section width	adhesive thickness
		[ $\mu\text{m}$ ]	[ $\mu\text{m}$ ]	[ $\mu\text{m}$ ]	[ $\mu\text{m}$ ]	[ $\mu\text{m}$ ]	[ $\mu\text{m}$ ]
ftg_kb-ob642	arithm. mean	195.20	93.55	8.03	6023.30	4990.90	38.22
	std. deviation	3.90	1.37	3.25	387.19	341.34	6.26
	inaccuracy (95% qua.) $\pm$	2.01	0.70	1.67	223.52	169.76	3.11
ftg_kb4552	arithm. mean	192.43	93.55	5.33	-	5179.25	20.72
	std. deviation	2.23	0.95	3.10	-	379.12	3.68
	inaccuracy (95% qua.) $\pm$	1.11	0.47	1.54	-	188.55	1.43

**Table 5.4.:** Summary and statistical analyses of surface roughness measurement data for Delo KB4552 and OB642.

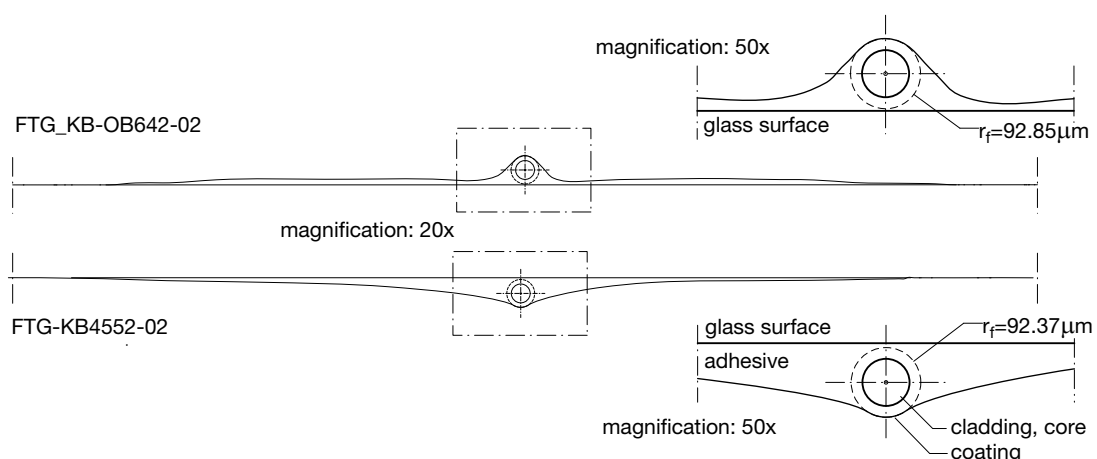


**Figure 5.29.:** Cross sections of fibres bonded to glass with either Delo KB OB642 or KB4552.

### 5.1.4. FBG Sensor Property Determination

#### 5.1.4.1. Gauge Factor Determination

The photo-elastic (strain-optic) coefficient  $p_e$  is described in section 5.1.1.7. It relates the axial strain of a bare optical fibre to the relative wavelength shift that it generates in a Bragg grating sensor, see eq. 5.33. It is convenient to use the strain sensitivity coefficient  $K_\varepsilon = 1 - p_e$  instead, which is often assumed to have a value of 0.78 for a bare fibre [VDE 10, p. 10]. Van Roosbroeck et al. [Van 09, p. 61] calculated a value of 0.7886 as the mean value from four test specimens. Flockhart et al. [Flo 04, p. 2750] obtained a value of 0.806 to 0.807 from strain testing. Jülich et al. [Jül 13, p. 6] determined a value of  $K_\varepsilon=0.783$  for a bare optical fibre type FBGS DTG-LBL-1550 used in the present work. This basic value is applied in this thesis as the reference value for an uncoated, free fibre. In eq. 5.46, 5.52, 5.60, the gauge factor  $k_\varepsilon$  as in [Jül 13] has been introduced for the FBG bonded to a substrate:

$$k_\varepsilon = \zeta_1 K_\varepsilon = \zeta_1 (1 - p_e)$$

The ratio of the strain transmission coefficient  $K_\varepsilon$  from the bare fibre suspension test and  $k_\varepsilon$  derived from four-point bending gives the strain transfer ratio value  $\zeta_1$ . A weak bond leads to  $\zeta_1 < 1$ . Based on eq. 5.60, the mechanically induced wavelength shift at constant temperature of an FBG bonded to a substrate is

$$\frac{\Delta\lambda(\varepsilon)}{\lambda_{B,0}} = k_\varepsilon \varepsilon_{1,s,m} \quad (5.102)$$

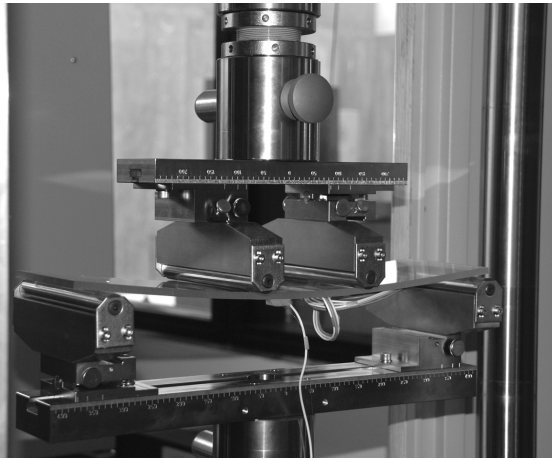


Figure 5.30.: Four-point bending testing facility.

The four point bending test procedure, as in fig. 5.30, suggested in the VDI guideline 2660 [VDE 10, pp. 33-34] is applied in the present work to determine the gauge factor  $k_\varepsilon$  and the strain transfer ratio  $\zeta_1$ , which depicts the individual strain transfer properties provided by the bond of the FBG to the substrate. If both negative and positive strain is measured with FBGs bonded to the top and to the bottom surface of the bent test specimen, the gauge factor can be determined by eq. 5.103 as in the VDI guideline

$$k_\varepsilon = \frac{\left| \frac{\Delta\lambda_t}{\lambda_{B,0,t}} \right| + \left| \frac{\Delta\lambda_c}{\lambda_{B,0,c}} \right|}{\left| \varepsilon_{1,s,e,t} \right| + \left| \varepsilon_{1,s,e,c} \right|} \quad (5.103)$$

with the indices  $t$  and  $c$  indicating tension and compression, respectively. The strain values  $\varepsilon_{1,s,e}$  for tension ( $t$ ) or compression ( $c$ ) used here is the strain in the fibres corrected with respect to their distance from the substrate's surface by means of eq. 5.61 or 5.62. Application of this procedure necessitates a constant bonding geometry of the FBG to the substrate and constant bending strain. The gauge factor can be determined from the wavelength shift ratios  $\Delta\lambda/\lambda_{B,0}$  and longitudinal, bending-corrected reference strain values  $\varepsilon_{1,s,e}$  for tension ( $t$ ) or compression ( $c$ )

$$k_\varepsilon = \zeta_1 K_\varepsilon = \frac{\Delta\lambda}{\lambda_{B,0}} \frac{1}{\varepsilon_{1,s,e}} = \frac{\Delta\lambda}{\lambda_{B,0}} \frac{1}{\varepsilon_{1,s} \left[ \frac{1}{r_{\varepsilon,s}} + \frac{(t_s+r_f+t_a)\left(1-\frac{1}{r_{\varepsilon,s}}\right)}{t_s} \right]} \quad (5.104)$$

For obtaining  $k_\varepsilon$ , the reference strain on the glass surface at the sensor location has to be known. In bending tests, the glass strain can be calculated with the deformation data of the specimen measured by means of path transducers and linear bending theory as shown in [VDE 10, p. 34]. In the present work, this setup could not be realised; the bending force and the displacement recorded by the testing machine were used instead to determine the glass strain from a finite element model. Both the bending and membrane strain in the glass are thus considered.

As glass cannot be easily analysed in axial tests, a four-point bending test setup was chosen according to fig. 5.31 and C.1 in appendix C.1. This test is particularly well suited, as it allows the fixing of the sensors in an unobstructed area between the stress rollers, where constant bending moments and, consequently, constant longitudinal strain conditions prevail.

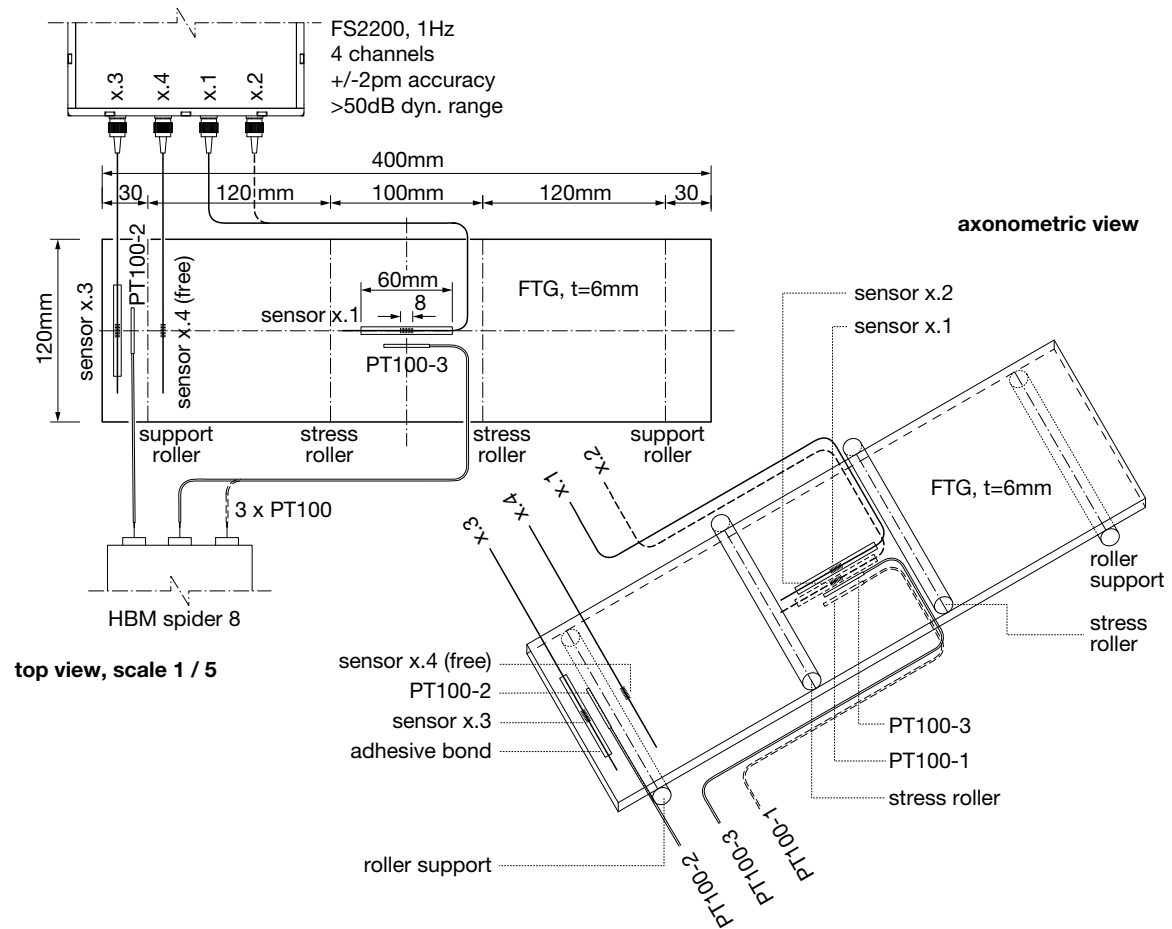


**Figure 5.31.:** Four-point bending test setup. The fibre-Bragg grating sensors in the centre of the glass plate are bonded to the plate's top (x.1) and bottom (x.2) surface. PT 100 temperature gauges are fixed nearby each Bragg sensor.

Contrary to the VDI 2660 [VDE 10, p. 33], the test has been effectuated force-controlled in order to avoid an increasing load at rising temperature caused by the expansion of the metallic connection cylinders. A Zwick-Roell Z100 testing machine was used in combination with a climatic chamber Mytron WT160 LN. The specimen used were made up of 3.848mm thick, 400mm by 120mm FTG plates with arrised, polished edges, equipped with two sensors 3.1 (top, compression), 3.2 (bottom, tension) for mechanical strain measurement in the centre, fig. 5.31 and fig. C.3 in appendix C.1, and one lateral sensor 3.3 for temperature compensation purposes. A fourth, free bare sensor 3.4, was not exploited in this test setup. Sensors 3.1 to 3.3 were glued applying UV-curing OB642 modified epoxy resin as shown in section 5.1.3. No broadening of the Bragg sensor spectra was monitored after the UV activation of the adhesive as shown in fig. C.2 in appendix

C.1. Three PT100 resistance temperature detection thermometers were placed directly adjacent to the bonded FBG.

Loads were applied in eight steps ranging from 25N to 200N with increments of 25N. The load was kept constant for 30s, followed by another 30s in an unloaded state, fig. 5.32. Load increment series were performed at 24.6°C and 141.0°C. The gauge factor and the photoelastic coefficient were determined by eq. 5.103, 5.104; the reference strain was calculated by FEM. Volumetric, 8-node elements were used in the model with an element size of 2mm; this allowed for two layers of elements through the thickness. The model was loaded with the forces recorded by the testing machine and solved by geometrical non-linear analysis. The wavelength shifts and reference strain values from the eight load increments were then used to determine the gauge factor by linear regression.



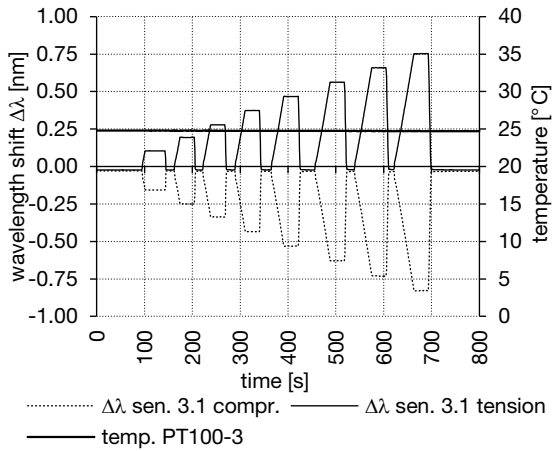


**Figure 5.32.:** Detail from the stepwise increased load application at constant temperature.

In analogy to Jülich et al. [Jül13, pp. 4-5], the reference strain on the glass surface calculated by FEA and the wavelength shift  $\Delta\lambda$  related to  $\lambda_{B,0}$  are plotted in fig. 5.33 for room temperature and 141°C for both the compressed and the tensile region. The dashed line is determined by linear regression from all tension and compression wavelength shift and reference strain values. Strain gauge values  $k_\epsilon$  are calculated by linear regression of the wavelength and strain terms in eq. 5.103. At room temperature (24.6°C),  $k_\epsilon=0.7898$  and at the autoclave temperature of 141°C, a slightly increased  $k_\epsilon=0.7925$  are determined in this way. In comparison with a bare fibre  $K_\epsilon$  of 0.783, the strain transfer ratio at 24.6°C becomes  $\phi_1=1.009$  and  $\phi_1=1.012$  at 141°C.

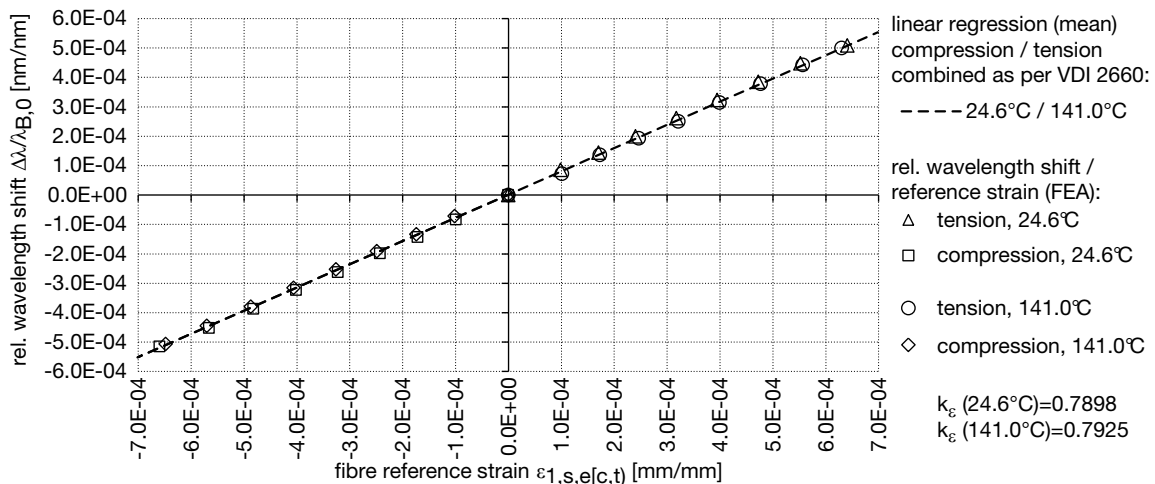


**Figure 5.33.:** Relative wavelength shift plotted against numerically derived strain from four-point bending for both tension and compression at 24.6°C and 141.0°C. The dotted curve is obtained by linear regression of the combined compression and tensile results as in VDI 2660.

The quantity of results from the tests explained above is not sufficient to derive further information on a potential temperature-dependency of the gauge factor. Further testing is necessary to determine the exact behaviour of  $k_\epsilon$  and  $p_\epsilon$  with respect to temperature. Schlüter [Sch10, pp. 129-131] mentions gauge factors in a range of 0.71-0.83 at 23°C for Ormocer®-coated fibres bonded with various adhesives. The values having been determined experimentally in the present work are in this range; subsequently, for FBG analyses at room temperature a common gauge factor of  $k_\epsilon=0.7898$  has been applied in this work. For comparison, theoretical gauge factors are calculated from numerical models in section 5.1.6.



#### 5.1.4.2. Determination of the Thermo-Optic Coefficient

As discussed in section 5.1.1.7, both the thermal expansion of the fibre-Bragg grating sensor itself and the temperature-induced change of the refractive index cause the Bragg wavelength to shift. In the case of a fibre optic sensor bonded to an object, as described in section 5.1.1.8, the thermal expansion of this object mainly influences the expansion of the fibre-Bragg sensor bonded to its surface. The coefficient of thermal expansion  $\alpha_g$  of silica optical fibres is usually assumed to have a value of  $0.55 \cdot 10^{-6} 1/K$  in the literature [Sch 10, p. 13], [Leb 04, pp. 2-8], [Oth 99, p. 99]; other authors give a value of  $0.51 \cdot 10^{-6} 1/K$  [Gab 12, p. 49] or  $0.50 \cdot 10^{-6} 1/K$  [Ste 97, p. 6], [Fra 01, p. 11], which is a very small compared with other materials. The strain transfer from the object into the fibre core is again expressed through the gauge ratio discussed in the previous section. In section 5.1.1.7, eq. 5.34

$$\frac{\Delta\lambda}{\lambda_{B,0}} = \Delta T \left( \alpha_g + \frac{1}{n_0} \frac{dn_0}{dT} \right)$$

illustrates the definition of the temperature-induced change of the refractive index of the fibre,  $\alpha_n$ , and the relationship of the relative wavelength shift of a free FBG attributable to changing temperature  $\Delta T$ .  $\alpha_n$  is the thermo-optic coefficient of the fibre. An FBG applied to measure mechanically induced strain measures the temperature-induced effects in parallel. Thus, the obtained strain result of such a measurement consists of the mechanical part, the temperature part related to the substrate and the apparent strain caused by the temperature effects on the refractive index. The temperature-induced strain part must be distinguishable from the total result in order to determine the mechanically-induced strain part. Single-mode fibres with inscribed FBGs do not permit the temperature-induced and mechanically induced wavelength shift portions to be distinguished. Therefore, either the temperature of the sensor and the coefficient of thermal expansion of the fibre and the substrate have to be known exactly in order to calculate the temperature-induced wavelength shift and subsequently to identify the mechanical strain or a sensor not being subjected to any mechanical strain has to be used in parallel to obtain the temperature-related part and to subtract this portion from the results obtained with a sensor exposed to mechanical and to temperature loads. The problem of separating the mechanical and temperature parts is a central topic in the

literature and in research. In the literature, values for  $\alpha_n$  cover a range from 5 to  $8.6 \cdot 10^{-6} 1/K$  [Ste 97, p. 6], [Sch 10, p. 13], [Leb 04, pp. 2-8]. The influence of temperature on the wavelength shift of a free fibre is about 8.6 to 14.2pm/K, whereas a  $1 \mu\epsilon$  ( $=1 \cdot 10^{-4} \% = 1 \mu m/m$ ) mechanical strain causes 1.22pm of wavelength change (a 1% strain thus results in  $\Delta\lambda = 12.2nm$ ). The above discussion shows the importance of identifying the coefficient  $\alpha_n$  of the FBGs used in this work in order to permit the correct derivation of the apparent and mechanical strain in the testing of laminates.

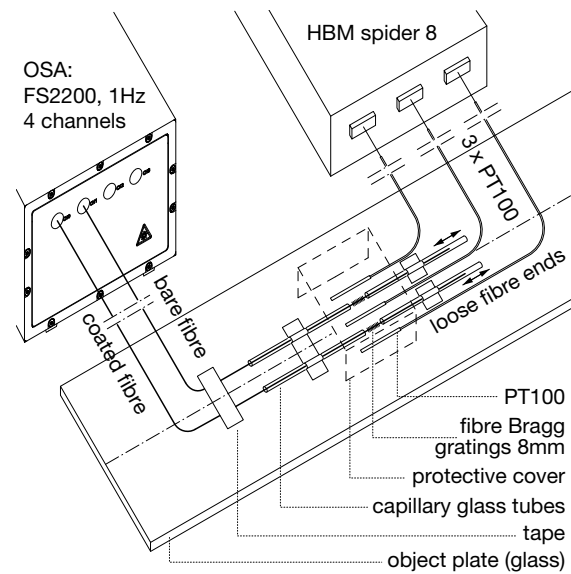


**Figure 5.34.:** Test setup for the determination of the thermoelastic coefficient of a free FBG.

By rearranging eq. 5.34, the thermo-optic coefficient of a free fibre can be determined as

$$\frac{1}{n_0} \frac{dn_0}{dT} = \alpha_n = \frac{\Delta\lambda}{\lambda_{B,0}} \frac{1}{\Delta T} - \alpha_g \quad (5.105)$$

In the test performed for this work, therefore, the relative wavelength shift  $\Delta\lambda/\lambda_{B,0}$  of an Ormocer<sup>®</sup>-coated DTG-LBL-1550 and a bare FBG of the same type were measured at various distinct, constant temperature levels  $T$ ; this permits the determination of  $\alpha_n$  by using the measured values of  $\Delta T$  and the constant  $\alpha_g = 0.55 \cdot 10^{-6} 1/K$ . The test was performed in a Mytron WT160 LN2 climatic chamber. As depicted in fig. 5.34, the test setup consists of a glass plate placed in the volumetric centre of the climatic chamber. In this way, heated air inside the chamber could flow around the entire plate.

Two capillary glass tubes of  $l=100\text{mm}$  /  $d=1\text{mm}$  were installed on the glass with a spacing of  $12\text{mm}$  between them. The coated fibre  $d=0.195\text{mm}$  was passed through both tubes and the FBG of a length of  $8\text{mm}$  was placed in the spacing of the tubes. The fibre was fixed by tape at one end, whereas the other end was left free to slide longitudinally along the tubes. The same setup was established with the bare fibre ( $0.125\text{mm}$  diameter). A protective silicone cover was placed above the spacing with some distance to the sensors. Both the cover and the tubes protected the fibre from the hot air stream flowing through the chamber, thus avoiding local temperature differences and vibrations of the fibres. As in the previous section, the FBG were measured with an FS2200 OSA operating at  $1\text{Hz}$ . Three PT100 resistance thermometers were placed directly adjacent to the sensors as shown in fig. 5.34.

Starting at room temperature ( $\sim 22.5^\circ\text{C}$ ), the temperature in the climatic chamber was increased by  $10^\circ\text{C}$  every 45 minutes until it reached  $\sim 143.7^\circ\text{C}$ , fig. 5.35. Temperature was measured with the PT100. Once constant temperature and wavelength response levels were reached in each step, the wavelength and respective temperature were recorded and  $\Delta\lambda/\lambda_{B,0}$  and  $\Delta T$  were calculated from these values.

The test wavelength and temperature results are used to determine the thermo-optic coefficient by fitting a curve to the measured values by application of regression analysis with least squares method. This is performed both by simple linear regression to obtain a linear curve and by multiple linear regression to obtain a quadratic curve as fits. For the coated fibre, simple and multiple regressions lead to a nearly identical curve, fig. 5.36. The temperature-dependent behaviour of an Ormocer<sup>®</sup> NM850-coated fibre of this type can thus be approximated by a linear function  $\lambda = 0.01259 \cdot T + 1544.75\text{nm}$  or  $\Delta\lambda = 0.01259 \cdot \Delta T - 0.00643\text{nm}$ . Compared with a similar test performed by the manufacturer of the FBGs, both curves present approximately the same slope. From the gradient of the linear curve, the thermo-optic coefficient is obtained as a constant value for  $20\text{-}140^\circ\text{C}$  by applying eq. 5.105:  $\alpha_n=0.760 \cdot 10^{-6} 1/\text{K}$ .

If the same procedure is applied to the results obtained from the bare fibre, the results from simple

and multiple linear regression analyses differ, fig. 5.37. The quadratic function,  $\lambda = 1.018 \cdot 10^{-5} \cdot T^2 + 0.00948 \cdot T + 1547.51\text{nm}$ , delivers the better fit to the experimental data than the linear function  $\lambda = 0.01115 \cdot T + 1547.45\text{nm}$ . Thus, the bare fibre shows non-linear temperature-dependent behaviour. The thermo-optic coefficient calculated from the quadratic function of wavelength and temperature increases linearly with temperature from  $5.87 \cdot 10^{-6}$  at  $22.5^\circ\text{C}$  to  $6.67 \cdot 10^{-6}$  at  $143.7^\circ\text{C}$ .

This non-linearity phenomenon is also described in literature: Flockhart et al. [Flo 04, pp. 2744-2751] determined the temperature-induced wavelength change of an FBG coated with DeSolute 950-200 acrylate as a quadratic function of temperature for a temperature range of  $-70^\circ\text{C}$  to  $+80^\circ\text{C}$ . Frank [Fra 01, p. 12] shows a slightly non-linear curve for the thermo-optic coefficient, with values of  $\alpha_n=5.6 \cdot 10^{-6} 1/\text{K}$  at  $0^\circ\text{C}$  and  $8.1 \cdot 10^{-6} 1/\text{K}$  at  $150^\circ\text{C}$ , but for a  $830\text{nm}$ -sensor. Schlüter [Sch 10, p. 12] also mentions the non-linear behaviour of  $\alpha_n$  at higher temperature. Manufacturers generally deliver a constant  $\alpha_n$  for a limited temperature range, e.g. [Int 12] give  $5.95 \cdot 10^{-6}$  for the range of  $0^\circ\text{C}$  to  $70^\circ\text{C}$ .

The summary of the results is shown in table 5.5, including the minimum and maximum  $\alpha_n$  derived by multiple regression with a quadratic function for the bare fibre. For analyses performed in this work at constant room temperature, the bare fibre value of  $6.655 \cdot 10^{-6}$  is typically applied. This is because the effect of the coating in the case of a bonded fibre is contained in the gauge factor  $k_e$ , which also influences the transfer of temperature-induced strain from the substrate into the fibre.

obtained from:	bare fibre		coated (Ormocer)
	multiple regression	simple regression	simple regression
$K_T \lambda_{B,0} = \Delta\lambda/\Delta T$	0.00948	0.01115	0.01259
$\alpha_g$ [1/K]	5.500E-07	5.500E-07	5.500E-07
$K_T$	-	7.205E-06	8.152E-06
$\alpha_n$ [1/K]	see below	6.655E-06	7.600E-06
$\lambda_{B,0}$ [nm]	1547.506 nm	1547.453 nm	1544.752 nm
mult. regr.	5.8722E-05 at $22.5^\circ\text{C}$		
range $\alpha_n$ :	6.6694E-06 at $143.7^\circ\text{C}$		

**Table 5.5.:** Thermo-optic coefficient results.

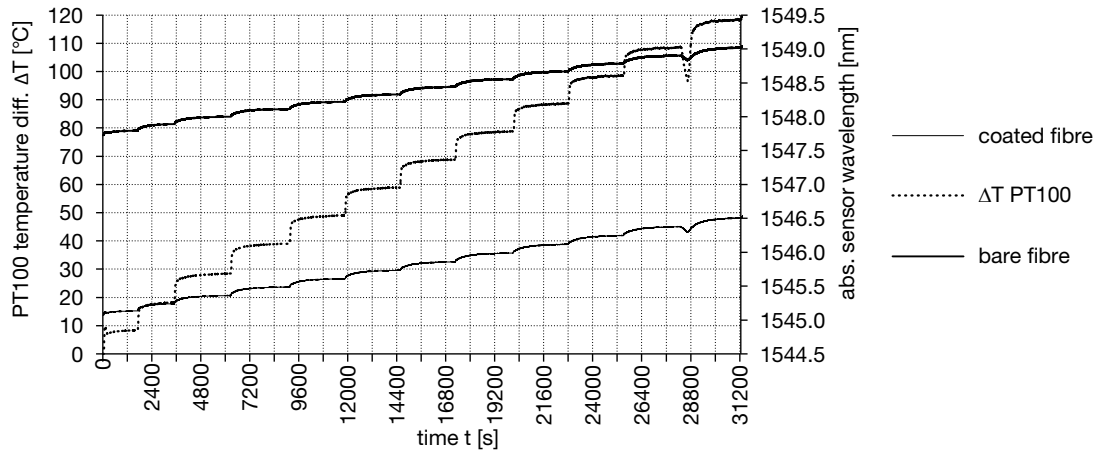


Figure 5.35.: Temperature devolution and related Bragg sensor wavelength of the temperature test.

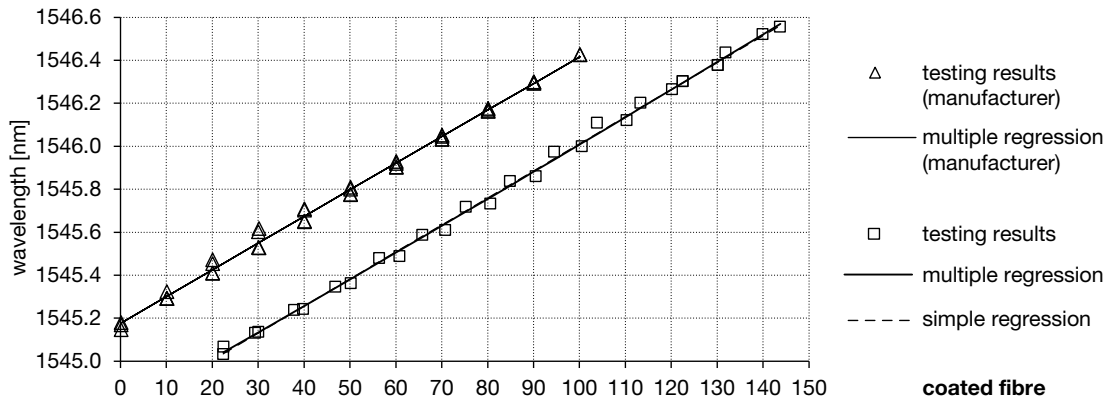


Figure 5.36.: Testing results of the Bragg sensor wavelength plotted against temperature and related linear and square regression curves for a coated fibre.

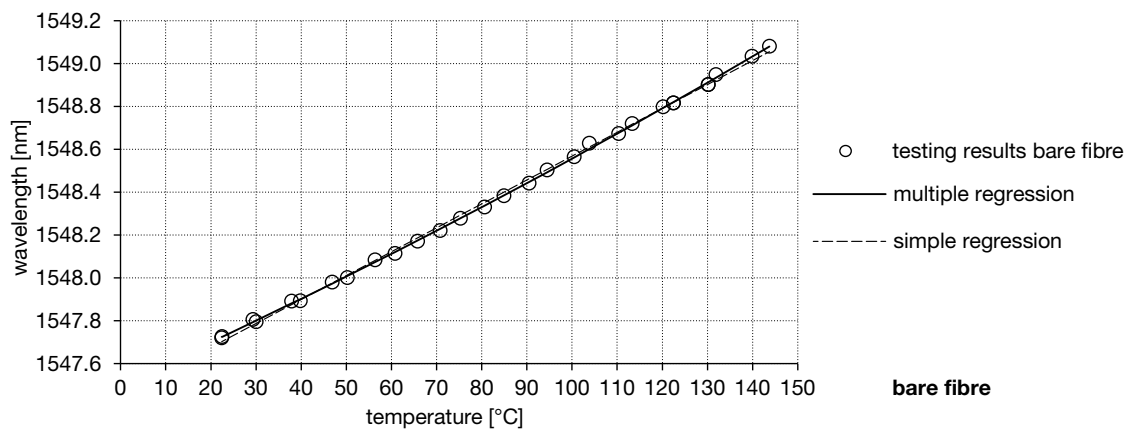


Figure 5.37.: Testing results of the Bragg sensor wavelength plotted against temperature and related linear and square regression curves for a bare fibre.

#### 5.1.4.3. Transverse Strain Effects

As explained in section 5.1.1.7, transverse strain acting on the sensor fibre causes birefringence resulting in double-peaks that often become visible as broadened spectra of the reflected wavelength. If the latter phenomenon occurs, then identification of the desired wavelength shift caused by longitudinal fibre strain becomes difficult. Therefore, transverse strain influence is regarded as an undesired perturbation in the context of this thesis. In the following cases transverse strain influence might occur for the case of cold bent lamination-stabilised glass:

- Birefringence can be caused by the adhesive used for the fibre bonding [Sto 97], [Hel 14], e.g. through possible shrinkage of the glue during cure.
- The cold bending of the glass causes transverse, in-plane strain  $\epsilon_{22}$  that can affect the fibre. However, the transmission of this strain component into the sensor happens in a transverse direction to the adhesive joint and to the fibre axis and the influence on the fibre is potentially very small.
- During the bending of the stacked glass panes and interlayer films on the bending mould, pressure orthogonal to the glass surface can occur locally, as shown in section 7.1.1. This happens mainly in contact areas of the bent glass to the mould and in areas directly forced down by the transverse bending bar. Theoretically, this effect is only maintained as long as the loose uncoupled interlayer sheets between the glass panes are in a solid state.
- The evacuation of the vacuum bag surrounding the bent glass-interlayer-stacks leads to pronounced birefringence effects in a number of sensors, as all the glass panes and interlayers are pressed against each other.
- When the interlayer material softens or liquefies in the autoclave lamination process, the transverse pressure is released from the sensors. Subsequently, birefringence is supposed to vanish.
- After the autoclave process, the release of the laminate from the bending mould causes elastic springback and long-term relaxation effects, which lead to a change of the geometrical shape

and the enclosed interior bending strain. Some transverse strain might occur and might affect the fibre.

- Exterior actions such as wind load on a cold bent lamination-stabilised glass can cause transverse strain acting on the fibre. This transverse strain in the  $\epsilon_3$ -direction, however, is very small compared with the in-plane strain  $\epsilon_{1,2}$  in the laminate.

A large number of research publications is available on the topic of birefringence attributable to transverse strain. The following paragraphs give a summary of some characteristic examinations of FBG birefringence. The findings are discussed in view of the application of FBGs in cold bent glass laminates:

Storoy and Johannessen [Sto 97] have examined birefringence in a polarimetric sensor and an FBG inscribed in an SMF caused by the curing process of a thin cyanoacrylate bond and thick epoxy embedment. They report birefringence up to  $3.6 \cdot 10^{-5}$ , corresponding to 38pm peak separation or a measurement uncertainty of 0.0032%, for the cyanoacrylate because of its high cure shrinkage and the development of anisotropic stress in the fibre attributable to the bond shrinkage. No birefringence was seen with the thick epoxy bond surrounding the cross section of the fibre. In the present work, adhesives exhibiting no or small post-cure effects are sought, see section 5.1.3. Polymer post-curing strain effects on embedded FBGs have also been examined by Parlevliet et al. [Par 10, pp. 291-301] with an FBG sensor directly immersed into the polymer resin. The gel point and the glass transition were identified by the increasing fibre compression from the shrinkage strain of the polymer. No such effects were actually encountered in the experiments performed in the present work, even though post-cure effects in adhesives have been identified, section 5.1.3.4. In the monitoring of a glass compound performed during the autoclave process, however, the impact of the temperature-dependent stiffness and the melting point of the interlayer on the FBG-measurement became visible, see section 7.1.

Gafsi and El-Sherif [Gaf 00, pp. 299-323] present analytical calculations applying coupled mode theory to investigate the influence of transverse loads on an FBG acting either as plane stress or plane strain. The authors have found that the

Bragg wavelength changes more strongly under the assumption of plane stress compared with plane strain. Another major aspect is the examination of the possibility of reducing birefringence by applying an appropriate soft coating to the embedded fibre in the grating region, a topic that has also been examined by Gabler [Gab 12]. In the present work, the coating of the fibre is first of all of importance for providing full shear transfer from the substrate to the fibre. This necessitates a high Young's modulus of the coating.

Lai et al [Lai 13] performed multi-axial loading tests and numerical analyses with a bare SMF embedded in an isotropic epoxy material subjected either to biaxial transverse strain or hydrostatic pressure. If the strain components  $\varepsilon_{2,3}$  orthogonal to the fibre axis differed, the single Bragg wavelength peak splits into two peaks with the difference being given by eq. 5.106 below. The authors used an effective photoelastic coefficient by replacing Poisson's ratio in eq. 5.32 by the biaxiality strain ratio  $\varepsilon_2/\varepsilon_3$ . In general, the wavelength-strain shift expression 5.31 is applicable in all cases of dominating axial strain  $\varepsilon_1$  even with relatively large transverse strain. In the present work, the various bending and relaxation stages of cold bent glass are examined numerically and the related gauge factors  $k_\varepsilon$  are determined.

Bosia et al. [Bos 03, pp. 925-934] performed tests and numerical analyses with both an SMF and a polarisation-maintaining (PM) bow-tie fibre subjected to a two-dimensional transverse strain field (biaxial load) acting directly on a fibre or on the fibre included in an epoxy block. The peak separation of the SMF attributable to birefringence for the principal strains in directions 2 (y) and 3 (z) is given as follows:

$$\frac{\Delta\lambda_3 - \Delta\lambda_2}{\lambda_{B,0}} = -\frac{n_0^2}{2} (p_{12} - p_{11}) (\varepsilon_3 - \varepsilon_2) \quad (5.106)$$

If the Young's modulus  $E$  of a material surrounding the FBG differs strongly from  $E$  of the fibre, then the strains in the fibre and the surrounding materials differ in transverse directions. The maximum disturbance can be found in the coating. This effect corresponds to the micro-modelling findings in this thesis, e.g fig. D.3 in section 5.1.6. The axial fibre strain, however, is not affected by this phenomenon.

Most of the research on transverse loads acting on FBGs is made in the field of polarisation-

maintaining fibres, typically Panda or bow-tie fibres. Linearly polarised light propagating in such fibres retains its polarisation during migration and therefore shows two clearly distinguishable polarisation modes. These modes have two different phase velocities. Basically, this polarisation state corresponds to birefringence and yields two peaks in the spectra.

Botero-Cadavid et al. [Bot 10, pp. 1291-1297] applied transverse local pressure to a PM Panda fibre and examined the effect on the spectral response of the FBG experimentally, numerically and analytically. They furthermore studied the various peak separations depending on the transverse load application angle to the section of the fibre.

Helminger, Daitche and Roths [Hel 14] also used a high birefringence PM Panda fibre and an SMF to study the development of the birefringence of sensors bonded to a substrate during the thermal curing process at 100°C on applying the epoxy adhesive EPO-TEK 353ND and during the following cooling of the bond zone. In their experiment, transverse strain acted on the fibre mainly in the cooling process, triggered by the various coefficients of thermal expansion of the fibre and the adhesive and the shrinkage of the latter. The transverse strain causes birefringence in the fibre and leads to two different Bragg conditions for linearly polarised light in two directions corresponding to the slow and fast axis of the fibre. The authors estimated the birefringence caused in a PM and also in the SMF to be approximately 36pm with an additional uncertainty of 36pm. The experiment shows that polarisation maintaining fibres are attractive for strain measurement in multiple directions. However, this necessitates an azimuthal alignment of the slow / fast axis of the PM fibre with the two principal strain directions of interest in the substrate; this is technically complex compared with an SMF.

In section 5.1.6, 5.1.6.5, transverse load applications to an FBG inside a two-ply glass laminate with PVB or SG interlayers are numerically examined and gauge factors / strain transmission coefficients are calculated, see table 5.12. For in-plane strain in the glass orthogonal to the fibre, the mean gauge factor for strain in the  $\varepsilon_2$ -direction is about -0.184 and exhibits a maximum variation of  $\pm 0.0029$  attributable to birefringence effects; this corresponds to a variation in strain of about 0.052nm per % strain.

For strain being both orthogonal to the glass panes and the FBG in  $\varepsilon_3$ -direction, the gauge coefficient is about -0.54 with a birefringence of  $\pm 0.035$  corresponding to 0.54nm per % strain which is a strong influence. If the strain in this direction remains small, these effects are, however, limited. To evaluate this for cold bent glass in the springback and relaxation phase, in which the interlayer is solid and bonded to the glass surfaces, respective studies are also included in the micro-mechanical model explained in section 5.1.6. The bending strain applied in the models is in the order of magnitude of the maximum strain in the real-scale cold bent glass specimens. For a gauge factor of about 0.8, the maximum birefringence-induced variation is only  $\pm 0.00048$ , which corresponds to 0.0074nm per % strain. The strain caused by

cold bending is in a range of 0.06% and thus the expected spectrum birefringence is approximately  $\pm 0.0005$ nm. For a control, the spectral width and its change with time in the FBGs employed in the real-scale glass specimens is monitored to detect possible broadening, see section 7.1.1.

#### 5.1.4.4. FBG Sensor Property Summary

A summary of the principal coefficients and parameters of fibre Bragg gratings drawn from a literature review is given in the following table 5.6 (in the table, (b) means bare fibre and (c) coated fibre):

parameter	$n_0$	$\alpha_T$	$\alpha_n$	$K_\varepsilon$	$p_{12}$	$p_{11}$
author	[-]	$[\frac{10^{-6}}{K}]$	$[\frac{10^{-6}}{K}]$	[-]	[-]	[-]
[Ste 97]	1.456	0.50	8.24	0.708	0.17	0.36
[Fra 01]	1.45	0.50	5.54	0.81	0.168	0.247
[Flo 04]	-	-	6.11	0.807	-	-
[Leb 04]	1.482	0.55	7.422	0.787	0.113	0.252
[Sch 10]	1.482	0.55	8.6	0.78	-	-
[Bot 10]	1.4608	0.54	-	-	0.121	0.27
[Gab 12]	1.4682	0.51	7.424	0.791	0.113	0.252
[Int 12]	1.454	-	6.5 (7.37)	0.78	0.112 $\pm$ 0.008	0.256 $\pm$ 0.017
[Jül 13]	-	-	-	0.783 $\pm$ 0.004	-	-
thesis	-	-	6.655(b), 7.60(c)	0.7898	-	-

**Table 5.6.:** Summary of the principal FBG parameters and coefficients

### 5.1.5. Testing of Glass-Bonded Bragg Sensors

#### 5.1.5.1. Test Setup

In addition to the assessment of an adhesive suitable for the bonding of an FBG in the context of glass laminates, the reliability and performance of a sensor glued to glass needs to be examined for the various conditions encountered in the envisaged use with cold bent, lamination-stabilised glass. These conditions are:

- Strain measurement on the surface of glass bent to a radius of approximately 5m, corresponding to a maximum strain level of approximately  $\pm 6.5 \cdot 10^{-4} \text{ mm/mm}$  ( $= 650 \mu\text{m/m} = 0.65\%$ ).
- Resistance to the conditions during lamination of glass in an autoclave: constant temperature of  $140^\circ\text{C}$  during three to four hours plus heating and cooling time.
- Operability of the bonded FBG after lamination.
- For constantly applied bending throughout the process, no or low bending pre-strain loss after the autoclave cycle compared with the measured bending strain prior to the thermal cycle.
- The fibres shall not be stripped of their coating, as this strongly reduces their mechanical strength and could lead to fibre rupture during lamination. Thus, the entire system of glass substrate / adhesive joint / fibre coating / silica fibre has to function during the glass laminate manufacturing process and in later practical use.

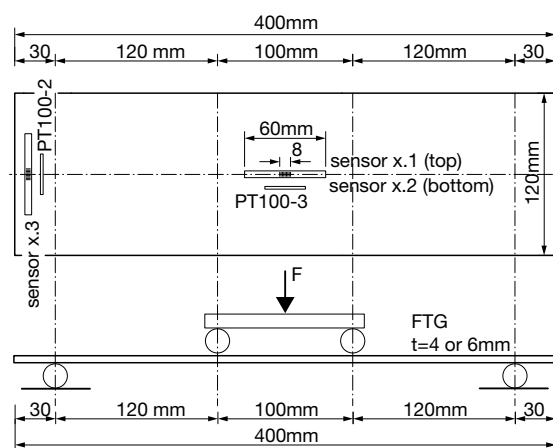


**Figure 5.38.:** Plan view and elevation of the four-point bending setup.

The necessary functionality tests were performed by subjecting rectangular glass specimens with

bonded FBG sensors to four-point bending, fig. C.1, in a climatic chamber. Through four-point bending, constant bending and constant strain conditions can be produced in the portion of the specimen situated between the two load application rollers, fig. 5.38. This situation corresponds well with the conditions occurring in cold bent glass in which relatively constant bending is generated in the deformation process into a shape close to a cylindrical arc. Furthermore, a sensor bonded at the centre of the glass plate is not obstructed or touched by the load application rollers. Four-point bending tests can also be executed inside a climatic chamber, which allows for reproducing the temperature cycle of an autoclave.

The influence of the pressure in an autoclave and the influence of the vacuum bag have not been tested. The lamination process itself, which involves the softening of the interlayer material by temperature and the successive hardening and adhesion to the glass in the cooling process are also not reproduced experimentally in the four-point bending tests, as this would necessitate a complex test set-up including vacuum bagging. The four-point bending tests in the climatic chamber are thus limited to combining the effects of bending and temperature loads, both of which are regarded as the principal parameters influencing the FBG bonding feasibility for cold bent lamination-stabilised glass.

The specimens were 400mm in length by 120mm in width with a glass thickness of either 6mm or 4mm. Two testing series were performed: In the first series, including test nos. 1 to 15, both an FBG and an electrical strain gauge (ESG) were glued to the centre at the bottom of the glass plate. Three thermocouples were applied for temperature control. In the second series, namely tests nos. 16 to 19, three FBGs were bonded to each specimen. One FBG was attached to the top, one at the bottom at the centre of the glass and a third in a zone without bending action and serving as temperature compensation. Three resistance temperature detectors (RTD) of PT100-type were placed in direct proximity to the FBGs. An overview of the specimens is given in table 5.7. All adhesive bonds were cured at room temperature following the manufacturer's instructions as in table B.1 in appendix B.1. The minimum time elapsed after UV-curing or thermal cure before testing was 48h. For calculating the fibre strain results, the geometrical data of the fibre bonds displayed in table 5.4 in section 5.1.3.5 are used.

no.	x	code	definition	cure
1-5	1-5	ANG_KB4552_x	annealed glass t=6mm, 1 centre bottom FBG, 1 centre bottom ESG, three thermocouples, path-controlled u=2.1mm	60s UV 60mW/cm <sup>2</sup> , 43% hum.
6-10	1-5	ANG_EP353ND_x	annealed glass t=6mm, 1 centre bottom FBG, 1 centre bottom ESG, three thermocouples, path-controlled u=2.1mm	100°C 15 Min., 65% hum.
11-15	1-5	ANG_UV681_x	annealed glass t=6mm, 1 centre bottom FBG, 1 centre bottom ESG, three thermocouples, path-controlled u=2.0mm	5s UV 60mW/cm <sup>2</sup> , 41% hum.
16-17	2, 4	FTG_KB-OB642_x	fully toughened glass t=4mm, 3 FBGs: centre-bottom, centre-top, lateral-top; 3 PT100 RTDs, load controlled F=194.24N	30s UV 60mW/cm <sup>2</sup> , 65% hum.
18-19	2, 3	FTG_KB4552_x	fully toughened glass t=4mm, 3 FBGs: centre-bottom, centre-top, lateral-top; 3 PT100 RTDs, load controlled F=194.24N	60s UV 60mW/cm <sup>2</sup> , 47% hum.

**Table 5.7.:** Overview of the specimens tested in four-point bending.

#### 5.1.5.2. Four-Point Bending Preliminary Tests

The first test series nos. 1 to 15, serving basically to examine the behaviour of FBGs bonded to glass with various adhesives, was conducted with the UV-curing adhesives Delo KB4552, Permabond UV681 and the thermal-curing Epoxy Technology EPO-TEK 353ND. The testing procedure as in fig. 5.39 consisted of a path-controlled load of 2.1mm applied to the 6mm-thick annealed glass specimens at room temperature for 5 min (instance 1). The FBG-sensors and electrical strain gauges were bonded to the bottom of the glass and were therefore subjected to tension during bending. Afterwards, the samples were heated in a climatic chamber to 140°C. When constant temperature was reached (instance 2), the initial load was applied again for one hour (3-4). Thereafter, the temperature was kept constant for another 10 more min (5) prior to cooling the samples back to room temperature again. Then, the initial load was applied for a third time (7). Whether the mechanical load at instances 1, 3-4 and 7 led to different sensor measurement results attributable to the influence of temperature on the adhesive was determined. The control of cooling during testing was limited, as the available climatic chamber was not equipped with nitrogen cooling. These tests, however, are of a preliminary nature and are therefore only dealt with briefly here.

FBG wavelength and temperature measurement diagrams plotted against time for three exemplary specimens covering all three adhesives are given in figure 5.40. The figures clearly exhibit differences in the FBG results during stages 3-4 in which a bending load was applied to the specimen heated to a constant temperature of 140°C. The testing results were examined by calculating the difference of the FBG-wavelength shift  $\Delta\lambda_m$  attributable to mechanical load and the  $\Delta\lambda_m$  attributable to a constant temperature state prior to the loading sequence. The  $\Delta\lambda_m$ -differences for instances 1-0, 3-2, 5-4, 7-6 and 8-7 were calculated first and were then divided by the corresponding force  $F_i$  applied by the testing machine:  $\Delta\lambda_m/F_i$ . Furthermore, normalised values were calculated from the above results related to the wavelength shift / force fractions at the beginning (1-0). All results and the respective arithmetic mean values can be seen in table C.1 in appendix C.2.

The mean values in the table reveal that the normalised  $\Delta\lambda_m/F_i$ -values vary by less than -6% for adhesive EP353ND and by about 3% for KB4552 at 140°C during instances 3-4 with respect to the bending measured at room temperature at instance 1. The adhesive UV681 even shows values of about -20% less. The measurement of a bending load at an autoclave thermal process with a UV681-bonded fibre therefore would result in a mistake of around -20%.



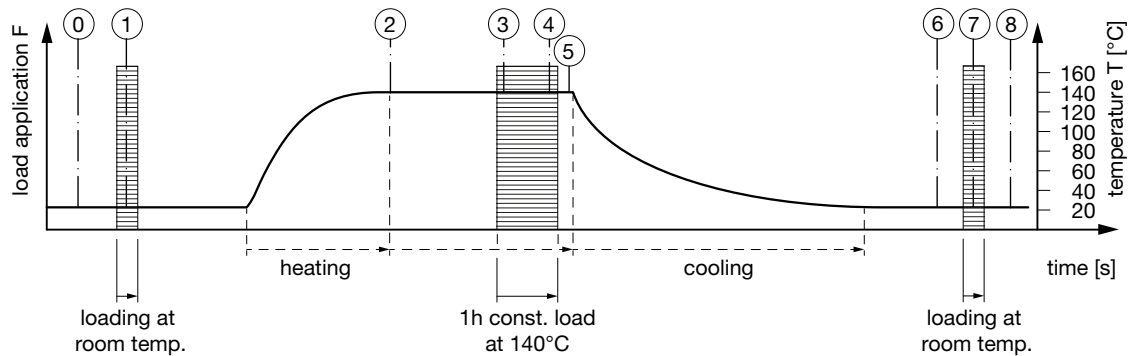


**Figure 5.39.:** Testing procedure for short term load application during autoclave thermal cycle.

However, if a load is applied at instance 7 after the thermal process, all adhesives exhibit relatively small mean measurement differences of  $-0.75\%$  to  $0.56\%$  compared with the same load at instance 1. With all adhesives, a change of about less than 3% in the relative wavelength shift / force results is observed during the load application stage at  $140^{\circ}\text{C}$  of one hour, if the results from 3-2 and 5-4 are compared. Whether these changes are related to the adhesives, the fibre / coating or to the test setup is not clear. Analytical and numerical stress calculation for the glass surface was corresponding with the stress determined by the FBG-measurements at room temperature.

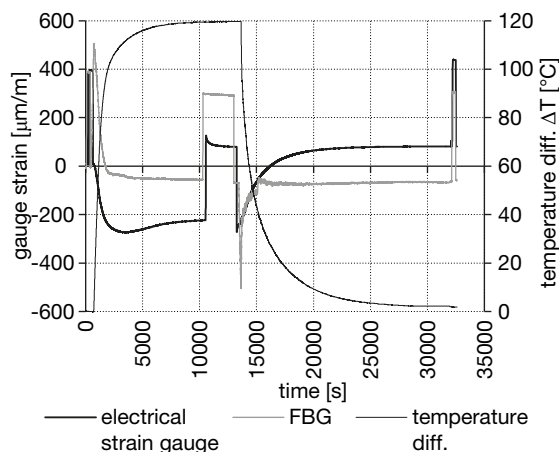


**Figure 5.41.:** Comparison of the mechanical strain measurement results of an electrical strain gauge and an FBG. Note the creep behaviour of the electrical strain gauge at  $140^{\circ}\text{C}$ . The gauges show a time lag / inertia with regard to temperature compensation.

The electrical strain gauges of the type linear-Y with Polyimide patches and a temperature compensation for titanium were glued to the glass

with the same adhesive types as used for the bonding of the FBGs. The comparison measurement results provided by the electrical strain gauges during the load cycle at instances 3 and 4 at  $140^{\circ}\text{C}$ , however, were unemployable because of a pronounced creep loss. The creep is attributed to the fact that the bonding length of the Polyimide patch was not sufficient to obtain full strain transfer in the measuring grid of the gauge. Further problems resulted from the temperature compensation of the electrical strain gauges. An example for adhesive EP353ND is shown in fig. 5.41.

In conclusion, the adhesive Permabond UV681 can be excluded for the task of fibre bonding to glass subjected to later autoclave conditions, as it does not provide sufficient stiffness for full load transfer during the thermal phase of lamination. Neither EP353ND nor Katiobond 4552 shows such a pronounced loss. The amber-coloured two-component EP 353ND is also excluded, as a thermal curing process is not easily applicable to glass pane sizes for architectural or automotive applications and would be an additional cost-intensive process step in the manufacturing of glass laminates equipped with FBG. Only the UV-curing single-component KB 4552 is thus retained from this pretesting cycle, as it exhibits the least wavelength shift measurement changes during and after the thermal process. However, the results from these preliminary tests only permit the identification of principal trends for the choice of appropriate adhesives. Furthermore, the load application duration in the above tests is relatively short compared with the permanent bending load acting on the sensor in a process involving cold bent glass.

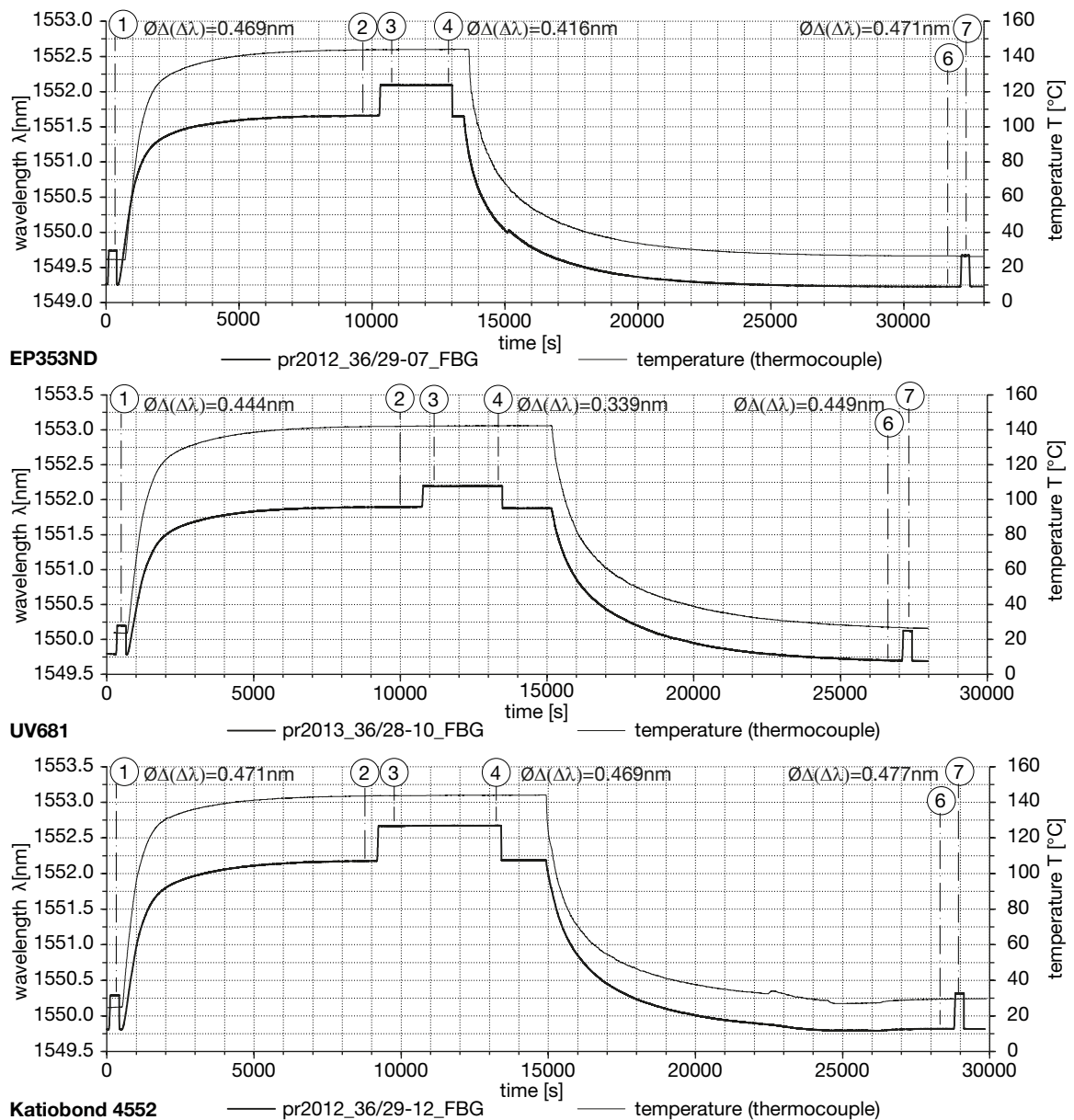


Figure 5.40.: Measured absolute FBG wavelength and temperature plotted against time for three different adhesives.

### 5.1.5.3. Four-Point Bending Constant Load Tests

Based on the experience from the tests described in the previous section, the test setup was changed. Samples made of fully toughened glass (FTG)  $t=4\text{mm}$  allowing for higher deformation and equipped with three sensors as described in section 5.1.4.1 were used. The full setup is shown in fig.5.31 and C.1 in section C.1. Whereas the centre sensors on the top (x.1) and bottom (x.2) of the glass allow for measuring compressive and tensile surface strain, a third FBG (sensor x.3) bonded to the lateral end of the glass beyond the roller support bearings acts as thermal compensation sensor, as it is applied to a zone with nearly vanishing strain. For calculating the mechanically induced strain, eq. 5.55 was used. For comparison reasons, only two promising adhesives, Delo KB4552 and KB OB642, were applied in the samples. A constant load was now applied during the entire temperature cycle, fig. 5.42, consisting of a phase at room temperature (instance 1), a ramped heating phase of 90 min, 240 min of constant temperature (instances 2, 3) at  $140^\circ\text{C}$  and a cooling phase of up to 8 hours for returning to room temperature level (instance 4). Only then, was the load removed. The sensor results were recorded during the entire process. Comparison of the results was made by using the measurements at the distinct instances 1 to 5 shown in fig. 5.42. Results were both evaluated relative to the absolute initial conditions at  $t=0$  at the beginning of the test but also relative to the respective antecedent instance. The temperature cycle was adapted to a typical autoclave protocol as used for cold bent glass lamination. The permanent load application combined with such a temperature regime corresponded to the situation encountered in the cold bending and autoclave lamination process from the real-scale tests in section 6.1.

To control possible thermal expansion effects from the vertical load-transferring metallic connection cylinders of the testing device, these tests were run in a force-controlled manner. This also permits an evaluation of the creep behaviour at constant temperature between instances 2 and 3. As sensor x.3 is not subjected to mechanical loading, effects from the thermal expansion of the substrate can be distinguished from the mechanically induced action on the sensors x.1, x.2. Apart from the relaxation study, the test mainly serves to examine the sensor measurement of a mechanically induced load during an autoclave-like thermal cycle. As the sensor behaviour mainly depends on

the temperature-related adhesive performance, the suitability of the bond for the lamination process is also examined by this test.

The spectra of each sensor were monitored prior to and after the test procedure, as shown by the example of sensor 2.3 in fig. 5.43. Table 5.8 contains a summary of the spectral width at  $-3\text{dBm}$  identified for all sensors on the four specimens. The control of the spectral width serves basically to identify possible transverse strain effects on the FBG resulting from post-cure effects of the adhesive.

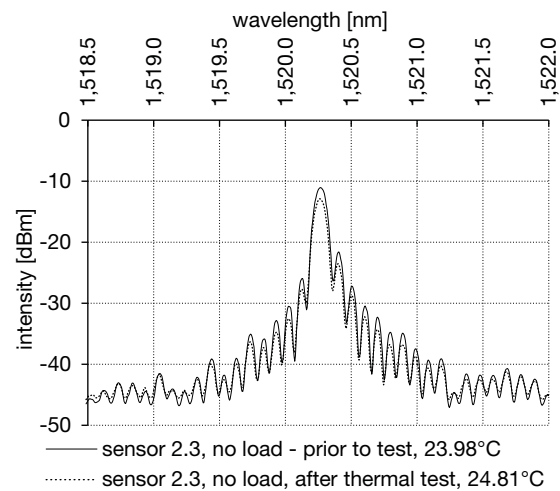


**Figure 5.43.:** Exemplary spectrum prior to and after thermal and load cycle.

The table indicates that the maximum absolute change in spectral width is  $0.0091\text{nm}$ . The spectral width alteration for these specimens for FBG bonded with KB OB642 is generally smaller than that for the FBG fixed by KB4552. These very small spectral width changes during the test and the subsequent lack of visible birefringence lead to the conclusion that the autoclave temperature cycle does not cause strong transverse strain effects by thermal post-cure of the adhesives. From their tests with highly birefringent Panda fibres glued with EPOTEK 353ND thermal curing epoxy, Helminger et al. [Hel 14] give an estimation of a residual birefringence of  $0.036\text{nm}$  for an SMF. This value is about four to ten times more than the spectrum broadening encountered here and can be explained on the basis that the adhesives used here are UV-curing and therefore only suffer very small thermal post-cure effects and subsequently also only small peak broadening attributable to birefringence.

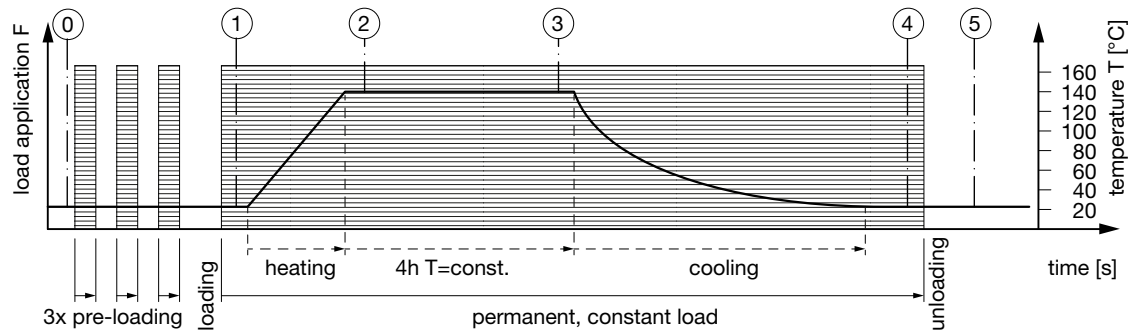


Figure 5.42.: Testing procedure for permanent load application during thermal autoclave cycle.

specimen	FBG	prior to testing		after testing		change $\Delta\lambda_{sw}$ [nm]	mean change [nm]	std. deviat. [nm]
		T	$\Delta\lambda_{sw}$	T	$\Delta\lambda_{sw}$			
		at -3dB [°C]	at -3dB [nm]	at -3dB [°C]	at -3dB [nm]			
FTG_KB-OB642_02	2.1	23.94	0.1048	23.97	0.1088	0.0040	0.0002	0.0034
	2.2	23.61	0.1009	23.65	0.0984	-0.0024		
	2.3	23.98	0.0913	24.81	0.0905	-0.0009		
FTG_KB-OB642_04	4.1	23.94	0.1067	21.63	0.1032	-0.0034	0.0009	0.0038
	4.2	23.73	0.0951	21.39	0.0982	0.0030		
	4.3	26.04	0.0936	22.37	0.0969	0.0032		
FTG_KB4552_02	2.1	24.02	0.0965	23.49	0.0947	-0.0018	0.0018	0.0063
	2.2	23.73	0.1033	23.28	0.1124	0.0091		
	2.3	25.51	0.1145	26.00	0.1127	-0.0018		
FTG_KB4552_03	3.1	24.19	0.1080	21.80	0.1088	0.0008	0.0018	0.0063
	3.2	23.86	0.1110	21.55	0.1196	0.0086		
	3.3	25.96	0.1071	22.87	0.1031	-0.0040		

Table 5.8.: Spectral width control at -3dB prior to and after the thermal and load cycle.

The post-cure effects monitored in the DSC analysis of KB 4552 in section 5.1.3.4 coincide with the increased spectral width change of this adhesive in table 5.8 compared to the KB OB642-adhesive. The volume shrinkage of the adhesives as given by the manufacturer is 3.7% for the KB4552 and 4.0% for KB OB642. Shrinkage should, however, mostly take place during the UV activation / curing of the adhesive. As shown by DSC in fig. 5.25, KB4552 is subject to strong post-cure effects at temperatures around 80-140°C, whereas KB OB642 only exhibits minor temperature post-cure. The coating material of the fibre, Ormocer NM850, does not show any thermal post-cure effects, fig. B.5. As the tests performed in the context of this work have been made to explore the feasibility of FBG use with glass laminates, the change in the spectral width of the bonded sensors for the two adhesives KB4552 and KB OB642 are assumed to be negligible.

The second aspect examined by the four-point bending tests is the effect of the thermal (autoclave) procedure on the measurement of mechanical strain via FBG. The principal information to be obtained is whether the pre-stress introduced into the fibre attributable to cold bending can be preserved throughout the process and whether this quantity is correctly measured after autoclaving. For this aspect, the sensor wavelength shift measurements at several instances are compared: at  $t=0$ , prior to the application of the bending load  $F=194.2\text{N}$  and the thermal load  $T=140^\circ\text{C}$ , at instance 1 when  $F$  has been applied at room temperature, at instance 4 after the thermal process back to room temperature and at instance 5 when the load  $F$  is relieved. Related to the initial conditions at  $t=0$  with an absolute Bragg wavelength  $\lambda_{B,0}$ , both the total wavelength shift  $\Delta\lambda_{tot,0}$  from temperature  $T$  plus the bending load  $F$  and the mechanically induced wavelength shift  $\Delta\lambda_{m,0}$  only attributable to  $F$  are calculated.

The latter is obtained by compensation of the sensors x.1, x.2 by the sensor x.3 as in eq. 5.55. As the installation area of FBG x.3 nevertheless is subjected to a small amount of bending strain, the sensor result measurement is reduced by this quantity prior to compensation. All results are given in table C.2 in appendix C.2.

The instances 1-5 are fixed at times when constant temperature conditions prevail. The wavelength shifts at these instances are calculated as mean values during 30 to 50 seconds. The individual geometry of each bond is taken into account in the strain / stress calculation for the necessary reduction of the sensor results to obtain the surface strain of the substrate as in eq. 5.61. The stress values for mechanically induced fibre strain related to the initial conditions at  $t=0$ ,  $\sigma_{xx,m,0}$ , are calculated from  $\Delta\lambda_{m,0}$ . The stress values can be seen to vary during the thermal phase. Therefore, the stress has additionally been calculated between the adjacent instances. A comparison of the stress measured at instance 1 related to  $t=0$  and at instance 5 related to instance 4 results in stress values differing less than in the case when the stress is related to  $t=0$ : the variation of the stress measured in instance 5 to the stress at instance 1 reaches peak values of 10% (approximately 4MPa) in the case of the results related to  $t=0$ , whereas less than 3% occur if the calculation is related to the precedent instance. The differences of the mechanically induced stress values calculated at instances 1 and 5 either relative to the initial conditions ( $t=0$ ),  $\Delta\sigma_{xx,m,abs}$ , or to the preceding instance (0-1 and 4-5),  $\Delta\sigma_{xx,m,rel}$ , are listed in table 5.9.

specimen	FBG	stress change relative to	
		inst. 5 to 1	inst. 5 to 4
		$\Delta\sigma_{xx,m,abs}$ (F)	$\Delta\sigma_{xx,m,rel}$ (F)
		[MPa]	[MPa]
ftg_kb-ob642-02	2.1	-2.8249	0.2028
	2.2	-0.7047	0.2435
ftg_kb-ob642-04	4.1	-4.0112	-0.9822
	4.2	0.4127	0.4877
ftg_kb4552-02	2.1	-3.7979	-1.1962
	2.2	-0.1370	-0.8262
ftg_kb4552-03	3.1	-0.3067	-1.1382
	3.2	2.3769	-0.7186

**Table 5.9.:** Residual stress summary relative to phases 1, 4 or 5 for FBGs bonded with different adhesives.

The stress differences  $\Delta\sigma_{xx,m,rel}$  are slightly smaller for FBG bonded with KB OB642 than for the KB4552 specimens. The results also show, that the deviation of strain or stress measurement increases, if the bonded fibre is subjected to thermal processes such as lamination. Thus, measurement related to intermediate stage results having the identical constant temperature as performed here is recommended.

In the top diagram in fig. 5.44, the temperature-compensated wavelength shift curves show the same level during stages of constant or slowly changing temperature. However, if temperature varies strongly and fast, such as during the heating or cooling phase, the compensation sensor 2.3 is not subjected to the same conditions as the other sensors 2.1, 2.2. Hence, the calculated mechanically induced wavelength shift deviates. As a result, values stemming from stages with temperature gradients should not be used for comparison or compensation of other sensors but constant conditions have to be established prior to record compensated FBG measurements from the test. The results for specimens with KB4552 are given in the appendix, C.2, fig. C.4.

The third aspect analysed in these tests is the identification of possible relaxation effects of the fibre bond to the glass substrate attributable to constant strain loading from the bent glass substrate. The shear modulus of the adhesives decreases with rising temperature; this can also have an influence on the FBG measurements. For determining the relaxation at constant temperature, the wavelength shift of all three sensors x.1, x.2, x.3 between the instances 2 and 3 has been examined and corresponds to a duration of 145 to 166 min. The related three diagrams for the sensors are plotted in fig. 5.44 for the specimen as an example; an additional diagram for the adhesive KB4552, namely fig. C.4, can be found in appendix C.2. Temperature rises slightly by about 0.06 to 0.08°C during this time, as shown in table 5.10. The same table gives the hypothetical maximum wavelength shift that can be caused by this temperature difference attributable to the various thermal expansion coefficients of the materials working as a compound, glass, adhesive and silica fibre; this accounts for less than 0.022nm between the fibre and the adhesive and <0.0021nm between the adhesive and the glass substrate. These estimations are, however, hypothetical and on the safe side.

With all tested specimen, sensors x.1, subjected to compression from bending and positive expansion from temperature, show a relaxation by about -0.0055nm to -0.0065nm, table 5.10. The sensors x.2, subject to mechanically induced tensile strain and positive thermal expansion, exhibit only a very small decrease in wavelength shift of less than 0.001nm. The wavelength shift “loss” of sensors x.3 of -0.0046 to 0.0058nm is similar to the results encountered with x.1. This type of behaviour is the same for all specimens. Adhesive or coating shrinkage attributable to thermal post-cure cannot explain this phenomenon, as this would lead to a decrease in wavelength shift  $\Delta\lambda$  of a similar magnitude for all sensors. Relaxation would also cause all sensors to exhibit a similar decrease in  $\Delta\lambda$ . At 140°C, all sensors are subjected to tensile stress because of the prevailing thermal expansion

of the substrate. Only sensors x.2 subjected to an initial mechanically induced tensile strain deviate from the relaxation behaviour encountered with the other two sensors. The test does not provide the data or conditions to identify the reasons for this different sensor behaviour clearly. As all specimens, albeit having two different adhesives applied, exhibit similar behaviour, the adhesive bond is unlikely to be the reason. The available results only permit the conclusion, that the mechanically induced tensile pre-strain in the fibre and the fibre with its coating itself are probably involved in causing sensors x.2 to behave differently from the other FBG x.1 and x.3. In conclusion, however, the relaxation loss of pre-strain in the fibre corresponds to a wavelength shift of less than -0.0065nm at a temperature of 140°C applied during 2 to 3 hours and is therefore assumed to be negligible in the context of this work.

specimen	FBG	instance 2			instance 3		inst. 3 - inst. 2		FBG	mean changes		hyp. $\Delta\lambda$ caused by $\Delta T^*$		
		time $\Delta t$	$T_2$	$\Delta\lambda_2$	$T_3$	$\Delta\lambda_3$	change $\Delta T$	change $\Delta\lambda$		$\Delta T$	$\Delta\lambda$	$\lambda_{B,0}$	$\Delta\lambda_T$ (glass-fibre)	$\Delta\lambda_T$ (fibre-adhesive)
FTG_		[s]	[°C]	[nm]	[°C]	[nm]		[nm]		[°C]	[nm]	[nm]	[nm]	[nm]
KB-OB642_02	2.1	10,000	140.829	1.611	140.894	1.604	0.0648	-0.0069	x.1	0.0778	-0.0065	1562.51	0.0012	0.0138
	2.2		141.359	3.059	141.427	3.057	0.0679	-0.0020				1535.19	0.0013	0.0142
	2.3		140.829	2.418	140.894	2.413	0.0648	-0.0045	x.2	0.0711	-0.0010	1520.27	0.0012	0.0134
KB-OB642_04	4.1	10,000	140.500	1.651	140.591	1.645	0.0909	-0.0062				1562.51	0.0017	0.0193
	4.2		141.155	3.091	141.229	3.091	0.0743	0.0001	x.3	0.0778	-0.0058	1535.19	0.0014	0.0155
	4.3		140.500	2.372	140.591	2.365	0.0909	-0.0070				1520.27	0.0017	0.0188
KB4552_02	2.1	10,000	140.483	1.575	140.593	1.570	0.1097	-0.0050	x.1	0.0718	-0.0055	1533.09	0.0021	0.0218
	2.2		141.102	3.112	141.192	3.113	0.0900	0.0014				1567.58	0.0017	0.0183
	2.3		140.483	2.418	140.593	2.413	0.1097	-0.0045	x.2	0.0620	0.0007	1575.03	0.0021	0.0224
KB4552_03	3.1	8,800	140.321	1.605	140.355	1.599	0.0340	-0.0060				1579.92	0.0007	0.0070
	3.2		140.946	3.114	140.980	3.114	0.0339	-0.0001	x.3	0.0718	-0.0046	1572.42	0.0007	0.0069
	3.3		140.321	2.383	140.355	2.379	0.0340	-0.0048				1564.86	0.0007	0.0069

\*  $\alpha_a$  (KB4552) = 158.0E-6;  $\alpha_a$  (OB642) = 166.0E-6;  $\alpha_g$  (fibre) = 0.55E-6;  $\alpha_s$  (glass) = 9.0E-6;  $\alpha_n$  = 5.58E-6;

Table 5.10.: Temperature and wavelength shift changes during 2.5 to 2.75 hours at constant temperature of 140°C and related relaxation estimation.

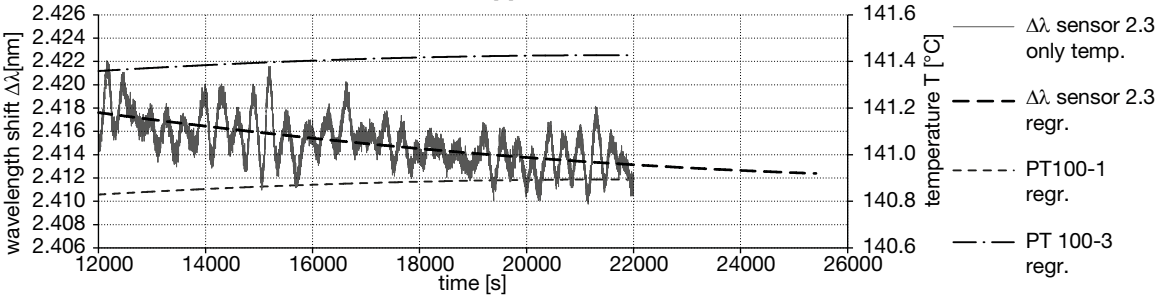
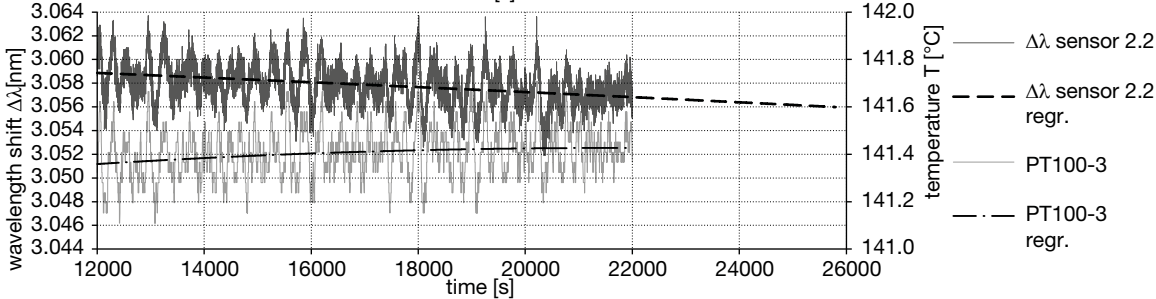
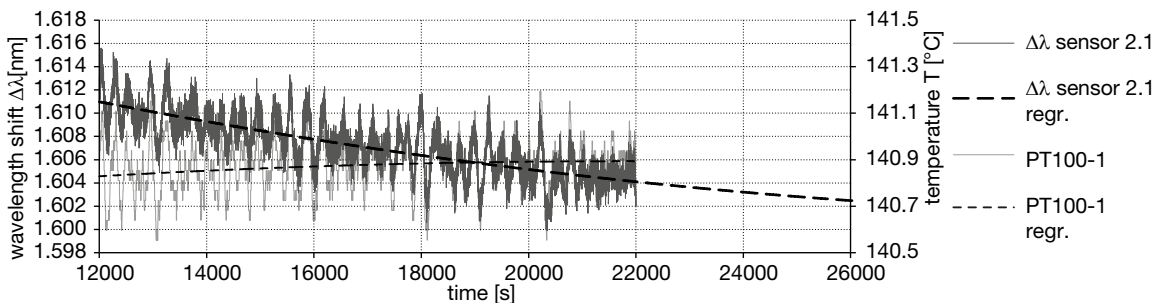
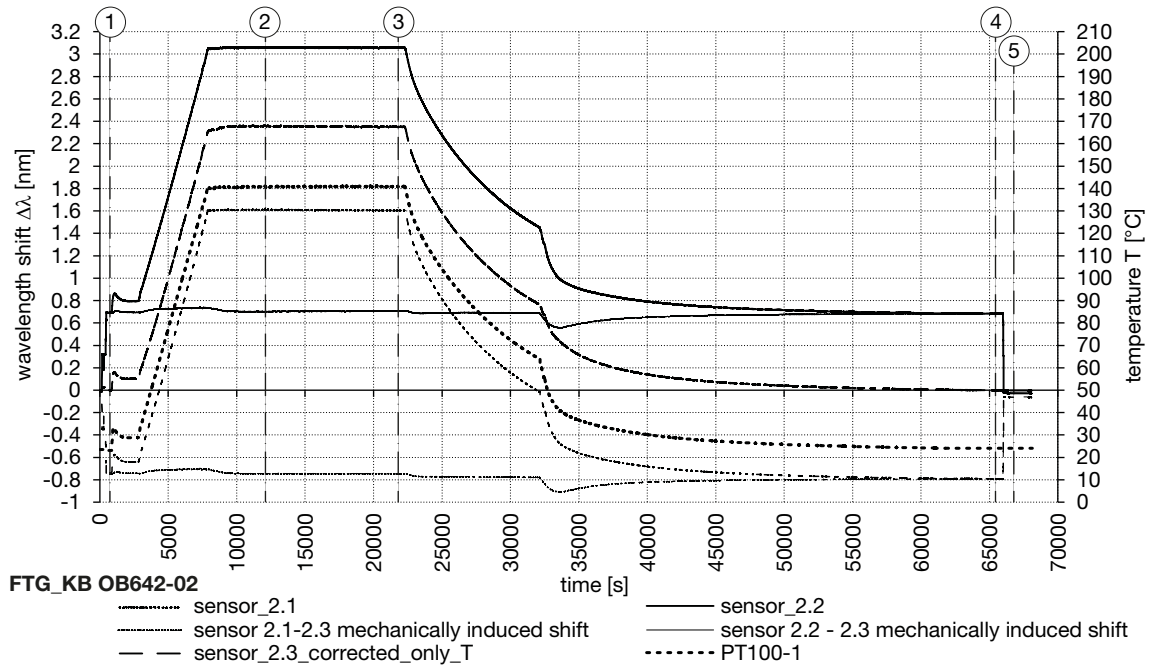


**Figure 5.44.:** Top diagram: testing procedure results total and compensated wavelength shift  $\Delta\lambda$  / temperature  $T$  vs. time of specimen FTG KB-OB642-02; bottom diagrams: relaxation behaviour at load  $F$  and constant  $T$ : wavelength shift / temperature vs. time between instances 2 and 3.

## 5.1.5.4. Summary

In conclusion, the following preliminary assumptions can be met for the bonding of fibre Bragg grating sensors to glass undergoing a thermal autoclave process for lamination:

- The test is performed by applying a permanent constant load  $F$  to a glass specimen equipped with an FBG bonded to the tensile and the compressed surface and an additional FBG glued in an area without mechanical strain. The specimen is then subjected to a temperature cycle corresponding to an autoclave process: 90 min heat ramping  $23^{\circ}\text{C}$  to  $140^{\circ}\text{C}$ , maintaining  $140^{\circ}\text{C}$  for 240 min, and cooling back to room temperature during 6 to 8 hours. After reaching  $23^{\circ}\text{C}$  again, the load is removed.
- Two UV-curing transparent epoxy adhesives used in this project are tested: Delo Katiobond 4552 and Katiobond OB642. Both adhesives withstand the thermal conditions of constant  $140^{\circ}\text{C}$  during four hours.
- No major systematic spectrum broadening of the sensors prior to and after the thermal process is encountered. The spectral width at  $-3\text{Bbm}$  is  $<0.0091\text{nm}$  with KB4552 and  $<0.0040$  with KB OB642. The possible peak measurement tolerance of a sensor response is estimated negligible for this work.
- Comparison of the stress measured by means of the wavelength shift of the sensor at the beginning of the loading with  $F$  and after the thermal process show a change in the stress measurement of  $+2.4$  to  $-4.0$  MPa for a total applied mechanical stress of approx.  $+39 / - 41\text{MPa}$ . This is attributable to changes of the polymer bond and coating material and the development of residual stress in the compound at the various thermal stages. If the stress measurement is not related to the initial sensor wavelength conditions at  $t=0$  but is calculated relatively to the precedent loading phase at constant temperature<sup>26</sup>, the stress difference reduces to less than  $-1.2\text{MPa}$  for KB4552 and  $-0.98$  to  $0.24\text{MPa}$  for KB OB642. These quantities are not negligible and show

the importance of the adhesive and the coating polymers, their bond section geometry and their curing.

- At constant temperature conditions for 2.5 to 2.75 hours with a load of 294N applied, sensors bonded to the glass surface subjected to compression and to tension show little relaxation of less than  $-0.0065\text{nm}$  related to a total of  $\pm 0.74\text{nm}$  wavelength shift from mechanically induced strain and  $+2.4\text{nm}$  from thermal expansion of the substrate ( $<0.4\%$ ). The FBG subjected to mechanically induced tension suffers less relaxation than the temperature compensation sensor and the sensor fixed onto the compressed glass surface. Both glass-adhesive-fibre-bonds show similar relaxation behaviour. The relaxation behaviour of the bonded sensors subjected to both tensile and compressive pre-strain is thus assumed to be negligible in the context of this work.
- The stress calculated from FBG measurements complies with the glass surface stress determined numerically for the sensor locations.

As mentioned before, the test setup is not designed to provide an analysis of potential residual strain developing in the FBG from the interlayer of a glass laminate. This possibility is basically examined by transient thermal FE models and through the bent glass specimen in section 6.1.

<sup>26</sup>This is the measured wavelength difference prior to load  $F$  application (time instance 0) and directly afterwards (time instance 1) and after the thermal process directly before (instance 4) and after the load removal (instance 5)



**5.1.6. FE Micro-Modeling**

A mechanical finite element model of microscopic scale is used to numerically analyse the behaviour of the bonded fibre. The models serves to explore the triaxial strain state developing in the fibre core because of various load cases applied to the glass or to the laminate. Inspired by the procedure used by Gabler [Gab12, pp. 74-111], the strain transmission attributable to mechanical or temperature load and possible birefringence effects related to the stress states in the fibre are calculated. For evaluation, gauge factors  $k_e$  (mechanical influence) and  $k_T$  (thermal influence) and their variation attributable to birefringence are determined from the principal strain in the fibre and the related strain or temperature at the surface of the substrate. The examination focuses on the question, if the gauge factor changes in the cold bending and relaxation process and if birefringence occurs.

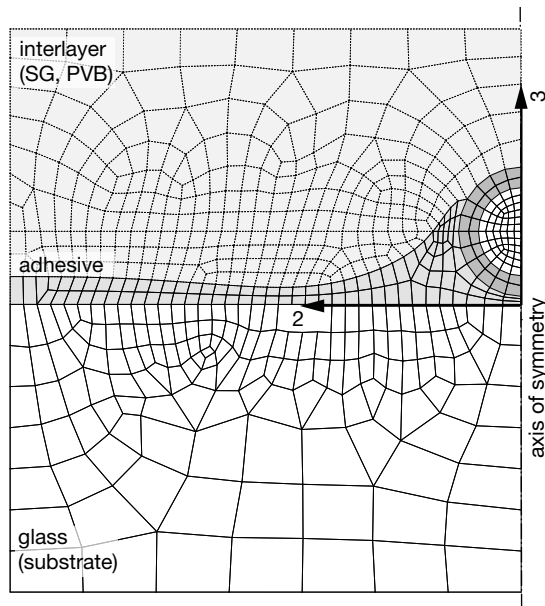


**Figure 5.45.:** Transverse section of the fibre bond zone mesh of the 3D micro-model.

The software applied is ANSYS vs. 13 and 14 with APDL scripts. The model is adapted to the conditions of the four-point bending tests performed in the previous section 5.1.5.2. The models have mesh element sizes of 5-10 $\mu$ m in the area of the fibre and the adhesive bond, fig. 5.45. In addition, the different stages of the cold bending and lamination process are simulated to examine the resulting strain states the fibre. Therefore, various material compositions, bond geometries and load

cases are considered. From the strain states, the wavelength shift  $\Delta\lambda$  in the sensor is determined and the gauge factors and their variation are calculated in comparison to the strain on the glass surface.

**5.1.6.1. Micro Model Setup**

Generally, the two different bond geometries A and B known from previous sections, fig. 5.46, are simulated in the micro model. All calculations are performed assuming linear-elastic or viscoelastic, isotropic material properties. Basically adapted to the DMA analyses in section 5.1.3, the shear modulus of the adhesive is fixed to either 10MPa or 570MPa, where 10MPa represents a low shear modulus e.g. at a temperature of 140°C during the autoclave process, whereas 570MPa is approximately the shear modulus for the adhesive Katiobond OB642 at room temperature.

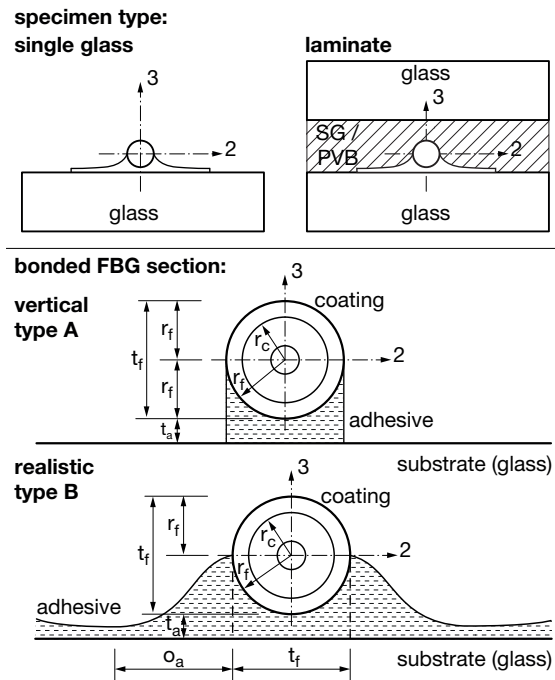


**Figure 5.46.:** Bond sections type A and type B.

Summarising, the simplified material property assumptions used in the models are:

- Adhesive:  $E_a=1,700\text{MPa}$ ,  $G_a=570\text{MPa}$ ,  $\nu=0.49$
- Fibre coating (Ormocer<sup>®</sup>):  $E_a=1,500\text{MPa}$ ,  $\nu=0.49$
- Silica fibre:  $E=73,000\text{MPa}$ ,  $\nu=0.16$
- Glass substrate:  $E_s=71,200\text{MPa}$ ,  $\nu=0.23$
- SG and PVB interlayer: modelled as in section 5.3

The geometry of the model is adapted to the measurement results documented in section 5.1.3.5. The related geometrical assumptions are:

- Glass thickness  $t_s=3.848\text{mm}$
- Bond thickness below the fibre  $t_a=0.012\text{mm}$
- Fibre cladding radius  $r_c=0.0625\text{mm}$
- Fibre coating radius  $r_f=0.09177\text{mm}$
- Bond section width:  $2o_a + 2r_f=1.5\text{mm}$  for bond type B and  $0.2\text{mm}$  for the bond type A.
- Total model dimensions: length= $30\text{mm}$ , width= $4\text{mm}$
- Model composition: either one glass layer with a surface-bonded fibre or a two-layered glass laminate with an SG or PVB interlayer of  $1.52\text{mm}$  thickness.

The model consists of SOLID185, 8-node volume elements. Enhanced strain formulation for reducing shear-locking effects is used. In critical zones, such as the adhesive layer below the fibre, three volume elements are applied through the section. Comparison with an identical model from 20-node volume elements SOLID186 has been made but the differences in the results between the two model types were found to be negligible; the analysis with 20-node elements is extremely time-consuming. The applied load cases as in fig. 5.47 are:

- Axial load: strain applied to the glass in longitudinal fibre direction (axis 1) corresponds to a normal strain of  $0.00054\text{mm/mm}$
- Bending: bending loads are adapted to the four-point bending tests performed in this work. Bending radii are  $3552\text{mm}$ , which corresponds to a surface strain of  $\pm 0.00054\text{mm/mm}$ . Bending of single glass plates and the entire cold bending /relaxation process are simulated.
- Transverse loads in direction 2 have been found exerting minor influence and are not shown here.
- Uniform temperature: heating or cooling by  $\pm 30^\circ\text{C}$

The gauge factors for each configuration and load case have been found being independent from the size of the applied load. Symmetry and support conditions are applied in the model as shown in fig. 5.47. The analysis is performed geometrically non-linearly. An overview of all model compositions is given in table 5.11.

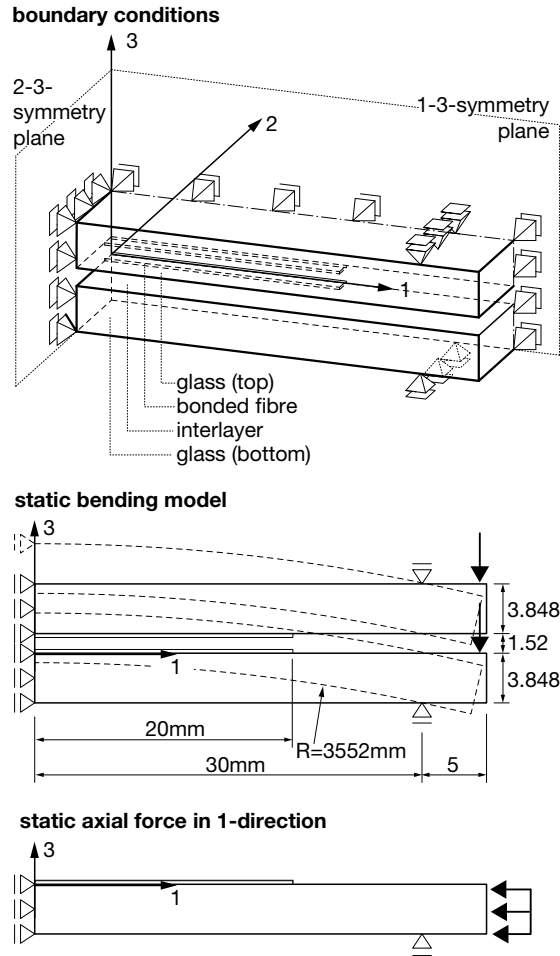


Figure 5.47.: Boundary conditions and load cases applied to the micro-model.

Therefore, the ratio of the strain actually determined in the core of the fibre  $\varepsilon_{i,f}, i = \{1 \dots 3\}$  and the surface strain  $\varepsilon_{i,s}, i = \{1 \dots 3\}$  of the substrate, extrapolated with eq. 5.62 to give the ideal full-transfer strain  $\varepsilon_{i,s,e}, i = \{1 \dots 3\}$  expected in the fibre, is calculated for bending loads. For thermal or axial loads, no bending extrapolation is necessary. The aim is to determine the gauge factors  $k_\varepsilon$  and  $k_T$  as defined in eq. 5.60. For mechanically induced bending strain, the first term of this equation

$$k_\varepsilon = \frac{\Delta\lambda(\varepsilon, T)}{\lambda_{B,0}} \frac{1}{\varepsilon_{1,s,e}} \quad (5.107)$$

applies and, for the temperature part, the second term

$$k_T = \frac{\Delta\lambda(\varepsilon, T)}{\lambda_{B,0}} \frac{1}{\Delta T} \quad (5.108)$$

can be used.

model						applied loads				
geometry			modeled system		glue	cold bending process			other loads	
glass layers	inter-layer	bond section	modeled fraction	boundary cond.	shear mod. G	bending (rot. about axis 2)	spring-back 0.01s	relaxation 3 months	axial (transl. in 1)	temperat. static uniform
			[-]	[-]	[MPa]	[mm/mm]	[mm/mm]	[mm/mm]	[mm/mm]	[°C]
1	-	type A vertical	1/4 syst.	sym.	10	0.00054	-	-	0.00054	-
		type B realistic	1/4 syst.	sym.	570	0.00054	-	-	0.00054	-
		PVB type B realistic	1/4 syst.	sym.	10	± 0.00054	-	-	0.00054	-
		SG type B realistic	1/4 syst.	sym.	570	0.00054	-	-	± 0.00054	-30
2	-	PVB type B realistic	1/4 syst.	sym.	10	-	-	-	-	-
		SG type B realistic	1/4 syst.	sym.	570	-	-	-	-	± 30
						± 0.00054	→ ±ε <sub>1</sub> *	→ ±ε <sub>1</sub> *	-	± 30

\* springback and relaxation analyses for a sensor subjected to compression and to tension

**Table 5.11.:** Summary of micro-mechanical models, boundary conditions and load cases.

Substituting the relative wavelength shift by eq. 5.58 and the extrapolated strain  $\varepsilon_{1,s,e}$  by eq. 5.62, the expressions for the gauge factors read

$$k_{\varepsilon} = \frac{1}{\varepsilon_{1,s} \left[ \frac{1}{r_{\varepsilon,s}} + \frac{(t_s + r_f + t_a) \left(1 - \frac{1}{r_{\varepsilon,s}}\right)}{t_s} \right]} \cdot \left[ \varepsilon_{1,f} \left(1 - \frac{n_0^2}{2} p_{12}\right) - \frac{n_0^2}{2} \left( \left( \frac{p_{11} + p_{12}}{2} \right) \cdot (\varepsilon_{2,f} + \varepsilon_{3,f}) \pm \left( \frac{p_{11} - p_{12}}{2} \right) (\varepsilon_2 - \varepsilon_3) \right) \right] \quad (5.109)$$

for mechanically-induced bending strain and

$$k_T = \frac{1}{\Delta T} \left[ \varepsilon_{1,f} \left(1 - \frac{n_0^2}{2} p_{12}\right) - \frac{n_0^2}{2} \left( \left( \frac{p_{11} + p_{12}}{2} \right) \cdot (\varepsilon_{2,f} + \varepsilon_{3,f}) \pm \left( \frac{p_{11} - p_{12}}{2} \right) (\varepsilon_{2,f} - \varepsilon_{3,f}) \right) + \Delta T \cdot \left( \alpha_n + (\alpha_s - \alpha_g) \left(1 - \frac{n_0^2}{2} (p_{12} - \nu(p_{11} + p_{12}))\right) \right) \right] \quad (5.110)$$

for temperature load. For the cases of purely axial load, no bending extrapolation is made for the glass surface stress and  $\varepsilon_{1,s}$  is used for axial loads instead of  $\varepsilon_{i,s}$ :

$$k_{\varepsilon,t} = \frac{1}{\varepsilon_{i,s}} \left[ \varepsilon_{1,f} \left(1 - \frac{n_0^2}{2} p_{12}\right) - \frac{n_0^2}{2} \left( \left( \frac{p_{11} + p_{12}}{2} \right) \cdot (\varepsilon_{2,f} + \varepsilon_{3,f}) \pm \left( \frac{p_{11} - p_{12}}{2} \right) (\varepsilon_2 - \varepsilon_3) \right) \right] \quad (5.111)$$

For evaluating all the gauge factors, a comparison

with the corresponding analytical values for a blank fibre is made.

Furthermore, the degree of birefringence can be determined and expressed through the variation of the gauge factors or directly through the wavelength shift variation. In the first case, the term

$$k_{\varepsilon} = \frac{1}{\varepsilon_{i,s,(e)}} \left( -\frac{n_0^2}{2} \right) \left[ \pm \left( \frac{p_{11} - p_{12}}{2} \right) (\varepsilon_2 - \varepsilon_3) \right] \quad (5.112)$$

delivers the variation of the gauge factor attributable to birefringence in the case of bending. To calculate the respective wavelength shift caused by the strain state in the fibre, eq. 5.58 can be used directly by permutation to  $\Delta\lambda$ . The Pockels coefficients  $p_{11}, p_{12}$  are set to 0.112 and 0.256 and  $n_0=1.454$ , as provided by the manufacturer of the fibre. The birefringence-caused wavelength peak separation calculated in this way corresponds to the analysis by using equation

$$\lambda_{B,2} - \lambda_{B,3} = \lambda_{B,0} \frac{n_0^2}{2} (p_{12} - p_{11}) (\varepsilon_2 - \varepsilon_3) \quad (5.113)$$

e.g. proposed by Helminger et al. [Hel 14], where  $\lambda_{B,2}$  and  $\lambda_{B,3}$  are the Bragg reflections from the two transverse axes of the fibre section.

For the analyses, a mean wavelength  $\lambda_{B,0}$  of 1550nm is assumed, where necessary. For temperature influence, the following values are used:  $\alpha_n=6.655 \cdot 10^{-6} 1/K$  (bare fibre, simple regression),  $\alpha_g=0.55 \cdot 10^{-6} 1/K$ ,  $\alpha_s=9.00 \cdot 10^{-6} 1/K$ . For simplification of the calculation of the gauge factors, the individual terms of the above equations are solved with these coefficients, basically following the example of Gabler [Gab 12, p. 78]:

$$\begin{aligned}
1 - \frac{n_0^2}{2} p_{12} &= 0.729393 \\
\frac{n_0^2}{2} \left( \frac{p_{11} + p_{12}}{2} \right) &= 0.194499 \\
\frac{n_0^2}{2} \left( \frac{p_{11} - p_{12}}{2} \right) &= -0.076108 \\
(\alpha_s - \alpha_g) \left( 1 - \frac{n_0^2}{2} (p_{12} - \nu(p_{11} + p_{12})) \right) + \alpha_n \\
&= 1.334 \cdot 10^{-5}
\end{aligned} \tag{5.114}$$

The temperature factor takes into account that the sensor is bonded to a soda-lime silica glass substrate. Calculation of the same factor for a free bare fibre gives a value of  $7.205 \cdot 10^{-6}$ .

With the gauge factors and birefringence values calculated by FEA, the influence of various loads, boundary conditions, FBG bond properties and laminate compositions on FBG measurements can be examined and evaluated with respect to the strain transfer conditions from the substrate into the core of the fibre. This also allows the verification of the applicability of eq. 5.60 for glass laminates; this is only possible, if the principal strain alignment of the fibre and substrate holds. If gauge factors determined by FEA are to be used to calculate the surface strain by FBG-measurement of a real glass laminate, a parallel verification by testing is necessary, see section 5.1.5.

The gauge factors calculated in this way can be compared with the typical factors given in the literature, e.g. Jülich et al. [Jül13, p.6], or with the gauge factor from a surface-bonded sensor as determined in this work,  $k_\varepsilon=0.7898 \approx 0.79$ . Birefringence effects are expressed by the variation of  $k_\varepsilon$  or by the deviation of the measured wavelength shift. The strain distribution along section 1-1, which follows the symmetry axis of the FE model shown in fig. 5.45, is used for analysing the related sensor measurements. Section 1-1 encompasses the two glass plates of the laminate and passes through the adhesive joint, the sensor coating and the centre of the silica fibre. The section is orthogonally oriented to the surfaces of the glass plate. The suitability of employment of principal strain values for the fibre sensitivity analyses was examined by verifying whether the shear strain components  $\tau_{ij}$  vanish.

### 5.1.6.2. Bending Load Application

Bending is applied to the model as described in the previous section 5.1.6.1. The principal strain components  $\varepsilon_{1,2,3}$  determined by FEA are substituted into eq. 5.109 to obtain the gauge factor and its variation attributable to birefringence (eq. 5.112).

The first models,  $f_t$ ,  $g_t$  and  $g_c$ , with a realistic adhesive joint section of the type B, serve to analyse the positive or negative strain caused by bending in a fibre bonded to a single glass pane with an adhesive having a shear modulus of either 10MPa or 570MPa. Figure D.1 in appendix D shows the distribution of the principal strain components along the section in the fibre core, the adjacent coating, the adhesive and the glass. The principal stress component  $\varepsilon_1$  can be seen to have a straight constant gradient along the section in the case of the stiffer adhesive. For the adhesive with a low  $G_a=10$ MPa, a decreased gradient of  $\varepsilon_1$  occurs in the adhesive bond and less strain transfer into the fibre is thus achieved. No differences in the strain distribution occur for a sensor subjected either to tension ( $g_t$ ) or to compression ( $g_c$ ). Division of the strains  $\varepsilon_2$  or  $\varepsilon_3$  by  $\varepsilon_1$  in both cases approximately yields the expected Poisson's coefficient of the fibre,  $\nu=0.16$ . In the coating and the adhesive bonding layers, the two components 2,3 are disturbed because of the discontinuity of the material stiffness of the compound formed by the fibre, coating, adhesive and the glass. The gauge factors  $k_\varepsilon=0.792$  calculated from the strain results with eq. 5.109 for the bond with the high adhesive shear modulus of 570MPa, fig. 5.48, are slightly bigger than  $k_\varepsilon=0.79$  derived from four-point bending tests in section 5.1.5. Minor birefringence effects in the order of less than 0.12% of the wavelength shift are caused by the bending, table 5.12. For a low adhesive shear modulus of 10MPa,  $k_\varepsilon=0.790$  becomes slightly smaller and no birefringence occurs.

For comparison with the analytical strain transfer method in section 5.1.2.2, analyses have also been carried out for the simplified type A bond geometry, fig. D.2 in appendix D. For  $G_a=10$ MPa, less strain transfer than with the type B bond section is achieved and the gauge factor  $k_\varepsilon=0.788$  becomes slightly smaller. For  $G_a=570$ MPa,  $k_\varepsilon=0.792$  is identical for both bond types A and B, fig. 5.48. Birefringence is close to zero for the vertical bond type A for small and large share moduli of the adhesive.

The study thus confirms the strong influence of the shear stiffness of the adhesive on the strain transfer pointed out previously in section 5.1.2.2.

Following the same method of principal strain interpretation as performed above, the entire cold bending, springback and relaxation process used to simulate the manufacturing and time-dependent behaviour of cold bent lamination-stabilised glass is examined with the FE micro-model. An adhesive shear modulus  $G_a=570\text{MPa}$  and realistic bond geometry of the type B as derived in section 5.1.3.5 are assumed and the sensors are subjected to either tension or compression from the cold bending process of the two glass panes. After the bending (models  $g_t$  or  $g_c$ ), the SG interlayer is activated and the springback at 0.01s upon release from the bending mould is analysed ( $h_t$  or  $h_c$ ). Relaxation of the laminate is examined after three months ( $i_t$  or  $i_c$ ). The material model as in section 5.3.2 is applied for the SG interlayer. Strain results are shown for the three steps in figures 5.49 below and D.3 in appendix D for the cases of tension and compression, respectively.

Regarding the strain transfer behaviour, no principal differences occur for the load cases with the fibre being subjected to tension or to compression. The strain component  $\epsilon_1$  reduces with time as a result of relaxation and the related loss of curvature. The gradient of  $\epsilon_1$  along the section in the glass and the fibre is constant for cold bending for the cold bent state in both models  $g_t, g_c$ . The related gauge factor in the cold bent state is  $k_\epsilon=0.792$ , fig. 5.48. In the springback and relaxation phases  $h_t, h_c$  and  $i_t, i_c$ , the gradient of the  $\epsilon_1$  strain distribution curve is larger along the section of the fibre than along the section of the glass. As a consequence, the ratio of the fibre strain to the glass surface strain rises and the gauge factor is increasing to 0.80 at the springback ( $h_t, h_c$ ) and to 0.81 after three months of relaxation ( $i_t, i_c$ ). The effects of birefringence decrease from initially 0.12% to 0.08% of the total wavelength shift  $\Delta\lambda$ , see table 5.12.

The strain components  $\epsilon_{2,3}$  along the section 1-1 are slightly different in all three phases  $g, h, i$ ; subsequently, the  $\nu$  calculated for the isotropic fibre varies between 0.158 and 0.165. The difference between  $\epsilon_{2,3}$  reduces during the three months of relaxation.

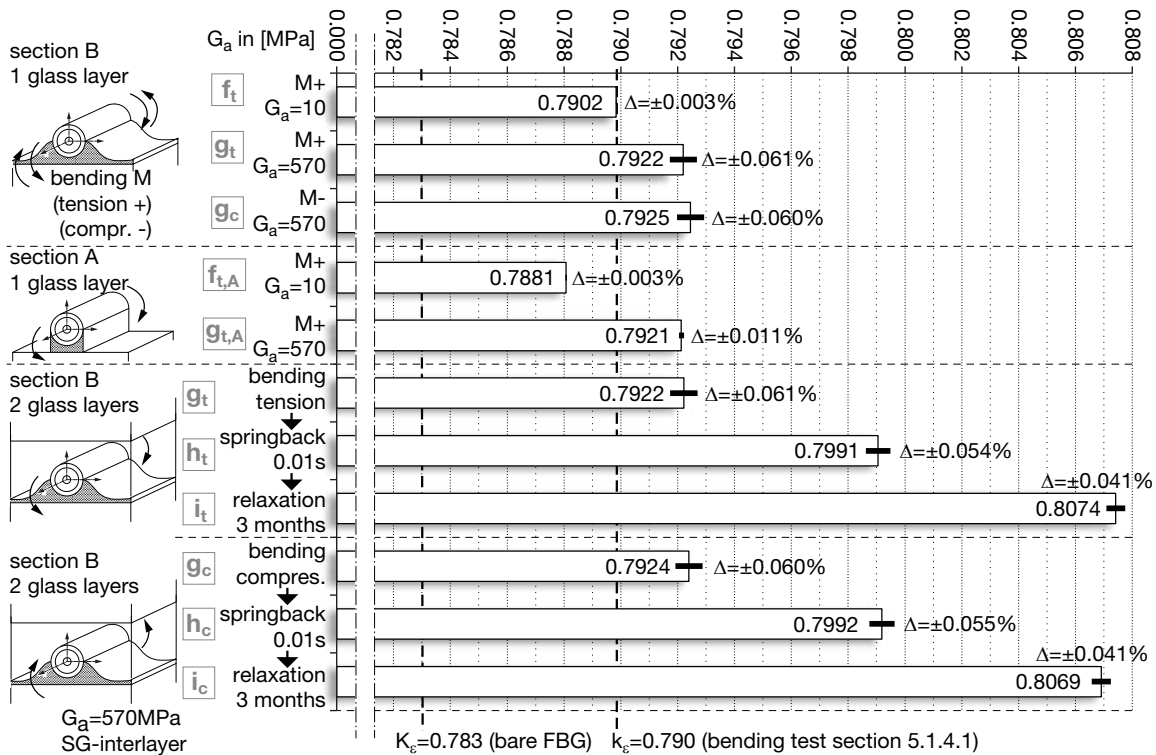
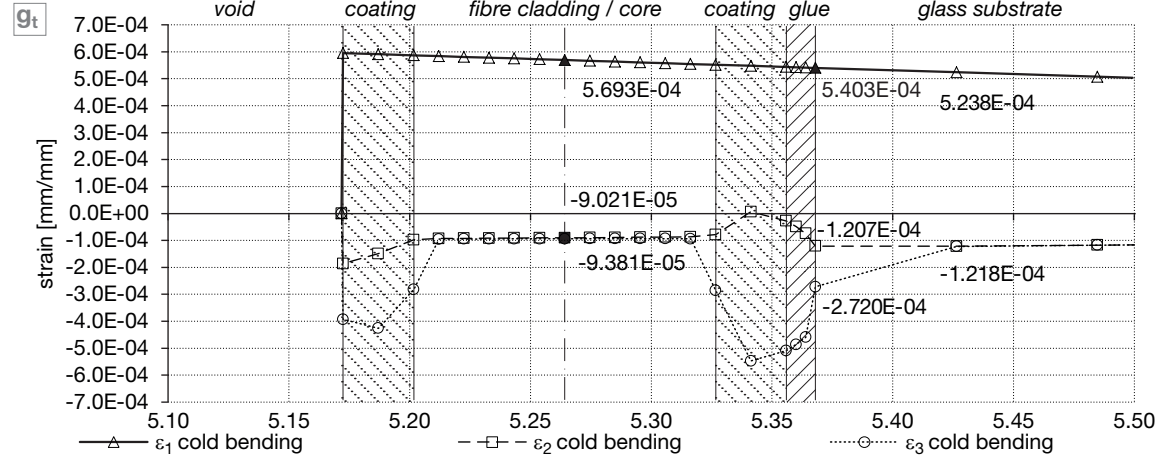


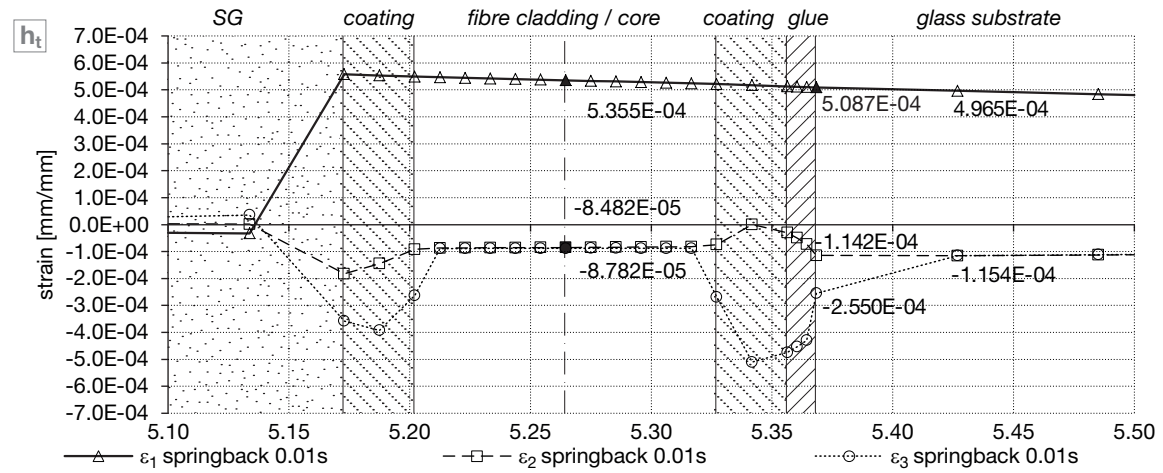
Figure 5.48.: Comparison of the  $k_\epsilon$  gauge factors and birefringence effects for bending.

section B, SG laminate, bending (tension) - springback - relaxation

bending / tension,  $G_a=570\text{MPa}$  (two separate glass layers)



springback 0.01s,  $G_a=570\text{MPa}$  (laminated)



relaxation 3 months,  $G_a=570\text{MPa}$  (laminated)

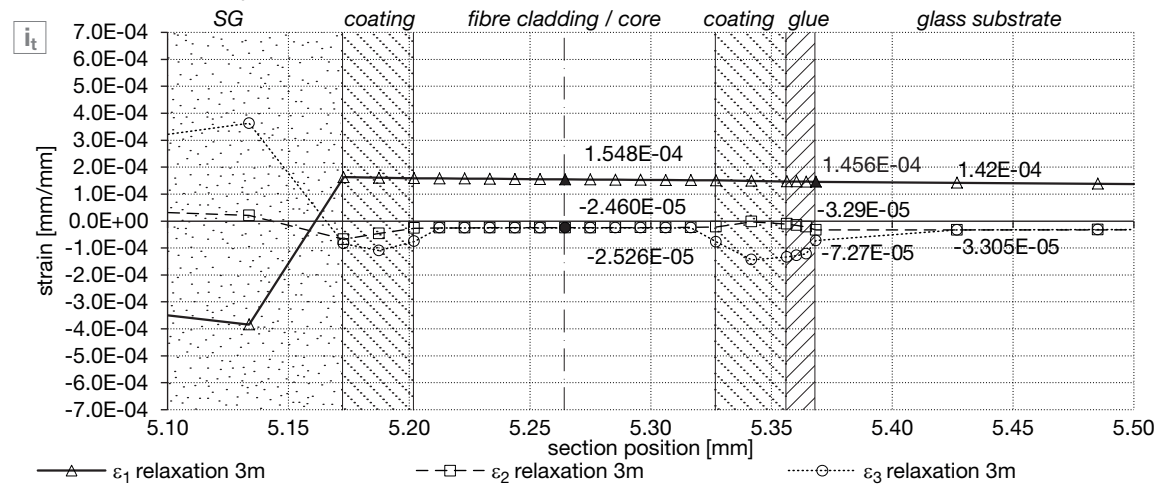


Figure 5.49.: Principal strain distribution from tensile bending loads along section 1-1 for a two-ply glass laminate in cold bent (top), initial springback after 0.01s (centre) and relaxation state after 3 months (bottom).



5.1.6.3. Axial Load Application

Axial strain in the order of 0.00054mm/mm is generated in single glass panes equipped with an FBG sensor bonded with an adhesive having a high shear stiffness  $G_a=570\text{MPa}$  (models  $c_t$ ,  $c_c$ ) or a low  $G_a=10\text{MPa}$  (model  $b_t$ ). The strain orientation corresponds to the fibre axis direction 1. The principal strain components induced in the fibre attributable to the tensile or compressive strain of the glass substrate is shown in figure D.4 in appendix D. For the adhesive bond section type B, the components  $\epsilon_{2,3}$  vary in the coating and adhesive zone but become constant across the section of the fibre core. A Poisson's coefficient in the order of  $\nu=0.16$  can be correctly determined for the fibre from the three strain components. As previously,  $\epsilon_{2,3}$  show slight differences in the case of a fibre bonded with the stiff adhesive  $G_a=570\text{MPa}$ , fig.

D.4. The gauge factor for the model  $b_t$  with a low adhesive stiffness  $G_a=10\text{MPa}$  is 0.79 and increases to  $k_\epsilon=0.792$  for the high adhesive shear modulus  $G_a=570\text{MPa}$  in the models  $c_t$ ,  $c_c$ , see fig. 5.50. The axial strain  $\epsilon_1$  in the fibre core corresponds exactly to the strain in the glass for the large adhesive shear modulus, whereas  $\epsilon_1$  reduces in the case of a fibre bonded with an adhesive having a small shear modulus  $G_a=10\text{MPa}$ . The deviation of the wavelength shift attributable to birefringence is zero for  $G_a=10\text{MPa}$  and augments to 0.09% for  $G_a=570\text{MPa}$ .

For the simplified bond section type A, the gauge factor obtained for small adhesive shear modulus is 0.788 and is 0.792 for a large modulus, fig. 5.50. Practically no birefringence effects occur in both cases.

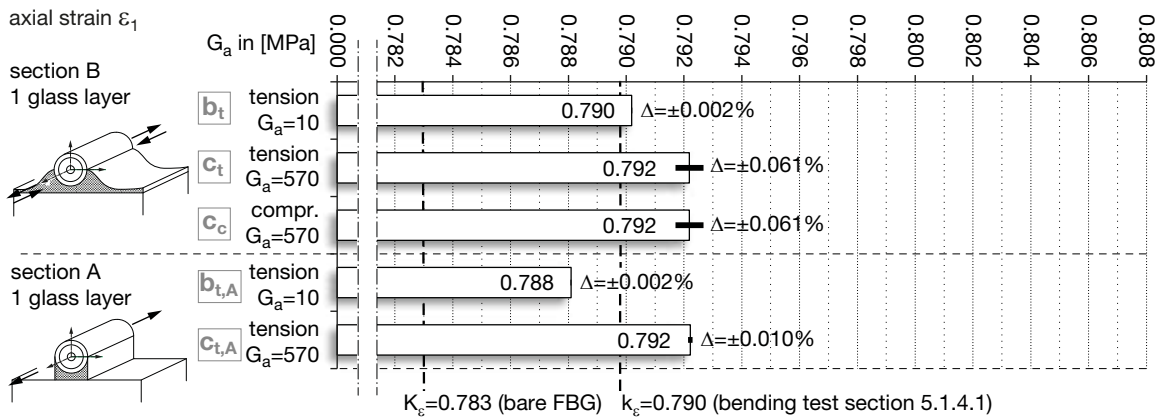


Figure 5.50.: Comparison of the  $k_\epsilon$  gauge factors and birefringence effects for axial load in 1-direction.

5.1.6.4. Thermal Load Application

In all thermal models, the residual axial strain in the fibre is significant. It is caused by the differential thermal expansion of the surrounding materials and the fibre itself, in particular the coating and the adhesive. Fig. D.5 in appendix D<sup>27</sup> reveals, that the laminates with different interlayers from PVB or SG (models  $q$ ,  $r$ ) and the surface-bonded fibre on a single glass plate (model  $p$ ) exhibit practically the same axial fibre strain  $\epsilon_1$ . Thus, the influence of the interlayer on the axial strain of the fibre is assumed to be small.

The effect of the coating and of the adhesive bond to the glass substrate and the related different thermal expansion coefficients are decisive for the build-up of residual strain in the fibre. However,

the chosen model approach is theoretical, as it does not account for the temperature-dependent non-linear material behaviour of the interlayer, the coating and the adhesive and assumes a uniform temperature in the specimen. The thermal gauge factors  $k_T$  of all models ( $p_{-}$ ,  $q_{\pm}$ ,  $r_{\pm}$ ) are in the range of  $2 \cdot 10^{-5} 1/K$ , fig. 5.51, which corresponds to an approximately 0.03nm wavelength shift per K temperature change. Birefringence effects, related to the proportionality factors, are about  $\pm 0.0004 \text{nm/K}$  for the PVB laminate and increase to  $\pm 0.0009 \text{nm/K}$  for the SG interlayer. A uniform temperature change in the laminate thus affects the fibre strain to a higher degree as calculated analytically for a bare fibre perfectly bonded to glass, where  $k_T = 1.33 \cdot 10^{-5}$ , corresponding to a wavelength shift of 0.021nm/K.

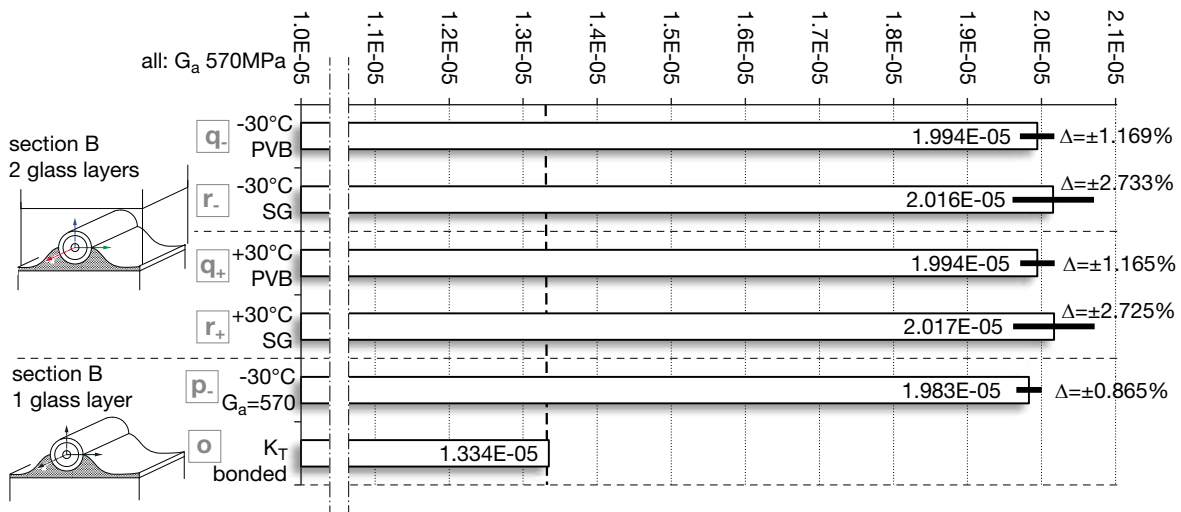


Figure 5.51.: Comparison of the  $k_T$  factors and birefringence effects for uniform thermal load.

<sup>27</sup>The strain distribution shows the residual mechanical strain only.



### 5.1.6.5. Summary

Regarding the fibre, the difference of bending and axial load cases can be concluded to be extremely small for all numerical cases studied in this work in which bending radii are always  $>3.00\text{m}$ . However, if the adhesive bond thickness below the fibre and / or the bending curvature increase, this hypothesis is assumed to result in an increasing error. Notably, however, the bending analysis results are corrected with respect to their distance from the surface of the substrate, see eq. 5.61. Generally, bonded FBG subjected to tension or compression show an identical behaviour with respect to  $k_\epsilon$  in the models and thus, share identical gauge factors.

All gauge factors  $k_\epsilon$  for bonded fibres with coating determined by tests and the FE micro-models in this work exceed the given value  $k_\epsilon=0.783$  of a bare, free fibre [Jül 13]. The gauge factors  $k_\epsilon$  for uniaxial bending and for loads in the direction of the fibre axis are in a range of 0.790 to 0.792. This corresponds approximately with the  $k_\epsilon = 0.790$  determined by the four-point bending test as in section 5.1.4.1. During the springback / relaxation of a cold bent lamination-stabilised glass,  $k_\epsilon$  increases to 0.81; this indicates an increased ratio of the fibre strain and the surface strain of the glass attributable to the influence of the interlayer. The difference between the gauge factors 0.792 for the cold bent state and 0.81 for the relaxed state corresponds to less than 1MPa stress calculated from the typical wavelength shift measurement of about 0.7nm ( $\approx 40\text{MPa}$ ) from cold bending.

An increase in the shear modulus  $G_a$  of the adhesive results in an increasing gauge factor and rising birefringence effects. An FBG bonded by means of an adhesive joint with an overhang (type B) is subjected to stronger birefringence effects and exhibits larger differences between  $\epsilon_2$  and  $\epsilon_3$

than an FBG bonded without overhang (type A). Thus, the adhesive bond geometry affects the triaxial strain state in the fibre, particularly with respect to transverse strain.

For all bending cases, birefringence effects  $\pm\Delta k_\epsilon$  are extremely small and account for less than  $\pm 0.06\%$  variation of  $k_\epsilon$ , which causes a maximum deviation of the measured wavelength shift by 0.12%, as can be seen in table 5.12. Laminate relaxation of cold bent glass leads to a decrease in birefringence. As a result, the hypothesis of negligible birefringence influence throughout the cold bending and the lamination and in the springback and relaxation processes is supported by the FE model.

For the theoretical assumption of a homogeneous thermal load acting in the entire laminate,  $k_T \approx 2 \cdot 10^{-5}$  has been determined in the FE analyses. The difference with regard to the theoretical value of a bare fibre ideally bonded to a glass surface  $k_T = 1.33 \cdot 10^{-5}$  can be explained by the influence of the coating and the adhesive, which have significantly higher thermal expansion coefficients than the fibre and the glass substrate. The influence of the interlayer in the present models is small. Thermal loads can cause non-negligible birefringence effects in the fibre.

In section 7.1, the behaviour of a fibre bonded to glass and laminated afterwards is examined in a transient temperature load finite element model. This model serves to identify the effects of the cooling of the laminate on the build-up of residual stress in the fibre. The variable material properties of the coating, the adhesive and the interlayer are included in the mentioned studies. A summary of the gauge factors and birefringence effects for the principle models is given in table 5.12.

		gauge factors						wavelength shift		
	no. load case	layers	$G_a$ [MPa]	inter-layer	$\emptyset k_{e,T}^*$ [-]	$\emptyset \zeta$ [-]	$\pm \Delta k_{e,T}$ biref. [%]	$\pm \Delta k_{e,T} / k_{e,T}$ [%]	$\Delta \lambda$ [nm]	$\Delta(\Delta \lambda)$ [nm]
FEM	test <b>a</b>	axial load, free fibre [Jül 13]	-	-	<b>0.783</b>	<b>1.000</b>	n.s.	-	-	-
	<b>b<sub>t,c</sub></b>	axial 1-direction	1 (glass)	10	-	0.790	1.009	0.00002	<b>0.002</b>	0.662 0.0000
	<b>c<sub>t,c</sub></b>			570	-	0.792	1.012	0.00048	<b>0.061</b>	0.664 0.0006
test	<b>d</b>	4-pt.-bending test [Jül 13]	1 alumin.	n.s.	-	0.778	0.994	n.s.	-	-
	<b>e</b>	4-pt.-bending test [this work]	1 (glass)	570	-	0.790	1.008	n.s.	-	-
	<b>f<sub>t</sub></b>	cold bending	1 (glass)	10	-	0.790	1.009	0.00002	<b>0.003</b>	0.698 0.0000
FEM	<b>g<sub>t,c</sub></b>			570	-	0.792	1.011	0.00048	<b>0.061</b>	0.700 0.0008
	<b>h<sub>t,c</sub></b>	cold bend. springback 0.01s	2 (glass)	570	SG	0.799	1.021	0.00044	<b>0.055</b>	0.658 0.0007
	<b>i<sub>t,c</sub></b>	cold bend. relax. 3 months	laminate	570	SG	0.807	1.030	0.00033	<b>0.041</b>	0.191 0.0002
theory	<b>n</b>	free fibre uniform temp., $\alpha_n + \alpha_g$	-	-	-	7.205E-06	-	-	-	-
	<b>o</b>	bonded fibre unif. temp. **	1 (glass)	-	-	1.334E-05	-	-	-	-
FEM	<b>p.</b>	$\Delta T = -30^\circ\text{C}$ cooling	1 (glass)	570	-	1.983E-05	-	5.495E-07	<b>2.771</b>	0.922 0.0159
	<b>q<sub>t</sub></b>	$\Delta T = \pm 30^\circ\text{C}$ heating / cooling	2 (glass)	570	PVB	1.994E-05	-	2.327E-07	<b>1.167</b>	0.927 0.0216
	<b>r<sub>t</sub></b>		laminate	570	SG	2.016E-05	-	5.502E-07	<b>2.729</b>	0.937 0.0512

\* related to a mean Bragg wavelength of  $\lambda_{B,0} = 1550\text{nm}$

\*\*  $(\alpha_s - \alpha_g) [1 - \rho_0^2 / 2 (\rho_{12}^{-1} (\rho_{11} + \rho_{12}))] + \alpha_n$

**Table 5.12.:** Summary of the gauge factors and birefringence effects from the micro-mechanical model.

## 5.2. Close Range Photogrammetry Principle

Photogrammetry comprises passive contactless remote sensing measurement and analysis methods for determining 3D shape data or location data of an object from photographs depicting the object of interest. For the derivation of 3D data from 2D photographic depictions, the camera device and the process involved in the creation of the picture have to be known in addition to access to the photograph. Photogrammetry 3D reconstruction of transparent objects, such as is necessary for this work, is particularly difficult because of the transparency of the glass specimens. The above-mentioned data have to be interpreted and measured with respect to the corresponding image and object points. The mathematical transformation “[...] between image and object space [...]” [Luh 14, p. 3] then allows the modelling of the object of interest. Various photogrammetry categories exist, of which offline (non real-time) close range photogrammetry (photographic distance <300m) and multi-image photogrammetry with more than two photographs for engineering purposes [Luh 14, p. 6] are the techniques applied in this work.

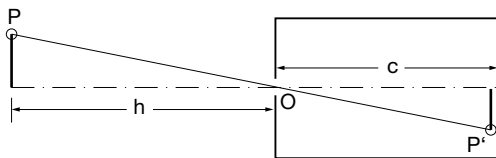


**Figure 5.52.:** Schematic depiction of the pinhole camera principle.

3D measurement with photogrammetry is mathematically and geometrically based on central projection. As described by Luhmann [Luh 14, p. 7], the shape “[...] and position of an object are determined by reconstructing bundles of rays in which, for each camera, each image point  $P'$ , together with the corresponding perspective centre  $O'$ , defines the spatial direction of the ray to the corresponding object point  $P'$ .” A point of the object of interest can be determined spatially if a minimum of two corresponding image rays, which are separated in space, intersect. The internal geometric parameters of the camera are specified by the *interior orientation*.

A pinhole camera model, fig. 5.52, can be used to describe the principal parameters of the interior orientation; these are central perspective centre  $O$ , the projection  $P'$  of the object point  $P$  to the image plane in the camera, the object distance  $h$  and the distance  $c$  between the image plane and  $O$ . The interior orientation describes the position of  $O$  relative to the image coordinate system.

The image coordinate system has only two dimensions with the coordinates  $x', y'$ . Addition of a  $z'$  axis orthogonal to the image plane establishes the local camera coordinate system with its origin in the perspective centre  $O'$  of the photo. The view orientation and position of a camera in space, expressed by the local camera coordinate system<sup>28</sup>, is defined relative to the global object coordinate system with the axes  $X, Y, Z$  by the six parameters of the *exterior orientation*. These are the coordinates of the perspective centre in global coordinates and the rotation angles of the image coordinate system relative to the global coordinate system. The exterior orientation is determined only after measurement of sufficient image coordinates of object points in the photogrammetry process. A vector  $X_0$ , extending from the origin of the global coordinate system towards the perspective centre  $O'$  at  $X_0, Y_0, Z_0$ , determines the location of the image coordinate system in space. The spatial angular orientation is given by a 3x3 rotation matrix  $R$ , which comprises three rotations  $\omega, \phi, \kappa$  about the global coordinate axes  $X, Y, Z$ , see [Luh 14, pp. 258-259]. The nine entries of the matrix  $R$  are named  $r_{ij}; i, j = \{1 \dots 3\}$ . The following equation defines the projection of an image point on the photo into the respective object point [Luh 14, p. 260]

$$\begin{bmatrix} X \\ Y \\ Z \end{bmatrix} = \begin{bmatrix} X_0 \\ Y_0 \\ Z_0 \end{bmatrix} + m \begin{bmatrix} r_{11} & r_{12} & r_{13} \\ r_{21} & r_{22} & r_{23} \\ r_{31} & r_{32} & r_{33} \end{bmatrix} \begin{bmatrix} x' \\ y' \\ z' \end{bmatrix} \quad (5.115)$$

where the scale factor  $m$  is different for each object / image point and  $x', y'$  are the entries of the image vector with  $z' = -c$ .

<sup>28</sup>The origin of the local camera coordinate system is situated at the perspective centre of the photograph

“Every measured image point corresponds to a spatial direction from projection centre to object point. The length of the direction vector is initially unknown [...]. The object point can be located on the image ray, and thereby absolutely determined in object space, only by intersecting the ray with an additional known geometric element such as a second spatial direction or an object plane.” [Luh 14, pp. 8-9]. Intersection of bundles of such rays from several photographs and the performance of bundle triangulation [Luh 14, p. 9] allows the orientation and determination of the respective object points in space. So-called *additional observations*, e.g. scale bars or fix points determined with other measurement methods, are used in photogrammetry to relate and scale the calculated 3D object point to absolute geometric units. In this thesis, an Aicon carbon fibre scale bar with two points distanced by 539.36mm was used for this purpose.

the object are identified and numbered. By starting from an initial approximation of the point data by the resection of all images, bundle adjustments are performed in which the interior and exterior orientation and the point coordinates are iteratively calculated and an optimisation / error reduction is undertaken during the process. From the bundle results, object point coordinates can be analysed and used further, for example, as data tables, for graphical representation or 3D modelling. In multi-image acquisition, which is the photogrammetric configuration used here, the coordinates of the object of interest are calculated via multi-image triangulation and then typically through bundle adjustment. Therefore, a minimum of two photographs taken from various positions must show every object point. In order to obtain uniform accuracy for all measurement points, at least 3 photographs are recommended by Luhmann [Luh 14, p. 138].

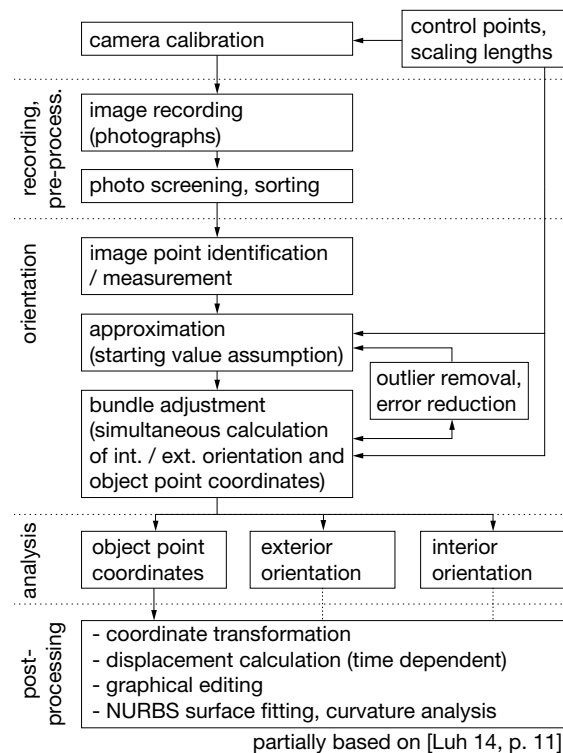


**Figure 5.53.:** Schematic process diagram of photogrammetry analysis.

The general procedure of photogrammetry application is shown in fig. 5.53. After calibration of the camera with respect to its interior orientation, pictures of the object of interest are taken. These images are imported into photogrammetry software in which the target points / object points of

Photogrammetry image and object point recognition can be made either by pattern recognition or by artificial target marks applied to the object. In the case of the nine 2.40m x 0.80m glass laminate test samples in the context of this work, pattern recognition was not possible because of the transparency of the specimens and the application of a black and white random speckle pattern coating or projection to the curved glass also was not feasible. Thus, an array of circular black numbered points as in fig. E.1 in section 6.1.3 was applied to the glass. This method allows semi-automated point recognition by the photogrammetry software. Moreover, identical object points measured at various monitoring time steps can be directly compared in order to calculate the displacement with time and accuracy can be improved [Luh 14, p. 221]. Luhmann [Luh 14, p. 225] reports at least 5 pixels as a minimum diameter for the target points on digital photographs; a minimum of 9-10 pixels is recommended for better precision.

Collinearity equations [Luh 14, p. 261] are the fundamental expressions in photogrammetry. They “[...] effectively describe image generation inside a camera by the geometry of a central projection.” [Luh 14, p. 262]. The object coordinates  $X, Y, Z$  are transformed into the respective image coordinates  $x', y'$  under the assumption of central projection and as “[...] functions of the interior orientation parameters ( $x'_0, y'_0, c, \Delta x', \Delta y'$ ) and exterior orientation parameters ( $X_0, Y_0, Z_0, \omega, \varphi, \kappa$ ) of one image.” [Luh 14, p. 261]:

$$\begin{aligned} x' &= x'_0 + z' \frac{r_{11}(X-X_0) + r_{21}(Y-Y_0) + r_{31}(Z-Z_0)}{r_{13}(X-X_0) + r_{23}(Y-Y_0) + r_{33}(Z-Z_0)} + \Delta x' \\ y' &= y'_0 + z' \frac{r_{12}(X-X_0) + r_{22}(Y-Y_0) + r_{32}(Z-Z_0)}{r_{13}(X-X_0) + r_{23}(Y-Y_0) + r_{33}(Z-Z_0)} + \Delta y' \end{aligned} \quad (5.116)$$

In these equations,  $c$  is the principal distance of the perspective centre from the image plane, which approximately corresponds to the focal length of the lens and  $\omega, \varphi, \kappa$  designate three rotations about the coordinate axes  $X, Y, Z$  independently from each other and serve to build the rotation matrix defining the angular orientation of the image coordinate system. The parameters  $r_{ij}$  form the 3x3 rotation matrix  $R$  defining the spatial angular orientation.

Error estimation is an important issue in every photogrammetric measurement. The possible precision, accuracy and trueness of measurement<sup>29</sup> that can be attained with photogrammetric procedures largely depend on the applied camera, the photographic quality and the object of interest. Luhmann [Luh 14, p. 562] mentions a possible best measurement accuracy of  $10\mu\text{m}$ . In the photogrammetric work undertaken for this thesis, no accuracy or trueness information could be gained for the glass specimen because of a lack in other applicable measurement technology for comparison. Laser-scanning by application of reflective label points and matt-finish contrast surface spray on the glass proved technically unsuccessful. Thus, only relative error estimation in the sense of measurement precision is applied based on the photogrammetric software calculations. “Measurement precision

is usually expressed numerically by measures of imprecision, such as standard deviation, variance, or coefficient of variation under the specified conditions of measurement.” [JCG 12, p. 22].

For the processing of the photographs, the camera data and camera calibration, for the establishment of the interior / exterior orientation and the bundle adjustment and for the determination of the 3D coordinates of the numbered points, the close-range photogrammetry software Australis was used at the IFP / University of Stuttgart. The software allows off-line photogrammetry processing of images and data from digital reflex cameras. The deviations of the adjustment results are given as root mean square errors (RMS), which are the square root of the sum of the squares of  $n$  given values. These given values are typically differences between measured  $X_i$  and nominal  $\bar{X}$  values [Luh 14, p. 93]:

$$RMS = \sqrt{\frac{\sum_{i=1}^n (X_i - \bar{X})^2}{n}} \quad (5.117)$$

The standard deviation and RMS of object and image coordinates or the camera parameters are calculated in Australis and the RMS of the 2D image coordinates referring to the rear projection is given in [ $\mu\text{m}$ ]. As a rule of thumb, the RMS of the image coordinates has to be equal or smaller than the 1/10 pixel size of the applied camera to obtain good quality and high precision. The camera data from all calibrations made for this thesis can be seen in table E.1 in appendix E.1. The above criterion is approximately met with all cameras except the EOS50D, which reaches only an RMS of 1/5 to 1/4 of the pixel size in some cases. This can be explained by the instability of the lens of this camera. In the bundle adjustment, standard errors from the six parameters of the exterior orientation are calculated. For all target points in various overlapping photographs, standard errors from limiting errors and total error propagation are calculated and three total RMS values are summarised for the 3D-object space coordinates  $X, Y, Z$  that are used in this thesis to estimate the relative quality of the object coordinate measurement.

<sup>29</sup>Accuracy is the “closeness of agreement between a measured quantity value and a true quantity value of a measurand” [JCG 12, p. 21], whereas *measurement precision* means the “closeness of agreement between indications or measured quantity values obtained by replicate measurements on the same or similar objects under specified conditions” [JCG 12, p. 22]. The *measurement trueness* is the “closeness of agreement between the average of an infinite number of replicate measured quantity values and a reference quantity value” [JCG 12, p. 21].

## 5 | ANALYSIS, DIAGNOSTIC

A bundle adjustment is shown in fig. 5.54.

	X	Y	Z	RMS	#	Sightings			
2456	0.1320	0.1118	0.0863	0.2363	0.1632	0.1459	1.5	5	YNNYYYYYNNNNNN
2457	0.1373	0.1029	0.0855	0.2466	0.1334	0.1327	1.7	6	YYNNYYYYNNNNNN
2458	0.1762	0.0932	0.0954	0.2926	0.1249	0.1411	1.4	6	YYNNYYYYNNNNNN
2459	0.2670	0.1069	0.1334	0.3627	0.1418	0.1714	1.4	5	YYNNYYYYNNNNNN
2460	0.3573	0.0922	0.1486	0.4501	0.1376	0.1920	2.1	4	YYNNYYYYNNNNNN
2861	0.1867	0.7848	0.5210	0.2133	0.8511	0.5731	1.2	3	NNNNNNNNYYNYNY
2862	0.0640	0.4410	0.3723	0.0864	0.4846	0.4103	1.2	4	NNNNNNNNYYNYNY
2863	0.0958	0.3168	0.3094	0.1204	0.3561	0.3526	0.7	4	NNNNNNNNYYNYNY
2864	0.1109	0.1467	0.1854	0.1505	0.1873	0.2501	1.6	5	NNNNNNNNYYNYNY
2865	0.1484	0.1143	0.1753	0.2044	0.1506	0.2570	1.6	5	NNNNNNNNYYNYNY
2866	0.0675	0.0567	0.0679	0.1177	0.0917	0.1100	1.1	5	NNNNNNNNYYNYNY
2871	0.3421	0.0800	0.2815	0.4129	0.1154	0.3254	1.2	4	YYNNYYYYNNNNNN
2872	0.1954	0.0791	0.2144	0.2530	0.1028	0.2484	1.1	5	YYNNYYYYNNNNNN
2873	0.0909	0.0558	0.1170	0.1521	0.0791	0.1656	1.7	8	YYNYNYNYNNNNNN
2874	0.0774	0.0589	0.1067	0.1118	0.0784	0.1460	1.5	7	YYNYNYNYNNNNNN
2875	0.0956	0.0721	0.1312	0.1140	0.1007	0.1684	1.1	5	YYNYNYNYNNNNNN
2876	0.0608	0.0719	0.1047	0.0806	0.1249	0.1628	1.7	5	YYNYNYNYNNNNNN

	Summary of Limiting STD Error Estimates	Summary of Total STD Error Estimates
RMS is at point	X, Y, Z	X, Y, Z
Minimum is at point	0.1448, 0.1755, 0.1585	0.1960, 0.2181, 0.2037
Maximum is at point	0.3573, 0.7848, 0.5210	0.4501, 0.8511, 0.5731

Label	X	Y	Z	RMS	#	Sightings
1011	-7124.5563	2000.1526	-1045.0611	2.5	2	11111111112222222222
1012	-6860.3391	2701.6090	-990.0832	2.5	4	123456789012345678901234567890
1013	-6600.9985	3405.4120	-955.4131	0.0	0	NNNNYYYYNNNNNN
1014	-6344.5471	4103.5612	-917.5886	0.0	0	YY*NNN*YY*NNNNNN
1021	-7113.9026	1932.9048	-288.9254	1.8	2	*NNNNNNYYNNNNNN
1022	-6849.1461	2653.3559	-240.2675	1.8	2	N*NNNN*YYNNNNNN
1023	-6588.9889	3354.7886	-197.6758	0.0	0	NN*NNNN*NNNNNN
1319	-6227.0291	873.6707	-1135.3340	1.7	4	NNNNNNNNNY*YNY
1324	-2712.2445	-441.8951	-537.0521	1.9	2	NNNNNNNNNYNYNY
1325	-3415.1586	-187.0937	-510.0979	2.0	3	NNNNNNNNNYNNYNY
1326	-4116.1016	66.5345	-485.0348	1.8	2	NNNNNNNNNYNNNYN
1327	-4752.0804	294.3786	-459.6548	1.0	2	NNNNNNNNNYNNNYN
1328	-5523.8873	575.7503	-436.3195	1.1	3	NYNNNNNN*NNYNYN
1329	-6214.8834	824.9267	-404.9102	1.8	4	NYNNNNNNNYNYNYN
1338	-5519.5218	518.0192	-323.2733	0.0	0	N*NNNNNNNNNN*NN
1339	-6201.4635	767.0734	-357.8140	0.0	0	NN*NNNNNNNNNN*NN
1466	-3932.0265	2198.1906	-1327.2347	1.6	2	NN*YNNNNNNNNNNNN

Figure 5.54.: Exemplary bundle adjustment result output of the software Australis.

The relative precision of measurement, expressed through the total RMS values of the standard deviation of the object coordinates calculated by the software, in this thesis shows an RMS of 0.03mm to 0.04mm for measurement with three synchronised cameras (three photographs) and of 0.1mm to 0.34mm for single cameras with a fixed focal length objective (14-24 photographs) of the glass object from various locations. The RMS error values depending on the applied camera and monitoring phase are given in table 6.2 in section 6.1.3.

For the production of images suited for photogrammetry, metric cameras or semi-metric cameras can be used. Metric cameras are optically and mechanically stable [Luh 14, p. 149] and do not need new interior orientation parameter calibration every time that they are used. In the context of this thesis, such cameras were not available and thus digital reflex cameras were applied. Recalibration of these cameras was often necessary as their interior orientation parameters were not constant over a long period of time. The cameras used were: Canon EOS7D, 40D, 50D and Nikon D2X, D80, D5000. The first three cameras (Canon) were employed simultaneously for taking synchronised photographs during the initial springback of the glass laminates. For the long-term monitoring with multiple photographs, a single camera with a fixed lens (20mm) was applied. A comparison of all camera calibrations can be seen in fig. E.1 in appendix E.1.

For the point clouds obtained from photogrammetry, coordinate transformation with a homogeneous transformation matrix was performed to establish an identical coordinate system for all monitoring time steps per specimen, see section 6.1.3. Based on this, the relative change of the point coordinates with time attributable to relaxation was calculated. The results were then compared with corresponding finite element displacement analyses and NURBS surfaces were created by least-square approximation from the 3D point clouds of each monitoring time step for glass curvature and smoothness analysis.

### 5.3. Material Models for Numerical Simulation

#### 5.3.1. Glass Laminates

Glass laminates are assembled from flat glass panes adhesively connected by polymer interlayers. Glass is characterised as “[...] an inorganic product of fusion, which has been cooled to a rigid condition without crystallization.” Glass does not “[...] consist of a geometrically regular network of crystals, but of an irregular network of silicon and oxygen atoms with alkaline parts in between [...]” [Hal 08, p. 4]. The typical glass product used in building is soda-lime silica glass, which is mainly made from about 69-74% of silica sand  $\text{SiO}_2$ , 5-14% calcium oxide  $\text{CaO}$  and 10-16% soda  $\text{Na}_2\text{O}$  [Wel 10, p. 17]. Glass is a viscous substance but with an extremely high viscosity of about  $10^{20}$  dPa s at ambient temperature [Hal 08, pp. 6-7]. The flow of glass is thus neglected for construction purposes and glass is considered an elastic isotropic material and exhibits brittle behaviour without a plastic zone prior to failure. This lack of ductility limits pure glass application in construction. To overcome this and to add ductility to glass elements, it is often laminated by means of an interlayer, which should keep any broken glass pieces together because of its flexibility and its adhesion to the glass. Soda-lime silica glass is usually assumed to have a density of  $2500\text{kg/m}^3$ , a Poisson’s ratio of  $\nu=0.20$  to  $0.23$  and a Young’s modulus of  $70,000\text{MPa}$ . The last-mentioned value, however, can vary depending on the exact chemical composition and on temperature, as shown, for example, by Sackmann [Sac 08, pp. 75-77]. Glass could also be subjected to temperature-dependent creep under long-term loading [Wör 06], but this can be considered negligible in the context of this work. For cold bending, which causes permanent compressive and tensile stress in the bent glass, heat strengthened or fully toughened glass is typically used to allow for sufficient curvature and to retain a reserve for additional loads. Chemically strengthened glass is theoretically applicable, but no publications have been found referring to this topic.

Typical polymer interlayer products used in building construction are [Sie 12b, pp. 66-73] the commonly used, thermoplastic polyvinyl butyral (PVB), the thermoplastic elastomer ethylene vinyl acetate (EVA), thermoplastic ionomer material such

as SentryGlas® (SG), thermoplastic polyurethane (PU) and acrylic cast resins. In this work, the characteristic interlayer materials PVB and SG are applied, which cover the range from a soft (PVB) to a shear-stiff (SG) material. Polymer materials are modelled by input of time-dependent shear modulus or Young’s modulus values and the related Poisson’s coefficients to create linear viscoelastic material definitions in ANSYS. No temperature shift functions are directly used in the software but various material models are created for each considered temperature level. With regard to the temperature variation measured in the testing facilities during a time of 10 months, levels of  $15^\circ\text{C}$  to  $25^\circ\text{C}$  are examined primarily as two typical boundaries. The necessary values are derived from the literature.

#### 5.3.2. Ionomer Interlayer

Thermoplastic ionomers, a designation given by the manufacturer DuPont, are created by the insertion of ionic groups into the polymer backbone up to an ion content of max. 10% [Kot 13, p. 33]. Methacrylic acid monomers are co-polymerised with olefinic monomers and the included ionic groups form metallic salts [Sie 12b, p. 71]. The polymer backbone is principally constituted from ethylene and butadiene [Kot 13, p. 33]. The polymer chains are not linked through chemical bonds; the metallic ions are used as cross-linking base points. Because of their thermoplastic properties, ionomers are also called ionoplasts [Ben 13, p. 7].

SentryGlas®, an ionomer product for glass lamination<sup>30</sup>, has to be stored in a conditioned atmosphere and is laminated in a vacuum bag in an autoclave procedure at approximately  $140^\circ\text{C}$  and 12 to 13 bar pressure. The manufacturer [DuP 15] reports a density of  $0.95\text{g/cm}^3$ , a melting point of  $94^\circ\text{C}$ , a glass transition temperature of  $43^\circ\text{C}$  (heat deflection temperature), a thermal expansion coefficient of  $100$  to  $150 \cdot 10^{-6} 1/\text{K}$  at  $-23$  to  $32^\circ\text{C}$  and a tensile strength of  $34.5\text{MPa}$  with an elongation at failure of 400%. DMA tests performed at the TU Dresden [Kot 13, pp. 95-96] revealed a glass transition of  $46^\circ\text{C}$  (onset  $E'$ ) to  $59-65^\circ\text{C}$  (peak  $\tan \delta$ ) followed by a flow zone at increasing temperature. The storage and loss moduli from the DMA tests at 1Hz are plotted in fig. 5.55.

<sup>30</sup>originally fabricated by DuPont but recently sold to Kuraray

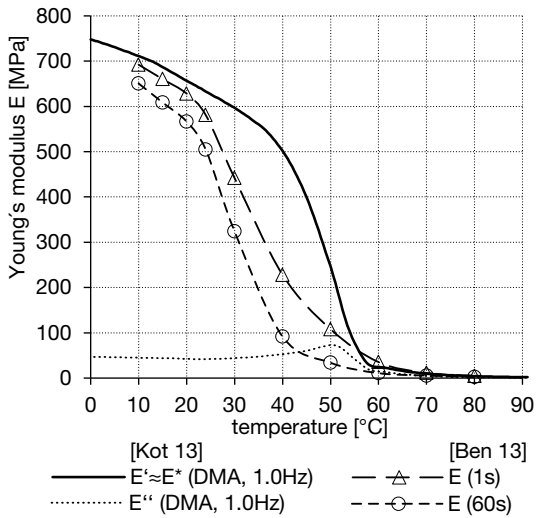


**Figure 5.55.:** Temperature-dependent Young's modulus of SG ionomer measured at 1Hz in DMA by M. Kothe, 2013. The results of Bennison are added for comparison.

For comparison, the temperature-dependent values given for the Young's modulus by Bennison et al. [Ben 13] are added to the diagram<sup>31</sup> fig. 5.55. The curve shapes are basically similar with the results of Bennison. The latter expose slightly smaller module and glass transition results for the given

durations of 1s and 60s. Thus, the data of the manufacturer can be supposed being on the safe side. In [Ben 13] a full dataset of  $E$ ,  $G$  and  $\nu$  is provided for the modelling of SentryGlas<sup>®</sup>, of which  $G$  and  $\nu$  are shown depending on time in the diagram fig. 5.56 for temperatures ranging from 10°C to 60°C. At room temperature, the material shows an elastoplastic behaviour [Ben 13, p. 20]. In this thesis, the shear values from diagram 5.56 for 15°C and 20°C are applied together with the respective Poisson coefficients. For the underlying elasticity necessary for FE analyses, secant modulus values related to the short-term Young's modulus have been calculated; these are 636MPa for 20°C and 667MPa for 15°C.

In the present work, the shear deformation of the interlayer of the glass-SG laminates after 10 months of testing time reaches maximum values of 1.6° with two-ply laminates on testing and 1.4° with three-ply laminates along the short edge of the specimens. This corresponds to maximum shear strain values of 0.035mm/mm and 0.03mm/mm, respectively. These shear angles and shear strain values, which are calculated via FEA, are considered small.

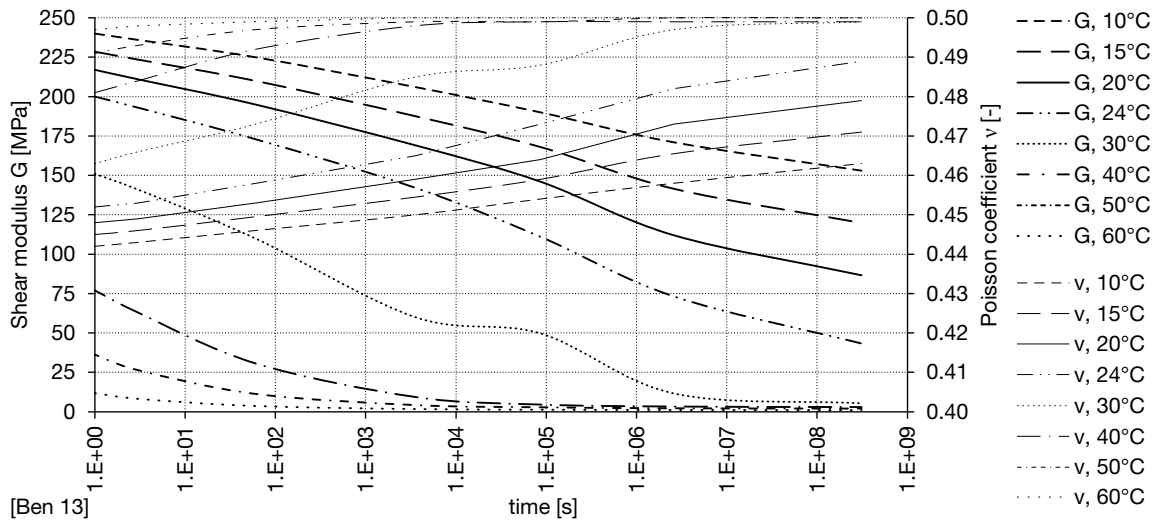


**Figure 5.56.:** Time- and temperature-dependent shear moduli and Poisson's coefficients of SG ionomer as published by Bennison et al.

<sup>31</sup>The storage modulus  $E'$  given here and the elastic material values  $E(t, T)$  for various times and temperatures as published by Bennison do not designate exactly the same type of modulus. Thus, the comparison of both values has to be interpreted qualitatively rather than quantitatively.



### 5.3.3. Viscoelastic PVB Interlayers

Polyvinyl butyral (PVB) is the most typical and widespread interlayer material used in glass lamination. PVB is made by the reaction of approximately 80% hydroxyl groups of polyvinyl alcohol with butyraldehyde [Kot 13, p. 31]. No cross-linking of the molecular chains occurs in the substance and, hence, the polymer undergoes phase changes from solid to plastic to liquid when it is heated. Thus, PVB is thermoplastic. Strong adhesion with glass is established through hydrogen bonds between the remaining hydroxyl groups and their OH-counterparts on the glass surface. As pure PVB is a relatively stiff material, plasticisers and other additives are appended. For providing sufficient adhesion to glass, the humidity content of the PVB has to be limited to about 0.4-0.5% [Kot 13]. Typical standard thickness values of PVB products are 0.38mm, 0.76mm and 1.52mm. Generally, standard PVB products have a density of about  $1.07\text{g/cm}^3$ , a coefficient of thermal expansion in a range of  $80 \cdot 10^{-6} 1/\text{K}$ , an elongation above 250% at failure and a tensile strength  $>20\text{MPa}$ . The melting temperature is at approximately  $75^\circ\text{C}$  and the glass transition occurs at  $8^\circ\text{C}$  (onset decrease  $E'$ ),  $15\text{-}25^\circ\text{C}$  (turning point  $E'$ ),  $30\text{-}38^\circ\text{C}$  (peak  $\tan \delta$ ) [Kot 13, p. 92], [Hal 08, p. 15]. The PVB product used for the testspecimens for this thesis is Trosifol<sup>®</sup> BG R20 provided by Kuraray.

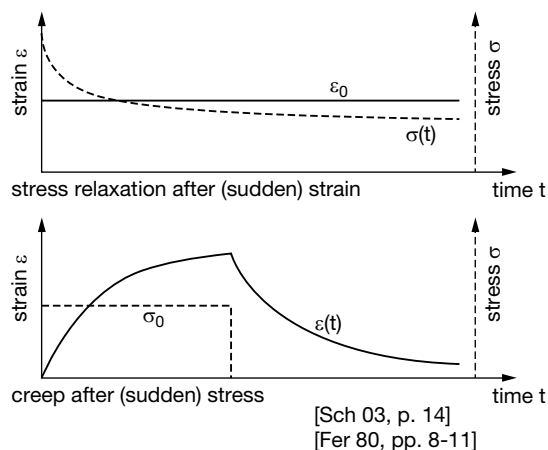


**Figure 5.57.:** Principles of stress relaxation because of sudden, constant strain (top) and creep from sudden stress (bottom).

PVB material behaviour is typically characterised as viscoelastic [And 14], which describes the time-lagged reversible deformation behaviour of a

substance subjected to an exterior load and is also called entropy-elastic. This is expressed either as creep, where deformation / strain increases under constant stress load, or as relaxation, where stress reduces because of an applied constant strain / deformation, fig. 5.57.

In the theory of linear visco-elasticity, the momentary strain or stress state of a polymer material only depends on temperature and time, regardless of the applied load. This is valid for the case of small deformations only. Schuler [Sch 03, p. 15] defines strain of less than 0.1 to 0.5% as a limit for viscoelastic behaviour. Other authors mention values up to 10% for the applicability of linear visco-elasticity [Sac 08, p. 16]. Sackmann [Sac 08, p. 16] cites shear angles  $\gamma < 42$  as a limiting criterion for  $xz$ -shear deformation of PVB interlayers for linear visco-elasticity. In the present thesis, shear angles in the 1.52mm thick PVB interlayer gained from finite element analysis in the springback and relaxation process after 10 months are always smaller than  $21.3^\circ$ . This value coincides with the displacement data from photogrammetry attributable to the relaxation and opposed mutual displacement of the bonded glass layers to each other. The related  $xz$ -shear strain is 0.37mm/mm, which corresponds to 37%. The maximum shear angle and shear strain in the interlayer locally occur along the short edge of the glass, where the mutual displacement of the glass layers also reaches its maximum. The shear angle gradually reduces longitudinally in the direction of the centre. As the exact limits in the literature remain vague, the finite element calculation of the glass laminates in ANSYS is employed as a simplified engineering approach with a viscoelastic PVB model based on the curve-fitting of testing results and a resulting 11-parameter Maxwell-Wiechert representation. However, the problem of non-linear visco-elasticity in PVB interlayers of glass laminates subjected to long-term gradual changes in large shear strain remains a topic for future research.

For the description of visco-elasticity, rheological models from combinations of Hookean springs, representing elasticity via a modulus  $E_i$  or  $G_i$ , and Newtonian dashpot for viscous damping  $\eta_i$  are used. Creep (retardation) can be modelled by a parallel spring and dashpot connected in series to an additional spring, the Kelvin-Voigt element.

Relaxation is modelled via Maxwell elements, consisting of a spring  $E_i$  ( $G_i$ ) and a dashpot  $\eta_i$  connected in series. The Maxwell model generally describes a viscous liquid. The complex behaviour of a viscous material can only be approximated by several Maxwell elements connected in parallel, called the generalised Maxwell model [Fer 80, pp. 15-16]. Addition of a single spring  $E'$  or  $G'$  in parallel to this model allows the description of a solid polymer. This model is called a Maxwell-Wiechert model, fig. 5.58. In the literature [Sch 03], [Sac 08], relaxation models are usually applied for the description of the behaviour of glass laminates.

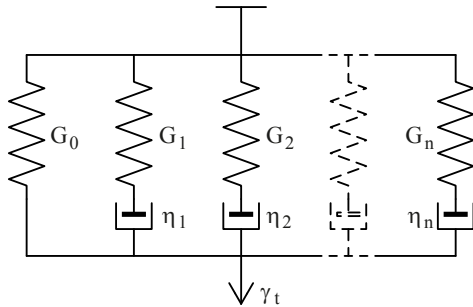


Figure 5.58.: Schematic Maxwell-Wiechert model.

The relaxation modulus  $G(t)$  is defined by [Sch 03, p. 21]

$$\frac{\tau(t)}{\gamma_0} = G(t) = G_0 + \sum_{i=1}^n G_i e^{-\frac{t}{\eta_i}} \quad (5.118)$$

where  $\eta_i$  is the damping. The application of linear visco-elasticity is based on the Boltzmann superposition principle and the correspondence principle. Superposition of the single mechanical responses of each step of a time  $t$ , e.g. the shear strain  $\gamma_i(t)$ , gives the final material response, e.g. the total shear strain  $\gamma_{tot}(t)$ , [And 14, p. 3], [Sch 03, p. 22], [Fer 80, p. 17]. This superposition principle allows the establishment of equations describing the material behaviour at various times  $t$  and constant temperature based on the load history. The time-dependent shear stress for a load history starting at  $t = 0$  can then be calculated via the relaxation modulus  $G(t)$  and the shear rate  $\dot{\gamma}$  [And 14, p. 3]:

$$\tau(t) = G(t) \gamma(0) + \int_0^t G(t-t') \dot{\gamma}(t') dt' \quad (5.119)$$

In this equation,  $t$  is the current time,  $t'$  a time in the past and  $(t - t')$  is the time interval between two steps considered.

The correspondence principle defines the applicability of linear-elastic theory to linear viscoelastic behaviour. Equation

$$G(t) = \frac{E(t)}{2(1+\nu(t))} \quad (5.120)$$

for the linear relationship of the shear and Young's modulus also applies under these conditions [Sac 08, p. 12].

The necessary material properties can be determined either through transient or periodic experiments [And 14, p. 3]. Periodic experiments, such as DMA on bulk PVB specimens or rheometer testing, are preferable [And 14, p. 3], as they allow the performance of dynamic tests at various oscillation or torsion frequencies and diverse temperatures without massive test expense and in a relatively short time [Men 99]. In a periodic test with a sinusoidal oscillation at an angular frequency  $\omega$  applied to a specimen, the resulting tensile or shear stress in the sample exposes a phase-shift  $\delta$  related to the respective strain. The shear stress and strain are then related by [And 14, p. 3], [Sac 08, p. 14]:

$$\tau(t) = \gamma_0 [G'(\omega) \sin(\omega t) + G''(\omega) \cos(\omega t)] \quad (5.121)$$

In this expression, the time-dependent behaviour of a viscoelastic material is defined by the shear storage modulus  $G'$  and the shear loss modulus  $G''$  related by the phase shift [Men 99, p. 66]

$$\tan \delta = \frac{G'}{G''} \quad (5.122)$$

The dynamic stress and strain from such tests can be expressed as complex quantities with the complex shear modulus [And 14, p. 4]

$$G^*(\omega) = G'(\omega) + iG''(\omega) = \frac{\tau^*}{\gamma^*} \quad (5.123)$$

The relaxation shear modulus  $G(t)$  for frequency scans of a viscoelastic material can be calculated from the experimentally determined storage and loss moduli  $G'$ ,  $G''$  by using the equation of Ninomiya and Ferry [Fer 80, p. 90]:

$$G(t) = G'(\omega) - 0.4G''(0.4\omega) + 0.014G''(10\omega); \quad \omega = \frac{1}{t} \quad (5.124)$$

Rheometer or DMA tests can be typically undertaken for frequencies in the range of 0.001Hz to 100Hz [And 14, p. 4] and at various temperature levels. The principle of time-temperature shift is used practically in order to superimpose test results determined for various frequencies and temperature levels to build a master-curve for  $G(t)$  (or  $E(t)$ ) with respect to a reference temperature  $T_0$ . This curve can be shifted parallel to the logarithmic time axis to obtain moduli for another temperature. A time period significantly larger than the original frequencies 0.001Hz to 100Hz can be covered through the shift. The Williams-Landel-Ferry (WLF) equation [Fer 80, p. 274] permits the calculation of horizontal shift factors  $\alpha_T(T)$

$$\log_{10} \alpha_T(T) = \frac{-c_1 (T - T_0)}{c_2 + T - T_0} \quad (5.125)$$

The coefficients  $c_{1,2}$  vary with different authors. The shift functions do not permit the calculation of relaxation moduli valid for every time  $t$ ; the short- and long-term time limits have to be chosen depending on the available test data.

The discrete test data obtained from a frequency analysis for the storage and loss moduli  $G'(\omega)$ ,  $G''(\omega)$  are typically approximated by a curve fit. These functions can then be applied to determine the relaxation modulus  $G(t)$  by means of eq. 5.124. For expressing the relaxation moduli via the Maxwell-Wiechert model, a curve fit can be made by applying a Prony series with  $n$  relaxation moduli values  $G_i$ , the respective relaxation times  $\lambda_i$  and the temperature shift factor  $\alpha_T(T)$ :

$$G(t, T) = \sum_{i=1}^n G_i e^{-\frac{t}{\alpha_T \lambda_i}} \quad (5.126)$$

In the context of the present work, various linear viscoelastic PVB models from the literature have been applied in comparison with the tests performed on cold bent glass. An overview of the available research approaches on PVB is given by table E.2 in appendix E.2. Other authors using the Maxwell-Wiechert type model for linear visco-elasticity in the domain of glass lamination interlayers include Galuppi et al. [Gal 12], [Gal 14b].

The most recent publication on PVB (Trosifol® BG R20) by Andreozzi et al. [And 14] is based on cyclic torsion testing in a rheometer. The obtained values for  $G'$  and  $G''$  are used to calculate curve fits with a polynomial-logarithmic function.

Master curves through horizontal shifting with the WLF-function eq. 5.125 are created for 30°C and WLF coefficients  $c_1 = 12.5 \pm 0.1$ ,  $c_2 = 89.0 \pm 1$  are reported. The shear relaxation modulus is calculated from this by eq. 5.124 and is approximated with a Maxwell-Wiechert model by using a Prony series representation with 10 elements. The resulting  $G(t)$  curves for 10°C to 50°C are shown in fig. 5.59 and the full Prony series is given in fig. E.3 in appendix E.2. The authors limit the validity from 0.1s to  $1 \cdot 10^7$ s. The  $G(t)$  curves, however, suggest a possible use of up to  $1 \cdot 10^8$  for temperatures equal to or lower than 20°C, but this is not experimentally covered. In the tests with cold bent Trosifol® BGR20-PVB-laminated glass made for this thesis, FE-analyses have been performed with these recent PVB model results, as they offer convenient time limits also covering short-time loads. The latter strongly affect the first moments of springback / relaxation during the release of the glass and therefore can have a major influence on the degree of curvature loss that a cold bent glass laminate shows during its lifetime. With this model, a good correspondence of the real-scale tests and the finite element analyses has been found, see fig. 6.12 in section 6.3.1.

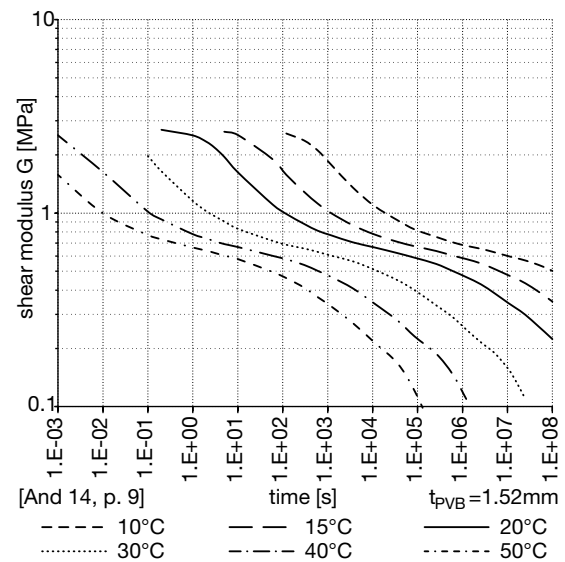


**Figure 5.59.:** Time- and temperature-dependent shear moduli of PVB Trosifol® BGR20 from the research of Andreozzi et al. (double-logarithmic).

Other research and test results for PVB were also applied in the finite element calculation of cold bent glass, but exhibited higher deviations from the test results of cold bent glass than the above approach.

- V. Sackmann [Sac 08, p. 142] has applied cyclic four-point bending tests with PVB-laminated glass (Trosifol® MB) to obtain a master curve for  $G(t)$  at  $T_0=20^\circ\text{C}$  and shift coefficients  $c_{1,2}$  depending on the temperature above and below glass transition. The Maxwell-Wiechert model with 12 parameters and the related  $G(t)$  curves are shown in fig. E.2 in appendix E.2.
- Schuler [Sch 03, pp. 140-141] conducted four-point bending tests and single lap shear tests by using glass-PVB laminate strips to calculate  $G(t)$ , to formulate a logarithmic function and a Maxwell-Wiechert model with three parameters for Trosifol® MB.
- Kutterer [Kut 03] has examined Trosifol® MB and has developed a logarithmic function for the PVB based on testing of cylindrical glass-PVB laminates subjected to shear at  $23\text{-}25^\circ\text{C}$ .

Comparison of the shear relaxation moduli  $G(t)$  at  $20^\circ\text{C}$  in fig. 5.60 reveals similar curve shapes for the models of most authors. Nevertheless, particularly for short-term situations  $t < 100\text{s}$  the relaxation moduli of the different tests can be seen to exhibit strong differences. For the sake of comparison, the shear moduli obtained by Van Duser [Dus 99] and Bennison [Ben 99, pp. 1761-1770] for another PVB product, Butacite®, are also shown. The behaviour of bulk PVB used in tensile DMA as in [Dus 99] / [Ben 99] results in extremely high short-term shear moduli and obviously differs from PVB bonded between two glass layers, as performed by the other mentioned authors either in four-point bending tests and / or transient shear tests [Sac 08], [Sch 03], [Kut 03] or in rheometer experiments [And 14].

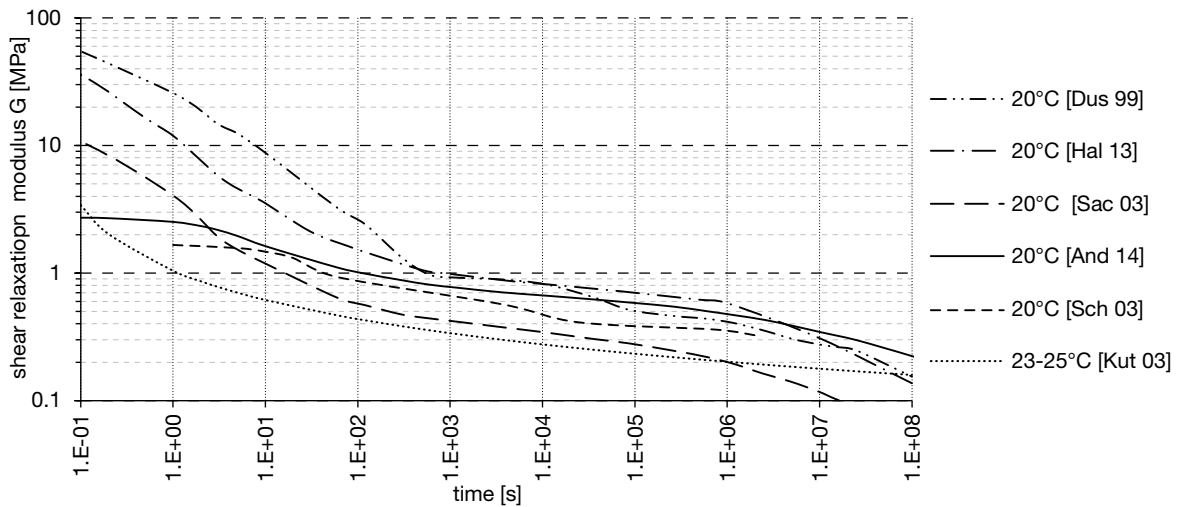


**Figure 5.60.:** Comparison of the time-dependent shear moduli at room temperature from different authors (double-logarithmic representation).

## **6 Application, Comparison**

## 6.1. Real Scale Testing

### 6.1.1. Real Scale Test Setup

For performing the testing and monitoring tasks defined in sections 3, p.21, and 4, p.25, nine cold bent glass laminates with three different compositions were fabricated as shown in figs. 4.1, 4.2 and explained in section 6.3. Prior to lamination, these glass panes were equipped with fibre optic sensors bonded to discrete points on the interior surfaces, as shown in section 6.1.2 (p.119) and with numbered points for use with photogrammetry attached to the exterior surfaces, section 6.1.3 (p.122). These nine laminates, made from either two fully toughened glass plies laminated with a PVB Trosifol® BG R20 and SentryGlas® ionomer (SG) interlayer or three SG-laminated glass plies, were used for long-term relaxation testing over a period of eight months. The dimensions of the bottommost glass pane were  $l/h=2400 \times 800$ mm, the other glass layers of each specimen being adapted in length to avoid an offset / stepping along the small edges in the bent, curved state. A summary of the nine specimens, 2esg\_pvb-01 to 03, 2esg\_sgp-01 to 03, 3esg\_sgp-01 to 03, their specifications and the related tests and numerical models is given in table 6.1.

After cold bending and lamination, the curved glass laminates were transported to the testing room while still being firmly attached to the bending mould. Prior to and during release from the horizontally placed mould, the deformation and interior stress were monitored by using the FBGs and close range photogrammetry. Following the release process, which took a maximum of five minutes, the specimens were placed on a permanent base for long-term monitoring, fig. 6.2.

Monitoring of the stress and displacement was undertaken simultaneously. Even though some continuous measurements were made with FBGs during the bending process and release from the mould, the spectra of each sensor were typically recorded at each measurement run. The time intervals between each measurement set, consisting of a sensor stress record and a photogrammetry displacement record, only represented a few minutes during the release process. The measurements were taken shortly after positioning on the base pedestal and switched to one set per day afterwards.

The influence of self weight on the relaxation process was eliminated by placing the glass in an upright position with one of the curved edges being supported by 14 low-friction sliding bearings of PTFE and POM, fig. 6.1. The supports allowed translation in all horizontal directions. At the short straight symmetry axis, the glass was supported at the bottom and constrained against translation; at the top, an additional constraint perpendicular to the glass surface prevented the laminate from toppling. Thus, the relaxation movement of the laminates was zero along the short axis of symmetry, and the recovery deformation developed symmetrically towards both extremities of the glass.

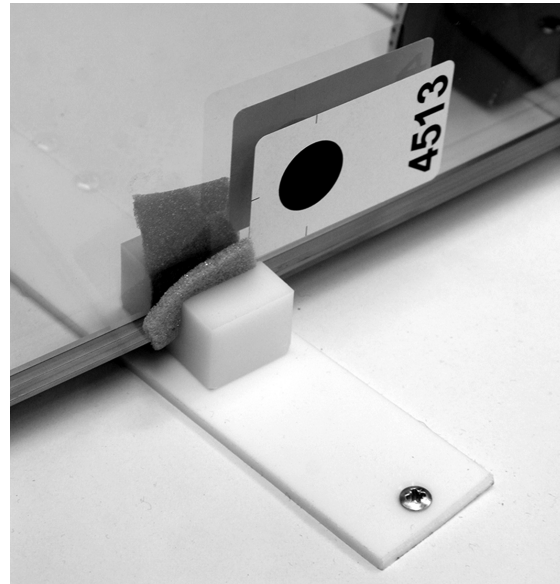


**Figure 6.1.:** Sliding support of a cold bent glass sample. The setting block is of POM, the flat sliding contact surface is of PTFE.

Gradually, with the passage of time, fewer monitoring sets needed to be recorded, as a few results were sufficient to follow the long-term recovery of the laminates. Testing was complete after 239 days, about eight months.

Based on the experience gained with the nine laminates, two additional specimens with four layers of low-iron white FTG were produced the same way and were equipped with a dense sensor network. These specimens served as a sensitive walkable arch demonstrator and were presented at the glasstec

specimen no.	composition	testing	FBGs	FE model type	max. $u_z$	temp.	interlay. model
2esg_pvb- 1,2,3	2x6mm FTG, 1.52mm PVB BG R20	cold bending, springback relax. 239d	6 pos. 2, 6 pos. 3	FSD.1.1 (cylind.), FSD.2.2 (contact)	124mm	15-25 °C	[And 14]
2esg_sgp- 1,2,3	2x6mm FTG, 1.52mm SG	cold bending, springback relax. 232d	6 pos. 2, 6 pos. 3	FSD.1.1 (cylind.), FSD.2.2 (contact)	124mm	15-25 °C	[Ben 13]
3esg_sgp- 1,2,3	3x6mm FTG, 1.52mm SG	cold bending, springback relax. 225d	6 pos. 2, 12 pos. 3-4, 6 pos. 5	FSD.1.1 (cylind.), FSD.2.2 (contact)	124mm	15-25 °C	[Ben 13]
4esg_sgp- 1,2	4x6mm FTG, 1.52mm SG	cold bending, springback relax. 2h	3x15 pos. 2, 3x15 pos. 7	FSD.1.1 (cylind.), FSD.2.2 (contact)	131mm, 135mm	20 °C	[Ben 13]

**Table 6.1.:** Summary of the real scale tests and related FE analyses performed on specimens l/h=2400x800mm, R=5000mm (cold bent)

2014 trade fair in Düsseldorf, fig. 6.3. The integrated sensor network permitted real-time monitoring of the stress distribution in the arch attributable to a load, e.g. a person on the arch and the position of this person. The permanently included cold bending stress and the actual stress from an exterior load were shown as a contour map on a screen place besides the arch. Furthermore, the FBG signals were used to switch on the LED illumination of the glass as long as a person was standing or moving on the arch. The real-time stress interpretation of the sensor network and the switching of the LEDs were achieved by a routine written with NI LabVIEW and by relay control. For these two laminates, namely 4esg\_sgp-01 and -02, the bending process, the moment prior to release from the bending mould after the autoclave process and two hours of springback / relaxation following the release were recorded by the spectra of the fibre-optic sensors. All measurements taken after release were made while the glass was in a horizontal position on the mould, at which point the self-weight of the laminate acted against the springback. In addition, a measurement was also made when 4esg\_sgp-02 was placed on two lateral linear supports along the small edges and functioned as an arch.

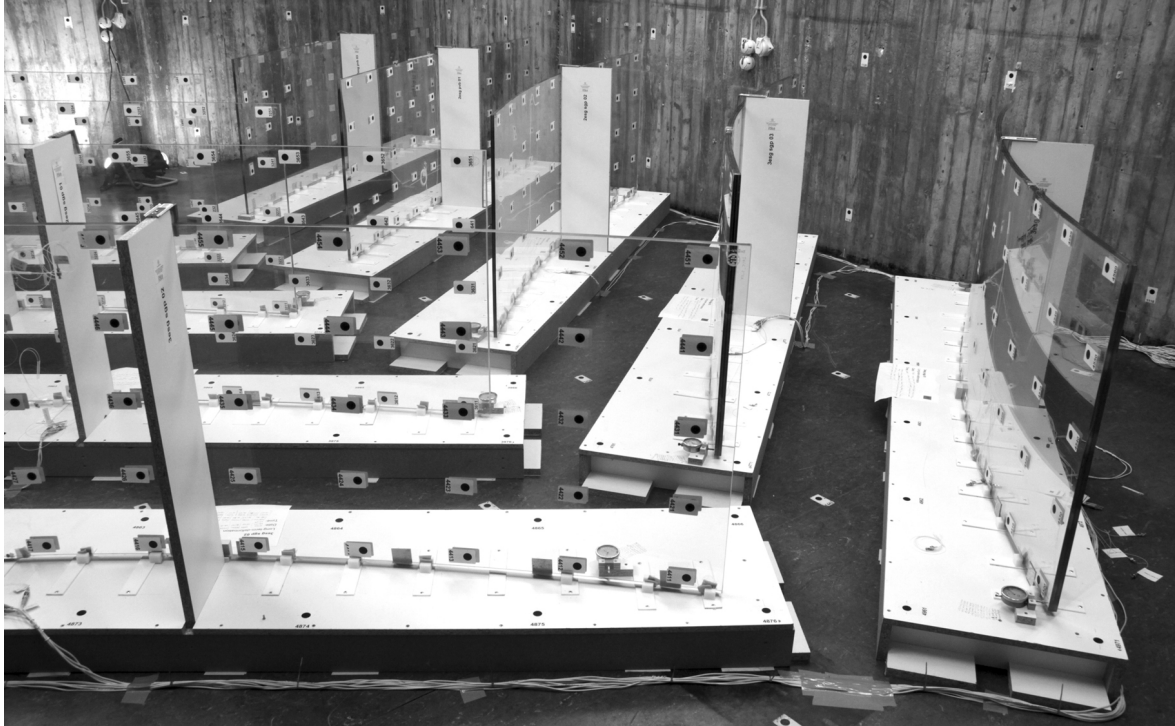


Figure 6.2.: Setup of the long-term testing of 9 cold bent glass specimens with three different compositions.

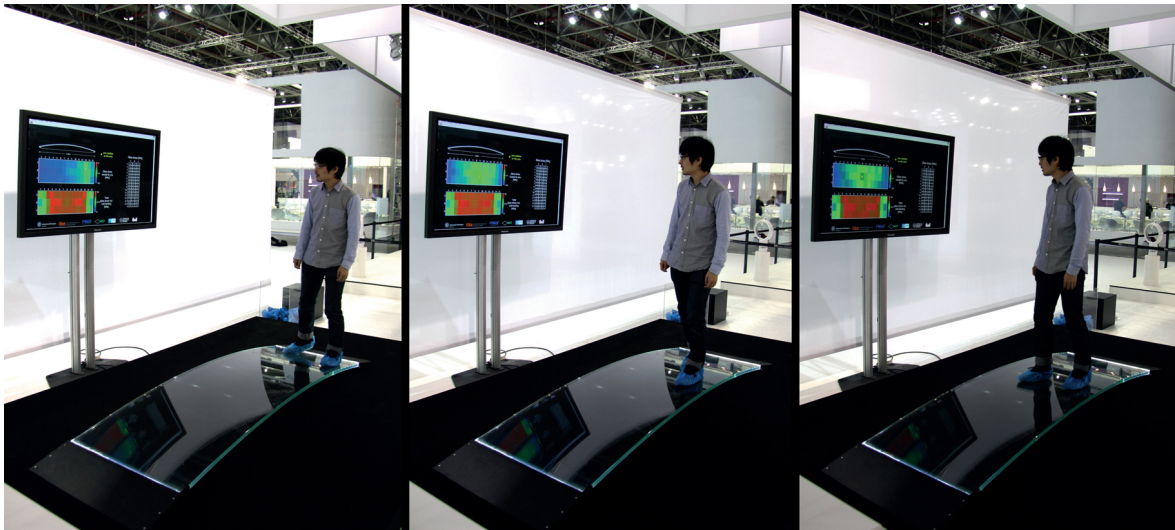


Figure 6.3.: Sensitive glass arch demonstrator with a 90 FBG sensor array presented at the glasstec 2014 trade fair.



**6.1.2. Equipment of the Samples with FBG**

The two and three-ply laminates produced were equipped with FBG acting as discrete strain sensors. Six sensors were attached to each interior face of the nine glass specimens 2esg\_pvb, 2esg\_sgp and 3esg\_sgp at the same locations, as listed in table 6.1. The bonding was performed with the adhesive KB4552, although it exhibited a yellowish aspect after UV cure and lamination. Figure 6.4 depicts the cross sections of the laminates and the respective FBG sensors glued to the numbered surface positions. The sensors glued to the same surface are numbered 1 to 6, 1 to 12 or 1 to 15 depending on the specimen type. The position number, addressed for example as *pos. 2*, specifies the glass surface to which a sensor fibre is attached. Glass surface numbering always starts with *pos. 1* at the exterior surface on the upper convex glass pane. The exact location and orientation of each sensor are shown in fig. 6.5. In order to reduce the cost, only one half of each interior glass surface was equipped with FBG. No temperature compensation FBG into the laminate could be successfully implemented.

Gluing a sensor to a location subjected to mechanically induced strain was not possible, as the entire glass panes experience such a strain.

The introduction of a loose sensor in a capillary into the interlayer also led to technical problems. Only the air temperature adjacent to the specimens was tracked; this was performed by an air thermometer and a loose sensor fibre laid onto the platforms of the specimens. The real temperature reigning inside a specimen thus remained subject to uncertainty. As thermal influence on the sensor measurements is not negligible, this fact is a critical point in the tests and necessitates a solution for future measurements. Sensors 2 to 4 and 9 to 11 were applied to measure the strain at the extremities of the bent panes. As strain becomes extremely small towards the ends, these sensors delivered indistinguishable results attributable to the overlaid scatter and temperature effects. Sensors 1, 6, 7 and 12 were bonded at points at the curved boundaries where the maximum longitudinal stress  $\sigma_x \approx \sigma_1$  was expected. Only these sensors are interpreted in the present work.

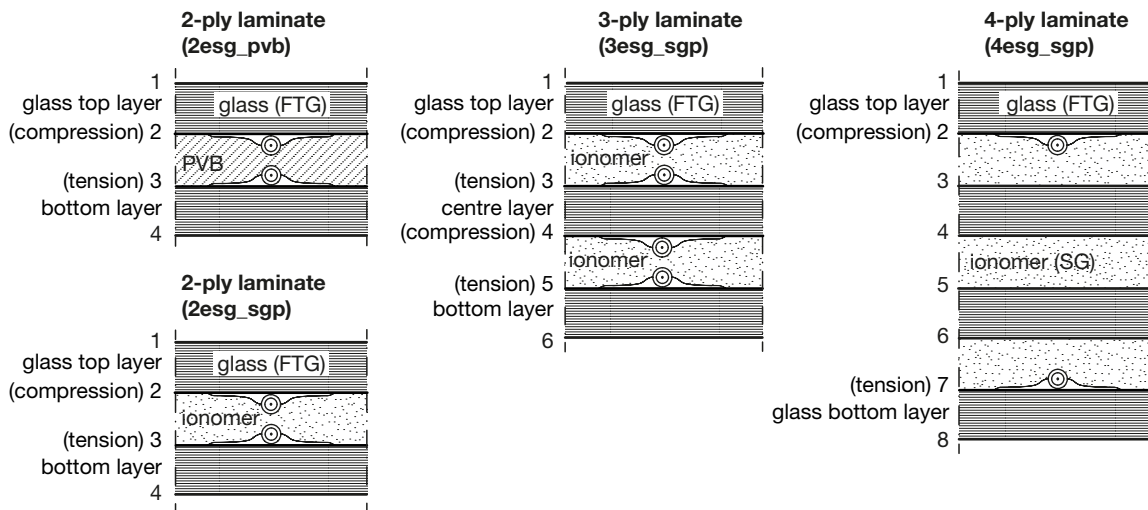


**Figure 6.4.:** Schematic cross sections and sensor positions of all laminate types produced for this research (not to scale).

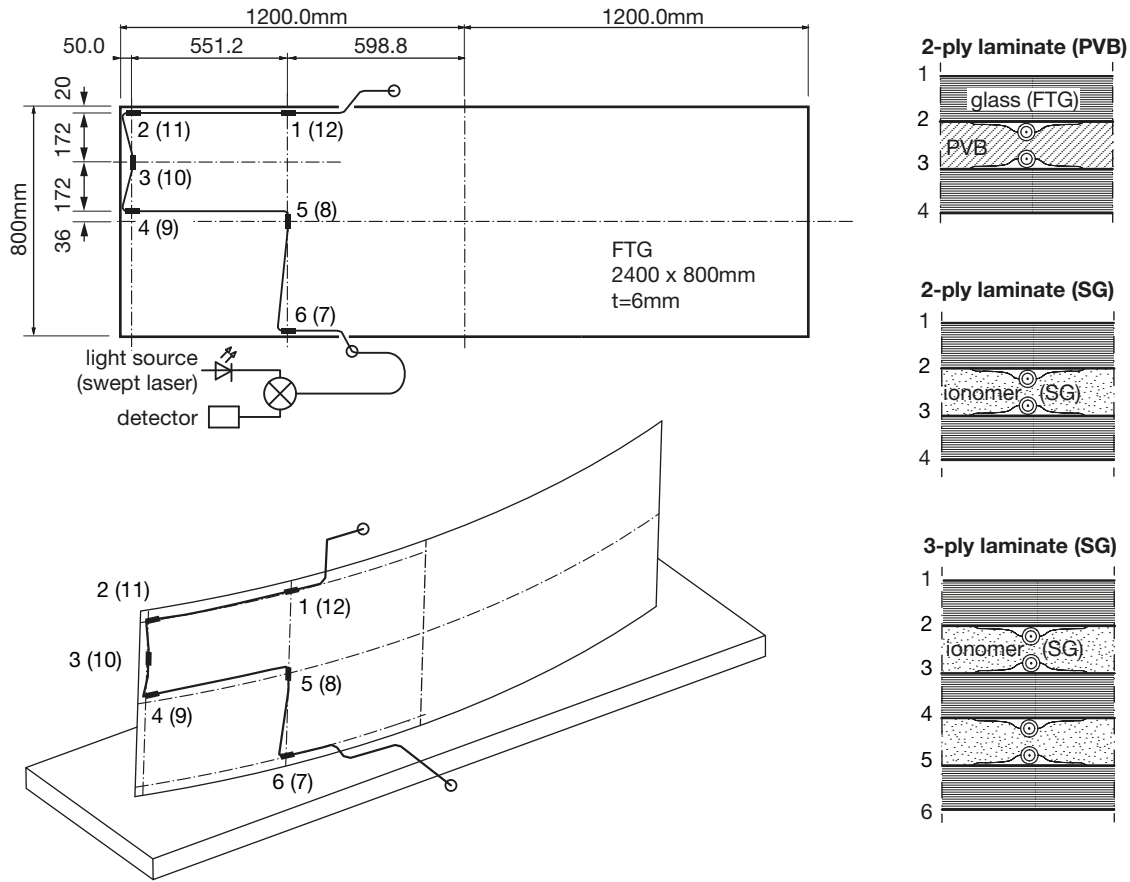
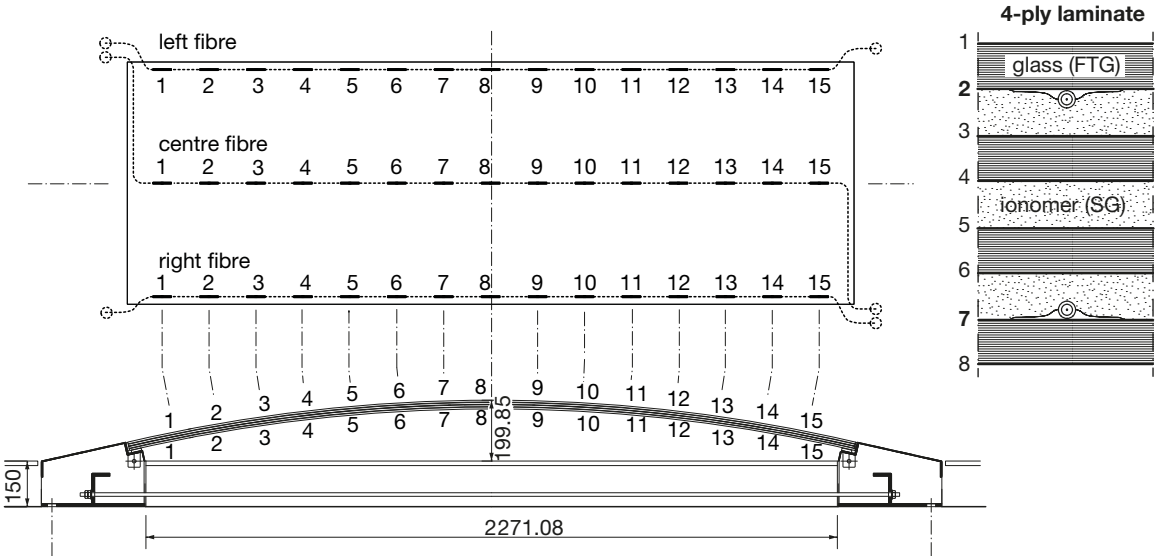


Figure 6.5.: Sensor layout and positions for the two- and three-ply laminates.

As shown in fig. 6.4, the four-ply glass laminates 4esg\_sgp have sensors only at glass surfaces pos. 2 and pos. 7, which are the bottom surface of the topmost glass and the top surface of the bottommost glass pane. The maximum glass strain / stress inside of the laminate is expected on these surfaces. Three fibres containing 15 sensors each are laid out parallel to the curved boundaries and in the centre on each of the two layers at pos. 2 and 7, fig. 6.6. The FBG are equally spaced by 155mm on the fibre. The fibres have a transverse distance of 365mm. Thus, an array of sensors is established in the laminate being sufficiently dense to determine the position of a load on the glass arch and to derive a stress contour map of the entire glass surfaces at positions 2 and 7. As a result of the adhesive analyses, a different product, Katiobond OB642, was applied for

bonding the sensors for the four-ply laminate. As pointed out in section 5.1.3, this adhesive shows a higher shear modulus at autoclave temperature than the previously used KB4552 and results in a fully transparent bond, even after lamination.

Figure 6.7 illustrates the preparation of a four-ply glass-interlayer stack with glued sensors slightly visible on the left hand side. The lead-out of the fibres from the laminate is performed at the ends of the curved edges of the glass. With all specimens, both fibre ends are led out and equipped with FC/APC connectors for redundancy reasons. The point at which the fibres are led out of the glass laminate proved to be the most sensitive area of the FBG layout regarding fibre breakage.



**Figure 6.6.:** Plan view and elevation of the four-ply laminate with the sensor layout at the interior faces of the top and bottom glass panes. The longitudinal spacing of the FBGs is 155mm and the transverse spacing is 356mm. The total arch length is 2400mm at the bottommost glass for a width of 800mm.



**Figure 6.7.:** Layout of sensors in the four-ply glass laminate prior to lamination.

### 6.1.3. Photogrammetry Application to the Specimens

Details concerning the principles of close range photogrammetry, concerning the applied cameras and concerning the software-based analysis of the photographs and measured points are given in section 5.2. The photographic procedure explained in the above-mentioned section was applied to the nine specimens 2esg\_pvb, 2esg\_sgp and 3esg\_sgp, which were equipped with an array of 5x10 numbered points as in fig. E.1 in appendix E.1 on both exterior surfaces. These points were regarded as slowly moving with time as a result of the relaxation of the laminates. The testing room itself had 188 fixed points used for reference.

For the tests described in the current work, two types of multi-image photogrammetry were applied: For the monitoring of the short-term springback and initial relaxation of the cold bent glass during release from the bending mould, accuracy in time is important, as the deformation process of the laminates happens quickly. Thus, three synchronised digital reflex cameras were used to take pictures of the top surface of the laminate from three fixed positions, fig. 6.8 and fig. 6.9. Hence, at each monitoring time step, three photographs are available. Each photograph shows all points on the top glass surface. The bottom points cannot be traced in this phase, as they are masked by the bending mould.

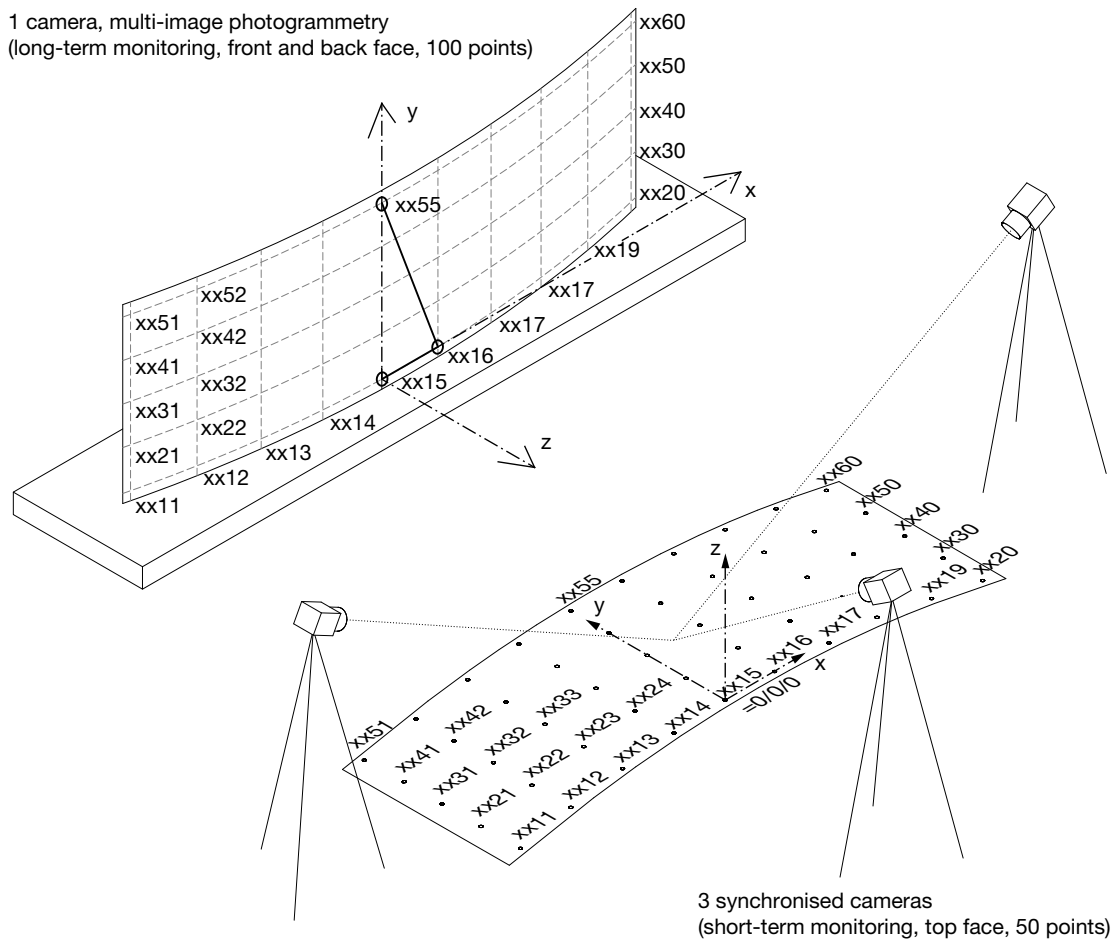


**Figure 6.8.:** Exemplary target point numbering system applied to the top glass surface in vertical and horizontal sample position. Note the three locations of the three synchronised cameras for short-term photogrammetry monitoring.



**Figure 6.9.:** Left: Setup of long-term testing of nine glass specimens; right: Photogrammetry setup at release of the glass samples from the bending mould.

For the long-term monitoring of the specimens resting on the sliding supports upon platforms as per figs. 6.8, 6.9 (left side), only one camera was applied and multiple overlapping photos were taken covering the entire specimen from all sides and viewing angles. In particular, the photographs focusing the vertical edges proved difficult, as the accuracy of measurement was reduced as a result of the acute viewing angles of the points on either curved surface of the glass. These photographs, however, are of importance for merging the concave and convex glass surfaces into one 3D representation exposing the correct laminate thickness. As a consequence of the large amount of point coordinate data calculated during testing, only the convex surface point data have been analysed in this work. Precision obtained with one camera was not sufficient to compare reliably the gradual shift, with time, of two points opposing each other on the concave and convex surface: this would have allowed the calculation of the changing shear angle with ongoing relaxation of the laminates.

Semi-automatic identification of the points on the photographs was carried out with the software Australis, see section 5.2 and fig. 6.10. This was undertaken for all nine specimens and for each monitoring step and resulted in a large amount of coordinate data. After bundle adjustment, each point cloud representing a glass specimen at a monitoring time step is related to the coordinate system calculated by the photogrammetry software. As these coordinate systems differ from time step to time step, no comparison of the displacement of the

target points on the glass surface is possible directly.

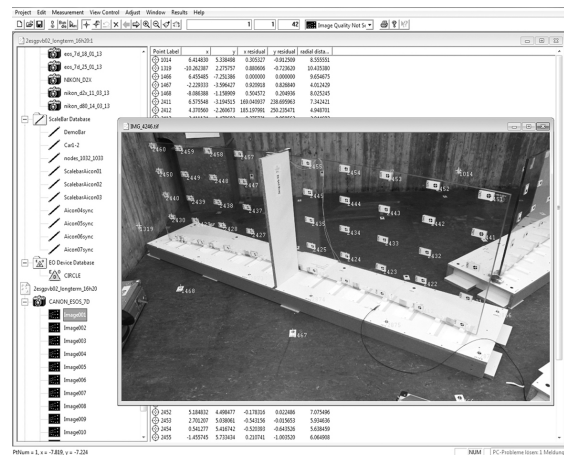


**Figure 6.10.:** Photogrammetry object target point identification in the Australis software.

To achieve comparability, the coordinate systems of all time steps for the same glass specimen have to be identically oriented and to have the same base point. Application of a homogeneous transformation matrix  $H_{transf}$ , which incorporates translation and rotation of the coordinate reference, solves this issue:

$$H_{transf} = \begin{bmatrix} R_{11} & R_{12} & R_{13} & T_X \\ R_{21} & R_{22} & R_{23} & T_Y \\ R_{31} & R_{32} & R_{33} & T_Z \\ 0 & 0 & 0 & 1 \end{bmatrix} \quad (6.1)$$

In this 4x4-matrix,  $R_{ij}$  is the rotational and  $T_k$  the translational part. For calculating the respective entries of the matrix, three points are chosen on the glass surface to orient the coordinate reference. To minimise the error caused by relative movement of the points during glass relaxation, they are chosen in the centre part of the curved surface, where the least changes are expected. Point xx15 is always chosen as base point 0/0/0. A vector  $\bar{v}_2$  is calculated from the direction of xx15 towards xx55, fig. 6.11. A second vector  $\bar{v}_{1,i}$  points from xx15 towards xx16. Both vectors have their bases in xx15. They are not precisely orthogonal to each other, as the accuracy of the target-point label positions on the glass surface is not sufficient. The cross product of  $\bar{v}_2 \times \bar{v}_{1,i}$  yields a vector  $\bar{v}_3$  normal to  $\bar{v}_2$  and  $\bar{v}_{1,i}$ . The cross product  $\bar{v}_2 \times \bar{v}_3$  then leads to a new vector  $\bar{v}_1$ . All vectors  $\bar{v}_{1,2,3}$  are normal to each other. The norms of these vectors are used as rotational entries  $R_{ij}$  for the matrix  $H$ .  $T_k$  is given by the point coordinates  $X, Y, Z$  of the base point xx15.

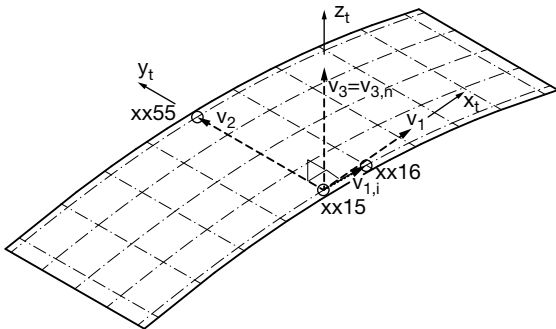


**Figure 6.11.:** Coordinate transformation orientation referring to the target points on the glass surface.

Multiplication of the coordinates  $X, Y, Z$  of each object point  $P_{local}$  with the inverse  $H^{-1}$  of the 4x4 homogeneous transformation matrix gives the object point coordinates  $P_{global}$  related to the new global coordinate system base in xx15:

$$H_{transf}^{-1} P_{local} = P_{global} \quad (6.2)$$

A summary of the total standard deviation errors (RMS) is given in table 6.2.

total standard deviation error estimates			
RMS [mm]	X	Y	Z
<b>short term</b>			
EOS 7D, 40D, 50D	0.0440	0.0430	0.0325
<b>long term</b>			
EOS 50D	0.3403	0.2526	0.2740
EOS 7D	0.5177	0.5421	0.7306
Nikon D80	0.2116	0.1868	0.1850
Nikon D5000	0.1399	0.1049	0.1456

**Table 6.2.:** RMS summary of the total standard deviation errors for the applied cameras.

## 6.2. Finite Element Model Setup

### 6.2.1. FE Models Adapted to the Tests

For the finite element analysis performed in ANSYS, a cold bending and relaxation model as close as possible to the experimental set-up is chosen. According to the modelling method classification from section 4.2, fig. 4.5, type FSD.2 with contact elements corresponding to the real bending mould from fig. 4.3 is applied. Adapted to the real tests with cold bent glass units, model type FSD.2 starts from a given bending shape with a single curvature radius of 5m at the bottom surface of the bottommost glass. Geometrical non-linear analysis is applied for the cold bending analysis in which the glass layers are forced to the mould by a linear force at the small edge of the glass, which corresponds to the transverse beam used for deformation in the tests, see fig. 4.2. As the experimental setup is double-symmetric to the longitudinal and transverse axes, a quarter model with symmetrical boundary conditions is produced. The glass panes  $t=6\text{mm}$  and interlayers  $t=1.52\text{mm}$  are each built up from one volume element through the thickness. Both 8-node SOLID185 and 20-node SOLID186 volume elements have been tested with varying mesh densities. SOLID185 elements of 15mm edge length have been found to represent an optimum with respect to analysis time and result precision. In order to prevent shear-locking, enhanced strain formulation is chosen. The bending mould is modelled with target elements TARGE170 and contact elements CONTA173 are applied along the surface of the glass panes forced to the mould. The applied displacement of the transverse beam for deforming the glass is adapted to the deformation results determined via photogrammetry as shown in section 6.3.1.

Corresponding to the tests, four different models as in fig. 6.4 and table 6.1 are created and examined. All of these shapes are based on a cylindrical mould shape with a constant radius of  $R=5\text{m}$ :

- 2esg\_pvb: 2x6mm FTG  $t=6\text{mm}$ , laminated with 1.52mm PVB BG R20
- 2esg\_sgp: 2x6mm FTG  $t=6\text{mm}$ , laminated with 1.52mm ionomer (SG)
- 3esg\_sgp: 3x6mm FTG  $t=6\text{mm}$ , laminated with 1.52mm ionomer (SG)
- 3esg\_sgp: 4x6mm FTG  $t=6\text{mm}$ , laminated with 1.52mm ionomer (SG)

In addition to the contact element model type FSD.2, an FE model based on a forced displacement of the lateral nodes along the glass edges of type FSD.1.1 into a perfect cylindrical shape with a radius of 5m was performed. The necessary modelling and analysis time consumption of such a simplified model is much less expensive than the contact element model. In section 7.2, the various models are compared in order to determine their possible use and accuracy for the general structural analysis of cold bent glass.

To choose the interlayer model for the PVB, the viscoelastic models given in section 5.3 are applied in ANSYS by input of either the experimental data for a curve-fitting or directly of the Prony series determined in this work. The analysis time in the FEM software covers the entire bending and test process during 8 months. The time steps for the springback / relaxation analysis are chosen in correspondence to the real time measured in the testing during the release from the bending mould and the long-term monitoring. Comparison of both the short- and long-term deformation behaviour and the stress during springback / relaxation of the laminates in the simulation with various PVB interlayer models and the photogrammetry / sensor testing results allowed to identify the PVB-testing results published by Andreozzi et al. [And 14] as the best fitting approach. As for the ionomer interlayer, the temperature- and time-dependent shear moduli published by Bennison et al. [Ben 13] were applied and led to results corresponding to the tests. In all cases, the FE analyses were performed for three temperature levels of 15°C, 20°C and 25°C. The temperature in the testing room typically varied over a range of 17-23°C during the 8 months of testing time. The underlying elastic modulus, which proved to be decisive for the initial springback at release, is given by the short-term secant modulus as shown in section 5.3.2. For the glass material, a Young's modulus of  $E=70.000\text{MPa}$  and a Poisson's coefficient of  $\nu=0.23$  are applied and linear elasticity and isotropy are assumed.

### 6.2.2. Form-Finding FE Models

Furthermore, four models of 3x3m glass panes bent into single- and double-curved shapes are made. These dimensions correspond to the approximate maximum width feasible with a standard autoclave<sup>32</sup>. For the length, 3.00m is chosen as well, because an increase in length usually does not result in increased glass stress for the same curvature. Differing from the models used for comparison with the testing results, the four above models were analysed with respect to obtaining a desired final shape after springback and relaxation. This approach is of interest for determining the bending mould shape necessary for the production of a precise desired glass geometry. Therefore, the iterative form-finding approach by fixed-point iteration FPI explained in section 4.2 and in figs. 4.5, 7.13 was applied. The cold bending results and the springback / relaxation after 8 months at 20°C were analysed for these models and the cold bending shape for obtaining a pre-defined final shape was determined. Four archetypical basic shapes, being of use for the cladding of double-curved building skins, with the following target curvature radii were examined:

- Paraboloid (synclastic): principal minimum curvature radii  $R_1 = R_2 = 35m$ ; 3x6mm FTG laminated with 1.52mm SG.
- Saddle (anticlastic):  $R_1 = R_2 = 35m$ ; 3x6mm FTG laminated with 1.52mm SG.
- Hyperbolic paraboloid (HP, anticlastic):  $R_1 = R_2 = 35m$ ; 3x6mm FTG laminated with 1.52mm SG.
- Cylindrical shape (single curvature):  $R = 5m$ ; 3x6mm FTG laminated with 1.52mm SG.

The models and their results are discussed in section 7.2. However, the analyses of these four exemplary models can only give a characteristic outline of the possibilities, limits and problems occurring in cold bending; this serves as a base for further research. The difference of the bending mould shape needed to achieve a particular final laminate geometry after lamination, springback and relaxation is of particular interest here. The cold bending stress referring to this mould shape and possible stability effects occurring with double curvature truly define the limits for the shape that can finally be obtained after relaxation. They also give an impression of the feasibility of the intended geometry and of its sensitivity to geometrical changes during relaxation.

<sup>32</sup>The standard maximum glass width is 3.21m. Here, 3m is chosen with respect to a bending mould and the necessary clamps to fix the laminate to the mould.



### 6.3. Comparison of FEA and Testing Results

#### 6.3.1. Displacement Results

As described in section 6.1.3 above, the coordinates of the numbered points attached to both exterior surfaces of the curved specimens are determined at various moments during the release from the bending mould and during the following eight months of testing time. By comparing the coordinates of a point at various times, the relative displacement values  $u_{x,y,z}$  in the direction of the unified coordinate axes can be calculated. Here, the displacement in the z-direction is used to characterise the recovery behaviour of the laminates. Usually, these values are shown and evaluated for the points along the narrow side of the curved laminates with the numbers xx21, xx31, xx41, xx51 and xx20, xx30, xx40, xx50, xx30 (compare fig. 6.8), which show the maximum displacement and are therefore characteristic for the recovery behaviour of the laminate. From the single displacement values of each numbered point, the arithmetic mean values of the displacement with time in the z-direction can be calculated for each specimen type 2esg\_pvb, 2esg\_sgp and 3esg\_sgp.

Some characteristic mean displacement values of the corner photogrammetry points are shown in table 6.3 for various times: 22 minutes after release from the bending mould, the two-ply laminates with SG and PVB interlayers suffered a mean springback of 20mm or above, whereas the three-ply SG laminate exhibited a much smaller springback below 8mm. Thus, the initial short-term springback is mainly influenced by the number of glass plies and the thickness of the laminate and less by the interlayer shear stiffness. This can be explained by the fact that the short-term interlayer shear modulus is relatively high for both SG and PVB (figs. 5.56 on p.110, E.3 on p.223 in section 5.3). With progressing relaxation time, the low long-term shear modulus of PVB leads to an ongoing recovery of the PVB-laminated specimens; this recovery accounts for a loss of 43% after 8 months. Both SG laminates show less recovery attributable to the high long-term shear modulus of the ionomer interlayer. The two-ply SG laminate recovers by 17% and the three ply SG laminate by 7%.

time	springback, relaxation: mean $\Delta u_z(t)$		
	2esg_pvb	2esg_sgp	3esg_sgp
[min,d]	[mm]	[mm]	[mm]
<b>cold bent (initial)</b>	122.20	122.60	123.80
<b>22 min</b>	-26.37	-19.85	-7.76
<b>126 min</b>	-29.04	-20.19	-8.00
<b>5d</b>	-39.87	-20.11	-8.57
<b>231d</b>	-52.41	-20.45	-8.78

**Table 6.3.:** Summary of the mean springback / relaxation in z-direction for different times calculated as mean values from the photogrammetry points along the narrow side of the glass.

Figure 6.12 shows a comparison of the mean z-coordinates<sup>33</sup> of the corner points of each specimen type derived from photogrammetric analysis and from FEA with contact elements. This diagram is derived from the results of all corner points of the glass measured by photogrammetry and from FEA with various interlayer material models as shown in appendix E.3, in fig. E.4:

- The PVB-model based on [And 14] used in the FE analysis leads to an overestimation of the recovery for short-term behaviour but corresponds to the test results for long-term relaxation.
- The continuous strong relaxation of the PVB laminate with progressing time is exhibited by both the FE approach and the tested specimens. The PVB-specimens do not to preserve a relevant curvature in the long term.
- Both SG finite element models with two and three glass plies based on [Ben 13] correspond with the testing results during all stages (1) to (4) and after 8 months. The z-coordinates attained after positioning on the platform for long-term monitoring (4) remain approximately constant.
- The three-ply specimens with SG interlayer exhibit the lowest level of initial springback and long-term relaxation.
- The general devolution of the springback-relaxation curves derived from the FE analysis corresponds well to the test results. The steps (1) to (4) from the test process as in fig. 6.12 can be simulated and are recognisable in the diagram.

<sup>33</sup>The maximum standard deviation of the z-coordinates occurring for the entire set of points within a group of three test laminates of the same type are given in table 6.4 in section 6.3.2

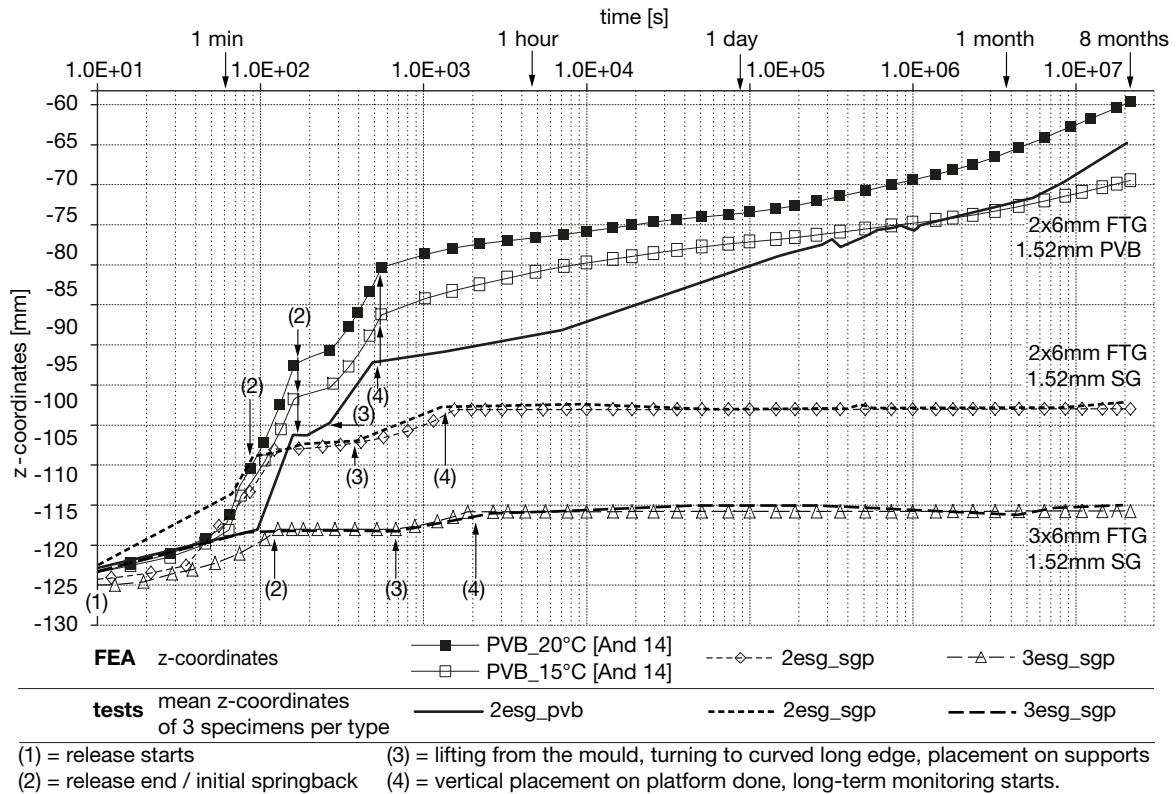


Figure 6.12.: Mean z-coordinate for points along the narrow side of the glass determined via photogrammetry plotted against logarithmic time scale; comparison to corresponding FE results.

### 6.3.2. Surface Curvature Quality

The entire geometry of the glass, which is of importance for understanding and controlling the shape achieved by cold bending and subsequent springback / relaxation, is determined by fitting a NURBS surface through the photogrammetry point array of 50 points per surface by applying the 3D software Rhinoceros®. Once such an approximated surface is determined, it can be used for principal curvature analysis, for example, by calculating the principal radii  $R_{1,2}$  or the Gaussian curvature  $\kappa$  for a given set of surface points. The main advantage of using such a surface is that a uniform arbitrary point array can be applied to all surfaces independently of the original photogrammetry point array. However, a surface fit is only an approximation to the real glass surface geometry and depends on the accuracy of the original point measurement by photogrammetry.

Furthermore, the fitting process might also lead to an approximation error<sup>34</sup>. For the sake of reducing the large number of points and surfaces used for result interpretation in this work, a new uniform point array was projected to the surfaces from each specimen series, thus allowing for calculating a mean surface.

The maximum standard deviation of the z-coordinates occurring for the entire set of points within a group of three test laminates of the same type are given in the first result column in table 6.4. The deviation of the z-coordinates of the mean surface from the individual specimens after 8 months is also provided and exhibits a maximum range of -2mm to +4mm.

<sup>34</sup>In order to control the presence of surface approximation errors regarding the curvature and geometry, the fitted surfaces from all specimens were compared with each other. In particular, the photogrammetry point monitoring with synchronised cameras, which lead to more precise results than the single-camera monitoring, was used to derive surfaces for this comparison.

	max. std. deviation z-coord. 3 specimens	deviation z-coord. of mean surface from specimen surfaces	
		max.	min.
specimen stage	[mm]	[mm]	[mm]
2esg_pvb cb	2.707	1.914	-1.183
	ar (8m)	2.003	1.157
2esg_sgp cb	3.648	4.003	-0.867
	ar (8m)	3.249	3.565
3esg_sgp cb	1.659	1.787	-1.049
	ar (8m)	1.099	1.056

**Table 6.4.:** Standard deviation of the z-coordinate of the three specimens per laminate type for the cold bent state (cb) and after 8 months of relaxation (ar). To the right, the deviation of the z-coordinates of the mean surface from the individual specimens are given.

The qualitative Gaussian curvature pattern of the mean glass surfaces derived via photogrammetry and via FE analysis is visualised in fig. 6.13 for the PVB laminates 2esg\_pvb and in fig. 6.14 for the two-ply SG laminates 2esg\_sgp. The curvature pattern for the three-ply type 3esg\_sgp is not shown, as it closely resembles the type 2esg\_sgp. The greenish areas tend towards single curvature.

Generally, both the FE model and the photogrammetry analysis exhibit the presence of anticlastic curvature along the curved longitudinal edges of the laminates in the cold bent state. In the centre, synclastic curvature zones occur. Towards the narrow sides of the glass, the curvature vanishes or exposes local anticlastic perturbations. After springback / relaxation of 8 months, the two laminate types exhibit some differences attributable to the differing degree of recovery and the interlayer shear properties. The PVB laminate in fig. 6.13 has a smooth surface with a small single curvature prevailing because of the large loss in bending deformation. With the two-ply laminate 2esg\_sgp in fig. 6.14, the zones of synclastic curvature shown in the centre and the anticlastic curvature visible in the boundary zones are preserved locally. The cause therefore is the small springback and small deformation loss with this laminate type.

The curvature radii of a regular pattern of 24 uniform points for all mean surfaces derived from FE analyses and testing with photogrammetry are depicted in figs. E.5, E.6 and E.7 in appendix E.4, pp. 226 to 228, for the cold bent state and the relaxation state after 8 months.

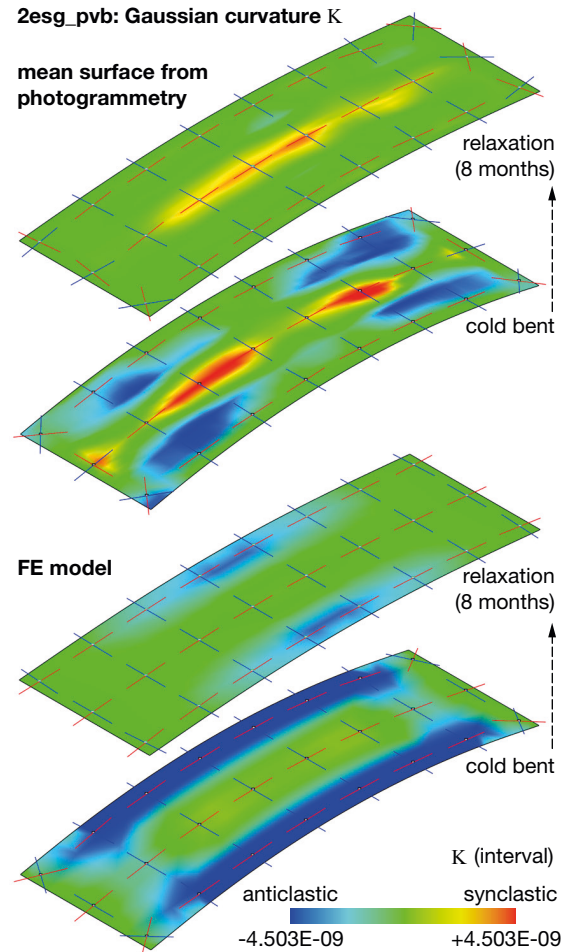


**Figure 6.13.:** Schematic Gaussian curvature plot of the mean surface from photogrammetry and the FE model for the cold bent state and after 8 months of relaxation for specimen type 2esg\_pvb.

The direction of the curvature radii  $R_{1,2}$  is shown for each point by two lines perpendicular to each other. The loss in deformation in z-direction  $\Delta u_z$  between the two states is also shown. The single curvature radius of the bending mould is 5m. Results for the convex top surface are as follows:

Cold bending shape:

- The curvature achieved in cold bending on the mould with  $R=5\text{m}$  is in a range of 4.60m to 5.20m in both analyses by FE and by photogrammetry. The zone exhibiting a regular curvature in longitudinal direction of about 5m encompasses 1/2 to 2/3 of the length of the laminate. Towards the narrow ends, the curvature gradually vanishes.

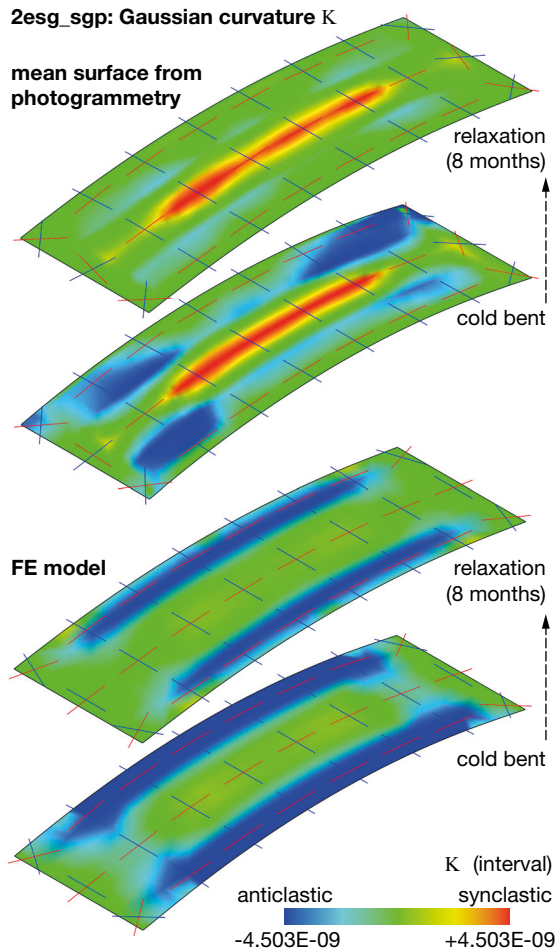


**Figure 6.14.:** Schematic Gaussian curvature plot of the mean surface from photogrammetry and the FE model for the cold bent state and after 8 months of relaxation for specimen 2esg\_sgp.

- Local anticlastic curvature zones with the principal radii pointing in diagonal directions are found in the corners.
- Along the curved longitudinal edges, an anticlastic curvature zone is derived from the FE model with minimal radii of -30m in the transverse direction as shown in figs. 6.13, 6.14. This effect is less pronounced in the photogrammetry results with minimum transverse radii of -50m.

Shape after 8 months of springback / relaxation:

- The PVB laminate 2esg\_pvb exhibits a curvature of 7.5m-9.5m. The anticlastic boundary zones reduce strongly in the photogrammetric monitoring. In the FE model, local anticlastic zones of small curvature remain, fig. E.5.

- The two-ply SG laminate 2esg\_sgp has remaining curvature of about 5.5m-6.0m. The anticlastic boundary zones remain after relaxation. The FE-model shows minimum transverse radii of -32m, whereas photogrammetry gives much larger transverse radii; see fig. E.6.
- The remaining curvature of the three ply SG laminate 3esg\_sgp is 5.0m-5.5m. The preservation of the anticlastic boundary zone is accentuated in the FE results (transverse R=-30m) but is less visible in the photogrammetric results; fig. E.7.

An example for the curvature analysis described above is given in fig. 6.15 for the three-ply SG laminate 3esg\_sgp. The preservation of the initial cold bending curvature after relaxation and the local synclastic or anticlastic zones can be seen for the discrete surface points.

With regard to the comparison, the point cloud density of the photogrammetric monitoring with 50 points was much inferior in comparison with the FE mesh. Nevertheless, in summary, both methods led to corresponding curvature and displacement results. In the tests and the models, the desired cold bending curvature of 5.00m given by the mould is achieved in an area encompassing one half up to two-thirds of the entire glass length. Most of the principal curvature directions are aligned with the longitudinal and transverse axes of the glass. After springback / relaxation of eight months at 20°C, the curvature in the longitudinal direction with the PVB laminates is reduced to 7.5m-9.0m, whereas the two-ply SG laminate still shows about 6.0m and the three-ply laminate preserves 5.1m-5.5m. Both SG laminates show anticlastic zones along the boundaries after relaxation, whereas such zones vanish in the PVB laminates. All laminate types have nearly planar zones in a zone of approximately 20cm to 30cm depth seen from the narrow edges with the SG laminates and 40cm with the PVB-laminated type. The SG laminates are more prone to preserving double-curved or uneven areas because of the shear stiffness of the interlayer leading to a small loss of curvature by springback / relaxation.

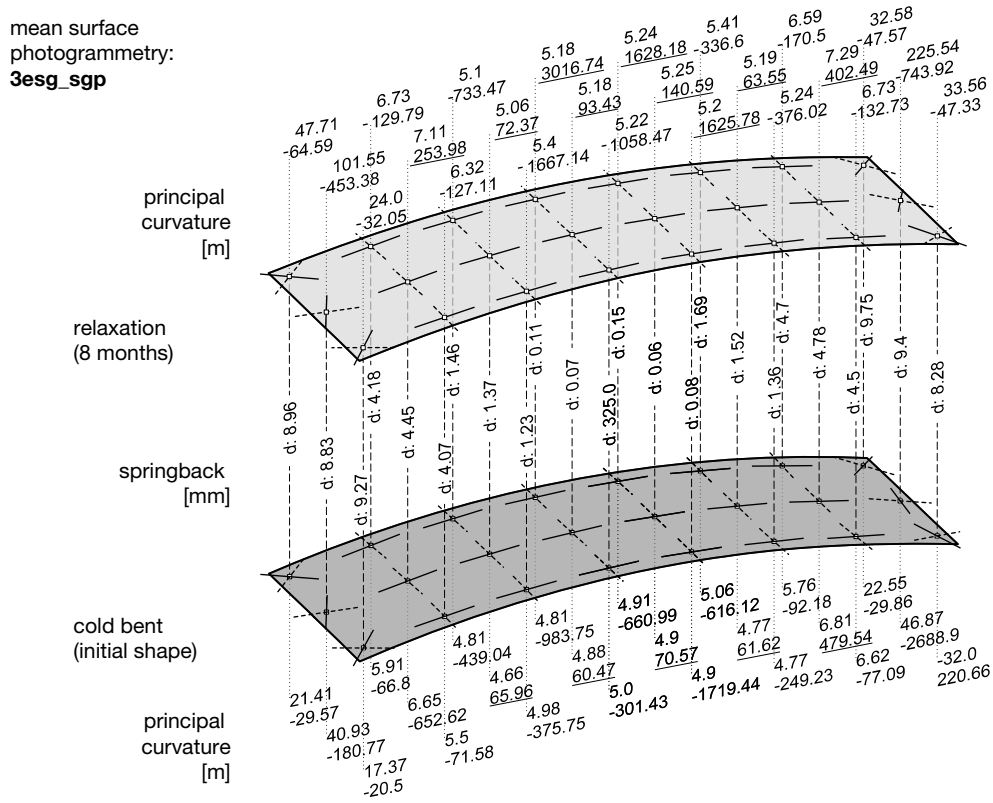


**Figure 6.15.:** Comparison of the principal curvature radii from photogrammetry on the top surface of the laminate 3esg\_sgp from three cold bent glass panes with SG-interlayer for the cold bent state and after 8 months of relaxation. In addition, the springback value  $u_z$  after 8 months relaxation is given.

**6.3.3. Strain and Stress Results**

The stress depicted in all following diagrams is determined from the strain, which itself is calculated by eq. 5.60 from the wavelength shift of the sensor and the temperature difference, by multiplying with the Young’s modulus of 70,000MPa. The strain transfer from the glass to the fibre core is calculated with the coefficients determined in sections 5.1.4.1, 5.1.4.2 and with respect to the assumptions examined in the micro-mechanical models in section 5.1.6.2. The influence of the distance between the sensor core of the fibre and the glass surface is taken into account for the bending strain calculation via eq. 5.61. The fibre Bragg grating sensors measure the stress corresponding to the orientation of the fibre, which is the longitudinal direction  $x$  of the glass laminates corresponding to the curved direction, in all cases examined here.

**6.3.3.1. Results from the Two- and Three-Ply Specimens**

The springback and relaxation behaviour measured with sensors no. 1 or 6 and 7, 12 in the nine curved laminates during short- and long-term monitoring exhibit large differences depending on the composition of the laminate, notably the interlayer material.

Figures 6.16, 6.17 and 6.18 depict a comparison of the mean stress  $\sigma_x$  results from the FBG monitoring and the FEA stress calculated for three temperature levels 15°C, 20°C and 25°C. Table 6.5 provides a comparative summary of the mean sensor stress and the related FEA results for different test stages.

The mean temperature in the test room during 8 months was 20°C. Compression results are treated as an absolute quantity in the following sections for a better description of increasing or decreasing stress. The mean standard deviation of the stress results from the various sensors and all nine specimens is in a range of 2.3MPa to 3.8MPa referring to the entire measurement period of 8 months.

Time-dependent behaviour of the laminates:

- For the PVB laminates 2esg\_pvb, the FBG and FEA results exhibit a strong decrease in compressive and tensile glass stress at the positions 2 and 3 in the laminate in the moment of the initial springback after release, fig. 6.16. 24 hours after the release, the initial tensile stress is reduced by 30% and the initial compressive stress by less than 25%, table 6.5. At 20°C, relaxation and the related decrease in stress are continuous and do not stabilise at a constant level; the PVB-laminated specimens will preserve only a small curvature and little stress after a long relaxation time. After 8 months, the initial cold bending stress is cut in half at 20°C.
- During springback, the two-ply SG laminate 2esg\_sgp exhibits an increase of compressive stress (pos. 2) and a constant level of tensile stress (pos. 3) in comparison with the initial cold bending stress, fig. 6.17. Afterwards, the stress remains stable during 8 months test time.
- With the three-ply SG laminate 3esg\_sgp, the initial bending stress on the outermost laminated glass surfaces pos. 2 and 5 increases at the moment of release and springback. The stress of the interior glass surfaces pos. 3, 4, being more close to the neutral axis, decreases slightly. During the following 8 months of the test, the stress remains constant on the level achieved after the springback, fig. 6.18.

Comparison of the results from the FBG and FEA:

- The general trend of the stress change with time exhibited by the FBG-sensors and the FE simulations is in good agreement for all laminate types and specimens. The stress curves for cold bending, the springback and the relaxation period calculated from the FBG exhibit the same behaviour and gradients as the stress from finite element analysis.

- For all laminate types, the mean stress values for the compression determined with the FBG comply well with the finite element results for the entire time of the testing process. The stress curves calculated by FEA and from the FBG are congruent, figs. 6.16, 6.17 and 6.18.
- After the autoclaving process, still being fixed to the bending mould, most of the FBG subjected to tension exhibit wavelength shift and stress results reduced by a mean value of 17% in comparison with the level measured in the cold bent state prior to lamination.
- The mean stress measured by the FBG subjected to tension is 10% to 35% below the finite element results during 8 months of relaxation. Cold bending tensile stress results show a better agreement in a range from -9% to +3%. As a consequence, the tensile stress curves from the FBG measurements in figs. 6.16, 6.17 and 6.18 run parallel below the respective FEA stress curves with an offset of 5MPa to 10MPa.
- The two-ply SG laminate 2esg\_sgp exhibits a slight decrease in FBG-measured tensile stress during 8 months; in contrast, the FE analysis results remain constant, fig. 6.17. Sensors subjected to compression show constant stress during the test period.

In appendix E.3 on page 225, all wavelength shift and stress results are given in tables E.3, E.4. The individual  $\sigma_x$  stress results determined from the FBG sensors 1, 6 (and 7, 12 for 3esg\_sgp) in the laminate and the resulting mean stress are also shown in detail in figs. E.8, E.9.



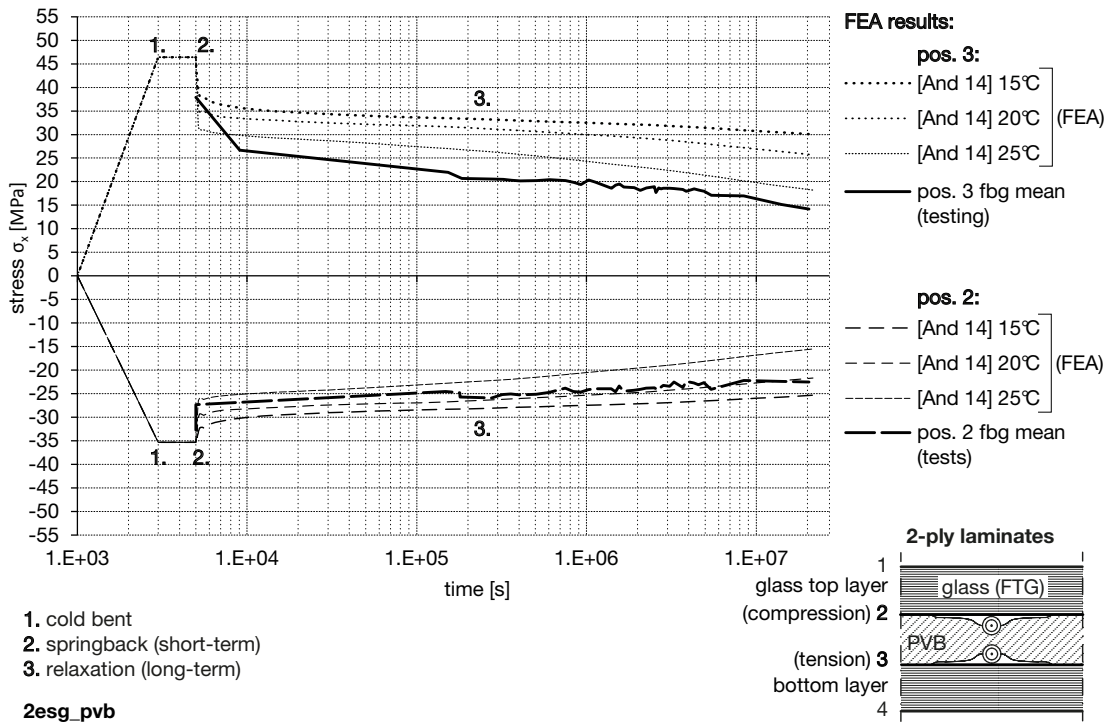


Figure 6.16.: Two-ply PVB laminate glass stress  $\sigma_x$  calculated from FBG 1 and 6 during 8 months of monitoring compared with finite element simulation for  $T=15^\circ\text{C}$ ,  $20^\circ\text{C}$  and  $25^\circ\text{C}$ .

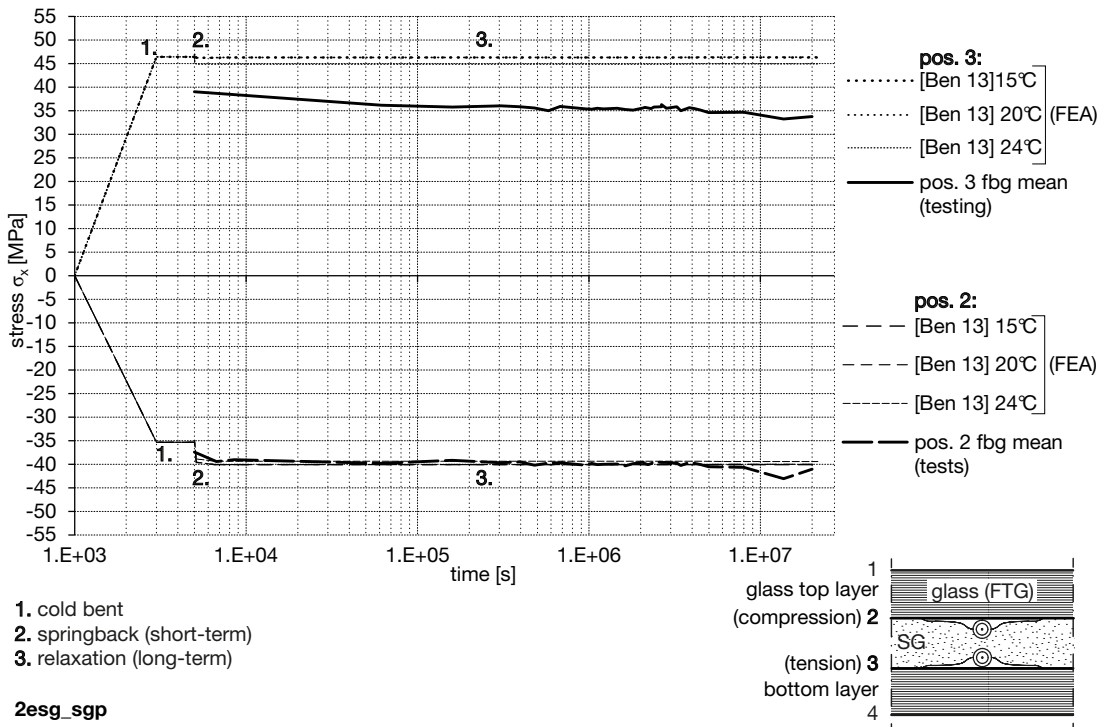


Figure 6.17.: Two-ply SG laminate glass stress  $\sigma_x$  calculated from FBG 1 and 6 during 8 months of monitoring compared with finite element simulation for  $T=15^\circ\text{C}$ ,  $20^\circ\text{C}$  and  $25^\circ\text{C}$ .

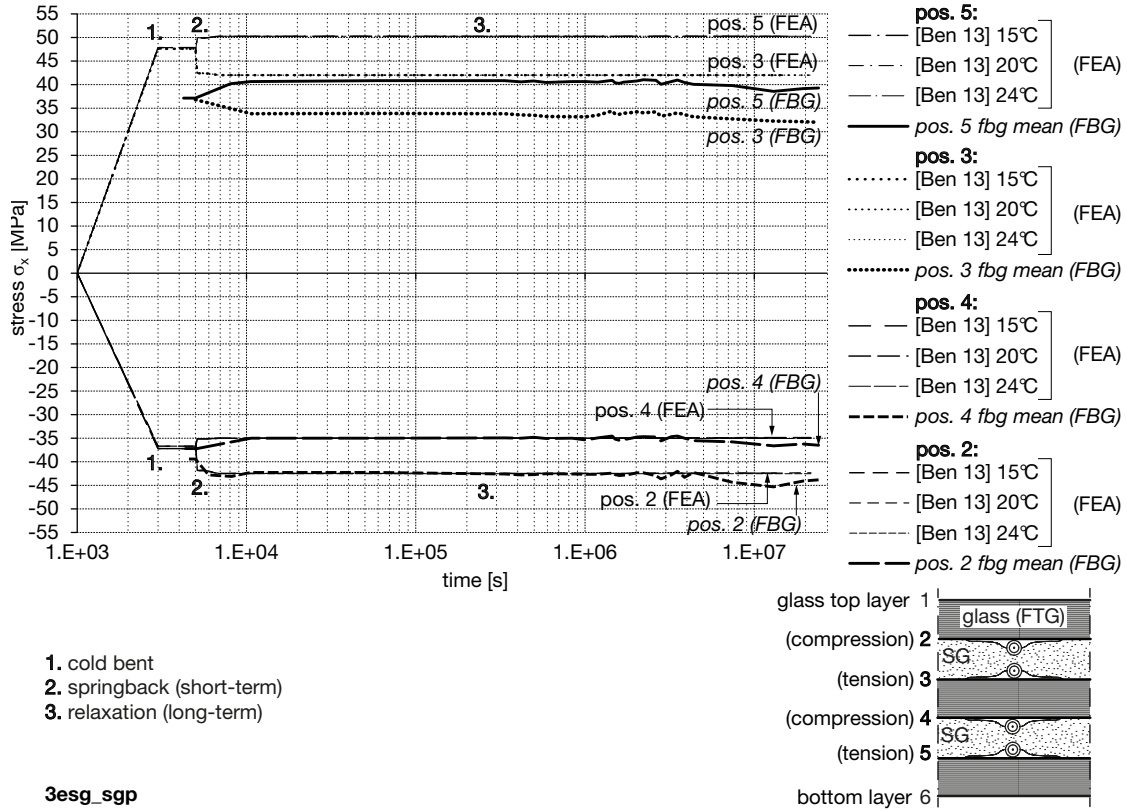


Figure 6.18.: Three-ply SG laminate glass stress  $\sigma_x$  calculated from FBG 1 and 6 during 8 months of monitoring compared with finite element simulation for  $T=15^\circ\text{C}$ ,  $20^\circ\text{C}$  and  $25^\circ\text{C}$ .

specimen	pos.	$\sigma_x$ (cb)			$\sigma_x$ (ac)	$\sigma_x$ (ar, 24h)			$\sigma_x$ (ar, 8m)			ratio ar(8m) / cb	
		FBG	FEA	$\sigma_{x(\text{FBG})} / \sigma_{x(\text{FEA})}$ [%]		FBG	FBG	FEA	$\sigma_{x(\text{FBG})} / \sigma_{x(\text{FEA})}$ [%]	FBG	FEA	$\sigma_{x(\text{FBG})} / \sigma_{x(\text{FEA})}$ [%]	FBG
		[MPa]	[MPa]	[%]	[MPa]	[MPa]	[MPa]	[%]	[MPa]	[MPa]	[%]	[%]	[%]
2esg_pvb	2	-	-35.34	-	-32.73	-24.50	-26.92	91.0	-22.51	-21.69	103.8	-	61.4
	20°C	47.11	46.39	101.6	37.89	23.35	31.85	73.3	14.20	25.68	55.3	30.1	55.4
2esg_pvb	2	see above					-25.35	96.7		-25.35	88.8		71.7
	15°C	see above					30.02	77.8		30.02	47.3		64.7
2esg_sgp	2	-40.01	-35.34	113.2	-37.42	-39.82	-40.09	99.3	-41.06	-40.03	102.6	102.6	113.3
	3	35.83	46.39	77.2	37.44	35.58	46.28	76.9	33.73	46.33	72.8	94.1	99.9
3esg_sgp	2	-40.76	-36.67	111.1	-39.41	-42.53	-42.47	100.2	-43.90	-42.37	103.6	107.7	115.5
	3	48.92	47.61	102.7	30.69	28.74	42.00	68.4	26.66	41.99	63.5	54.5	88.2
	4	-35.81	-37.18	96.3	-37.29	-34.78	-34.97	99.5	-36.50	-34.89	104.6	101.9	93.9
	5	43.41	47.84	90.7	37.10	40.82	50.26	81.2	39.29	50.25	78.2	90.5	105.0

cb=cold bent ac=after autoclave process ar (24h)=24 hours after release ar (8m)=8 months after release

Table 6.5.: Comparison and change of stress in x-direction as calculated by FEA and measured with FBG at different test stages.



### 6.3.3.2. Results from the Four-Ply Specimens

As explained above in fig. 6.6 in section 6.1.2, the four-ply laminates 4esg\_sgp were equipped with fibres and FBG running in curvature direction along the central symmetry axis and along both lateral edges and being situated on the outermost laminated glass surfaces positions 2 and 7. FBG measurements were performed in the cold bent state (cb), after the autoclaving process but still being fixed on the mould (ac), 15min and 2h after release (ar) and in the built-in state as a double-hinged arch (sw). As the FBG and FEA results at 15min. and 2h after release are nearly identical, only the situation 15min after release is used in the following.

The detailed sensor measurement  $\sigma_x$  stress results for all tests phases, including cold bending, after autoclaving, springback after release and built-in as an arch subjected to self weight, from the specimens 4esg\_sgp-01 and -02 are depicted in in appendix E.3 in the diagrams fig. E.10 for position 2, where the sensors are subjected to compression stress, and fig. E.11 for position 7, where tension occurs. The wavelength shift and stress results are also provided in appendix E.3 in table E.5.

The mean values calculated for the fibres in the centre and along the boundaries are shown in comparison with  $\sigma_x$  values calculated by FEA in fig. 6.19 below. Results calculated from the FBG and from finite element analysis are plotted in comparison. As local deformation differences in the cold bending process are possible attributable to fabrication tolerances, two finite element studies for maximum arch rises of 131mm and 135mm are given. In table 6.6, the mean results calculated from the sensors 4 to 12, which exhibit similar stress values, are compared with corresponding finite element results for the four measurement stages cb, ac, ar and sw. The right-hand side of table 6.6 lists the wavelength and stress differences between the successive stages, for example, (ac-cb) means the difference occurring between the results after autoclaving and the cold bent state. Thus, the changes occurring between two stages can be directly compared.

The principal results are (compression results are treated as an absolute quantity for a better description of increasing or decreasing stress):

- The stress curves calculated from the FBG along the left and right boundaries (lateral) of the

laminates are either situated between the FEA results for an initial deformation of 131mm and 135mm or lie close to the 131mm approach. FBG results in the centre fibre mostly lie below the 131mm FE results. Generally, the stress measured with sensors 4-12 is better covered by the 131mm FE calculation, fig. 6.19.

- The stress caused by cold bending is approximately 45MPa at position 7 (tension) and -40MPa at position 2 (compression).
- In comparison with the cold bending stress, FBG sensors at position 2 show a compression stress increased by 11% after the autoclaving process, see table 6.6.
- Compared with the cold bent state, FBG sensors at position 7 exhibit a decrease in tensile stress by 8% after the autoclaving process.
- After release (ar), compression stress (pos. 2) monitored with the FBGs rises by 3.5MPa relative to the stress measured after the autoclaving process (ac), fig. 6.19 and table 6.6. FEA simulation gives a slightly higher absolute stress increase.
- After release (ar), tensile stress measured by FBG rises by 1MPa compared with the stress after the autoclaving process (ac). Stress results from the FE analysis indicate an increase of 4MPa to 5MPa.
- Tensile cold bending  $\sigma_x$  at position 7 along the boundaries is bigger than along the centre line, whereas compressive stress  $\sigma_x$  at position 2 is smaller along the boundaries and bigger along the centre line.
- With the laminate acting as an arch subjected to self-weight, the absolute stress measured by FBG slightly rises by 1MPa to 2MPa.

With regard to the stress distribution trend along the curved laminate and the behaviour in different fabrication stages, the stress calculated from the sensors and via finite element analysis demonstrates good agreement. After autoclaving, the tensile FBG stress exhibits a decrease and the compressive stress an increase with respect to the stress in the cold bent state.

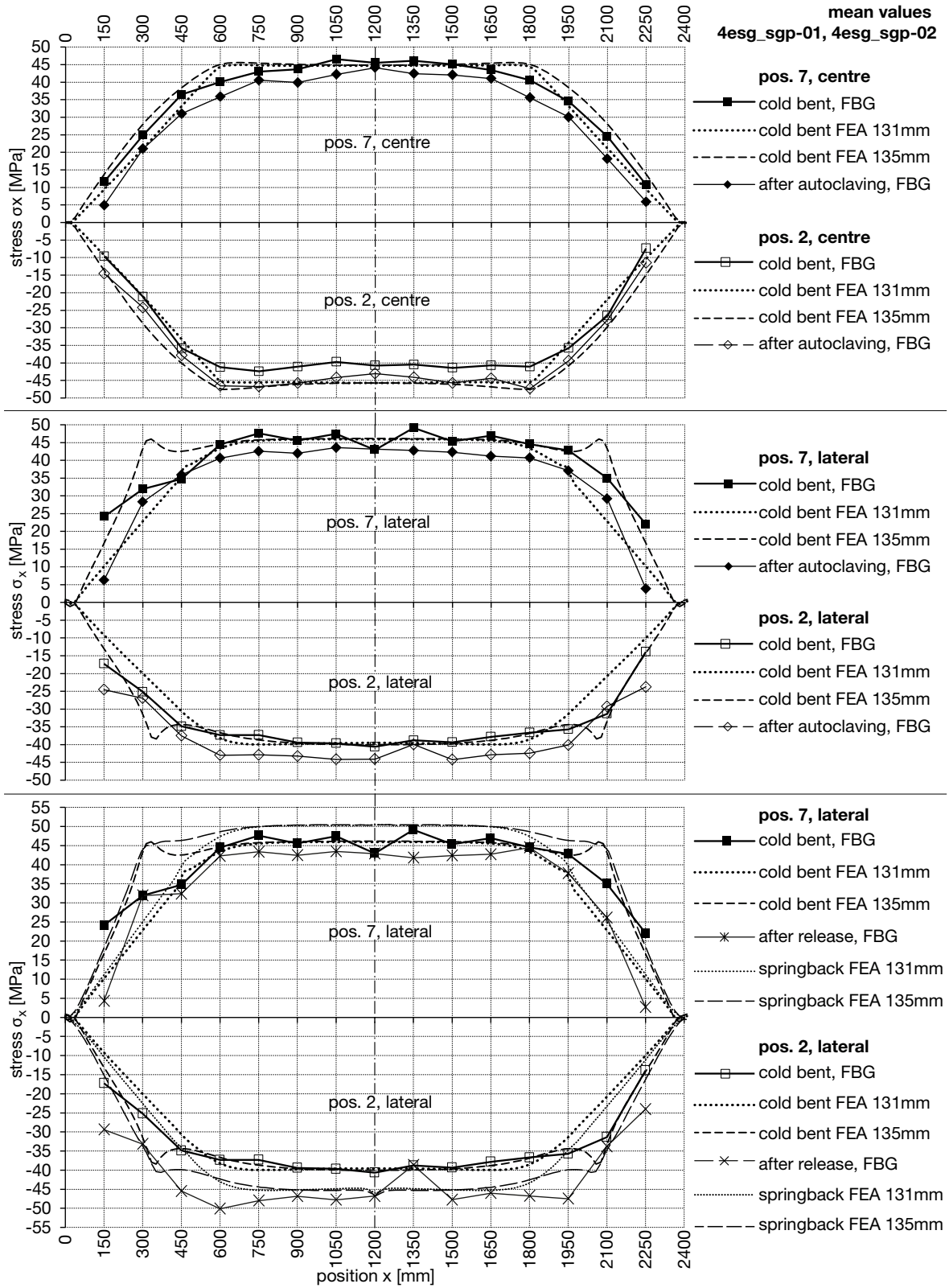


**Figure 6.19.:** Mean  $\sigma_x$  stress distribution from FBG and FE analyses for cold bending, after the autoclave process and after release / springback along the curved direction of laminate type 4esg\_sgp. Top: positions 2 and 7 along the central symmetry axis of the laminate; centre: positions 2 and 7 along the boundary of the laminate; bottom: positions 2 and 7 along the boundary of the laminate

testing and FE-analysis results							differences between stages			
pos.	stage	testing (FBG)		FEA (131mm)	FEA (135mm)	mean $\sigma_{x(\text{FBG})}$ / $\sigma_{x(\text{FEA131})}$	stages $\Delta_{i,j}$	testing		FEA (131mm)
		mean $\Delta\lambda$ [nm]	mean $\sigma_x$ [MPa]	mean $\sigma_x$ [MPa]	mean $\sigma_x$ [MPa]	[%]		$\Delta\lambda_{i,j}$ [nm]	$\Delta\sigma_{x,i,j}$ [MPa]	$\Delta\sigma_{x,i,j}$ [MPa]
7 lateral	cb	0.88	46.00	45.33	45.72	101.48	cb-in	0.88	46.00	45.33
	ac	0.73	42.03	45.33	45.72	92.71	ac-cb	-0.16	-3.92	0.00
	ar	0.75	42.81	49.15	49.47	87.10	ar-ac	0.03	0.78	3.82
	sw	0.71	44.83	-	-	-	sw-ar	-0.04	2.02	-
centre	cb	0.84	43.78	44.71	45.11	97.92	cb-in	0.84	43.78	44.71
	ac	0.70	40.40	44.71	45.11	90.37	ac-cb	-0.14	-3.37	0.00
	ar	-	-	49.67	50.34	-	ar-ac	-	-	4.96
	sw	-	-	-	-	-	sw-ar	-	-	-
2 lateral	cb	-0.63	-38.55	-39.36	-38.84	97.95	cb-in	-0.63	-38.55	-39.36
	ac	-0.78	-42.99	-39.36	-38.84	109.22	ac-cb	-0.16	-4.44	0.00
	ar	-0.83	-46.51	-44.68	-44.53	104.10	ar-ac	-0.05	-3.52	-5.32
	sw	-0.93	-47.67	-	-	-	sw-ar	-0.10	-1.16	-
centre	cb	-0.67	-40.99	-45.44	-46.44	90.20	cb-in	-0.67	-40.99	-45.44
	ac	-0.83	-45.32	-45.44	-46.44	99.72	ac-cb	-0.16	-4.33	0.00
	ar	-	-	-49.99	-51.04	-	ar-ac	-	-	-4.55
	sw	-	-	-	-	-	sw-ar	-	-	-

stages, boundary conditions:

in initial

cb cold bent

ac after autoclaving, prior to release

ar after release, resting on the mould

sw laterally supported arch, self weight

FE-model:

FEA (131):

FEA (135): max. deformation  $u_z=131\text{mm}$

max. deformation  $u_z=135\text{mm}$

stage differences  $i, j$ : e.g. ac-cb=stress difference

between cold bending (cb) and after autoclaving (ac)

**Table 6.6.:** FBG sensor wavelength shift and x-stress results at different testing stages compared with FE analyses with maximum displacements of 131mm or 135mm.

### 6.3.4. Summary of the Testing Results

Close range photogrammetry is applicable for 3D shape / displacement measurement and reaches high precision and accuracy depending on the quality of the photographic monitoring. FEA with viscoelastic interlayer models for PVB as in [And 14] and for SG as in [Ben 13] complies with the testing results from photogrammetry and FBG sensing  $\sim 20^\circ\text{C}$  and can be used to simulate the laminate behaviour with a contact element model FSD.2.

PVB specimens show a continuous strong relaxation at  $20^\circ\text{C}$  during the test time of 8 months and cannot preserve a relevant curvature or stress level in the long term. During this period, the two-ply PVB laminates lose 40% of their initial cold bending deformation. The SG laminates preserve a constant level of curvature and of stress after springback and show practically now further relaxation at room temperature. The two-ply SG laminates recovers by 17% and the three ply SG laminate by 7% during 8 months.

Planar or low curvature zones develop at the narrow ends of the bent glass laminates that stretch by less than 15% (SG) or less than 30% (PVB) in the curvature direction. Anticlastic disturbance zones along the laminate boundaries from cold bending vanish with PVB laminates during relaxation, but are partially preserved in SG laminates.

specimen	pos.	FBG	FEA
2esg_pvb	2 (compr.)	-	61%
	3 (tens.)	30%	55%
2esg_sgp	2 (compr.)	103%	113%
	3 (tens.)	94%	100%
3esg_sgp	2 (compr.)	108%	116%
	5 (tens.)	91%	105%
4esg_sgp	2 (compr.)	120%	114%
	7 (tens.)	93%	108%

**Table 6.7.:** Summary of the stress ratio after 8 months to the cold bending stress level (=100%) for FE and sensor analysis. (\* Ratio of the stress after autoclaving and after release.)

Comparing the stress results both from the FBG and finite element analysis of the cold bent state and after 8 months of relaxation, as shown in table 6.7, the tendencies exhibited by the FBG sensors and the numerical analyses are identical. The maximum stress occurs during springback at the outermost interfaces of glass and the interlayer. It can exceed the initial cold bending stress by 10%. With an increasing laminate thickness or increasing number of glass layers or higher shear stiffness of the interlayer, the laminate shows a

decreasing springback and relaxation behaviour and an increase of the additional glass stress during the springback. With the PVB laminates 2esg\_pvb, both the tensile and the compression stress are continuously reduced with ongoing relaxation time. With both SG-laminates 2esg\_sgp and 3esg\_sgp, the stress increases with relaxation time compared with the cold bent state. After springback, the SG laminates constantly preserve this stress level.

specimen	pos.	$\sigma_x$ (cb)	$\sigma_x$ (ac)	$\sigma_{x(ac)} /$
		(mean)	(mean)	$\sigma_{x(cb)}$
		[MPa]	[MPa]	[%]
2esg_pvb	2	-	-32.73	-
	3	47.11	37.89	80.4
2esg_sgp	2	-40.01	-37.42	93.5
	3	35.83	37.44	104.5
3esg_sgp	2	-40.76	-39.41	96.7
	3	48.92	30.69	62.7
	4	-35.81	-37.29	104.1
	5	43.41	37.10	85.5
	7	-38.55	-42.99	111.5
4esg_sgp	7 <sub>l</sub>	46.00	42.03	91.4
	2 <sub>c</sub>	-40.99	-45.32	110.6
	7 <sub>c</sub>	43.78	40.40	92.3
	7 <sub>l</sub>	46.00	42.03	91.4

**Table 6.8.:** Comparison of the mean stress values in the x-direction for the stages cold bent (cb) and after autoclaving (ac).

The trend of the development of the stress in cold bent lamination-stabilised glass during cold bending, after lamination and during the springback / relaxation after release from the bending mould measured with fibre Bragg grating sensors corresponds to the results from FEA. Even slight changes in exterior loading or temperature trigger a real-time response of the FBG. The fibre-optic sensors, their coating and the adhesive bond resist the autoclave conditions and they are barely visible in the glass laminate.

However, differences occur in the tensile and compressive stress level prior to and after the autoclaving process. The systematic representative decrease in tensile stress by 8% and the increase in absolute compression stress by 11% as in table 6.8 seen with laminate type 4esg\_sgp give rise to assumptions related to the temperature-dependent behaviour of the different materials bonded to each other, e.g. the fibre, its coating, the adhesive, the glass substrate and the polymer interlayer. Investigations undertaken in this context are presented in the following section 7.1, 7.1.2.

## **7 Discussion, Transfer**

## 7.1. Monitoring Feasibility of Glass Laminates by Applying Fibre Optic Sensors

### 7.1.1. FBG Transverse Effect Results and Sensor Robustness

In order to obtain valid strain results in the axial direction of the FBG, the presence of birefringence in the sensor must be excluded; this effect is typically caused by transverse loads orthogonal to the fibre section, see fig. 5.9 in section 5.1.1.7.

Studies of the stress states acting in bonded and laminated FBG and the related birefringence of the FBG by numerical micro-mechanical models are shown in section 5.1.6. In brief, the birefringence determined with the models for a surface-bonded fibre embedded into an SG interlayer in the context of cold bent glass is  $\pm 0.0004\text{nm}$  for a total  $\Delta\lambda$  of  $0.7\text{nm}$ , table 5.12 in section 5.1.6.5. This quantity is estimated as being negligible in this work. The gauge factor of  $k_\epsilon$  of  $0.790$  is applicable and slightly rises to  $0.80$  with ongoing relaxation time. Other than the process of vacuum bagging, large transverse strain orthogonal to the glass surface is not expected to occur often, as glass laminates usually work in bending and the strain in the thickness direction is a minor component in the related strain states. This has also been shown by the micro-mechanical FE studies in section 5.1.6.2.

The spectral width of the wavelength peak signal of an FBG can be used as a control parameter for the occurrence of birefringence. Therefore, the spectral width at  $-3\text{dB}$  (or at  $50\%$  of the peak amplitude in the normalised representation) is determined from the spectra during the testing period. Typical spectral width results of the FBG used in this research are in a range of  $0.09\text{nm}$  to  $0.1\text{nm}$ . Broadening of the spectrum or double peaks can thus be identified in comparison with this basic width value. In section 5.1.5.3, table 5.8, spectral width monitoring of the four-point bending test specimens with surface-bonded sensors prior to and after the autoclave-like temperature cycle of  $140^\circ\text{C}$  has been performed previously. No systematic substantial spectrum broadening has occurred in this testing procedure.

The principle of using FBG in glass laminates for glass surface stress measurement is based on the hypothesis that potential local transverse loads acting on the sensors during the cold bending process<sup>35</sup> or in the vacuum bag vanish in the autoclave process because of the interlayer melting (SG) or softening (PVB) at the process temperature of  $140^\circ\text{C}$ . Thus, transverse loads are no longer transferred by the interlayer or they are evenly distributed over the entire surface and so have minor influence on the FBG. In the testing of all specimen types 2esg\_pvb, 2esg\_sgp, 3esg\_sgp and 4esg\_sgp, stress monitoring with the FBG has been exclusively based on the measurement of spectra. This enables the control of the spectra with respect to spectrum broadening / double peaks as an indicator for transverse load influence.

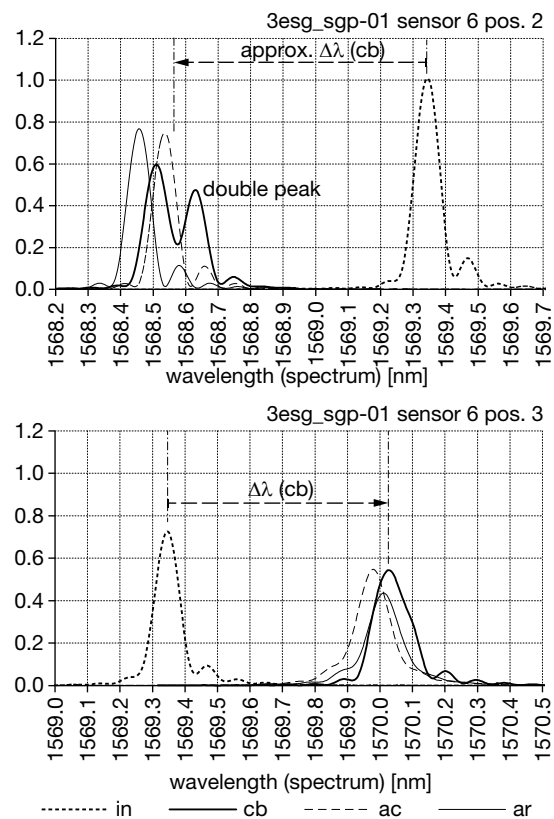


**Figure 7.1.:** Example FBG-spectra from laminate 3esg\_sgp-01 for the process stages cold bending (cb), after autoclaving (ac) and after release from the bending mould (ar). Top: FBG subjected to compression, double peak occurs during cold bending. Bottom: Tensile strain acting in the FBG.

<sup>35</sup>Loads perpendicular to the glass surface can occur at locations at which the glass-interlayer stacks are directly pressed against the mould during cold bending. Vacuum drawing of the vacuum bag is another important reason causing transverse forces.

<b>summary:</b>	<b>pos. 2</b>	<b>pos. 3</b>	<b>pos. 4</b>	<b>pos. 5</b>	<b>pos. 7</b>	<b>total (mean)</b>	<b>unit</b>
applied sensors:	144	54	18	18	90	324	[-]
sensor losses*:	0	9	0	0	15	24	[-]
birefringence at cold bending (incl. vacuum)	14	10	12	3	3	42	[-]
permanent birefringence (double peaks):	5	3	0	2	1	11	[-]
mean initial spectral width (in):	0.0887	0.0883	0.0846	0.0878	0.0970	0.0893	[nm]
spectral width at cold bending (cb)	0.1161	0.1370	0.1381	0.1217	0.1578	0.1341	[nm]
spectral width cold bent with vacuum (cb(ev))	0.1525	0.2357	0.1710	0.1079	-	0.1668	[nm]
mean spectral width after autoclaving (ac)	0.1000	0.1042	0.1023	0.1145**	0.1030	0.1024	[nm]
mean spectral width after release (ar)	0.0961	0.1031	0.1017	0.1731**	0.1029	0.1009	[nm]

\*sensor losses: 15 not connectable due to breakage of the fibre at the exit

9 due to fibre rupture between two sensors plus breakage of the fibre at the exit

\*\* result distortion by large double-peak outliers (thus excluded from total mean results)

**Table 7.1.:** Summary of the spectral width values for all cold bent glass specimens and sensor robustness statistics.

Examples of spectra from the characteristic testing stages initial (in) with the reference Bragg wavelength  $\lambda_{B,0}$ , during cold bending (cb), after autoclaving (ac) and after release (ar) are shown for specimen 3esg\_sgp-01 in fig. 7.1. The top diagram demonstrates, that a double peak occurs at sensor 6 in position 2 (concave glass surface, compression) in the cold bent state. After autoclaving, the birefringence effect vanishes as expected and does not occur again after release. The spectra of the same process stages are shown at the bottom of the diagram for a sensor at position 3 (tensile strain). No significant spectrum broadening or double peaks are identified here. In some cases, spectra have been monitored during vacuum drawing of the laminate enclosed in the vacuum bag. In this stage, many sensors show double peaks, as pronounced transverse forces act on the glass-interlayer stacks and subsequently on the sensors. As the sensors are not yet laminated, they react as in similar way as a free FBG to transverse forces and exhibit a high transverse force sensitivity causing strong birefringence.

A systematic spectral width monitoring is depicted in fig. 7.2 for the laminate 4esg\_sgp-02 for the stages initial / after sensor gluing (ag), cold bent (cb), after autoclave (ac), after release from the mould (ar) and as an arch subjected to self-weight (sw). Out of the 45 FBG shown, four exhibit significant spectral width broadening.

In two cases, this phenomenon has been related to a brittle failure of the adhesive bond, which probably occurred prior to the lamination. In two cases, the birefringence is kept upright after lamination in the autoclave. The mean spectral width values from all cold bending specimens tested here are listed in table 7.1. The total mean spectral width, which is initially about 0.089nm, broadens to 0.13nm (or to 0.167nm in the vacuum bag) in the cold bent stage. After autoclaving and during the rest of the tests, the mean spectral width drops to 0.1nm again. This clearly supports the initial hypothesis of vanishing birefringence during autoclaving. An entire summary of the double peaks identified in all curved glass specimens is provided in table E.6 in appendix E.3.

In total, 324 FBG were installed in this first experimental approach. Out of 24 sensors that did not respond after the autoclaving process, 15 could not be contacted because the fibre was broken at both exits from the laminate. Thus, a real loss of only 9 sensors has to be accounted for that is mainly attributable to fibre breakage at tight curves in the nine laminates of the two-ply and three-ply test series. Permanent transverse load influence and the respective sensor birefringence during the entire testing period have been identified for 11 sensors out of 324. Transverse load influence and the related birefringence of the FBG are thus not a major issue in cold bending with lamination.

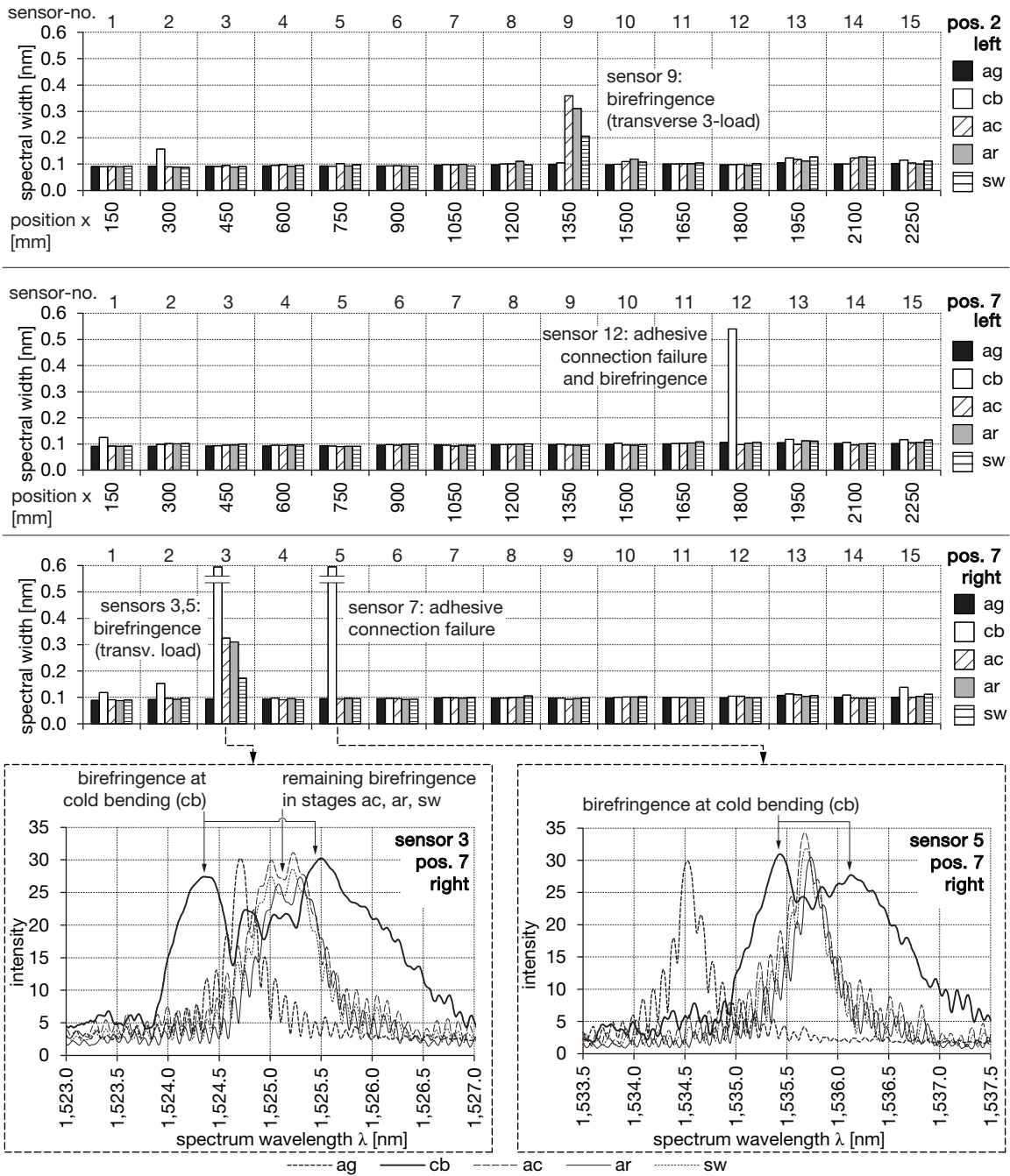


**Figure 7.2.:** Spectral width monitoring of three chains of 15 FBGs each from specimen 4esg\_sgp-02 at pos. 2 (left) and pos. 7 (left, right). Spectra for sensors 3,5 at pos. 7 (right) are given as an example at the bottom. The process stages are: ag=initial zero-state after sensor bonding, cb=cold bent state, ac=bent state after autoclaving, still fixe to the mould, ar=15 minutes after release from the mould, sw=built-in as arch subjected to self-weight.



### 7.1.2. FBG Result Evaluation

As shown in the table 7.2, the stress measured with the FBGs after the autoclave process shows a decrease of the tensile and an increase of the (absolute) bending stress in comparison with the cold bending stress. For tension, a mean reduction to 86% of the cold bending stress and for compression a mean increase to 104% are identified. The sensor wavelength shift throughout the entire testing period has therefore been referenced to the wavelength measured on the planar glass prior to the bending procedure. An attempt to equate the wavelength measured after lamination with the wavelength in the cold bent state prior to autoclaving has been successful for correcting the above stress variation in a few cases but has generally been found to be too sensitive with respect to potential deviations of the wavelength results from cold bending. Thus, results from this method are not shown in this work.

specimen	pos.	FBG			FEA	
		$\sigma_x$ (cb)	$\sigma_x$ (ac)	$\sigma_{x(ac)} / \sigma_{x(cb)}$	$\sigma_x$ (cb)	$\sigma_{x(ac)} / \sigma_{x(cb)}$
		(mean)	(mean)	[%]	[MPa]	[%]
2esg_pvb	2	-	-32.73	-	-35.34	92.61
	3	47.11	37.89	80.4	46.39	81.68
2esg_sgp	2	-40.01	-37.42	93.5	-35.34	105.88
	3	35.83	37.44	104.5	46.39	80.70
3esg_sgp	2	-40.76	-39.41	96.7	-36.67	107.46
	3	48.92	30.69	62.7	47.61	64.46
	4	-35.81	-37.29	104.1	-37.18	100.31
	5	43.41	37.10	85.5	47.84	77.56
4esg_sgp	2 <sub>l</sub>	-38.55	-42.99	111.5	-39.76	108.12
	7 <sub>l</sub>	46.00	42.03	91.4	45.33	92.72
	2 <sub>c</sub>	-40.99	-45.32	110.6	-45.44	99.74
	7 <sub>c</sub>	43.78	40.40	92.3	44.71	90.36

indices: c=centre; l=lateral (right / left side)

**Table 7.2.:** Comparison of the mean x-stress in the cold bent state (cb) and after autoclaving (ac) derived from FBGs and finite element analysis.

Table 6.7 reveals, that, subsequently, the long-term tensile stress measured with the sensors is also lower compared with that of the finite element calculations. However, a comparison of FEA-data to sensor results necessitates careful evaluation, as a model cannot fully integrate or cover all the potential imperfections, aberrations and real material behaviour occurring in a physical test. Various hypotheses have been examined for explaining the variation of the FBG-calculated stress values prior to and after autoclaving and from the stress determined by finite element analysis. As the variation occurs

between the stress introduced by cold bending and the stress measured after the autoclaving process, the discussion notably concerns the influence of temperature on the fibre bond and on the compound with the interlayer.

- The strain distribution along a cross section of the fibre in the bent laminate after strong relaxation influence studied with the FE micro-model is shown in section 7.1.2.1.
- The influence of the temperature on the adhesive bond of the fibre during the autoclave process is discussed as a potential reason of the measurement variation of the FBGs on the basis of the tests from previous chapters in section 7.1.2.2.
- For a basic evaluation of the behaviour of FBGs bonded to glass in an autoclave lamination process, a brief examination of the monitoring of such a process involving FBGs is performed in section 7.1.2.3.
- As the effect of the heating and cooling process in the autoclave and its effect on the residual fibre stress caused by the different thermal expansion of the bonded materials has not been monitored, a transient finite element model is used to simulate the temperature gradients in the laminate, see section 7.1.2.4.
- In section 7.1.2.5, the handling, applicability, quality and operability of fibre-optic sensors with Bragg gratings for the use in glass laminates is discussed.

7.1.2.1. Analysis with the Micro-Mechanical FE Model

Fig. 7.3 shows a cross section of the SG laminate in the zone of the fibre bond and the SG interlayer from the micro-mechanical studies undertaken in section 5.1.6.2. In the cold bent state, the bending strain in the fibre only depends on the bond quality; the gradient of the bending strain in the glass and the fibre is constant and the strain distribution curve is linear. During the springback, strain develops in the interlayer from the shear compound and from the bending moment developing in the compound that stabilises against the return moments of the glass. The interlayer strain grows with ongoing relaxation time and exhibits a non-linear increase in the proximity of the fibre. The gradient of the strain distribution in the fibre now differs from the bending strain gradient in the glass.

From the model it cannot be clearly distinguished, if the fibre is subjected to additional normal forces from the sandwich effect during the recovery of the laminate; an influence of the surrounding interlayer on the interior strain state of the fibre can be assumed. In the case of this model configuration, the strain in the fibre core during springback / relaxation is slightly larger than it would be expected for a perfect bond of a fibre to the glass, compare section 5.1.6.2. However, the influence of the interlayer is extremely small and the fibre bending strain still depends mainly on the strain state of the glass substrate. The model delivers no explanation for the decrease in tensile strain and the increase in compressive strain after the autoclave process but permits to exclude the influence of the interlayer during relaxation as a potential source of strain deviation.

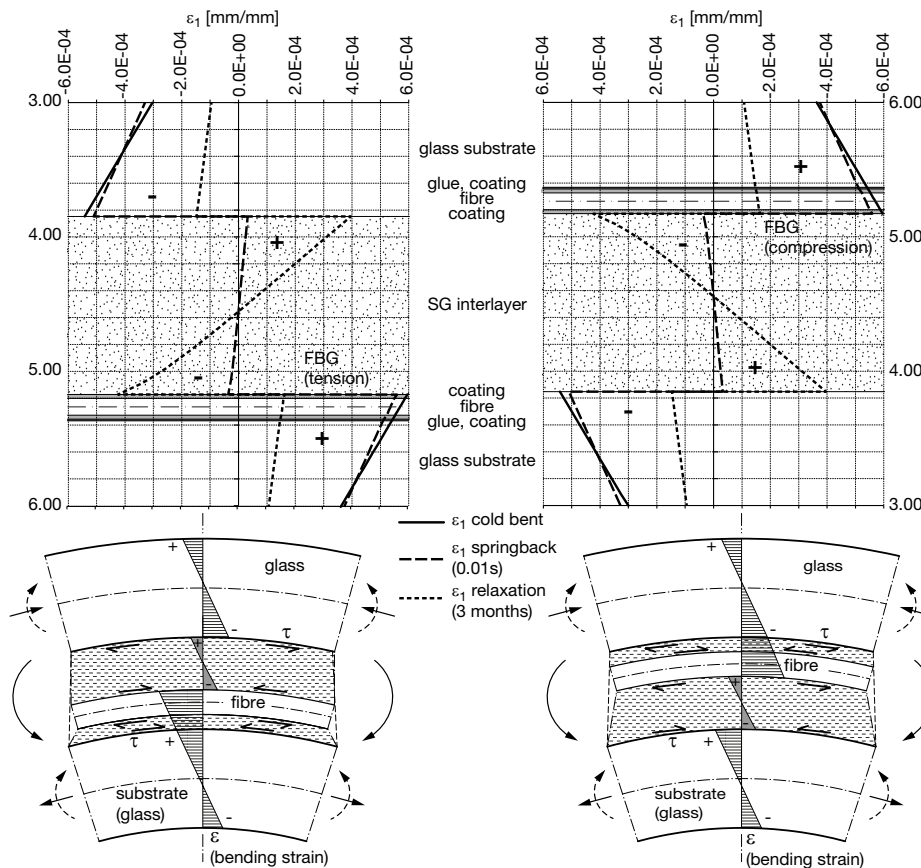


Figure 7.3.: Cross section of the fibre bond and the interlayer depicting the  $\epsilon_1$  strain distribution during springback and relaxation of a two-ply SG glass laminate.

### 7.1.2.2. Potential Influence of the Adhesive Bond

A potential reason for the modified wavelength shift measurement of the FBGs after autoclaving is a temperature-induced change of the adhesives used for the fibre bonding or an alteration of the bond itself. The examination of the adhesives in section 5.1.3 and the four-point bending tests described in section 5.1.5.3 allow an evaluation of these influences.

All adhesives applied for the fibre bonding in this work are cured by UV-light. Post-cure from temperature influence is described in the literature, for example, [Sch 10, p. 104], as a possible reason for the shrinkage of epoxy adhesives. Such shrinkage can cause compression in a bonded fibre or can lead to birefringence effects as examined by [Hel 14], [Sto 97] and [Par 10]. The DSC-analyses shown in section 5.1.3.4 have therefore been performed to identify potential chemical reactions of adhesives subjected to increasing temperature after UV cure, compare [Wel 11a]. The analysis results of the two adhesives mainly applied for the specimens in this work are depicted in fig. 5.25. The adhesive KB4552 used for the bonding of the FBG with the nine specimens for long-term testing, 2esg\_pvb, 2esg\_sgp and 3esg\_sgp, exhibits a pronounced post-cure reaction in a temperature range of 90°C to 135°C. The manufacturer indicates a volume shrinkage of 3.7% [Del 14] for this product. The second product, KB OB642, which has been used with the sensitive glass arches 4esg\_sgp, shows only minor temperature-related changes.

The temperature-related behaviour of FBG bonded to a glass specimen has additionally been examined by four-point bending, as described in section 5.1.5.3. Both adhesives mentioned above have been used in the tests. A simultaneous measurement of the influence of tension and compression on the sensor measurement has been made possible by the bonding of FBG to the top and bottom surface of the glass. The tests simulated the temperature cycle of an autoclave process. The wavelength measured at the unloaded state after the tests differed by a maximum of about  $\pm 0.07\text{nm}$  from the initial wavelength prior to testing, which corresponds to a maximum stress variation of  $\pm 4\text{MPa}$ . No dependency of this deviation on the tensile or compressive strain state of the FBG during the tests was revealed. These results thus do not allow to a conclusion to be drawn regarding a

systematic loss of tensile stress and an increase in absolute compression strain, as seen with the cold bent real scale laminates.

The adhesive KB4552 does not suffer a more pronounced negative wavelength shift after the test than does KB OB642. From this, we can conclude that possible post-cure and shrinkage effects do not affect the adhesives in a different way. The sensor spectra prior to and after the four-point bending tests have not revealed a relevant broadening in spectral width; a significant influence of birefringence on the measurement of a surface-bonded fibre caused by the reaction of the adhesives to temperature can thus be excluded here. The creep / relaxation studies regarding the fibre bond to the glass substrate in section 5.1.5.3, fig. 5.44, table 5.10 and section 5.1.5.4 have identified a creep loss of wavelength shift in the order of only 0.0065nm measured during the constant temperature and load phase of approximately three hours. With sensors subjected to tension, this creep effect is lower than that of sensors under compression.

Hence, the creep / relaxation behaviour, potential adhesive effects or residual compressive stress from cooling of the fibre bonded to glass identified in the four-point bending tests are not suited to explain entirely the change in wavelength by about -0.10nm after the autoclaving process. Remarkably, however, that the four-point bending tests revealed the potential, relatively large scatter of the wavelength shift results after the thermal cycle.

Ganß [Gan 15, pp. 361-371] has recently performed tests with FBG integrated into the structural adhesive bond of two glass panes made with an epoxy and an acrylate glue to study the change of the properties of the adhesive bond subjected to thermo-mechanical loads. In cyclic temperature loading, the FBG integrated into the joint made with the acrylate adhesive exhibit an increasing wavelength shift with each new temperature cycle. This indicates modifications of the adhesive caused by the temperature cycles. However, the nature of these changes and the interdependencies of the modification of the adhesive, the FBG and the glass cannot be deduced directly and show the complexity of monitoring effects with FBG inside bonded material compounds.

7.1.2.3. Autoclave Process Monitoring

The monitoring of an autoclave process with FBG was performed in the context of a research project at the ITKE with glass laminates having a different composition and interlayer material<sup>36</sup> than used in this thesis. However, the interpretation of the monitoring results is of interest with regard to knowledge of the principal influence of the autoclave process on the sensor wavelength shifts at the beginning, during the course and at the end of the process. The process started with a temperature level of 21.2°C. After autoclaving, the laminate was removed from the autoclave at a temperature of about 25°C. A vacuum bag was applied. Fig. 7.4 shows the process, the temperature and measured wavelength shifts of a sensor bonded to a glass surface in the laminate at position 3 (the top surface of the second glass layer) and of a nearby free temperature compensation FBG.

The diagram shows that, even after a certain time at constant maximum air temperature, the bonded sensor still has not reached a constant measurement level. The wavelength shift still rises, although with a decreasing gradient, until the start of the

cooling phase. This example shows that sufficient time is necessary for a laminate to reach uniform temperature through its entire thickness. Whether this FBG behaviour is only caused by the delayed heating of the interior of the laminate compared with the constant air temperature cannot be deduced. The temperature behaviour of the adhesive and the coating of the fibre can also have an influence. The expected wavelength shift of the bonded sensors at maximum temperature is 1.92nm and 1.03nm for the free sensor. These values are approximately signalled by the sensors at the end of the constant temperature phase: the maximum mean wavelength shift measured with the bonded sensor is 1.82nm and about 1.05nm with the free sensor.

Calculation of the stress caused in the fibre by the differential thermal strain of the fibre and the glass substrate results in 46-51MPa tensile fibre stress at maximum measured air temperature, as calculated from the sensor wavelength shift of the bonded fibre in the laminate and of the free temperature-compensation sensor. On the assumption of a perfect bond of the fibre and the glass and no disturbing influence from the adhesive and the coating, a maximum idealised stress of 55MPa is expected.

<sup>36</sup>An interlayer material softer than PVB was applied.

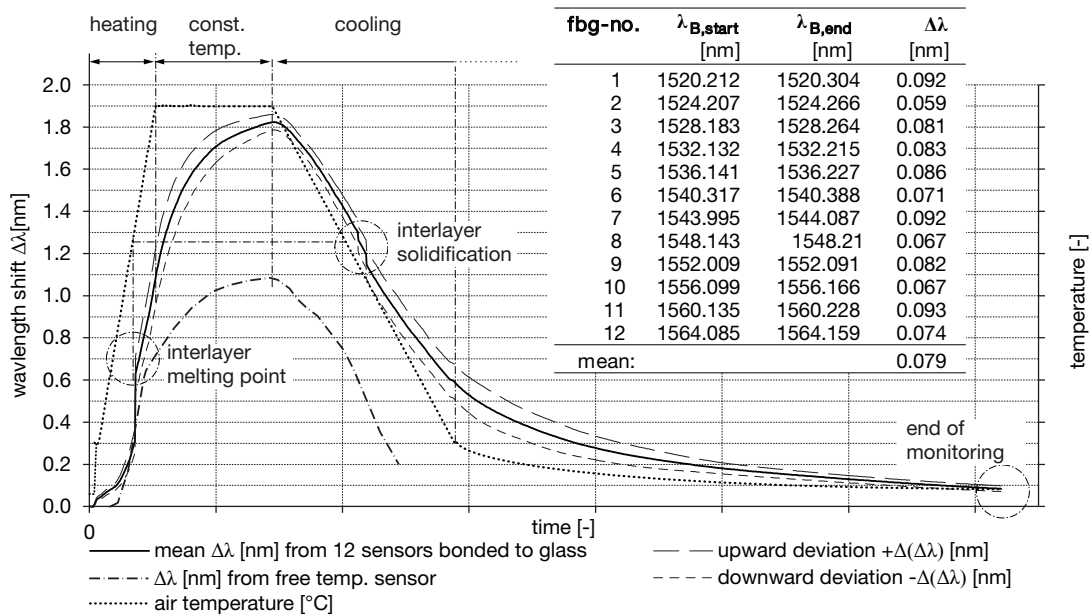


**Figure 7.4.:** Example of the monitoring of an autoclave process with FBG bonded to glass and a free FBG for temperature compensation. The table at the right shows the difference of the initial and final wavelength of the 12 bonded sensors.

The disturbances in the continuity of the gradients of  $\Delta\lambda$  of the bonded sensor during heating and cooling indicated in fig. 7.4 can be interpreted as the melting and solidification point of the polymer interlayer; this corresponds well to the property data provided by the manufacturer.

After the process, the sensors exhibit a mean wavelength difference of +0.08nm with respect to the initial conditions. The air temperature at the end of the entire process was about 3°C to 4°C higher than the initial temperature of 21.2°C. This temperature difference can partially be a cause of the wavelength difference. Even though the exact temperature inside of the glass laminate is not known, the sensors nearly return to their initial level of Bragg wavelength. Thus, the autoclave lamination process in this case apparently does not cause a major negative shift in the sensor signal. This conclusion is of interest, as the diverse thermal expansion and temperature-dependent stiffness of the bonded adjacent materials, which are the glass substrate, adhesive, coating, the silica fibre core and the interlayer, might cause residual stress in the fibre during the cooling of the laminate, when the bonding of all components is established by the solidifying interlayer. Whether the same behaviour applies for PVB or SG interlayers cannot be stated with certainty but the monitoring nevertheless gives emphasis to the hypothesis that no major strain is introduced into a glass-bonded fibre during the autoclave process. As the autoclave monitoring described above was performed with a planar laminate, we cannot conclude whether a prestressed fibre on a cold bent glass would react the same way.

With regard to other reasons of potential residual stress introduced to the sensors during the heating and cooling in autoclave process, additional hypotheses can be assumed. Figure 7.5 schematically illustrates the entire process of the cold bending and lamination in an autoclave and subsequent cooling. During the heating, the free part of a fibre between two bonded sensor locations might be stretched because of the thermal expansion of the glass substrate being 16 times greater than the expansion of the fibre. In cases in which the fibre between two bonds has no additional relief length to compensate the different thermal expansion values, the sensor bonds can be subjected to additional tension; this causes creep at the sensor locations and subsequent permanent wavelength shift loss  $\Delta(\Delta\lambda)_{bond}$ .

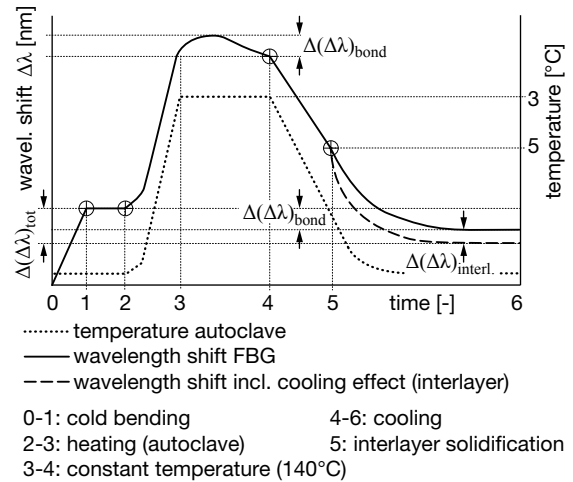


**Figure 7.5.:** Hypothetical influence of the adhesive bond of the fibre and of the interlayer solidification during the cooling process on the wavelength shift measured with an FBG.

As seen above with the soft interlayer material in fig. 7.4, the solidification of the interlayer during cooling is visible in the wavelength shift of a sensor bonded to glass. The negative expansion of the interlayer is usually 10-20 times higher than the thermal expansion of the glass; this can cause compression and the respective wavelength shift change  $\Delta(\Delta\lambda)_{interl.}$  in the parts of the fibre being in contact with the surrounding interlayer. Neither could be verified practically in the scope of this work, however.

In the 2015 report [Int 15], 10 hours of storage of the coated fibre at a temperature of 150°C are shown to lead to a decrease of the measured wavelength by 0.055nm. This is close to the 8% to 10% wavelength change after autoclaving, equivalent to 0.056 to 0.07nm, identified in this work. Following the report, the decrease in wavelength is attributable to post cure effects, which, however, have not been identified by DSC in this work, see fig. B.5 in section B.2.

#### 7.1.2.4. Transient Numerical Model

Three transient finite element models, which simulate the temperature gradient through the thickness of the laminate during the autoclave process have been studied in the context of this work. The heating and cooling phase of the process is taken into account by convection of the even glass surface and the increasing or decreasing temperature of the air flowing around the laminate. The temperature-dependent material moduli of the interlayer, the adhesive and fibre coating from sections 5.3.2 and 5.1.3 are integrated into the model. Three approaches have been studied, which are briefly discussed below.

A entire specimen of the type 2esg\_sgp from 2x6mm FTG subjected to cold bending deformation ( $\pm 45\text{MPa}$ ) and subsequent lamination with 1.52mm SG was analysed to examine cooling effects after the autoclave process on potential residual stress in the laminate. Below a temperature of  $55^\circ\text{C}$ , the SG-interlayer was assumed to be sufficiently stiff to permit full load transfer. Therefore, only the cooling process in the autoclave from  $55^\circ\text{C}$  to  $25^\circ\text{C}$  (flowing air, increased convection) for a period of 2.5h followed by 7.5h of cooling from  $25^\circ\text{C}$  to  $23^\circ\text{C}$  with stationary air (less convection) was simulated. As a result, the absolute compressive stress from cold bending increased by 2% (1MP) and the tensile stress decreased by 1% (0.5MPa). This glass stress alteration can thus explain a small portion of the stress change experienced with the FBG from the tests.

The entire geometry of a sensor bonded to glass, the cold bending, the lamination and cooling were examined with a transient micro multi-physics model of 2x4mm FTG and 1.52mm SG-interlayer based on the setup shown in section 5.1.6.1. Only the cooling process was assumed in the model. Therefore, the interlayer is actuated at  $55^\circ\text{C}$  and the entire laminate was cooled to  $25^\circ\text{C}$  and then to  $23^\circ\text{C}$ , as explained above. As a result, the sensor fibre was subjected to a high residual compressive stress of about -19 MPa at the end of 10 hours of cooling. The respective stress strain at  $25^\circ\text{C}$  and at  $23^\circ\text{C}$  are depicted in fig. 7.6. The axial strain  $\epsilon_x$  remains constant through the thickness of the fibre core but the components  $\epsilon_{y,z}$  vary and therefore birefringence occurs, similar as in the uniform cooling studies in section 5.1.6.4. Even though this remaining compression strain in the fibre is too high, the study,

however, shows that residual compressive stress in the fibre can develop in the fibre during the cooling process. This effect is largely dependent on the thermal expansion coefficient, the adherence, the solidification temperature and the stiffness of the involved materials. A weakness of the model is the simplified assumption of a sudden solid interlayer actuation at  $55^\circ\text{C}$ .

The decrease in tensile stress and the increase in (absolute) compressive stress in the sensors particularly visible in figure 6.19 can be explained by the compression developing in the bonded fibre during cooling after solidification.

With respect to the extensive analysis time necessary for the above micro-model, a study of the entire autoclave process has been performed for a sensor bonded to only one glass pane ( $t=4\text{mm}$ ). The material moduli depending on temperature are integrated into the model. Time steps of 1.5h of heating to  $140^\circ\text{C}$ , 3h at constant  $T=140^\circ\text{C}$ , 3h of cooling to  $25^\circ\text{C}$  and an additional 7h of cooling to  $23^\circ\text{C}$  are simulated in the transient model. As a result, a negligible residual stress remains in the fibre core after the entire process. As the model does not take into account the interlayer and lamination, this model does not explain the behaviour of the bonded fibre after the autoclaving. However, the question of the fibre behaviour after autoclaving can be narrowed to the influence of the interlayer on the fibre during the cooling process.

As the real softening and solidification behaviour and the relative adhesion or cohesion of all materials involved is not exactly known, the transient model studies can only serve as a basic sensitivity analysis here.

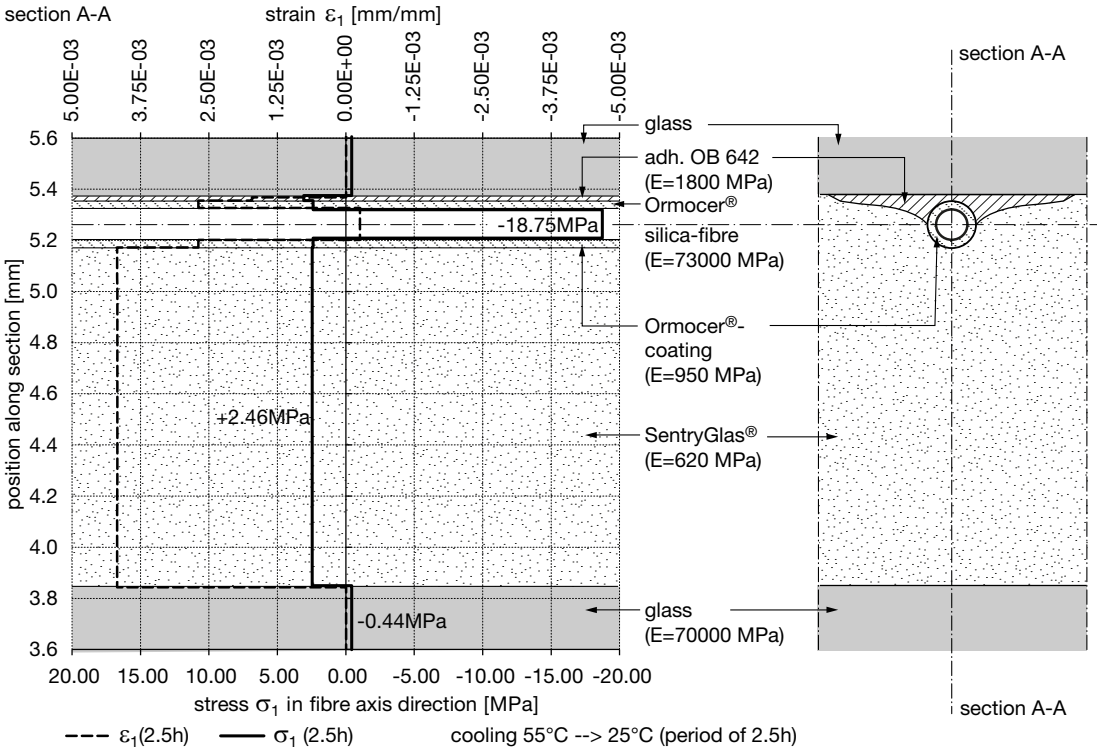


Figure 7.6.: Compression axial strain  $\sigma_x$  and transverse components  $\sigma_{y,z}$  developing in a bonded fibre during cooling from 55°C to 23°C. A section along the z-axis through the centre of the fibre is shown.



#### 7.1.2.5. Handling, Application Feasibility and Operation of Fibre-Optic Sensors

The manufacturing of a reproducible bond to the substrate with constant geometrical properties is decisive for the quality and reliability of the strain transfer into the FBG and thus for the strain measurement. The development of an application procedure for a transparent autoclave-resistant bond necessary for this work has been highly time-consuming and has varied with the properties of the applied adhesive.

During the development of an application procedure for a transparent autoclave-resistant bond for optical fibres in the context of this work, the use of UV-curing adhesives has been determined as the method of choice, as it permits the fibre to be positioned and oriented prior to the initiation of the polymerisation of the glue. With the optical quality of the fibre application being of utmost importance for an application in laminated glass, considerable attention has to be paid, during the fibre installation, to keep the glass surfaces clean and to avoid sharp transitions of the adhesive joint and the glass substrate. The fibre should be laid loosely and have additional length to compensate for the differential thermal expansion of the fibre and the substrate. The resulting slight undulation of the fibre might cause undesirable optical effects in the laminate, particularly in the case of an irregular layout. The shifting of interlayer sheets and glass panes against each other during the preparation of the laminate can cause fibre breakage.

With regard to the two adhesives chosen for the bonding, the KB4552 epoxy revealed a slight yellowish aspect after the UV cure and this colour intensified during the autoclave process, see fig. 7.7. The second epoxy applied, KB OB642, did not suffer any colour changes after UV cure and autoclaving, as shown in figure 7.8.

A major issue is the leading-out of the fibres from the glass laminate, which constitutes the most sensitive part of this measurement method set-up. The exit location of the fibre from the laminate has to be chosen according to the intended framing or substructure of the glass and an appropriate exit angle has to be chosen. The installation of a protective tubing or similar devices at the fibre exit can cause air bubbles in the interlayer during lamination, if any remaining air is not fully sucked out by vacuum drawing. The fibres and sensors positioned inside the glass laminates are

well protected; only a few losses occurred during manufacturing and these were mainly attributable to fibre breakage at the exit point. All fibres and FBGs in operation prior to lamination also functioned after the autoclave process.

When handling lengthy fibres with multiple sensors, the tendency of the fibres to coil and their bending resistance must be considered. Manipulation of the fibre on a transparent material such as glass easily leads to breakage of the barely visible fibre. FC/APC-plugs usually do not stand the autoclave conditions. They have to be cut off after the cold bending process to be spliced to the fibre endings again after autoclaving. Development of a robot-assisted lay-out, mounting and bonding process for FBG and the respective fibres is encouraged, as the installation of a larger fibre set and the cleanliness and precision necessary to produce a transparent bond result can be time-consuming.

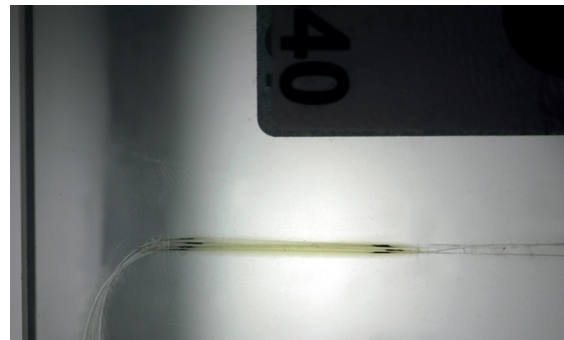


**Figure 7.7.:** Sensors in a three ply glass laminate glued with Delo KB4552. The adhesive shows a yellowish aspect after UV cure and autoclaving.



**Figure 7.8.:** Sensor glued to the interior glass surface of the four-ply laminate with Delo KB OB642.





## 7.2. Numerical Cold Bent Glass Analysis Method Evaluation

The measurement results gained from the four different types of cold bent glass laminates with fibre optic sensors and by photogrammetry have principally confirmed the finite element modelling assumptions and boundary conditions used for the detailed numerical models with contact elements (FSD.2.2 as in table 4.5). The results are analysed and compared in section 6.3 and the deviations seen with the FBG-sensors are discussed in the previous section 7.1.

In the following section 7.2.1, the stress results from testing and contact element models are principally interpreted and compared with simplified finite element approaches. The form-finding numerical modelling approach aiming at the determination of the cold bending shape necessary to achieve a desired final laminate shape is developed on this basis. In section 7.2.2, the developed analysis methodology is used to study numerically four basic archetypical glass bending shapes as examples. The chosen principle shapes are aimed at establishing a fundamental understanding of the behaviour of cold bent glass stabilised by lamination and at pointing out analysis methods and design basis strategies.

### 7.2.1. Analysis of Cold Bent Glass Behaviour and Appropriate Modelling Methods

#### 7.2.1.1. Test Result Interpretation

The stress distribution across the section of the various laminate types can be determined from the finite element analyses and FBG-measurement results shown in section 6.3.3. In figure 7.9, the section distribution of  $\sigma_x$  for the four laminate types studied above is shown for the sensor positions 1 (or 6), located at a distance of approximately 600mm from the narrow edge of the specimens in x-direction and 20mm from the curved edge, compare fig. 6.5. The glass surface stress of all positions across the thickness determined via FEA is used to plot the stress distribution; the respective sensor results are shown in comparison. The FE-model type applied for these calculations is the contact element model FSD.2.2.

With all four laminate types<sup>37</sup>, the tensile stress from the cold bending process at the top of the glass exceeds the absolute compressive stress at the bottom surface by 4MPa to 10MPa. Thus, the glass panes are not in a pure bending state but additional tensile membrane forces act that can be explained by the conditions along the boundary layer discussed by de Vericourt [Roy 11, p. 379] based on the inextensional theory by Mansfield [Man 89] and Ashwell [Ash 63]. By bending the glass plate, moments occur in curvature direction  $x$  and in transverse direction  $y$ . The plate develops an anticlastic curvature along the boundary region; this has been monitored in this work both by photogrammetry and FEA as in fig. 6.14. This double-curved situation causes a tensile membrane force parallel to the edge and an out-of plane force equilibrating the bending moment decreasing to zero. As a consequence, the maximum tensile force in single-curvature bending is expected along the longitudinal curved boundaries.

At a short time after release, the stress acting on the exterior surfaces has drastically reduced because of the springback effect. The initial elastic springback activates the shear compound of the glass panes via the interlayer. The bending stress reduces depending on the loss of curvature from springback but, in parallel, the glass panes on the convex side (top) of the laminate experiences additional compressive membrane stress and the glass on the concave (bottom) side experiences tensile membrane stress. Figure 7.10 depicts this mechanism. The membrane compression stress acting in the upper pane reduces the tensile bending stress on the glass surface of position 1 and increases the compression stress on the glass surface next to the interlayer at position 2. At the bottommost glass pane, the tensile bending stress at position 3 in a 2-ply laminate (or pos. 5 or 7 with the other laminate types) increases by the tensile membrane stress and the compressive bending stress at the exterior concave surface is subsequently reduced. This effect is, in principle, comparable to the combined bending and normal force load-bearing behaviour of a sandwich plate with thick, bending-stiff top and bottom layers [Sta 74, p. 85].

<sup>37</sup>The four-ply laminates 4esg\_sgp were less deformed during cold bending than the other three laminates and subsequently showed less stress and smaller differences than the other specimens.

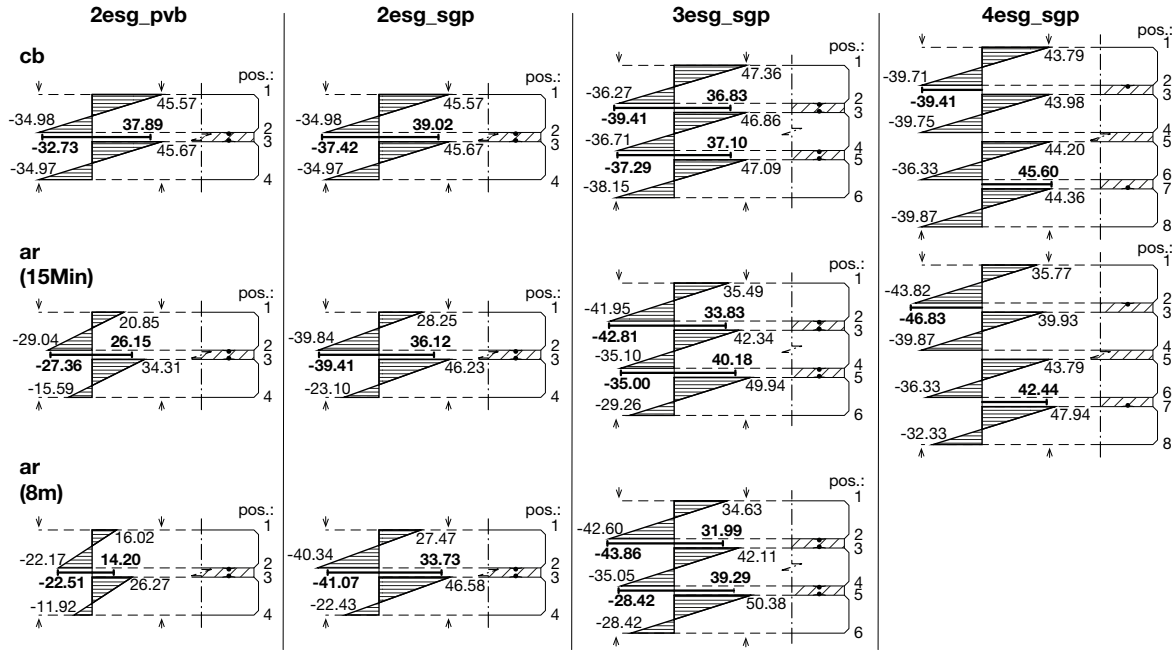


**Figure 7.9.:** Glass stress  $\sigma_x$  distribution across the section of all four laminate types for the locations of the sensors 1 or 6 as calculated by FEA. The thick lines indicate the same mean stress calculated for the glass surface with the FBG sensors.

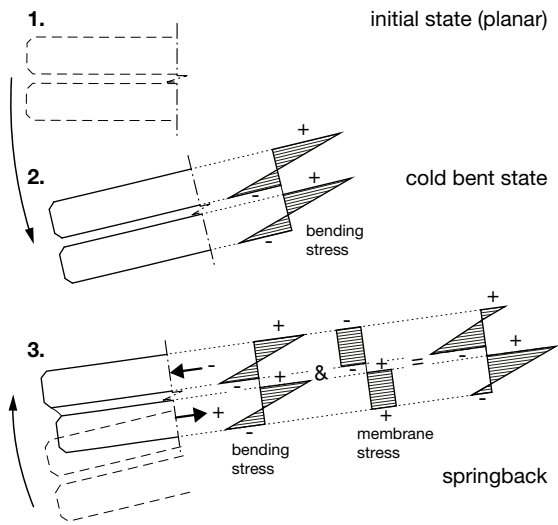


**Figure 7.10.:** Schematic depiction of the bending stress for single curvature cold bending and the development of additional membrane stress from springback.

The maximum tensile and compressive glass stress in the curvature direction occurs at the interfaces of the exterior glass plates and the respective interlayers (positions 2 and 3 or 5 or 7), fig. 7.9.

The PVB interlayer causes a high loss of curvature with time and an equivalent loss in stress can be observed attributable to the the low shear modulus of the interlayer material leading to pronounced creep / relaxation behaviour. In the present tests, the compressive stress decreases to  $\sim 65\%$  of the initial cold bending stress and the tensile stress to  $\sim 55\%$  during 8 months at  $15^\circ\text{C}$  to  $25^\circ\text{C}$ .

Laminates with the SG interlayer, having a high shear modulus, exhibit less springback and relaxation effects, as shown in section 6.3.3. The sensors and FEA show a rise in absolute compressive and tensile stress of up to 10% of the cold bending stress during springback for the glass surfaces at the interfaces of the exterior glass plates and the respective interlayers. This increased stress level reached after springback was preserved during 8 months test time and was not visibly reduced by relaxation. The stress introduced by cold bending to the glass panes situated in the centre of the laminate (positions 3 to 6 in the three- and four-ply laminates) was approximately preserved during the period of 8 months, as shown by FEA and the FBG sensors.

## 7.2.1.2. Cylindrical Model

Modelling of the cold bending and recovery process with contact elements by the FE model type FSD.2 (4.5) permits precise results to be obtained for the manufacturing process of cold bent glass laminates, as shown in the previous sections. However, the modelling process is expensive with respect to the necessary working time. Thus, a comparison with a simplified approach by applying forced nodal displacement into a perfect cylindrical cold bending shape, model type FSD.1, has been analysed in comparison with the contact element model and with the FBG results. The results for one half of a curved symmetrical glass laminate are shown in fig. 7.12 for the laminate types 2esg\_sgp and 4esg\_sgp. Laminates types 2esg\_pvb and 3esg\_sgp are presented in appendix E.4, fig. E.12. However, the application of a perfect cylindrical bending shape along the entire length of a glass pane is a theoretical assumption. In practice, the laminate flattens towards the longitudinal ends and no curvature can be applied or preserved in the boundary zone along the narrow edge because of the discontinuity of the glass pane.

The cylindrical model FSD.1 in all cases exhibits a nearly constant stress  $\sigma_x$  along the entire curvature direction attributable to the constant bending moments. The tensile stress  $\sigma_x$  at positions 3, 5 or 7 is slightly underestimated with the cylindrical model and the absolute compressive stress  $\sigma_x$  at positions 2, 4 or 6 is overestimated, because the cylindrical model cannot simulate the contact situation of the glass on the mould. Local contact can cause local stress peak zones deviating from a constant bending stress level, as occurs with laminate 2esg\_sgp in fig. 7.12. As for long-term relaxation of 8 months, the stress distribution along the curved glass laminates calculated by the cylindrical and the contact element model correspond well for both two-ply laminate types. For 3esg\_sgp and 4esg\_sgp, the tensile stress after 8 months is slightly underestimated. In summary, the cylindrical model FSD.1 shows good agreement with the contact element approach FSD.2. As for tensile forces on the glass surfaces of positions 3, 5 and 7, the cylindrical approach can underestimate the occurring stress level depending on the mould shape and the applied deformation of the glass onto the mould. Verification of the correspondence of the real deformation applied to the glass during the cold bending process in manufacturing to the deformation used in the numerical simulation is recommended. As for the

stress close to the longitudinal ends of the laminate, the cylindrical model approach delivers results on the safe side, as the glass is constantly bent along its entire length.

Contrary to a plate being bent into a perfect cylindrical shape, the constraining of the narrow edge used in the tests to bend the glass onto a cylindrical mould does not cause an ideal constant bending moment in the curvature direction but leads to a variable bending influence depending on the contact positions of the glass and the mould. As can be seen from the studies with the two different bending deformations of 131mm and 135mm in fig. E.11, this leads to variable  $\sigma_x$  stress distributions in the curvature direction along the curved edge zone. Increased deformation at the ends causes the glass, which locally deforms in a parabolic or saddle shape, to touch the mould. This produces a slight lift-off in the adjacent areas and leads to a decrease of the bending stress.

Figure 7.11 illustrates the stress in x- and y-directions caused by cold bending onto the mould used for the manufacturing of the tested specimens. An additional contact point of the bent glass to the mould occurs at the centre of the region above the transverse mould beam at  $x=600\text{mm}$ . Here, a local maximum stress concentration also occurs.

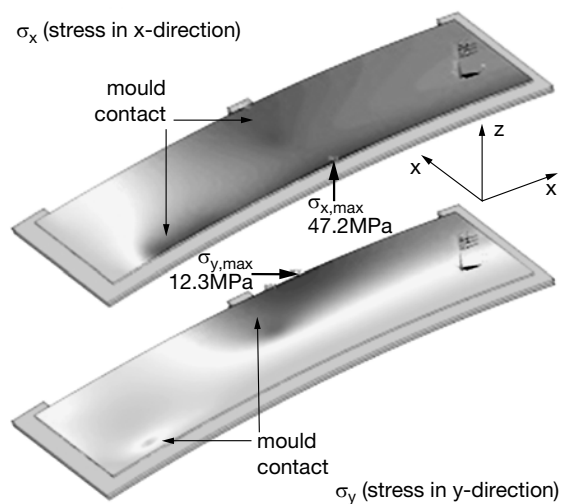


**Figure 7.11.:** Stress plots in x- and y-direction in a glass pane generated by cold bending on the mould. A quarter of the mould and glass panes is modelled, as symmetry conditions are applied.

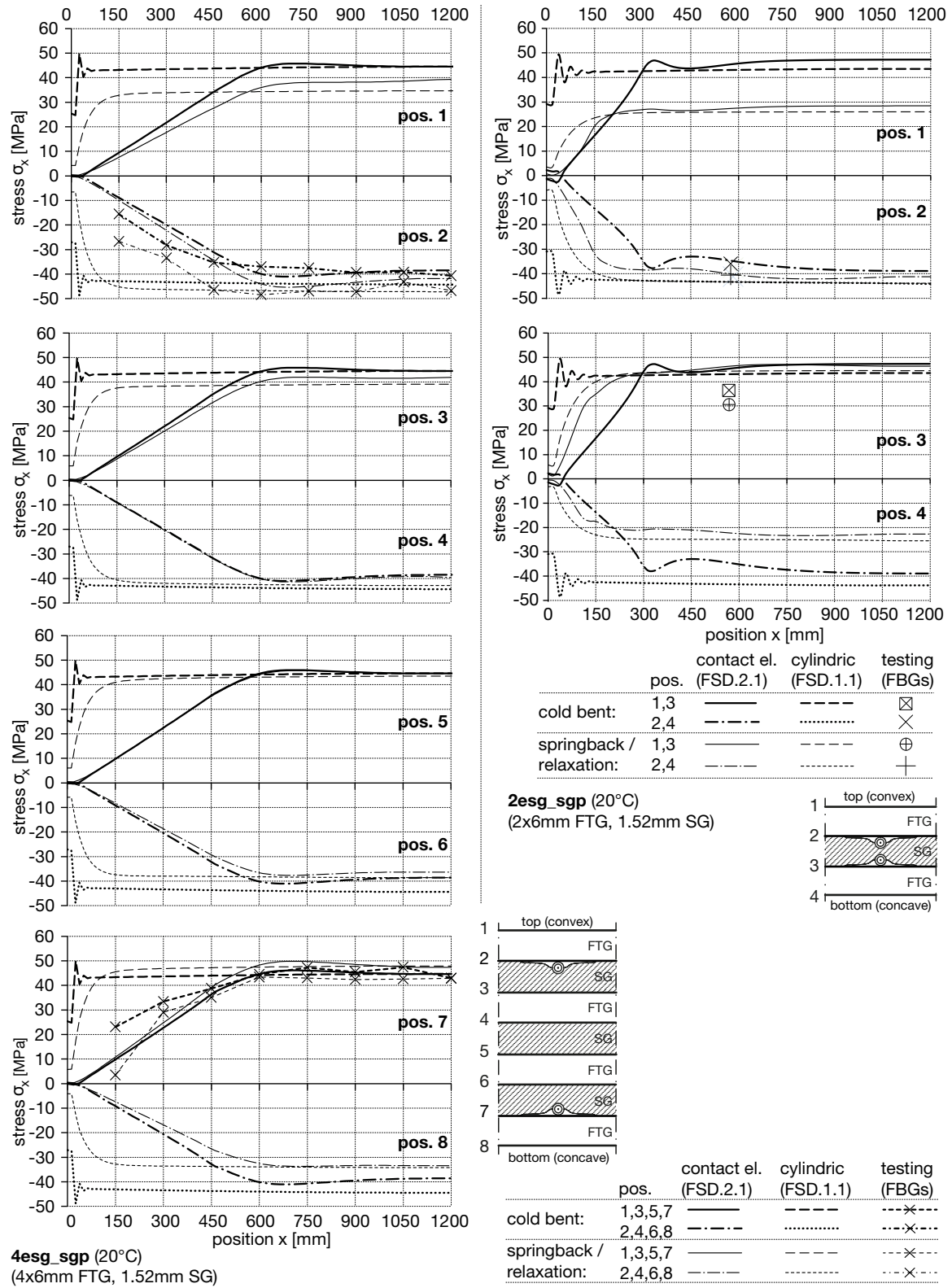


Figure 7.12.: Comparison of the stress results  $\sigma_1$  along a longitudinal section 20mm from the curved edge determined with the contact element model FSD.2.2, the cylindrical model FSD.1.1 and the FBG-results for 4esg\_sgp and 2esg\_sgp.

### 7.2.1.3. Fixed Point Iteration Model

For the numerical simulation of the tested specimens, only models of the type FSD have been used, as the initial bending shape is a given parameter. In practical applications, however, a stable *final* shape of the glass laminate will usually be demanded. Thus, the cold bending process has to be performed with a mould having a superelevated geometrical shape. The necessary superelevation depends on the desired final glass shape after springback / relaxation, on the relaxation time, the temperature level, the interlayer materials and the composition of the laminate.

As a practical manufacturing approach, Teich [Tei 14, p. 80] proposes a temperature treatment of six hours at 68°C of cold bent glass stabilised by lamination with SG-interlayers to anticipate the relaxation of the laminate with time and to minimise potential geometrical changes of the shape of the laminate in the built-in state. This technique is not considered in the present work.

A possible solution to the form-finding issue of the superelevated glass shape necessary to obtain a given desired final shape after springback and a specified relaxation time is proposed by model type FPI. Fixed-point iteration, as described in section 4.2, is used in a loop procedure including the entire manufacturing steps of cold bending, lamination and springback / recovery, see fig. 7.13. The procedure starts by applying the desired final shape as the first cold bending deformation geometry. The geometry obtained after springback / relaxation is compared with the desired target shape; subsequently, the difference of the respective shape coordinates is calculated and added to the initial cold bending shape. This modified deformation parameter is then applied for the next bending and springback iteration loop. The process is repeated until a given tolerance limit to the desired shape is met after springback / relaxation. If the analysis does not converge, this is a first indication that the desired shape cannot be manufactured. The number of iterations can be limited to avoid superfluous calculation time.

Displacement of the nodes of a glass pane by fixed vertical values, the latter representing a desired final shape described by the three final coordinates  $x, y, z$ , does not precisely result in this target shape. If the deformation is mostly inextensional (bending), the centre axis lengths between the nodes remains constant prior to and after deformation but the nodes

now lie in a curved surface. Thus, a geometrical  $x$  and  $y$  displacement of the nodes with respect to the planar initial configuration has also taken place. In the model, this is taken into account by performing subiterations in each cold bending step in order to correct the resulting slight deviation of the bending shape obtained in the first iteration substep. If double curvature shall be achieved, the deformation is not inextensional any more but shows additional in-plane strain. This membrane strain has a strong influence on the stress developing in the glass by cold bending. As double curvature deformations usually remain low, the geometrical part of the horizontal  $x$ - $y$ -shift is small compared with single curvature bending.

In this work, the FPI model uses the forced nodal displacement method (FPI.1). Combination with contact and target elements in order to take the mould into account is possible, but leads to a complex, expensive modelling / analysis process. Application examples of the FPI model are shown in the following section 7.2.2.

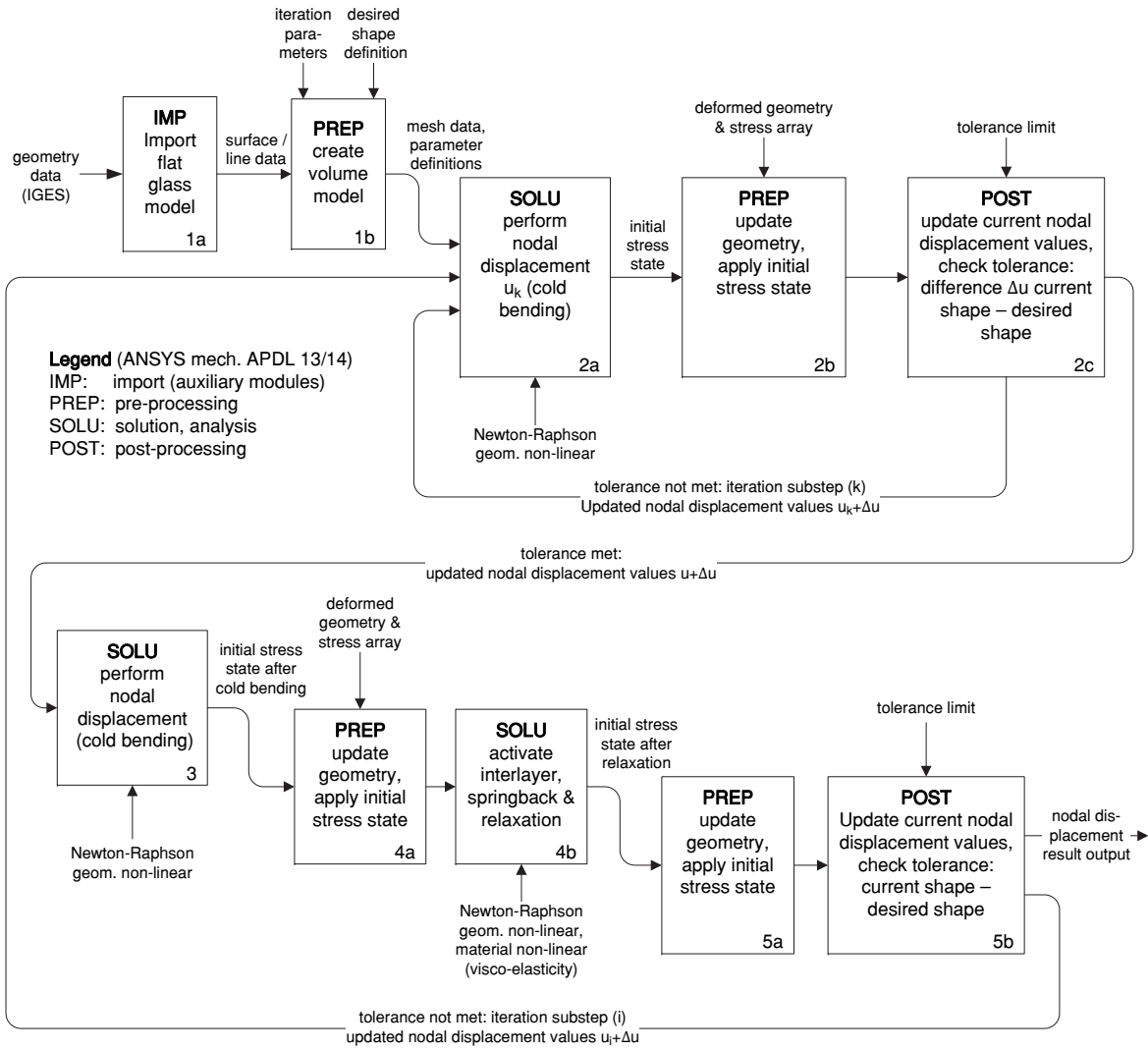
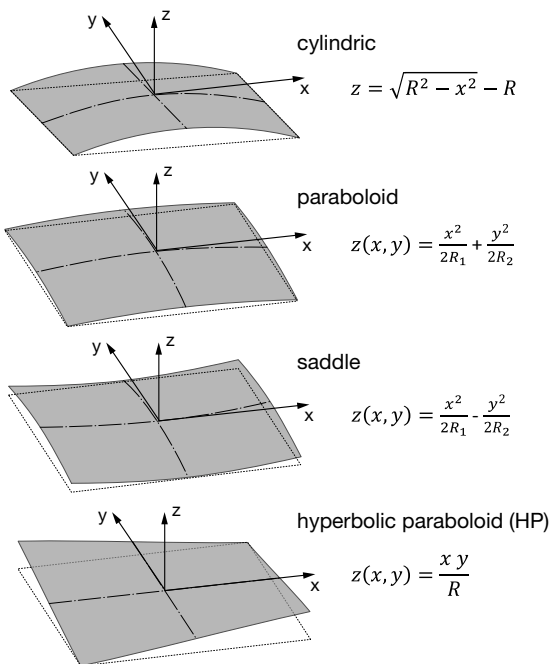


Figure 7.13.: Process diagram of the finite element fixed point iteration for cold bending of glass.

### 7.2.2. Examination of Principal Cold Bending Shapes

Four archetypical glass bending shapes, namely a single-curved cylindrical, a synclastic paraboloid, an anticlastic saddle and hyperbolic paraboloid, have been examined by applying model types FPI.1.1 and FPI.1.2. The target geometries, as shown in fig. 7.14, comprise bending radii of 35m for the double curved shapes and 5m for the cylindrical shape. All laminates examined are composed of 3x6mm FTG panes of 3x3m size and SG interlayer, see also 6.2.2.



**Figure 7.14.:** Explicit surface equations of the four basic cold bending shapes studied.

For the cold bending deformation by forced displacement of *some chosen* nodes as in model FPI.1.1, the edges of the glass panes and their diagonals (paraboloid) or straight rulings (saddle, HP) are set as boundary conditions for the forced displacement. This configuration could be used in practice in the setup of a bending jig with constraints along the glass edges and diagonals / rulings used for the shaping of the glass. The bending mould applied for producing the single curved specimens for the tests in this work, for example, offers curved support lines along the glass edges and additional straight transverse supports; constraint is only applied along the narrow edges by means of a vertically movable beam in order to deform the glass.

For the second type of deformation, *all* nodes are forced into the desired position (FPI.1.2). This method is an idealisation, as no fully functional practical manufacturing equivalent exists, see 2.2. Application of a deformation mode complying with the simultaneous forced deformation of all points on the glass surface is technically difficult and is not the state of technology of elastic bending. The approach of applying uniform compression to press the glass (with contact elements) onto a mould (target elements) for shaping, has been briefly studied in the context of this work; some example results from the preliminary model are presented below in fig. 7.17.

Even though the four bending shapes studied in this work cannot cover the entire field of cold bending options, they are suited to identifying, examining and discussing the principal parameters and issues influencing single- and double curvature cold bending in a representative way. Both the superelevated bending shape necessary to obtain the target shape after springback / relaxation and the final shape after eight months of relaxation at 20°C have been iteratively determined and compared with the desired target shape for both model types FPI.1.1 and FPI.1.2.

The main aspects of interest are the following parameters: the maximum principal tensile stress  $\sigma_1$ , the curvature radii  $R_{1,2}$  (double curvature) or  $R$  (single curvature), the Gaussian curvature  $\kappa$ , the vertical z-coordinates of the cold bent geometry  $z_{cb}$ , of the desired shape  $z_{des}$  and the difference of the z-coordinates of the desired and achieved shape after springback / relaxation,  $\Delta z$ . The curvature and smoothness of the glass surface after the springback / relaxation is of importance for the optical quality of the glass laminate. For the monitoring of the curvature and displacement parameters listed above, a matrix of nine characteristic points has been analysed on the superelevated (pre-camber) cold bent glass geometry and on the final surface obtained after eight months of relaxation. The results are shown for the hyperbolic paraboloid in fig. 7.16 and for the paraboloid in fig. 7.15 as characteristic examples of a synclastic and an anticlastic shape. The saddle and cylindrical geometry are provided in figs. E.14 and E.13 in appendix E.4. The Gaussian curvature is only shown for the springback shape in the mentioned figures, as the optical surface quality of these shapes is decisive for the application, for example, in a building. A summary and comparison of all parameters is provided in table 7.3.



no.	shape	bending method	cold bent (superelevated mould shape)						8 months of springback / relaxation					
			desired shape $z_{des}^a$	super-elevation $z_{cb}^a$	$z_{cb} / z_{des}$	max. $\sigma_1$	max. $\sigma_1$ at pos.	max. $\sigma_1$ location	min. $R_{1,cb}$ cold bent (range)	shape diff. $\Delta z^b$	max. $\sigma_1$	max. $\sigma_1$ at pos.	max. $\sigma_1$ location	min. $R_{1,relax}$ relaxed (range)
			[mm]	[mm]	[%]	[MPa]	[-]	[-] [m]	[mm]	[MPa]	[-]	[-] [m]		
C.1	cylindric (R=5m)	FPI.1.1	223.6	243.4	108.9	55.0 (335.4) <sup>c</sup>	1,3,5	perimeter	2.3-7.8	13.56	55.00	5	perimeter	4.1-8.1 (15.9 locally)
C.2		FPI.1.2	222.6	240.6	108.1	57.0 (124.9) <sup>d</sup>	1,3,5	perimeter	4.3-4.8	0.12	56.20	5	perimeter	4.9-6.5 (91.2 at the ends)
P.1	paraboloid	FPI.1.1	64.2	106.8	166.4	58.6	1,3,5	perimeter	6.4-17.0	4.0	41.2	5	perimeter	8.5-24.7
P.2	(R <sub>1,2</sub> =35m)	FPI.1.2	64.2	112.8	175.8	55.7	1,3,5	centre	19.1-22.7	3.3	40.9	5	centre	28.7-38.5
S.1	saddle	FPI.1.1	64.2	125.2	195.0	138.3	1,3,5	perimeter	3.3-21.1	4.1	70.3	5	perimeter	5.7-47.2
S.2	(R <sub>1,2</sub> =35m)	FPI.1.2	64.2	131.3	204.5	118.1	1,3,5	perimeter	14.6-30.2	1.4	49.3	5	perimeter	30.2-44.6
H.1	HP	FPI.1.1	128.3 no convergence achieved after 4 iterations						-	11.2	-	-	-	-
H.2	(R <sub>1,2</sub> =35m)	FPI.1.2	128.3	243.8	190.0	110.0	1 to 6	perimeter	15.1-19.5	1.8	26.6	1,2	perimeter	35.1-36.6

<sup>a</sup> max. z coordinate after deformation into the desired or the superelevated mould shape

<sup>b</sup> Maximum difference of the z-coordinates between the desired and the achieved shape after relaxation

FPI.1.1: fixed-point iteration, partial node set displacement

FPI.1.2: fixed-point iteration, entire nodes displaced

<sup>c</sup> local stress at corner (singularity)

<sup>d</sup> local stress near the narrow edge

**Table 7.3.:** FE-analysis results of the cold bent state and after 8 months of relaxation at 20°C for four basic bending shapes 3\*6mm FTG 3x3m laminated with 1.52mm SG. The maximum deformation, minimum radii and maximum principle tensile stress values for the desired shape, the superelevated bending shape and the achieved final geometry are documented.

- The Gaussian curvature studies of the four basic shapes reveal that the springback of glass deformed along the edges and diagonals or rulings as performed with model type FPI.1.1 results in surfaces with irregular curvature. In practice, this leads to visible stress patterns and bumps. The deviation  $\Delta z$  from the desired shape is more pronounced than with the model type FPI.1.2, see table 7.3. The radii after relaxation exhibit more variation with FPI.1.1 than with FPI.1.2.
- The forced deformation of partial node sets in model FPI.1.1 can lead to convergence problems in the analysis, as the unconstrained glass zones tend to buckle. Here, for example, the iterations for the HP have not converged with FPI.1.1.
- For obtaining double-curved shapes with radii of 35m after springback / relaxation, the cold bending superelevation has to be about 170% to 200% of the desired shape. This can lead to tight bending radii between 10m to 20m, see table 7.3.
- For obtaining the synclastic paraboloid bending shape (P.1, P.2) as in fig. 7.15, the necessary superelevation of  $\approx 175\%$  of the desired shape is smaller than for the anticlastic HP (H.1, H.2) and saddle (S.1, S.2) geometries, which necessitate a pre-camber of nearly 200%, figs. 7.16 and E.14.
- The cylindrical shape (C.1) shows a pronounced maximum deviation of up to 20mm from the

desired shape, if the deformation is only applied along three parallel curved longitudinal sections by model FPI.1.1. For the full nodal displacement with FPI.1.2, the deviation after springback is less than 0.1mm as shown in fig. E.13. The superelevation necessary to obtain a long-term radius of 5m is about 110% compared with the desired shape. This complies with the findings from the tests in this work.

In summary, the forced deformation model FPI.1.2 involving all glass mesh points permits the determination of the bending mould shapes, that lead to the bending and springback / relaxation behaviour of the bent glass coming close to the given target shape. However, this approach is still theoretical, as a corresponding bending device and the actual bending of the glass exactly to it in manufacturing are difficult to achieve. If only partial node sets are forced into a given shape (FPI.1.1), the final glass shape after springback / relaxation exhibits surface irregularities with local curvature radii variations from the target radii and visible deviations of the obtained and desired shape. The risk of local buckling, which leads to limited single curved zones, is particularly problematic with method FPI.1.1 and occurs especially with the anticlastic shapes. Generally, double curvature bending only permits low radii after springback / relaxation of about 35m, if tensile stress of up to 120MPa is accepted in the bending process. Through relaxation, this stress mostly reduces to values smaller than 60MPa.

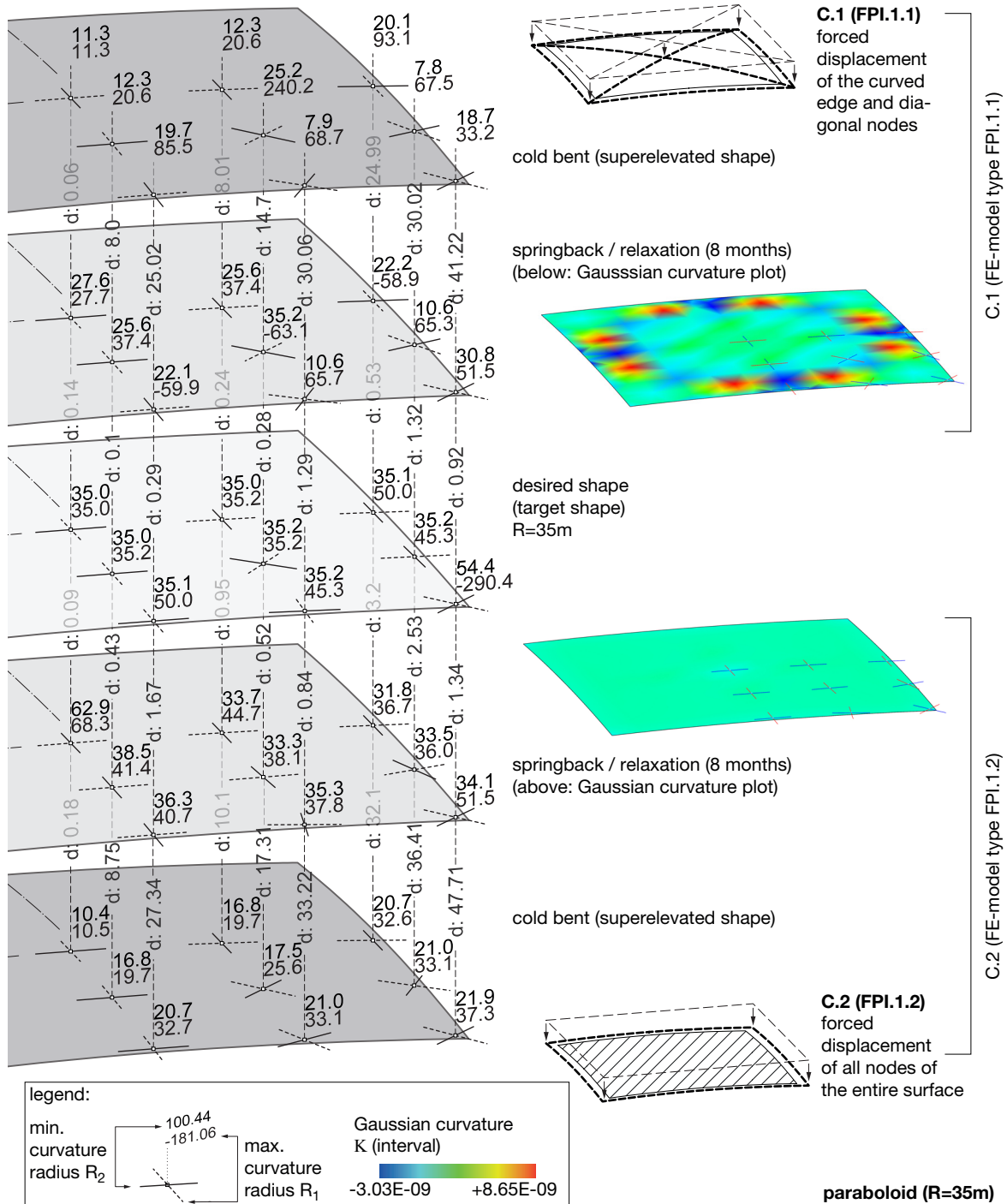


**Figure 7.15.:** Curvature analysis of a paraboloid shape from 3x6mm FTG (3x3m) laminated with 1.52mm SG analysed with model types FPI.1.1 and FPI.1.2. The principal curvature directions / results are shown for nine points on the surface of the topmost glass. The superelevated cold bending shape, the target shape and the achieved shape after 8 months of relaxation are shown. Values with a "d:" are the difference vectors of the points on the cold bent, relaxed and target glass shapes.

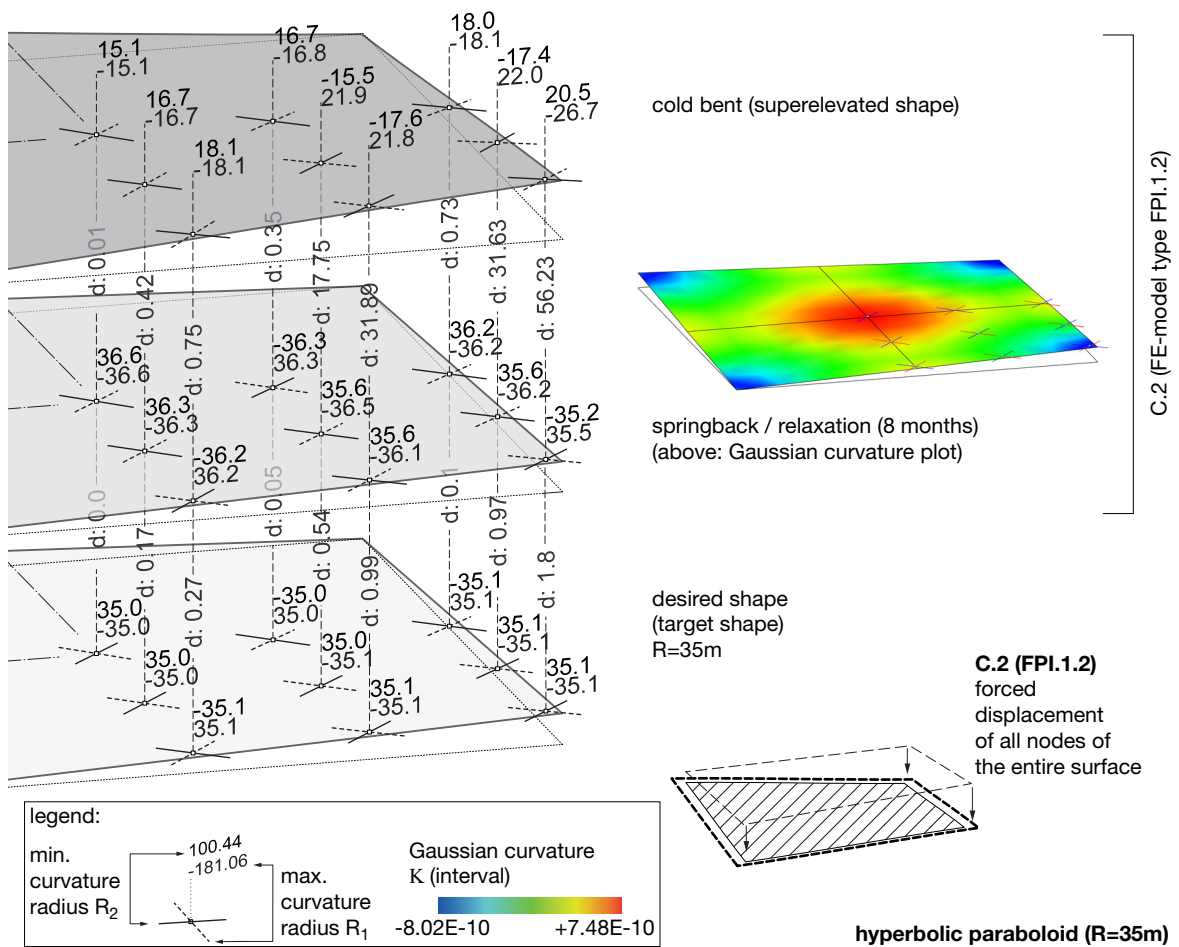


**Figure 7.16.:** Curvature analysis of a HP shape from 3x6mm FTG (3x3m) laminated with 1.52mm SG analysed with model type FPI.1.2. The principal curvature directions / results are shown for nine points on the surface of the topmost glass. The superelevated cold bending shape, the target shape and the achieved shape after 8 months of relaxation are shown. Values with a "d:" are the difference vectors of the points on the cold bent, relaxed and target glass shapes.

The bending geometries that can be achieved in the cold bending process mainly depend on the chosen technical procedure and on the stress developing in the glass. Bending into double curvature allows only a small curvature. This is because double-curved deformation leads to membrane stress developing across the entire cross section of the thin glass. As the membrane stiffness is high compared to the bending stiffness, the application of double curvature causes high membrane stress even at small deformation levels. Analysis of the stress distribution on the top and bottom surfaces and across the sections of the various glass bending shapes have shown that the double-curved bending geometries develop both membrane and bending stress components in the process.

In contrast, pure bending, which causes inextensional deformation with respect to the centroid axis of the glass pane, causes a linear stress distribution across the surface with the maximum stress on both surfaces of the glass depending on the thickness of the pane and on the applied curvature. As shown previously, practical cold bending of a glass plate into a cylindrical shape also causes some membrane stress particularly in the boundary zones along the curved edges.

A principal issue in the creation of double-curved shapes is that the entire glass surface has to be supported on both sides during the bending process in order to achieve the intended shape and to avoid buckling, as seen from the studies with model FPI.1.2. This could theoretically be achieved by a movable matrix of core and cavity punches or by vacuum-forming. Only the latter technique seems realistic to some degree. The application of surface pressure to form an object onto a mould is typical for metal sheet forming, for example, [Pap02] and [Chu 14], or for deforming polymer sheets. However, all these materials are deformed plastically. Cold bending of glass into a mould shape is an elastic process. Fig. 7.17 shows an example finite element study by using uniform pressure to elastically press-form 3x10mm fully toughened glass panes to a HP-shaped bending mould. Contact and target elements are applied to the glass bottom surfaces and the mould. The springback of the achieved bent shape after lamination with 0.9mm SG interlayer is also shown. This type of detailed modelling and numerical analysis is highly time-consuming and a convergence of the analysis cannot be achieved in some cases.

The latter gives an indication of the stability buckling issues encountered with cold bending into double-curvature. As only extremely small curvature can be realised, the related market opportunities are limited.

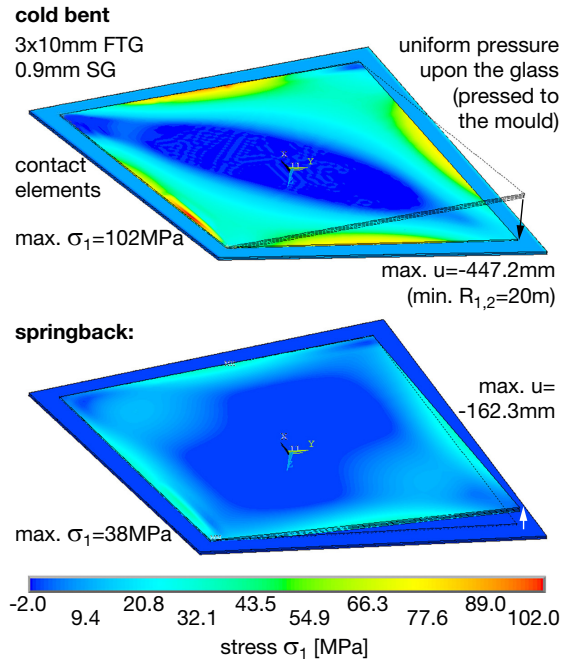


**Figure 7.17.:** Cold bending and springback principal tensile stress shown for 3x10mm FTG laminated with 0.9mm SG pressed upon a HP-shaped bending mould by means of uniform pressure.

Application of the forced displacement of all nodes of a glass plate of 3x3m and 6mm thickness as in model type FSD.1.2 allows the determination of the maximum tensile stress, minimum radii and maximum nodal displacement for the variable cold bending curvature of the four basic bending geometries discussed above. The results in fig. 7.18 indicate that the bending of glass into a parabolic shape causes less tensile stress in the glass for a given bending radius  $R$  or vertical displacement  $u_z$  than the HP and the saddle. The relationship of  $\sigma_1/R$  and  $\sigma_1/u_z$  is non-linear. By using the characteristic stress of fully toughened glass, the minimum cold bending radii of 18m can be reached for the saddle shape, 16-17m for the HP and 11m for the paraboloid. The allowable stress level of 50MPa from the TRLV permits bending radii of 27m for the saddle, 25m for the HP and 18m for the paraboloid to be obtained. When using this table, we must keep in mind that the values have been determined by forced nodal displacement (FSD.1.2), a method that has no real functional manufacturing counterpart.

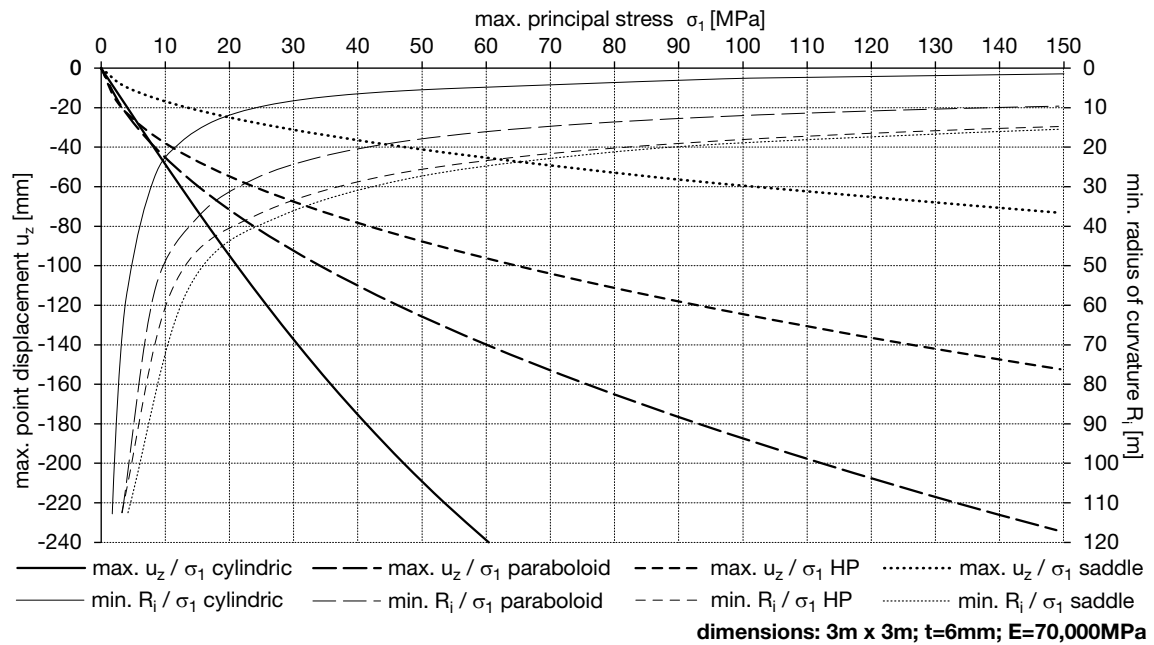


**Figure 7.18.:** Maximum principle tensile stress  $\sigma_1$ , minimum curvature radii  $R_1 = R_2$  and max. vertical displacement  $u_z$  for a 3x3m glass plate deformed into a cylindrical, saddle, HP or paraboloid geometry by cold bending. Note that the values are calculated by FEA using the method of forcing all FE mesh nodes situated of the bottom surface of the respective glass pane.



## 8 Conclusion

### 8.1. Cold Bent Glass Analysis and Monitoring

Elastically, cold bent lamination-stabilised glass is a promising product for application in smoothly curved building envelopes having a low curvature, as it combines a high optical surface quality with a relatively stable geometrical shape. The preservation and long-term stability of the bent shape mainly depends on the shear modulus of the interlayer in combination with the number of glass layers. However, for the purposeful and safe application of cold bent lamination-stabilised glass, the interior stress from the cold bending process and its time- and temperature-related behaviour during the lifetime of the product have to be known. Therefore, a stress monitoring solution is necessary that allows the continuous long-term recording of the glass stress states inside the laminate. For application in built-in glass elements, this monitoring technique must not obstruct the transparency of the glass. Furthermore, the interdependency of the stress, the feasible shapes, the cold bending process and the composition of the laminate are of interest.

Therefore, various numerical FE simulation methods have been developed and examined in comparison with test results from single-curved real-scale glass specimens. Four specimen series with two, three or four glass layers and PVB or SG ionomer interlayers have been fabricated. After cold bending and release from the bending mould, the springback and eight months of relaxation have been recorded at room temperature. The four-ply specimens have been used as a sensitive glass arch demonstrator indicating the stress pattern caused by exterior loads. The geometrical 3D shape of the glass specimens and the deformation behaviour with time have been tracked by applying close-range photogrammetry with point arrays. The monitoring of the glass stress inside the laminates has been performed with thin, barely visible, fibre optic sensors with Bragg gratings (FBG) bonded to the glass prior to the bending and lamination.

As this is the first application of FBG in laminated glass, a transparent adhesive bonding method for the coated FBG has been developed in this work. A constant reproducible joint geometry based on a UV curing epoxy adhesive has been identified by extensive tests of 22 adhesives. The chosen solution provides a shear modulus of sufficient value to permit full load transfer from the glass to the fibre at autoclaving conditions of 140°C.

The bond length, its thickness and the shear modulus of the adhesive have been identified as the main parameters influencing the strain transfer from the bent glass to the FBG by means of a simplified analytical bending formulation for the bonded fibre and by corresponding FE models. The gauge factor  $k_\epsilon$  of the chosen fibre bond, quantifying the strain transfer ratio from the bent glass substrate to the bonded fibre, has been determined as 0.79 by four point bending tests and by a corresponding micro-mechanical FE model. Springback and relaxation of the laminate can cause an increase to  $k_\epsilon=0.81$ . No birefringence of the FBG in the cold bent and in the laminated state has occurred. The well-known equations 5.58 and 5.60, linking the wavelength shift of the FBG and the homogeneous uniaxial strain of the isotropic fibre caused by the corresponding substrate strain, have been found to be applicable for FBG in cold bent glass laminates.

Principally, the FBG and their transparent adhesive bond have been successfully applied inside real scale cold bent glass laminates and they withstand the autoclaving process. Regarding the cold bending stress and the relative trend of the stress development during springback and relaxation, the tendencies exhibited by the FGB sensors and the numerical analyses have been identical. Real-time measurement of the glass stress caused by exterior loads applied to cold bent glass laminates proved possible. With the single-curved glass specimens, birefringence from the transverse load influence can locally occur with the sensors during cold bending and, more often, during vacuum drawing. It has been shown that these effects vanish in the autoclave process when the interlayer melts.

However, the Bragg wavelengths and the related stress measured in the cold bent state prior to the autoclaving process and afterwards exhibited a decrease for FBG subjected to tension and an absolute increase for sensors in compression by a mean value of  $\sim 10\%$ . No straightforward single reason has been identified for this behaviour, but post-cure shrinkage effects of the coating of the FBG in the autoclave and the different extents of thermal expansion of the of the silica fibre, the coating, the adhesive bond, the interlayer and the glass forming a compound are assumed to cause residual compressive stress in the fibre in the cooling process after lamination. Hence, if the cold bending stress state has to be taken into account, relative FBG measurement should be referenced to the cold bending stress measured prior to lamination.



Finite element modelling of the four types of single-curved cold bent glass specimens and the tests including 3D monitoring with photogrammetry and stress recording with FBG have successfully yielded comparable results and relaxation behaviour tendencies.

A detailed contact element FE model of the mould and the laminate has been used for comparison with the tests. It principally complies with the 3D displacement monitoring by photogrammetry and with the FBG stress measurements. Both the model and photogrammetry reveal the development of a shallow anticlastic curvature zone along the curved edges of single-curved bent glass. The initial springback of the laminated bent glass (5% to 20%) at release mainly depends on the number and thickness of glass layers and the elastic properties of the interlayer. In contrast, the long-term relaxation behaviour depends on the time- and temperature-dependent shear modulus of the interlayer. At room temperature, the initial bending deformation of the two-ply PVB laminates is reduced by 40% after 8 months, whereas the SG laminates exhibit no further recovery behaviour.

During the initial springback after release, the cold bending stress acting on the exterior glass surfaces of the laminates reduces, whereas the cold bending stress of the outermost laminated glass surfaces increases with the SG laminates by up to 10%. This is attributable to additional stabilising membrane stress in the glass from the springback. The maximum tensile stress occurs at the laminated surface of the outermost glass panes in the boundary zones along the curved edge. As a result, the permanent relaxation of the PVB laminates leads to a continuous loss in curvature and stress. Cold bent PVB laminates thus can only be used together with shape-stabilising clamping to a substructure. At 20°C, the SG laminates do not noticeably relax after the initial springback and mostly preserve their cold bent shape. The initial cold bending stress in the laminate is also preserved or increases and this has to be taken into account in the design.

The application of a simplified FE model based on the forcing of nodes into a perfect cylindrical shape leads to cold bending and relaxation stress results approximately corresponding to both the tests and the contact element model. In some cases, the tensile stress is slightly underestimated. The cylindrical model can be used for predimensioning with respect to stress but not for the determination of the exact final geometrical glass shape.

For the form finding of the superelevated mould shape necessary to obtain a final applicable desired cold bent glass geometry, a fixed-point iteration model has successfully been used with various examples of three-ply laminates. The superelevation depends on laminate composition, bent shape, temperature and time. Single-curved SG laminates at 20°C and eight months relaxation time approximately necessitate less than 15% additional superelevation of the desired shape, whereas double-curved SG laminates might require an additional 100%. A strong influence of the bending mould and bending method on the stress and geometry of the final glass shape in the cold bent state and during relaxation has been revealed. Cold bending of double-curved shapes permits a very small curvature to be achieved and can lead to local buckling effects of the glass panes involved.

The application potential of fibre optic sensors with Bragg gratings for laminated glass products lies in the field of the monitoring of complex architectural and vehicle glazing for spacecraft, aircraft, land-bound and marine use. Integration of the sensors in structural adhesive joints in glass construction is also possible [Gan 15]. The insights gained from FBG-usage for the extreme case of cold bent glass with lamination stabilisation can be transferred to all types of laminated glass products. In particular, the continuous long-term monitoring of very large, expensive glass panes used in buildings or prototypes justifies the use of FBGs. Examples are commercial and company buildings, such as [zee 15] and [ins 14], or freeform architecture. Sensitive glass laminates with integrated FBGs for stress monitoring can contribute to an enhancement of safety factors regarding the load influence from static and dynamic loads such as wind, waves, temperature, distortion or impact. The application of FBGs in the boundary zones of glass elements, where the sensor fibres affect the transparency even less, is of interest, because these zones are particularly sensitive to breakage and often exhibit the maximum stress. The use of FBGs for experimental stress or temperature monitoring purposes in research or for industrial glass processing are further possible applications.

## 8.2. Further Research, Future Work

The scope of the present work only allows an initiation into the topics of cold bent lamination-stabilised glass behaviour and of fibre Bragg gratings applied for stress monitoring and for identifying the potential, the principal working methods and issues involved in the use of such glass and sensing devices.

Systematic research on cold bent lamination-stabilised glass with SG interlayers is necessary regarding the relaxation behaviour at increased temperature above 30°C in cyclic or long-term temperature applications. An examination of the anticipated relaxation of cold bent glass by a temperature treatment prior to use [Tei 14] should also be undertaken. The influence of the bending mould geometry and of the glass deformation on the stress level and the optical surface quality of the laminate after autoclaving and springback is an important issue for the manufacturing process of cold bent lamination-stabilised glass. Related to this, the examination and monitoring of the geometrical surface smoothness and stress anisotropies and the comparison of bent glass after springback / relaxation to the target shape, for example by photogrammetry or phase measuring deflectometry, have to be adapted with regard to application to large, high quality, architectural glass.

Regarding the safety of cold bent lamination-stabilised glass, the post-breakage behaviour and potential micro-crack influence on the interior and exterior glass surfaces permanently subjected to tension are a matter of interest. Based on the results of this work, the application of fibre-optic sensors for the monitoring of large glass structures with respect to an enhancement of the safety factors for glass design is encouraged. Permanent real-time stress monitoring of new or critical glass constructions potentially permits an increased safety level.

As detailed finite element studies can be time-consuming, analytical approaches for the calculation of developable cold bending shapes and the time- and temperature-dependent springback / relaxation are necessary for the engineering design of cold bent lamination-stabilised glass [Gal 14b]. Standards or codes for the quality and calculation of design stress and material resistance of cold bent glass including partial safety and load duration factors have to be fixed additionally in order to ensure the more widespread use of this product.

The most pressing issue regarding the application of FBG in glass laminates is the development of an integrated temperature compensation method for discrete fibre optic sensors. Despite extensive research performed regarding temperature compensation of FBGs, no solution applicable with standard interrogation equipment exists to date. Polarisation-maintaining fibres combined with a Sagnac interferometer [Don07] or a loop mirror [She 13], polarisation-dependent loss (PDL) of FBG [Luy 12] or long period gratings with inter-grating spaces are among the recent approaches.

Further research concerning the behaviour of FBG bonded to glass being laminated by autoclaving are necessary to resolve the issue of the modified Bragg wavelength measured after the lamination process. These changes are thought to be related to post-cure effects of the coating in the autoclave and to residual stress from the different extents of the thermal expansion of the materials in the compound during cooling. In this context, the development of a transparent separation method of the fibre and the interlayer are a possible solution for avoiding the influence of the interlayer strain and its thermal expansion on the FBG.

The exit point of the optical fibre from the laminate is a fragile point regarding the practical use of FBG [Kin 14, pp. 7408-7410], for which a industrial robust standard solution adapted to autoclave conditions has to be developed.

The existing analytical strain models for FBG are mainly based on [Ste97] and cover either FBGs bonded to a surface or embedded in isotropic, orthotropic or anisotropic materials. For sandwich materials with soft isotropic interlayers and stiff cover layers, the development of an analytical approach regarding the multi-axial strain transfer to a FBG for the description of a coated fibre bonded by adhesive to the rigid cover surface and surrounded by an interlayer material is of interest.

In the near future, distributed strain and temperature sensing with OTDR and OFDR technology, 5.1.1.3, can be used to overcome the problem of discrete sensing with the FBG. A prerequisite, however, is to achieve a reduction of the high cost of the necessary technical equipment.

## References

- [Abe 08] Aben, H.; Anton, J.; Errapart, A.: Modern Photoelasticity for Residual Stress Measurement in Glass: Residual Stress in Glass, *Strain*, 44 (2008), 1, 40–48 (cit. on p. 28).
- [Abe 14] Aben, H. et al.: A new approach to edge stress measurement in tempered glass panels, conference contribution, *engineered transparency: glass - facade - energy*, engineered transparency. International Conference at glasstec 2014, Düsseldorf, 241 (cit. on p. 28).
- [Abe 10] Aben, H. et al.: On non-destructive residual stress measurement in glass panels, *Estonian Journal of Engineering*, 16 (2010), 2, 150 (cit. on p. 28).
- [And 14] Andreozzi, L. et al.: Dynamic torsion tests to characterize the thermo-viscoelastic properties of polymeric interlayers for laminated glass, *Construction and Building Materials*, 65 (2014), 1–13 (cit. on pp. 33, 111–114, 117, 125, 127, 138).
- [Ash 63] Ashwell, D. G.: The boundary layer in the bending of inextensible plates and shells, *The Quarterly Journal of Mechanics and Applied Mathematics*, 16 (1963), 2, 179–191 (cit. on pp. 14, 152).
- [Bag 10] Bagger, A.: *Plate shell structures of glass - Studies leading to guidelines for structural design*, PhD thesis, Lyngby: DTU Civil Engineering, 2010 (cit. on p. 10).
- [Bel 07a] Belis, J. et al.: Cold bending of laminated glass panels, *HERON Vol. 52, No. 1/2*, Vol. 52, No. 1/2 - 2007 (2007), 123–146 (cit. on pp. 12, 14, 23).
- [Bel 07b] Belis, J. et al.: Experimental assessment of cold-bent glass panels, conference contribution, *Glass Performance Days : conference proceedings, 2007, Tampere, Finland*. Glass Performance Days, Tampere, 2007, 115–117 (cit. on pp. 14, 32).
- [Ben 99] Bennison, S. J.; Jagota, A.; Smith, C. A.: Fracture of Glass/Polyvinyl Butyral (Butacite) Laminates in Biaxial Flexure, *Journal of the American Ceramic Society*, 82 (7) (1999), 82, 1761–1770 (cit. on p. 114).
- [Ben 13] Bennison, S.; Stelzer, I.; Czyzewicz, R.: “Structural Performance and Applications of Laminated Glass”, company reaerach and application presentation, Tampere, 2013 (cit. on pp. 109, 110, 117, 125, 127, 138).
- [BF 11] BF, B. F. e.V.: *BF Merkblatt 009/2011: Leitfaden für thermisch gebogenes Glas im Bauwesen*. Bundesverband Flachglas e.V., 2011 (cit. on pp. 17, 18).
- [Bos 03] Bosia, F. et al.: Characterization of the response of fibre Bragg grating sensors subjected to a two-dimensional strain field, *Smart Materials and Structures*, 12 (2003), 6, 925–934 (cit. on p. 83).

- [Bot 10] Botero-Cadavid, J.; Causado-Buelvas, J.; Torres, P.: Spectral Properties of Locally Pressed Fiber Bragg Gratings Written in Polarization Maintaining Fibers, *Journal of Lightwave Technology*, 28 (2010), 9, 1291–1297 (cit. on pp. 83, 84).
- [Buc 09] Bucak, Ö. et al.: Das Bauprodukt “warm gebogenes Glas” - Prüfverfahren, Festigkeiten und Qualitätssicherung, *Stahlbau*, 78 (2009), 23–28 (cit. on p. 17).
- [Buc 95] Buck, J. A.: *Fundamentals of optical fibers*, Wiley series in pure and applied optics, Wiley, New York, 1995 (cit. on pp. 37, 38).
- [Büs 01] Büstrich, R.; Kahlenberg, F.; Popall, M.: ORMOCER®s for Optical Interconnection Technology, *Journal of Sol-Gel Science and Technology*, (2001), 20, 181–186 (cit. on p. 65).
- [C14 11] C14 Committee: *ASTM C1464 - 06(2011): Specification for Bent Glass*, ASTM International, 2011 (cit. on pp. 16, 17).
- [Cac 04] Cachola Schmal, P., ed.: *Workflow: Struktur-Architektur = Architecture-engineering: Klaus Bollinger + Manfred Grohmann*, Birkhäuser-Verlag für Architektur, Basel ; Boston, 2004, 224 pp. (cit. on p. 2).
- [Che 05] Cheng, C.-C. et al.: An investigation of bonding-layer characteristics of substrate-bonded fiber Bragg grating, *Journal of Lightwave Technology*, 23 (2005), 11, 3907–3915 (cit. on p. 55).
- [Chi 13] Chinzi, G.: Curved glass surfaces: design, process definition and performances, conference contribution, *Glass Performance Days 2013: conference proceedings, Tampere, Finland*. Glass Performance Days 2013, Tampere, 336–344 (cit. on pp. 16, 17).
- [Chu 14] Chung, W. et al.: Finite element simulation of plate or sheet metal forming processes using tetrahedral MINI-elements, *Journal of Mechanical Science and Technology*, 28 (2014), 1, 237–243 (cit. on p. 162).
- [cri 15] cricursa: *curved glass*, curved glass, 21st Mar. 2015 (cit. on pp. 17, 19).
- [Dat 14] Datsiou, K.; Overend, M.: Behaviour of cold bent glass plates during the shaping process, conference contribution, *engineered transparency: glass - facade - energy*, engineered transparency: International conference at glasstec, Düsseldorf, 125–133 (cit. on pp. 12, 32).
- [Del 14] Delo: *DELO Technische Information Katiobond 4552*, DELO Technische Information Katiobond 4552, 28th Nov. 2014 (cit. on p. 145).
- [DIB 13] DiBt: *Allgemeine bauaufsichtliche Zulassung für thermisch gebogene, linienförmig gelagerte Glasscheiben Fini Curve Float und Fini Curve VSG*, ABZ Z704-146, Berlin, 8th Dec. 2013 (cit. on p. 18).
- [DIB 10] DiBt: *Allgemeine bauaufsichtliche Zulassung Z-70.4-163 für gebogenes Floatglas „SGG Contour“ und gebogenes VSG aus Floatglas „SGG Contour Stadip“*, ABZ Z-70.4-163, Berlin, 2010 (cit. on p. 18).
- [DiB 12] DiBt: *Allgemeine bauaufsichtliche Zulassung Z-70.3-175 für Glascobond Verbund-Sicherheitsglas mit Schubverbund*, Allgemeine bauaufsichtliche Zulassung Z-70.3-175, Berlin: DiBt, 1st Nov. 2012 (cit. on p. 14).
- [DiB 06a] DiBt: *Technische Regeln für die Bemessung und die Ausführung punktförmig gelagerter Verglasungen (TRPV)*, technical guideline RI 700, Berlin: DiBt, Aug. 2006 (cit. on p. 14).

- [DiB 03] DiBt: *Technische Regeln für die Verwendung von absturzsichernden Verglasungen (TRAV)*, technical guideline, Berlin: DiBt, 2003 (cit. on pp. 14, 18).
- [DiB 06b] DiBt: *Technische Regeln für die Verwendung von linienförmig gelagerten Verglasungen (TRLV)*, technical guideline RI 700, Berlin: DiBt, Aug. 2006 (cit. on pp. 14, 18).
- [DIN 00] DIN (NMP, N.: *DIN 1288-3 (09-2000): Bestimmung der Biegefestigkeit von Glas. Teil 3: Prüfung von Proben bei zweiseitiger Auflagerung (Vierschneiden-Verfahren)*, Deutsche Industrie-Norm, Berlin, 2000 (cit. on p. 17).
- [DIN 12] DIN (NMP, N.: *DIN EN 12150-1 Glas im Bauwesen – Thermisch vorgespanntes Kalknatron-Einscheibensicherheitsglas – Teil 1: Definition und Beschreibung; Deutsche Fassung prEN 12150:2012*, Deutsche Industrie-Norm, Berlin, 2012 (cit. on p. 18).
- [Don 07] Dong, X.; Tam, H. Y.; Shum, P.: Temperature-insensitive strain sensor with polarization-maintaining photonic crystal fiber based Sagnac interferometer, *Applied Physics Letters*, 90 (2007), 15, 151113 (cit. on p. 168).
- [DuP 15] DuPont: *SentryGlas Brochure. Typical Physical Properties of DuPont SentryGlas Interlayer*, SentryGlas Brochure, 25th Jan. 2015 (cit. on p. 109).
- [Dus 99] Duser, A. V.; Jagota, A.; Bennison, S. J.: Analysis of Glass/Polyvinyl Butyral Laminates Subjected to Uniform Pressure, *Journal of Engineering Mechanics*, 125 (1999), 4, 435–442 (cit. on p. 114).
- [Eck 10] Eckhardt, C.; Stahl, J.: New materials for transparent constructions, *Glass, facade, energy: engineered transparency ; international conference at Glastec [29.-30 Sept. 2010 at Düsseldorf]*, Schneider, J.; Weller, B. (ed.), Techn. Univers. Drsdn, Dresden, 2010, 431–439 (cit. on p. 2).
- [Eek 08] Eekhout, M.: Zappi Glass Structures and Constructions in Blob Architecture, conference contribution, *Challenging glass: Conference on Architectural and Structural Applications of Glass, Faculty of Architecture, Delft University of Technology, May 2008*, Challenging Glass 2008, Delft, 545–555 (cit. on p. 14).
- [Eek 07] Eekhout, M.; Lockefeer, W.; Staaks, D.: Application of cold twisted tempered glass panels in double curved architectural designs, conference contribution, *Glass Performance Days : conference proceedings, 2007, Tampere, Finland*. Glass Performance Days, Tampere, 2007, 213–220 (cit. on p. 14).
- [Eek 09] Eekhout, M.; Niderehe, S.: The New, Cold Bent Glass Roof of the Victoria & Albert Museum, London, conference contribution, *Glass Performance Days : conference proceedings, 2009, Tampere, Finland*. Glass Performance Days, Tampere, 408–412 (cit. on pp. 12, 14).
- [Eig 10] Eigensatz, M. et al.: Paneling architectural freeform surfaces, conference contribution, ACM Press, 2010, 1 (cit. on p. 10).
- [Ens 05] Ensslen, F.: *Zum Tragverhalten von Verbund-Sicherheitsglas unter Berücksichtigung der Alterung der Polyvinylbutyral-Folie*, PhD thesis, Bochum: Ruhr-Universität Bochum, 2005 (cit. on p. 29).
- [EOT 13] EOTA: *BTH & BAG curved glass, curved glass for use in buildings*, European Technical Approval ETA 13/0362, Brussels: EOTA, 27th June 2013 (cit. on p. 18).
- [Erd 97] Erdogan, T.: Fiber grating spectra, *Journal of Lightwave Technology*, 15 (1997), 8, 1277–1294 (cit. on pp. 43, 45, 46).

- [Est 13] Estrada, G.; Baldassini, N.; Royer de Vericourt, R.: Direct evaluation of internal forces in cold-bent plates, conference contribution, *Glass Performance Days 2013: conference proceedings, Tampere, Finland*. Glass Performance Days 2013, Tampere, 67–69 (cit. on pp. 14, 32).
- [Fed 13] Federation, G. G.: *The Glazing Manual*, Guideline, manual, London: Glass and Glazing Federation GGF, 2013, 89–104 (cit. on pp. 16, 17).
- [Fel 12] Feldmann, M.: *Glas für tragende Bauteile*, Werner Verlag, Köln, 2012, 263 pp. (cit. on p. 28).
- [Fel 13] Feldmann, M. et al.: *Guidance for European structural design of glass components: support to the implementation, harmonization and further development of the Eurocodes*. Publications Office, Luxembourg, 2013 (cit. on pp. 14, 16, 17).
- [Fer 80] Ferry, J. D.: *Viscoelastic properties of polymers*, 3d ed, Wiley, New York, 1980, 641 pp. (cit. on pp. 112, 113).
- [Fil 12a] Fildhuth, T.; Knippers, J.: Considerations Using Curved, Heat or Cold Bent Glass for Assembling Full Glass Shells, *Engineered transparency 2012 conference proceedings*, Weller, B.; Schneider, J. (ed.), 2012, 135 (cit. on pp. 3, 11, 32).
- [Fil 14a] Fildhuth, T.; Knippers, J.: Dehnungsmessung in Gekrümmten Glaslaminaten mit Faseroptischen Sensoren, *Glasbau 2014*, Weller, B.; Tasche, S. (ed.), Wiley-VCH Verlag GmbH, D-69451 Weinheim, Germany, 15th Apr. 2014, 289–300 (cit. on p. 29).
- [Fil 11] Fildhuth, T.; Knippers, J.: Double Curved Glass Shells from Cold Bent Glass Laminates, conference contribution, *Glass Performance Days 2011: conference proceedings, Tampere, Finland*. Glass Performance Days 2011, Tampere (cit. on pp. 11, 12).
- [Fil 14b] Fildhuth, T.; Knippers, J.: Feasibility studies on fibre optical sensor implementation in cold bent glass laminates, conference contribution, *engineered transparency: glass - facade - energy*, engineered transparency: International Conference at glasstec, Düsseldorf, 61–73 (cit. on p. 29).
- [Fil 14c] Fildhuth, T.; Knippers, J.: Interior stress monitoring of laminated, cold bent glass with fibre Bragg sensors. conference contribution, *Challenging Glass 4*, Lausanne, 105–112 (cit. on p. 29).
- [Fil 13] Fildhuth, T.; Knippers, J.: Permanent Strain Measurement Inside of Cold Bent Glass Laminates, conference contribution, *Glass Performance Days 2013*, Tampere (cit. on p. 29).
- [Fil 12b] Fildhuth, T.; Lippert, S.; Knippers, J.: Design and Joint Pattern Optimisation of Glass Shells, conference contribution, *IASS-ACPS Conference Proceedings 2012*, IASS-ACPS Conference Proceedings 2012, Seoul 2012, FF165, Seoul (cit. on p. 11).
- [Fil 14d] Fildhuth, T. et al.: Recovery behaviour of laminated cold bent glass – Numerical analysis and testing, *Challenging Glass 4 & COST Action TU0905 Final Conference*, Bos, F. et al. (ed.), CRC Press, 28th Jan. 2014, 113–121 (cit. on pp. 27, 31, 32).
- [Flo 04] Flockhart, G. M. H. et al.: Quadratic Behavior of Fiber Bragg Grating Temperature Coefficients, *Applied Optics*, 43 (2004), 13, 2744 (cit. on pp. 76, 80, 84).
- [Flö 13] Flöry, S. et al.: Ruled Free Forms, *Advances in Architectural Geometry 2012*, Hesselgren, L. et al. (ed.), Springer Vienna, Vienna, 2013, 57–66 (cit. on p. 11).
- [Fra 01] Frank, A.: *Dehnungs- und Temperaturmessung in Verbundwerkstoffen mit eingebetteten faseroptischen Bragg-Gitter-Sensoren*, EMPA-Bericht, Diss. ETH Nr. 14083, Zürich: Eidgenössische Technische Hochschule Zürich ETHZ, June 2001 (cit. on pp. 79, 80, 84).

- [Fre 09] Frey, H.: Fließende Grenzen - Freiformflächen im Spannungsfeld von Innen und Außen, conference contribution, *glasbau 2009*, glasbau 2009, Dresden, 145–159 (cit. on p. 10).
- [Fuc 09] Fuchs, A.; Lenzen, S.; Barf, H.: *Innovativ konstruieren Synergien im Bauprozess zwischen Herstellern und Planern*, Inst. für Internat. Architektur-Dokumentation, München, 2009 (cit. on p. 10).
- [Gab 12] Gabler, M.: *Funktionsintegrierte Faserverbundwerkstoffe - ein Beitrag zu strukturintegrierter Sensorik*, Inst. für Tragkonstruktionen u. Konstruktives Entwerfen, Univ., Stuttgart, 2012 (cit. on pp. 4, 45, 48, 50, 79, 83, 84, 95, 97, 193).
- [Gaf 00] Gafsi, R.; El-Sherif, M. A.: Analysis of Induced-Birefringence Effects on Fiber Bragg Gratings, *Optical Fiber Technology*, 6 (2000), 3, 299–323 (cit. on p. 82).
- [Gal 14a] Galuppi, L.; Massimiani, S.; Royer-Carfagni, G.: Large deformations and snap-through instability of cold-bent glass, *Challenging Glass 4 & COST Action TU0905 Final Conference*, Louter, C. et al. (ed.), CRC Press, 28th Jan. 2014, 681–689 (cit. on p. 32).
- [Gal 12] Galuppi, L.; Royer-Carfagni, G.: Laminated beams with viscoelastic interlayer, *International Journal of Solids and Structures*, 49 (2012), 18, 2637–2645 (cit. on p. 113).
- [Gal 15] Galuppi, L.; Royer-Carfagni, G.: Optimal cold bending of laminated glass, (2015) (cit. on pp. 23, 32).
- [Gal 14b] Galuppi, L.; Royer-Carfagni, G.: Rheology of cold-lamination-bending for curved glazing, *Engineering Structures*, 61 (2014), 140–152 (cit. on pp. 13, 15, 32, 33, 113, 168).
- [Gan 15] Ganß, M. et al.: Untersuchungen an thermo-mechanisch beanspruchten Glasklebeverbindungen mit integrierten faseroptischen Sensoren. conference contribution, *Glasbau 2015*, Glasbau 2015, Ernst & Sohn, Berlin, 2015, 361–371 (cit. on pp. 145, 167).
- [Gmb 14a] GmbH, E.: *evolute tools for Rhino - Proven rationalization tools for complex geometries*, evolute. the geometry experts, 11th Sept. 2014 (cit. on p. 10).
- [Gmb 14b] GmbH, S. T.: Bewegliches Faltdach, conference contribution, *Intelligent Glass - Documentation glass technology live 2014*, glass technology live, Düsseldorf, 56 (cit. on p. 15).
- [Haa 14] Haase, K.-H.: Load monitoring opportunity using optical fiber technology, conference contribution, *engineered transparency: glass - facade - energy*, engineered transparency. International Conference at glasstec, Düsseldorf, 249 (cit. on p. 29).
- [Hab 02] Habenicht, G.: *Kleben Grundlagen, Technologien, Anwendung*, Springer, Berlin; Heidelberg; New York; Barcelona; Hong Kong; London; Milan; Paris; Tokyo, 2002 (cit. on pp. 67, 68, 71).
- [Hal 08] Haldimann, M.; International Association for Bridge and Structural Engineering: *Structural use of glass*, Structural engineering documents 10, International Association for Bridge and Structural Engineering, Zürich, Switzerland, 2008, 215 pp. (cit. on pp. 109, 111).
- [Hel 14] Helminger, D.; Daitche, A.; Roths, J.: Glue-induced birefringence in surface-attached FBG strain sensors, conference contribution, 91577B (cit. on pp. 73, 82, 83, 89, 97, 145).
- [Her 11] Her, S.-C.; Huang, C.-Y.: Effect of Coating on the Strain Transfer of Optical Fiber Sensors, *Sensors*, 11 (2011), 12, 6926–6941 (cit. on pp. 56, 57).
- [Hil 78] Hill, K. O. et al.: Photosensitivity in optical fiber waveguides: Application to reflection filter fabrication, *Applied Physics Letters*, 32 (1978), 10 (cit. on p. 41).

- [Hil 97] Hill, K.; Meltz, G.: Fiber Bragg grating technology fundamentals and overview, *Journal of Lightwave Technology*, 15 (1997), 8, 1263–1276 (cit. on pp. 41–43).
- [Hof 87] Hoffmann, K.: *Eine Einführung in die Technik des Messens mit Dehnungsmeßstreifen*, GmbH, H. B. M. (ed.), Druckerei Drach Pfungstadt, Darmstadt, 1987, 289 pp. (cit. on p. 4).
- [Hua 14] Huard, M.; Eigensatz, M.; Bompas, P.: Planar Panelization with Extreme Repetition, conference contribution, *Advances in Architectural Geometry 2014*, Advances in Architectural Geometry 2014, London, 259–279 (cit. on p. 10).
- [ins 14] insider, apple: *Full scale segment of Apple's Campus 2 'spaceship' facade revealed in photos*, <http://appleinsider.com>, 18th Apr. 2014 (cit. on p. 167).
- [Int 12] International, F.: *Draw Tower Grating DTG-LBL-830 / DTG-LBL-1550. Product data sheet*. 2012 (cit. on pp. 80, 84).
- [Int 15] International, F.: *DTG coating Ormocer-T for Temperature Sensing Applications*, product report, Geel / Belgium: FBGS, Feb. 2015, 8 (cit. on p. 147).
- [Int 14] International, F.: *How big is the bending induced optical loss and strain?*, FBGS Draw Tower Gratings, 12th Oct. 2014 (cit. on p. 47).
- [JCG 12] JCGM: *International vocabulary of metrology – Basic and general concepts and associated terms (VIM) JCGM 200:2012*, guideline JCGM 200:2012. 3rd edition, Sèvres: JCGM, 2012, 108 (cit. on p. 107).
- [Jia 14] Jiang, C. et al.: Structures: Combining Geometry with Fabrication and Statics, conference contribution, *Advances in Architectural Geometry 2014*, Advances in Architectural Geometry 2014, London, 199–214 (cit. on p. 10).
- [Jül 13] Jülich, F. et al.: Gauge factors of fibre Bragg grating strain sensors in different types of optical fibres, *Measurement Science and Technology*, 24 (2013), 9, 094007 (cit. on pp. 52, 76, 78, 84, 103).
- [Kar 08] Karisola, J.; KREA Ltd., A. C. M.: *Innovations in bending and tempering boost the glass market*, GlassOnWeb.com, 2008 (cit. on p. 2).
- [Kas 03] Kasper, R.; Sedlacek, G.: A New Method to Determine the Bending Strength of Curved Glass Panels, conference contribution, *Glass Performance Days 2003: conference proceedings, Tampere, Finland*. Glass Performance Days, Tampere, 89–91 (cit. on p. 17).
- [Kas 11] Kassnel-Henneberg, B.: Purely structural glass building envelopes, conference contribution, *Glass and solar in sustainable development: Glass Performance Days : conference proceedings, 17-20 June 2011, Tampere, Finland*, Glass Performance Days, GPD, Tampere, 2011, 304–309 (cit. on pp. 4, 32).
- [Kel 12] Keller, C. M.: “Modellierung der Kaltverformung von Glas in doppelt gekrümmte Formen mit Platten- und Schalentheorien”, Diplomarbeit, Stuttgart, Jan. 2012 (cit. on pp. 15, 32).
- [Kel 14] Kelly, P.: *Properties of Materials*. 2, CRC Pr I Llc, 2014 (cit. on p. 57).
- [Kin 14] Kinet, D. et al.: Fiber Bragg Grating Sensors toward Structural Health Monitoring in Composite Materials: Challenges and Solutions, *Sensors*, 14 (2014), 4, 7394–7419 (cit. on p. 168).



- [Kna 04] Knauer, M. C.; Kaminski, J.; Hausler, G.: Phase measuring deflectometry: a new approach to measure specular free-form surfaces, conference contribution, 366–376 (cit. on p. 30).
- [Kna 09] Knauer, M. C. et al.: Deflektometrie macht der Interferometrie Konkurrenz Deflectometry Rivals Interferometry, *tm - Technisches Messen*, 76 (2009), 4 (cit. on p. 30).
- [Kot 13] Kothe, M.: *Alterungsverhalten von polymeren Zwischenschichtmaterialien im Bauwesen*, PhD thesis, Dresden: Technische Universität Dresden, 2013, 185 pp. (cit. on pp. 109, 111).
- [Kut 03] Kutterer, M.: *Verbundglasplatten: Näherungslösungen zur Berücksichtigung von Schubverbund und Membrantragwirkung*, Shaker\*\*\*5100500, Aachen, 2003 (cit. on p. 114).
- [Lai 13] Lai, M.; Karalekas, D.; Botsis, J.: On the Effects of the Lateral Strains on the Fiber Bragg Grating Response, *Sensors*, 13 (2013), 2, 2631–2644 (cit. on p. 83).
- [Leb 04] Lebid, S.: *Störungen in der Charakteristik von Faser-Bragg-Gitter-Sensoren durch lokale thermische und mechanische Einflüsse*, Wirtschaftsverl. NW, Verl. für Neue Wiss., Bremerhaven, 2004 (cit. on pp. 4, 50, 79, 84).
- [Lin 12] Lindner, E.: *Erzeugung und Eigenschaften hoch-temperaturstabiler Faser-Bragg-Gitter*, IPHT, Jena: Friedrich-Schiller-Universität Jena, Physikalisch-Astronomische Fakultät, 15th May 2012 (cit. on pp. 38, 42–45).
- [Liu 09] Liu, B.; Feng, X.; Zhang, S.-M.: The effective Young's modulus of composites beyond the Voigt estimation due to the Poisson effect, *Composites Science and Technology*, 69 (2009), 13, 2198–2204 (cit. on p. 58).
- [Lou 14] Louter, C. et al.: *Challenging Glass 4 and COST Action TU0905 Final Conference Proceedings, EPFL 2014*, 2014 (cit. on p. 3).
- [Luh 14] Luhmann, T.: *Close-range photogrammetry and 3D imaging*, 2nd edition, De Gruyter textbook, De Gruyter, Berlin, 2014, 684 pp. (cit. on pp. 31, 105–108).
- [Luy 12] Luyckx, G.; Kinet, D.; Lammens, N.: Temperature insensitive cure cycle monitoring of cross-ply composite laminates using the polarization dependent loss property of FBG, conference contribution, *15th european conference on composite materials*, 15th european conference on composite materials (ECCM15 - 2012), Venice (cit. on p. 168).
- [Mäh 13] Mähr, T.: Pushing the limits of structural glass design by applying close-range photogrammetry, conference contribution, *Glass Performance Days 2013: conference proceedings, Tampere, Finland*. Glass Performance Days 2013, Tampere, 415–418 (cit. on p. 28).
- [Man 89] Mansfield, E. H.: *The bending and stretching of plates*, 2nd ed, Cambridge University Press, Cambridge [England] ; New York, 1989, 228 pp. (cit. on pp. 14, 152).
- [Men 99] Menard, K. P.: *Dynamic mechanical analysis: a practical introduction*, CRC Press, Boca Raton, Fla, 1999, 208 pp. (cit. on pp. 67, 68, 112).
- [Mer 14] Mercier, B.: Non-contact 3D measurement of flat or bended glass for highest process control, conference contribution, *engineered transparency: glass - facade - energy*, engineered transparency. Interantional Conference at glasstec 2014, Düsseldorf, 215 (cit. on p. 31).
- [Mey 03] Meyberg, K.; Vachenauer, P.: *Differential- und Integralrechnung, Vektor- und Matrizenrechnung*, Springer, Berlin [u.a.], 2003 (cit. on p. 32).

- [Neu 09] Neugebauer, J.: A Design Concept for Bent Insulated Glasses for the Reading Room of the Berlin State Library, conference contribution, *Glass Performance Days: conference proceedings, 2009, Tampere, Finland*. Glass Performance Days, Tampere, 244–249 (cit. on p. 18).
- [Neu 08] Neugebauer, J.: Climatic loads in cruved insulated glasses, conference contribution, *Challenging glass: Conference on Architectural and Structural Applications of Glass, Faculty of Architecture, Delft University of Technology, May 2008*, Challenging Glass 2008, Delft (cit. on p. 18).
- [Neu 13] Neugebauer, J.: Conically shaped insulated glass, conference contribution, *Glass Performance Days 2013: conference proceedings, Tampere, Finland*. Glass Performance Days, Tampere, 92–94 (cit. on p. 18).
- [Nij 11] Nijssse, R.: Corrugated glass facades, conference contribution, *Glass Performance Days 2011: conference proceedings, Tampere, Finland*. Glass Performance Days, Tampere, 394–397 (cit. on p. 18).
- [Nor 13] Normung e. V, D. D. I. für: *DIN EN 6032 Luft- und Raumfahrt – Faserverstärkte Kunststoffe – Prüfverfahren – Bestimmung der Glasübergangstemperatur*, prEN 6032, Berlin: DIN Deutsches Institut für Normung e. V, July 2013 (cit. on p. 68).
- [nor 15] northglass: *AG1, AG12 and AG15 Glass Tempering Furnaces Main Parameters*, AG1, AG12 and AG15 Glass Tempering Furnaces Main Parameters, 3rd Dec. 2015 (cit. on pp. 16, 19).
- [Nöt 14] Nöther, N.: *Brillouin Optical Frequency Domain Analysis (BOFDA) based distributed fiber-optic sensing technology*, new fiber optic strain and temperature sensors, 2014 (cit. on p. 41).
- [Oth 99] Othonos, A.; Kalli, K.: *Fiber Bragg gratings: fundamentals and applications in telecommunications and sensing*, Artech House optoelectronics library, Artech House, Boston, Mass, 1999 (cit. on pp. 36, 42, 43, 79).
- [Oth 06] Othonos, A. et al.: Fibre Bragg Gratings, *Wavelength Filters in Fibre Optics*, Venghaus, H. (ed.), 123, Springer Berlin Heidelberg, 2006, 189–269 (cit. on p. 4).
- [Pap 02] Papeleux, L.; Ponthot, J.-P.: Finite element simulation of springback in sheet metal forming, *Journal of Materials Processing Technology*, 125-126 (2002), 785–791 (cit. on p. 162).
- [Par 10] Parlevliet, P. P.; Bersee, H. E.; Beukers, A.: Measurement of (post-)curing strain development with fibre Bragg gratings, *Polymer Testing*, 29 (2010), 3, 291–301 (cit. on pp. 73, 82, 145).
- [Pen 14] Penkova, N. et al.: Thermal load analysis of cylindrically bent insulating glass units, conference contribution, *Challenging Glass 4 & COST Action TU0905 Final Conference*, Challenging Glass 4, Lausanne, 123–132 (cit. on p. 18).
- [Pen 13] Pennetier, S.; Bindji-Odzili, F.: A numerical model for cold bending of laminated glass panels, conference contribution, *Glass Performance Days 2013: conference proceedings, Tampere, Finland*. Glass Performance Days 2013, Tampere, 286–289 (cit. on p. 13).
- [Poc 89] Pockels, F. C. A.: *Ueber den Einfluss elastischer Deformationen, speciell einseitigen Druckes, auf das optische Verhalten krystallinischer Körper*, Dissertation, Göttingen, 1889, PhD thesis, Göttingen, 1889 (cit. on p. 48).
- [Pot 08] Pottmann, H. et al.: Freeform surfaces from single curved panels, *ACM Transactions on Graphics*, 27 (2008), 3, 1 (cit. on p. 11).

- [Red 04] Redner, A. S.: Stress Measuring Methods for Quality Control and Process Optimization in Glass, *International Journal of Forming Processes*, 7 (2004), 4, 555–563 (cit. on p. 28).
- [Rör 14] Rörig, T. et al.: Surface Panelization Using Periodic Conformal Maps, conference contribution, *Advances in Architectural Geometry 2014*, Advances in Architectural Geometry 2014, London, 199–214 (cit. on p. 10).
- [Ros 13] Rose, K.: *UV curable Ormocer coatings*, Fraunhofer ISC Werkstoffchemie- hybride Schichten und-beschichtungstechnologie, 2013 (cit. on p. 65).
- [Roy 11] Royer de Vericourt, R.: Inextensional Theory Applied to Cold Bent Glass Built-in Stress Evaluation, conference contribution, *Glass and solar in sustainable development: Glass Performance Days : conference proceedings, 17-20 June 2011, Tampere, Finland*, Glass Performance Days, GPD, Tampere, 2011, 377–383 (cit. on pp. 13, 14, 32, 152).
- [Sac 08] Sackmann, V.: *Untersuchungen zur Dauerhaftigkeit des Schubverbunds in Verbundsicherheitsglas mit unterschiedlichen Folien aus Polyvinylbutyral*, PhD thesis, München: Technische Universität München, 2008 (cit. on pp. 109, 111, 112, 114).
- [Sal 91] Saleh, B. E. A.: *Fundamentals of photonics*, Wiley series in pure and applied optics, Wiley, New York, 1991 (cit. on pp. 36, 37, 39).
- [Sam 12] Samiec, D.: Distributed fibre-optic strain and temperature measurement with extremely high spatial resolution, *Photonik International*, (2012) (cit. on p. 41).
- [Sch 15] Schiffstechnik GmbH, T. I.-. und: *Tilsecure multi-functional yacht-glazing with Piezo-electric sensors*, Tilsecure multi-functional yacht-glazing, 2015 (cit. on p. 29).
- [Sch 13] Schiftner, A. et al.: Architectural Geometry from Research to Practice: The Eiffel Tower Pavilions, *Advances in Architectural Geometry 2012*, Hesselgren, L. et al. (ed.), Springer Vienna, Vienna, 2013, 213–228 (cit. on pp. 2, 10, 11, 14).
- [Sch 98] Schlaich, J.; Schober, H.: Glaskuppel für die Flußpferde im Zoo Berlin, *Stahlbau*, 67 (1998), 4, 307–312 (cit. on p. 10).
- [Sch 10] Schlüter, V. G.: *Entwicklung eines experimentell gestützten Bewertungsverfahrens zur Optimierung und Charakterisierung der Dehnungsübertragung oberflächenapplizierter Faser-Bragg-Gitter-Sensoren*, Bundesanstalt für Materialforschung und -prüfung (BAM), Berlin, 2010 (cit. on pp. 4, 50, 56, 57, 64, 75, 78–80, 84, 145, 194).
- [Sch 02] Schober, Hans; Schlaich, Jörg: Filigrane Kuppeln: Beispiele, Tendenzen und Entwicklungen, (2002) (cit. on p. 10).
- [Sch 03] Schuler, C.: *Einfluss des Materialverhaltens von Polyvinylbutyral auf das Tragverhalten von Verbundsicherheitsglas in Abhängigkeit von Temperatur und Belastung*, PhD thesis, München: Technische Universität München, 2003 (cit. on pp. 29, 111, 112, 114).
- [Sch 12] Schuler, C. et al.: Einsatz von gebogenem Glas im Bauwesen, *Stahlbau*, 81 (2012), 3, 190–196 (cit. on pp. 17, 18).
- [sed 15] sedak: *Fertigungskompetenzen sedak*, Fertigungskompetenzen sedak, 21st Mar. 2015 (cit. on pp. 16, 19).

- [She 13] Shen, C. et al.: Temperature-insensitive strain sensor using a fiber loop mirror based on low-birefringence polarization-maintaining fibers, *Optics Communications*, 287 (2013), 31–34 (cit. on p. 168).
- [Sie 12a] Siebert, G.: Aktueller Stand der Normenreihe DIN 18008, conference contribution, *10. Glas im konstruktiven Ingenieurbau 2012*, 10. Glas im konstruktiven Ingenieurbau 2012, 10, Hochschule München, Verein der Freunde des Stahlbaus an der Hochschule München e.V., München, 2012, 30 (cit. on p. 14).
- [Sie 12b] Siebert, G.; Maniatis, I.: *Tragende Bauteile aus Glas Grundlagen, Konstruktion, Bemessung, Beispiele*, Ernst & Sohn, Berlin, 2012 (cit. on pp. 16, 109).
- [Sin 12] Singh, P.; Jülich, F.; Roths, J.: Polarization dependence of the strain sensitivity of fiber Bragg gratings inscribed in highly birefringent optical fibers, conference contribution, 84391S (cit. on p. 37).
- [Sta 74] Stamm, K.: *Sandwichkonstruktionen; Berechnung, Fertigung, Ausführung*, Ingenieurbauten: Theorie und Praxis 3, Springer, Wien, New York, 1974, 337 pp. (cit. on pp. 13, 33, 152).
- [Sta 11a] Standardization, I. O. for: *ISO 11485-1:2011. Glass in building – Curved glass – Part 1: Terminology and definitions*, International Organization for Standardization, 2011 (cit. on p. 17).
- [Sta 11b] Standardization, I. O. for: *ISO 11485-2:2011. Glass in building – Curved glass – Part 2: Quality requirements*, International Organization for Standardization, 2011 (cit. on p. 17).
- [Sta 14] Standardization, I. O. for: *ISO 11485-3:2014. Glass in building - Curved glass - Part 3: Requirements for curved tempered and curved laminated safety glass*, International Organization for Standardization, 2014 (cit. on p. 17).
- [Ste 97] Steenkiste, R. J. V.: *Strain and temperature measurement with fiber optic sensors*, Technomic Pub. Co, Lancaster, Pa, 1997 (cit. on pp. XIII, 48, 52, 79, 84, 168, 192, 193).
- [Sto 97] Storøy, H.; Johannessen, K.: Glue induced birefringence in surface mounted optical fibres, *Electronics Letters*, 33 (1997), 9, 800 (cit. on pp. 73, 82, 145).
- [sun 14] sunglass: *sunglass company information provided at GPD 2013 by Gery Chinzi*, 2014 (cit. on p. 19).
- [Tei 14] Teich, M.; Kloker, S.; Baumann, H.: Curved glass: bending and applications, conference contribution, *engineered transparency: glass - facade - energy*, engineered transparency: glass - facade - energy, Düsseldorf (cit. on pp. 3, 12–14, 32, 156, 168).
- [Tim 14] Timm, C.; Chase, J.: Thermally curved glass for the building envelope, conference contribution, *Challenging Glass 4 & COST Action TU0905 Final Conference*, Challenging Glass 4, Lausanne, 141–149 (cit. on pp. 16, 17).
- [Tru 01] Trutzel, M. N.: *Dehnungsermittlung mit faseroptischen Bragg-Gitter-Sensoren : Grundlagen, Eigenschaften und Anwendungen*, PhD thesis, Berlin: Technische Universität Berlin, 2001 (cit. on pp. 46, 50–52, 64, 193).
- [Udd 06] Udd, E.: *Fiber optic sensors an introduction for engineers and scientists*, Wiley, New York [u.a.], 2006 (cit. on p. 4).
- [Van 09] Van Roosbroeck, J.; Vlekken, J.; Chojetzki, C.: A New Methodology for Fiber Optic Strain Gage Measurements and its Characterization, conference contribution, *Proceedings: Nürnberg*,

- Germany, 26-28 May 2009 ; [part of] *SENSOR + TEST Conference 2009*, OPTO 2009, AMA Service, Wunstorf, 2009, 59–64 (cit. on pp. 49, 54, 76).
- [Vau 13] Vaudeville, B. et al.: How Irregular Geometry and Industrial Process Come Together: A Case Study of the “Fondation Louis Vuitton Pour la Création”, Paris, *Advances in Architectural Geometry 2012*, Hesselgren, L. et al. (ed.), Springer Vienna, Vienna, 2013, 279–294 (cit. on pp. 2, 11, 14).
- [VDE 10] VDE, V. l.: *VDI/VDE 2660: Experimental stress analysis – Optical strain sensor based on fibre bragg grating – Fundamentals, characteristics and sensor testing*, July 2010 (cit. on pp. 54, 76, 77).
- [Vou 12] Vouga, E. et al.: Design of self-supporting surfaces, *ACM Transactions on Graphics*, 31 (2012), 4, 1–11 (cit. on pp. 10, 11).
- [Wal 11] Wallner, J.; Pottmann, H.: Geometric Computing for Freeform Architecture, *Journal of Mathematics in Industry*, 1 (2011), 1, 4 (cit. on p. 10).
- [Web 13] Weber, F.: Designing pleated curved glass structures for iconic greenhouses, conference contribution, *Glass Performance Days 2013: conference proceedings, Tampere, Finland*. Glass Performance Days, Tampere, 328–335 (cit. on pp. 14, 18).
- [Wel 10] Weller, B.: *Glasbau-Praxis: Konstruktion und Bemessung ; Vertikal- und Überkopfverglasungen, absturzsichernde Verglasungen, begehbare Verglasungen, Berechnungshilfen*, Bauwerk, Berlin, 2010 (cit. on pp. 17, 109).
- [Wel 11a] Weller, B.; Kothe, C.; Wunsch, J.: Study of the Photo Initiated Curing Process of Transparent Adhesives, conference contribution, *Taller, Longer, Lighter - Meeting growing demand with limited resources. IABSE-IASS Symposium 2011*, IABSE-IASS Symposium 2011, IABSE reports 98, IABSE reports, London, 566 (cit. on pp. 65, 145).
- [Wel 11b] Weller, B.; Krampe, P.: Bent glass in four-point bending test, conference contribution, *Glass Performance Days 2011: conference proceedings, Tampere, Finland*. Glass Performance Days, Tampere, 301–303 (cit. on p. 18).
- [Wel 14a] Weller, B.; Tautenhahn, L.: Evaluation of adhesively bonded mounting systems by comparing photogrammetry and FEM, conference contribution, *engineered transparency: glass - facade - energy*, engineered transparency. International Conference at glasstec 2014, Düsseldorf, 197 (cit. on pp. 28, 31).
- [Wel 14b] Weller, B.; Tautenhahn, L.; Sauerborn, T.: Strain distribution of thin out-of-plane loaded glass plates by photogrammetry, conference contribution, *Challenging Glass 4 & COST Action TU0905 Final Conference*, Challenging Glass 4, Lausanne, 541 (cit. on pp. 28, 31).
- [Wör 06] Wörner, J.-D.; Schneider, F.: Zeitabhängiges Materialverhalten von Glas, *Bauingenieur*, 81 (2006), 278–284 (cit. on p. 109).
- [Yin 08] Yin, S.; Ruffin, P. B.; Yu, F. T. S., eds.: *Fiber optic sensors*, 2nd ed, Optical science and engineering 132, CRC Press, Boca Raton, FL, 2008 (cit. on pp. 40, 41, 45, 47).
- [zee 15] zeen, de: *Foster and Partners completes Apple store in Hangzhou, China*, de zeen magazine, 18th Feb. 2015 (cit. on p. 167).
- [Zel 99] Zellner, P.: *Hybrid space: new forms in digital architecture*, Rizzoli, New York, 1999, 191 pp. (cit. on p. 2).



## List of Figures

1.1.	Funicular station “Congress” of the Nordkettenbahn at Innsbruck (Arch.: Zaha Hadid). . . . .	2
1.2.	Fondation Louis Vuitton pour la Création, Paris (Arch. F.O. Gehry). Photo: Courtesy of Niccolo Baldassini, Paris. . . . .	2
1.3.	Translational grid shell with quadrangular mesh, Bosch-Areal, Stuttgart (Arch.: Prof. Ostertag + Vornholdt; Eng.: Schlaich, Bergermann und Partner). . . . .	3
1.4.	MyZeil shopping mall with a triangulated glass grid shell façade, Frankfurt a. M. (Arch.: Massimiliano Fuksas architetto). . . . .	3
1.5.	Smooth, double curved façade from cold bent glass. Rendering: N. Jundt, ITKE . . . . .	3
1.6.	Cold bent glass façade of Strasbourg Central Station. . . . .	4
1.7.	Size comparison of an optical fibre and its FC/APC-plug. . . . .	5
1.8.	Research approach and methodology overview . . . . .	7
2.1.	Principle of the developable strip approximation and its application to a freeform façade. . . .	10
2.2.	Cold bent glass façade study with wind load and self weight. Top: normal joint forces; bottom: principal stress $\sigma_1$ . . . . .	11
2.3.	Cold bending form-finding studies of double curved, three-ply glass laminate panels for a paraboloid and a saddle shell. . . . .	11
2.4.	Cold bent glass on a mould in an evacuated vacuum bag. . . . .	13
2.5.	Schematic depiction of the principal heat bending processes. . . . .	16
2.6.	Optical distortion of a single curved, thermally bent insulating glass unit. . . . .	17
4.1.	Schematic workflow depiction of the glass cold bending, lamination and relaxation procedure applied for this research. . . . .	27
4.2.	Cold bending aluminium mould with glass-interlayer stacks wrapped in an evacuated vacuum bag applied in this research. . . . .	27
4.3.	Target and contact element configuration of a symmetric quarter model of the bending mould and glass panes. . . . .	33
4.4.	Schematic diagram depicting the principal phases of cold bent and lamination. . . . .	33
4.5.	Diagram of the applicable finite element design strategies for cold bending and relaxation modelling of glass. . . . .	34
5.1.	Fused silica preform for optical fibre drawing (top) and tip detail (bottom). Source: Courtesy of FBGS Technologies GmbH, Jena . . . . .	36
5.2.	Ray propagation types and relevant angles in step-index fibre . . . . .	38
5.3.	Radial distribution $R(r)$ for $l=0$ and $l=1$ . . . . .	39
5.4.	Function principle and reflection of a Bragg grating . . . . .	43
5.5.	Modulated index amplitude (AC) and the DC-index change (offset) of a FBG . . . . .	44
5.6.	Draw tower principle scheme (Image based on: <a href="http://www.fbgs.com/technology/dtg-technology/">http://www.fbgs.com/technology/dtg-technology/</a> ). . . . .	44
5.7.	Normalised reflectivity $R_e$ plotted against the normalised wavelength. . . . .	46
5.8.	Intensity plot ( $\log_{10}$ ) of a FBG spectrum for normalised wavelength $\lambda/\lambda_{max}$ . . . . .	47
5.9.	Modification of the polarisation fields attributable to transverse force deformation. . . . .	50

5.10. Stress in the cylindrical fibre due to transverse linear forces. . . . .	50
5.11. Sensor fibre and substrate strain directions . . . . .	51
5.12. Schematic axial and bending models of a FBG bonded to a substrate and inside of a laminate. . . . .	55
5.14. Schematic axial and bending models of a FBG bonded to a substrate and inside of a laminate. . . . .	56
5.13. Schematic transverse and longitudinal sections of a surface-bonded fibre. . . . .	57
5.15. Schematic depiction of a surface-bonded fibre subjected to bending. . . . .	58
5.16. Comparison of numerically and analytically determined bending strain for different $G_a$ and bond types A, B. . . . .	62
5.17. Bending strain transfer ratio with varying $G_a$ for $t_a=0.012\text{mm}$ . . . . .	62
5.18. Bending strain transfer ratio with varying $t_a$ for $G_a=10\text{MPa}$ (top) and $G_a=600\text{MPa}$ (bottom). . . . .	63
5.19. Infrared spectroscopy of Ormocer <sup>®</sup> NM850: Transmission spectrum (top left), reaction turnover (top-right) and detailed bands of the transmission spectrum (bottom). . . . .	66
5.20. UV-intensity measurement of UVA Hand 250 lamp depending on light source distance from cure object. . . . .	67
5.21. DMA testing device (Netzsch DMA 242 C). . . . .	68
5.22. DMA testing results $E'$ , $E''$ of Delo KB4552 and KB OB642 (top) and complex Young's modulus $E^*$ (bottom). . . . .	70
5.23. Bulk adhesive sample axial tensile testing with an Instron UPM 5881. . . . .	71
5.24. Tensile stress-strain diagrams for Delo KB4552 (top) and KB OB642 (bottom) after UV cure only and UV cure with autoclave-like tempering. . . . .	72
5.25. Comparison of DSC analyses for Delo KB4552, KB AD640 and KB OB642. . . . .	72
5.26. Mitutoyo SV-C3200-H4 surface roughness contour measurement device. . . . .	74
5.27. Surface roughness contour measurement gauge head. . . . .	74
5.28. Microscopic plan view images of surface-bonded FBGs. . . . .	74
5.29. Cross sections of fibres bonded to glass with either Delo KB OB642 or KB4552. . . . .	75
5.30. Four-point bending testing facility. . . . .	76
5.31. Four-point bending test setup. The fibre-Bragg grating sensors in the centre of the glass plate are bonded to the plate's top (x.1) and bottom (x.2) surface. PT 100 temperature gauges are fixed nearby each Bragg sensor. . . . .	77
5.32. Detail from the stepwise increased load application at constant temperature. . . . .	78
5.33. Relative wavelength shift plotted against numerically derived strain from four-point bending for both tension and compression. . . . .	78
5.34. Test setup for the determination of the thermoelastic coefficient of a free FBG. . . . .	79
5.35. Temperature devolution and related Bragg sensor wavelength of the temperature test. . . . .	81
5.36. Testing results of the Bragg sensor wavelength plotted against temperature and related linear and square regression curves for a coated fibre. . . . .	81
5.37. Testing results of the Bragg sensor wavelength plotted against temperature and related linear and square regression curves for a bare fibre. . . . .	81
5.38. Plan view and elevation of the four-point bending setup. . . . .	85
5.39. Testing procedure for short term load application during autoclave thermal cycle. . . . .	87
5.41. Comparison of the mechanical strain measurement results of an electrical strain gauge and an FBG. . . . .	87
5.40. Measured absolute FBG wavelength and temperature plotted against time for three different adhesives. . . . .	88
5.43. Exemplary spectrum prior to and after thermal and load cycle. . . . .	89
5.42. Testing procedure for permanent load application during thermal autoclave cycle. . . . .	90
5.44. Top diagram: testing procedure results total and compensated wavelength shift $\Delta\lambda$ / temperature T vs. time of specimen FTG KB-OB642-02; bottom diagrams: relaxation behaviour at load F and constant T: wavelength shift / temperature vs. time between instances 2 and 3. . . . .	93
5.45. Transverse section of the fibre bond zone mesh of the 3D micro-model. . . . .	95
5.46. Bond sections type A and type B. . . . .	95
5.47. Boundary conditions and load cases applied to the micro-model. . . . .	96
5.48. Comparison of the $k_E$ gauge factors and birefringence effects for bending. . . . .	99



5.49. Principal strain distribution from tensile bending loads along section 1-1 for a two-ply glass laminate in cold bent (top), initial springback after 0.01s (centre) and relaxation state after 3 months (bottom). . . . .	100
5.50. Comparison of the $k_e$ gauge factors and birefringence effects for axial load in 1-direction. . . . .	101
5.51. Comparison of the $k_T$ factors and birefringence effects for uniform thermal load. . . . .	102
5.52. Schematic depiction of the pinhole camera principle. . . . .	105
5.53. Schematic process diagram of photogrammetry analysis. . . . .	106
5.54. Exemplary bundle adjustment result output of the software Australis. . . . .	108
5.55. Temperature-dependent Young's modulus of SG ionomer measured at 1Hz in DMA by M. Kothe, 2013. The results of Bennison are added for comparison. . . . .	110
5.56. Time- and temperature-dependent shear moduli and Poisson's coefficients of SG ionomer as published by Bennison et al. . . . .	110
5.57. Principles of stress relaxation and creep. . . . .	111
5.58. Schematic Maxwell-Wiechert model. . . . .	112
5.59. Time- and temperature-dependent shear moduli of PVB Trosifol <sup>®</sup> BGR20 from the research of Andreozzi et al. . . . .	113
5.60. Comparison of the time-dependent shear moduli at room temperature from different authors. . . . .	114
6.1. Sliding support of a cold bent glass sample. . . . .	116
6.2. Setup of the long-term testing of 9 cold bent glass specimens with three different compositions. . . . .	118
6.3. Sensitive glass arch demonstrator with a 90 FBG sensor array presented at the glasstec 2014 trade fair. . . . .	118
6.4. Schematic cross sections and sensor positions of all laminate types produced for this research (not to scale). . . . .	119
6.5. Sensor layout and positions for the two- and three-ply laminates. . . . .	120
6.6. Plan view and elevation of the four-ply laminate with the sensor layout at the interior faces of the top and bottom glass panes. . . . .	121
6.7. Layout of sensors in the four-ply glass laminate prior to lamination. . . . .	121
6.8. Exemplary target point numbering system applied to the top glass surface in vertical and horizontal sample position. . . . .	122
6.9. Photogrammetry setup of long-term testing of nine glass specimens and at release of the glass samples from the bending mould. . . . .	123
6.10. Photogrammetry object target point identification in the Australis software. . . . .	123
6.11. Coordinate transformation orientation referring to the target points on the glass surface. . . . .	124
6.12. Mean z-coordinate for points along the narrow side of the glass determined via photogrammetry plotted against logarithmic time scale; comparison to corresponding FE results. . . . .	128
6.13. Schematic Gaussian curvature plot of the mean surface from photogrammetry and the FE model for the cold bent state and after 8 months of relaxation for specimen type 2esg_pvb. . . . .	129
6.14. Schematic Gaussian curvature plot of the mean surface from photogrammetry and the FE model for the cold bent state and after 8 months of relaxation for specimen 2esg_sgp. . . . .	130
6.15. Comparison of the principal curvature radii from photogrammetry on the top surface of a laminate from three cold bent glass panes with SG interlayer for the cold bent state and after 8 months of relaxation. . . . .	131
6.16. Two-ply PVB laminate glass stress in the x-direction calculated from FBG 1 and 6 during 8 months of monitoring; comparison with FEA results. . . . .	133
6.17. Two-ply SG laminate glass stress in the x-direction calculated from FBG 1 and 6 during 8 months of monitoring; comparison with FEA results. . . . .	133
6.18. Three-ply SG laminate glass stress in the x-direction calculated from FBG 1 and 12 during 8 months of monitoring; comparison with FEA results. . . . .	134
6.19. Mean $\sigma_x$ stress distribution from FBG and FE analyses along the curved direction of laminate type 4esg_sgp. . . . .	136
7.1. Example spectra from lamimnate 3esg_sgp-01. . . . .	140

7.2.	Spectral width monitoring of three chains of 15 FBGs each from specimen 4esg_sgp-02 at pos. 2 (left) and pos. 7 (left, right). Spectra for sensors 3,5 at pos. 7 (right) are given as an example at the bottom. . . . .	142
7.3.	Cross section of the fibre bond and the interlayer depicting the $\epsilon_1$ strain distribution during springback and relaxation of a two-ply SG glass laminate. . . . .	144
7.4.	Example of the monitoring of an autoclave process with FBG bonded to glass and a free FBG for temperature compensation. . . . .	146
7.5.	Hypothetical influence of the adhesive bond of the fibre and of the interlayer solidification during the cooling process on the wavelength shift measured with an FBG. . . . .	147
7.6.	Compression axial strain $\sigma_x$ and transverse components $\sigma_{y,z}$ developing in a bonded fibre during cooling from 55°C to 23°C. A section along the z-axis through the centre of the fibre is shown. . . . .	149
7.7.	Sensors in a three ply glass laminate glued with Delo KB4552. The adhesive shows a yellowish aspect after UV cure and autoclaving. . . . .	150
7.8.	Sensor glued to the interior glass surface of the four-ply laminate with Delo KB OB642. . . . .	150
7.9.	Glass stress $\sigma_x$ distribution across the section of all four laminate types for the locations of the sensors 1 or 6 as calculated by FEA. . . . .	153
7.10.	Schematic depiction of the bending stress for single curvature cold bending and the development of additional membrane stress from springback. . . . .	153
7.11.	Stress plots in x- and y-direction in a glass pane generated by cold bending on the mould. . . . .	154
7.12.	Comparison of the stress results $\sigma_x$ along a longitudinal section 30mm from the curved edge determined with the contact element model FSD.2.2, the cylindrical model FSD.1.1 and the FBG-results for 4esg_sgp and 2esg_sgp. . . . .	155
7.13.	Process diagram of the finite element fixed point iteration for cold bending of glass. . . . .	157
7.14.	Explicit surface equations of the four basic cold bending shapes studied. . . . .	158
7.15.	Curvature analysis of a paraboloid shape from 3x6mm FTG (3x3m) laminated with 1.52mm SG analysed with model types FPI.1.1 and FPI.1.2. The principal curvature directions / results are shown for nine points on the surface of the topmost glass. . . . .	160
7.16.	Curvature analysis of a HP shape from 3x6mm FTG (3x3m) laminated with 1.52mm SG analysed with model type FPI.1.2. The principal curvature directions / results are shown for nine points on the surface of the topmost glass. . . . .	161
7.17.	Cold bending and springback principal tensile stress shown for 3x10mm FTG laminated with 0.9mm SG pressed upon a HP-shaped bending mould. . . . .	162
7.18.	Maximum principle tensile stress $\sigma_1$ , minimum curvature radii $R_1 = R_2$ and max. vertical displacement $u_z$ for a 3x3m glass plate deformed into a cylindrical, saddle, HP or paraboloid geometry by cold bending. . . . .	163
B.1.	DMA testing results $E'$ and $E''$ for adhesives from Delo, Permabond, Fraunhofer ISC and Panacol (temp.=tempering during 3.5h at 140°C). . . . .	197
B.2.	DMA testing results $E'$ and $E''$ for adhesives from Wellmanntech, Polytec, Dymax, Henkel and 3m (temp.=tempering during 3.5h at 140°C; thix.=thixotropic version of Catiowell 3052). . . . .	198
B.3.	Axial tensile testing results E for adhesives from Delo, Wellmanntech, Polytec and Dymax (temp.=tempering during 3.5h at 140°C; thix.=thixotropic version of Catiowell 3052). . . . .	199
B.4.	Axial tensile testing results E for adhesives from Panacol, Henkel, Fraunhofer ISC, Permabond and 3m. . . . .	200
B.5.	DSC testing results for adhesives from Wellmanntech, Polytec, Fraunhofer ISC, Permabond and Panacol. . . . .	201
B.6.	Surface roughness measurement results across FBG bond of the specimen FTG OB642-02 and -03. . . . .	204
B.7.	Surface roughness measurement results across FBG bond of the specimen FTG KB4552-02 and -03. . . . .	205
C.1.	Four-point bending device and climatic chamber . . . . .	208
C.2.	Spectra of sensors 3.1 to 3.3 prior to and after UV cure of the adhesive. . . . .	209

C.3.	Type specimen for the four-point bending tests. . . . .	209
C.4.	Top diagram: Testing procedure results total and compensated wavelength shift $\Delta\lambda$ / temperature T vs. time of specimen FTG KB4552-02; bottom diagrams: Relaxation behaviour at load F and constant T: Wavelength shift / temperature vs. time between instances 2 and 3. . . . .	212
D.1.	Principal strain distribution from bending loads along section 1-1 for a single glass plate with a realistic type B bond geometry. . . . .	214
D.2.	Principal strain distribution from bending loads along section 1-1 for a single glass plate with a simplified type A bond geometry. . . . .	215
D.3.	Principal strain distribution from compression bending loads along section 1-1 for a two-ply SG glass laminate in cold bent, springback and relaxation state. . . . .	216
D.4.	Principal strain distribution from axial loads in direction 1 along section 1-1 for a single glass. . . . .	217
D.5.	Principal strain distribution from uniform thermal cooling loads for a two-ply glass laminate and a single glass pane. . . . .	218
E.1.	Setup of the target point numbering in the testing room and positions of the glass specimens. . . . .	221
E.2.	Shear modulus and Maxwell model for PVB as per Sackmann. . . . .	222
E.3.	Time- and temperature-dependent shear moduli of PVB Trosifol BGR20 from the research of Andreozzi et al. . . . .	223
E.4.	Relaxation behaviour of the three curved laminate types 2esg_pvb (top), 2esg_sgp (centre) and 3esg_sgp (bottom). . . . .	225
E.5.	Comparison of the principal curvature radii from photogrammetry (top) and FE analysis (bottom) on the top surface of laminate from two cold bent glass panes with PVB interlayer for the cold bent state and after 8 months of relaxation. . . . .	226
E.6.	Comparison of the principal curvature radii from photogrammetry (top) and FE-analysis (bottom) on the top surface of laminate from two cold bent glass panes with DG-interlayer for the cold bent state and after 8 months of relaxation. . . . .	227
E.7.	Comparison of the principal curvature radii from photogrammetry (top) and FE-analysis (bottom) on the top surface of laminate from three cold bent glass panes with SG-interlayer for the cold bent state and after 8 months of relaxation. . . . .	228
E.8.	Two-ply PVB and SG laminate glass stress in the x-direction calculated from FBG 1 and 6 during 8 months of test monitoring. . . . .	231
E.9.	Three-ply SG laminate glass stress in the x-direction calculated from FBG 1, 6, and 12 during 8 months of test monitoring . . . . .	232
E.10.	Stress at position 2 in x-direction as measured with FBG-sensors and calculated by finite element analysis along the glass in longitudinal bending direction. . . . .	234
E.11.	Stress at position 7 in x-direction as measured with FBG-sensors and calculated by finite element analysis along the glass in longitudinal bending direction. . . . .	235
E.12.	Comparison of the stress results $\sigma_1$ along a longitudinal section 30mm from the curved edge from the contact element model FSD.2.2, the cylindrical model FSD.1.1 and the FBG-results for 3esg_sgp and 2esg_pvb. . . . .	237
E.13.	Curvature analysis of a cylindric shape from 3x6mm FTG (3x3m) laminated with 1.52mm SG analysed with model types FPI.1.1 and FPI.1.2. The principal curvature directions / results are shown for nine points on the surface of the topmost glass. . . . .	238
E.14.	Curvature analysis of a saddle shape from 3x6mm FTG (3x3m) laminated with 1.52mm SG analysed with model types FPI.1.1 and FPI.1.2. The principal curvature directions / results are shown for nine points on the surface of the topmost glass. . . . .	239



## List of Tables

2.1. Comparative summary of curved glass manufacturing methods and properties. . . . .	19
5.1. Summary of the principal control parameters of optical waveguides . . . . .	39
5.2. Overview of the tests carried out with different adhesives. . . . .	66
5.3. Mean storage and loss moduli from DMA at temperatures of 30°C, 115°C and 140°C. . . . .	69
5.4. Summary and statistical analyses of surface roughness measurement data for Delo KB4552 and OB642. . . . .	75
5.5. Thermo-optic coefficient results. . . . .	80
5.6. Summary of the principal FBG parameters and coefficients . . . . .	84
5.7. Overview of the specimens tested in four-point bending. . . . .	86
5.8. Spectral width control at -3dB prior to and after the thermal and load cycle. . . . .	90
5.9. Residual stress summary relative to phases 1, 4 or 5 for FBGs bonded with different adhesives. . . . .	91
5.10. Temperature and wavelength shift changes during 2.5 to 2.75 hours at constant temperature of 140°C and related relaxation estimation. . . . .	92
5.11. Summary of micro-mechanical models, boundary conditions and load cases. . . . .	97
5.12. Summary of the gauge factors and birefringence effects from the micro-mechanical model. . . . .	104
6.1. Summary of the real scale tests and related FE analyses performed on specimens l/h=2400x800mm, R=5000mm (cold bent) . . . . .	117
6.2. RMS summary of the total standard deviation errors for the applied cameras. . . . .	124
6.3. Summary of the mean springback / relaxation in z-direction for different times calculated as mean values from the photogrammetry points along the narrow side of the glass. . . . .	127
6.4. Standard deviation of the z-coordinate of the three specimens per laminate type for the cold bent state (cb) and after 8 months of relaxation (ar). . . . .	129
6.5. Comparison and change of stress in x-direction as calculated by FEA and measured with FBG at different test stages. . . . .	134
6.6. FBG sensor wavelength shift and x-stress results at different testing stages compared with FE analyses with maximum displacements of 131mm or 135mm. . . . .	137
6.7. Summary of the stress ratio after 8 months to the cold bending stress level for FE and sensor analysis. . . . .	138
6.8. Comparison of the mean stress values in the x-direction for the stages cold bent (cb) and after autoclaving (ac). . . . .	138
7.1. Summary of the spectral width values for all cold bent glass specimens and sensor robustness statistics. . . . .	141
7.2. Comparison of the mean x-stress in the cold bent state (cb) and after autoclaving (ac) derived from FBGs and finite element analysis. . . . .	143
7.3. FE-analysis results of the cold bent state and after 8 months of relaxation at 20°C for four basic bending shapes 3*6mm FTG 3x3m laminated with 1.52mm SG. . . . .	159
A.1. Sensor types and categories . . . . .	192

| LIST OF TABLES

B.1. Overview of the technical datasheet properties of the preselected adhesives. . . . .	196
B.2. Synopsis and comparison table of all adhesive testing results, part 1. . . . .	202
B.3. Synopsis and comparison table of all adhesive testing results, part 2. . . . .	203
C.1. Ratio of wavelength shift $\Delta\lambda$ and applied force $F$ , normalised and statistical values. . . . .	210
C.2. All FBG measurement wavelength shift results and related strain / stress calculations for the tested instances 0 to 5. . . . .	211
E.1. Summary of the principal camera calibration data and RMS. . . . .	220
E.2. Overview of PVB interlayer material characterisations from different research works. . . . .	222
E.3. Results summary of the test series involving specimens 2esg_pvb-01 to -03 and 2esg_sgp-01 to -03. . . . .	229
E.4. Results summary of the test series involving specimens 3esg_sgp-01 to -03. . . . .	230
E.5. FBG and numerical results summary of the test series involving specimens 4esg_sgp-01 and -02. . . . .	233
E.6. Summary of double peaks encountered with laminates 2esg_pvb, 2esg_sgp, 3esg_sgp and 4esg_sgp. . . . .	236

## Appendix





## **A Bragg Grating Sensors**

### A.1. Fibre Optic Sensor Categories

operation principle	related sensor types	region	configuration
phase modulation (interference-based)	<ul style="list-style-type: none"> <li>- low coherence fibre-optic interferom. (LCFOI)</li> <li>two light beams:</li> <li>- Michelson interferometer</li> <li>- Mach-Zehnder interferometer</li> <li>- Sagnac interferometer</li> <li>multi light beams:</li> <li>- ring resonator</li> </ul>	intrinsic	all-fibre sensing, interferometric
intensity modulation (intensity-based)	<ul style="list-style-type: none"> <li>- differential intensity type</li> <li>- evanescent wave type</li> <li>- Fabry-Perot interferometer / etalon (reflection / transmission)</li> <li>- micro-bending sensors</li> </ul>	extrinsic  intrinsic	discrete single sensors
wavelength / spectrum modulation (spectrally-based)	optical time domain reflectometry OTDR: <ul style="list-style-type: none"> <li>- Brillouin scattering</li> <li>- Raman scattering</li> </ul> optical frequency domain reflectometry OFDR: <ul style="list-style-type: none"> <li>- Rayleigh scattering</li> </ul>	intrinsic	distributed sensors
	<ul style="list-style-type: none"> <li>- fibre Bragg gratings (FBG)</li> <li>- blackbody sensors</li> <li>- fluorescent fibre optic sensors</li> <li>- absorption type sensors</li> </ul>	intrinsic  extrinsic	discrete sensors or quasi-distributed sensors (network, multiplexing)
polarisation modul.	- birefringent fibre (fibre polarimetric sensor)	intrinsic	discrete sensors

**Table A.1.:** Sensor types and categorisation by operation principle, sensor location and configuration.

### A.2. Photoelasticity

$p_{ij}$  are the Pockels coefficients that describe the dependency of the refractive index on an electrical field as an electro-optic effect. The photoelastic Pockels matrix and its coefficients  $p_{ij}$  for an isotropic material such as the fibre silica core, are defined as follows [Ste 97, p. 277]:

$$\begin{aligned}
 p_{12} &= p_{23} & p_{22} &= p_{11} & p_{55} &= p_{44} \\
 p_{22} &= p_{33} & p_{44} &= \frac{p_{22} - p_{23}}{2} & p_{12} &= p_{13} \\
 p_{55} &= p_{66} & p_{46} &= p_{56} = p_{65} & p_{ij} &= 0
 \end{aligned}$$

$$[p_{ij}] = \begin{bmatrix}
 p_{11} & p_{12} & p_{12} & 0 & 0 & 0 \\
 p_{12} & p_{11} & p_{12} & 0 & 0 & 0 \\
 p_{12} & p_{12} & p_{11} & 0 & 0 & 0 \\
 0 & 0 & 0 & \frac{p_{11} - p_{12}}{2} & 0 & 0 \\
 0 & 0 & 0 & 0 & \frac{p_{11} - p_{12}}{2} & 0 \\
 0 & 0 & 0 & 0 & 0 & \frac{p_{11} - p_{12}}{2}
 \end{bmatrix} \quad (\text{A.1})$$

### A.3. Strain and Temperature Sensitivity of FBGs

The derivations given here are mainly based on the works of Trutzel [Tru 01], v. Steenkiste [Ste 97] and Gabler [Gab 12]. The optical axes of the optically isotropic fibre are aligned with the principal axes of the fibre; subsequently, the photoelastic Pockels matrix eq. A.1 above links the electrical field and the strain. Two axes  $p, q$  are introduced, which lie in the  $x_2$ - $x_3$ -plane normal to the longitudinal 1-axis (or  $z$ ) of the sensor.  $n_p, n_q$  are the refractive indices referring to these two axes. The change  $\Delta n_{p,q}$  caused by mechanically induced strain and temperature strain is solved for principals strain conditions and results in the expression

$$\begin{aligned} \frac{\Delta n_{p,q}}{n_0} = & -\frac{n_0^2}{2} \left[ p_{12} \varepsilon_1 + (p_{11} + p_{12}) \left( \frac{\varepsilon_2 + \varepsilon_3}{2} \right) \pm \right. \\ & \left. \pm \left( \frac{p_{11} - p_{12}}{2} \right) (\varepsilon_2 - \varepsilon_3) \right] + \\ & + \frac{n_0^2}{2} (p_{11} + 2p_{12}) \Delta T \alpha_g + \frac{\Delta T}{n_0} \frac{dn_0}{dT}, \end{aligned} \quad (\text{A.2})$$

This equation gives the relative change of the refractive indices for the two polarisation directions  $p, q$  depending on terms for strain and for temperature. The coefficients  $p_{ij}$  are the photoelastic Pockels proportionality coefficients from eq. A.1 [Ste 97, p. 277].

For small deformation or small differences / increments, the infinitesimal small values of  $d\lambda$ ,  $d\varepsilon_i$  and  $dT$  in eq. 5.28 can be approximately replaced by  $\Delta\lambda$ ,  $\Delta\varepsilon_i$  and  $\Delta T$ . The differential  $d$  is then assumed to be a linear function of  $\Delta$ :  $d \approx \Delta$ . The differences from OSA-measurements  $\Delta\lambda$  have to be related to initial reference values  $\lambda_{B,0}$ ,  $\varepsilon_{0,i}$  and  $T_0$  and eq. 5.28 becomes:

$$\begin{aligned} \frac{\Delta\lambda}{\lambda_{B,0}}(\varepsilon_i, T) = & \left( \frac{\Delta \bar{n}_{eff}(\varepsilon_i)}{\bar{n}_{eff,0}} + \frac{\Delta\Lambda(\varepsilon_i)}{\Lambda_0} \right) + \\ & + \left( \frac{\Delta \bar{n}_{eff}(T)}{\bar{n}_{eff,0}} + \frac{\Delta\Lambda(T)}{\Lambda_0} \right). \end{aligned} \quad (\text{A.3})$$

The period  $\Lambda$  can only change in an axial fibre direction because of mechanical strain and / or temperature influence:

$$\begin{aligned} \Delta\Lambda(\varepsilon_1, T) &= \Delta\varepsilon_1 \Lambda_0 + \Delta T \alpha_g \Lambda_0 \\ \Leftrightarrow \frac{\Delta\Lambda(\varepsilon_1, T)}{\Lambda_0} &= \Delta\varepsilon_1 + \Delta T \alpha_g \end{aligned} \quad (\text{A.4})$$

The relative refractive index change is given in eq.A.2 for the  $p, q$ -polarisation directions. Temperature causes an expansion of the sensor fibre in the principal directions  $i$ , which depends on the coefficient of thermal expansion of the silica, as in

$$\Delta\varepsilon_1 = \Delta\varepsilon_2 = \Delta\varepsilon_3 = \Delta T \alpha_g \quad (\text{A.5})$$

but it also causes a change of the refractive index  $n$ . With the above formulations, eq. A.2 for principal strain conditions in the fibre calculates separately for mechanically induced strain and apparent temperature strain:

$$\begin{aligned} \frac{\Delta n_{p,q}(\varepsilon_i)}{n_0} = & -\frac{n_0^2}{2} \left[ p_{12} \varepsilon_1 + \frac{p_{11} + p_{12}}{2} (\varepsilon_2 + \varepsilon_3) \pm \right. \\ & \left. \pm \frac{p_{11} - p_{12}}{2} (\varepsilon_2 - \varepsilon_3) \right] \end{aligned} \quad (\text{A.6})$$

$$\begin{aligned} \frac{\Delta n_{p,q}(T)}{n_0} = & -\frac{n_0^2}{2} \left[ p_{12} \alpha_g \Delta T + \frac{p_{11} + p_{12}}{2} 2 \alpha_g \Delta T \right] + \\ & + \frac{n_0^2}{2} \left[ \Delta T \alpha_g (2p_{12} + p_{11}) \right] + \frac{\Delta T}{n_0} \frac{dn_0}{dT} \end{aligned} \quad (\text{A.7})$$

As explained, for example, with Schlüter [Sch 10, p. 14], the mean effective refractive index change  $\Delta \bar{n}_{eff}$  of the loaded sensor related to  $\bar{n}_{eff,0}$ , the index prior to load application, are replaced by the respective mean effective refractive indices for the polarisation directions  $p, q$ . In this work,  $\bar{n}_{eff,0}$  is replaced by  $n_0$  for simplicity reasons. In the case of uniaxial strain and isotropy,  $\Delta \bar{n}_{eff} = \Delta n_p = \Delta n_q$  applies.

The full expression for a free fibre Bragg grating subjected to mechanically induced strain and temperature is determined through substitution of eqs. A.4, A.6 and A.7 into eq. A.3, which causes some terms to cancel out:

$$\begin{aligned} \frac{\Delta \lambda}{\lambda_{B,0}} = & \varepsilon_1 \left( 1 - \frac{n_0^2}{2} p_{12} \right) - \frac{n_0^2}{2} \left[ \left( \frac{p_{11} + p_{12}}{2} \right) (\varepsilon_2 + \varepsilon_3) \right. \\ & \left. \pm \left( \frac{p_{11} - p_{12}}{2} \right) (\varepsilon_2 - \varepsilon_3) \right] + \Delta T \left( \alpha_g + \frac{1}{n_0} \frac{dn_0}{dT} \right) \end{aligned}$$

## **B Adhesive Bonding of Fibres**

B.1. Adhesive Classification

manu- facturer	brand name	glass trans.T <sub>g</sub>	viscosity	strength	E	thermal exp. pre (post) T <sub>g</sub>	temp. range [°C]	cure			colour			
								tens. glass		method		time	intens.	wavel.
								[mPa·s]	[N/mm <sup>2</sup> ]					
DELO	KB4552	1K 130	1300	24	24	1100	158	-40-150	UV	60	55-60	320-550	amber-transp.	
	KB OB642	1K 90 (136)	10000	46	23	2000	67 (166)	-40-150	UV	10	55-60	320-440	transp.-clear	
	KB AD 640	1K 100	9000	45	22	2000	93 (163)	-40-150	UV	15	55-60	320-440	yellowish	
dymax	ultra light-weld 431	1K 115	500	27	31	570	54 (206)	-55-250	UV	2	50	320-400	colorless	
Epoxy Tech.	353ND	2K ≥90	4000			3564			thermal	150°C: 60 120°C: 30			amber	
Fraunhofer	Ormocer NM850	1K				<1500		<180	UV				transp.-clear	
ISC	Ormocer AL1029	1K						<180	UV				transp.-clear	
hbm	x 280	2K	7000			2800		-200-280	thermal	95°C: 3600			grey-opaque	
	z 70		8-14				70 (80)	-30-100	room temp.	20°C: 300			transp.-clear	
henkel	loctite 3301	1K	160	19		738		-40-130	UV	80	30	365	transp.-clear	
	loctite 3494	1K 31	6000	22.5		520	87 (250)	-40-120	UV	30	100	365	transp.-clear	
	loctite 4090	2K 88 (122)		7.1		565	71 (175)		room temp.				hazy yellow	
panacol	vitalit 1605	1K > 150	300-500	17.3		3132	75	-40-180	UV	60	60		transp.-clear	
	vitalit 2020	1K > 125	200-400				130	-40-160	UV	60	90		transp.-clear	
	vitalit UC 1608	1K > 120	500-1000			6000	50	-40-175	UV	90	60		transp.-clear	
perma- bond	UV 632	1K	200-300	13				<150	UV	60	<10	365-420	colorless	
	UV 681	1K	80-100	10-12				<150	UV	4	33	320-420	colorless	
polytec	polytec UV 2144	1K 167	15000					-40-150	UV	5			transp.-clear	
Wellmann- tech	Catowell 3052	1K	113					-40-150	UV	95	< 1	395	yellow-clear	
	Photowell 1044	1K 167	15000						UV	5	80	350-240	transp.-	
3M	scotch-Weld DP804	2K	8000	9	8			0-100	room temp.	23°C: 21600			colorless	
	scotch-Weld UV50	1K	6500	10				-50-130	UV	< 3	10	365	clear	

Table B.1.: Overview of the technical datasheet properties of the preselected adhesives.

**B.2. Adhesive Testing Results**

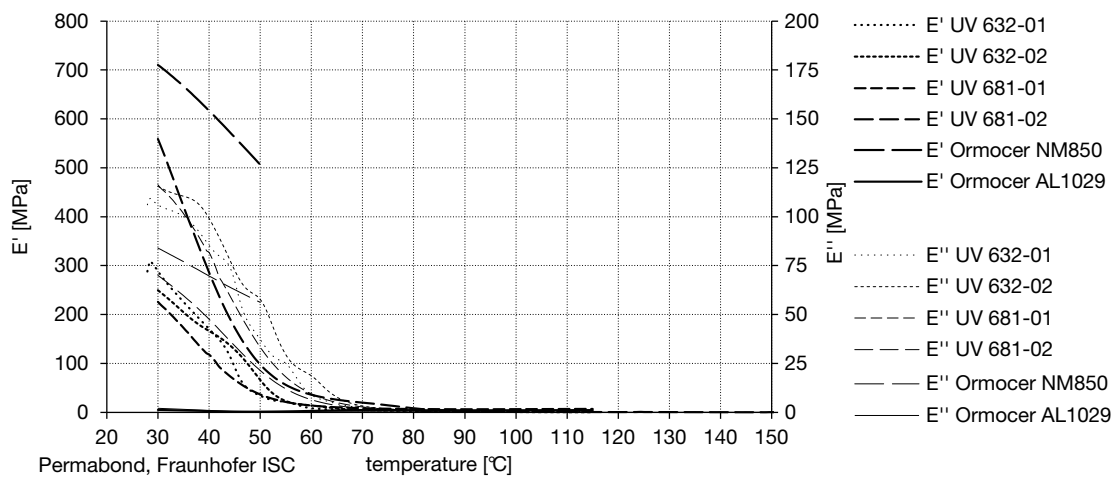
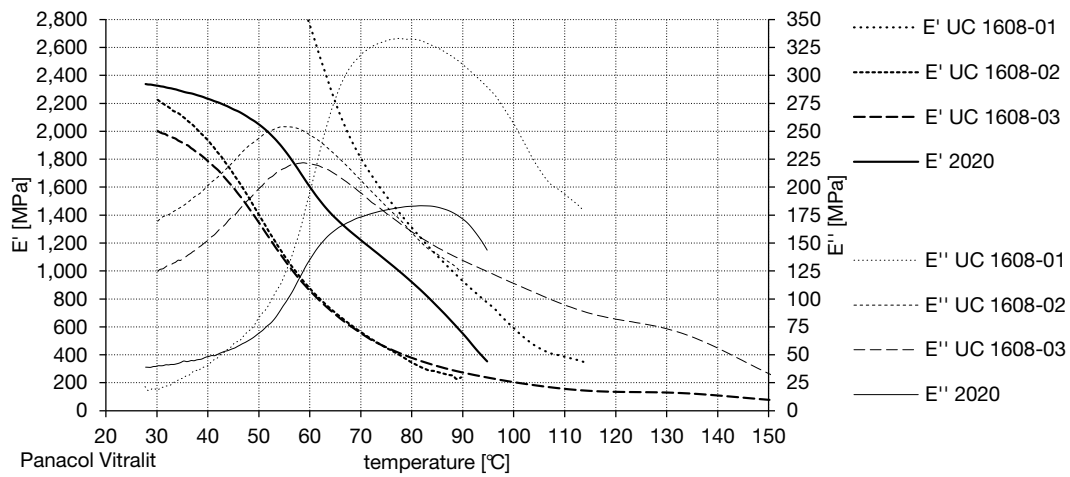
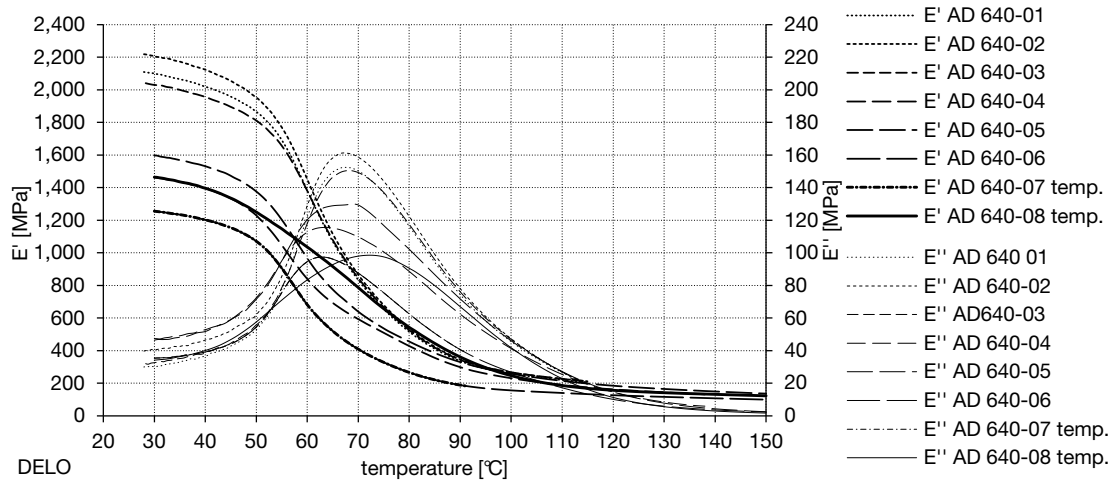


**Figure B.1.:** DMA testing results E' and E'' for adhesives from Delo, Permabond, Fraunhofer ISC and Panacol (temp.=tempering during 3.5h at 140°C).

B | ADHESIVE BONDING OF FIBRES

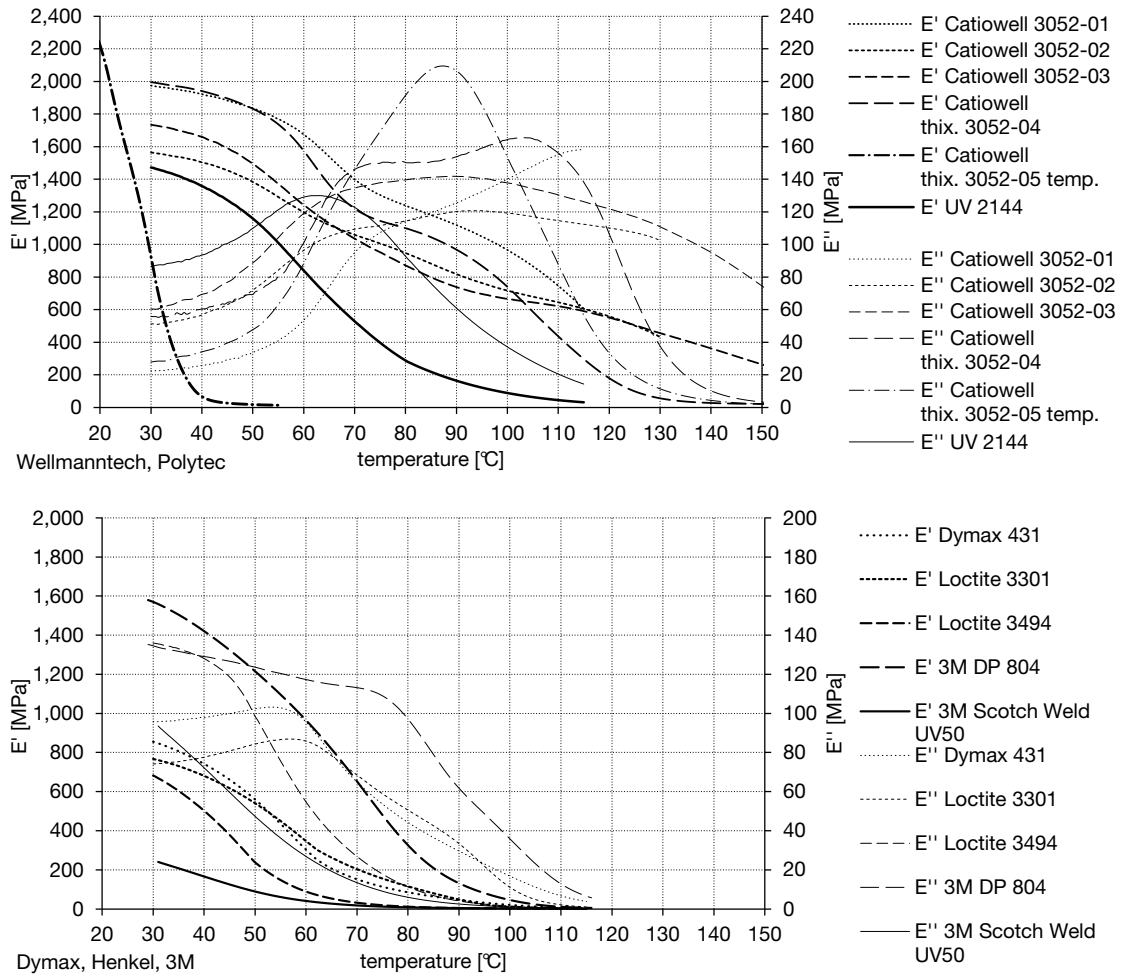


**Figure B.2.:** DMA testing results E' and E'' for adhesives from Wellmann, Polytec, Dymax, Henkel and 3m (temp.=tempering during 3.5h at 140°C; thix.=thixotropic version of Catiowell 3052).



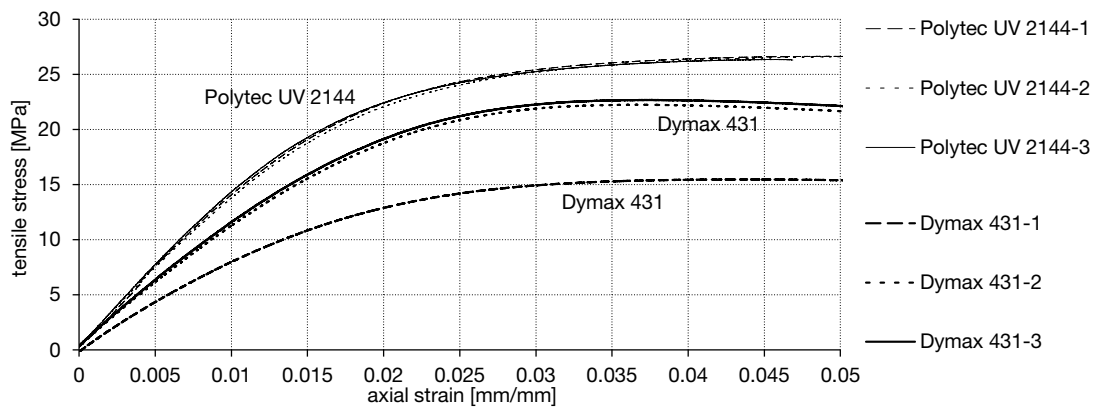
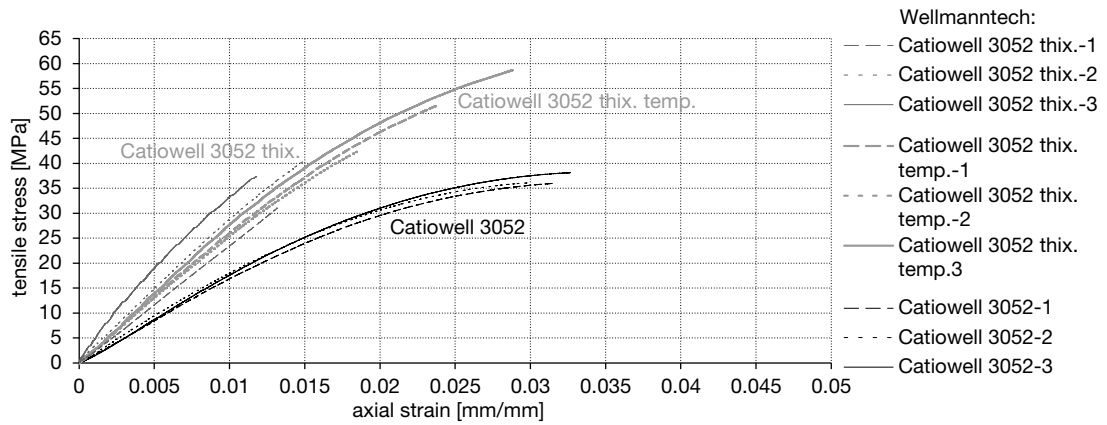
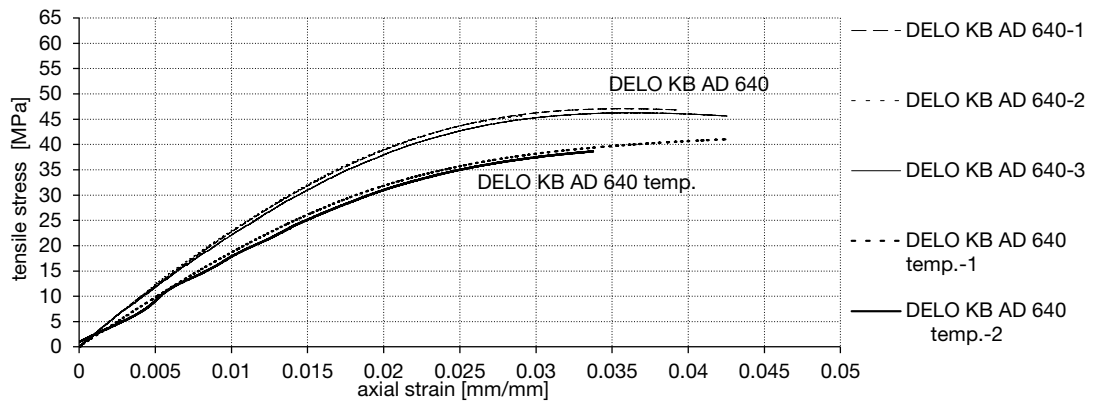


**Figure B.3.:** Axial tensile testing results E for adhesives from Delo, Wellmanntech, Polytec and Dymax (temp.=tempering during 3.5h at 140 °C; thix.=thixotropic version of Catiowell 3052).

B | ADHESIVE BONDING OF FIBRES

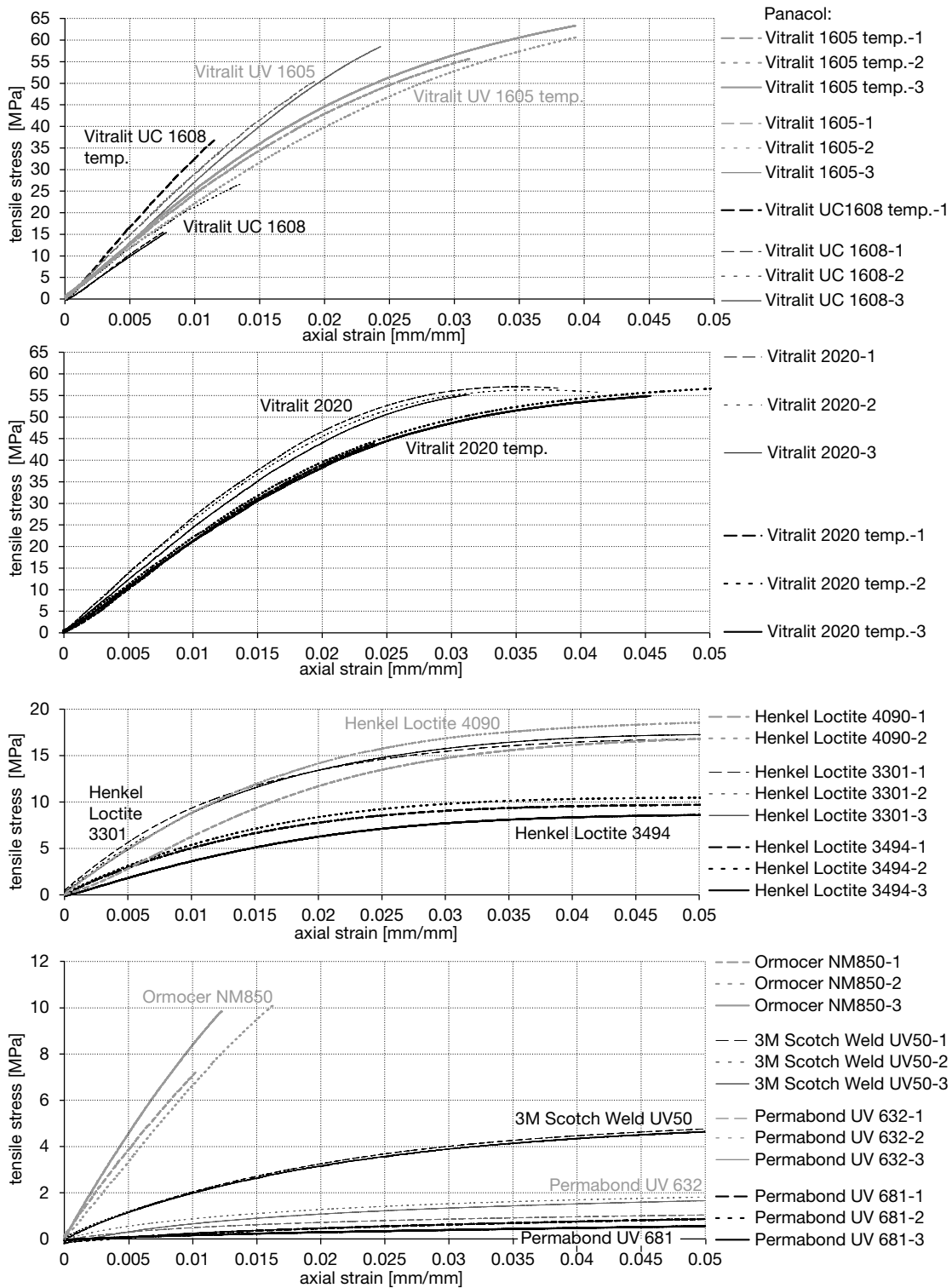
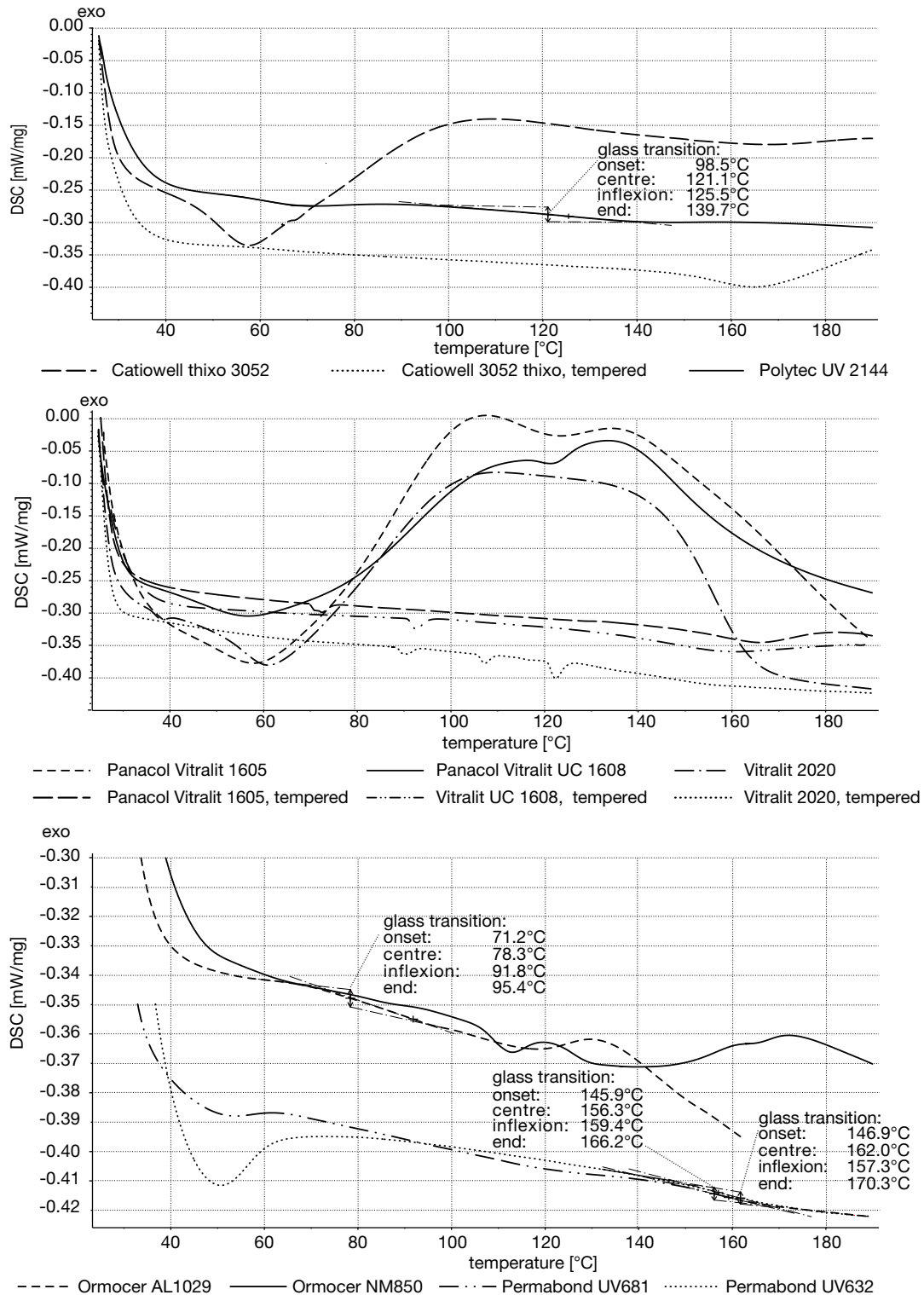


Figure B.4.: Axial tensile testing results E for adhesives from Panacol, Henkel, Fraunhofer ISC, Permabond and 3m.



**Figure B.5.:** DSC testing results for adhesives from Wellmanntech, Polytec, Fraunhofer ISC, Permabond and Panacol (temp.=tempering during 3.5h at 140°C; thix.=thixotropic version of Catiowell 3052).

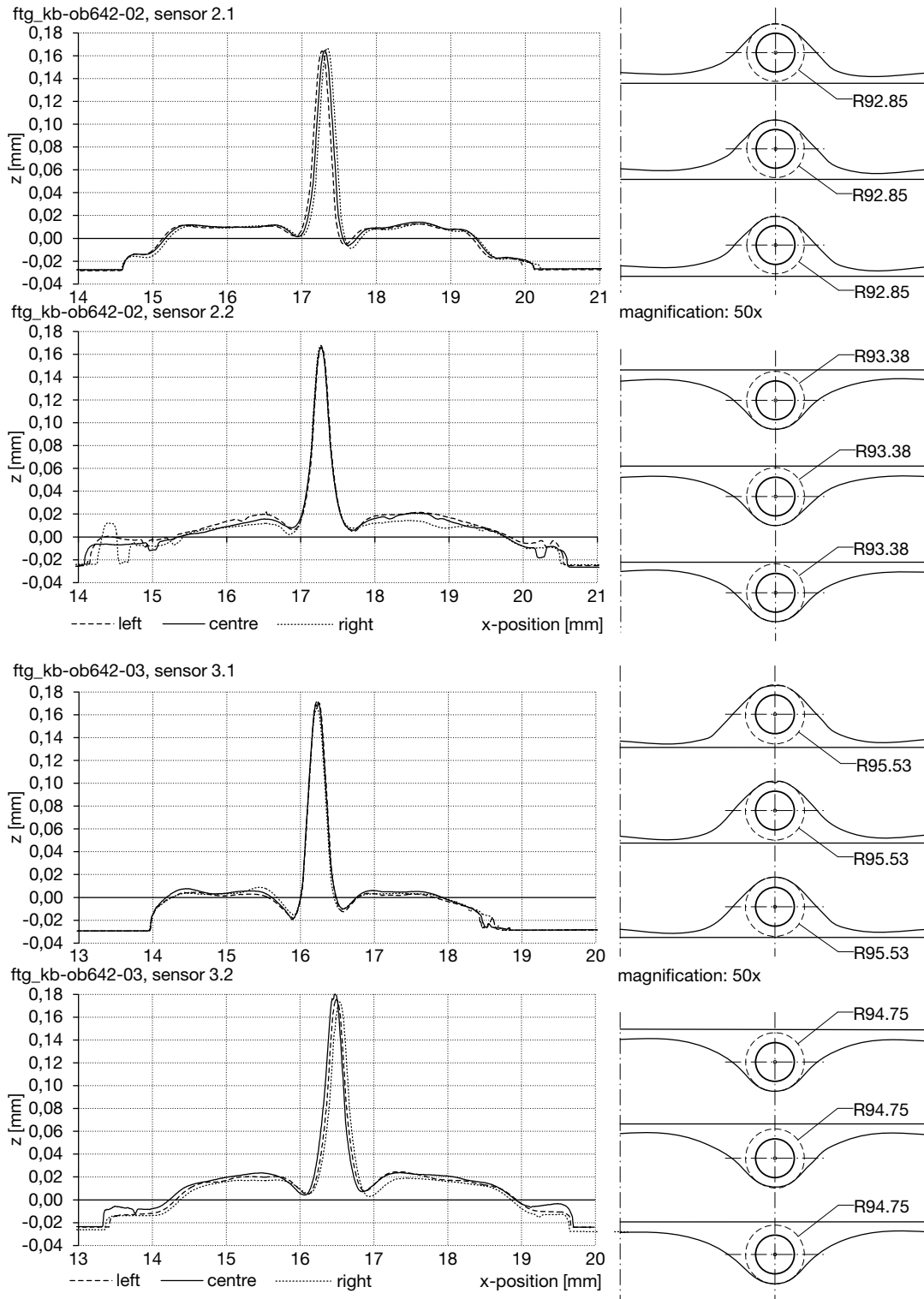
		UV-cured									
manu- facturer	no.	brand name	DSC			DMA			tensile test (21-24°C)		
			$\Delta$ heat flux (post-cure) [mW/mg]	T <sub>g</sub> [°C]	E' (30°C) [MPa]	E' (140°C) [MPa]	T <sub>g</sub> <sup>*</sup> [°C]	E <sub>avg</sub> [MPa]	std. dev. [MPa]	$\sigma_{ult, avg}$ [MPa]	$\epsilon_{ult, avg}$ [mm/mm]
DELO	1	KB4552	0.30 (80-117°C)	unidentifiable	1524.62	25.08	peak tan $\delta$ : 105-110 peak E'': 66	1881.82	50.18	40.10	0.0357
	2	KB AD640	0.04 (60-80°C) inflexion: 121.8 centre: 126.2	onset: 110.2 unidentifiable	1773.69	129.19	onset drop E': 50 peak tan $\delta$ : 83-90 peak E'': 65-67	2460.73	44.49	40.10	0.0338
	3	KB OB642	0.07 (65-109°C)	unidentifiable	1802.68	176.45	onset drop E': 54 peak tan $\delta$ : 70, 122 peak E'': 71	2516.34	319.27	20.72	0.0095
Dymax	4	Ultra Light-Weld 431	-	-	855.17	-	onset drop E': 53, 97 peak tan $\delta$ : 108 peak E'': 55	1113.68	164.32	21.40	0.0390
Epoxy T.	5	EPO-TEK 353ND	0.01 (145-170°C)	unidentifiable	710.27	**	unidentifiable**	807.78	146.90	9.07	0.0130
Fraunhofer ISC	6	Ormocer NM850	0.003 (120-130°C)	onset: 71.2 centre: 78.2 inflexion: 91.8	4.86	-	peak tan $\delta$ : 30	33.43	1.47	2.65	0.1007
Henkel	8	Loctite 3301	-	-	767.65	-	peak tan $\delta$ : 103 peak E'': 58	1004.01	89.40	16.87	0.0369
	9	Loctite 3494	-	-	682.70	-	onset drop E': 45 peak tan $\delta$ : 80 onset drop E': 37	571.73	146.04	9.62	0.0566
	10	Loctite 4090	-	-	-	-	-	840.11	213.70	18.48	0.1088
Panacol	11	Vitralit UV1605	0.38 (60-135°C)	unidentifiable	**	**	-	2955.94	145.57	47.78	0.0185
	12	Vitralit UV2020	0.30 (60-135°C)	unidentifiable	2338.08	**	peak E'': 83	2595.54	159.21	56.17	0.0344
	13	Vitralit UC1608	0.28 (57-133°C)	unidentifiable	2701.69	108.49	onset drop E': 50 peak tan $\delta$ : 115 peak E'': 57-78	2356.17	218.24	19.28	0.0097
Perma- bond	14	UV632	0.016 (50-65°C)	onset: 146.9 centre: 162.0 inflexion: 157.3	268.76	-	onset drop E': 47-50 peak tan $\delta$ : 53-57	91.35	27.42	2.14	0.2100
	15	UV681	0.003 (53-62°C)	onset: 145.9 centre: 156.3 inflexion: 159.4	182.87	0.06	peak tan $\delta$ : 50	24.51	8.09	25.87	0.1400

Table B.2.: Synopsis and comparison table of all adhesive testing results, part 1.

UV-cured											
manu- facturer	no.	brand name	DSC			DMA			tensile test (21-24°C)		
			Δ heat flux (post-cure) [mW/mg]	T <sub>g</sub> [°C]	E' (30°C) [MPa]	E' (140°C) [MPa]	T <sub>g</sub> <sup>*</sup> [°C]	E <sub>avg</sub> [MPa]	std. dev. [MPa]	σ <sub>ult, avg</sub> [MPa]	ε <sub>ult, avg</sub> [mm/mm]
Polytec	16	UV2144	~0	onset: 98.5 centre: 121.1 inflexion: 125.5	1471.92	-	peak tanδ: 110 peak E'': 64 onset drop E': 46	1496.75	32.58	26.54	0.0501
Wellmann- tech	17	Catiowell 3052	-	-	1757.67	362.23	peak E'': 92-96 (115) onset drop E': 50, 102	1860.72	96.57	36.73	0.0313
	18	Catiowell 3052 (thixotr.)	0.19 (56-108°C)	-	1995.76	27.22	peak tanδ: 128 peak E'': 102 onset drop E': 54, 92	3155.64	780.42	36.31	0.0110
	19	Photowell 1044	-	-	-	-	-	-	-	-	-
3M	20	Scotch-W. UV50	-	-	240.69	-	unidentifiable	226.20	7.93	6.48	0.1905
	21	Scotch-Weld DP804	-	-	1570.09	-	peak tanδ: 112 peak E'': 70-75 onset drop E': 53	-	-	-	-
* Values separated by a "; : two onset points distinguishable in DMA											
** Bulk specimen being too brittle for testing											
UV-cured and tempered											
manu- facturer	no.	brand name	DSC			DMA			tensile test (21-24°C)		
			Δ heat flux (post-cure) [mW/mg]	T <sub>g</sub> [°C]	E' (30°C) [MPa]	E' (140°C) [MPa]	T <sub>g</sub> <sup>*</sup> [°C]	E <sub>avg</sub> [MPa]	std. dev. [MPa]	σ <sub>ult, avg</sub> [MPa]	ε <sub>ult, avg</sub> [mm/mm]
DELO	1	KB4552	~0	unidentifiable	1582.55	80.10	peak tanδ: 105 peak E'': 70-75 onset drop E': 44, 70	1464.89	163.35	34.74	0.0615
	2	KB AD640	-	-	1290.30	131.57	peak tanδ: 78 peak E'': 62-71 onset drop E': 49-52	2042.62	123.86	39.99	0.0381
	3	KB OB642	~0	unidentifiable	2412.95	100.26	peak tanδ: 145 peak E'': 130 onset drop E': 55, 115	2610.46	272.27	25.06	0.0107
Panacol	11	Vitralit UV1605	~0	unidentifiable	-	-	-	2472.17	114.56	59.93	0.0367
	12	Vitralit UV2020	~0	unidentifiable	-	-	-	2203.75	43.82	51.80	0.0398
	13	Vitralit UC1608	~0	unidentifiable	-	-	-	3579.82	-	36.78	0.0115
Permbd.	14	UV632	~0	unidentifiable	-	-	-	3579.82	-	36.78	0.0115
Wellmann- tech	18	Catiowell 3052 (thixotr.)	~0	unidentifiable	2595.29	21.15	peak tanδ: 115 peak E'': 89	2729.03	95.14	50.84	0.0237

Table B.3.: Synopsis and comparison table of all adhesive testing results, part 2.

**B.3. Adhesive Bond Section Data**



**Figure B.6.:** Surface roughness measurement results across FBG bond of the specimen FTG OB642-02 and -03.

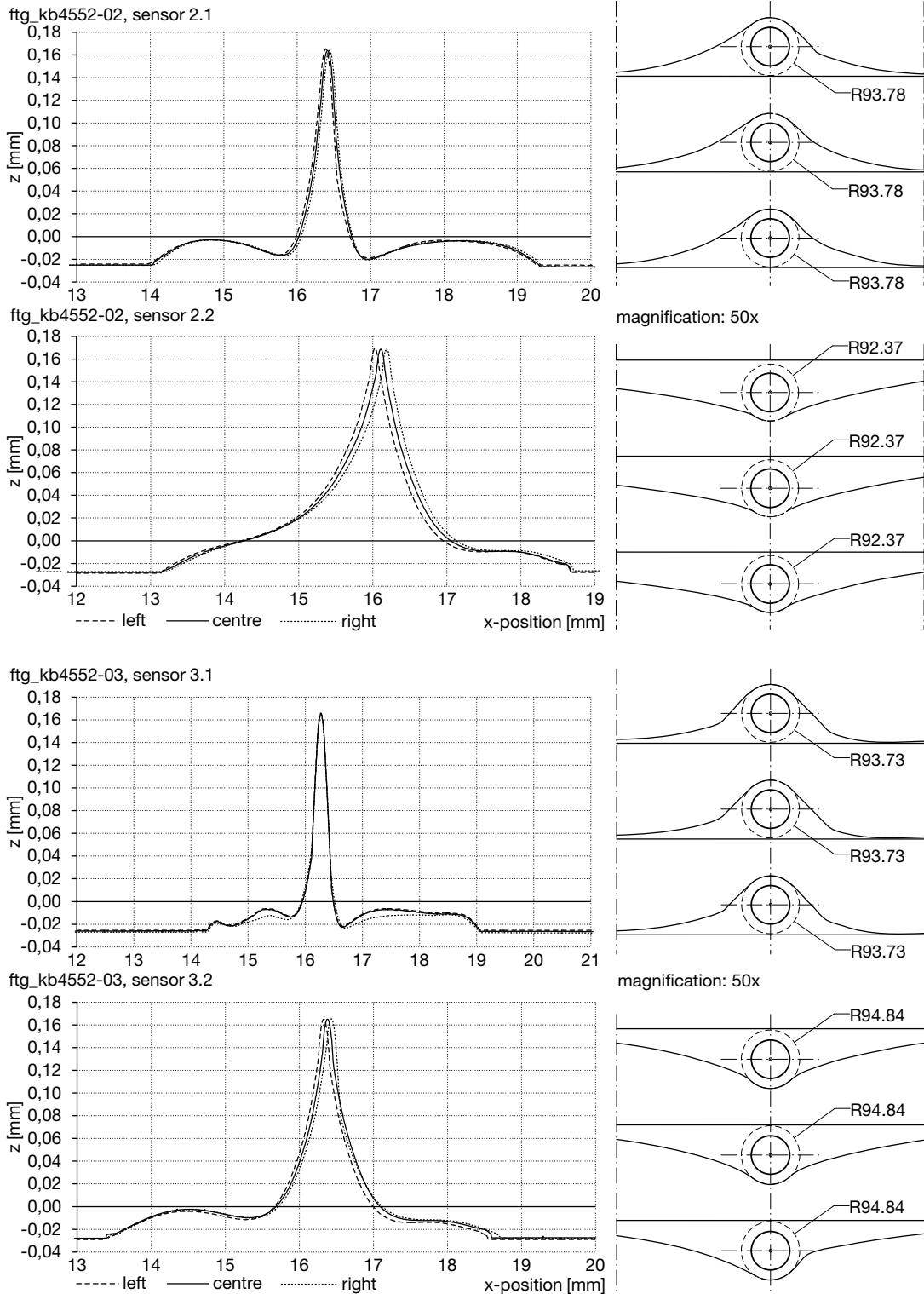


Figure B.7.: Surface roughness measurement results across FBG bond of the specimen FTG KB4552-02 and -03.





## **C Sensor Property Testing Results**

C.1. FBG Coefficient Determination

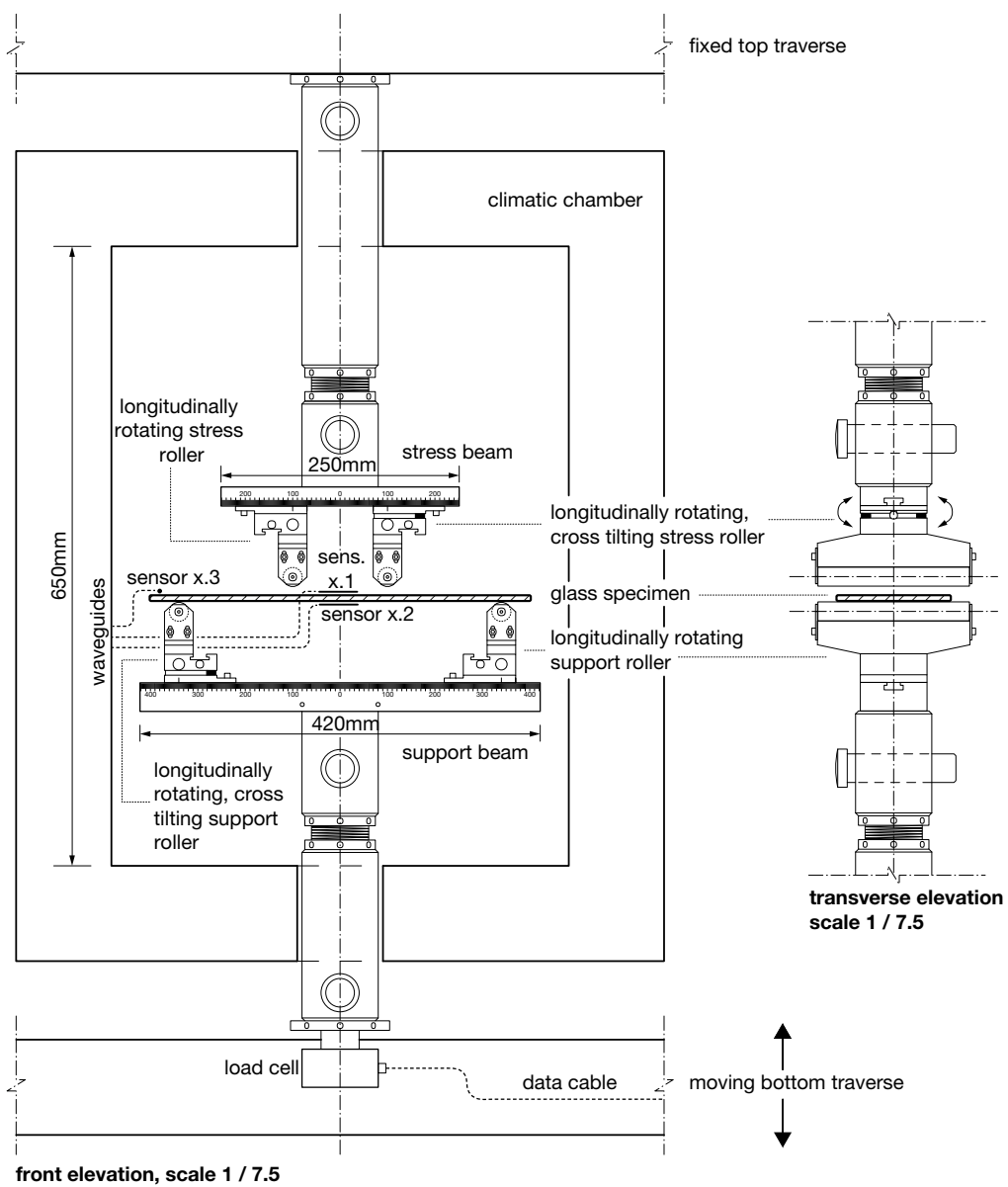
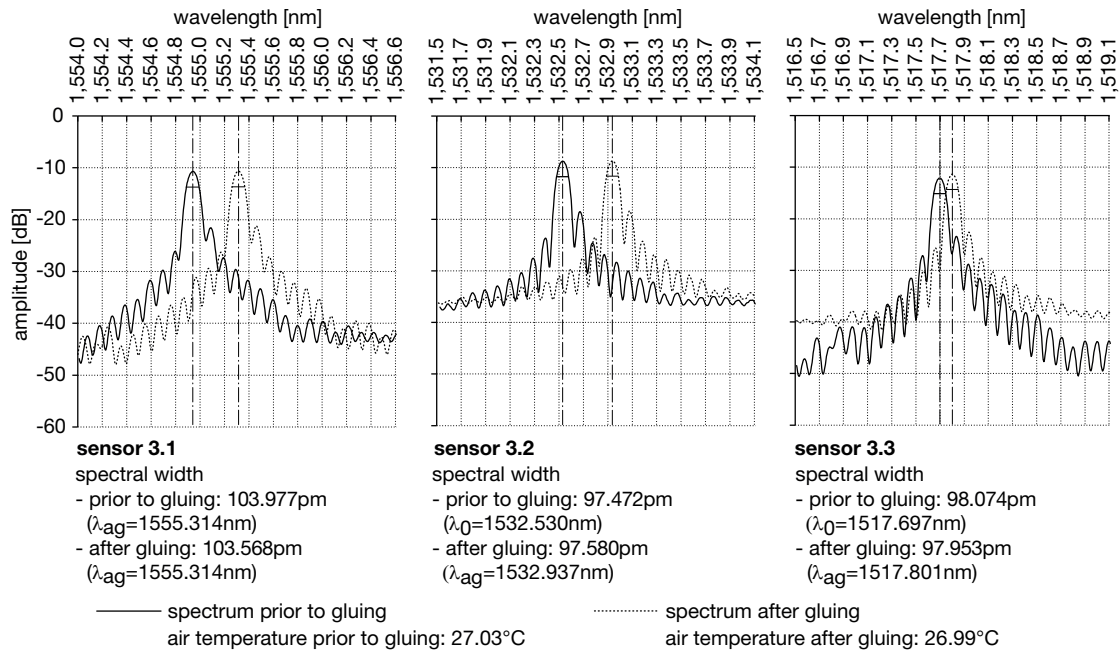
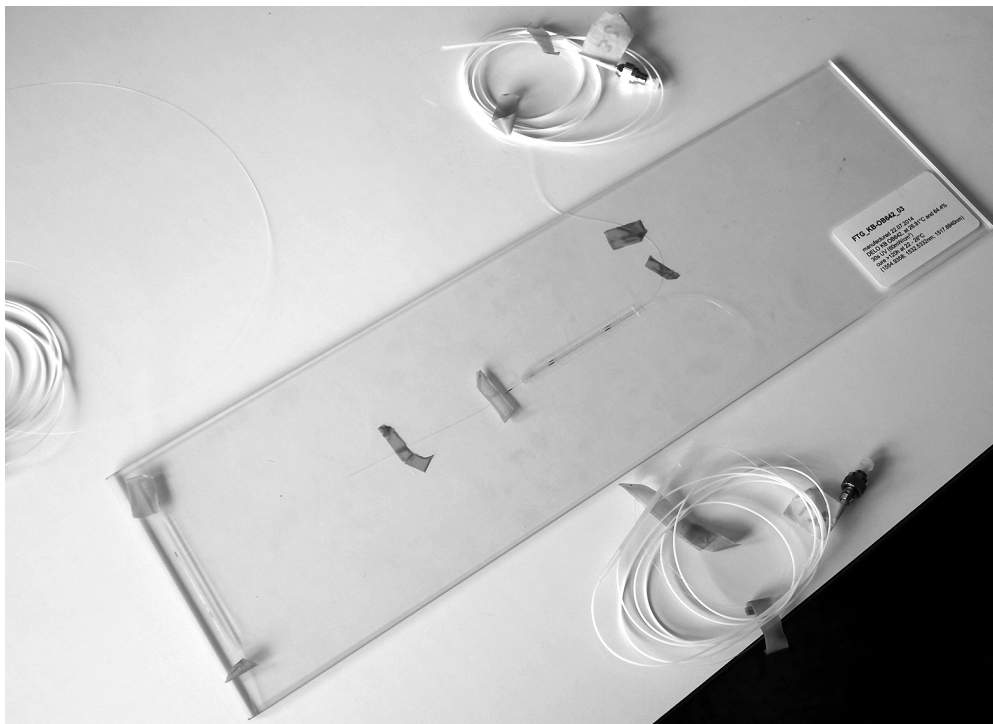


Figure C.1.: Four-point bending device and climatic chamber used in this research.



**Figure C.2.:** Spectra of sensors 3.1 to 3.3 prior to and after UV cure of the adhesive. The spectral width remains nearly unchanged in the process. The shift of the spectra is supposedly caused by heating of the glass and fibre from the UV-lamp, which could not be recorded. Another possibility is strain introduced from differential temperature of the fibre and the glass during heating and subsequent cooling after cure.



**Figure C.3.:** Type specimen for the four-point bending tests.

C.2. Four-Point Bending Tests of FBGs Bonded to Glass

FL_EP353ND-		$\Delta\lambda / F$ [pm/N]				
no.	sensor-no.	1-0	3-2	5-4	7-6	8-7
1	PR2012_36_29-07	1.63820	1.51978	1.53422	1.57741	1.59228
2	PR2012_36_29-03	1.59777	1.51183	1.55935	1.59059	1.60407
3	PR2012_36_29-04	1.60580	1.50867	1.57165	1.61030	1.60198
4	PR2012_36_29-05	1.60202	1.50487	1.55939	1.61617	1.60362
arithm. mean		1.61095	1.51129	1.55615	1.59862	1.60048
standard deviation		0.01846	0.00634	0.01573	0.01788	0.00555
normalised values						
1	PR2012_36_29-07	1.000	0.928	0.937	0.963	0.972
2	PR2012_36_29-03	1.000	0.946	0.976	0.996	1.004
3	PR2012_36_29-04	1.000	0.940	0.979	1.003	0.998
4	PR2012_36_29-05	1.000	0.939	0.973	1.009	1.001
arithm. mean		1.000	0.938	0.966	0.993	0.994
standard deviation		0.000	0.008	0.020	0.020	0.015
deviation $\Delta_H$ to 1-0 [%]		0.00%	-6.18%	-3.38%	-0.75%	-0.64%

FL_UV681-		$\Delta\lambda / F$ [pm/N]				
no.	sensor-no.	1-0	3-2	5-4	7-6	8-7
1	PR2013_36_29-17	1.53883	1.36349	1.38300	1.56294	1.51596
2	PR2013_36_28-10	1.58012	1.15285	1.18670	1.58664	1.59257
3	PR2013_36_29-14	1.59068	1.28333	1.32357	1.59913	1.60863
4	PR2013_36_29-15	1.59988	1.24981	1.29764	1.59436	1.59448
5	PR2013_36_29-16	1.65399	1.12853	1.19284	1.66434	1.65867
arithm. mean		1.59270	1.23560	1.27675	1.60148	1.59406
standard deviation		0.04145	0.09637	0.08525	0.03779	0.05121
normalised values						
1	PR2013_36_29-17	1.000	0.886	0.899	1.016	0.985
2	PR2013_36_28-10	1.000	0.730	0.751	1.004	1.008
3	PR2013_36_29-14	1.000	0.807	0.832	1.005	1.011
4	PR2013_36_29-15	1.000	0.781	0.811	0.997	0.997
5	PR2013_36_29-16	1.000	0.682	0.721	1.006	1.003
arithm. mean		1.000	0.777	0.803	1.006	1.001
standard deviation		0.000	0.077	0.070	0.007	0.010
deviation $\Delta_H$ to 1-0 [%]		0.00%	-22.28%	-19.72%	0.56%	0.08%

FL_KB4552-		$\Delta\lambda / F$ [pm/N]				
no.	sensor-no.	1-0	3-2	5-4	7-6	8-7
1	PR2012_36_20-01	1.55901	1.60150	1.60690	1.55877	1.55035
2	PR2012_36_29-02	1.52792	1.57403	1.60268	1.53062	1.53873
3	PR2012_36_29-11	1.52077	1.57650	1.58696	1.52837	1.48871
4	PR2012_36_29-12	1.55055	1.58907	1.58360	1.55628	1.54929
5	PR2012_36_29-13	1.57918	1.59501	1.61345	1.58230	-
arithm. mean		1.54748	1.58722	1.59872	1.55127	1.53177
standard deviation		0.02368	0.01180	0.01291	0.02233	0.02918
normalised values						
1	PR2012_36_20-01	1.000	1.027	1.031	1.000	0.994
2	PR2012_36_29-02	1.000	1.030	1.049	1.002	1.007
3	PR2012_36_29-11	1.000	1.037	1.044	1.005	0.979
4	PR2012_36_29-12	1.000	1.025	1.021	1.004	0.999
5	PR2012_36_29-13	1.000	1.010	1.022	1.002	-
arithm. mean		1.000	1.026	1.033	1.002	0.995
standard deviation		0.000	0.010	0.013	0.002	0.012
deviation $\Delta_H$ to 1-0 [%]		0.00%	2.58%	3.32%	0.25%	-0.51%

Table C.1.: Ratio of wavelength shift  $\Delta\lambda$  and applied force  $F$ , normalised and statistical values.

fl_kb-ob642-02				instance-no. i						
FBG	$\lambda_{B,0}$	result, sensor FBG	unit	0 (no load)	1 (F)	2 (F, T)	3 (F, T)	4 (F)	5 (no load)	
	[nm]	$\Delta\lambda_{tot,0}$ (F,T)	2.1 [nm]	0.0000	-0.7340	1.6224	1.6145	-0.7822	-0.0522	
2.1	1562.506	mech./Temp.	2.2 [nm]	0.0000	0.7021	3.0696	3.0677	0.6934	-0.0133	
2.2	1535.194		2.3 [nm]	0.0000	0.0017	2.3601	2.3521	0.0009	-0.0007	
2.3	1520.267	$\Delta\lambda_{m,0}$ (F)	2.1 [nm]	0.0000	-0.7340	-0.7352	-0.7351	-0.7806	-0.0489	
bond geometry:				2.2 [nm]	0.0000	0.7021	0.7120	0.7181	0.6950	-0.0101
	[mm]	T (PT100-1)	- [°C]	23.4724	23.0954	140.7847	140.8593	24.1882	24.1444	
$t_s$	3.8490	$\sigma_{xx,m,0}$ (F)	2.1 [MPa]	0.0000	-40.4009	-44.1136	-44.0928	-43.0054	-2.8249	
$r_{f,1}$	0.0929		2.2 [MPa]	0.0000	39.1694	38.3780	38.7273	38.7253	-0.7047	
$r_{f,2}$	0.0934	$\epsilon_{xx,m,i}$ (F)	2.1 [mm/mm]	-	-5.6610E-04	-9.5577E-07	1.2012E-07	-3.5125E-05	5.6458E-04	
$t_{a,1}$	0.0067	(prev. inst.)	2.2 [mm/mm]	-	5.5147E-04	7.7338E-06	4.8405E-06	-1.8151E-05	-5.5355E-04	
$t_{a,2}$	0.0050	$\sigma_{xx,m,i}$ (F)	2.1 [MPa]	-	-40.3060	-0.0681	0.0086	-2.5009	-40.1981	
		(prev. inst.)	2.2 [MPa]	-	39.2644	0.5506	0.3446	-1.2924	39.4130	

fl_kb-ob642-04				instance-no. i						
FBG	$\lambda_{B,0}$	result, sensor FBG	unit	0 (no load)	1 (F)	2 (F, T)	3 (F, T)	4 (F)	5 (no load)	
		$\Delta\lambda_{tot,0}$ (F,T)	4.1 [nm]	0.0000	-0.7122	1.6423	1.6389	-0.7378	-0.0144	
4.1	1552.787	mech./Temp.	4.2 [nm]	0.0000	0.6784	3.0795	3.0796	0.7585	0.0649	
4.2	1530.292		4.3 [nm]	0.0000	-0.0023	2.3624	2.3588	0.0632	0.0569	
4.3	1515.39	$\Delta\lambda_{m,0}$ (F)	4.1 [nm]	0.0000	-0.7122	-0.7260	-0.7258	-0.8069	-0.0773	
bond geometry:				4.2 [nm]	0.0000	0.6784	0.7112	0.7148	0.6893	0.0020
		T (PT100-1)	- [°C]	21.8562	22.0616	140.5357	140.5852	25.0551	24.3090	
$t_s$	3.8520	$\sigma_{xx,m,0}$ (F)	4.1 [MPa]	0.0000	-39.1546	-42.9362	-42.9186	-44.2675	-4.0112	
$r_{f,1}$	0.0918		4.2 [MPa]	0.0000	38.0833	38.8236	39.0293	38.8658	0.4127	
$r_{f,2}$	0.0970	$\epsilon_{xx,m,i}$ (F)	4.1 [mm/mm]	-	-5.5178E-04	-1.0731E-05	1.7873E-07	-6.2865E-05	-5.6557E-04	
$t_{a,1}$	0.0113	(prev. inst.)	4.2 [mm/mm]	-	5.3303E-04	2.5792E-05	2.8610E-06	-2.0026E-05	5.3988E-04	
$t_{a,2}$	0.0071	$\sigma_{xx,m,i}$ (F)	4.1 [MPa]	-	-39.2865	-0.7640	0.0127	-4.4760	-40.2687	
		(prev. inst.)	4.2 [MPa]	-	37.9515	1.8364	0.2037	-1.4258	38.4392	

ftg_kb4552-02				instance-no. i						
FBG	$\lambda_{B,0}$	result, sensor FBG	unit	0 (no load)	1 (F)	2 (F, T)	3 (F, T)	4 (F)	5 (no load)	
		$\Delta\lambda_{tot,0}$ (F,T)	2.1 [nm]	0.0000	-0.7125	1.5869	1.5840	-0.7560	-0.0454	
2.1	1533.092	mech./Temp.	2.2 [nm]	0.0000	0.7172	3.1212	3.1219	0.7448	0.0195	
2.2	1567.575		2.3 [nm]	0.0000	0.0070	2.4234	2.4210	0.0450	0.0221	
2.3	1575.029	$\Delta\lambda_{m,0}$ (F)	2.1 [nm]	0.0000	-0.7125	-0.8289	-0.8295	-0.7934	-0.0600	
bond geometry:				2.2 [nm]	0.0000	0.7172	0.7054	0.7084	0.7074	0.0050
		T (PT100-1)	- [°C]	23.7599	24.1171	140.5475	140.5988	25.4527	24.0115	
$t_s$	3.8480	$\sigma_{xx,m,0}$ (F)	2.1 [MPa]	0.0000	-40.7946	-43.7839	-43.8173	-45.3595	-3.7979	
$r_{f,1}$	0.0938		2.2 [MPa]	0.0000	39.2321	39.1805	39.3467	38.6684	-0.1370	
$r_{f,2}$	0.0924	$\epsilon_{xx,m,i}$ (F)	2.1 [mm/mm]	-	-5.6105E-04	-9.1770E-05	-4.1415E-07	2.8423E-05	-5.7785E-04	
$t_{a,1}$	0.0021	(prev. inst.)	2.2 [mm/mm]	-	5.5008E-04	-9.0524E-06	2.3160E-06	-7.9385E-07	5.3848E-04	
$t_{a,2}$	0.0118	$\sigma_{xx,m,i}$ (F)	2.1 [MPa]	-	-39.9466	-6.5341	-0.0295	2.0237	-41.1428	
		(prev. inst.)	2.2 [MPa]	-	39.1657	-0.6445	0.1649	-0.0565	38.3395	

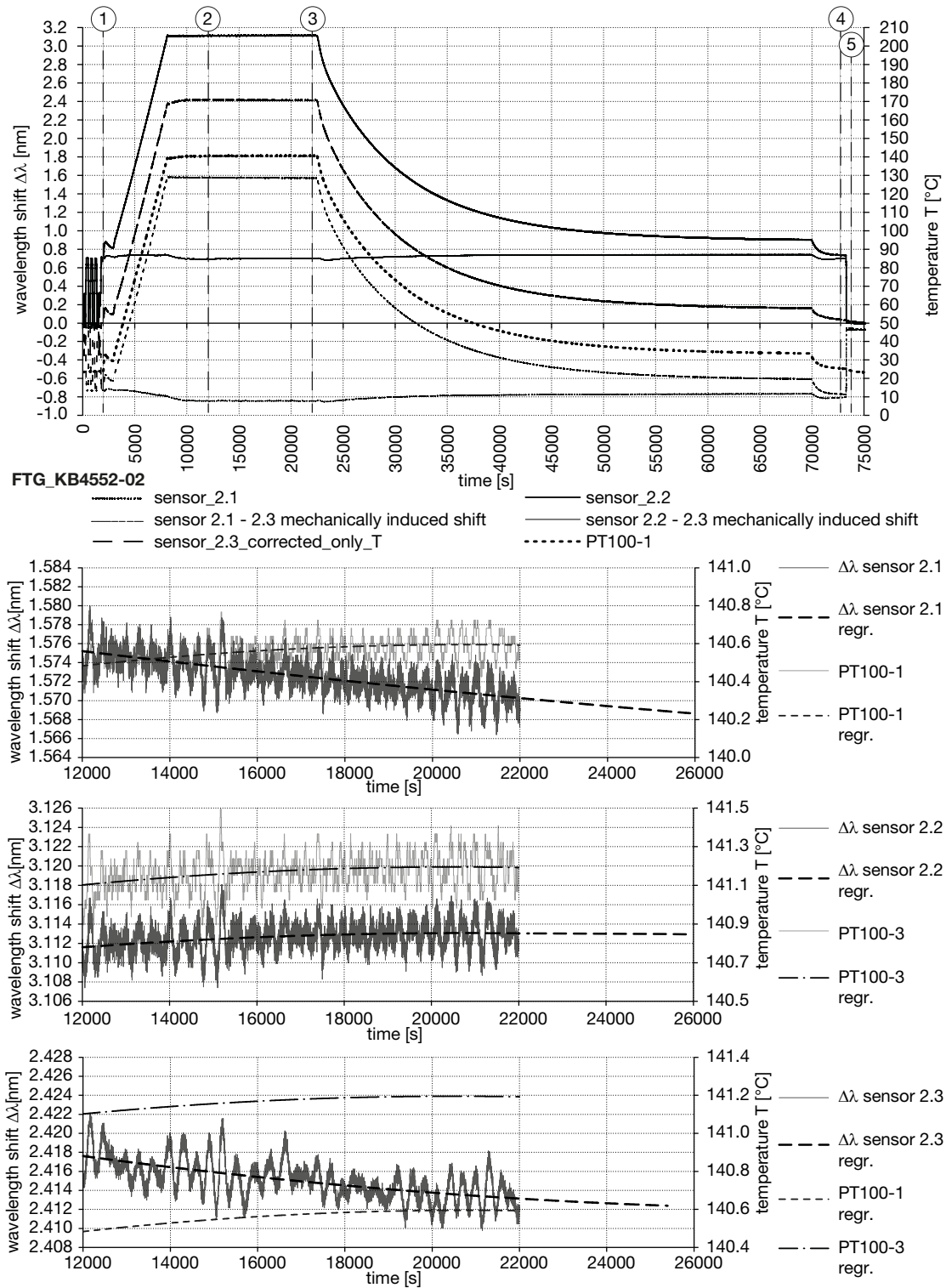
ftg_kb4552-03				instance-no. i						
FBG	$\lambda_{B,0}$	result, sensor FBG	unit	0 (no load)	1 (F)	2 (F, T)	3 (F, T)	4 (F)	5 (no load)	
		$\Delta\lambda_{tot,0}$ (F,T)	3.1 [nm]	0.0000	-0.7382	1.6379	1.6338	-0.8163	-0.0731	
3.1	1579.922	mech./Temp.	3.2 [nm]	0.0000	0.7182	3.1481	3.1395	0.6969	-0.0242	
3.2	1572.421		3.3 [nm]	0.0000	0.0117	2.4019	2.3988	-0.0513	-0.0669	
3.3	1564.865	$\Delta\lambda_{m,0}$ (F)	3.1 [nm]	0.0000	-0.7382	-0.7446	-0.7456	-0.7456	0.0132	
bond geometry:				3.2 [nm]	0.0000	0.7182	0.7570	0.7601	0.7676	0.0621
		T (PT100-1)	- [°C]	23.4422	23.4398	140.3316	140.3614	21.7408	21.6527	
$t_s$	3.8460	$\sigma_{xx,m,0}$ (F)	3.1 [MPa]	0.0000	-41.2463	-43.2883	-43.3421	-42.0440	-0.3067	
$r_{f,1}$	0.0937		3.2 [MPa]	0.0000	39.0182	40.0935	40.2669	41.3317	2.3769	
$r_{f,2}$	0.0948	$\epsilon_{xx,m,i}$ (F)	3.1 [mm/mm]	-	-5.6368E-04	-4.8834E-06	-7.7251E-07	2.1304E-08	-5.7967E-04	
$t_{a,1}$	0.0035	(prev. inst.)	3.2 [mm/mm]	-	5.5076E-04	2.9703E-05	2.3941E-06	5.7095E-06	5.4067E-04	
$t_{a,2}$	0.0035	$\sigma_{xx,m,i}$ (F)	3.1 [MPa]	-	-40.1342	-0.3477	-0.0550	0.0015	-41.2724	
		(prev. inst.)	3.2 [MPa]	-	39.2143	2.1148	0.1705	0.4065	38.4958	

$\Delta\lambda_{tot,0}$  (F, T) total wavelength shift due to load F and temperature T, related to initial  $\lambda_{B,0}$  at  $t=0$   
 $\Delta\lambda_{m,0}$  (F) mech. induced wavelength shift caused by load F related to initial  $\lambda_{B,0}$  at  $t=0$ :  $\Delta\lambda_{tot,0}(F,T) - \Delta\lambda_s(T)$   
T (PT100-1) temperature measured by PT100-1  
 $\sigma_{xx,m,0}$  (F) mech. induced stress from load F, related to initial  $\lambda_{B,0}$  at  $t=0$   
 $\epsilon_{xx,m,i}$  (F) mech. induced strain due to load F, related to the previous instance i  
 $\sigma_{xx,m,i}$  (F) mech. induced stress due to load F, related to the previous instance i

Table C.2.: All FBG measurement wavelength shift results and related strain / stress calculations for the tested instances 0 to 5 shown in fig. 5.42.

C | SENSOR PROPERTY TESTING RESULTS



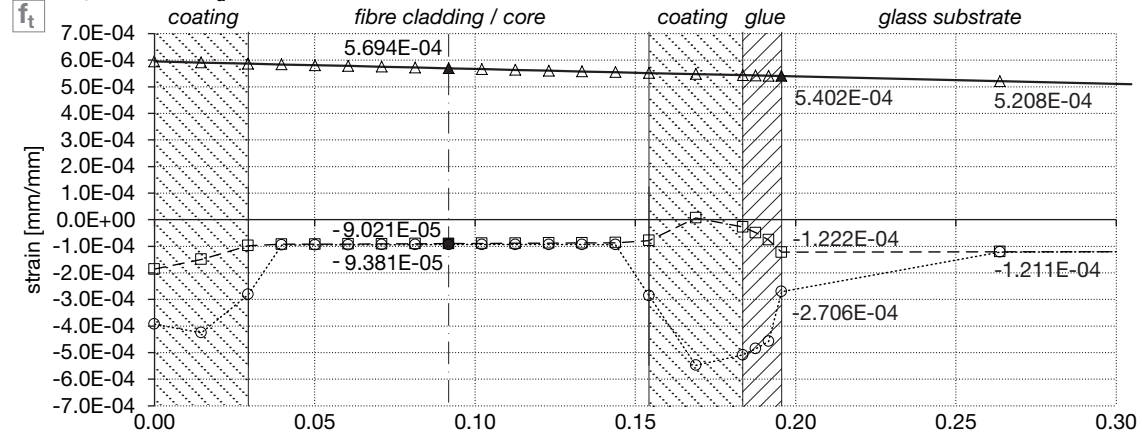
**Figure C.4.:** Top diagram: Testing procedure results total and compensated wavelength shift  $\Delta\lambda$  / temperature T vs. time of specimen FTG KB4552-02; bottom diagrams: Relaxation behaviour at load F and constant T: Wavelength shift / temperature vs. time between instances 2 and 3.

## **D Micro-Mechanical FEM Results**

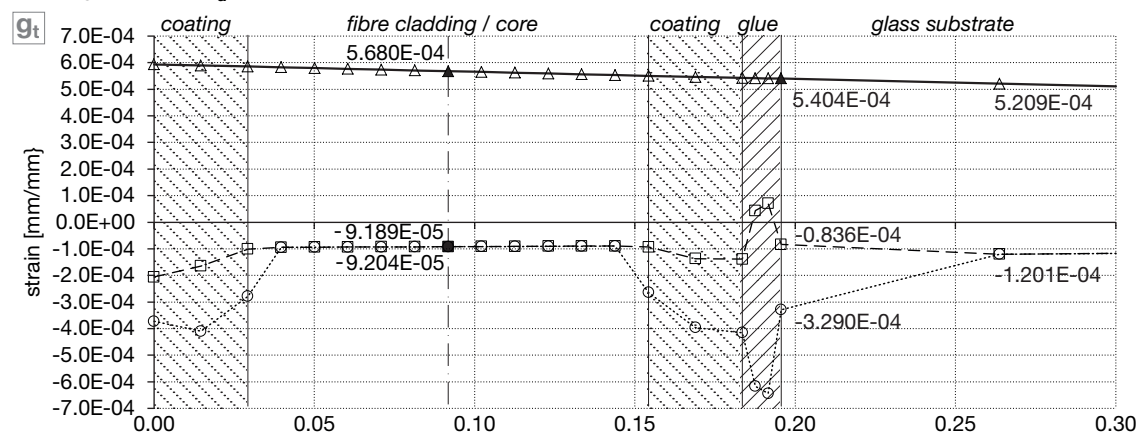
D | MICRO-MECHANICAL FEM RESULTS

section B, 1 glass layer, bending

bending / tension,  $G_a=570\text{MPa}$



bending / tension,  $G_a=10\text{MPa}$



bending / compression,  $G_a=570\text{MPa}$

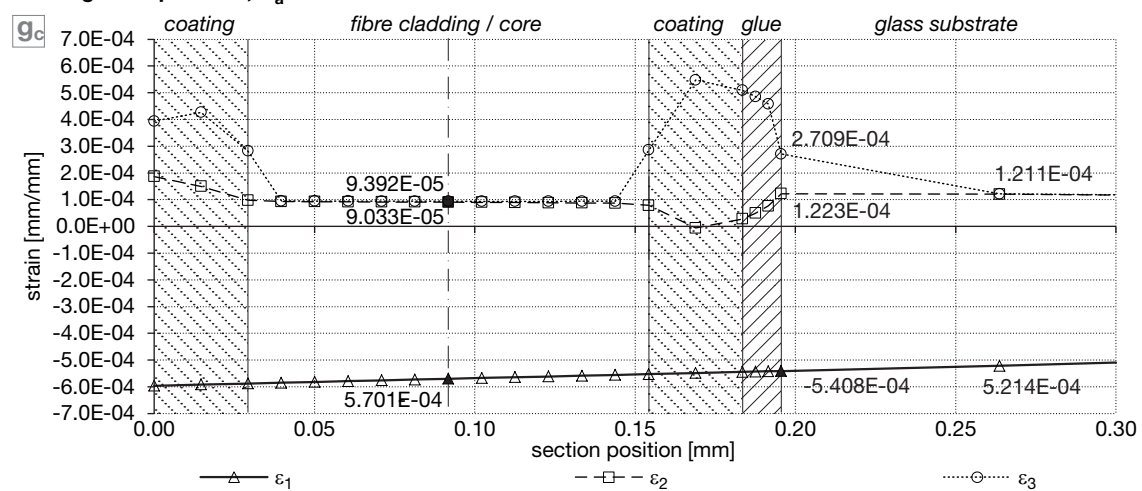
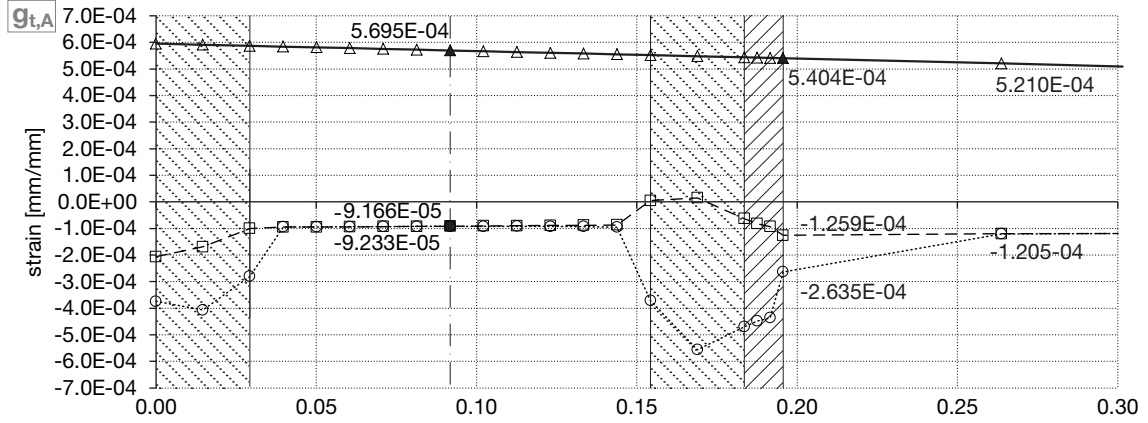


Figure D.1.: Principal strain distribution from bending loads along section 1-1 for a single glass plate with a realistic bond geometry. Top: tensile bending,  $G_a=570\text{MPa}$ ; centre: tensile bending,  $G_a=10\text{MPa}$ ; bottom: compression bending,  $G_a=570\text{MPa}$ .



section A, 1 glass layer, bending

bending / tension,  $G_a=570\text{MPa}$



bending / tension,  $G_a=10\text{MPa}$

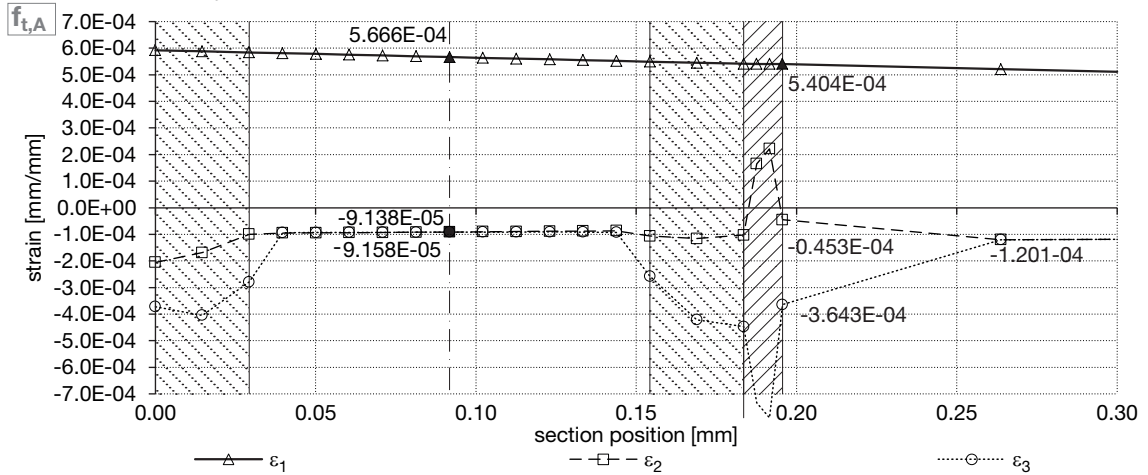
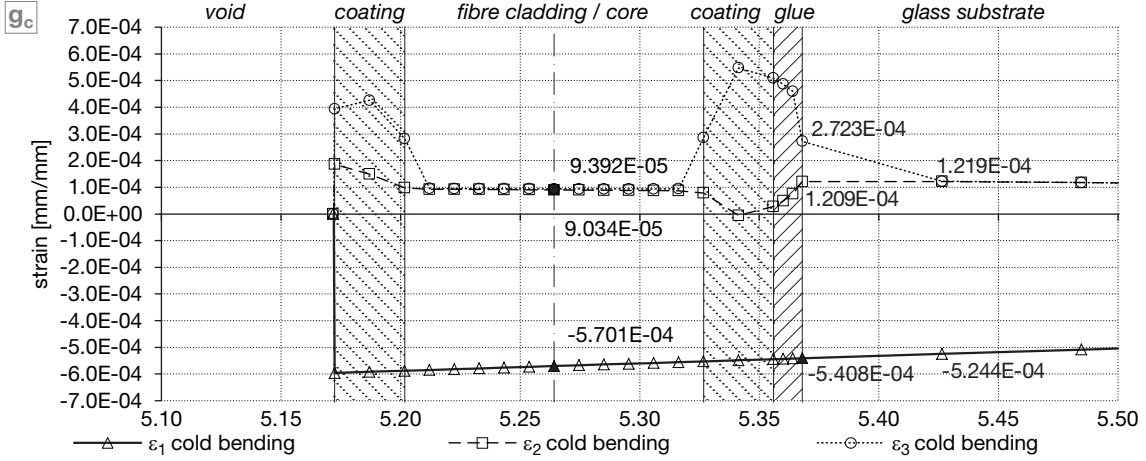


Figure D.2.: Principal strain distribution from bending loads along section 1-1 for a single glass plate with a simplified type A bond geometry. Top: tensile bending,  $G_a=570\text{MPa}$ ; bottom: tensile bending,  $G_a=10\text{MPa}$ .

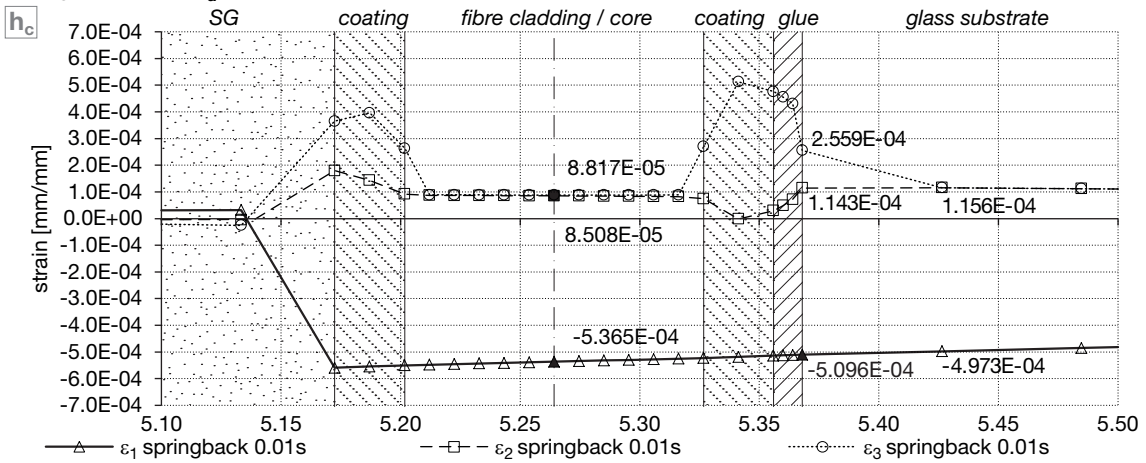
D | MICRO-MECHANICAL FEM RESULTS

section B, SG laminate bending (compression) - springback - relaxation

bending / compression  $G_a=570\text{MPa}$  (two separate glass layers)



springback 0.01s,  $G_a=570\text{MPa}$  (laminated)



relaxation 3 months,  $G_a=570\text{MPa}$  (laminated)

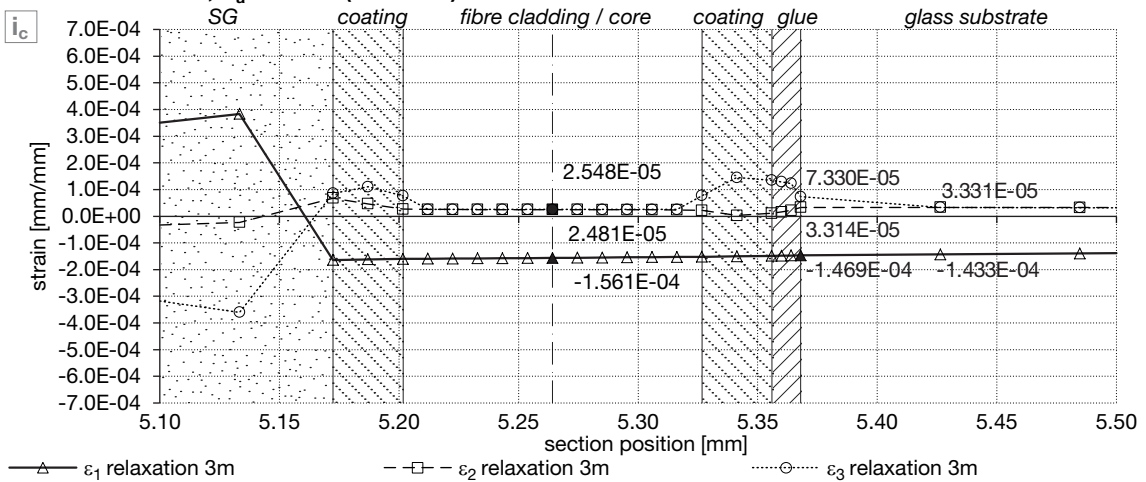
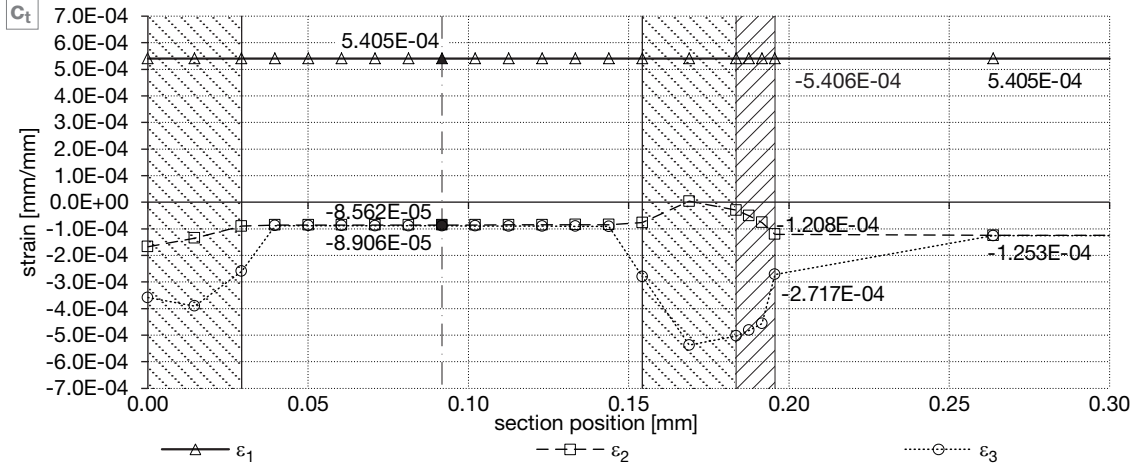


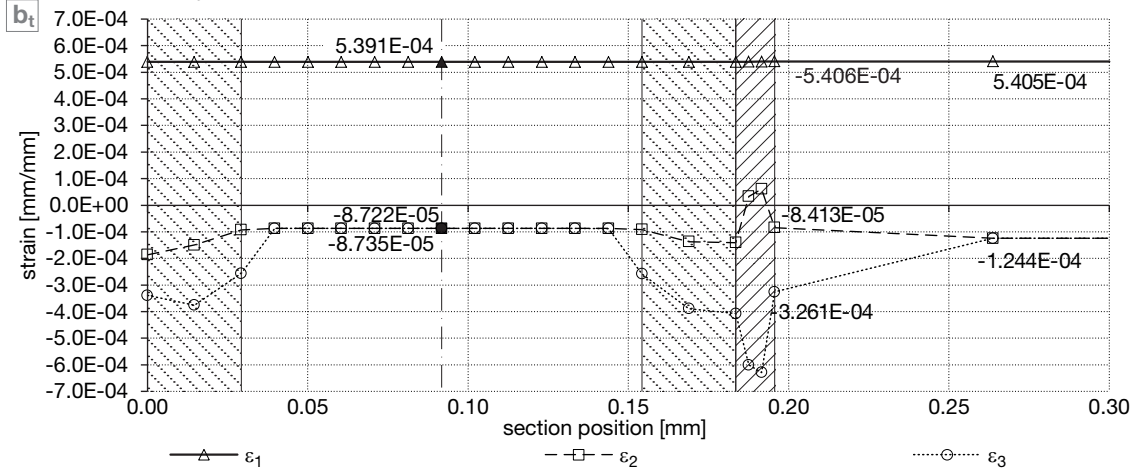
Figure D.3.: Principal strain distribution from compression bending loads along section 1-1 for a 2-ply SG glass laminate in cold bent (top), initial springback after 0.01s (centre) and relaxation state after 3 months (bottom).

section B, 1 glass layer, axial load in 1-direction

axial 1 / tension,  $G_a=570\text{MPa}$



axial 1 / tension,  $G_a=10\text{MPa}$



axial 1 / compression,  $G_a=570\text{MPa}$

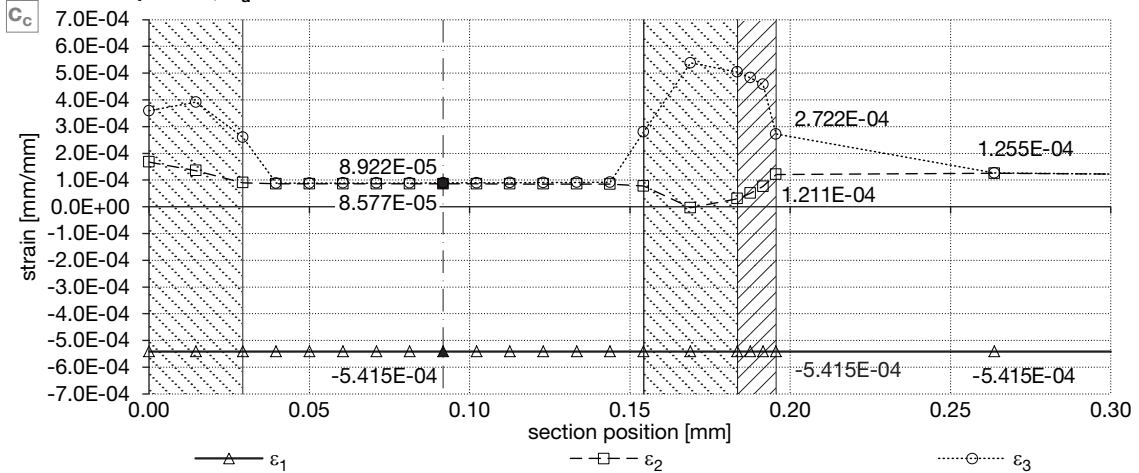
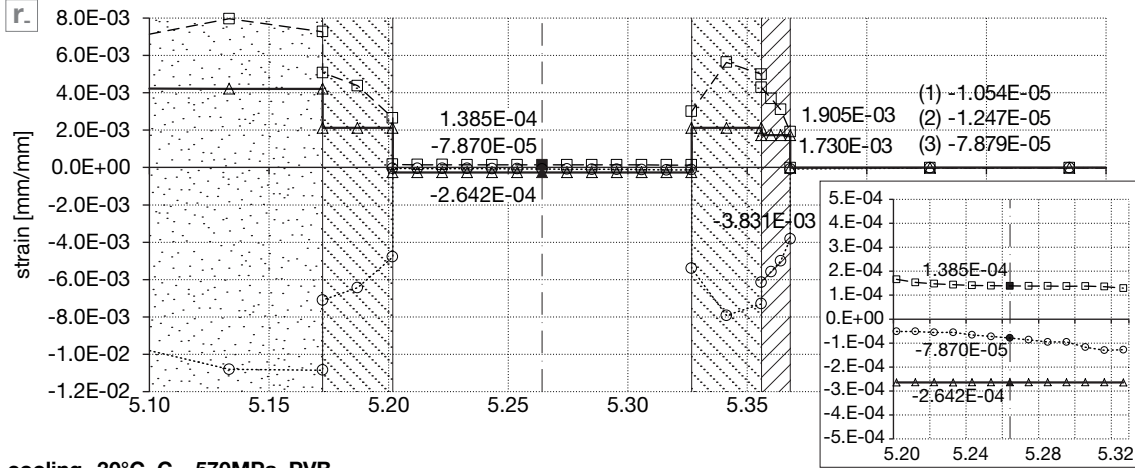


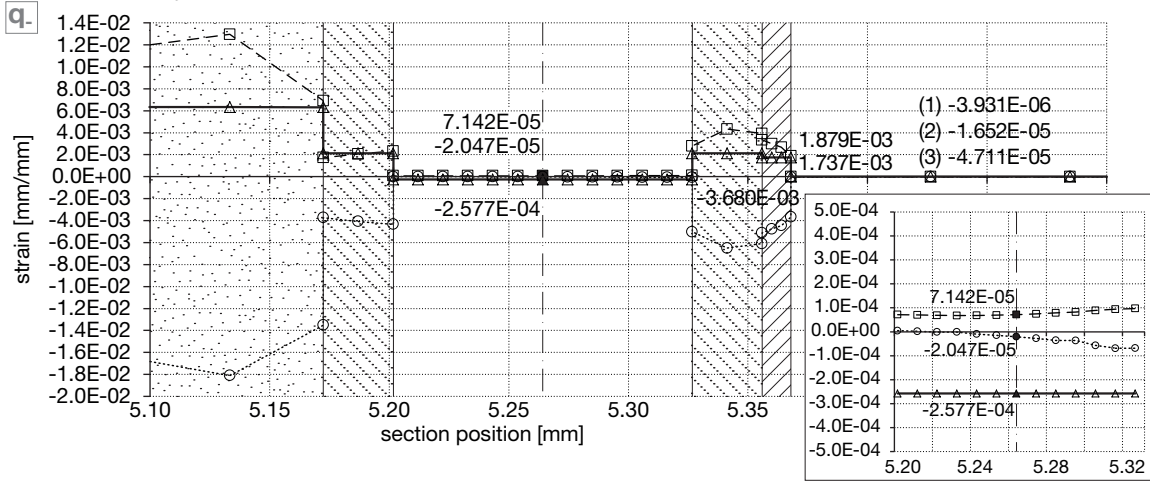
Figure D.4.: Principal strain distribution from axial loads in direction 1 along section 1-1 for a single glass. Top: tension,  $G_a=570\text{MPa}$ ; centre: tension,  $G_a=10\text{MPa}$ ; bottom: compression,  $G_a=570\text{MPa}$ .

D | MICRO-MECHANICAL FEM RESULTS

section B, laminate (2 glass layers), thermal load (uniform cooling)  
cooling -30°C,  $G_a=570\text{MPa}$ , SG



cooling -30°C,  $G_a=570\text{MPa}$ , PVB



section B, 1 glass layer, thermal load  
cooling -30°C,  $G_a=570\text{MPa}$

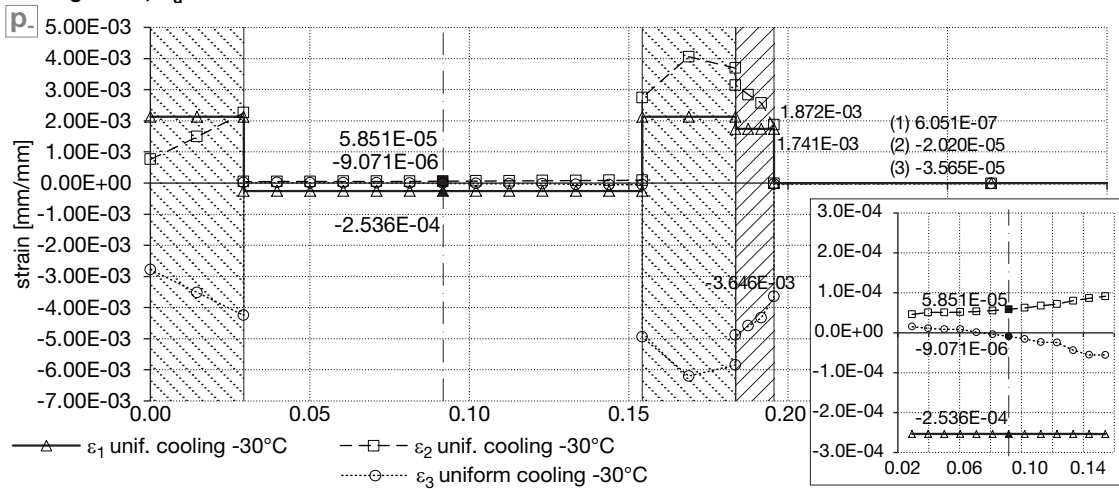


Figure D.5.: Principal strain distribution from uniform thermal cooling loads (-30°C) for a two-ply glass laminate and a single glass pane. Top: SG interlayer,  $G_a=570\text{MPa}$ ; centre: PVB interlayer,  $G_a=570\text{MPa}$ ; bottom: single glass,  $G_a=570\text{MPa}$ .

## **E Real Scale Tests**

## E.1. Photogrammetry

camera	date	(calibrated)		RMS bundle			pixel
		focal length	RMS image coord.	x	y	z	size
		-	-	x	y	z	-
		[mm]	[ $\mu$ m]	[mm]	[mm]	[mm]	[ $\mu$ m]
<b>Canon EOS 50D</b>	11.01.2013	-	-	-	-	-	4.672
	13.01.2013	18.8369	0.98	0.0682	0.0901	0.0496	4.672
	15.01.2013	20.1370	3.32	0.1531	0.1923	0.1162	4.672
	20.01.2013	18.9349	0.95	0.2100	0.3271	0.1785	4.672
	25.01.2013	18.3726	1.03	0.0682	0.1126	0.0588	4.672
	25.01.2013	18.5531	0.79	0.2013	0.2973	0.1752	4.672
	26.01.2013	18.6720	0.81	0.1523	0.1343	0.1123	4.672
	01.02.2013	18.8613	1.10	0.1372	0.1846	0.1108	4.672
	11.02.2013	18.8937	0.98	0.2063	0.2117	0.1717	4.672
18.02.2013	18.9262	1.24	0.2682	0.2661	0.1762	4.672	
<b>EOS 40D</b>	13.01.2013	19.9129	0.68	0.0441	0.0501	0.0268	5.710
	18.01.2013	19.0485	0.53	0.0299	0.0277	0.0214	5.710
	25.01.2013	20.4601	0.77	0.0338	0.0498	0.0274	5.710
<b>EOS 7D</b>	11.01.2013	20.0720	0.42	0.1167	0.1294	0.0842	4.300
	18.01.2013	19.7510	0.40	0.1365	0.1079	0.1144	4.300
	25.01.2013	18.5333	0.55	0.2035	0.1965	0.1806	4.300
<b>Nikon D2X</b>	08.03.2013	20.4300	0.47	0.0129	0.0206	0.0110	5.500
	11.03.2013	20.4160	0.34	0.0652	0.0694	0.0516	5.500
<b>D80</b>	14.03.2013	20.4219	0.60	0.1285	0.1073	0.0848	6.090
	02.09.2013	20.5328	0.45	0.0660	0.0731	0.0305	6.090
<b>D5000</b>	18.04.2013	20.4168	0.38	0.0470	0.0229	0.0204	5.500

Table E.1.: Summary of the principal camera calibration data and RMS.

**developed walls and floor  
scale 1/100**

walls: 128 points  
 floor: 60 points  
 speximens: 9\*90=810 points  
 total: 998 array points

1000 (wall)

point marker  
 scale 1/2

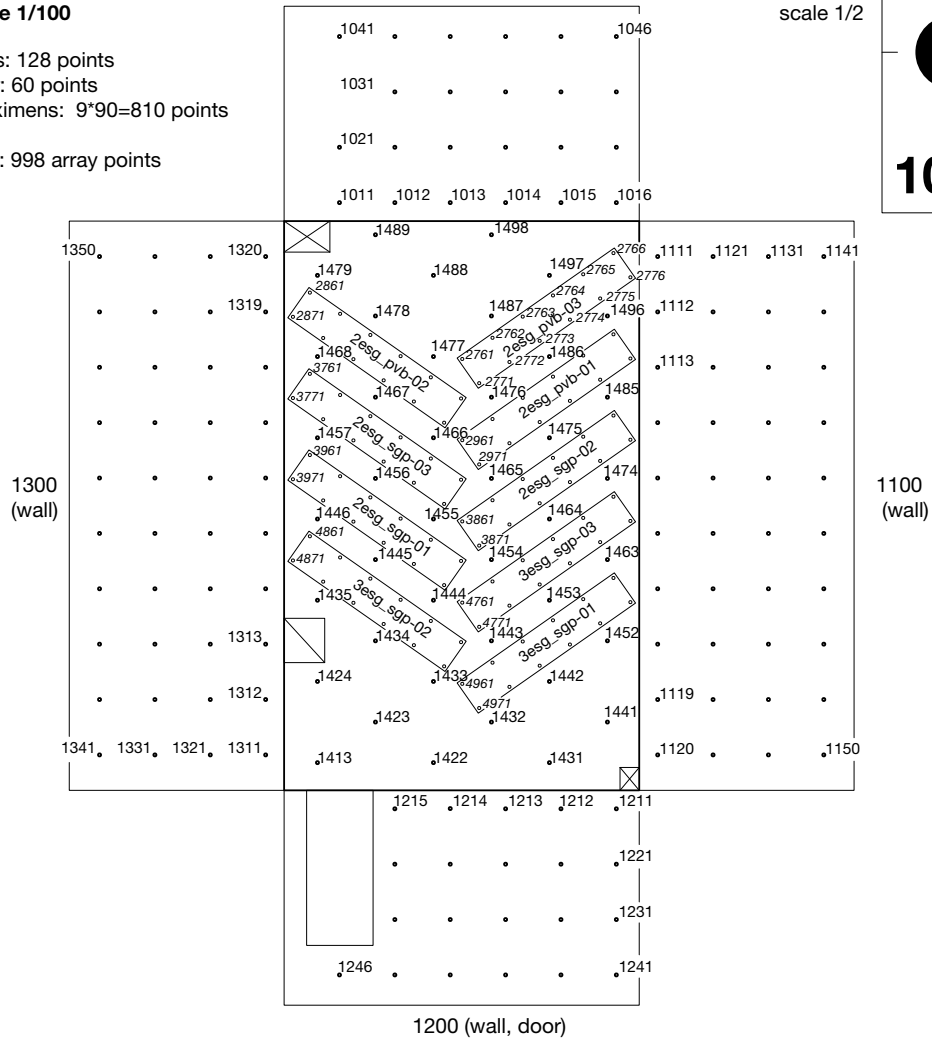
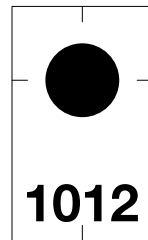


**Figure E.1.:** Setup of the target point numbering in the testing room and positions of the glass specimens.

E.2. Numerical Cold Bending Model

author	material	manu- facturer	product label	test	specimen	results	test range	models, fit	master curve	valid fit range
Weller, B. et al., FKG (ed.)	ionomer	DuPont (Kuraray)	SentryGlas®	tensile DMA	bulk material	E', E'' (T)	-50 to 100°C	-	-	-
Bennison et al.	ionomer	DuPont (Kuraray)	SentryGlas®	DMA	n.a.	E(t,T) G(t,T)	10 to 80°C	-	n.a.	1s to 10 years
van Duser et al.	PVB	DuPont (Kuraray)	Butacite®	tensile DMA	bulk material	E', E'' (t,T) corresp. G	0 to 70°C	11-param. Maxwell- Wiechert, WLF	20°C	10 to 60°C
Kutterer, M.	PVB	HT Troplast AG (Kuraray)	Trosifol® MB	single-lap shear	cylindrical glass-PVB- laminates d=30mm, 10-0.38 to 0.76-10mm	G(t,T)	0 to 60°C, 23-25°C	non-linear model as per Weng [Wen 88], logarithmic fit	-	0 to 60°C, 0.1 to 1E+07s
Schuler, C.	PVB	HT Troplast AG (Kuraray)	Trosifol® MB	single-lap shear and 4-pt.-bending	grazed strips 250x80mm from glass-PVB-materials, 6- 1.52-6mm	G(t,T)	5 to 60°C	3-param. Maxwell- Wiechert, logarithmic law	-	0 to 70°C, 1s to 3 months
Sackmann, V.	PVB	HT Troplast AG (Kuraray)	Trosifol® MB	static and cyclic 4-point-bending	glass-PVB-laminates 1100x200mm, 6-1.52-6mm (static), 8-0.76-8mm	G(t, T)	0 to 60°C and 0 to 40°C	12-param. Maxwell- Wiechert, WLF	20°C	0 to 70°C, 1s to 6 months
Andreozzi et al.	PVB	Kuraray	Trosifol® BG R20	cyclic torsion, rheometer	cylindrical drill-core glass- PVB-laminates d=23mm, 8-0.76-8mm / 8-1.52-8mm	G', G'' (t,T) G(t,T)	30 to 80°C, 0.0001 or 0.1 to 100Hz	10-param. Maxwell- Wiechert, WLF	30°C	30 to 50°C, 0.1 to 1E+07s

Table E.2.: Overview of PVB interlayer material characterisations from different research works.

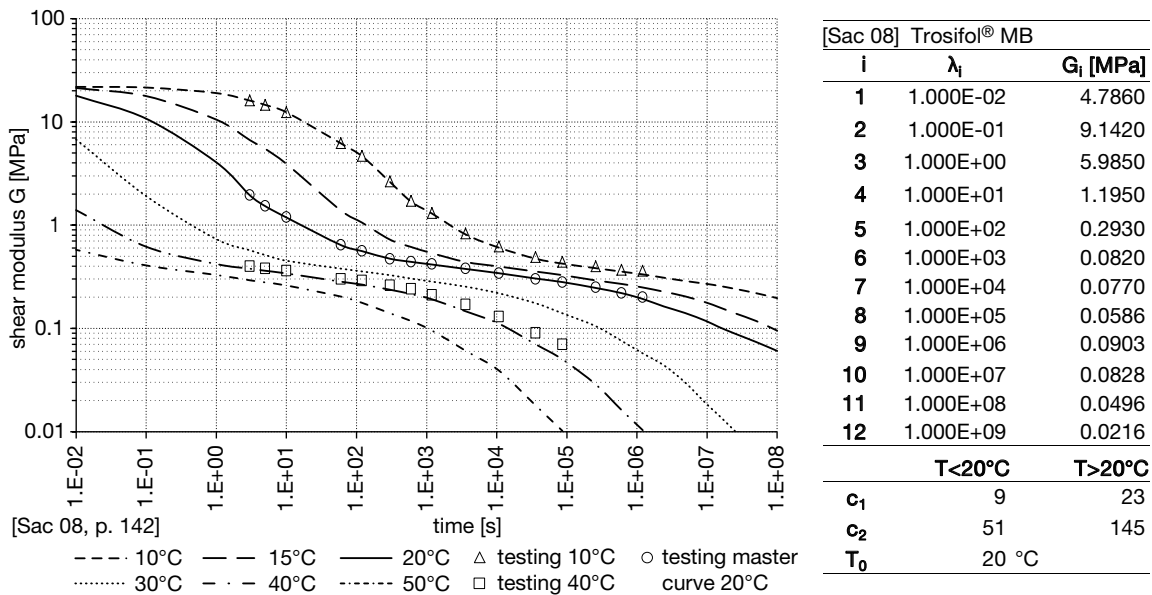
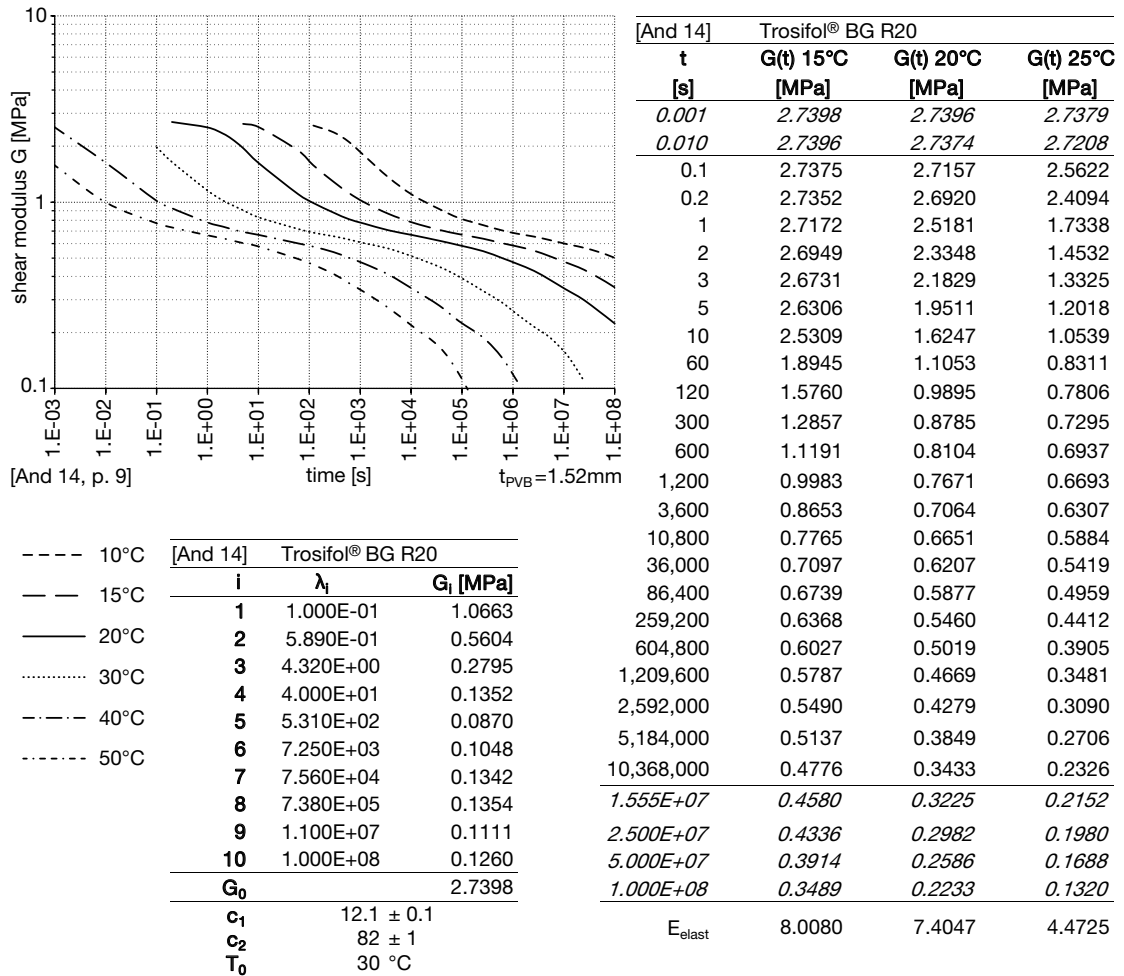


Figure E.2.: Shear modulus and Maxwell model for PVB as per Sackmann (top) for Trosifol® MB.





**Figure E.3.:** Time- and temperature-dependent shear moduli of PVB Trosifol® BGR20 from the research of Andreozzi et al. (double-logarithmic). The related generalised Maxwell model (Prony series) is shown a the bottom-left and tabled G(t) values calculated with the Maxwell model are shown on the right.



E.3. Real Scale Testing Results

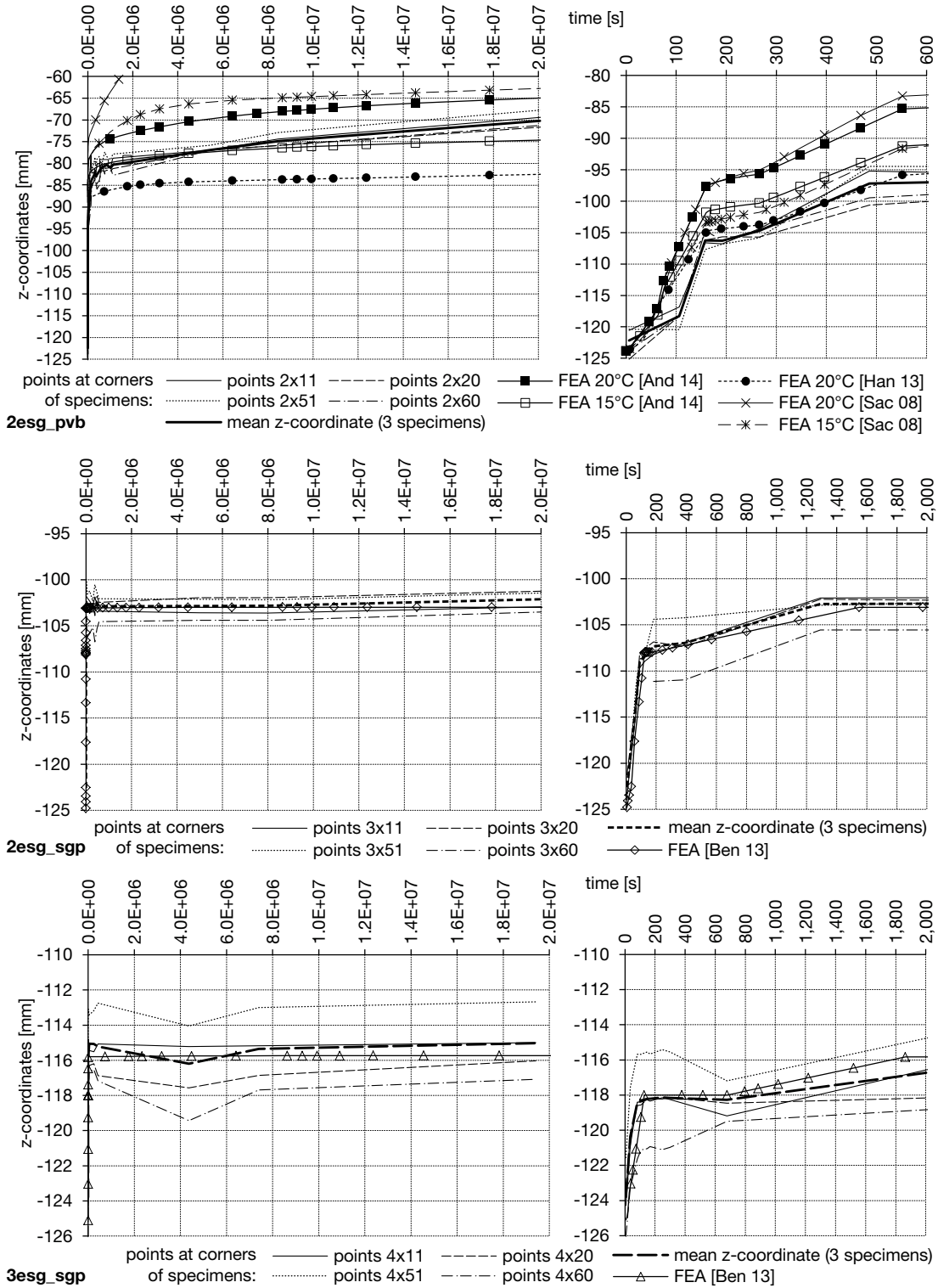
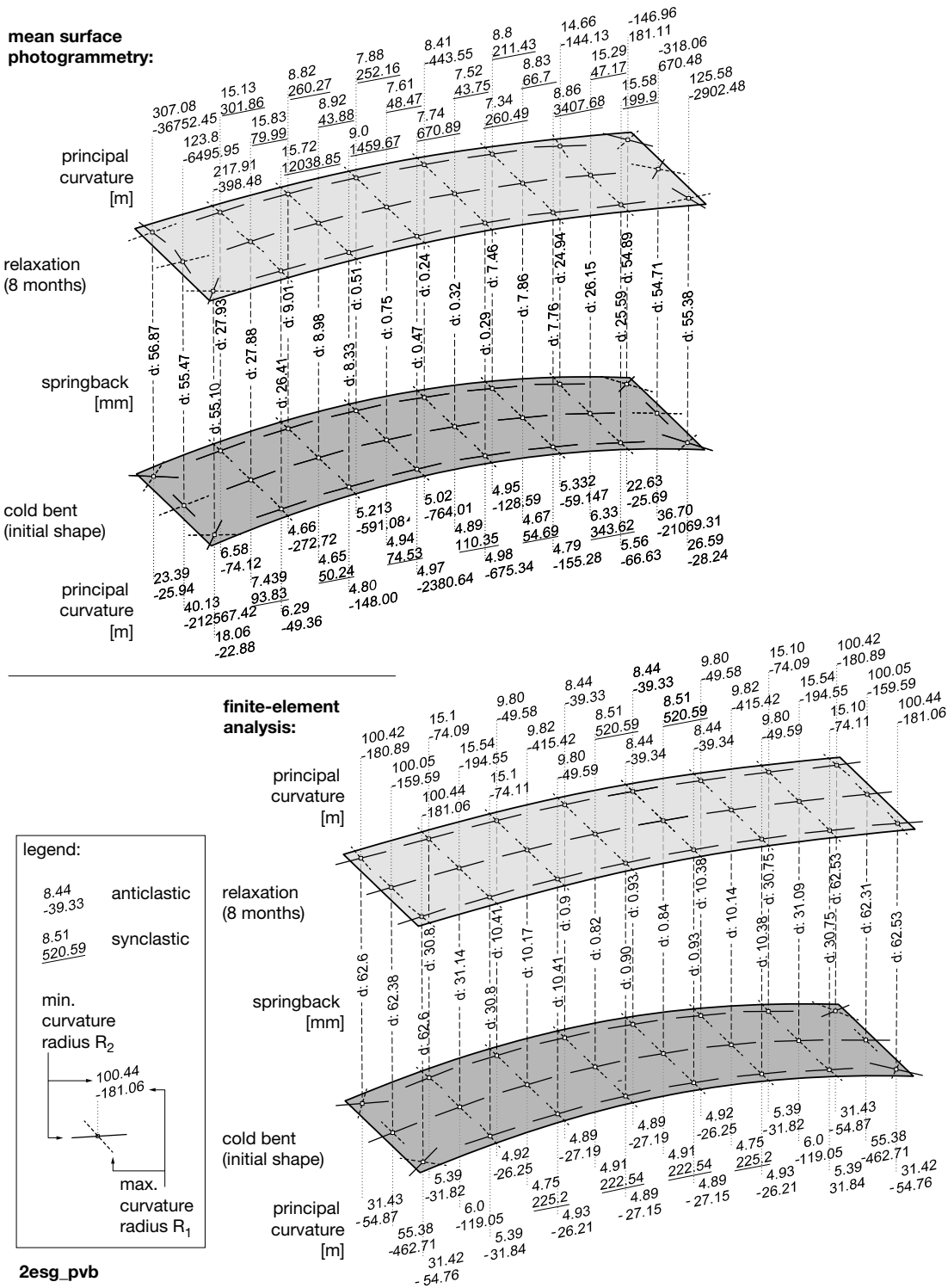
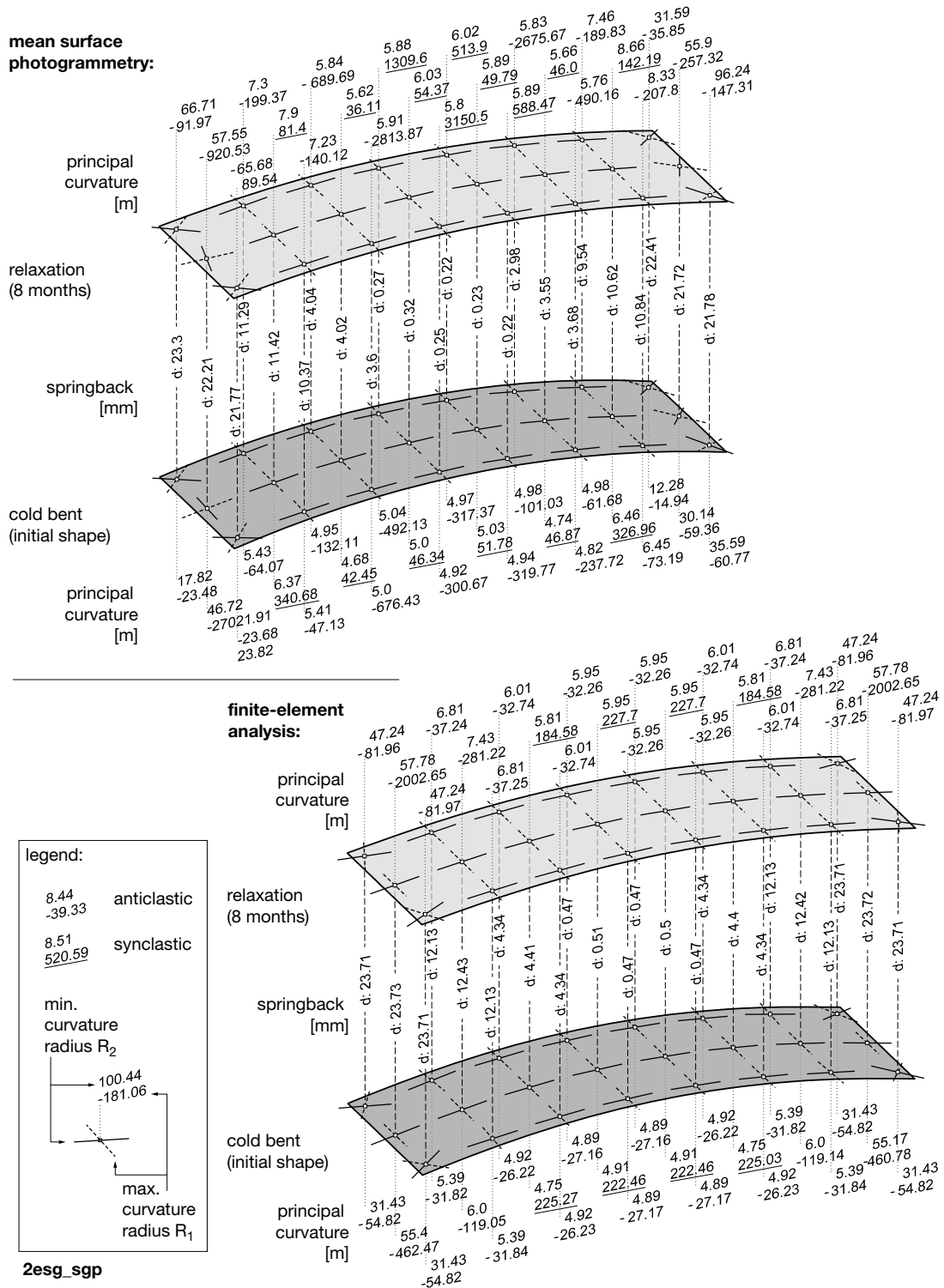


Figure E.4.: Relaxation behaviour of the three curved laminate types 2esg\_pvb (top), 2esg\_sgp (centre) and 3esg\_sgp (bottom), expressed via the changing z-coordinate of the corner points xx21, xx51, xx20 and xx60 plotted against time. On the right hand side, the short term springback behaviour is shown. The mean values of these points and various FE-results are shown in comparison.



**Figure E.5.:** Comparison of the principal curvature radii from photogrammetry and FE analysis on the top surface of laminate from two cold bent glass panes with PVB interlayer for the cold bent state and after 8 months of relaxation. In addition, the springback value  $u_z$  after 8 months relaxation is given.



**Figure E.6.:** Comparison of the principal curvature radii from photogrammetry and FE-analysis on the top surface of laminate from two cold bent glass panes with SG-interlayer for the cold bent state and after 8 months of relaxation. In addition, the springback value  $u_z$  after 8 months relaxation is given.

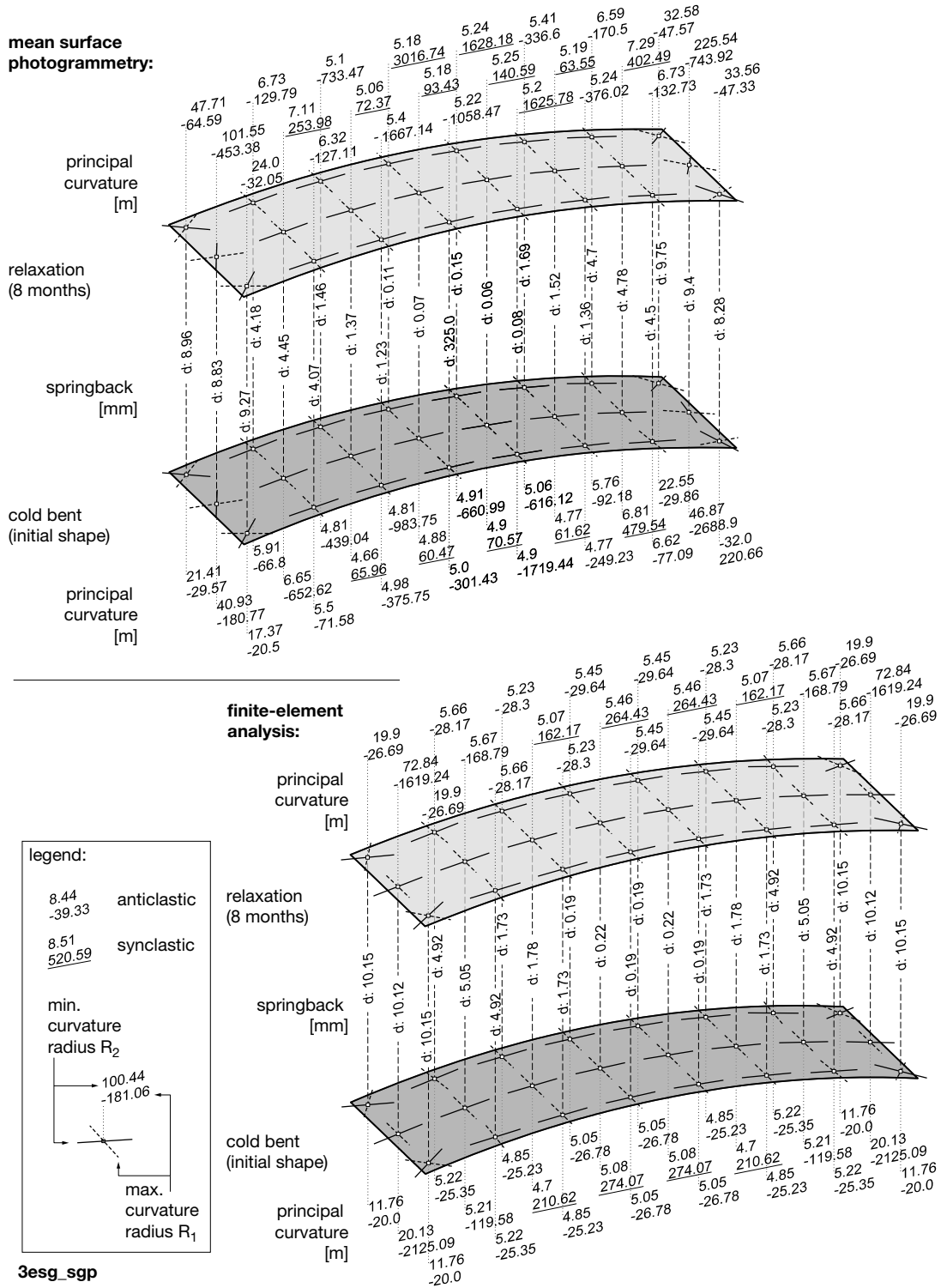


**Figure E.7.:** Comparison of the principal curvature radii from photogrammetry and FE-analysis on the top surface of laminate from two cold bent glass panes with PVB-interlayer for the cold bent state and after 8 months of relaxation. In addition, the springback value  $u_z$  after 8 months relaxation is given.

specimen	pos. fbg	cold bending			after autoclave process				24h relaxation				9m relaxation				
		$\lambda_B$ [nm]	$\Delta\lambda_{cb}$ [nm]	$\sigma_x$ [MPa]	$\lambda_B$ [nm]	$\Delta\lambda_{sp}$ [nm]	$\Delta\lambda_{sp}-\Delta\lambda_{cb}$ [nm]	$\sigma_{x,0}$ [MPa]	$\Delta\sigma_{x,rel}$ [MPa]	$\lambda_B$ [nm]	$\Delta\lambda_{24h}$ [nm]	$\sigma_{x,0,24h}$ [MPa]	$\sigma_{x,rel}$ [MPa]	$\lambda_B$ [nm]	$\Delta\lambda_{9m}$ [nm]	$\sigma_{x,0,9m}$ [MPa]	$\sigma_{x,rel}$ [MPa]
2esg_pvb-01	1	1519.760	ne	-	1519.132	-0.628	-	-35.08	-	1519.249	-0.511	-28.18	-	1519.418	-0.343	-28.88	-
	6	1569.311	ne	-	1568.731	-0.580	-	-31.39	-	1568.842	-0.469	-24.99	-	1569.005	-0.306	-26.30	-
	1	1519.786	ne	-	1520.537	0.751	-	41.32	-	1520.266	0.480	25.30	-	1520.207	0.421	17.17	-
	6	1569.416	ne	-	1570.155	0.739	-	39.33	-	1569.923	0.507	25.95	-	1569.849	0.433	17.03	-
	2	1519.575	ne	-	1518.965	-0.610	-	-33.43	-	1519.096	-0.479	-24.99	-	1519.265	-0.310	-20.26	-
	6	1569.248	ne	-	1568.555	-0.693	-	-37.42	-	1568.791	-0.458	-23.57	-	1568.949	-0.300	-19.77	-
2esg_pvb-02	1	1519.534	1520.342	0.808	sl	sl	-	-	sl	sl	-	-	sl	sl	-	-	
	6	1569.244	1570.152	0.908	1569.799	0.555	-0.353	32.00	17.11	1569.577	0.332	19.11	38.21	1569.515	0.271	11.03	30.13
	2	1519.613	ne	-	1518.979	-0.635	-	-33.09	-	1519.098	-0.515	-26.77	-	1519.256	-0.358	-23.72	-
	6	1569.296	ne	-	1568.772	-0.524	-	-25.98	-	1568.917	-0.379	-18.52	-	1569.068	-0.229	-16.11	-
	1	1519.564	ne	-	1520.252	0.688	-	40.80	-	1519.995	0.431	25.92	-	1519.917	0.353	15.95	-
	6	1569.317	ne	-	1569.938	0.622	-	36.00	-	1569.661	0.344	20.47	-	1569.568	0.251	9.83	-
arithmetic mean	2	-	-	-	-	-	-32.73	-	-	-0.469	-24.50	-	-	-0.307	-22.51	-	-
3	-	-	-	-	-	-	37.89	-	-	0.419	23.35	-	-	0.346	14.20	-	-
2esg_sgp-01	1	1519.674	ne	-	1518.904	-0.770	-	-41.27	-	1518.916	-0.758	-40.98	-	1519.008	-0.666	-41.68	-
	6	1569.352	ne	-	1568.588	-0.764	-	-39.60	-	1568.604	-0.748	-39.10	-	1568.680	-0.672	-40.83	-
	1	1519.623	1520.347	0.724	1520.344	0.721	-0.003	41.37	-2.96	1520.266	0.643	36.65	36.81	1520.315	0.692	33.54	33.70
	6	1569.295	1569.801	0.506	1569.956	0.661	0.155	36.89	-11.51	1569.891	0.596	32.97	24.58	1569.954	0.659	30.54	22.15
	2	1519.689	ne	-	1519.068	-0.621	-	-31.82	-	1519.006	-0.683	-36.00	-	1519.085	-0.604	-37.23	-
	6	1569.337	ne	-	1568.618	-0.719	-	-36.01	-	1568.551	-0.786	-40.37	-	1568.635	-0.702	-41.48	-
2esg_sgp-02	1	1519.711	ne	-	1520.350	0.639	-	38.42	-	1520.342	0.631	37.22	-	1520.421	0.710	36.06	-
	6	1569.299	ne	-	1569.949	0.650	-	37.89	-	1569.950	0.651	37.18	-	1570.040	0.741	36.44	-
	2	1519.775	1519.063	-0.712	1519.074	-0.701	0.010	-36.67	-3.33	1519.025	-0.750	-40.25	-43.59	1519.100	-0.675	-41.55	-44.88
	6	1569.264	1568.283	-0.981	1568.494	-0.770	0.211	-39.14	-14.14	1568.453	-0.811	-42.23	-56.38	1568.529	-0.735	-43.63	-57.77
	1	1519.668	1520.343	0.675	1520.265	0.597	-0.078	35.97	1.63	1520.266	0.598	35.13	39.51	1520.334	0.666	33.43	37.81
	6	1569.326	1570.104	0.778	1569.908	0.582	-0.196	34.08	7.86	1569.928	0.602	34.30	44.91	1569.994	0.668	32.39	43.00
arithmetic mean	2	-	-	-	-0.846	-46.65	-	-	-0.724 v	-	-37.42	-49.96	-	-0.676	-41.06	-51.33	
3	-	-	-	-	0.671	35.63	-	-	0.641	0.111	37.44	-1.25	-	0.620	35.58	36.45	

ne=no entry  
sl=sensor loss  
italics: sensor birefringence

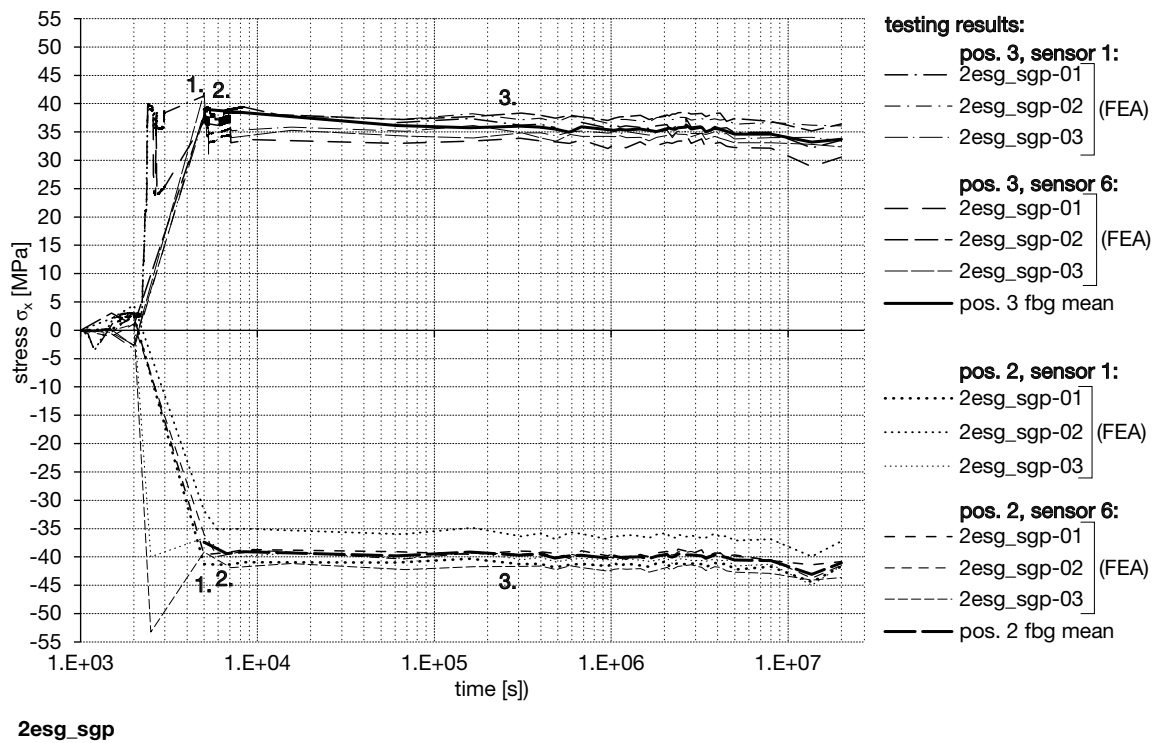
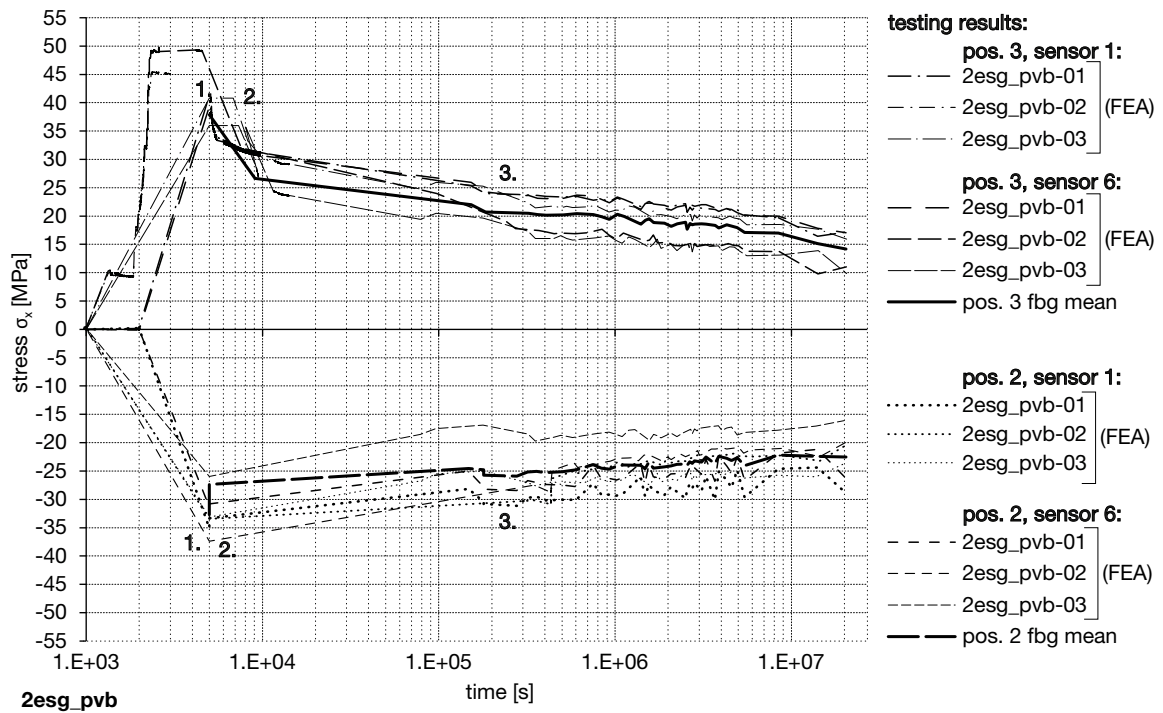
Table E.3.: Results summary of the test series involving specimens 2esg\_pvb-01 to -03 and 2esg\_sgp-01 to -03.

specimen	pos. fbg initial	cold bending			after autoclave process				24h relaxation				9m relaxation				
		$\lambda_B$ [nm]	$\Delta\lambda_{cb}$ [nm]	$\sigma_x$ [MPa]	$\lambda_B$ [nm]	$\Delta\lambda_{ac}$ [nm]	$\Delta\lambda_{ac}-\Delta\lambda_{cb}$ [nm]	$\sigma_{x,0}$ [MPa]	$\Delta\sigma_{x,rel}$ [MPa]	$\lambda_B$ [nm]	$\Delta\lambda_{24h}$ [nm]	$\sigma_{x,0,24h}$ [MPa]	$\sigma_{x,rel}$ [MPa]	$\lambda_B$ [nm]	$\Delta\lambda_{9m}$ [nm]	$\sigma_{x,0,9m}$ [MPa]	$\sigma_{x,rel}$ [MPa]
<b>3esg_sgp-01</b>	1	1519.795	-0.750	-40.02	1518.877	-0.810	-0.104	-40.76	e	1518.972	-0.715	-37.81	-31.98	1519.050	-0.637	-40.08	-34.25
	2	1569.343	-0.827	-42.84	1543.789	-0.820	-0.201	-40.55	8.42	1543.903	-0.705	-36.62	-25.57	1543.987	-0.622	-38.66	-27.62
	3	1549.566	0.890	50.65	1550.456	0.516	-	33.30	-	1520.319	0.641	37.93	-	1520.430	0.752	37.53	-
	4	1519.687	-0.706	-37.56	1569.847	0.537	-	33.53	-	1569.984	0.674	38.58	-	1570.083	0.773	37.31	-
	5	1519.678	-	-	1518.919	-0.825	0.013	-41.18	-1.84	1518.869	-0.874	-45.59	-44.87	1518.951	-0.793	-47.64	-46.92
	6	1544.608	-0.619	-32.13	1568.847	-0.784	-0.028	-39.06	0.40	1568.784	-0.847	-42.54	-44.07	1568.892	-0.738	-43.29	-44.82
<b>3esg_sgp-02</b>	1	1519.744	-	-	1574.890	0.649	-	39.84	-	1574.871	0.630	37.20	-	1574.945	0.704	34.61	-
	2	1569.631	-0.784	-38.65	1550.121	0.627	-	39.23	-	1550.095	0.601	36.17	-	1550.166	0.672	33.46	-
	3	1574.241	-	-	1519.071	-0.712	0.077	-34.89	-5.40	1519.140	-0.643	-32.86	-36.94	1519.219	-0.564	-34.88	-39.16
	4	1519.783	-0.789	-40.29	1543.907	-0.748	-	-36.23	-	1543.988	-0.667	-33.38	-	1544.080	-0.575	-34.96	-
	5	1519.626	0.765	46.49	1520.275	0.649	-0.117	41.09	5.40	1520.364	0.738	44.47	47.62	1520.446	0.820	42.41	48.94
	6	1544.655	-	-	1570.024	0.676	-0.161	41.45	7.58	1570.124	0.776	45.23	50.16	1570.205	0.857	43.00	51.70
<b>3esg_sgp-03</b>	1	1519.692	-0.779	-39.26	ne	-	-	-	-	1518.899	-0.793	-41.29	-	1518.988	-0.704	-42.95	-
	2	1569.279	-	-	1568.514	-0.764	-	-37.22	-	1568.465	-0.813	-41.00	-	1568.549	-0.730	-43.11	-
	3	1574.210	0.856	48.54	1574.871	0.661	-0.195	37.91	10.63	1574.838	0.629	35.03	45.54	1574.926	0.716	33.12	43.63
	4	1549.574	0.825	47.56	1550.133	0.559	-0.266	32.85	14.70	1550.109	0.536	30.47	45.05	1550.200	0.626	28.81	43.39
	5	1519.708	-0.678	-35.51	1519.064	-0.644	0.034	-33.74	-1.76	1519.105	-0.603	-32.55	-34.44	1519.209	-0.499	-33.36	-35.25
	6	1544.568	-0.653	-33.54	1543.844	-0.724	-0.071	-37.56	4.02	1543.898	-0.670	-35.69	-31.79	1543.994	-0.574	-37.04	-33.14
arithmetic mean	1	1519.723	0.741	41.02	1520.420	0.697	-0.044	38.92	2.11	1520.490	0.767	41.21	43.69	1520.571	0.848	39.14	41.62
	2	1569.345	0.693	37.08	1569.979	0.634	-0.058	34.30	2.78	1570.068	0.724	37.52	40.67	1570.170	0.825	36.37	39.53
	3	-	-0.795	-40.76	-	-0.802	-0.012	-39.41	-1.18	-	-0.824	-42.53	-42.94	-	-0.729	-43.90	-44.05
	4	-	0.643	48.92	-	0.507	-0.202	30.69	13.90	-	0.495	28.74	35.79	-	0.558	26.66	33.99
	5	-	-0.689	-35.81	-	-0.743	-0.053	-37.29	1.32	-	-0.667	-34.78	-32.14	-	-0.578	-36.50	-33.88
	6	-	0.759	43.41	-	0.618	-0.095	37.10	4.47	-	0.720	40.82	45.53	-	0.813	39.29	45.45

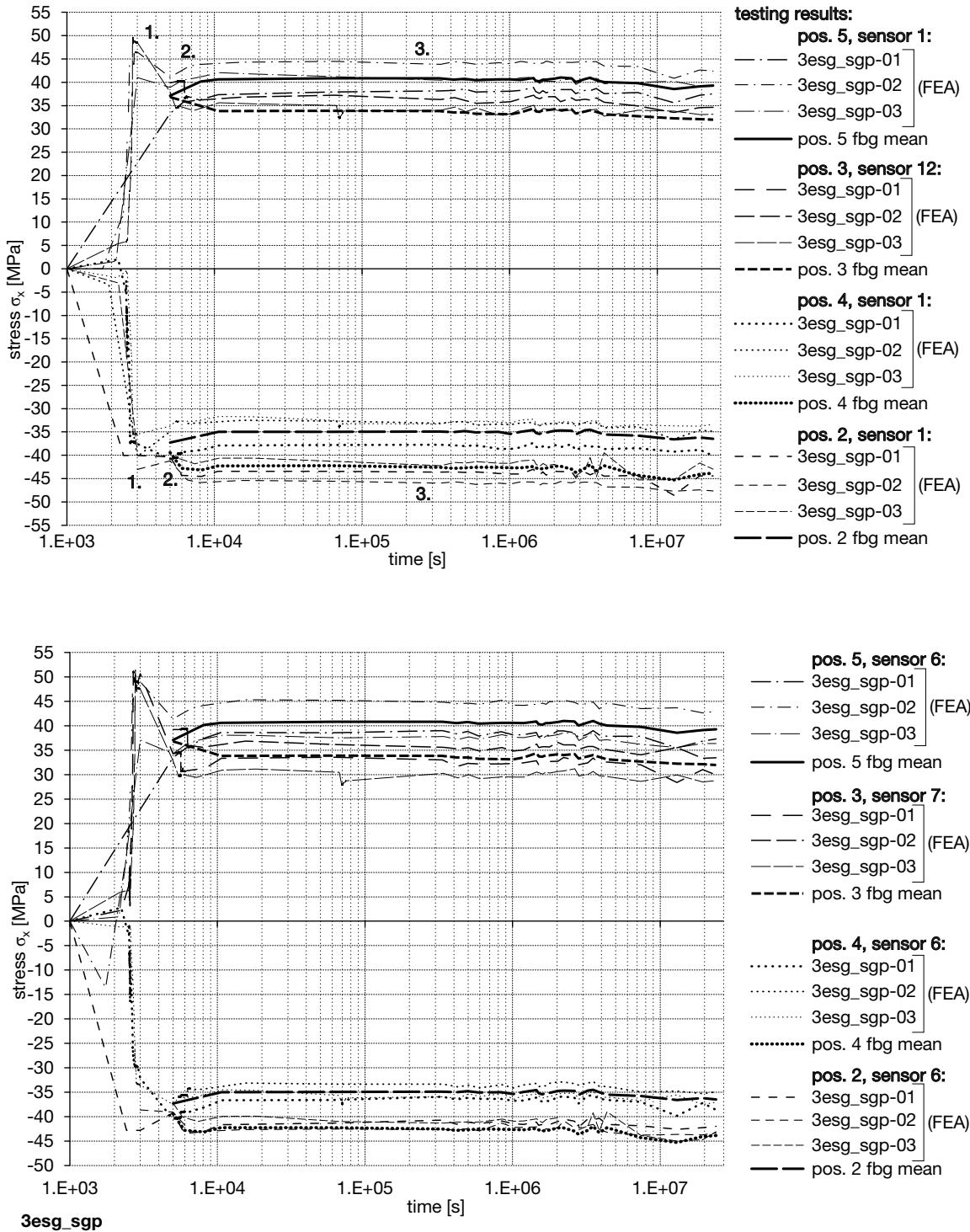
ne=no entry *sl*=sensor loss *italics*: sensor birefringence

Table E.4.: Results summary of the test series involving specimens 3esg\_sgp-01 to -03.





**Figure E.8.:** Glass stress  $\sigma_x$  calculated from FBG 1, 6 for the three two-ply specimens with PVB interlayer (top) and for the three two-ply specimens with SG interlayer (bottom) during 8 months of monitoring.



**Figure E.9.:** Glass stress  $\sigma_x$ , calculated from FBG 1, 12 (top) and FBG 6, 7 (bottom) during 8 months of monitoring of the three specimens 3esg\_sgp01 to -03 with three glass plies and SG interlayer.

		mean wavelength shift $\Delta\lambda$ [nm]															T
sensor-no.:		1	2	3	4	5	6	7	8	9	10	11	12	13	14	15	[°C]
pos.	pos x [mm]:	150	300	450	600	750	900	1050	1200	1350	1500	1650	1800	1950	2100	2250	
7	lateral cb	0.477	0.614	0.666	0.838	0.896	0.864	0.943	0.823	0.935	0.871	0.902	0.906	0.390	0.694	0.344	21.1 / 31.3
	ac	0.087	0.472	0.607	0.691	0.732	0.720	0.755	0.746	0.741	0.735	0.717	0.718	0.456	0.507	-0.103	22.7 / 23.1
	ar	0.068	0.550	0.560	0.735	0.757	0.743	0.764	0.755	0.738	0.751	0.760	0.794	0.675	0.466	0.042	24
	sw	0.023	0.489	0.499	0.679	0.715	0.707	0.731	0.725	0.710	0.713	0.710	0.734	0.607	0.394	-0.030	20.5
centre	cb	0.259	0.492	0.696	0.761	0.816	0.830	0.884	0.868	0.881	0.866	0.839	0.790	0.683	0.505	0.256	21.1 / 31.3
	ac	0.068	0.348	0.524	0.610	0.695	0.685	0.729	0.765	0.738	0.733	0.717	0.621	0.523	0.310	0.087	22.7 / 23.1
	ar	-	-	-	-	-	-	-	-	-	-	-	-	-	-	-	24
	sw	-	-	-	-	-	-	-	-	-	-	-	-	-	-	-	20.5
2	lateral cb	-0.242	-0.380	-0.552	-0.597	-0.598	-0.637	-0.644	-0.663	-0.632	-0.644	-0.619	-0.600	-0.585	-0.507	-0.192	21.1 / 31.3
	ac	-0.446	-0.489	-0.676	-0.774	-0.775	-0.783	-0.802	-0.804	-0.732	-0.811	-0.789	-0.784	-0.744	-0.550	-0.452	22.7 / 23.1
	ar	-0.517	-0.584	-0.802	-0.885	-0.851	-0.833	-0.853	-0.838	-0.696	-0.860	-0.832	-0.848	-0.864	-0.619	-0.444	24
	sw	-0.582	-0.645	-0.872	-0.968	-0.937	-0.937	-0.961	-0.931	-0.804	-0.963	-0.934	-0.945	-0.958	-0.702	-0.530	20.5
centre	cb	-0.109	-0.311	-0.568	-0.665	-0.687	-0.667	-0.645	-0.665	-0.663	-0.681	-0.802	-0.680	-0.585	-0.421	-0.073	21.1 / 31.3
	ac	-0.276	-0.445	-0.685	-0.839	-0.846	-0.831	-0.806	-0.788	-0.810	-0.841	-0.841	-0.875	-0.735	-0.526	-0.232	22.7 / 23.1
	ar	-	-	-	-	-	-	-	-	-	-	-	-	-	-	-	24
	sw	-	-	-	-	-	-	-	-	-	-	-	-	-	-	-	20.5

*$\Delta\lambda$ -values are not temperature-compensated.*

		mean stress $\sigma_x$ [MPa]															T
sensor-no.:		1	2	3	4	5	6	7	8	9	10	11	12	13	14	15	[°C]
pos.	pos x [mm]:	150	300	450	600	750	900	1050	1200	1350	1500	1650	1800	1950	2100	2250	
7	lateral cb	24.12	31.90	34.76	44.45	47.60	45.59	47.44	42.96	49.14	45.35	46.95	44.55	42.77	34.96	22.07	21.1 / 31.3
	ac	6.24	28.28	35.91	40.61	42.55	41.96	43.56	43.19	42.77	42.30	41.16	40.69	37.07	29.22	3.88	22.7 / 23.1
	ar	4.31	31.91	32.39	42.29	43.38	42.44	43.48	42.88	41.79	42.38	42.71	44.50	37.75	26.11	2.69	24
	sw	6.05	32.80	33.25	43.41	45.38	44.78	45.98	45.52	44.54	44.59	44.32	45.52	38.36	26.48	3.17	20.5
centre	cb	11.60	24.90	36.48	40.03	43.01	43.69	46.56	45.49	46.10	45.09	43.46	40.57	34.47	24.53	10.81	21.1 / 31.3
	ac	4.95	21.01	31.02	35.85	40.55	39.86	42.20	44.11	42.43	42.05	41.02	35.56	30.05	18.18	5.90	22.7 / 23.1
	ar	-	-	-	-	-	-	-	-	-	-	-	-	-	-	-	24
	sw	-	-	-	-	-	-	-	-	-	-	-	-	-	-	-	20.5
2	lateral cb	-17.24	-25.14	-34.88	-37.33	-37.30	-39.42	-39.66	-40.64	-38.80	-39.35	-37.81	-36.67	-35.72	-31.34	-13.87	21.1 / 31.3
	ac	-24.53	-26.95	-37.53	-43.01	-42.90	-43.25	-44.16	-44.10	-39.96	-44.24	-42.84	-42.44	-40.11	-29.25	-23.76	22.7 / 23.1
	ar	-29.36	-33.15	-45.47	-50.08	-47.99	-46.82	-47.78	-46.77	-38.66	-47.72	-46.01	-46.76	-47.46	-33.78	-24.04	24
	sw	-28.76	-32.30	-45.17	-50.42	-48.52	-48.34	-49.54	-47.67	-40.35	-49.13	-47.31	-47.79	-48.32	-34.01	-24.43	20.5
centre	cb	-9.63	-21.16	-35.83	-41.24	-42.39	-41.09	-39.73	-40.74	-40.50	-41.40	-40.70	-41.09	-35.75	-26.55	-7.36	21.1 / 31.3
	ac	-14.57	-24.22	-37.85	-46.53	-46.74	-45.77	-44.18	-43.04	-44.13	-45.73	-44.40	-47.32	-39.38	-27.75	-11.48	22.7 / 23.1
	ar	-	-	-	-	-	-	-	-	-	-	-	-	-	-	-	24
	sw	-	-	-	-	-	-	-	-	-	-	-	-	-	-	-	20.5

*$\sigma_x$ -values are temperature-compensated.*

		FE-model stress $\sigma_x$ [MPa] for max. $u_x=131\text{mm}$ and max. $u_x=135\text{mm}$															
sensor-no.:		1	2	3	4	5	6	7	8	9	10	11	12	13	14	15	
pos.	pos x [mm]:	150	300	450	600	750	900	1050	1200	1350	1500	1650	1800	1950	2100	2250	
7	lateral cb	131	9.94	22.41	35.88	43.61	45.58	45.88	45.95	45.96	45.95	45.88	45.58	43.61	35.88	22.41	9.94
	135	16.33	42.45	42.51	44.75	45.77	46.02	46.11	46.13	46.11	46.02	45.77	44.75	42.51	42.45	16.33	
	ar	131	10.94	24.59	38.76	47.64	49.95	50.30	50.30	45.96	50.30	50.30	49.95	47.64	38.76	24.59	10.94
	135	17.85	43.53	46.31	48.77	50.00	50.36	50.43	46.13	50.43	50.36	50.00	48.77	46.31	43.53	17.85	
centre	cb	131	9.28	20.74	32.62	44.63	44.81	44.69	44.71	44.73	44.71	44.69	44.81	44.63	32.62	20.74	9.28
	135	13.52	27.63	38.07	45.24	45.39	45.05	44.88	44.83	44.88	45.05	45.39	45.24	38.07	27.63	13.52	
	ar	131	10.38	23.21	36.46	48.82	50.04	49.93	49.97	49.52	49.97	49.93	50.04	48.82	36.46	23.21	10.38
	135	15.05	30.94	42.71	50.29	50.83	50.39	50.20	49.65	50.20	50.39	50.83	50.29	42.71	30.94	15.05	
2	lateral cb	131	-9.06	-19.76	-30.25	-38.00	-39.96	-39.79	-39.60	-39.54	-39.60	-39.79	-39.96	-38.00	-30.25	-19.76	-9.06
	135	-12.86	-30.83	-34.35	-36.55	-38.63	-39.64	-39.96	-40.03	-39.96	-39.64	-38.63	-36.55	-34.35	-30.83	-12.86	
	ar	131	-10.17	-22.26	-33.74	-42.75	-45.23	-45.16	-44.85	-46.12	-44.85	-45.16	-45.23	-42.75	-33.74	-22.26	-10.17
	135	-14.84	-33.25	-39.86	-42.22	-44.33	-45.21	-45.30	-46.68	-45.30	-45.21	-44.33	-42.22	-39.86	-33.25	-14.84	
centre	cb	131	-9.25	-20.81	-32.87	-44.90	-45.56	-45.51	-45.65	-45.72	-45.65	-45.51	-45.56	-44.90	-32.87	-20.81	-9.25
	135	-13.49	-28.45	-39.80	-47.26	-46.97	-46.09	-45.79	-45.72	-45.79	-46.09	-46.97	-47.26	-39.80	-28.45	-13.49	
	ar	131	-10.29	-23.09	-36.41	-48.49	-50.39	-50.39	-50.58	-50.25	-50.58	-50.39	-50.39	-48.49	-36.41	-23.09	-10.29
	135	-14.80	-31.19	-43.63	-51.34	-51.67	-50.89	-50.68	-50.22	-50.68	-50.89	-51.67	-51.34	-43.63	-31.19	-14.84	

*stages, boundary conditions: ac after autoclaving, prior to release*  
*in initial ar after release, resting on the mould*  
*cb cold bent sw laterally supported arch, self weight*

Table E.5.: FBG and numerical results summary of the test series involving specimens 4esg\_sgp-01 and -02.

E | REAL SCALE TESTS

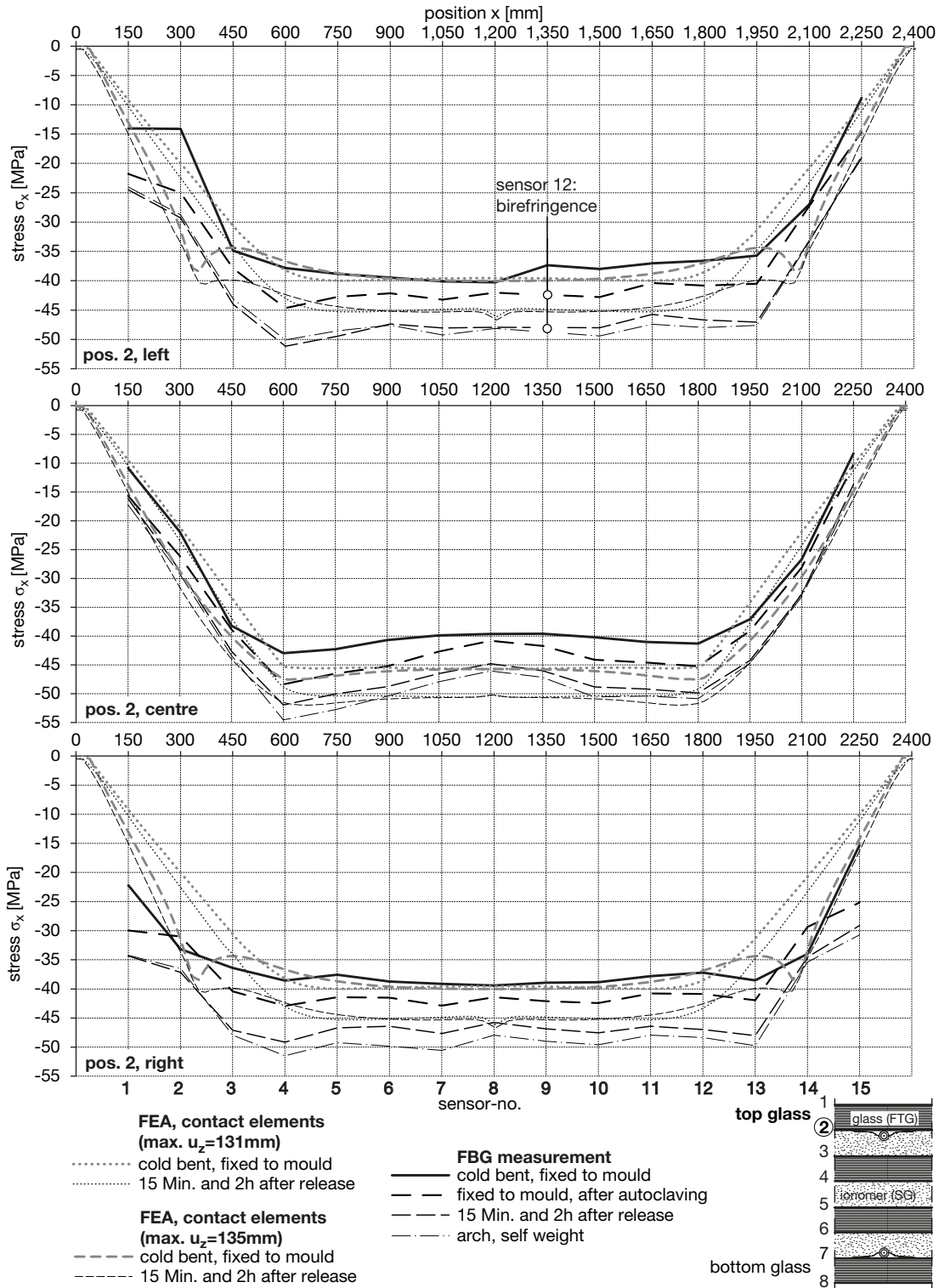
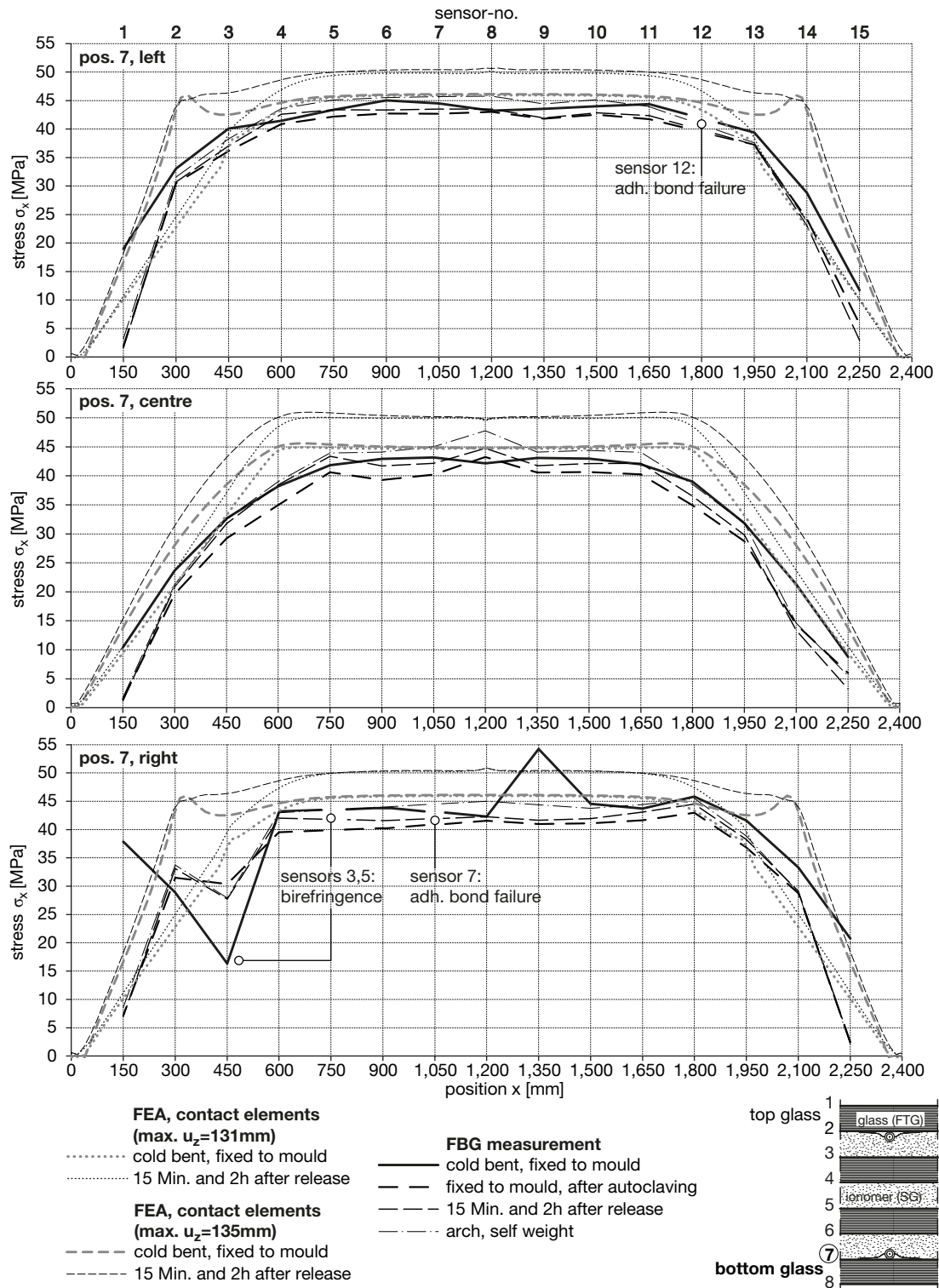


Figure E.10.: Stress at position 2 in x-direction as measured with FBG-sensors and calculated by finite element analysis along the glass in longitudinal bending direction. The sensor spacing is 150mm.



**Figure E.11.:** Stress at position 7 in x-direction as measured with FBG-sensors and calculated by finite element analysis along the glass in longitudinal bending direction. The sensor spacing is 150mm.

E | REAL SCALE TESTS

Birefringence (double peaks)					
A		stages, sensor-no.			
specimen	pos.	cb	ac, ar	remark	
4esg_sgp-01	2 left	-	-	-	
	centre	11	11	adh. bond fail.	
	right	-	-	-	
	7 left	4,5,8,10,13	-	-	
	centre	-	-	-	
	right	15	-	-	
4esg_sgp-02	2 left	9	9	-	
	centre	-	-	-	
	right	-	-	-	
	7 left	12	-	adh. bond fail.	
	centre	-	-	-	
	right	2,3,5,7	3,7	7: adh. bond fail.	
C		stages, sensor-no.			
specimen	pos.	cb	ac, ar	remark	
2esg_sgp-01	2	ne	-	-	
	3	ne	-	-	
2esg_sgp-02	2	ne	-	-	
	3	ne	-	-	
2esg_sgp-03	2	1,2,3,5,6	-	vacuum cb(ev)	
	3	1,2,3,6	1,2,6	vacuum cb(ev)	
D		stages, sensor-no.			
specimen	pos.	cb	ac, ar	remark	
2esg_pvb-01	2	ne	-	-	
	3	ne	-	-	
2esg_pvb-02	2	-	-	-	
	3	-	-	-	
2esg_pvb-03	2	ne	-	-	
	3	ne	-	-	
<i>ne:</i>		<i>no entry</i>			
<i>- :</i>		<i>no birefringence occurs</i>			

**Table E.6.:** Summary of double peaks encountered with laminates 2esg\_pvb, 2esg\_sgp, 3esg\_sgp and 4esg\_sgp during the process stages cold bending (cb), after autoclaving (ac) and after release from the bending mould (ar).

E.4. Result Comparison

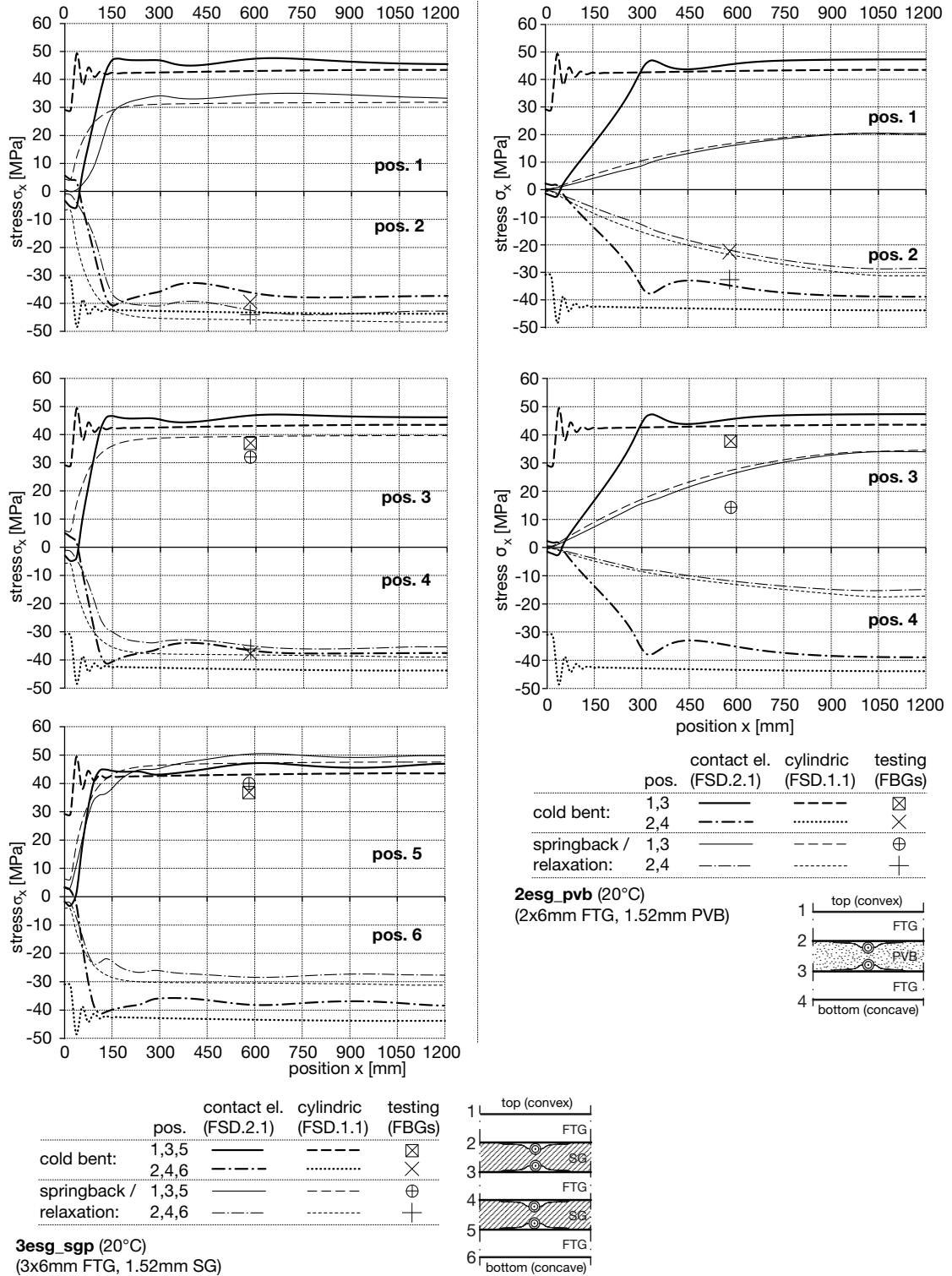
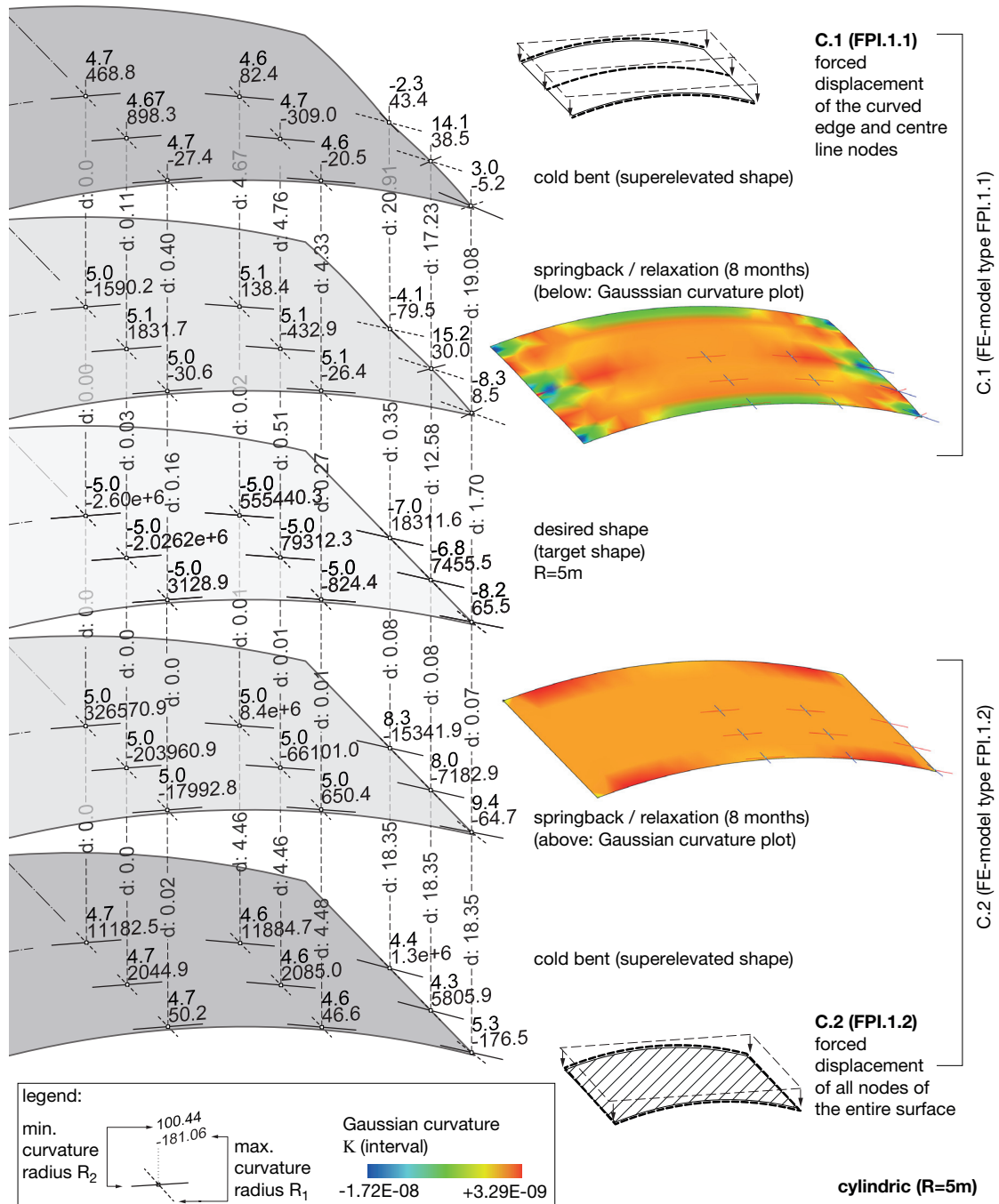


Figure E.12.: Comparison of the stress results  $\sigma_1$  along a longitudinal section 30mm from the curved edge from the contact element model FSD.2.2, the cylindrical model FSD.1.1 and the FBG-results for 3esg\_sgp and 2esg\_pvb.





**Figure E.13.:** Curvature analysis of a cylindric shape from 3x6mm FTG (3x3m) laminated with 1.52mm SG analysed with model types FPI.1.1 and FPI.1.2. The principal curvature directions / results are shown for nine points on the surface of the topmost glass. The superelevated cold bending shape, the target shape and the achieved shape after 8 months of relaxation are shown. Values with a "d:" are the difference vectors of the points on the cold bent, relaxed and target glass shapes.



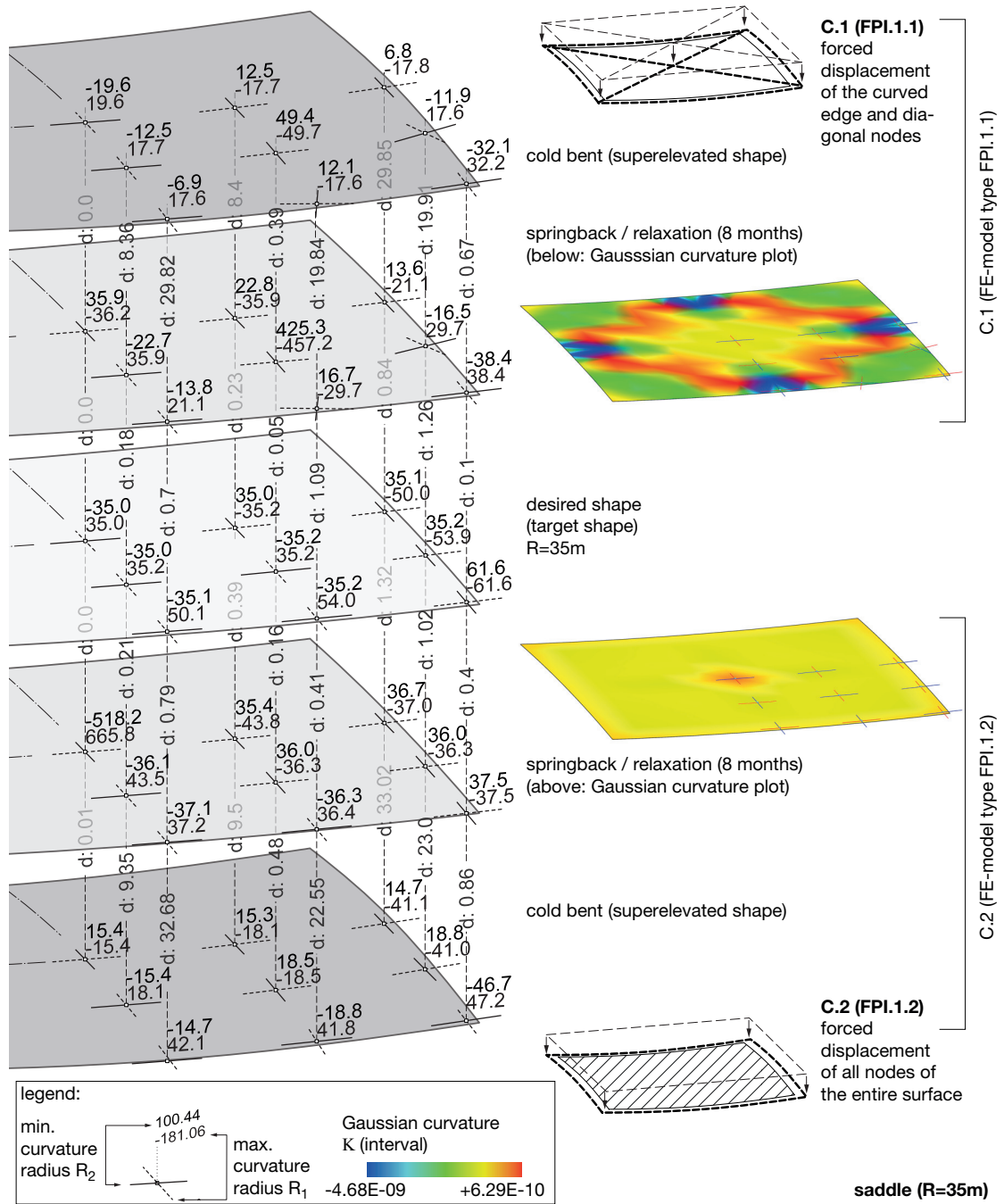


**Figure E.14:** Curvature analysis of a saddle shape from 3x6mm FTG (3x3m) laminated with 1.52mm SG analysed with model types FPI.1.1 and FPI.1.2. The principal curvature directions / results are shown for nine points on the surface of the topmost glass. The superelevated cold bending shape, the target shape and the achieved shape after 8 months of relaxation are shown. Values with a "d:" are the difference vectors of the points on the cold bent, relaxed and target glass shapes.



## **F Curriculum Vitae**



**Dipl.-Ing. Thiemo Fildhuth**

1972	Born in Bad Pyrmont, Germany
1992	A-levels (Abitur) at the Schiller-Gymnasium, Hameln, Germany
1992-1993	Civil service in Hameln as a paramedic-assistant on Red Cross Ambulances
1993-2001	Studies of architecture at the Darmstadt Institute of Technology (TUD), Germany
1998-1999	Civil engineering studies at the ISTG - Grenoble Institute of Science and Technology at the Joseph Fourier University (UJF), France
1997-2000	German National Academic Foundation Scholarship (Studienstiftung des Deutschen Volkes), grant awarded for excellency in studies
2001	Graduated (Dipl.-Ing. Univ.) in Architecture at the Darmstadt Institute of Technology
2002-2005	Studies of civil engineering at the University of Applied Sciences at Mainz, Germany
2002	Internship at RFR Stuttgart, Germany
2003	Internship semester at Schlaich, Bergermann and Partner, Stuttgart, Germany
2005	Graduation (Dipl.-Ing. (FH)) in Civil Engineering at the Mainz University of Applied Sciences; diploma work: Development of Long Span Sandwich Glass Box Girders (Prof. Dr.-Ing. K. Berner, Dr.-Ing. M.Kutterer)
2005-2007	B+G Engineers Bollinger and Grohmann GmbH, Frankfurt a. M., main project contributions: EPFL Learning Center / Lausanne; Nordkettenbahn funicular/Innsbruck; Musée des Confluences/Lyon
since 2007	Member of the Lower Saxony Chamber of Engineers
2007-2009	RFR Paris, participation in the following projects: Fondation Louis Vuitton pour la Création, Paris; Al Raha Beach development infrastructure project, Abu Dhabi
2009-2015	Research associate and doctoral candidate at the Institute of Building Structures and Structural Design ITKE, University of Stuttgart (head: Prof. Dr.-Ing. Jan Knippers)
2009-2011	AiF-ZIM research project KF2386401: Kalt gekrümmte Glaslaminat - Herstellung und Verwendungschancen. Industry partner: seele-sedak GmbH & Co. KG, Gersthofen
2012-2013	European research project ARC IAPP 230520 participation, assigned by RFR, partners: BGT, Bretten; INGLAS, Friedrichshafen and the IFP, University of Stuttgart
2013-2014	AiF-ZIM research project KF2386407: Messung und Optimierung von Glaslaminaten in Prozess und Anwendung unter Einsatz optischer Sensorik. Industry partner: GuS GmbH & Co. KG, Lübbecke
since 2013	Managing partner of the Rainer Fildhuth KG, Lügde (HRA 4625) and vice chairman of the non-profit Schwering & Hasse trust
2014	Exhibition of a stress-sensitive glass arch as a demonstrator of fibre Bragg grating sensor application in curved glass laminates at the glasstec international trade fair, Düsseldorf, Germany
since 2015	Knippers Helbig Advanced Engineering, Stuttgart





Herausgeber: Professor Dr.-Ing. Jan Knippers